QUANTIFYING AND CONTROLLING THE NANO-ARCHITECTURE OF NEURONAL SYNAPSES

EDITED BY: Xiaobing Chen, Thomas A. Blanpied and Thomas Kuner
PUBLISHED IN: Frontiers in Synaptic Neuroscience

frontiers Research Topics

ISSN 1664-8714
ISBN 978-2-83250-084-2
DOI 10.3389/978-2-83250-084-2

About Frontiers

Frontiers is more than just an open-access publisher of scholarly articles: it is a pioneering approach to the world of academia, radically improving the way scholarly research is managed. The grand vision of Frontiers is a world where all people have an equal opportunity to seek, share and generate knowledge. Frontiers provides immediate and permanent online open access to all its publications, but this alone is not enough to realize our grand goals.

Frontiers Journal Series

The Frontiers Journal Series is a multi-tier and interdisciplinary set of open-access, online journals, promising a paradigm shift from the current review, selection and dissemination processes in academic publishing. All Frontiers journals are driven by researchers for researchers; therefore, they constitute a service to the scholarly community. At the same time, the Frontiers Journal Series operates on a revolutionary invention, the tiered publishing system, initially addressing specific communities of scholars, and gradually climbing up to broader public understanding, thus serving the interests of the lay society, too.

Dedication to Quality

Each Frontiers article is a landmark of the highest quality, thanks to genuinely collaborative interactions between authors and review editors, who include some of the world's best academicians. Research must be certified by peers before entering a stream of knowledge that may eventually reach the public - and shape society; therefore, Frontiers only applies the most rigorous and unbiased reviews.
Frontiers revolutionizes research publishing by freely delivering the most outstanding research, evaluated with no bias from both the academic and social point of view. By applying the most advanced information technologies, Frontiers is catapulting scholarly publishing into a new generation.

What are Frontiers Research Topics?

Frontiers Research Topics are very popular trademarks of the Frontiers Journals Series: they are collections of at least ten articles, all centered on a particular subject. With their unique mix of varied contributions from Original Research to Review Articles, Frontiers Research Topics unify the most influential researchers, the latest key findings and historical advances in a hot research area! Find out more on how to host your own Frontiers Research Topic or contribute to one as an author by contacting the Frontiers Editorial Office: frontiersin.org/about/contact

QUANTIFYING AND CONTROLLING THE NANO-ARCHITECTURE OF NEURONAL SYNAPSES

Topic Editors:
Xiaobing Chen, National Institutes of Health (NIH), United States
Thomas A. Blanpied, University of Maryland, United States
Thomas Kuner, Heidelberg University, Germany

Citation: Chen, X., Blanpied, T. A., Kuner, T., eds. (2022). Quantifying and Controlling the Nano-Architecture of Neuronal Synapses.
Lausanne: Frontiers Media SA. doi: 10.3389/978-2-83250-084-2

Table of Contents

frontiers | Frontiers in Synaptic Neuroscience

TYPE Editorial
PUBLISHED 07 September 2022
DOI 10.3389/fnsyn.2022.1024073

Editorial: Quantifying and controlling the nano-architecture of neuronal synapses

Xiaobing Chen[1]*, Thomas Kuner[2]* and Thomas A. Blanpied[3]*

[1]Laboratory of Neurobiology, National Institute of Neurological Diseases and Stroke, National Institutes of Health, Bethesda, MD, United States, [2]Department of Functional Neuroanatomy, Institute for Anatomy and Cell Biology, Heidelberg University, Heidelberg, Germany, [3]School of Medicine, University of Maryland, Baltimore, MD, United States

KEYWORDS

synapse, nano-architecture, dynamics, super-resolution imaging, volume EM, EM tomography, correlated microscopy

Check for updates

OPEN ACCESS

EDITED AND REVIEWED BY
P. Jesper Sjöström,
McGill University, Canada

*CORRESPONDENCE
Xiaobing Chen
chenx@ninds.nih.gov
Thomas A. Blanpied
tblanpied@som.umaryland.edu
Thomas Kuner
thomas.kuner@uni-heidelberg.de

RECEIVED 20 August 2022
ACCEPTED 24 August 2022
PUBLISHED 07 September 2022

CITATION
Chen X, Kuner T and Blanpied TA (2022) Editorial: Quantifying and controlling the nano-architecture of neuronal synapses.
Front. Synaptic Neurosci. 14:1024073.
doi: 10.3389/fnsyn.2022.1024073

Editorial on the Research Topic
Quantifying and controlling the nano-architecture of neuronal synapses

About 2 years ago when the journal gave us the opportunity to launch this Research Topic, the three of us were excited by the rapid growth of cutting-edge imaging approaches now illuminating the architecture and molecular organization of synapses. Since its launch, we received enthusiastic responses from many authors and in the end, we published 15 articles in this volume.

These articles, including original research, reviews, and opinion, present a snapshot of several key active areas of ongoing work. They fall roughly into three areas: technical advances in single-molecule imaging and analysis, dynamics of molecular organization within the synapse, and advances in electron microscopy that are propelling new insights.

Technical advances in single-molecule imaging and analysis

This group of papers illustrates well how light-based super-resolution imaging is providing important new routes to visualize and analyze the distribution of proteins in single synapses. Particularly including single-molecule, expansion microscopy, and SIM. New methods are achieving ever-better resolution while also making these technically challenging approaches easier to use by more laboratories. Here, Unterauer and Jungmann provided an updated review of DNA PAINT technology which provides single-nanometer resolution with straightforward routes to molecular counting along with highly multiplexed imaging. A great advantage of the approach is that with a single labeling step, antibodies conjugated with short DNA oligonucleotides can label multiple targets that are subsequently imaged by sequential exchange of fluorophore-labeled complementary oligonucleotides, avoiding chromatic aberration. Narayanasamy et al. then further expanded the use of DNA-PAINT by demonstrating multiplexed imaging of multiple pre- and post-synaptic proteins in brain slices, demonstrating the viability of this important approach for analyzing synaptic nanostructure *in vivo*. In a Perspective, Specht argued that single-molecule imaging provides a powerful approach to determining protein copy number, providing both high throughput and high subcellular spatial resolution to interpret such counts. Copy number of key postsynaptic density (PSD) proteins have been studied using calibrated fluorescent light microscopy (Sugiyama et al., 2005) or scanning transmission electron microscopy (STEM) (Chen et al., 2005), and these numbers have been used to estimate the copy number of many other PSD proteins using quantitative mass spectrometry (Cheng et al., 2006; Martinez-Sanchez et al., 2021) and a recent study demonstrated estimation of protein number copy in individual spines by coupling super-resolution imaging and quantitatively mass spectrometry (Helm et al., 2021). New single-molecule methods are likely to offer an opportunity to map changes of the copy number of key synaptic proteins during synaptic activity.

Several new advances within this arena were also introduced in this Topic. Kuhlemann et al. demonstrated site-specific labeling of the extracellular domain of γ-aminobutyric acid type A (GABA_A) receptor subunits by genetic code expansion with unnatural amino acids combined with bio-orthogonal click-chemistry labeling with tetrazine dyes. Gagliano et al. provided a comprehensive review of single molecular tracking and super-resolution imaging of synaptic proteins in 3D enabled by new light sheet illumination approaches. Sneve and Piatkevich provided an overview of new insights that may arise from using expansion microscopy to map synapses in neuronal circuits. These contributions highlight the enormous potential of combining novel labeling approaches with novel microscopy techniques.

Dynamics of molecular organization within the synapse

A second group of papers focused on new aspects of molecular dynamics that support synaptic functional diversity. Piao and Sigrist provided a detailed review of work from Drosophila which shows how the active zone protein (M)Unc13 defines the behavior of individual release sites of the active zone. More generally, the work illustrates that isoform-specific components of the vesicle release machinery may drive functional presynaptic heterogeneity, revealing principles likely at play in the mammalian brain as well. In new research, Maschi et al. imaged release of individual vesicles (Tang et al., 2016; Maschi and Klyachko, 2017) to determine that Myosin V regulates both temporal and spatial utilization of release sites during two main forms of synchronous release in the presynaptic active zone. Using a modeling approach, they describe Myosin V function as controlling a gradient of release site release probability across the active zone, thereby uniting spatial and temporal functions of Myosin V in uni-vesicular and multi-vesicular release. Westra et al. reviewed our current understanding of how several lipids specifically enriched the synapse are organized at the synaptic membrane. They bring together compelling arguments that organization of the membrane itself in fact could contribute to protein distribution at the synapse and to synaptic transmission. They conclude with a call for new technologies to define and test the influence of synaptic lipid nanoscale organization of synaptic proteins.

In recent years, many studies using super-resolution light microscopy techniques including PALM, dSTORM, single-molecule tracking, STED, SIM, and Expansion Microscopy have found that key scaffolding proteins in the excitatory PSD such as PSD-95, and receptors such as NMDARs and AMPARs, are located subsynaptically in areas of high density termed nanoclusters or nanodomains (Fukata et al., 2013; MacGillavry et al., 2013; Nair et al., 2013; Broadhead et al., 2016; Tang et al., 2016; Goncalves et al., 2020). This work has focused attention on the potential that discrete adhesion molecule systems may control transsynaptic alignment (Haas et al., 2018; Ramsey et al., 2021). Expanding this investigation in inhibitory synapses, Gookin et al. report synaptic nanoclusters of the adhesion protein neuroligin-2, which are arrayed similarly to nanoclusters of the $\text{GABA}_\text{A}\text{R}$ (Crosby et al., 2019), suggesting an important role in establishing synapse nanoarchitecture. Through direct quantitative comparison of super-resolution methods, they report further that dSTORM provided a more detailed view of the protein density landscape of neuroligin-2. This is an important observation in part because combining nanostructure with trafficking and diffusion dynamics of proteins is a rich area for incoming work. A powerful approach to this general problem applied specifically to the case of adhesion molecules like the neuroligins is provided by Lagardère et al. who demonstrated the use of FluoSIM, a new simulator of membrane protein dynamics for fluorescence microscopy. Correlating high-resolution imaging experiments with simulations of Neurolin1 at synaptic vs. extrasynaptic sites enabled biological and biophysical interpretation of the imaging data, and advanced new ideas about how Neuroligin-Neurexin interactions play essential roles in organizing the synaptic cleft.

Emphasized by all these findings, it is clear that further exploration is still needed of how subsynaptic protein nanoclusters/nanodomains govern synapse function. The importance of this undertaking is even further emphasized by work here from Sun et al., who used dSTORM to image the nanometer-scale trans-synaptic alignment of key proteins in the active zone and PSD during synaptic development and maturation. They report that despite profound changes in the abundance and nanoarchitecture of these proteins across early development in culture—or even following prolonged, total blockade of neuronal activity—transcellular protein nano-alignment remained robust.

Progress in electron microscopy of synapses

The field of electron microscopy is teeming with technical advances in microscopy (e.g., significantly larger, faster, and more sensitive electron detection cameras, much better optics and much more stable stages and more efficient computer-driven automated image acquisition schemes), new and improved sample preparation techniques and advances in image processing software development are all powering new discoveries.

Here we collected three EM related papers as vignettes of this blooming field. To further dissect structural basis of synaptic transmission, information of subsynaptic structures/organelles now often need to be quantified in specifically designed experiments. Watanabe et al. reported their development of sets of image analysis programs for aiding quantitative morphometric analysis (e.g., location and number) of subcellular organelles such as vesicles, endosomes in synaptic terminals, this would be especially useful for large bulk of serial section EM images where manually analysis might be too daunting and unproductive; they also introduce a scheme to address sampling biases in image analysis, a much needed feature to have.

Petralia et al. provided a review of a class of underappreciated structures called invaginations, small outward projections from one cell membrane to another in various synaptic junctions, which is often too small to be seen by light microscopy and was often misidentified by traditional thin section EM. Invaginations appear to be important for further understanding processes in synaptic development, maintenance, and plasticity. Now, focused ion beam-scanning electron microscopy (FIB-SEM), one of the new 3D EM or volume EM methods, makes tracing and detailed analysis of these invaginating structures possible.

3D volume EM uses fixed, heavy metal-stained, and plastic-embedded brain tissues imaged by serial block-face scanning EM (SBEM), requiring either mechanical serial sectioning (Denk and Horstmann, 2004) or FIB milling (Knott et al., 2008; Wu et al., 2017; Xu et al., 2021) and imaging with back-scattered electrons. Larger sample volumes are imaged by the automated tape-collecting ultramicrotome (ATUM), where ∼30 nm thick serial sections are imaged by SEM (Kasthuri et al., 2015) or by transmission EM (Yin et al., 2020) to allow reconstruction and mapping of thousands of synapses in the neuropil (Hua et al., 2015). The resulting huge 3D datasets requires machine learning based automated segmentation (Heinrich et al., 2021). For volumes $< \sim 100$ cubic micrometers, thick-section bright field scanning transmission EM (STEM) tomography of 1–2 µm thick plastic embedded sections provide 3–4 nm isotropic resolution without sectioning resulted in reconstructions of entire ribbons in rat rod bipolar cell ribbon synapses (Graydon et al., 2014) and smaller spines or entire PSDs (Chen et al., 2014, 2015) in rat hippocampal cultures. Another useful technique is the development of the conjugate light and EM array tomography (Collman et al., 2015), which enables mapping the transmitter types in large numbers of synapses in brain tissue in great detail.

Finally, Szule provided detailed hypotheses of molecular identities of various structures in the regular array of a large macromolecular assembly, the active zone material, a dedicated molecular machinery responsible for vesicle retention, delivery and fusion at the presynaptic terminal of the frog neuromuscular junction (NMJ). The organization of these active zone materials and its structural model was based on 3D reconstructions from EM tomography of fixed or freeze-substituted frog NMJ. A molecular level structural model detailing vesicle fusion processes at the presynaptic terminal of the NMJ active zone might have broader implications for understanding the molecular basis of synaptic transmission in other types of synapses in general. Super-resolution light microscopy is now revealing the molecular organization of active zone proteins at NMJ (Badawi and Nishimune, 2020). It would be of great interest to see a unified molecular structural model based on EM and LM in the near future.

Transmission EM tomography of synapses has allowed the creation of 3D reconstructions to delineate organization of subsynaptic organelles, key synaptic proteins, and macromolecular complexes at pre and postsynaptic terminals in fixed or high pressure frozen and freeze-substituted neuronal culture, brain slice culture or nerve tissue (Harlow et al., 2001; Chen et al., 2008; Burette et al., 2012; Watanabe et al., 2013; Imig et al., 2014) and in vitrified hydrated synapses in neuronal cultures or isolated synaptosomes using cryo-EM tomography (Zuber et al., 2005; Fernandez-Busnadiego et al., 2013; Tao et al., 2018; Martinez-Sanchez et al., 2021). Structures reconstructed by EM tomography provide size, shape, and location of protein complexes, subcellular organelles in synapses, but at current 2–4 nm resolution, cannot guarantee unambiguous molecular identification of individual structures at synapses. Matching the size and shape of structures in tomograms to high resolution structures of individual proteins such as PSD-95 MAGUKs (Nakagawa et al., 2004) or extracellular domains of glutamate receptors (Nakagawa et al., 2005; Sobolevsky et al., 2009) may lead to molecular identity. Efforts were made to combine immunogold labeling (Chen et al., 2008, 2011) or miniSOG (Chen et al., 2018) with EM tomography to identify a certain class of structures at synapses such as PSD-95 as vertical filaments at the PSD. In other cases, KO animals (Fernandez-Busnadiego et al., 2013; Imig et al., 2014; Schrod et al., 2018) or protein knockdown (Chen et al., 2011,

2015) were combined with EM tomography to test hypotheses regarding molecular identity of classified structures. Recent work using averaging techniques in cryo EM tomograms (Liu et al., 2020; Martinez-Sanchez et al., 2021) showed that individual receptors at synapses might be identifiable by their extracellular domain morphology. Finally, it will be exciting to see how two major approaches to molecular nanostructure, direct imaging of proteins in cryo-fixed samples using cryo-ET combined with subsequent identification of protein identity vs. imaging of fluorescently labeled proteins using super-resolution microscopies, with MINFLUX (Balzarotti et al., 2017) reaching nanometer resolution, will converge on synaptic nanoarchitecture.

Together, the articles of this Research Topic highlight that synaptic nanoarchitecture is a blossoming field helping to grow and propagate important technical advances and unearthing new insight to synaptic function. We close this volume of the topic with hope that we will come back to this lively garden of ours in due time to welcome more papers that highlight exciting new progress and development in this vibrant field. We look forward to seeing you then!

Author contributions

XC, TK, and TB conceived the main ideas and wrote the manuscript. All authors contributed to the article and approved the submitted version.

Funding

XC is supported by the NINDS intramural program. TB is supported by R37MH080046. TK is supported by grants of the Baden-Württemberg Stiftung.

Acknowledgments

We thank Tom Reese and Richard Leapman for their critical reading of the manuscript.

Conflict of interest

The authors declare that the research was conducted in the absence of any commercial or financial relationships that could be construed as a potential conflict of interest.

Publisher's note

References

Badawi, Y., and Nishimune, H. (2020). Super-resolution microscopy for analyzing neuromuscular junctions and synapses. *Neurosci. Lett.* 715, 134644. doi: 10.1016/j.neulet.2019.134644

Balzarotti, F., Eilers, Y., Gwosch, K. C., Gynna, A. H., Westphal, V., Stefani, F. D., et al. (2017). Nanometer resolution imaging and tracking of fluorescent molecules with minimal photon fluxes. *Science* 355, 606–612. doi: 10.1126/science.aak9913

Broadhead, M. J., Horrocks, M. H., Zhu, F., Muresan, L., Benavides-Piccione, R., DeFelipe, J., et al. (2016). PSD95 nanoclusters are postsynaptic building blocks in hippocampus circuits. *Sci. Rep.* 6, 24626. doi: 10.1038/srep24626

Burette, A. C., Lesperance, T., Crum, J., Martone, M., Volkmann, N., Ellisman, M. H., et al. (2012). Electron tomographic analysis of synaptic ultrastructure. *J. Comp. Neurol.* 520, 2697–2711. doi: 10.1002/cne.23067

Chen, X., Levy, J. M., Hou, A., Winters, C., Azzam, R., Sousa, A. A., et al. (2015). PSD-95 family MAGUKs are essential for anchoring AMPA and NMDA receptor complexes at the postsynaptic density. *Proc. Natl. Acad. Sci. USA* 112, E6983–6992. doi: 10.1073/pnas.1517045112

Chen, X., Nelson, C. D., Li, X., Winters, C. A., Azzam, R., Sousa, A. A., et al. (2011). PSD-95 is required to sustain the molecular organization of the postsynaptic density. *J. Neurosci.* 31, 6329–6338. doi: 10.1523/JNEUROSCI.5968-10.2011

Chen, X., Vinade, L., Leapman, R. D., Petersen, J. D., Nakagawa, T., Phillips, T. M., et al. (2005). Mass of the postsynaptic density and enumeration of three key molecules. *Proc. Natl. Acad. Sci. USA* 102, 11551–11556. doi: 10.1073/pnas.0505359102

Chen, X., Winters, C., Azzam, R., Li, X., Galbraith, J. A., Leapman, R. D., et al. (2008). Organization of the core structure of the postsynaptic density. *Proc. Natl. Acad. Sci. USA* 105, 4453–4458.

Chen, X., Winters, C., Crocker, V., Lazarou, M., Sousa, A. A., Leapman, R. D., et al. (2018). Identification of PSD-95 in the postsynaptic density using MiniSOG and EM tomography. *Front. Neuroanat.* 12, 107. doi: 10.3389/fnana.2018.00107

Chen, X. B., Winters, C., Azzam, R., Sousa, A. A., Leapman, R. D., and Reese, T. S. (2014). Nanoscale imaging of protein molecules at the postsynaptic density. *Nanoscale Imag. Synap. New Concepts Oppor.* 84, 1–21. doi: 10.1007/978-1-4614-9179-8_1

Cheng, D., Hoogenraad, C. C., Rush, J., Ramm, E., Schlager, M. A., Duong, D. M., et al. (2006). Relative and absolute quantification of postsynaptic density proteome isolated from rat forebrain and cerebellum. *Mol. Cell. Proteomics* 5, 1158–1170. doi: 10.1074/mcp.D500009-MCP200

Collman, F., Buchanan, J., Phend, K. D., Micheva, K. D., Weinberg, R. J., and Smith, S. J. (2015). Mapping synapses by conjugate light-electron array tomography. *J. Neurosci.* 35, 5792–5807. doi: 10.1523/JNEUROSCI.4274-14.2015

Crosby, K. C., Gookin, S. E., Garcia, J. D., Hahm, K. M., Dell'Acqua, M. L., and Smith, K. R. (2019). Nanoscale subsynaptic domains underlie the organization of the inhibitory synapse. *Cell Rep.* 26, 3284-3297 e3283. doi: 10.1016/j.celrep.2019.02.070

Denk, W., and Horstmann, H. (2004). Serial block-face scanning electron microscopy to reconstruct three-dimensional tissue nanostructure. *PLoS Biol.* 2, e329. doi: 10.1371/journal.pbio.0020329

Fernandez-Busnadiego, R., Asano, S., Oprisoreanu, A. M., Sakata, E., Doengi, M., Kochovski, Z., et al. (2013). Cryo-electron tomography reveals a critical role of RIM1alpha in synaptic vesicle tethering. *J. Cell Biol.* 201, 725–740. doi: 10.1083/jcb.201206063

Fukata, Y., Dimitrov, A., Boncompain, G., Vielemeyer, O., Perez, F., and Fukata, M. (2013). Local palmitoylation cycles define activity-regulated postsynaptic subdomains. *J. Cell Biol.* 202, 145–161. doi: 10.1083/jcb.201302071

Goncalves, J., Bartol, T. M., Camus, C., Levet, F., Menegolla, A. P., Sejnowski, T. J., et al. (2020). Nanoscale co-organization and coactivation of AMPAR, NMDAR, and mGluR at excitatory synapses. *Proc. Natl. Acad. Sci. USA* 117, 14503–14511. doi: 10.1073/pnas.1922563117

Graydon, C. W., Zhang, J., Oesch, N. W., Sousa, A. A., Leapman, R. D., and Diamond, J. S. (2014). Passive diffusion as a mechanism underlying ribbon synapse vesicle release and resupply. *J. Neurosci.* 34, 8948–8962. doi: 10.1523/JNEUROSCI.1022-14.2014

Haas, K. T., Compans, B., Letellier, M., Bartol, T. M., Grillo-Bosch, D., Sejnowski, T. J., et al. (2018). Pre-post synaptic alignment through neuroligin-1 tunes synaptic transmission efficiency. *Elife* 7, 31755. doi: 10.7554/eLife.31755

Harlow, M. L., Ress, D., Stoschek, A., Marshall, R. M., and McMahan, U. J. (2001). The architecture of active zone material at the frog's neuromuscular junction. *Nature* 409, 479–484. doi: 10.1038/35054000

Heinrich, L., Bennett, D., Ackerman, D., Park, W., Bogovic, J., Eckstein, N., et al. (2021). Whole-cell organelle segmentation in volume electron microscopy. *Nature* 599, 141–146. doi: 10.1038/s41586-021-03977-3

Helm, M. S., Dankovich, T. M., Mandad, S., Rammner, B., Jahne, S., Salimi, V., et al. (2021). A large-scale nanoscopy and biochemistry analysis of postsynaptic dendritic spines. *Nat. Neurosci.* 24, 1151–1162. doi: 10.1038/s41593-021-00874-w

Hua, Y., Laserstein, P., and Helmstaedter, M. (2015). Large-volume en-bloc staining for electron microscopy-based connectomics. *Nat. Commun.* 6, 7923. doi: 10.1038/ncomms8923

Imig, C., Min, S. W., Krinner, S., Arancillo, M., Rosenmund, C., Sudhof, T. C., et al. (2014). The morphological and molecular nature of synaptic vesicle priming at presynaptic active zones. *Neuron* 84, 416–431. doi: 10.1016/j.neuron.2014.10.009

Kasthuri, N., Hayworth, K. J., Berger, D. R., Schalek, R. L., Conchello, J. A., Knowles-Barley, S., et al. (2015). Saturated reconstruction of a volume of neocortex. *Cell* 162, 648–661. doi: 10.1016/j.cell.2015.06.054

Knott, G., Marchman, H., Wall, D., and Lich, B. (2008). Serial section scanning electron microscopy of adult brain tissue using focused ion beam milling. *J. Neurosci.* 28, 2959–2964. doi: 10.1523/JNEUROSCI.3189-07.2008

Liu, Y. T., Tao, C. L., Zhang, X., Xia, W., Shi, D. Q., Qi, L., et al. (2020). Mesophasic organization of GABAA receptors in hippocampal inhibitory synapses. *Nat. Neurosci.* 23, 1589–1596. doi: 10.1038/s41593-020-00729-w

MacGillavry, H. D., Song, Y., Raghavachari, S., and Blanpied, T. A. (2013). Nanoscale scaffolding domains within the postsynaptic density concentrate synaptic AMPA receptors. *Neuron* 78, 615–622. doi: 10.1016/j.neuron.2013.03.009

Martinez-Sanchez, A., Laugks, U., Kochovski, Z., Papantoniou, C., Zinzula, L., Baumeister, W., et al. (2021). Trans-synaptic assemblies link synaptic vesicles and neuroreceptors. *Sci. Adv.* 7(10). doi: 10.1126/sciadv.abe6204

Maschi, D., and Klyachko, V. A. (2017). Spatiotemporal regulation of synaptic vesicle fusion sites in central synapses. *Neuron.* 94, 65–73. doi: 10.1016/j.neuron.2017.03.006

Nair, D., Hosy, E., Petersen, J. D., Constals, A., Giannone, G., Choquet, D., et al. (2013). Super-resolution imaging reveals that AMPA receptors inside synapses are dynamically organized in nanodomains regulated by PSD95. *J. Neurosci.* 33, 13204–13224. doi: 10.1523/jneurosci.2381-12.2013

Nakagawa, T., Cheng, Y., Ramm, E., Sheng, M., and Walz, T. (2005). Structure and different conformational states of native AMPA receptor complexes. *Nature* 433, 545–549. doi: 10.1038/nature03328

Nakagawa, T., Futai, K., Lashuel, H. A., Lo, I., Okamoto, K., Walz, T., et al. (2004). Quaternary structure, protein dynamics, and synaptic function of SAP97 controlled by L27 domain interactions. *Neuron* 44, 453–467. doi: 10.1016/j.neuron.2004.10.012

Ramsey, A. M., Tang, A. H., LeGates, T. A., Gou, X. Z., Carbone, B. E., Thompson, S. M., et al. (2021). Subsynaptic positioning of AMPARs by LRRTM2 controls synaptic strength. *Sci. Adv.* 7, eabf3124. doi: 10.1126/sciadv.abf3126

Schrod, N., Vanhecke, D., Laugks, U., Stein, V., Fukuda, Y., Schaffer, M., et al. (2018). Pleomorphic linkers as ubiquitous structural organizers of vesicles in axons. *PLoS ONE* 13, e0197886. doi: 10.1371/journal.pone.0197886

Sobolevsky, A. I., Rosconi, M. P., and Gouaux, E. (2009). X-ray structure, symmetry and mechanism of an AMPA-subtype glutamate receptor. *Nature* 462, 745–756. doi: 10.1038/nature08624

Sugiyama, Y., Kawabata, I., Sobue, K., and Okabe, S. (2005). Determination of absolute protein numbers in single synapses by a GFP-based calibration technique. *Nat. Methods* 2, 677–684.

Tang, A.-H., Chen, H., Li, T. P., Metzbower, S. R., MacGillavry, H. D., and Blanpied, T. A. (2016). A trans-synaptic nanocolumn aligns neurotransmitter release to receptors. *Nature* 536, 210–214. doi: 10.1038/nature19058

Tao, C. L., Liu, Y. T., Sun, R., Zhang, B., Qi, L., Shivakoti, S., et al. (2018). Differentiation and characterization of excitatory and inhibitory synapses by cryo-electron tomography and correlative microscopy. *J. Neurosci.* 38, 1493–1510. doi: 10.1523/JNEUROSCI.1548-17.2017

Watanabe, S., Rost, B. R., Camacho-Perez, M., Davis, M. W., Sohl-Kielczynski, B., Rosenmund, C., et al. (2013). Ultrafast endocytosis at mouse hippocampal synapses. *Nature* 504, 242–247. doi: 10.1038/nature12809

Wu, Y., Whiteus, C., Xu, C. S., Hayworth, K. J., Weinberg, R. J., Hess, H. F., et al. (2017). Contacts between the endoplasmic reticulum and other membranes in neurons. *Proc. Natl. Acad. Sci. USA.* 114, E4859–E4867. doi: 10.1073/pnas.1701078114

Xu, C. S., Pang, S., Shtengel, G., Muller, A., Ritter, A. T., Hoffman, H. K., et al. (2021). An open-access volume electron microscopy atlas of whole cells and tissues. *Nature* 599, 147–151. doi: 10.1038/s41586-021-03992-4

Yin, W., Brittain, D., Borseth, J., Scott, M. E., Williams, D., Perkins, J., et al. (2020). A petascale automated imaging pipeline for mapping neuronal circuits with high-throughput transmission electron microscopy. *Nat. Commun.* 11, 4949. doi: 10.1038/s41467-020-18659-3

Zuber, B., Nikonenko, I., Klauser, P., Muller, D., and Dubochet, J. (2005). The mammalian central nervous synaptic cleft contains a high density of periodically organized complexes. *Proc. Natl. Acad. Sci. USA* 102, 19192–19197. doi: 10.1073/pnas.0509527102

frontiers in Synaptic Neuroscience

METHODS
published: 18 December 2020
doi: 10.3389/fnsyn.2020.584549

SynapsEM: Computer-Assisted Synapse Morphometry

Shigeki Watanabe[1,2]*, *M. Wayne Davis*[3], *Grant F. Kusick*[1], *Janet Iwasa*[4] *and Erik M. Jorgensen*[3]*

[1]*Department of Cell Biology, Johns Hopkins University School of Medicine, Baltimore, MD, United States,* [2]*Solomon H. Snyder Department of Neuroscience, Johns Hopkins University School of Medicine, Baltimore, MD, United States,* [3]*Department of Biology and Howard Hughes Medical Institute, University of Utah, Salt Lake City, UT, United States,* [4]*Department of Biochemistry, University of Utah, Salt Lake City, UT, United States*

The structural features of a synapse help determine its function. Synapses are extremely small and tightly packed with vesicles and other organelles. Visualizing synaptic structure requires imaging by electron microscopy, and the features in micrographs must be quantified, a process called morphometry. Three parameters are typically assessed from each specimen: (1) the sizes of individual vesicles and organelles; (2) the absolute number and densities of organelles; and (3) distances between organelles and key features at synapses, such as active zone membranes and dense projections. For data to be meaningful, the analysis must be repeated from hundreds to thousands of images from several biological replicates, a daunting task. Here we report a custom computer program to analyze key structural features of synapses: SynapsEM. In short, we developed ImageJ/Fiji macros to record x,y-coordinates of segmented structures. The coordinates are then exported as text files. Independent investigators can reload the images and text files to reexamine the segmentation using ImageJ. The Matlab program then calculates and reports key synaptic parameters from the coordinates. Since the values are calculated from coordinates, rather than measured from each micrograph, other parameters such as locations of docked vesicles relative to the center of an active zone can be extracted in Matlab by additional scripting. Thus, this program can accelerate the morphometry of synapses and promote a more comprehensive analysis of synaptic ultrastructure.

Keywords: electron microscopy, synapse, morphometry, ultrastructural analysis, SynapsEM

Edited by:
Xiaobing Chen,
National Institutes of Health (NIH),
United States

Reviewed by:
Thomas Uram,
Computing, Environment and Life
Sciences Directorate, Argonne
National Laboratory, United States
Jae Hoon Jung,
National Institutes of Health (NIH),
United States

Correspondence:
Shigeki Watanabe
shigeki.watanabe@jhmi.edu
Erik M. Jorgensen
jorgensen@biology.utah.edu

Received: *17 June 2020*
Accepted: *30 November 2020*
Published: *18 December 2020*

Citation:
Watanabe S, Davis MW, Kusick GF,
Iwasa J and Jorgensen EM
(2020) SynapsEM:
Computer-Assisted Synapse
Morphometry.
Front. Synaptic Neurosci. 12:584549.
doi: 10.3389/fnsyn.2020.584549

INTRODUCTION

Understanding the mechanisms of synaptic transmission requires detailed characterizations of synapses at the ultrastructural level. To release neurotransmitters, synaptic vesicles fuse at a specialized membrane domain of the presynaptic terminal called the active zone (Couteaux and Pécot-Dechavassine, 1970; Heuser et al., 1979). A subset of vesicles are docked, that is, in contact with the active zone membrane by morphology (Schikorski and Stevens, 1997; Hammarlund et al., 2007; Imig et al., 2014), and fuse in response to calcium influx (Heuser et al., 1979; Heuser and Reese, 1981). Following fusion, these vesicles are recycled locally *via* endocytosis and components sorted in an endosome to sustain synaptic transmission (Ceccarelli et al., 1972; Heuser and Reese, 1973; Dittman and Ryan, 2009; Saheki and De Camilli, 2012; Watanabe et al., 2013a,b, 2014; Kononenko and Haucke, 2015). However, the structures involved in synaptic membrane trafficking are extremely small. For example, synaptic vesicles are 30–50 nm in diameter (Zhang et al., 1998), and a few hundred vesicles are clustered within a synaptic bouton (Schikorski and Stevens, 1997; Shepherd and Harris, 1998), which is only ∼0.5–1 μm in diameter. Moreover, a vesicle may move only a few nanometers to fully engage the active zone membrane during docking (Hammarlund et al., 2007; Imig et al., 2014), and this state is quite dynamic (Chang et al., 2018; Kusick et al., 2020). Given these dimensions, synaptic morphometry requires the resolution of electron microscopy.

Morphometry is typically performed on an electron micrograph of a single synaptic profile from a 30–70 nm-thick section. Analyses from ∼200 synaptic profiles are then summed, and results are compared between controls and experimental samples, such as mutants or drug-treated neurons. In each image, the following features are analyzed: the size of membrane-bound structures such as vesicles and other organelles, the number of these structures, and the distance of these structures from the active zone membrane, the plasma membrane, and if apparent, electron-dense cytomatrix (dense projection) that presumably harbors calcium channels. The organelles identified in serial electron micrographs can be "segmented" by tracing and characterized manually by measuring the sizes of the organelles and distances of these structures to the relevant membranes. Thus, manually measuring features in electron micrographs is labor-intensive, requiring extra effort to record annotated features in such a way that they can be easily reexamined.

To overcome these issues, we developed an analysis workflow, SynapsEM, that integrates ImageJ macros and Matlab scripts for the morphometry of synapses from electron micrographs (**Figure 1**). Specifically, the Matlab scripts first shuffle images from different conditions, which are pooled into a single folder (**Figure 1A**). This shuffling procedure reduces potential bias during annotation. These images are imported into ImageJ as a sequence (**Figure 1A**). With the freehand line tool, the contours of the plasma membrane and the active zone membrane are traced, and their x,y-coordinates are recorded in the ROI manager (**Figure 1B**). Then, the diameters of vesicles are traced using a straight line tool (**Figure 1B** inset), and the x,y-coordinates at the centroid of vesicles are recorded. Additionally, the membrane of endosomes can be traced with a freehand selection tool, and x,y coordinates of the contour line recorded. Once all structures are annotated from an image, the values in the ROI are exported as a text file (**Figures 1B,C**). The text file can be imported back to ImageJ for re-evaluation by independent researchers. This re-evaluation step is not required but independent confirmation of segmentation calls makes the annotation more accurate. When all images are analyzed, the resulting text files are unblinded and imported into Matlab (**Figure 1C**). The custom scripts then calculate the distances of membrane-bound structures to the active zone membrane as well as the plasma membrane. The numbers and diameters of these structures are also determined. These data are then compared between different conditions computationally; the researcher remains blinded to individual images. The outputs of the scripts can be saved or exported to other programs for statistical analysis. SynapsEM can be applied to serial-section data, but one must be cautious about overcounting structures that span in multiple sections. Overall, this workflow expedites the analysis of synaptic ultrastructure, reduces the experimental biases associated with manual image annotation, and unifies the method of analysis across many labs.

MATERIALS AND EQUIPMENTS

The following materials are required for the procedures described in this manuscript.

- Electron micrographs, preferably acquired with the same camera setting on the same microscope for a set of experiments.
- A computer (no specific requirements as long as it meets the system requirement for the Matlab program).
- A computer keyboard with a numeric keypad.
- Matlab, MathWorks (The scripts were originally written in Matlab 2008, and have been added to in versions up to Matlab 2020).
- Matlab custom scripts (available from https://github.com/shigekiwatanabe/SynapsEM).
- Fiji (or ImageJ).
- Macros (available from https://github.com/shigekiwatanabe/SynapsEM).
- Maya for 3-D rendering (optional).
- Wacom tablet (Cintiq 22HD), or another pen tablet (optional, but makes annotating many images easier).

METHODS

Randomizing Images

Images from multiple samples should be analyzed in a batch to minimize the potential bias during the analysis. Shuffling removes any possibility of conscious or unconscious bias between samples, eliminating any variables in analysis apart from different samples themselves. Even with blinded, but not scrambled images, the analysis can be skewed when they are analyzed in different batches: this can range from an obvious phenotype making it clear which condition a sample is, to simple day-to-day differences in the segmentation, to a novice improving the accuracy of their segmentation as they work through more images in an experiment. For this purpose, all images for single experiments are pooled into one folder (**Figure 1A**). These images should be duplicates of the original images to keep the original data intact. To ensure the original images are safe, the program asks whether the images should be duplicated when the "randomize" code is run in Matlab. Answering "yes" to this question will make copies of the images and randomize the duplicated images, leaving the original data untouched. In the popup window, select the directory (folder) that contains all images for an experiment. After the selection, another window pops up, prompting the user to select all images. Select all images to be randomized. At the end of the program, randomized images are found in the "randomized" folder, nested in the directory where the original images are (**Figure 1A**). The key is named "key.mat" and is also saved in the "randomized"

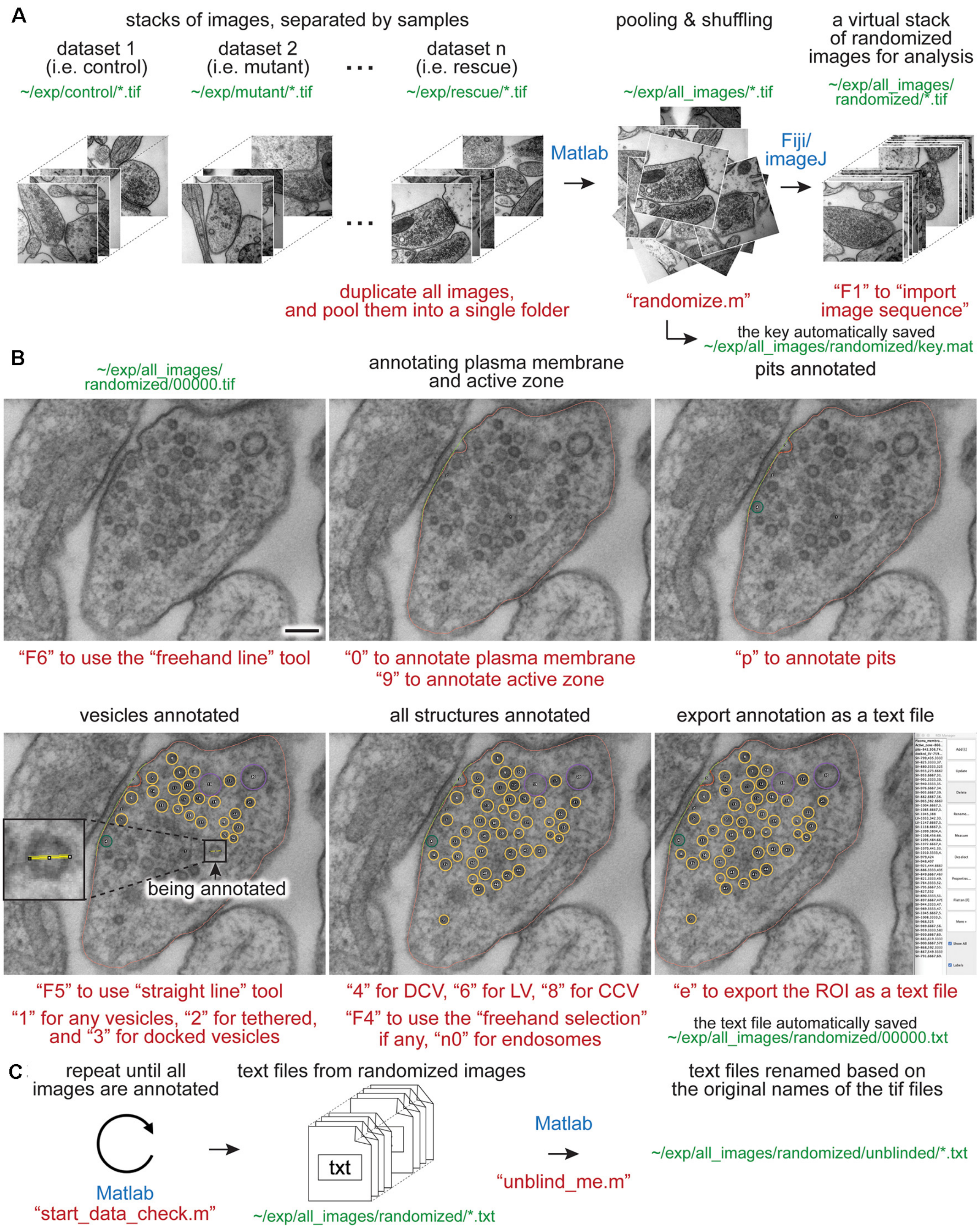

FIGURE 1 | Synapse morphometry using synapsEM. **(A)** A schematic showing the image randomization procedure. In each experiment, images are collected from multiple samples (i.e., control, mutants, drug-treated). Ideally, image acquisition should also be done blinded. These images are pooled into the same folder and then randomized using the "randomize.m" Matlab script. Running this program creates a new folder, named "randomized," and transfers the images into this folder with the randomized number assigned to each image. These images should be opened in ImageJ or Fiji as a virtual stack using the F1 key after installing the "synapsEM_analysis_macro.txt" macro. **(B)** A schematic showing the procedure for image annotation. After opening the images in ImageJ/Fiji, membranes can be traced using specific tools and hot keys (as denoted in red). Note that all structures annotated are recorded into the ROI manager. For vesicles, draw a line across the vesicle membrane as shown in the inset. After pressing a hot key corresponding to the structure (i.e., "1" for synaptic vesicle in this case), the macro draws a circle using the drawn line as a diameter for the vesicle. When the annotation is complete, the structures listed in the ROI manager can be exported by simply pressing "e" on the computer keyboard. **(C)** A schematic showing the final steps of the morphometry. After all images in the dataset are annotated, the resulting text files must be first checked for errors using the "start_data_check" script in Matlab. After corrections, the text files can be decoded based on the original names of the corresponding images using the "unblind_me" script. This script duplicates the text files, decode the copied files, and move them to the "unblinded" folder. The decoded text files can be further processed for analysis. The sentences in red, green, and blue indicate the commands, the directory of files, and the software used, respectively. Scale bars = 100 nm.

folder (**Figure 1A**). This file must be kept safe until the analysis is complete.

Opening Images

Morphometry is performed in Fiji. Start Fiji, and install the "synapsEM_analysis_macro.txt" by navigating to the plugin dropdown menu, clicking on "Macros" and then "Install," and selecting the "synapsEM_analysis_macro.txt" file. For easy access to the file, it is highly recommended to store this macro in the ∼/Fiji/macros directory so it is readily accessible. To skip this installation procedure, the contents of "synapsEM_analysis_macro.txt" can be copied into the StartupMacros.fiji.ijm, which is found in the ∼/Fiji/macros directory, since all the macros in this file are activated as Fiji starts up.

To start the analysis, the randomized images should be opened as a stack (**Figure 1A**). Press the "F1" key to import the image sequence as a virtual stack—the pixel size information on tif files will be converted such that each pixel is one arbitrary unit when the "F1" hotkey is used. If images are opened through "File, Import, Image sequence" or simply dragging a folder to Fiji, it is important to "set scale" through the "Analyze" drop-down menu and type in 1 for the "distance in pixels" and 1 for the "known distance." This conversion of the pixel size can also be performed by pressing "F2." When working with a large dataset, it is highly recommended that images are opened as a virtual stack.

Segmenting Images

The eventual goal of segmentation is to determine the size of vesicles and other membrane-bound organelles, the numbers or density of these structures, and the distribution of these structures relative to the plasma membrane or active zone membrane. The macros are set up to record x,y-coordinates of the structures of interest and their size information in the ROI manager window. These macros are accessed through hot keys, as listed in **Tables 1**, **2**. Three sets of line tools are used to trace different features at synapses. A straight line tool (the Fiji tool #1) is accessed with "F5" and used to annotate closed and near-uniformly circular structures like synaptic vesicles, large vesicles, and dense-core vesicles. A freehand selection tool (the Fiji tool #3, "F4") is used to segment closed and irregularly-shaped structures such as endosomes. A freehand line tool (the Fiji tool #7, "F6") is used to segment open-ended structures, such as plasma membranes, active zone membranes, and pits.

When an appropriate tool in Fiji is selected (**Table 1**), objects in the micrograph can be segmented using hot keys listed in **Table 2** (**Figure 1**). For open-ended membranes, trace the contour of the membranes as closely as possible using the freehand line tool. From each micrograph, one plasma membrane ("0") and at least one active zone membrane ("9") must be segmented. Since some synapses have multiple active zones (**Figures 2A,B**), judged based on the presence of postsynaptic density in the juxtaposed membranes, more than one active zone can be defined per micrograph. However, a single plasma membrane should be drawn in each image. In some synapses, presynaptic dense projections are prominent in the active zone (Zhai and Bellen, 2004; Watanabe et al., 2013a), and they can be traced using the same tool and added to the ROI Manager by pressing "d" for dense projection and "r" for the synaptic ribbon. If membranes are deflected inward, towards the cytoplasm (**Figures 1A–C**, **2E,F**), they can be traced as pits ("U"), although the exact nature of these membrane invaginations, whether exocytic, endocytic, or simple membrane ruffles, must be determined with careful experiments (Watanabe et al., 2013a,b, 2014). If any of these pits are clearly covered with electron-dense materials indicative of clathrin-coats (Heuser and Reese, 1973), they can be annotated as clathrin-coated pits ("7"). Note that the active zone membrane is drawn under the pit where the plasma membrane would have been before exocytosis when prominent pits like the one in **Figure 1B** are present within the active zone. Pits are classified as being "within the active zone" (**Figure 1B**) if their segmentation overlaps with the traced active zone membrane at two points or if both ends are within 5 nm of the active zone membrane (that is, the entire pit is in the active zone). Otherwise, pits are classified as being "outside the active zone" (**Figures 2E,F**). Thus, these features must be traced carefully so that pits inside and outside the active zone are properly distinguished from each other.

For vesicles, use the straight line tool to draw a line across the outer edges of a vesicle (**Figure 1D**). By doing so, the diameter of a vesicle as well as the x,y-coordinates at the center of the line are recorded in the ROI manager. A circle is drawn on the vesicle based on the diameter. Synaptic vesicles can be manually categorized (**Figures 2G,H**) into docked—no lighter pixels between vesicle membrane and plasma membrane ("3"), tethered when a vesicle is close but not docked and has visible tethers to the plasma membrane ("2"), and all other vesicles in the terminal ("1"; **Figures 2G,H**). If not categorized, docking will be determined by the overlap between the vesicle membrane and the plasma membrane. However, tethered vesicles must be annotated by visual inspection, since they are defined as having a physical tether to the plasma membrane (Watanabe et al., 2013b). The same line tool is used to annotate other types of vesicles including clathrin-coated vesicles ("8," **Figures 2C,D**), dense-core vesicles ("4" and "5" if docked, **Figures 2E–H**), and large vesicles ("6," **Figure 1B**). Large vesicles are clear-core vesicles with a diameter of 60–100 nm that may be involved in exocytosis (He et al., 2009; Borges-Merjane et al., 2020; Maus et al., 2020), endocytosis (Watanabe et al., 2013a,b, 2014; Kononenko et al., 2014), and cargo trafficking (Ou et al., 2010; Vukoja et al., 2018). If preferred, all vesicles can be annotated as synaptic vesicles using "1."

Endosomes are also quite prevalent at presynaptic terminals. Although their identity is difficult to determine from single profiles, we define structures as endosomes if they are larger than 100 nm by visual inspection or have irregular shapes (**Figures 2E,F**; Watanabe et al., 2014, 2018). To trace endosomes, the freehand selection tool ("F4") is used to follow the contour of the putative endosomal membrane, and press "0" from the numeric keypad to add the coordinates ("n0"—hereafter, when a number is preceded by n, it will refer to the number key on the numeric keypad). Their areas are also recorded

TABLE 1 | A list of hot keys, encoded in macros for ImageJ/Fiji.

Analysis tools in ImageJ/Fiji	Tool#	Hot keys
Freehand selection tool	3	F4
Straight line tool	1	F5
Freehand line tool	7	F6

TABLE 2 | A list of hot keys, encoded in macros for ImageJ/Fiji.

Structures to be segmented	Hot keys	Analysis tools in ImageJ/Fiji
Synaptic vesicles	1	Straight line tool
Tethered synaptic vesicles	2	Straight line tool
Docked synaptic vesicles	3	Straight line tool
Dense-core vesicles	4	Straight line tool
Docked dense-core vesicles	5	Straight line tool
Large vesicles	6	Straight line tool
Clathrin-coated pits	7	Freehand line tool
Clathrin-coated vesicles	8	Straight line tool
Active zone membrane	9	Freehand line tool
Plasma membrane	0	Freehand line tool
Endosomes	n0	Freehand selection tool
Ferritin+ synaptic vesicles	n1	Straight line tool
Ferritin+ tethered synaptic vesicles	n2	Straight line tool
Ferritin+ docked synaptic vesicles	n3	Straight line tool
Ferritin+ large vesicles	n4	Straight line tool
Ferritin+ clathrin-coated vesicles	n5	Straight line tool
Ferritin+ pits	n6	Freehand line tool
Ferritin+ multivesicular bodies	n7	Freehand selection tool
Ferritin+ endosomes	n8	Freehand selection tool
Ferritin+ buds on endosomes	n9	Freehand line tool
Pits	u	freehand line tool
Multivesicular bodies	m	Freehand selection tool
Particles	p	Straight line tool
Import a text file	i	N/A
Export ROI as a text file	e	N/A
Synaptic ribbon	r	Freehand line tool
Dense projection	d	Freehand line tool
Buds on endosomes	j	Freehand line tool

in the ROI manager. For multivesicular bodies (MVBs), press "m." Currently, endosomes and MVBs are the only such structures traced in our study, but this analysis can be extended to other irregularly shaped structures like mitochondria and autophagosomes.

Ferritin or gold particles, as well as organelles that contain them, can also be tracked as distinct structures (**Figures 2I–L**). Ferritin is typically used as a fluid phase marker to track recently endocytosed membranes (Watanabe et al., 2013b, 2014, 2018), while gold particles are often conjugated with antibodies or other moieties for affinity interaction to probe proteins of interest (Li et al., 2020). In addition to the plasma membrane and active zone membrane, pits with particles can be annotated using the freehand line tool and recorded with "n6" on the numeric keypad. For particle-containing vesicles, use the straight line tool, and add them to the ROI manager by pressing "n1" for any vesicles, "n2" for tethered vesicles, "n3" for docked vesicles, "n4" for large vesicles, and "n5" for clathrin-coated vesicles (**Table 2**). The particles themselves can be annotated using the same tool and hitting the "p" on the keyboard. Particle-positive endosomes and MVBs are traced using the freehand selection tool and recorded with "n8" and "n7," respectively.

For other structures, the best practice is to annotate using hot keys of structures similar to the structures of interest. For example, mitochondria can be marked as "particle-positive MVBs (n7)" or "particle-positive endosomes (n8)" for the analysis purpose. Likewise, any vesicular structures can be annotated with particle-positive vesicles (n1-n5) since these structures are normally not annotated unless ferritin or something similar is used in the study. Be sure to take notes on what keys are used.

As a cautionary note, the distance between membranes is calculated at the minimum, that is, from the outer leaflet of a vesicle to the inner leaflet of the plasma membrane or active zone membrane. Accordingly, it is highly recommended to use images acquired at a sufficient spatial resolution (i.e., less than 1 nm/pixel) and use a pen tablet to trace objects. Since electron micrographs might not be acquired at the same settings, the contrast should be adjusted in each image to make the features-of-interest appear clear for analysis.

Exporting as a Text File

When segmentation is completed from an image, the annotated structures in the ROI manager can be exported as a text file. Press "e" on the keyboard (**Figure 1B**). This macro then generates a text file containing all the segmented structures in the order of the ROI manager list. The text file is named after the image and automatically saved in the folder where the image is. The Fiji screen advances to the next image after the text file is saved. In the text file, the record of each structure is organized as follows: the tool used to annotate (by its Fiji tool number), the name of a structure, area or length of a structure if it is not a vesicle, x-coordinate(s), y-coordinate(s), and radius of a vesicle if it is a vesicle. These values are separated by a tab character (ASCII 09). The record in the ROI manager will be erased after the export is complete.

Importing a Text File

After completing the analysis for all images, it is important to check whether all the essential components are segmented in every image and the text files are compatible with the Matlab codes. To check, run the "start_data_check" function in Matlab (**Figure 1C**). If any data are missing or more than one plasma membrane are annotated, this function returns the names of the files and the description of the problems associated with the files in the command window. To fix the problems or reevaluate the annotations, the records in a text file can be imported back to the correct image in a stack. On the image of interest, press "i" to import the text file. If there is a text file corresponding to this image in the folder, the segmentation will automatically pop up and the records in the ROI manager. If the list in the ROI manager is modified, press "e" again to export the modified list to the text file. Note that this process will overwrite the existing file.

Unblinding the Text Files

After ensuring that all images are annotated correctly, the resulting text files can be unblinded for further analysis by the Matlab scripts (**Figure 1C**). To unblind the shuffled text files, use the "unblind_me" script in Matlab. This script prompts users to define the directory where the key is and where the text files are.

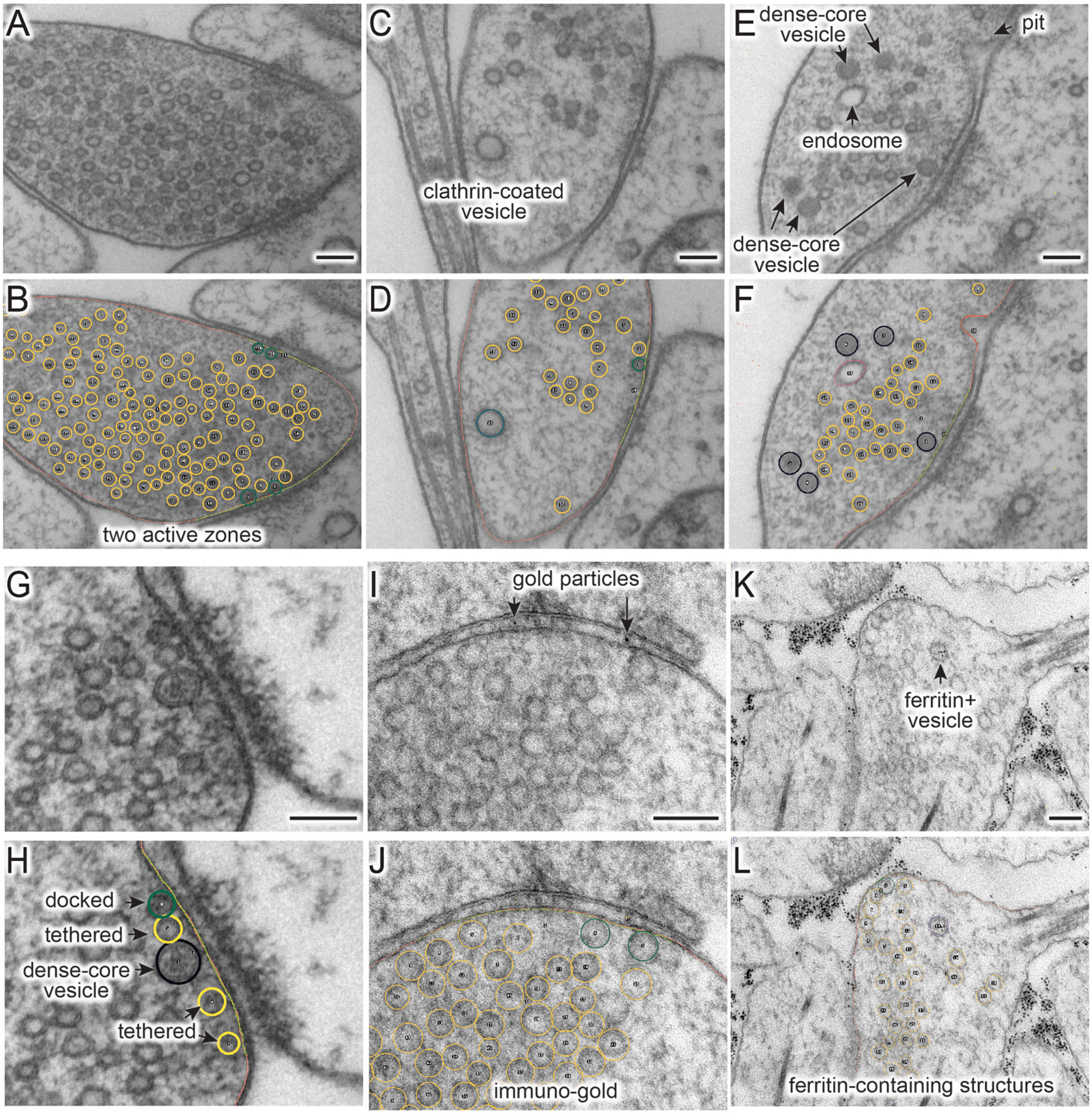

FIGURE 2 | (A–L) Example micrographs **(A,C,E,G,I,K)** and their annotations **(B,D,G,H,J,L)**, showing structures that can be traced using the ImageJ/Fiji macros ("synapsEM_analysis_macro.txt"). **(A,B)** Multiple active zones in a single synaptic profile. **(C,D)** Clathrin-coated vesicle. **(E,F)** Dense-core vesicles and endosomes. **(G,H)** Docked or tethered synaptic vesicles in active zones. **(I,J)** Gold particles. **(K,L)** Ferritin-containing vesicles. See **Table 2** for the full list of structures and hot keys to enter into the ROI manager. Scale bars = 100 nm.

After selecting the files, the text files will be renamed based on the names of the original images and copied into a new folder, called "unblinded," nested within the folder with the shuffled text files. Matlab analysis should be performed using the unblinded text files.

Running Matlab Scripts

The Matlab scripts are designed to use the spatial coordinates and size information of annotated structures to calculate the distances among them and extract count data for annotated features (numbers of synaptic vesicles, docked vesicles, endosomes, etc). To start, select the directory where all the scripts are located, and then type in "start_analysis" in the command line. Since the data analysis for each sample must be run separately, we typically define the name of the sample at this stage (i.e., control_1 = start_analysis;). The program prompts users to input the pixel size for the images (nm/pixel) and the size of the bin (i.e., 50 nm), which is used for plotting the distribution data such as locations of vesicles relative to the active zone. Then, a user interface pops up, first asking to choose the directory where the text files are and then to select all the text files. The files are then loaded into Matlab for processing.

The scripts are designed to perform the following three calculations: size, number, and distribution of distances from the plasma membrane and active zone, of the vesicles and endosomes. First, the sizes of the structures are calculated based on the pixel size, and the mean and median diameter of vesicles, as well as 1-D surface area of and 2-D space within endosomes, are determined from the sample. These numbers are available as an average in a single image or an average for the sample. For pits, the diameter is calculated at the full-width half-maximum. Besides, the scripts also calculate the depth (height), the width at the base, and the surface area of the pits. These data are available as a number array in the final dataset.

Second, the total numbers of structures are calculated from each profile and then their mean and median are determined. The total numbers are additionally sorted based on their locations relative to the active zone and plasma membrane. For example, if a vesicle is within 30 nm of the plasma membrane and also within 30 nm of the active zone, this vesicle is counted towards the vesicle-associated with the active zone. If a vesicle is within 30 nm of the plasma membrane but not associated with the active zone membrane (>30 nm), this vesicle will be categorized as a vesicle in the periactive zone. If neither condition is met, the object is considered cytoplasmic. The distinction between vesicles above the active zone vs. the periactive zone is somewhat arbitrary but useful for detecting certain vesicle pools. For example, synaptic vesicles within 30 nm of the active zone membrane (about two rows of vesicles) are thought to contribute to the readily releasable pool (Schikorski and Stevens, 2001), and their numbers are often reported (Richmond et al., 2001; Hammarlund et al., 2007). Vesicles or pits in the periactive zone reflect endocytic events since they correlate with the internalization of fluid phase markers and are typically observed hundreds of milliseconds after an action potential (Watanabe et al., 2013b, 2014, 2018). In contrast, pits within the active zone represent fusing vesicles since they appear a few milliseconds after an action potential (Watanabe et al., 2013a,b; Kusick et al., 2018). The distance threshold in nanometers can be moved by changing the number in line number 65 in the source code (vesicle_count.m) from 30 to the desired number. After the analysis, the number of data is available in the "vesicle_number" table as a number array. The key to interpreting the array is listed in **Supplementary Table 2**.

Third, they calculate the minimal distance from each structure to the plasma membrane and active zone membrane and determine the distribution of each structure relative to these membranes. For a vesicle, the distance from the center to every point on the plasma membrane, active zone, and if annotated, dense projection is calculated, and the radius of the vesicle is subtracted such that the distance is determined from the outer edge of the vesicle to the membrane. Then, the minimal distance is reported as the final distance. If the distance is calculated to be 0 nm from the plasma membrane, the vesicles are considered docked, and they will be categorized into the docked pool for the numerical calculations. For endosomes and other irregularly shaped organelles, to determine the distance to the plasma membrane and active zone, we calculate numerous distances from the organelle membrane to the synaptic membrane and find their minimum. The distances can be plotted as continuous frequency distribution with no binning if enough data are collected. However, the distribution of structures is typically determined by calculating the number of the structures at certain distances away from the active zone membrane or if annotated, the dense projection based on the bin the user specifies (i.e., 50 nm). The resulting tables show their average number and normalized abundance at each bin (**Supplementary Table 1**).

The output of the Matlab scripts appears in the workspace as a structure array and can be compared between different conditions or samples (e.g control vs. mutants, or glutamatergic vs. GABAergic neurons). To compare, all other samples in a single experiment should be processed by the same procedure (i.e., mutant_1 = start_analysis; in the command line). After all the samples are processed, the workspace should be saved in .mat format.

For plotting the data and statistical analysis, we export the data to Prism. Several optional scripts are available to re-organize the data for exporting. Please refer to the **Supplementary Information**. Step-by-step protocols are also available in the **Supplementary Information**.

RESULTS

To validate program scripts, the computed data were compared to manually segmented data. Specifically, we segmented 10 images using the procedures described above and calculated distances from ∼25–30 vesicles to the active zone membrane using the Matlab scripts (**Figure 3A**: diameter of synaptic vesicles). Then, we manually measured the distances from those vesicles to the nearest active zone membrane based on visual inspection. We repeated the measurements three times to estimate errors caused by manual measurement. We then plotted the disparities between distances determined by the different methods. On average, the difference between the calculated and measured distances was 1.4 nm (**Figure 3B**; median and 95% CI). This number is similar to the error made by repeating the manual measurements three times on the same set of images (1.3 nm median, **Figure 3B**). The overall distribution of synaptic vesicles is also unchanged (**Figure 3C**). Thus, the calculations based on the x,y-coordinates of structures are valid and produce data as accurate as manual measurements.

Based on the data from these 10 images, we determined key synaptic parameters of synapses from cultured mouse hippocampal neurons (14 days *in vitro*). The diameter of synaptic vesicles was 39.6 ± 0.2 nm (mean ± SEM) when all vesicles in the set were pooled, and 40.1 ± 0.6 nm (mean ± SEM), when the numbers were first averaged per profile and then the mean of means was determined from the entire dataset (**Figure 3D**). The mean of means would better represent the population average. The average number of synaptic vesicles per profile was 51 (**Figure 3E**, median, and 95% CI shown). About four vesicles were found within 30 nm of the active zone membrane; of these, ∼2 vesicles were docked

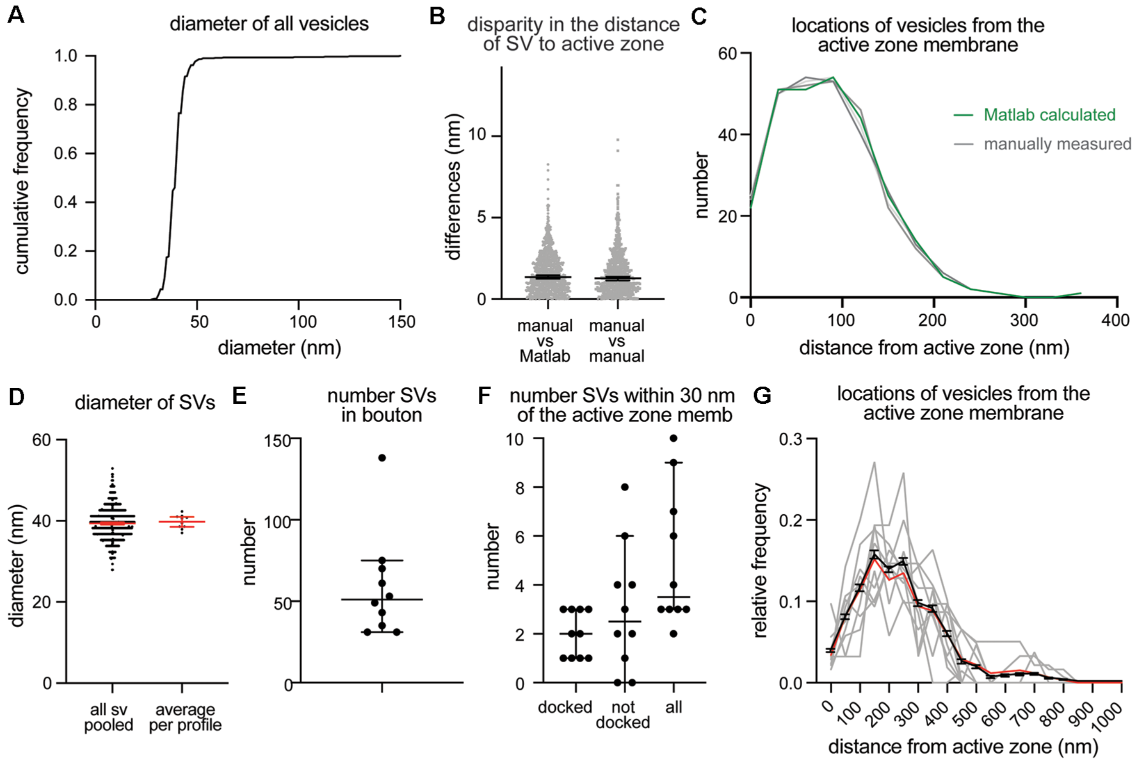

FIGURE 3 | Example plots that can be readily generated with the synapsEM. **(A)** A cumulative plot showing the diameter of all vesicles annotated from 10 sample images used in this study. A total of 590 vesicles are annotated. **(B)** A scatter plot showing the disparity in distances of vesicles to the active zone membrane between the Matlab calculated and manually measured (left) or among three manually measured (right). Each dot = one measurement. The medians are 1.4 nm and 1.3 nm, respectively, (p = 0.8, unpaired t-test). **(C)** A plot showing the distribution of vesicle distances from the active zone membrane. No difference is observed between the Matlab calculated and manually measured ($p > 0.99$, Kruskal–Wallis test with Dunn's multiple comparison test). **(D)** A plot showing the diameter of synaptic vesicles, averaged from all vesicles pooled (left, 39.6 ± 0.2 nm, mean ± SEM) and means of each profile (right, 40.1 ± 0.6 nm, mean ± SEM). **(E)** A plot showing the number of vesicles in the terminal. Each dot = the number in each profile. **(F)** A plot showing the number of vesicles docked or tethered at the active zone or all vesicles within 30 nm of the active zone membrane. Each dot = the number in each profile. **(G)** A plot showing the distribution of synaptic vesicle distances to the active zone. Gray lines = the normalized distance distribution from each profile. Black line = average from 10 profiles. Red line = the normalized abundance from the pooled data.

on average (**Figure 3F**). It is sometimes useful to normalize vesicle numbers and docking to the size of the active zone. To accommodate this calculation, the length of active zones is accessible in the output (**Supplementary Table 2**), and the average is also determined (median = 385 nm). Although n is small, these numbers are surprisingly close to the numbers we have obtained from thousands of images across many experiments (Watanabe et al., 2013b, 2014; Kusick et al., 2018; Li et al., 2020). The distribution of distances from synaptic vesicles to the active zone can be mapped from each synaptic profile (gray lines), averaged numbers per profile (black line, mean ± SEM), and the data all combined (**Figure 3G**, red line). Thus, typical synaptic parameters can be measured and plotted using SynapsEM.

SynapsEM was used to segment data from other model systems. We performed the same analysis using serial sections of *C. elegans* neuromuscular junctions (**Figure 4**, n = 5 reconstructed synapses). In these reconstructions, the numbers can be calculated per synaptic profile containing a dense projection or per fully reconstructed synapse (end-to-end of a synaptic bouton defined by the presence of synaptic vesicles). The average number of synaptic vesicles per profile and per reconstructed synapse were 35.5 and 394, respectively (**Figures 4A–C,E**). Of the ∼5 vesicles within 30 nm of the active zone membrane in single profiles, an average of 3 are docked per synaptic profile (**Figure 4D**), thus, 8.5% of the total vesicle pool are docked in the active zone. Similarly, 9% of the total vesicles in the reconstructed boutons were docked (**Figure 4F**). Thus, the docked pool can be estimated from the synaptic profile data, as has been done in previous publications (Hammarlund et al., 2007; Watanabe et al., 2013a). Since dense projections are apparent at these synapses (**Figure 4A**), distances between synaptic vesicles and docked vesicles and the dense projection can be calculated (**Figures 4G,H**). The median radial distance from the dense projection for all vesicles was 140 nm, while the median radial distance from the dense projection for docked vesicles was 67 nm, suggesting that vesicles tend to dock near the dense projections, where voltage-gated calcium channels are harbored (Gracheva et al., 2008). Thus, SynapsEM works with both 2D and 3D datasets from multiple model systems.

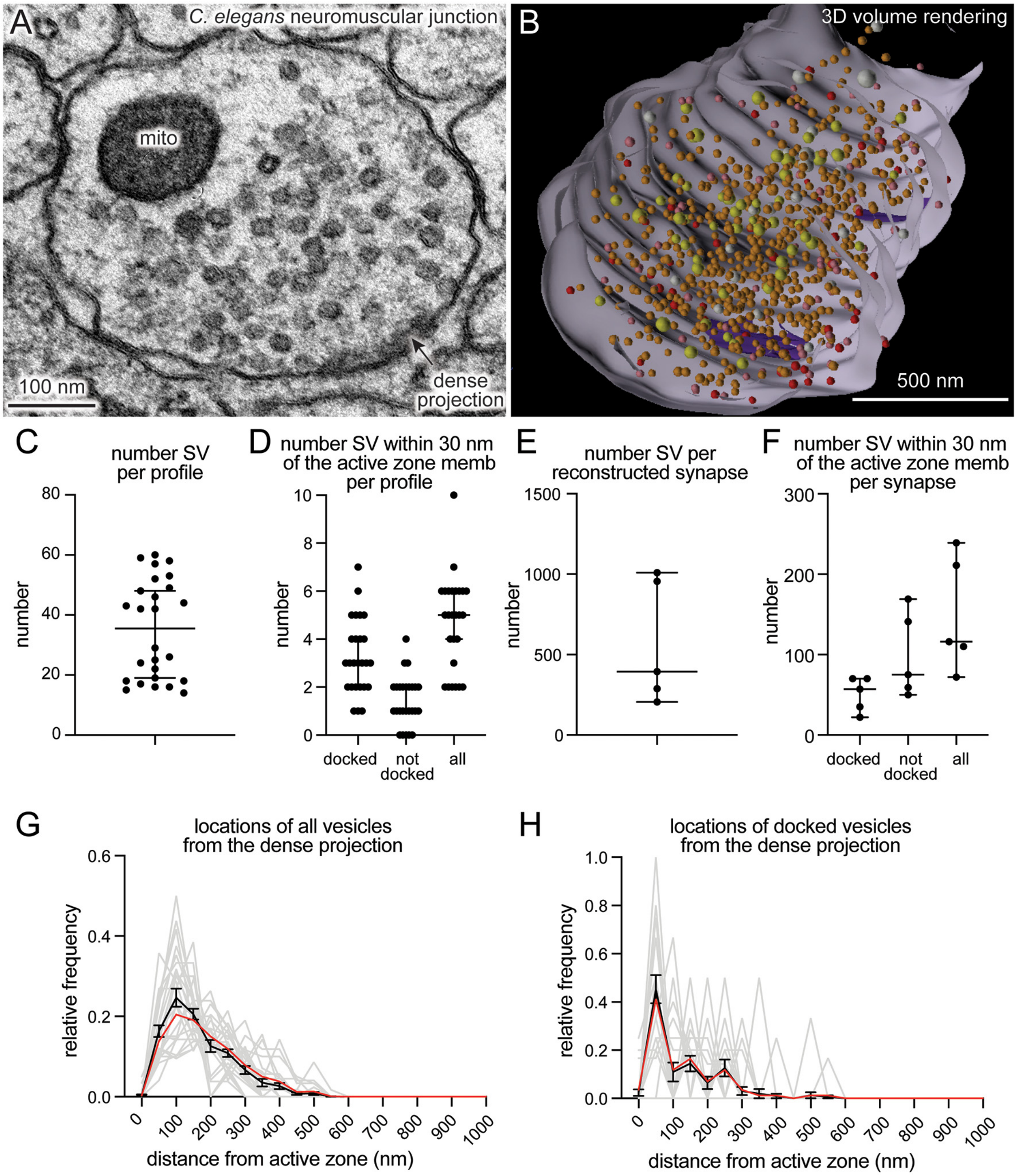

FIGURE 4 | SynapsEM works with other model systems and with 3D reconstruction programs. **(A)** An example micrograph from a serial reconstruction of a *C. elegans* neuromuscular junction, shown in **(B)**. Fourty-eight raw electron micrographs (33 nm each) in series are segmented in Fiji, and x,y-coordinates of each structure exported into text files (i.e., x,y-coordinates from the contour of endosomes, dense projections, plasma membrane). Using x,y-coordinates, polygonal meshes on membranes and dense projections are created using the "loft" command, and vesicles created using the "sphere" command in Maya (see **Supplementary Information**). The z-coordinates for all structures in each slice were determined based on the slice number and increments of 33 nm. **(B)** A snap-shot of the reconstructed synapse using Maya, based on the x,y-coordinates collected from each profile in this study. Red = docked synaptic vesicles; Orange = synaptic vesicles; yellow = dense-core vesicles; white = large vesicles; purple = dense projections. **(C)** A plot showing the number of vesicles in single synaptic profiles. Each dot = the number in a profile. **(D)** A plot showing the number of vesicles within 30 nm of the active zone membrane per profile, and the number of those vesicles docked or tethered at the active zone. Each dot = the number in each profile. **(E)** The total number of synaptic vesicles from synapses fully reconstructed from serial electron micrographs. **(F)** the number of vesicles within 30 nm of the active zone membrane per profile and the number of those vesicles docked or tethered at the active zone from fully reconstructed synapses. **(G)** A plot showing the distribution of synaptic vesicle distances to the dense projection. **(H)** A plot showing the distribution of docked synaptic vesicle distances to the dense projection. In **(G,H)**, gray lines = the normalized distribution from each profile. Black line = average from 26 profiles. Red line = the normalized abundance from the pooled data.

DISCUSSION

Ultrastructural analysis of synapses has been performed by many labs over the years. Excellent programs, for example, IMOD (Kremer et al., 1996), TrakEM2 (Cardona et al., 2012), and Reconstruct (Fiala, 2005; SynapseWeb, Kristen Harris), provide visualization software for data acquired from either serial sections or tomograms. SynapseEM is a Fiji plug-in designed to quantify morphometric data from electron micrographs. IMOD, TrakEM2, and Reconstruct can all perform similar measurements but focus more on 3-D data, with in-depth features for handling and rendering serial images or tomograms not included in SynapsEM. TrakEM2 in particular offers similar quantification procedures; SynapsEM's benefit is an all-in-one package, from scrambling raw images to outputting final data tables, that is fast and easy to use even for those completely unfamiliar with Fiji or Matlab, but also easily modified. These procedures have been used by everyone from novices to experts to quantitate tens of thousands of 2-D images and over a thousand 3-D reconstructions (Watanabe et al., 2013b, 2014, 2018; Kusick et al., 2018; Li et al., 2020). Although SynapsEM handles serial-section data, it is difficult to annotate structures like endosomes and multivesicular bodies that span across multiple sections, since images are randomized. Thus, for serial-section data, careful re-evaluation is necessary after unblinding. Alternatively, one can skip the randomization step if desired.

Several features streamline and standardize the characterization of synaptic features. First, this approach allows multiple experimenters to assess the validity of annotations, reducing potential errors in the analysis. Second, automated shuffling of images from different conditions reduces potential bias in the analysis. Third, additional parameters can be extracted from the dataset *post hoc*, since the positions of structures are all recorded. For example, the locations of pits relative to the center of an active zone can be calculated based on their coordinates (Kusick et al., 2018; Li et al., 2020; also see **Supplementary Information**). Fourth, this approach can also be applied to serial-sections to calculate distances in three-dimensions (Kusick et al., 2018), similar to IMOD (Kremer et al., 1996) and Reconstruct (Fiala, 2005; SynapseWeb, Kristen Harris). Fifth, the 3D dataset can be rendered into a segmented volume in Maya based on the x,y-coordinates of the structures and their sizes (**Figure 4B**; see **Supplementary Information** for the procedure). Thus, SynapsEM is a versatile approach for the morphometry of synapses. For truly universal and automated analysis, the implementation of the machine-learning-based algorithms into the SynapsEM platform is awaited. It is hoped that SynapsEM will promote data sharing and consistent morphometry of synaptic ultrastructure among labs.

DATA AVAILABILITY STATEMENT

All the data underlying this study can be found in the **Supplementary Material**. Data Sheet 2 includes text files generated by Fiji, Data Sheet 3 includes the Matlab files generated by running analysis on these text files, and Data Sheet 4 includes final data tables used to generate the figures.

AUTHOR CONTRIBUTIONS

SW, MD, and EJ conceived and designed the experiments and wrote the manuscript. GK and SW wrote the protocols. MD wrote the original macro for ImageJ/Fiji. SW wrote the Matlab scripts. JI wrote the Maya code for volume rendering. All authors contributed to the article and approved the submitted version.

FUNDING

SW and this work were supported by start-up funds from the Johns Hopkins University School of Medicine, Johns Hopkins Discovery funds, Johns Hopkins Catalyst Award, the National Science Foundation (1727260), the National Institutes of Health (1DP2 NS111133-01 and 1R01 NS105810-01A1) awarded to SW. SW is an Alfred P. Sloan fellow, McKnight Foundation Scholar, and Klingenstein and Simons Foundation scholar. GK was supported by a grant from the National Institutes of Health to the Biochemistry, Cellular and Molecular Biology program of the Johns Hopkins University School of Medicine (T32 GM007445) and is a National Science Foundation Graduate Research Fellow (2016217537). MD's work was supported by the National Institutes of Health (R01 NS034307) awarded to EJ. EJ is an Investigator of the Howard Hughes Medical Institute.

ACKNOWLEDGMENTS

We thank H. James de St. Germain for training SW on Matlab coding and Marc Hammarlund for discussion. We are also indebted to Edward Hujber, Thien Vu, Morven Chien, and Stephen Alexander Lee for additional MatLab routines.

SUPPLEMENTARY MATERIAL

The Supplementary Material for this article can be found online at: https://www.frontiersin.org/articles/10.3389/fnsyn.2020.584549/full#supplementary-material.

REFERENCES

Borges-Merjane, C.,Kim, O., and Jonas, P. (2020). Functional electron microscopy ("Flash and Freeze") of identified cortical synapses in acute brain slices. *Neuron* 105, 992–1006.e6. doi: 10.1016/j.neuron.2019.12.022

Cardona, A., Saalfeld, S., Schindelin, J., Arganda-Carreras, I., Preibisch, S., Longair, M., et al. (2012). TrakEM2 software for neural circuit reconstruction. *PLoS One* 7:e38011. doi: 10.1371/journal.pone.0038011

Ceccarelli, B., Hurlbut, W. P., and Mauro, A. (1972). Depletion of vesicles from frog neuromuscular junctions by prolonged tetanic stimulation. *J. Cell Biol.* 54, 30–38. doi: 10.1083/jcb.54.1.30

Chang, S., Trimbuch, T., and Rosenmund, C. (2018). Synaptotagmin-1 drives synchronous Ca^{2+} triggered fusion by C2B domain-mediated synaptic vesicle-membrane attachment. *Nat. Neurosci.* 21, 33–40. doi: 10.1038/s41593-017-0037-5

Couteaux, R., and Pécot-Dechavassine, M. (1970). Synaptic vesicles and pouches at the level of "active zones" of the neuromuscular junction. *C. R. Hebd. Seances Acad. Sci. Ser. Sci. Nat.* 271, 2346–2349.

Dittman, J., and Ryan, T. A. (2009). Molecular circuitry of endocytosis at nerve terminals. *Annu. Rev. Cell Dev. Biol.* 25, 133–160. doi: 10.1146/annurev.cellbio.042308.113302

Fiala, J. C. (2005). Reconstruct: a free editor for serial section microscopy. *J. Microsc.* 218, 52–61. doi: 10.1111/j.1365-2818.2005.01466.x

Gracheva, E. O., Hadwiger, G., Nonet, M. L., and Richmond, J. E. (2008). Direct interactions between *C. elegans* RAB-3 and Rim provide a mechanism to target vesicles to the presynaptic density. *Neurosci. Lett.* 444, 137–142. doi: 10.1016/j.neulet.2008.08.026

Hammarlund, M., Palfreyman, M. T., Watanabe, S., Olsen, S., and Jorgensen, E. M. (2007). Open syntaxin docks synaptic vesicles. *PLoS Biol.* 5:e198. doi: 10.1371/journal.pbio.0050198

He, L., Xue, L., Xu, J., McNeil, B. D., Bai, L., Melicoff, E., et al. (2009). Compound vesicle fusion increases quantal size and potentiates synaptic transmission. *Nature* 459, 93–97. doi: 10.1038/nature07860

Heuser, J. E., and Reese, T. S. (1973). Evidence for recycling of synaptic vesicle membrane during transmitter release at the frog neuromuscular junction. *J. Cell Biol.* 57, 315–344. doi: 10.1083/jcb.57.2.315

Heuser, J. E., and Reese, T. S. (1981). Structural changes after transmitter release at the frog neuromuscular junction. *J. Cell Biol.* 88, 564–580. doi: 10.1083/jcb.88.3.564

Heuser, J. E., Reese, T. S., Dennis, M. J., Jan, Y., Jan, L., and Evans, L. (1979). Synaptic vesicle exocytosis captured by quick freezing and correlated with quantal transmitter release. *J. Cell Biol.* 81, 275–300. doi: 10.1083/jcb.81.2.275

Imig, C., Min, S.-W., Krinner, S., Arancillo, M., Rosenmund, C., Südhof, T. C., et al. (2014). The morphological and molecular nature of synaptic vesicle priming at presynaptic active zones. *Neuron* 84, 416–431. doi: 10.1016/j.neuron.2014.10.009

Kononenko, N. L., and Haucke, V. (2015). Molecular mechanisms of presynaptic membrane retrieval and synaptic vesicle reformation. *Neuron* 85, 484–496. doi: 10.1016/j.neuron.2014.12.016

Kononenko, N. L., Puchkov, D., Classen, G. A., Walter, A. M., Pechstein, A., Sawade, L., et al. (2014). Clathrin/AP-2 mediate synaptic vesicle reformation from endosome-like vacuoles but are not essential for membrane retrieval at central synapses. *Neuron* 82, 981–988. doi: 10.1016/j.neuron.2014.05.007

Kremer, J. R., Mastronarde, D. N., and McIntosh, J. R. (1996). Computer visualization of three-dimensional image data using IMOD. *J. Struct. Biol.* 116, 71–76. doi: 10.1006/jsbi.1996.0013

Kusick, G. F., Chin, M., Lippmann, K., Adula, K. P., Davis, M. W., Jorgensen, E. M., et al. (2018). Synaptic vesicles undock and then transiently dock after an action potential. *BioRxiv*

Kusick, G. F., Chin, M., Raychaudhuri, S., Lippmann, K., Adula, K. P., Hujber, E. J., et al. (2020). Synaptic vesicles transiently dock to refill release sites. *Nat. Neurosci.*, 23, 1329–1338. doi: 10.1038/s41593-020-00716-1

Li, S., Raychaudhuri, S., Lee, S. A., Wang, J., Kusick, G. F., Prater, C., et al. (2020). Release sites are positioned to activate NMDA receptors. *BioRxiv* [Preprint]. doi: 10.1101/2020.05.01.072157

Maus, L., Lee, C., Altas, B., Sertel, S. M., Weyand, K., Rizzoli, S. O., et al. (2020). Ultrastructural correlates of presynaptic functional heterogeneity in hippocampal synapses. *Cell Rep.* 30, 3632–3643.e8. doi: 10.1016/j.celrep.2020.02.083

Ou, C.-Y., Poon, V. Y., Maeder, C. I., Watanabe, S., Lehrman, E. K., Fu, A. K. Y., et al. (2010). Two cyclin-dependent kinase pathways are essential for polarized trafficking of presynaptic components. *Cell* 141, 846–858. doi: 10.1016/j.cell.2010.04.011

Richmond, J. E., Weimer, R. M., and Jorgensen, E. M. (2001). An open form of syntaxin bypasses the requirement for UNC-13 in vesicle priming. *Nature* 412, 338–341. doi: 10.1038/35085583

Saheki, Y., and De Camilli, P. (2012). Synaptic vesicle endocytosis. *Cold Spring Harb. Perspect. Biol.* 4:a005645. doi: 10.1101/cshperspect.a005645

Schikorski, T., and Stevens, C. F. (1997). Quantitative ultrastructural analysis of hippocampal excitatory synapses. *J. Neurosci.* 17, 5858–5867. doi: 10.1523/JNEUROSCI.17-15-05858.1997

Schikorski, T., and Stevens, C. F. (2001). Morphological correlates of functionally defined synaptic vesicle populations. *Nat. Neurosci.* 4, 391–395. doi: 10.1038/86042

Shepherd, G. M. G., and Harris, K. M. (1998). Three-dimensional structure and composition of CA3→CA1 axons in rat hippocampal slices: implications for presynaptic connectivity and compartmentalization. *J. Neurosci.* 18, 8300–8310. doi: 10.1523/JNEUROSCI.18-20-08300.1998

Vukoja, A., Rey, U., Petzoldt, A. G., Ott, C., Vollweiter, D., Quentin, C., et al. (2018). Presynaptic biogenesis requires axonal transport of lysosome-related vesicles. *Neuron* 99, 1216–1232.e7. doi: 10.1016/j.neuron.2018.08.004

Watanabe, S., Liu, Q., Davis, M. W., Hollopeter, G., Thomas, N., Jorgensen, N. B., et al. (2013a). Ultrafast endocytosis at Caenorhabditis elegans neuromuscular junctions. *eLife* 2:e00723. doi: 10.7554/eLife.00723

Watanabe, S., Rost, B. R., Camacho-Pérez, M., Davis, M. W., Söhl-Kielczynski, B., Rosenmund, C., et al. (2013b). Ultrafast endocytosis at mouse hippocampal synapses. *Nature* 504, 242–247. doi: 10.1038/nature12809

Watanabe, S., Mamer, L. E., Raychaudhuri, S., Luvsanjav, D., Eisen, J., Trimbuch, T., et al. (2018). Synaptojanin and endophilin mediate neck formation during ultrafast endocytosis. *Neuron* 98, 1184–1197.e6. doi: 10.1016/j.neuron.2018.06.005

Watanabe, S., Trimbuch, T., Camacho-Pérez, M., Rost, B. R., Brokowski, B., Söhl-Kielczynski, B., et al. (2014). Clathrin regenerates synaptic vesicles from endosomes. *Nature* 515, 228–233. doi: 10.1038/nature13846

Zhai, R. G., and Bellen, H. J. (2004). The architecture of the active zone in the presynaptic nerve terminal. *Physiology* 19, 262–270. doi: 10.1152/physiol.00014.2004

Zhang, B., Koh, Y. H., Beckstead, R. B., Budnik, V., Ganetzky, B., and Bellen, H. J. (1998). Synaptic vesicle size and number are regulated by a clathrin adaptor protein required for endocytosis. *Neuron* 21, 1465–1475. doi: 10.1016/S0896-6273(00)80664-9

Conflict of Interest: The authors declare that the research was conducted in the absence of any commercial or financial relationships that could be construed as a potential conflict of interest.

frontiers in Synaptic Neuroscience

ORIGINAL RESEARCH
published: 15 April 2021
doi: 10.3389/fnsyn.2021.650334

Myosin V Regulates Spatial Localization of Different Forms of Neurotransmitter Release in Central Synapses

*Dario Maschi[1], Michael W. Gramlich[2] and Vitaly A. Klyachko[1]**

[1] *Department of Cell Biology and Physiology, Washington University School of Medicine, St. Louis, MO, United States,*
[2] *Physics Department, Auburn University, Auburn, AL, United States*

Synaptic active zone (AZ) contains multiple specialized release sites for vesicle fusion. The utilization of release sites is regulated to determine spatiotemporal organization of the two main forms of synchronous release, uni-vesicular (UVR) and multi-vesicular (MVR). We previously found that the vesicle-associated molecular motor myosin V regulates temporal utilization of release sites by controlling vesicle anchoring at release sites in an activity-dependent manner. Here we show that acute inhibition of myosin V shifts preferential location of vesicle docking away from AZ center toward periphery, and results in a corresponding spatial shift in utilization of release sites during UVR. Similarly, inhibition of myosin V also reduces preferential utilization of central release sites during MVR, leading to more spatially distributed and temporally uniform MVR that occurs farther away from the AZ center. Using a modeling approach, we provide a conceptual framework that unites spatial and temporal functions of myosin V in vesicle release by controlling the gradient of release site release probability across the AZ, which in turn determines the spatiotemporal organization of both UVR and MVR. Thus myosin V regulates both temporal and spatial utilization of release sites during two main forms of synchronous release.

Keywords: synaptic transmission, neurotransmitter release, myosin V, release site, vesicle docking, release probability, active zone

Edited by:
Thomas Kuner,
Heidelberg University, Germany

Reviewed by:
Stefan Hallermann,
Leipzig University, Germany
Ruud Toonen,
Vrije Universiteit Amsterdam,
Netherlands

****Correspondence:***
Vitaly A. Klyachko
klyachko@wustl.edu

Received: *07 January 2021*
Accepted: *03 March 2021*
Published: *15 April 2021*

Citation:
Maschi D, Gramlich MW and Klyachko VA (2021) Myosin V Regulates Spatial Localization of Different Forms of Neurotransmitter Release in Central Synapses. Front. Synaptic Neurosci. 13:650334. doi: 10.3389/fnsyn.2021.650334

INTRODUCTION

Neurotransmitter release is governed by the fusion of synaptic vesicles at specialized release sites at the synaptic active zone (AZ). The number, spatial distribution and temporal utilization of release sites are thought to play important roles in regulating synaptic transmission (Neher, 2010). Nanoscale imaging techniques have recently made it possible to detect individual vesicle release events in central synapses revealing the presence of multiple discrete release sites within the individual AZ. The number of release sites vary widely across the synapse population with estimates ranging from 2 to 18 per AZ (Tang et al., 2016; Maschi and Klyachko, 2017; Sakamoto et al., 2018). These release sites are distributed throughout the AZ with the nearest-neighbor distances of ∼80–100 nm, and co-localize with clusters of pre-synaptic docking factors (Tang et al., 2016). Importantly, release site usage is not uniform across the AZ, but rather forms a gradient decreasing from the AZ center to periphery with a ∼fourfold difference in basal release probability between most central and most peripheral release sites (Maschi and Klyachko, 2020). Release site usage is also dynamically regulated: vesicle release preferentially occurs at more central release sites during low activity, but shifts away from AZ center toward more peripheral release sites during high-frequency stimulation (Maschi and Klyachko, 2017).

In addition to uni-vesicular release (UVR) when a single vesicle fuses in response to an action potential, a multi-vesicular release (MVR) is also prominent in many central synapses (Korn et al., 1994; Tong and Jahr, 1994; Auger et al., 1998; Auger and Marty, 2000; Wadiche and Jahr, 2001; Singer et al., 2004; Christie and Jahr, 2006; Huang et al., 2010; Leitz and Kavalali, 2011, 2014; Rudolph et al., 2011; Malagon et al., 2016; Chanaday and Kavalali, 2018). This form of synchronous release involves fusion of two or more vesicles in response to a single action potential in the same synapse and has been suggested to serve a wide range of functions including enhancing synaptic reliability, controlling synaptic integration and induction of several forms of plasticity (Rudolph et al., 2015). We recently found that MVR events exhibit spatial and temporal patterns of organization which are determined by the gradient of release site properties across the individual AZs. MVR events are also often not perfectly synchronized and are spatially organized with the first of the two events comprising MVR located closer to the AZ center (Maschi and Klyachko, 2020).

Thus the spatiotemporal organization of the two major forms of synchronous release, UVR and MVR, are both determined by the distribution of release site properties across individual AZs. Yet the mechanisms controlling the heterogeneity and utilization of release sites at the AZ in central synapses are only beginning to emerge. Recent studies suggest that release site refilling and utilization requires actin and myosins (Miki et al., 2016, 2018; Mochida, 2020). Among actin-dependent motors, myosin V is the principle motor known to be associated with presynaptic vesicles in central neurons (Takamori et al., 2006). We recently found that acutely inhibiting myosin V markedly reduces the probability of release site reuse, and causes a profound vesicle anchoring/docking defect (Maschi et al., 2018). This is consistent with EM observations of reduced number of docked vesicles in neuroendocrine cells upon myosin V inhibition (Desnos et al., 2007). Our single-vesicle tracking measurements revealed that vesicles undergo cycles of docking and undocking at the AZ and that myosin V controls vesicle retention at release sites in an activity-dependent manner, but not vesicle transport to the release sites (Maschi et al., 2018). This function is consistent with myosin V's ability to interact with SNARE proteins, including syntaxin 1A and synaptobrevin, and its transition from a transporting motor to a tether in a calcium-dependent manner (Prekeris and Terrian, 1997; Ohyama et al., 2001; Krementsov et al., 2004; Watanabe et al., 2005). In addition to this role for myosin V in supporting vesicle retention at release sites, our previous results suggested that spatial distribution of release is altered by myosin V inhibition. Here we extended these studies to examine the role of myosin V in determining spatial landscape of release site usage across individual AZs and its role in regulating spatial properties of UVR and MVR.

RESULTS

The Spatial Localization of Vesicle Docking and Release in the Active Zone Is Myosin V -Dependent

Our previous studies have shown that utilization of individual release sites within an AZ forms a gradient decreasing from the AZ center to periphery (Maschi and Klyachko, 2020). In other words, more central release sites have a higher release probability (Pr) and thus are preferentially used. We also found that myosin V plays an important role in refilling of the individual release sites with vesicles (Maschi et al., 2018) and therefore it actively regulates the utilization (and thus the Pr) of release sites. To explore the role of myosin V in spatially shaping the release probability landscape across the AZs, we analyzed these datasets using three independent approaches.

First, we examined the effects of acute myosin V inhibition on the spatial distribution of individual release events in the AZ of hippocampal boutons. Briefly, our imaging approach takes advantage of a pH-sensitive indicator vGlut1-pHluorin targeted to the synaptic vesicle lumen (Voglmaier et al., 2006; Balaji and Ryan, 2007; Leitz and Kavalali, 2011) allowing detection of single vesicle release events with ∼20–27 nanometer precision (Maschi and Klyachko, 2017). Single release events were evoked in individual synapses at 37°C by 1 AP stimulation at 1Hz for 120 s (or, in some experiments, with a 10Hz train for 10 s, repeated at 0.05 Hz with the same total recording time and number of stimuli per frequency) with a frame duration of 40ms. We previously observed that acute inhibition of myosin V with a selective agent Myovin-1 (Myo-1) or with Pentabromopseudilin (PBP) caused an increase in the average distance from release events to AZ center, particularly during high-frequency (10 Hz) stimulation (Maschi et al., 2018). Indeed, such a shift in location of vesicle release upon myosin V inhibition is also evident in cumulative plots of vesicle locations, particularly during high-frequency synaptic activity (10Hz) (**Figure 1B** and **Supplementary Table 1**).

To understand how this spatial shift arises, we examined changes in release site utilization upon myosin V inhibition. Individual release sites within each bouton were defined using hierarchical clustering algorithms with a cluster diameter of 50 nm (**Figure 1A**) as we described previously (Maschi and Klyachko, 2017). The observed spatial distribution of vesicle fusion events reflects a ∼fourfold gradient of release site usage within the individual AZs, in which release sites with higher release probability are localized closer to the AZ center, while the sites that are used less frequently are localized more peripherally

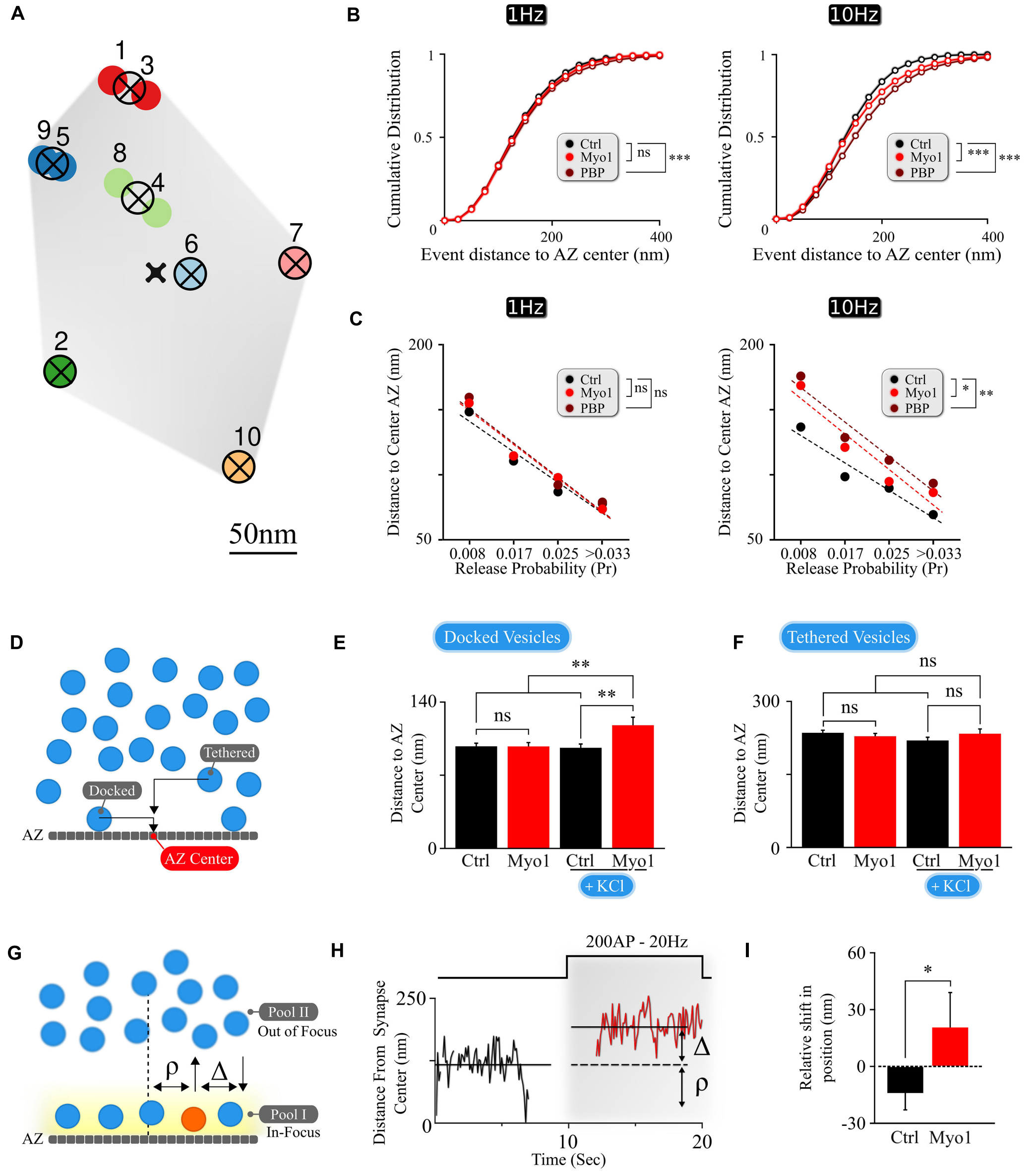

FIGURE 1 | The spatial localization of vesicle docking and release is myosin V -dependent. **(A)** Sample map of release events within a single hippocampal bouton evoked by 1 Hz stimulation, with 10 fusion events and 7 release sites. Hierarchical cluster analysis was used to define release event clusters [representing individual release sites (crossed circles)] with a clustering diameter of 50 nm. Events clustered into the same release site are shown by the same color. Scale bar = 50 nm. **(B)** Effects of myosin V inhibition with Myo-1 (red) or PBP (brown) on cumulative histograms of distances from vesicle release locations to the AZ center recorded at 1 Hz (left) or 10 Hz (right). **(C)** Effects of myosin V inhibition with Myo-1 (red) or PBP (brown) on the average distance to the AZ center for individual release sites for measurements at 1Hz (left) or 10 Hz (right), binned on the basis of their release probability. Note that errors of measurements are too small to be visible in this plot and the same data is presented as a bar-graph in **Supplementary Figure 1**. **(D)** Cartoon representation of the analysis of LaSEM measurements in individual hippocampal boutons in cultures depolarized (or not) by KCl application (55 mM) for 10 min in the presence or absence of Myo-1 (20 min), immediately followed by fixation. Vesicles were considered as 'docked' when the distance from the vesicle center to AZ was under 30 nm and 'tethered' when the distance was under 100 nm. **(E,F)** Effects of myosin V inhibition with Myo-1 on the localization of docked vesicles **(E)** or tethered vesicles **(F)**, with or without KCl depolarization, plotted as the mean distance to AZ center (nm). **(G)** Cartoon representation of vesicle re-docking measurements using single-vesicle tracking. Vesicle disappearance/reappearance events are caused by vesicle moving out-of/back in-to the focal plane near the AZ, due to vesicle shuttling between the docking locations at the AZ and the inner vesicle pool. The relative shift in vesicle position upon re-docking was determined as a difference (Δ) of vesicle initial docking location before disappearance (ρ) and its subsequent position after re-appearance/re-docking, both measured relative to the synapse center. **(H)** Example of a single vesicle track, measured relative to the synapse center, showing a disappearance/re-appearance event. Vesicle re-appeared (red) during a 200AP, 20 Hz stimulus train farther (by Δ nm) from the initial disappearance location (ρ). **(I)** Quantification of the shift in vesicle re-appearance/re-docking location. The shift in vesicle location was determined as a difference in the exponential fits to the aggregate distributions of vesicle locations (**Supplementary Figure 1C**) separated as toward synapse center versus toward periphery relative to the vesicle initial location (defined as a point of 0 shift). Errors are residual sum of squares from the exponential fits. Statistical significance was evaluated using KS-test of cumulative distributions toward the periphery for each condition. Two-sample *t*-test **(C,E,F)** or two-sample KS-test of cumulative distributions (B,I). $^*p < 0.05$, $^{**}p < 0.01$, $^{***}p < 0.001$, ns, not significant.

(**Figure 1C** and **Supplementary Figure 1A**). Most importantly, acute inhibition of myosin V resulted in a shift of release site utilization from the AZ center toward periphery at 1Hz and particularly at 10Hz stimulation (**Figure 1C**, **Supplementary Figures 1A,B**, and **Supplementary Table 1**), suggesting a role for myosin V in spatially controlling synaptic vesicle release. Given the overall reduction in vesicle release observed upon myosin V inhibition (Maschi et al., 2018), the increased distance to the AZ center, on average, for the groups of release sites with equivalent Pr in the presence of Myo1 or PBP is consistent with reduced utilization of central release sites upon myosin V inhibition.

To better understand the role of myosin V in spatial distribution of release, we analyzed the scanning electron microscopy (LaSEM) images of primary cultures of hippocampal neurons that were incubated (or not) with Myo-1 for 20 min and then acutely depolarized (or not) with 55 mM KCl for 10 min to induce vesicle release and recycling (Maschi et al., 2018). We examined both "docked" vesicles (previously defined as vesicles with the center within 30 nm from the AZ), and "tethered" vesicles (all vesicles with a center within 100 nm from the AZ) (**Figure 1D**). Within these definitions, we found that myosin V inhibition selectively affected the spatial distribution of "docked" vesicles, causing a significant increase in the distance of docked vesicles from the AZ center upon KCl stimulation (**Figure 1E** and **Supplementary Table 1**). This spatial shift in the localization of vesicles undergoing recycling and re-docking is in line with the spatial shift in the utilization of release sites caused by myosin V inhibition (**Figure 1C** and **Supplementary Table 1**). In contrast, no significant effect of Myosin V inhibition was observed in the absence of stimulation (**Figure 1E** and **Supplementary Table 1**), or within the "tethered" vesicle population in either condition (**Figure 1F** and **Supplementary Table 1**), suggesting the specific effects of myosin V inhibition on vesicle re-docking.

To further support these observations, we performed spatial analyses of the tracks of individual synaptic vesicles during recycling and docking in live hippocampal boutons, which we previously recorded in the presence (or not) of myosin V inhibitors (Maschi et al., 2018). Briefly, individual vesicles were labeled with a lipophilic FM-like dye SGC5 via compensatory endocytosis using a pair of stimuli at 100 ms. Single-vesicle tracking approach permitted us to follow the dynamics of individual vesicles with ∼20 nm precision. We previously observed that vesicles undergo rounds of docking/undocking and accompanying transitions between the membrane pool and the inner synaptic pool. These transitions are evident as disappearance and reappearance events when vesicles are moving out-of and in-to the field of view near the AZ (**Figure 1G**; Maschi et al., 2018). We thus quantified how myosin V inhibition affects the change in vesicle docking position by comparing its initial position before undocking/disappearance (ρ, **Figures 1G,H**) and its subsequent position upon reappearance/re-docking (i.e., relative shift in docking location: Δ, **Figures 1G,H**). We observed that in control conditions, vesicles have a tendency to re-appear slightly closer to the synapse center, resulting in a net negative re-appearance shift in location relative to their original docking location ($\Delta = -14 \pm 9$ nm, see Methods for definition) (**Figure 1I** and **Supplementary Table 1**), which is in line with the notion that more central release sites are preferentially utilized under basal conditions. In contrast, acute inhibition of myosin V with Myo-1 lead to a significant shift in relative vesicle re-docking position toward the synapse periphery upon re-appearance, resulting in a net positive re-appearance shift ($\Delta = +21 \pm 18$ nm; $P = 0.03$, two-tailed KS-test as compared to control condition) (**Figure 1I**, **Supplementary Figure 1C**, and **Supplementary Table 1**). PBP treatment also showed a tendency of vesicle re-docking to occur more peripherally, but this effect was not statistically significant (**Supplementary Figures 1C,D** and **Supplementary Table 1**). These differences could reflect the fact that the two agents have different mechanisms of action (Bond et al., 2013) and thus different effects on vesicle mobility: Myo-1 inhibits ADP release from actomyosin complex thus arresting myosin V on actin, while PBP reduces myosin-actin coupling by inhibiting ATP binding and hydrolysis; thus the two agents differentially affect the initial vesicle mobility state. Notably the vesicle tracking measurements are also not equivalent or directly comparable to the EM measurements or the vesicle release measurements above, because in our measurements vesicle displacement can only be defined relative to the 2D projection of the synapse center (as approximated by the geometric center of the total labeled recycling vesicle population, see section "Materials and Methods"), but not the actual AZ center. Nevertheless, the spatial shift in vesicle re-docking position toward synapse periphery upon myosin V inhibition supports the other two experimental observations that myosin V modulates the spatial location of vesicle docking.

Spatial Organization of MVR Events Is Myosin-V Dependent

Analyses presented above have thus far examined the effects of myosin V inhibition on spatial properties of UVR. Additionally, MVR is also a prominent form of synchronous release in central synapses. We previously showed that the spatiotemporal organization of MVR events is determined by the gradient of release probability across the AZ (Maschi and Klyachko, 2020). Since myosin V supports refilling of individual release sites, we hypothesized that it could also regulate the spatial organization of MVR. To approach this question, we detected and analyzed individual MVR events in the same dataset that we used for analyses of UVR events above, as we described previously (Maschi and Klyachko, 2020). Briefly, in our recordings the vast majority of MVR events are evident as a pair of fusion events evoked by a single AP. Depending on the distance between the two vesicle fusion events comprising an MVR, such events fall in two subcategories. First subcategory contains well-separated MVR events that have sufficient spatial separation to allow each event in the pair to be individually localized (Resolved events, **Figure 2A**). The second subcategory contain strongly overlapping, sub-diffraction distance MVR events that could not be resolved directly (Unresolved events), which required an alternative analysis approach comprising two separate steps. First, MVR event detection was achieved based on their amplitude (with a threshold set at two standard deviations above the mean quantal event amplitude determined individually for

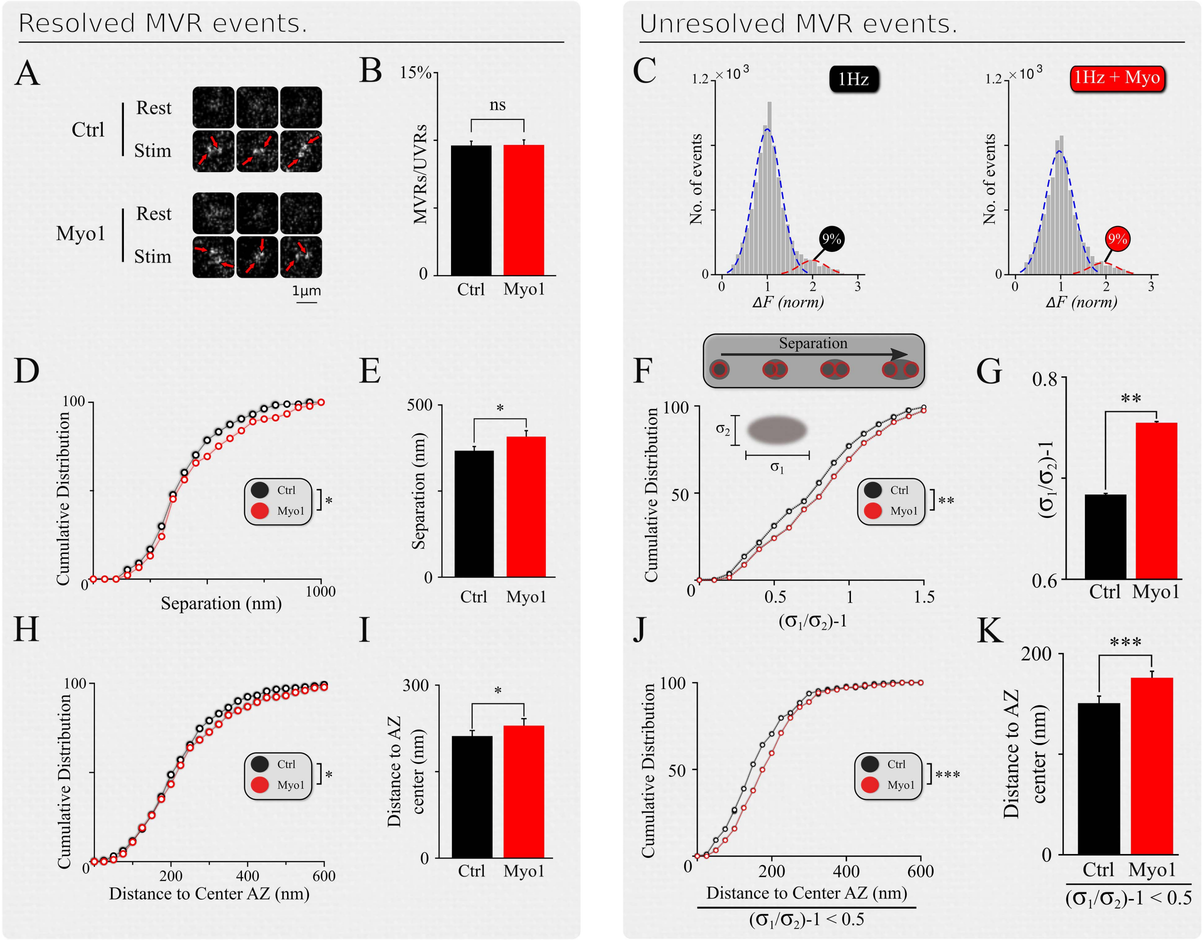

FIGURE 2 | Spatial organization of MVR events is myosin-V dependent. **(A)** Examples of resolved MVR events in different boutons in control conditions (top) and cultures treated with Myo1 (bottom) for 20 min. Scale bar = 1 µm. **(B,C)** Inhibition of myosin V with Myo-1 does not affect the ratio between detected MVR and UVR events for resolved **(B)** and unresolved **(C)** MVR events. For unresolved MVR events, ratio of UVR and MVR was calculated based on a multi-Gaussian fit **(C)**. **(D,E)** Effects of myosin V inhibition with Myo-1 on the distance between two fusion events comprising an MVR for resolved events. Cumulative plots **(D)** and mean values **(E)** are shown. **(F,G)** Same as **(D,E)** for unresolved MVR events. **(H,I)** Effects of myosin V inhibition with Myo-1 on the distance from MVR events to the AZ center for resolved events. Cumulative plots **(H)** and mean values **(I)** are shown. **(J,K)** Same as **(H,I)** for unresolved MVR events. Only a subpopulation of more symmetrical MVR events (asymmetry score < 0.5) were included in this analysis, because these more symmetrical events could be well-approximated by a single symmetrical Gaussian fit, making this analysis comparable to that of the resolved MVR events. Two-sample *t*-test (all panels). $^{*}p < 0.05$, $^{**}p < 0.01$, $^{***}p < 0.001$, ns, not significant.

each bouton). Second, the identified MVR events were analyzed on the basis of asymmetry considerations, using an asymmetric Gaussian model fit to determine the width (sigma) of the Gaussian fit in the maximal (longitudinal, $\delta1$) direction and the minimal (transverse, $\delta2$) direction (**Figure 2F**, insert). The ratio $\delta1/\delta2{-}1$ (asymmetry score) represents asymmetry of the double-event image, which correlates with the distance between the two sub-diffraction events forming the image (DeCenzo et al., 2010). We have previously shown that the two subcategories have the same spatiotemporal features and represent the same biological phenomenon of MVR (Maschi and Klyachko, 2020).

Inhibition of myosin V did not strongly affect the UVR/MVR event ratio for either population of resolved or unresolved MVR events (Myo-1: **Figures 2B,C**; PBP: **Supplementary Figures 2B,C**, and **Supplementary Table 1**). However, several spatial features of MVR were affected by myosin V inhibition. First, the separation distance between the two releases comprising an MVR event was significantly increased in the presence of Myo-1 or PBP, for both resolved and unresolved MVR events (Myo-1: **Figures 2D–G**; PBP: **Supplementary Figures 2D–G** and **Supplementary Table 1**). Second, both resolved and unresolved MVR events occurred further away from the AZ center when myosin V was inhibited (Myo-1: **Figures 2H–K**; PBP: **Supplementary Figures 2H–K** and **Supplementary Table 1**). These results are consistent with the above notion that myosin V inhibition causes a shift in utilization of release sites away from the AZ center.

To confirm and further explore the role of myosin V in the spatial aspects of release site utilization we analyzed the reuse of the release sites engaged in MVR. We observed that central release sites engaged in MVR events show a significant reduction of reuse upon myosin V inhibition, while the more peripheral release sites were not strongly affected (**Figure 3A**, **Supplementary Figure 3A**, and **Supplementary Table 1**). This observation thus provides a mechanistic basis for the increased distance from the MVR events to the AZ center and the correspondingly increased spatial separation within the MVR event pair that we observed above (**Figure 2** and **Supplementary Table 1**).

This observation also provides a testable prediction. We previously found that release sites closer to the AZ center are more likely to harbor UVR as well as MVR events during observation period (representing spatial "overlap" of UVR and MVR events). Thus reduced utilization of the central release sites upon myosin V inhibition predicts that the spatial overlap of UVR and MVR events at the same release sites is also reduced. To test this prediction, we analyzed the probability that the same release site is engaged in UVR and MVR during our observation time. As predicted, the overlap of MVR and UVR events at the same release sites was significantly reduced in the presence of Myo-1 or PBP (**Figures 3B,C**, **Supplementary Figures 3B,C**, and **Supplementary Table 1**).

Therefore, by reducing the preferential utilization of central release sites during MVR, inhibition of Myosin V not only results in increased distance from MVR events to the AZ center and increased spatial separation within individual MVR events, but it also reduces spatial overlap of MVR with the UVR events.

Inhibition of Myosin V Reduces Temporal Separation Within MVR Events

The pairs of release events comprising MVR are often not perfectly synchronized with each other, but exhibit a slight temporal separation on the order of 1–5 milliseconds (Auger et al., 1998; Auger and Marty, 2000; Crowley et al., 2007; Rudolph et al., 2011; Malagon et al., 2016; Maschi and Klyachko, 2020). We recently showed that this temporal separation arises because the first event in the MVR pair occurs closer to the AZ center, while the second event in the pair occurs more peripherally with a slight delay (Maschi and Klyachko, 2020). The extent of this temporal separation depends on the difference in radial distance of the two events comprising MVR from the AZ center and correlates with the distance between the two events (**Figure 4B** and **Supplementary Table 1**). Because the spatial localization of MVR events is altered by myosin V inhibition, we examined how the temporal separation is affected. To estimate the temporal separation within the MVR events we measured the amplitude differences between the two events in the same frame, which is an established approach to quantify the temporal separation (Maschi and Klyachko, 2020; **Figure 4A**). Here we found that in the presence of Myo-1 (**Figures 4D,E**) or PBP (**Supplementary Figures 4A,B**), the amplitude differences within the individual MVR events were no longer dependent on their relative distance (as compared to control, **Figures 4B,C**, and quantified in **Figure 4F**, **Supplementary Figure 4C**, and **Supplementary Table 1**). We note that a component of the amplitude differences likely arises from an uncertainty in determining the fusion event amplitude; which we previously estimated to be ∼10%. Thus, the amplitude differences remaining in our measurements in the presence of Myo-1 or PBP could be, to a large extent, accounted for by the intrinsic uncertainty in our measurements. These results suggest that inhibition of myosin V reduces the temporal separation within the MVR events. Thus myosin V regulates both spatial and temporal organization of MVR events as well as UVR.

DISCUSSION

Docking of synaptic vesicles at the release sites within the AZ is an essential mechanism controlling strength and timing of synaptic transmission. We previously showed that vesicle-associated molecular motor myosin V is a key regulator of release site refilling during synaptic activity by controlling vesicle anchoring and retention at the release sites. Here we extend these studies to demonstrate that myosin V also regulates the spatial organization of vesicle docking across the AZ during two main forms of synchronous release, the UVR and MVR. This is supported by three key observations: (i) Acute inhibition of myosin V shifts location of vesicle docking away from the AZ center toward periphery. Consequently the utilization of release sites during UVR also shifts away from the AZ center when myosin V is inhibited. (ii) Inhibition of myosin V reduces utilization of central release sites by MVR events. Consequently MVR events occur further away from the AZ center and have a larger separation distance within the event pair; (iii) Inhibition of myosin V reduces the temporal separation within the MVR events. Thus by regulating spatio-temporal organization of UVR and MVR events across the AZ, myosin V actions represent a mechanism that fine-tunes neurotransmitter release.

Myosin V Role in the Spatiotemporal Regulation of UVR and MVR

The spatial and temporal utilization of release sites during both UVR and MVR follows complex patterns that are determined by the gradient of release probability (Pr) across the AZ. Yet such apparent complexity often arises from simpler underlying principles thus posing a central question: given the function of Myosin V in vesicle anchoring/docking at release sites, could the observed effects of myosin V inhibition on release site utilization be explained simply by changes in the gradient of release site Pr? To approach this question, we created a basic model representation of an AZ with 12 discrete release sites arranged to form a center-to-periphery gradient of release probability (Pr) (**Schematic 1A**). Because the number of release sites per AZ vary widely across synapse population [in the range of 2–18 (Tang et al., 2016; Maschi and Klyachko, 2017; Sakamoto et al., 2018)], the model was formulated not to depend on the precise number of release sites, but rather on the gradient of release site Pr (central/peripheral) across the AZ (see Materials and Methods for model formulation). First, the model shows that reducing the center-to-periphery gradient of Pr across the AZ results in increased distance of UVR events to the AZ center (**Schematic 1B**), which is what we observed experimentally as a result of myosin V inhibition. Likewise, for the MVR events, the

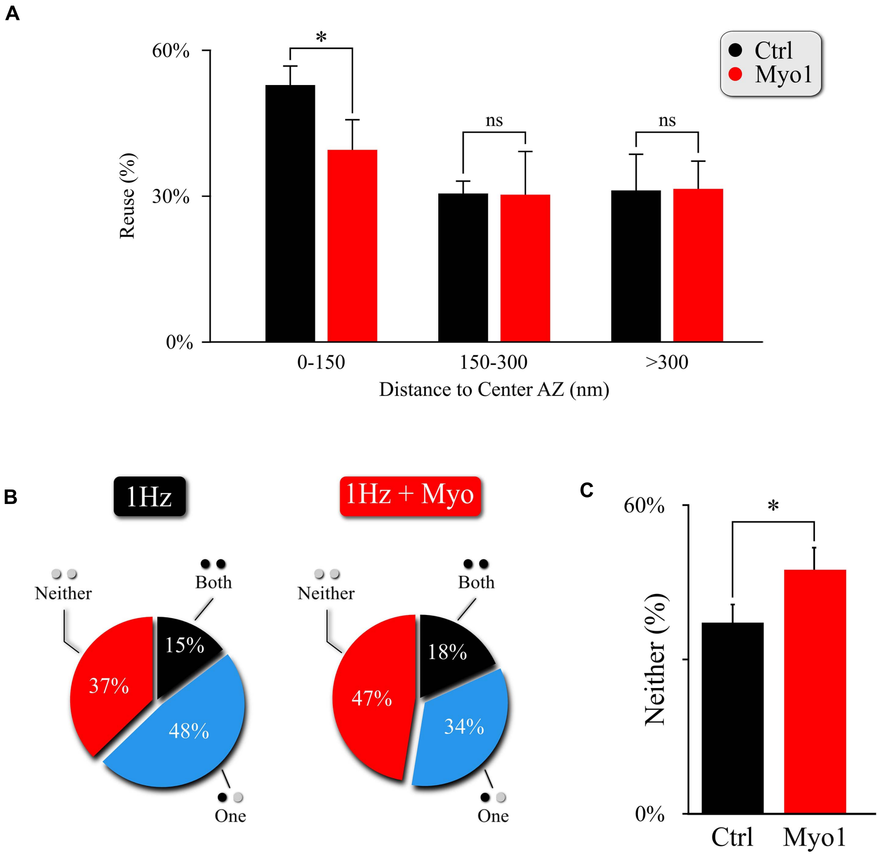

FIGURE 3 | Myosin V regulates utilization of release sites engaged in MVR. **(A)** Effect of myosin V inhibition with Myo-1 (red) on reuse of release sites engaged in MVR events. Reuse was quantified as the percentage of release sites engaged in MVR that are reused at least once during the 120 s observation period by either other MVR or UVR events. The reuse probability is highly dependent on the distance to AZ center; to account for this variability, we use a paired *t*-test with data binning at 50 nm. **(B,C)** Effect of myosin V inhibition with Myo-1 (red) on the spatial overlap of MVR and UVR events determined by the proximity analysis. Percentages of MVR events in which none (red), one (blue), or both (black) events in the pair occurred within ± 25nm of at least one UVR event (i.e., at the same at release site) during the observation period **(B)**, and quantification of the percentage of no overlap of MVR and UVR events **(C)**. Two-sample *t*-test **(A)** or Barnard's test **(C)**. $^{*}p < 0.05$, ns, not significant.

model shows that reducing the Pr gradient also leads to increased spatial separation of the two fusion events comprising an MVR (**Schematic 1C**), which we also observed following myosin V inhibition. Thus, the simplest working model that accounts for the observed spatial effects of myosin V inhibition is that by shifting utilization of release sites from more central to more peripheral, myosin V inhibition acts by reducing the Pr gradient effectively spreading the release to a larger area of the AZ.

The conceptual relationship between the steepness of the Pr gradient and spatial localization of release events also holds under conditions when Pr gradient becomes steeper than normal. For example, we previously observed that buffering intraterminal calcium with EGTA increased utilization of central release sites (thus making the center-to-periphery Pr gradient steeper). EGTA also caused a shift in spatial localization of UVR events toward the AZ center and reduced spatial separation within the MVR events (Maschi and Klyachko, 2017, 2020), both of which are recapitulated by the model (**Schematic 1B,C**).

Moreover, this framework also recapitulates the more complex relationship between the Pr gradient and the temporal features of MVR. Interestingly, both inhibition of myosin V and buffering intraterminal calcium with EGTA have the same effect of decreasing the temporal separation within MVR events, while having opposing effects on the Pr gradient. While appear paradoxical on the first glance, these results are also conceptually explained by our model. Specifically, our previous observations suggested that temporal separation within MVR events results from the first event occurring closer to the AZ center, while the second event in the pair occurring with a short 1–5 ms delay at a more peripheral site. This temporal separation thus depends on the difference in radial distance to AZ center of two fusion events comprising an MVR. Our model shows that this parameter has a bell-shape curve (**Schematic 1D**), reaching a maximum at ∼threefold to fourfold gradient of Pr, which is similar to experimentally observed value in control conditions. Therefore, either inhibition of myosin V or calcium buffering with EGTA, while having opposite effects on the steepness of the Pr gradient, both drive it away from the optimal value, resulting in reduced temporal separation. This temporal control, in combination with regulating spatial separation within the MVR events, may allow

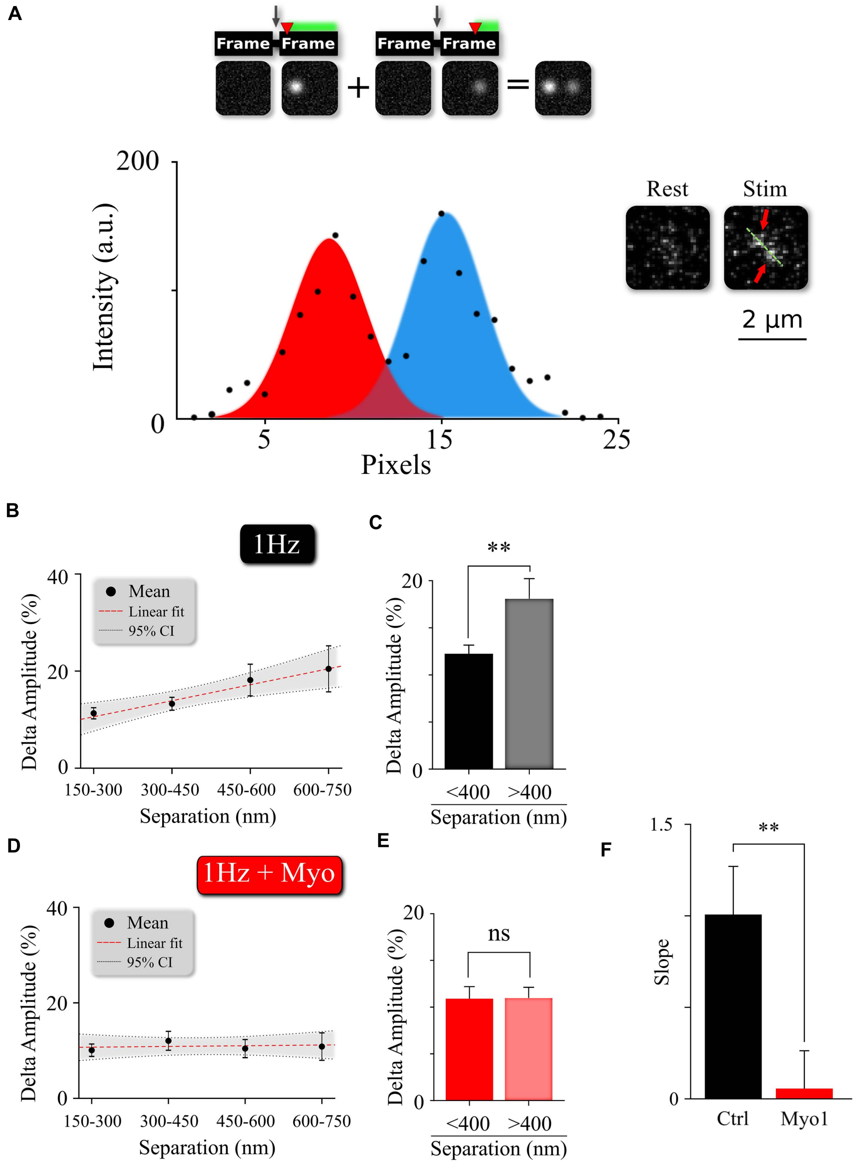

FIGURE 4 | Myosin V regulates temporal separation within MVR events. **(A)** Sample image and intensity profile of an MVR event with noticeable difference in intra-event amplitude. Top, Insert: A cartoon diagram shows the relationship between time delay (red arrow) of the second fusion after an action potential and the resulting amplitude difference within an MVR event pair recorded together in the same frame. **(B,C)** Amplitude difference of the two events comprising MVR as a function of intra-event distance. Linear fit **(B)** and *t*-test of pooled data **(C)** are shown. **(D,E)** Effect of myosin V inhibition with Myo-1 on the amplitude difference of the two events comprising MVR as a function of intra-event distance. Linear fit **(D)** and *t*-test of pooled data **(E)** are shown. **(F)** Quantification of the effects of Myo-1 in panel **(D)** assessed by comparing the slopes of the correlations in **(B,D)**. Two-sample *t*-test **(C,E)**. One-way analysis of covariance **(F)**. $^{**}p < 0.01$; ns, not significant.

myosin V to fine-tune the quantal size by adjusting the duration of neurotransmitter release during MVR while engaging spatially distinct subsets of postsynaptic receptors.

Myosin V and the Gradient of Release Site Properties

Our results do not necessarily imply that myosin V selectively serves as a docking factor only for the central release sites; the effect of myosin V inhibition could simply be more apparent for the central release sites because they are used much more frequently under normal conditions, while the limited duration of observation masks the effect on peripheral release sites which are used much less frequently. Thus we speculate that additional or alternative mechanisms may exist that makes usage of central release sites more frequent. One possible mechanism suggested by our previous study is the presence of center-to-periphery gradient of calcium elevation following an action potential (Maschi and Klyachko, 2020). Such calcium gradient could in turn control myosin V-dependent vesicle retention at release

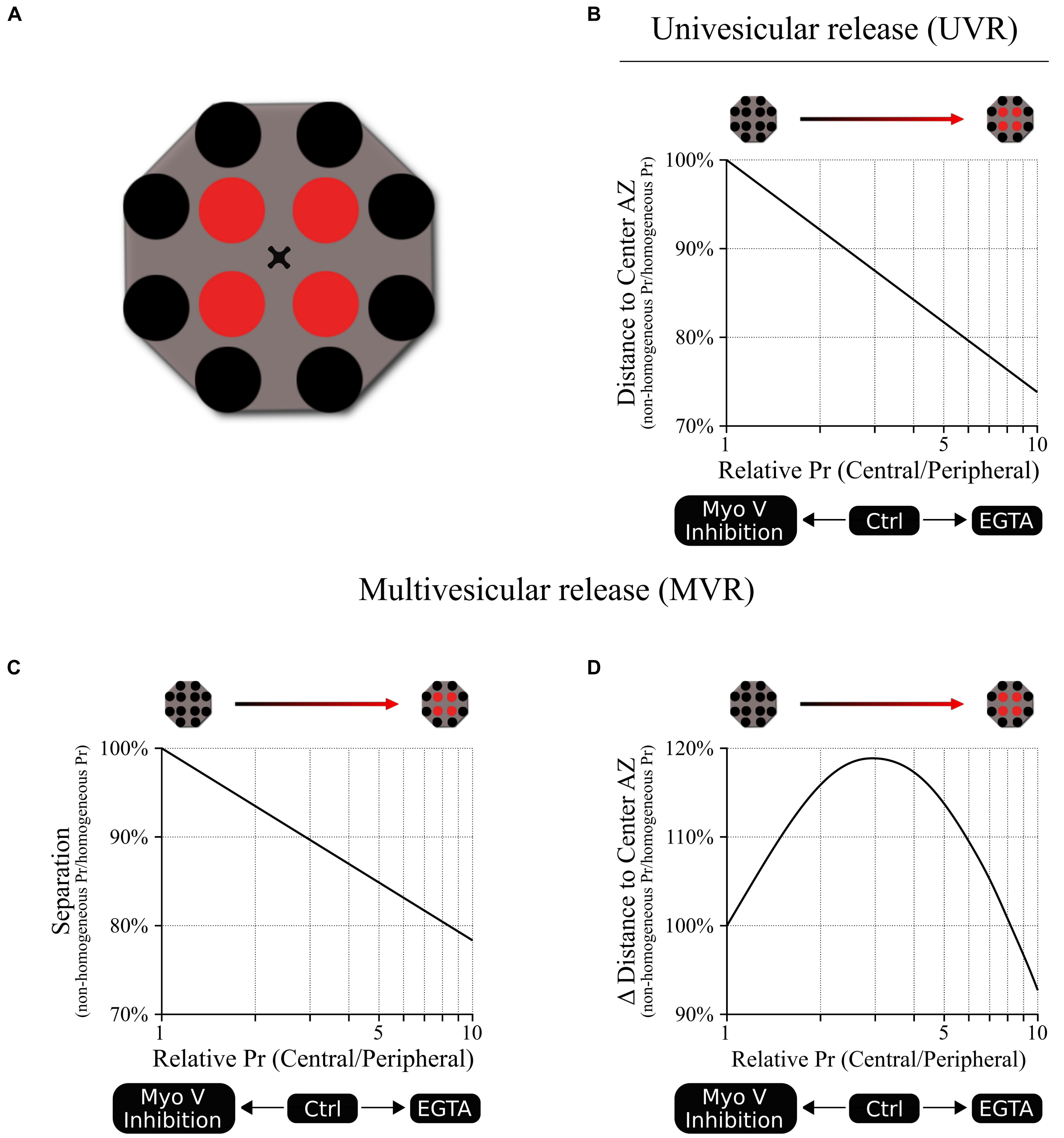

SCHEMATIC 1 | A model linking release site Pr gradient and spatiotemporal features of UVR and MVR events. **(A)** A cartoon representation of the model illustrating spatial distribution of 12 release sites within a single AZ. We used a Monte Carlo simulation to model the probability that a release event occurs in a given release site based on the release probability of the individual release sites. For this model, a shared probability was assigned for the four central release sites (red) and a different but also shared probability was assigned for the 8 peripheral release sites (black). In other words, the model could be represented by two concentric donuts with two different Pr values. Ten different central/peripheral Pr ratios (i.e., Pr gradients) were used (from 1 to 10); for each Pr ratio we run 1 million simulations, resulting in the outcome of 10 million points for each plot shown. The results were normalized to the values obtained at the Pr ratio = 1 (homogeneous distribution of Pr across the AZ). **(B)** Release events occur at shorter distances from the AZ center as the central/peripheral Pr ratio increases; in other words, the utilization of more central release sites increases as the Pr gradient increases. The opposite effect occurs when Pr ratio decreases, leading to larger distances from release events to the AZ center, representing an increased utilization of more peripheral release sites. **(C)** Spatial separation within the pair of release events comprising an MVR decreases as the central/peripheral Pr gradient increases. The opposite occurs when Pr gradient decreases, leading to increased spatial separation within the MVR events, as we observed when myosin V was inhibited. **(D)** Temporal separation between the two release events comprising an MVR depends on the difference in their radial distances to AZ center. This parameter has a bell-shape dependence on the central/peripheral Pr ratio. Either increase or decrease of the Pr ratio from the optimal value around 3–4 leads to smaller differences in the distances to the AZ center for the two events comprising an MVR. This predicts a reduced temporal separation of the two events comprising an MVR with either increase or decrease in the Pr gradient, as observed experimentally with EGTA or inhibition of myosin V, respectively.

sites thus creating a center-to-periphery gradient of release site Pr. Indeed, Myosin V function is calcium-dependent; calcium elevation drives transition of myosin V from a transporting motor to a tether and also regulates myosin V association with the SNARE proteins (Prekeris and Terrian, 1997; Ohyama et al., 2001; Rose et al., 2003; Krementsov et al., 2004; Watanabe et al., 2005; Eichler et al., 2006). Thus the differences in spatial utilization of release sites could be driven by the gradient of calcium elevation in the synaptic bouton following an AP, which determines the strength or duration of myosin V association with a release site. While the mechanistic basis for the gradient of calcium rise across the AZ will require further investigation, a number of possible mechanisms have been suggested in previous studies. A higher calcium elevation in the AZ center can simply result from larger density of release sites (assuming each is associated with a calcium channel) at the AZ center vs. periphery. Differential calcium channel mobility in the center vs. periphery of the AZ (Schneider et al., 2015) could also contribute to different stability of channel association with the release sites or its coupling with the vesicle (Eggermann et al., 2011; Miki et al., 2017). Alternatively, or additionally, a gradient of release site properties could arise from other, calcium/myosin V- independent mechanisms. For instance clusters of presynaptic proteins that are believed to represent the structural correlates of release sites exhibit a large degree of heterogeneity in size and composition across the AZ (Schneider et al., 2015; Tang et al., 2016; Glebov et al., 2017) presumably due to differential enrichment and mobility of many critical components, such as Bassoon, RIM, Munc13, Munc18, and Syntaxin-1 (Smyth et al., 2013; Schneider et al., 2015; Tang et al., 2016; Bademosi et al., 2017; Glebov et al., 2017). Clusters of several of these critical proteins are detected predominately near the AZ center (Tang et al., 2016), suggesting that more peripheral clusters are smaller and below the detection limit.

In summary, by modulating the landscape of release probability across the AZ, myosin V fine-tunes the spatio-temporal dynamics of neurotransmitter release during both UVR and MVR events to dynamically shape synaptic transmission.

MATERIALS AND METHODS

Neuronal Cell Cultures

Neuronal cultures were produced from the hippocampus of E16-17 rat pups of mixed gender as previously described (Peng et al., 2012; Maschi et al., 2018). Hippocampi were dissected from E16-17 pups, dissociated by papain digestion, and plated on coated glass coverslips containing an astrocyte monolayer. Neurons were cultured in Neurobasal media supplemented with B27. All animal procedures conformed to the guidelines approved by the Washington University Animal Studies Committee.

Lentiviral Infection

VGlut1-pHluorin was generously provided by Drs. Robert Edward and Susan Voglmaier (UCSF) (Voglmaier et al., 2006). Lentiviral vectors were generated by the Viral Vectors Core at Washington University. Hippocampal neuronal cultures were infected at DIV3.

Fluorescence Microscopy

Neurotransmitter Release Measurements

All experiments were conducted at 37°C within a whole-microscope incubator (*In vivo* Scientific) at DIV16–19 as described previously (Maschi et al., 2018). Neurons were perfused with bath solution (125 mM NaCl, 2.5 mM KCl, 2 mM CaCl2, 1 mM MgCl2, 10 mM HEPES, 15 mM Glucose, 50 mM DL-AP5, 10 mM CNQX, pH adjusted to pH 7.4). Fluorescence was excited with a Lambda XL lamp (Sutter Instrument) through a 100x 1.45 NA oil-immersion objective and captured with an EMCCD camera (Hamamatsu) or cooled sCMOS camera (Hamamatsu). Focal plane was continuously monitored, and focal drift was automatically adjusted with 10 nm accuracy by an automated feedback focus control system (Ludl Electronics). Field stimulation was performed by using a pair of platinum electrodes and controlled by the software via Master-9 stimulus generator (A.M.P.I.). Images were acquired using two frames with an acquisition time of 40ms, one 45ms before stimulation and one coincidently (0ms delay) with stimulation.

Single-Vesicle Tracking

Sparse vesicle labeling and functional synapse localization were performed following our previously developed procedures (Maschi et al., 2018). The same bath solution as above was used for the dye loading and imaging, except 0.2 mM $CaCl_2$, 1.0 mM $MgCl_2$ were used to wash excess dye from the sample. 10 μM SGC5 (Biotium) were added to the bath solution for the dye loading step. Samples were imaged for 50–70 s, at an exposure rate of 80 ms (with a total frame rate of 10Hz). Samples were stimulated for 10 s at 20 Hz with a 10 s delay after the first frame.

Pharmacology

MyoVin-1 (Millipore), Pentabromopseudalin (PBP, Fisher Scientific) or EGTA-AM (Millipore) were diluted in DMSO (Sigma-Aldrich) and stored at −20°C. Samples were incubated in imaging solution with 30 μM Myo-1 for 5–10 min or 5 μM PBP for 5 min, or 250 μM EGTA-AM for 20 min before dye loading. The effective final DMSO concentration was < 0.5%. Extended exposure to MyoVin-1 or PBP caused cell death, thus the bath solution during the experiment did not include Myo-1 or PBP. Our control measurements indicated that continuous presence of these blockers during the experiments did not have additional effects on vesicle motility beyond the effects of pre-incubation (data not shown).

Large-Area Scanning Electron Microscopy (LaSEM)

Cultures were fixed in a solution containing 2.5% glutaraldehyde and 2% paraformaldehyde in 0.15 M cacodylate buffer with 2 mM CaCl2, pH 7.4 that had been warmed to 37°C for 1 h. In experiments with KCl-induced depolarization, fixation was performed immediately following KCl application, and care was taken to complete the fixation procedure within a few seconds. Coverslips were rinsed in cacodylate buffer 3 times for 10 min each, and subjected to a secondary fixation for 1 h in 2% osmium tetroxide/1.5% potassium ferrocyanide in cacodylate buffer for

1 h, rinsed in ultrapure water 3 times for 10 min each, and stained in an aqueous solution of 1% thiocarbohydrazide for 1 h. After this, the coverslips were once again stained in aqueous 2% osmium tetroxide for 1 h, rinsed in ultrapure water 3 times for 10 min each, and stained overnight in 1% uranyl acetate at 4°C. The samples were then again washed in ultrapure water 3 times for 10 min each and en bloc stained for 30 min with 20 mM lead aspartate at 60°C. After staining was complete, coverslips were briefly washed in ultrapure water, dehydrated in a graded acetone series (50, 70, 90, and 100% x2) for 10 min in each step, and infiltrated with microwave assistance (Pelco BioWave Pro, Redding, CA, United States) into Durcupan resin. Samples were flat embedded in a polypropylene petri dish and cured in an oven at 60°C for 48 h. Post resin curing, the coverslips were exposed with a razor blade and etched off with concentrated hydrofluoric acid. Small pieces of the resin containing the cells was then cut out by saw and mounted onto blank resin stubs before 70 nm thick sections were cut in the cell culture growing plane and placed onto a silicon wafer chips. These chips were then adhered to SEM pins with carbon adhesive tabs and large areas ($\sim 330 \times 330\ \mu$m) were then imaged at high resolution in a FE-SEM (Zeiss Merlin, Oberkochen, Germany) using the ATLAS (Fibics, ON, Canada) scan engine to tile large regions of interest. High-resolution tiles were captured at $16{,}384 \times 16{,}384$ pixels at 5 nm/pixel with a 5 μs dwell time and line average of 2. The SEM was operated at 8 KeV and 900 pA using the solid-state backscatter detector. Tiles were aligned and export using ATLAS 5.

Image and Data Analysis

Localization of UVR events

The fusion event localization at subpixel resolution was performed using MATLAB code based on the uTrack software package (Jaqaman et al., 2008; Aguet et al., 2013). Release sites were defined using hierarchical clustering performed in MATLAB as we described previously (Maschi and Klyachko, 2017, 2020; Maschi et al., 2018). We previously found that the observed clusters do not arise from random distribution of release events, but rather represent a set of defined and repeatedly reused release sites within the AZs (Maschi and Klyachko, 2017).

Localization of MVR Events

Localization of resolved MVR events was performed using a mixture-model multi-Gaussian fit using in-built functions in uTrack (Jaqaman et al., 2008; Aguet et al., 2013) as we described previously (Maschi and Klyachko, 2020).

Unresolved MVR events were identified based on the event amplitude. The single event amplitude and its variability were determined for each bouton individually. Photobleaching was accounted for by fitting the event intensity changes over time. The threshold for MVR event detection was set at two standard deviations above the mean single event amplitude determined individually for each bouton. Localization of unresolved MVR events was determined using an asymmetrical Gaussian model fit based on the minimization of the residuals as described in (Maschi and Klyachko, 2020).

Release site reuse and release probability

Release probability of individual release sites was calculated based on the number of release events detected per release site and divided by the duration of the observation period. For MVR events, reuse was defined more broadly as the probability that the release site engaged in MVR is reused at least once during the 120 s observation period by either other MVR or UVR events.

Event proximity analysis

To determine probability of spatial overlap of MVR and UVR events at the same release sites during the observation period, a proximity analysis was performed in which overlap was defined as having at least one UVR event occurring within 25 nm of an MVR event during observation period.

EM analyses

Synapse identification and vesicle localization analysis were performed as described in Maschi et al. (2018). Distances to the AZ center were measured from the projection of the vesicle position on the AZ plane. "Docked" vesicles were defined as those with the distance from the membrane to the vesicle center less than 30 nm and "tethered" vesicle as those with the distance less than 100 nm.

Single-vesicle tracking

Individual vesicle track positions (x,y) were obtained using the MATLAB code based on uTrack software (Jaqaman et al., 2008) following our previously developed procedures (Forte et al., 2017; Gramlich and Klyachko, 2017; Maschi et al., 2018). Quantification of vesicle motion was performed using the three-frame moving average of vesicle position to mitigate the effects of noise. Vesicle tracks were converted from two-dimensional (x,y) spatial locations in the imaging plane to a one-dimensional radial distance (s) from the synapse center (x_s, y_s), $s = \text{sqrt}\ [(x - x_s)^2 + (y{-}y_s)]^2$. Synapse center was defined as a center of mass of the synapse image obtained following labeling the entire vesicle population with a strong stimulus of 400 APs at 20 Hz. When more than one disappearing and/or re-appearing tracks were observed sequentially in a given synapse, all tracks associated with the same bouton were grouped together to determine the criterion for analysis described below.

To ensure that only re-docking vesicles were included in the analysis, vesicles were accepted for the analysis based on the following conditions: [i] a vesicle must be localized within 600 nm of a synapse center within the first 20 frames and must be observed for at least 50 frames before disappearing; this condition excluded a small subset of vesicles that can "re-appear" in the neighboring synapses via intersynaptic vesicle exchange (Gramlich and Klyachko, 2017) [ii] Appearance events were only considered in the same subset of synapses in which vesicle disappearance was observed first, and re-appearing vesicle must be observed for at least 20 frames afterward to be included; the definitions of disappearance and reappearance events were the same as we described previously (Maschi et al., 2018); [iii] if multiple sequential re-appearance events occur for the same vesicle, each event is counted as a new re-appearance with the same requirements. Synapses where more than one vesicle was observed simultaneously were excluded from analysis. These restrictions combined with the low labeling probability of one vesicle per synapse in the vast majority of synapses under our stimulation conditions (Peng et al., 2012; Gramlich and Klyachko, 2017) ensured consideration of re-docking vesicles only.

Relative shift in vesicle location upon disappearance and re-docking was quantified as the difference in radial distances of vesicle re-appearance and disappearance positions. Average vesicle position before disappearance was quantified for the first five seconds of the track (ρ). Average position for the re-appeared vesicle was quantified for the entire time the track re-appeared ($t > 2$ sec). All vesicle shifts for each condition (Ctrl, Myo-1, PBP) were pooled and binned into 25 nm bin-size distributions centered around 0 nm. Each side of the distribution (representing a shift toward or away from the synapse center) was fit separately to an exponential decay and the overall shift was determined as the difference in the fit time courses. To evaluate the statistical significance of the small shift in vesicle position after re-appearance under different conditions, we used KS-tests of cumulative distributions toward the periphery for each condition. Cumulative distributions were obtained for vesicles shifts starting from no-shift and toward the periphery, because cumulative distributions more accurately measure small changes in distributions.

Vesicle disappearance and appearance oversampling correction

Vesicle disappearance and appearance distributions were sampled at a rate of 10 frames per second. However, the typical disappearance rate was on the order of 1 vesicle per second (1 vesicle per 10 frames) resulting in significant oversampling. Thus, we averaged the oversampled distributions with a five-frame moving average and plotted every fifth data point. Further, we performed statistical analysis on the averaged data to prevent over-sampling bias of the statistics.

Computational Model for the Spatial Distribution of Vesicle Release

A basic model of vesicle release across the AZ was built assuming a fixed distribution of release sites through the AZ. 12 discrete release sites were distributed across the AZ in two groups (central and peripheral) with four central release sites positioned symmetrically at a distance D to the AZ center and eight peripheral cites at twice the distance (2xD) (**Schematic 1A**). The model was formulated in terms of the gradient of release site Pr (central/peripheral) across the AZ. Pr of individual release sites was assigned to form a center-to-periphery gradient with a shared probability assigned to the four central release sites and a different but also shared probability assigned for the 8 peripheral release sites. The model could thus be represented by two concentric donuts with two different Pr values. Monte Carlo simulations were used to model the probability that a release event occurred in a given release site based on the release probability of the individual release sites. We assumed no interaction of any kind between consecutive fusion events in the same or different release sites and therefore the probability was calculated independently for each fusion event. Ten different central/peripheral Pr ratios (i.e., Pr gradients) were used (from 1 to 10); for each Pr ratio we ran 1 million simulations, with a combined total of 10 million points for each plot shown. The results were normalized to the values obtained at the Pr ratio = 1 (homogeneous distribution of Pr across the AZ).

The MatLab code of the model is freely available through GitHub.

Data Inclusion and Exclusion Criteria

A minimum of 5 detected release events per bouton was required for all analyses.

Statistical Analyses

Statistical analyses were performed in Matlab. Statistical significance was determined using two tailed Student's t-test, Kolmogorov-Smirnov (K-S) test, or a Barnard's test where appropriate. The Myo1 and PBP conditions were independent experiments; all comparisons were performed between 2 datasets, CT and Myo1, and supported by additional comparison of CT and PBP. With this experimental design, adjustment for multiple comparisons was not performed because we did not believe false positives/type-1 errors would be a significant contribution to overall error. Indeed, testing for overall effects with adjustment for multiple comparisons was consistent with all major conclusions obtained.

Data is reported as mean ± SEM; or ± 95% confidence interval; or ± residual sum of squares from fits to distributions, as indicated in the text, figure legends and **Supplementary Table 1**. $p < 0.05$ was considered statistically significant. The number of experiments reported reflects the number of different cell cultures tested and is provided in **Supplementary Table 1**. Statistical tests used to measure significance are indicated in each figure legend along with the corresponding significance level (p value). Analysis of the samples was not blinded to condition. Randomization and sample size determination strategies are not applicable to this study and were not performed.

DATA AVAILABILITY STATEMENT

The raw data supporting the conclusions of this article will be made available by the authors, without undue reservation.

ETHICS STATEMENT

The animal study was reviewed and approved by Washington University Animal Studies Committee.

AUTHOR CONTRIBUTIONS

DM, MG, and VK conceived the experiments, contributed analysis tools, and wrote the manuscript. DM and MG performed the experiments and analyzed the data. VK supervised the project and provided funding for the project. All authors contributed to the article and approved the submitted version.

FUNDING

This work was supported in part by a grant to VK from NINDS (R35 NS111596) and funds from Department of Cell Biology and Physiology at Washington University.

ACKNOWLEDGMENTS

We acknowledge the assistance of Matthew Joens and Dr. James Fitzpatrick at the Washington University Center for Cellular Imaging in EM studies.

SUPPLEMENTARY MATERIAL

The Supplementary Material for this article can be found online at: https://www.frontiersin.org/articles/10.3389/fnsyn.2021.650334/full#supplementary-material

Supplementary Figure 1 | Spatial effects of myosin V inhibition on release site utilization and vesicle re-docking. **(A,B)** Effects of myosin V inhibition with Myo-1 (left) or PBP (right) on the average distance to the AZ center for individual release sites in measurements at 1Hz (top) or 10 Hz (bottom), binned on the basis of their release probability. **(C)** Histograms of the shift in the distance to synapse center for vesicles undergoing a disappearance and a reappearance event in Control, Myo-1 and PBP. Locations of vesicle re-appearance were separated as toward synapse center versus toward periphery relative to the vesicle initial location (defined as a point of 0 shift) and each side of the histograms were fitted to a single exponential, the difference of which was used to determine the relative shift. **(D)** Quantification of the effect of PBP on the shift in vesicle re-appearance/re-docking location. Same analysis as in **Figure 1I**. Two-sample *t*-test **(A,B)**, two-sample KS-test of cumulative distributions **(C,D)**. *$p < 0.05$, **$p < 0.01$, ns, not significant.

Supplementary Figure 2 | Effects of myosin V inhibition with PBP on the spatial organization of MVR events. **(A)** Examples of resolved MVR events in cultures treated with PBP. Scale bar = 1 μm. **(B,C)** Inhibition of myosin V with PBP does not affect the ratio between MVR and UVR events for resolved **(B)** and unresolved MVR **(C)** events. For unresolved MVR events, ratio of UVR, and MVR was calculated based on a multi-Gaussian fit **(C)**. **(D,E)** Effects of myosin V inhibition with PBP on the distance between two fusion events comprising an MVR for resolved events. Cumulative plots **(D)** and mean values **(E)** are shown. **(F,G)** Same as **(D,E)** for unresolved MVR events. **(H,I)** Effects of myosin V inhibition with PBP on the distance from MVR events to the AZ center for resolved events. Cumulative plots **(H)** and mean values **(I)** are shown. **(J,K)** Same as **(H,I)** for unresolved MVR events. Only a subpopulation of more symmetrical MVR events (asymmetry score < 0.5) were included in this analysis, because these more symmetrical events could be well-approximated by a single symmetrical Gaussian fit, making this analysis comparable to that of the resolved MVR events. Two-sample *t*-test (all panels). *$p < 0.05$, **$p < 0.01$, ***$p < 0.001$, ns, not significant.

Supplementary Figure 3 | Effects of myosin V inhibition with PBP on the utilization of release sites engaged in MVR. **(A)** Effect of myosin V inhibition with PBP (brown) on reuse of release sites engaged in MVR events. Reuse was quantified as the percentage of release sites engaged in MVR that are reused at least once during the 120 s observation period by either other MVR or UVR events. The reuse probability is highly dependent on the distance to AZ center; to account for this variability, we use a paired *t*-test with data binning at 50 nm. **(B,C)** Effect of myosin V inhibition with PBP (brown) on the spatial overlap of MVR and UVR events determined by the proximity analysis. Percentages of MVR events in which none (red), one (blue), or both (black) events in the pair occurred within ± 25nm of at least one UVR event (i.e., at the same at release site) during the observation period **(B)**, and quantification of the percentage of no overlap of MVR and UVR events **(C)**. Two-sample *t*-test **(A)** or Barnard's test **(C)**. **$p < 0.01$, ns, not significant.

Supplementary Figure 4 | Effects of myosin V inhibition with PBP on the temporal separation within MVR events. **(A,B)** Effect of myosin V inhibition with PBP on the amplitude difference of the two events comprising MVR as a function of intra-event distance. Linear fit **(A)** and *t*-test of pooled data **(B)** are shown. **(C)** Quantification of the effects of PBP in panels **(A,B)** assessed by comparing the slopes of the correlations. Two-sample *t*-test **(B)**. One-way analysis of covariance **(C)**. *$p < 0.05$; ns, not significant.

Supplementary Table 1 | Table of all data values and statistical analyses. Data table columns are formatted as (i) corresponding figure location; (ii) conditions being statistically compared and separated by "/"; (iii) measurement; (iv) number of samples (synapses, dishes, and cultures) used for each test; (v) mean values and errors for each condition separated by "/" and corresponding to conditions in column (i); (vi) statistical test used for comparison; and (vii) *P*-value resulting from the statistical comparison.

REFERENCES

Aguet, F., Antonescu, C. N., Mettlen, M., Schmid, S. L., and Danuser, G. (2013). Advances in analysis of low signal-to-noise images link dynamin and AP2 to the functions of an endocytic checkpoint. *Dev. Cell* 26, 279–291. doi: 10.1016/j.devcel.2013.06.019

Auger, C., Kondo, S., and Marty, A. (1998). Multivesicular release at single functional synaptic sites in cerebellar stellate and basket cells. *J. Neurosci.* 18, 4532–4547. doi: 10.1523/jneurosci.18-12-04532.1998

Auger, C., and Marty, A. (2000). Quantal currents at single-site central synapses. *J. Physiol.* 526(Pt 1), 3–11. doi: 10.1111/j.1469-7793.2000.t01-3-00003.x

Bademosi, A. T., Lauwers, E., Padmanabhan, P., Odierna, L., Chai, Y. J., Papadopulos, A., et al. (2017). *In vivo* single-molecule imaging of syntaxin1A reveals polyphosphoinositide- and activity-dependent trapping in presynaptic nanoclusters. *Nat. Commun.* 8:13660.

Balaji, J., and Ryan, T. A. (2007). Single-vesicle imaging reveals that synaptic vesicle exocytosis and endocytosis are coupled by a single stochastic mode. *Proc. Natl. Acad. Sci. U.S.A.* 104, 20576–20581. doi: 10.1073/pnas.0707574105

Bond, L. M., Tumbarello, D. A., Kendrick-Jones, J., and Buss, F. (2013). Small-molecule inhibitors of myosin proteins. *Future Med. Chem.* 5, 41–52. doi: 10.4155/fmc.12.185

Chanaday, N. L., and Kavalali, E. T. (2018). Optical detection of three modes of endocytosis at hippocampal synapses. *Elife* 7:e36097.

Christie, J. M., and Jahr, C. E. (2006). Multivesicular release at Schaffer collateral-CA1 hippocampal synapses. *J. Neurosci.* 26, 210–216. doi: 10.1523/jneurosci.4307-05.2006

Crowley, J. J., Carter, A. G., and Regehr, W. G. (2007). Fast vesicle replenishment and rapid recovery from desensitization at a single synaptic release site. *J. Neurosci.* 27, 5448–5460. doi: 10.1523/jneurosci.1186-07.2007

DeCenzo, S. H., DeSantis, M. C., and Wang, Y. M. (2010). Single-image separation measurements of two unresolved fluorophores. *Optics Express* 18, 16628–16639. doi: 10.1364/oe.18.016628

Desnos, C., Huet, S., Fanget, I., Chapuis, C., Bottiger, C., Racine, V., et al. (2007). Myosin va mediates docking of secretory granules at the plasma membrane. *J. Neurosci.* 27, 10636–10645. doi: 10.1523/jneurosci.1228-07.2007

Eggermann, E., Bucurenciu, I., Goswami, S. P., and Jonas, P. (2011). Nanodomain coupling between Ca(2)(+) channels and sensors of exocytosis at fast mammalian synapses. *Nat. Rev. Neurosci.* 13, 7–21. doi: 10.1038/nrn3125

Eichler, T. W., Kogel, T., Bukoreshtliev, N. V., and Gerdes, H. H. (2006). The role of myosin Va in secretory granule trafficking and exocytosis. *Biochem. Soc. Trans.* 34, 671–674. doi: 10.1042/bst0340671

Forte, L. A., Gramlich, M., and Klyachko, V. A. (2017). Activity-dependence of synaptic vesicle dynamics. *J. Neurosci.* 37, 10597–10610. doi: 10.1523/jneurosci.0383-17.2017

Glebov, O. O., Jackson, R. E., Winterflood, C. M., Owen, D. M., Barker, E. A., Doherty, P., et al. (2017). Nanoscale structural plasticity of the active zone matrix modulates presynaptic function. *Cell Rep.* 18, 2715–2728. doi: 10.1016/j.celrep.2017.02.064

Gramlich, M. W., and Klyachko, V. A. (2017). Actin/Myosin-V- and activity-dependent inter-synaptic vesicle exchange in central neurons. *Cell Rep.* 18, 2096–2104. doi: 10.1016/j.celrep.2017.02.010

Huang, C. H., Bao, J., and Sakaba, T. (2010). Multivesicular release differentiates the reliability of synaptic transmission between the visual cortex and the somatosensory cortex. *J. Neurosci.* 30, 11994–12004. doi: 10.1523/jneurosci.2381-10.2010

Jaqaman, K., Loerke, D., Mettlen, M., Kuwata, H., Grinstein, S., Schmid, S. L., et al. (2008). Robust single-particle tracking in live-cell time-lapse sequences. *Nat. Methods* 5, 695–702. doi: 10.1038/nmeth.1237

Korn, H., Sur, C., Charpier, S., Legendre, P., and Faber, D. S. (1994). The one-vesicle hypothesis and multivesicular release. *Adv. Second Messenger Phosphoprotein Res.* 29, 301–322. doi: 10.1016/s1040-7952(06)80022-4

Krementsov, D. N., Krementsova, E. B., and Trybus, K. M. (2004). Myosin V: regulation by calcium, calmodulin, and the tail domain. *J. Cell Biol.* 164, 877–886.

Leitz, J., and Kavalali, E. T. (2011). Ca(2)(+) influx slows single synaptic vesicle endocytosis. *J. Neurosci.* 31, 16318–16326. doi: 10.1523/jneurosci.3358-11.2011

Leitz, J., and Kavalali, E. T. (2014). Fast retrieval and autonomous regulation of single spontaneously recycling synaptic vesicles. *Elife* 3:e03658.

Malagon, G., Miki, T., Llano, I., Neher, E., and Marty, A. (2016). Counting vesicular release events reveals binomial release statistics at single glutamatergic synapses. *J. Neurosci.* 36, 4010–4025. doi: 10.1523/jneurosci.4352-15.2016

Maschi, D., Gramlich, M. W., and Klyachko, V. A. (2018). Myosin V functions as a vesicle tether at the plasma membrane to control neurotransmitter release in central synapses. *Elife* 7:e39440.

Maschi, D., and Klyachko, V. A. (2017). Spatiotemporal regulation of synaptic vesicle fusion sites in central synapses. *Neuron* 94:e63.

Maschi, D., and Klyachko, V. A. (2020). Spatiotemporal dynamics of multivesicular release is determined by heterogeneity of release sites within central synapses. *Elife* 9:e55210.

Miki, T., Kaufmann, W. A., Malagon, G., Gomez, L., Tabuchi, K., Watanabe, M., et al. (2017). Numbers of presynaptic Ca(2+) channel clusters match those of functionally defined vesicular docking sites in single central synapses. *Proc. Natl. Acad. Sci. U.S.A.* 114, E5246–E5255.

Miki, T., Malagon, G., Pulido, C., Llano, I., Neher, E., and Marty, A. (2016). Actin- and myosin-dependent vesicle loading of presynaptic docking sites prior to exocytosis. *Neuron* 91, 808–823. doi: 10.1016/j.neuron.2016.07.033

Miki, T., Nakamura, Y., Malagon, G., Neher, E., and Marty, A. (2018). Two-component latency distributions indicate two-step vesicular release at simple glutamatergic synapses. *Nat. Commun.* 9:3943.

Mochida, S. (2020). Neurotransmitter release site replenishment and presynaptic plasticity. *Int. J. Mol. Sci.* 22:327. doi: 10.3390/ijms22010327

Neher, E. (2010). What is rate-limiting during sustained synaptic activity: vesicle supply or the availability of release sites. *Front. Syn. Neurosci.* 2:144. doi: 10.3389/fnsyn.2010.00144

Ohyama, A., Komiya, Y., and Igarashi, M. (2001). Globular tail of myosin-V is bound to vamp/synaptobrevin. *Biochem. Biophys. Res. Commun.* 280, 988–991. doi: 10.1006/bbrc.2001.4236

Peng, A., Rotman, Z., Deng, P. Y., and Klyachko, V. A. (2012). Differential motion dynamics of synaptic vesicles undergoing spontaneous and activity-evoked endocytosis. *Neuron* 73, 1108–1115. doi: 10.1016/j.neuron.2012.01.023

Prekeris, R., and Terrian, D. M. (1997). Brain myosin V is a synaptic vesicle-associated motor protein: evidence for a Ca2+-dependent interaction with the synaptobrevin-synaptophysin complex. *J. Cell Biol.* 137, 1589–1601. doi: 10.1083/jcb.137.7.1589

Rose, S. D., Lejen, T., Casaletti, L., Larson, R. E., Pene, T. D., and Trifaro, J. M. (2003). Myosins II and V in chromaffin cells: myosin V is a chromaffin vesicle molecular motor involved in secretion. *J. Neurochem.* 85, 287–298. doi: 10.1046/j.1471-4159.2003.01649.x

Rudolph, S., Overstreet-Wadiche, L., and Wadiche, J. I. (2011). Desynchronization of multivesicular release enhances Purkinje cell output. *Neuron* 70, 991–1004. doi: 10.1016/j.neuron.2011.03.029

Rudolph, S., Tsai, M. C., von Gersdorff, H., and Wadiche, J. I. (2015). The ubiquitous nature of multivesicular release. *Trends Neurosci.* 38, 428–438. doi: 10.1016/j.tins.2015.05.008

Sakamoto, H., Ariyoshi, T., Kimpara, N., Sugao, K., Taiko, I., Takikawa, K., et al. (2018). Synaptic weight set by Munc13-1 supramolecular assemblies. *Nat. Neurosci.* 21, 41–49. doi: 10.1038/s41593-017-0041-9

Schneider, R., Hosy, E., Kohl, J., Klueva, J., Choquet, D., Thomas, U., et al. (2015). Mobility of calcium channels in the presynaptic membrane. *Neuron* 86, 672–679. doi: 10.1016/j.neuron.2015.03.050

Singer, J. H., Lassova, L., Vardi, N., and Diamond, J. S. (2004). Coordinated multivesicular release at a mammalian ribbon synapse. *Nat. Neurosci.* 7, 826–833. doi: 10.1038/nn1280

Smyth, A. M., Yang, L., Martin, K. J., Hamilton, C., Lu, W., Cousin, M. A., et al. (2013). Munc18-1 protein molecules move between membrane molecular depots distinct from vesicle docking sites. *J. Biol. Chem.* 288, 5102–5113. doi: 10.1074/jbc.m112.407585

Takamori, S., Holt, M., Stenius, K., Lemke, E. A., Gronborg, M., Riedel, D., et al. (2006). Molecular anatomy of a trafficking organelle. *Cell* 127, 831–846.

Tang, A. H., Chen, H., Li, T. P., Metzbower, S. R., MacGillavry, H. D., and Blanpied, T. A. (2016). A trans-synaptic nanocolumn aligns neurotransmitter release to receptors. *Nature* 536, 210–214. doi: 10.1038/nature19058

Tong, G., and Jahr, C. E. (1994). Multivesicular release from excitatory synapses of cultered hippocampal neurons. *Neuron* 12, 51–59. doi: 10.1016/0896-6273(94)90151-1

Voglmaier, S. M., Kam, K., Yang, H., Fortin, D. L., Hua, Z., Nicoll, R. A., et al. (2006). Distinct endocytic pathways control the rate and extent of synaptic vesicle protein recycling. *Neuron* 51, 71–84. doi: 10.1016/j.neuron.2006.05.027

Wadiche, J. I., and Jahr, C. E. (2001). Multivesicular release at climbing fiber-Purkinje cell synapses. *Neuron* 32, 301–313. doi: 10.1016/s0896-6273(01)00488-3

Watanabe, M., Nomura, K., Ohyama, A., Ishikawa, R., Komiya, Y., Hosaka, K., et al. (2005). Myosin-Va regulates exocytosis through the submicromolar Ca2+-dependent binding of syntaxin-1A. *Mol. Biol. Cell* 16, 4519–4530. doi: 10.1091/mbc.e05-03-0252

Conflict of Interest: The authors declare that the research was conducted in the absence of any commercial or financial relationships that could be construed as a potential conflict of interest.

frontiers
in Synaptic Neuroscience

PERSPECTIVE
published: 24 May 2021
doi: 10.3389/fnsyn.2021.685052

Invaginating Structures in Synapses – Perspective

Ronald S. Petralia[1]*, Pamela J. Yao[2], Dimitrios Kapogiannis[2] and Ya-Xian Wang[1]

[1] Advanced Imaging Core, National Institute on Deafness and Other Communication Disorders/National Institutes of Health, Bethesda, MD, United States, [2] Laboratory of Clinical Investigation, National Institute on Aging/National Institutes of Health, Bethesda, MD, United States

Invaginating structures are common in the synapses of most animals. However, the details of these invaginating structures remain understudied in part because they are not well resolved in light microscopy and were often misidentified in early electron microscope (EM) studies. Utilizing experimental techniques along with the latest advances in microscopy, such as focused ion beam-scanning EM (FIB-SEM), evidence is gradually building to suggest that the synaptic invaginating structures contribute to synapse development, maintenance, and plasticity. These invaginating structures are most elaborate in synapses mediating rapid integration of signals, such as muscle contraction, mechanoreception, and vision. Here we argue that the synaptic invaginations should be considered in future studies seeking to understand their role in sensory integration and coordination, learning, and memory. We review the various types of invaginating structures in the synapses and discuss their potential functions. We also present several new examples of invaginating structures from a variety of animals including *Drosophila* and mice, mainly using FIB-SEM, with which we trace the form and arrangement of these structures.

Keywords: spine, spinule, retina, *Drosophila*, planaria, invagination

OPEN ACCESS

Edited by:
Xiaobing Chen,
National Institutes of Health,
United States

Reviewed by:
Joseph Szule,
Texas A&M University, United States
Joachim H. R. Lübke,
Julich-Forschungszentrum,
Helmholtz-Verband Deutscher
Forschungszentren (HZ), Germany
Tom Kornberg,
University of California,
San Francisco, United States

****Correspondence:***
Ronald S. Petralia
petralia@nidcd.nih.gov

Received: *24 March 2021*
Accepted: *28 April 2021*
Published: *24 May 2021*

Citation:
Petralia RS, Yao PJ,
Kapogiannis D and Wang Y-X (2021)
Invaginating Structures in Synapses –
Perspective.
Front. Synaptic Neurosci. 13:685052.
doi: 10.3389/fnsyn.2021.685052

INTRODUCTION

Invaginating structures are small outward projections found in a diverse array of cell types (Bastiani and Goodman, 1984; Petralia et al., 2015; Wood et al., 2021), including synapses of neurons of almost all animals (reviewed in Petralia et al., 2015, 2016, 2017, 2018). The invaginating structures involve cell membranes of two different cells, with the outward projection – the invaginating structure – from one cell being surrounded by the invaginated membrane of the other cell. Therefore, in cross-sectional views of transmission electron microscopy (TEM), the invaginating structures can appear as double membrane-covered vesicles. In neuronal synapses, the invaginating structures can be divided into two main groups depending on the presence or absence of active zones.

Invaginating structures can be important in synapse physiology, yet they often have been overlooked in studies of synaptic function. This is especially true for the smaller spinule types of invaginating structures because they are difficult to identify without TEM, and even with standard 2D TEM, the origins of the invaginating structures are often obscure. Today, super-resolution and other specialized light microscopy techniques allow better visualization of these invaginating structures in synapses (Ueda and Hayashi, 2013; Zaccard et al., 2020). Moreover, the new wave of

3D EM methods such as focused ion beam-scanning electron microscopy (FIB-SEM) makes tracing of these invaginating structures possible. These approaches are inspiring scientists to examine the role of invaginating structures in synapses and neurons. In this perspective, we describe some of the more interesting examples of invaginating structures including several new examples from across the animal kingdom. We also discuss the latest ideas about how they may be central to the regulation of synaptic and neuronal function.

RESULTS AND DISCUSSION

Invaginating Structures Associated With Mechanoreception and Photoreception (Figure 1A)

Some of the most elaborate arrangements of invaginating structures are found in synapses of the circuits involved in processing mechanoreception or photoreception and are adaptations to allow animals to respond very rapidly to changing environmental mechanical and visual stimuli (Petralia et al., 2017). They include various combinations of invaginating presynaptic terminals and postsynaptic spines (**Figure 1A**). The most amazing example is seen in cubozoan jellyfish, which have eyes as elaborate as those of higher animals even though they lack brains! These jellyfish exhibit complex behaviors involving vision, such as avoiding obstacles, prey capturing, and complex mating behaviors (e.g., Nilsson et al., 2005). They possess photoreceptor cells with prominent invaginating spines from postsynaptic cells or other photoreceptor cells (Gray et al., 2009). This suggests that the invaginating synapse was one of the earliest functional developments in animal nervous systems, even forming prior to the evolution of any form of "brain." Invaginating postsynaptic spines can be found in some invertebrate sensory cell synapses such as in the octopus statocyst involved in balance and hearing, and mechanoreceptor cells involved in the defensive gill-withdrawal reflex of the sea hare, *Aplysia* (Bailey and Thompson, 1979; Bailey et al., 1979). Interestingly, the invaginating spines of *Aplysia* have twice as many presynaptic vesicles as non-invaginating ones; the authors attribute this to the high degree of synaptic plasticity related to the reflex (Bailey and Thompson, 1979; Bailey et al., 1979). Hair cell synapses of the tunicate, *Ciona intestinalis*, can have invaginating structures at their base and these can be postsynaptic, presynaptic, or both (reciprocal – with presynaptic vesicles on both sides of the synapse; Rigon et al., 2018). In the octopus (**Figure 1A**), the photoreceptor terminals form large bag- or carrot-shaped structures that are filled with presynaptic vesicles and contain (1) invaginating postsynaptic spines, (2) presynaptic vesicle-filled "finger twigs" from adjacent carrots, and (3) "tunnel fibers" from small neurons (Dilly et al., 1963; Case et al., 1972). Structures like "finger twigs" also are found in squid photoreceptor terminal "carrots." Neither the finger twigs nor tunnel fibers show any distinctive signs of chemical synapses (no definitive active zones with densities), except for the synaptic vesicles in the finger twigs. Due to their deep invagination of the photoreceptor terminal, these structures are instead ideally arranged to mediate electrical field/ephaptic conduction (Cohen, 1973; Haghighat et al., 1984; Petralia et al., 2017).

Simple Brains (Figures 1B,C)

Flatworms are the simplest animals with bilateral symmetry, a head, and a brain. Even at this earliest stage in brain evolution, a variety of invaginating structures are evident including at postsynaptic dendrites or other cellular processes with or without synaptic active zones, and various presynaptic terminals invaginating and interdigitating with other terminals (**Figure 1B**; Petralia et al., 2015). Nematodes have a simple nervous system with a minimal "brain" structure composed of a circumpharyngeal nerve ring and associated neuron clusters including the ventral ganglion (White et al., 1986). Recent studies show that nematodes have a variety of types of spine synapses similar to those found in vertebrates (Cuentas-Condori et al., 2019). White et al. (1986) showed several examples of presynaptic terminals invaginating into postsynaptic processes, and postsynaptic processes (spines) invaginating into presynaptic terminals, as well as a motoneuron terminal invaginating into an interneuronal cell body. In **Figure 1C**, a presynaptic terminal invaginates a structure into the base of a neurite extending from a neuronal soma in the ventral ganglion. A possible junction may occur on the invaginating structure where the membranes appear denser and there are unidentified subsynaptic structures in the postsynaptic cell.

Vertebrate Brains (Figures 1D–H)

Invaginating structures are rather common in synapses of the vertebrate brain. For example, in a recent study of the human temporal cortex, Rollenhagen et al. (2020) found examples of postsynaptic spines invaginating into presynaptic terminals. They also found examples of presynaptic terminals with active zones and large non-synaptic structures from presynaptic terminals, both of which invaginate into dendrites. We have examined a FIB-SEM dataset from mouse nucleus accumbens showing various examples, including (1) postsynaptic spinules invaginating into presynaptic terminals, (2) invaginating structures from presynaptic terminals forming cup-shaped synapses with a more deeply invaginating portion, and (3) short presynaptic spinules invaginating into dendrites (**Figures 1D–H**). These will be discussed below in relation to the published literature.

Spinules from the postsynaptic spine invaginating into the presynaptic terminal (**Figures 1E–G**) have been described in many areas of the mammalian brain especially in the hippocampus (Westrum and Blackstad, 1962; Spacek and Harris, 2004; Yao et al., 2005; Tao-Cheng et al., 2009). An interesting example was documented in mouse barrel cortex, where some postsynaptic spines invaginate fully into the presynaptic terminals and then appear to extend a thick process, filled with various vesiculate structures and filaments, deeper within the terminal (Rodriguez-Moreno et al., 2018, 2020). Spinule formation is enhanced in hippocampal slice cultures following stimulation to induce long-term potentiation (LTP; Tao-Cheng et al., 2009) suggesting that spinules recycle extra postsynaptic

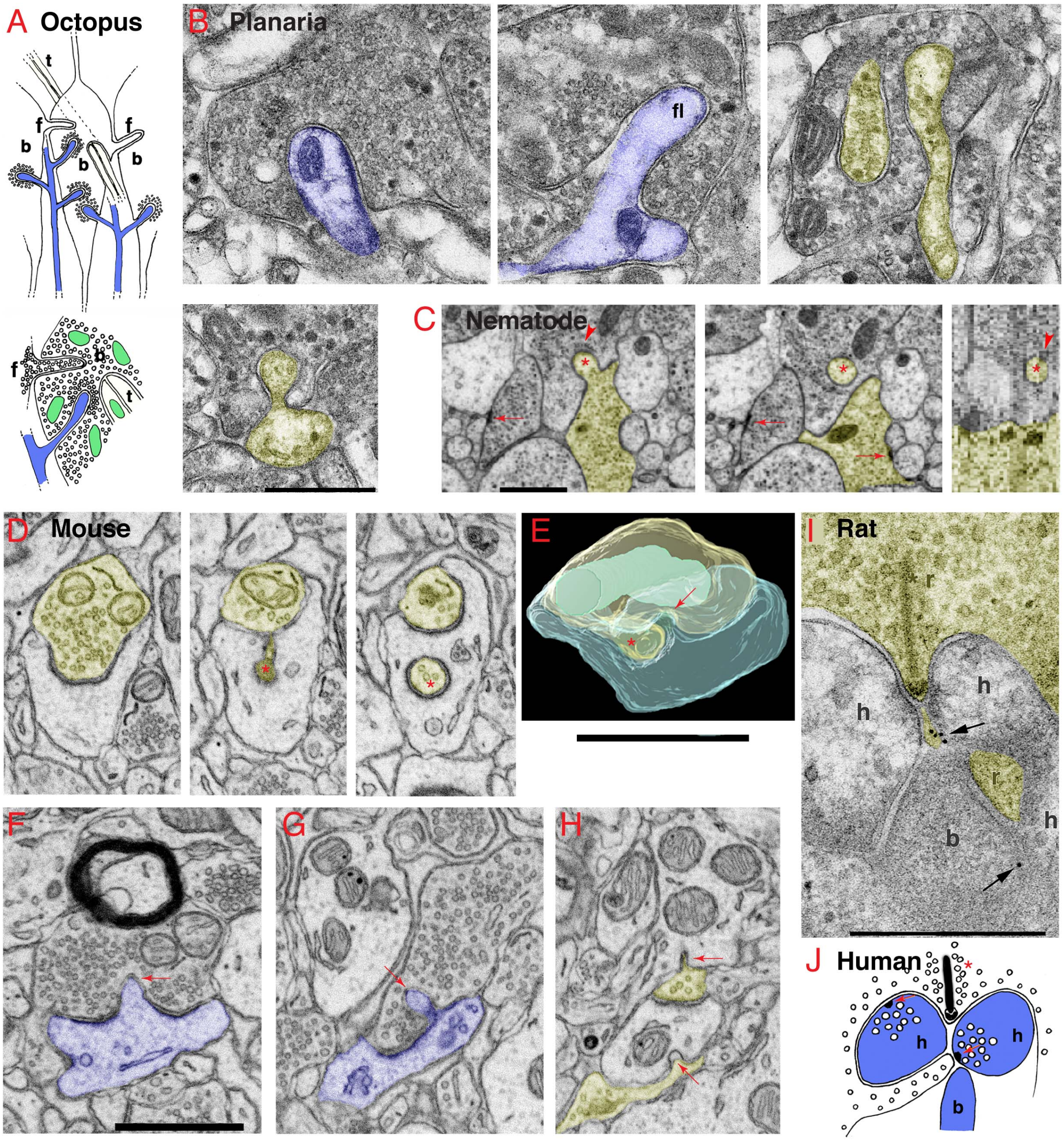

FIGURE 1 | Invaginating structures are common in animal synapses. **(A)** Drawings recapitulating the octopus's large *en passant* photoreceptor terminals, called "bags" (*b*) or "carrots." The bags are filled with synaptic vesicles (shown in lower drawing) and contain three types of invaginating structures from three different sources, including: (1) postsynaptic spines (*blue*) with a dense layer of synaptic vesicles surrounding the deeply invaginating spine heads; (2) presynaptic terminals, also called "finger twigs" (*f*), which are filled with synaptic vesicles (lower drawing), invaginating from adjacent bags; and (3) "tunnel fibers" (*t*), which are one or more nerve trunks passing in a "tunnel" through the bag at ~right angles to the invaginating spines and originating from small neurons called "microneurons." Mitochondria are *green*. Drawings are from Petralia et al. (2017) with slight modifications. **(B)** Electron microscopy (EM) images of the planaria brain synapses. The invaginating structures include an invaginating postsynaptic dendrite (*blue*, left image), an invaginating filopodium (*f*, middle image), and interdigitating axon terminals (*yellow* and *uncolored*, right image). In the EM image on the left in the 2nd row, an unidentified projection invaginates into an axonal terminal (*yellow*) with large dense-cored vesicles. **(C)** EM images show an invaginating structure from the ventral ganglion of the nematode, *Pristionchus pacificus* (Bumbarger et al., 2013; serial cross-section online data set in Neurodata OCP). An invaginating structure (*asterisk*) originates from an axon terminal (*yellow*), which is one of two vesicle-filled terminals that form typical nematode dyadic synapses with a presynaptic density (*arrows*) centered between two postsynaptic processes (lacking PSD; White et al., 1986; Hall and Russell, 1991). The invaginating process enters into the base of a neurite extending from a neuron soma of the ventral ganglion (cell matches descriptions of neurons by position and structure; Ware et al., 1975; White et al., 1986). A possible junction may occur on the dorsal aspect of the invaginating process where the membranes appear denser and there are unidentified subsynaptic structures (*arrowheads*) in the postsynaptic cell. The left two images are transverse sections (z positions 2017 and 2019 in the image stack), and the right image is a digitally reconstructed parasagittal section. **(D–H)** Invaginating structures in the mouse nucleus accumbens. **(D)** An invaginating presynaptic terminal (*yellow*). The z positions in the FIB-SEM image stack are 144, 202, and 237 for the three

(Continued)

FIGURE 1 | Continued
images. The main part of the terminal partly invaginates into the cup-shaped postsynaptic process, and it then invaginates a portion of the terminal deep within the postsynaptic process (*asterisk*). **(E)** A 3D reconstruction of a similar invaginating presynaptic (yellow) terminal (asterisk) from the same data set in panel **(D)**, turned about 90 degrees relative to the structure in panel **(D)**. The postsynaptic membrane also invaginates a short spinule (*arrow*) into the presynaptic terminal (yellow), similar to the one shown in panel **(F)**. The 3D reconstruction is reprinted, after slight modification, from Delgado et al. (2019). **(F,G)** Examples of postsynaptic (*blue*) membrane invaginating short spinules (arrows) into presynaptic terminals. The EM image in panel **(F)** also includes a myelinated axon in which the glial cytoplasm (oligodendrocyte) partly invaginates into the axon. **(H)** Two presynaptic terminals invaginate short spinules (arrows) into dendrites (adjacent EM image in *z* position to this EM image is published in Delgado et al., 2019). **(I)** ImmunoEM of rat brain synapse. Immunogold localization (*arrows*) of GABA-A receptors in invaginating structures in the rod spherule of the rod photoreceptor synaptic terminal complex (*r*) in the rat retina. As is typical in vertebrate retinas, a complex of processes (*b*, *h*) from bipolar and horizontal cells invaginate into the terminal adjacent to the active zone identified by the presynaptic ribbon (*asterisk*). The immunogold labeling for GABA-A (*arrow*) is concentrated between a horizontal cell process and a small projection extending from the presynaptic rod cytoplasm and directly subjacent to the active zone. **(J)** Drawing shows that in the human retina, rod photoreceptor synaptic terminals have a ribbon (*asterisk*) synapse with an invaginating structure from one bipolar and two horizontal cells (*b*, *h*) plus a small projection of cytoplasm from the rod terminal. Horizontal cell processes can form synapses (*red arrows*) with the rod terminal and its projection and with the bipolar cell process; they contain large vesicles and presynaptic densities (Linberg and Fisher, 1988). Panels **(I,J)** are reprinted from Petralia et al. (2017) with slight modifications. Scale bars **(B**,**I)** = 500 nm, **(C,E,F)** (apply **D**,**G,H**) = 1 μm.

membrane formed during enhanced synaptic activity. Indeed, some spinules are associated with the formation of the large, mushroom-shaped spines during synaptic plasticity such as that following LTP (Petralia et al., 2014, 2015, 2018). These mushroom-shaped spines enlarge since more membrane is added as additional glutamate receptor molecules are incorporated into the postsynaptic membrane; this increase in receptors likely enhances synaptic transmission. Apparently, this added membrane causes the PSD to become perforated in correlation with the increased density of glutamate receptors (Ganeshina et al., 2004a,b). At this point, a spinule may form at the perforation, invaginate into the presynaptic terminal (**Figure 1F**), and transfer excess postsynaptic membrane into the presynaptic terminal (Spacek and Harris, 2004; Tao-Cheng et al., 2009; Petralia et al., 2014, 2015, 2018). Coated pits often are seen at the ends of spinules (Westrum and Blackstad, 1962; Spacek and Harris, 2004; Yao et al., 2005; Tao-Cheng et al., 2009), mediating removal and absorption of spinule ends into the terminal. And recent studies with enhanced resolution 3D light microscopy have confirmed that neuronal activity induces spine-derived spinule elongation (Zaccard et al., 2020).

Invaginating structures originating from presynaptic terminals in many animals vary from small spinules (**Figure 1H**) to larger structures and are often filled with presynaptic vesicles (**Figures 1D,E**). In the mammalian forebrain, some spinules that invaginate into presynaptic terminals originate from adjacent axons or presynaptic terminals, from ∼12% in the CA1 region of the rat hippocampus (Spacek and Harris, 2004) to ∼35% in the visual cortex of the ferret (Campbell et al., 2020). Invaginating structures from adjacent presynaptic terminals that are filled with synaptic vesicles often enter each other; these "pseudopodial indentations" or "PSIs" are described in some vertebrate synaptic terminals and can sometimes form complex intertwinings (Boyne and Mcleod, 1979; Boyne and Tarrant, 1982; see invertebrate examples in **Figures 1B**, **2**). Such complex structures could act as "variable diffusion traps" to control levels of ions and other substances in the space between the processes (Boyne and Tarrant, 1982). Electrical stimulation of presynaptic terminals on the electrical organ of torpedo rays increases PSI frequency and size (∼27×; Boyne and Mcleod, 1979). Some inhibitory GABAergic terminals in the mammalian forebrain invaginate short structures into the postsynaptic cell. The postsynaptic membrane surrounding the invaginating structure contains an enzyme to synthesize cannabinoid that mediates a retrograde signal for tonic inhibition of synaptic activity (Yoshida et al., 2011; Omiya et al., 2015).

Cup-shaped spines are highly concave spines that wrap around partly or fully invaginating presynaptic terminals. They are common in cerebral cortex and hippocampus of mammals, and especially in the dentate gyrus (Desmond and Levy, 1983; Frotscher and Leranth, 1986; Petralia et al., 2017, 2018). Cup-shaped spines can be even more complex in the nucleus accumbens (Delgado et al., 2019; Yao et al., 2020), where the presynaptic terminal can continue in part as a deeper invagination with a synaptic active zone (**Figures 1D,E**; Delgado et al., 2019). Desmond and Levy (1983) found that high-frequency stimulation of entorhinal cortex input increases the number of concave spines in the dentate gyrus. Spines in CA1 slice cultures appear more cup-like after chemical induction of LTP (Nagerl et al., 2008), while the number of cup-shaped spines decreases after high-frequency electrical stimulation to induce LTP in CA1 slice cultures (Chang and Greenough, 1984). Cup-shaped spines appear to be more common in both slice and dissociated cultures compared to intact tissue (Roelandse et al., 2003; Mitchell et al., 2012; Petralia et al., 2017 and unpublished data). All of this suggests that formation of cup-shaped spines is a type of spine plasticity that is analogous in some ways to development of the large convex mushroom spines.

Drosophila: Brain (Figure 2) and Neuromuscular Junctions

One of the most striking recent revelations about invaginating structures in synapses has occurred for the insect brain. When we first reviewed the invaginating structures of all animals in 2015 (Petralia et al., 2015), such structures were almost unknown for the insect brain.

The only examples were glia-derived capitate projections invaginating into photoreceptor terminals in the *Drosophila* eye (Prokop and Meinertzhagen, 2006) and some interaxonal invaginating structures (Petralia et al., 2015). Then, in 2018, utilizing FIB-SEM, (Gruber et al., 2018) described the synaptic spinules of the olfactory circuit of the *Drosophila* brain, and it became apparent that synaptic spinules are common. As can be

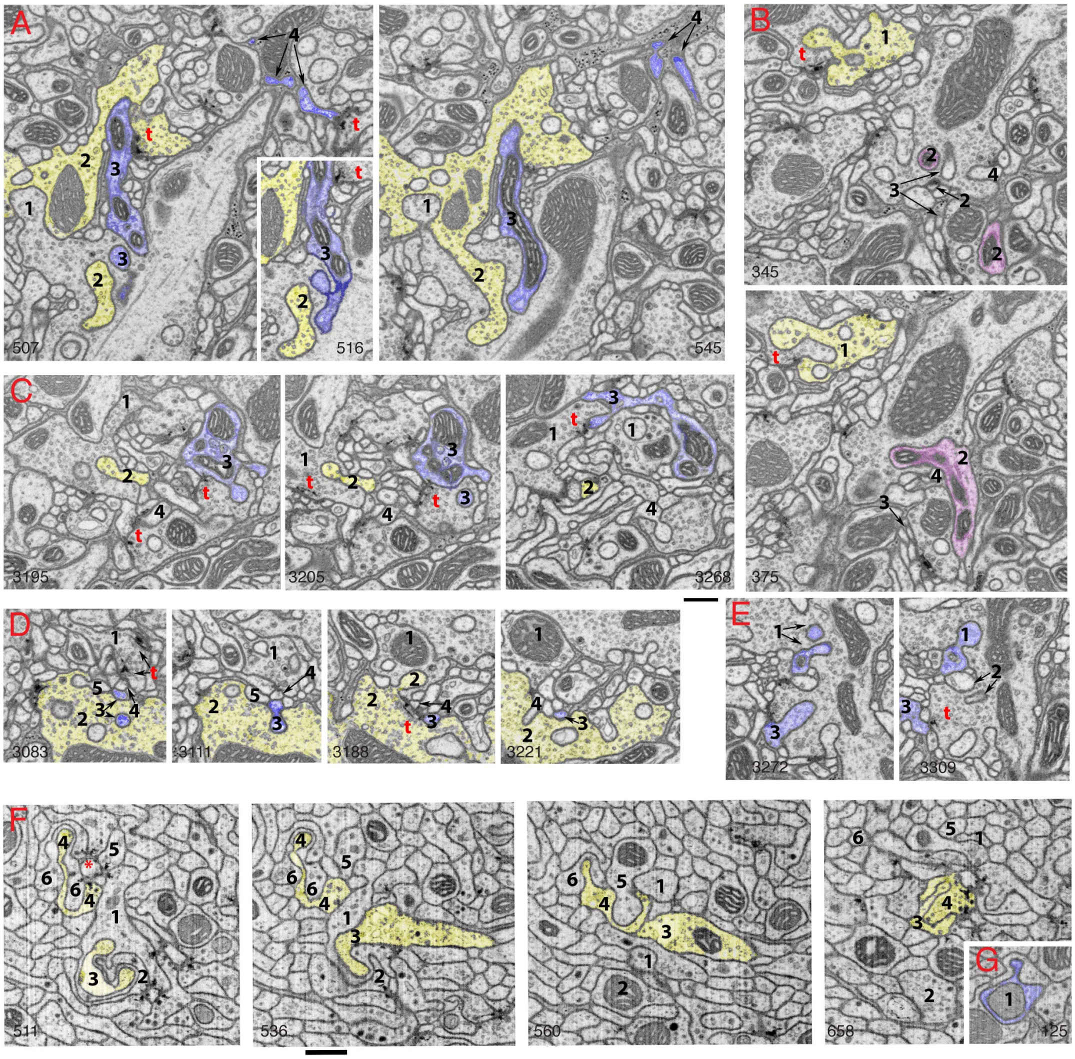

FIGURE 2 | Invaginating structures in the *Drosophila* brain. Examples are FIB-SEM image stacks of the protocerebral bridge **(A–E)** and mushroom body **(F,G)**. *Blue*, dendrite; *yellow*, axon; *magenta*, either dendrite or axon or both. Axon terminals were defined by accumulation of synaptic vesicles or were traced to a presynaptic T-bar; dendrites were traced to a postsynaptic process. Invaginating structures are defined as outward projections. **(A)** Neurites 1 and 2 are large axon terminals that co-invaginate (neurite 1 invaginates into neurite 2 while neurite 2 invaginates into neurite 1). Neurite 3 is a dendrite that invaginates into axon 1, and neurite 3 is one of the two postsynaptic processes of a T-bar synapse (*t*) of axon 2. Neurite 4 is a dendrite that invaginates into a glial cell process; neurite 4 also is one of two postsynaptic processes at a T-bar synapse in an adjacent axon terminal (left image). **(B)** Neurite 1 is an axon terminal that invaginates into an adjacent axon terminal; neurite 1 is also postsynaptic at a T-bar synapse in the adjacent terminal (bottom image). Neurites 2, 3, and 4 invaginate into the same large axon terminal; 3 and 4 are small dendrites. Neurite 2 (*magenta*) was traced for a long distance (>4 μm). This neurite 2 displays features of both presynaptic and postsynaptic structures and forms at least two or three T-bar synapses as well as two or three postsynaptic processes with different synapses (not shown). **(C)** Axon terminal 1 is invaginated by axon terminal 2 and also invaginates another terminal. Neurite 3 is a dendrite that forms four spine-like structures, including one that forms a postsynaptic process at a synapse with terminal 1 and another that invaginates into a subjacent terminal. Neurite 4 is a dendrite that also invaginates into the same subjacent terminal. **(D)** A structure from axon terminal 2 invaginates into axon terminal 1, while structures from dendrites 3, 4 and 5 invaginate into terminal 2. **(E)** Neurites 1, 2, and 3 are projections from dendrites that invaginate into the same large axon terminal; neurite 1 has two invaginating structures. Neurite 3 also bears some T-bar like structures (not shown). Invaginating structures from axon terminals can be filled with synaptic vesicles as seen in panels **(A,B)**, or devoid of vesicles as evident in panel **(D)**. **(F)** Neurites 1-6 are all small axon terminals with relatively few synaptic vesicles. These axons invaginate with each other and also often cluster to form synapses on central dendrite processes. **(G)** An example of a dendrite (1) invaginating into an axon terminal. The number in the lower left or lower right corner of each micrograph indicates its z position in the FIB-SEM image stack. *t* = T-bar (only selected ones are labeled). Scale bars are 500 nm for panels **(A–E)** and **(F–G)**. Note that the protocerebral bridge neuropil **(A–E)** contains abundant invaginating processes from large axon terminals and dendrites, while the mushroom body neuropil **(F,G)** contains abundant invaginating processes from small axon terminals but few from dendrites.

seen for two areas of the *Drosophila* brain in **Figure 2**, there is a high abundance of invaginating neuronal processes into axonal terminals, derived from either dendrites or other axonal terminals. This pattern appears to be the rule for the *Drosophila* brain. Interestingly, some of the invaginating structures are derived from neurites with reciprocal synaptic functions, acting as both axon and dendrite. One such example is shown in **Figure 2B**: neurite 1 is a vesicle-filled axonal terminal but also forms one of the two postsynaptic elements of a photoreceptor terminal T-bar synapse, and neurite 2 was traced to different portions (not shown) containing postsynaptic processes or presynaptic T-bars. Similar reciprocal structures in interneurons are described for the ocellar photoreceptor terminal complex of *Drosophila* (Stark et al., 1989) that shows an example of a vesicle-filled interneuron invaginating into a photoreceptor terminal. However, photoreceptor terminals in both compound eyes and ocelli of *Drosophila* are invaginated mainly by specialized glial processes, rather than axonal or dendritic ones (reviewed in Prokop and Meinertzhagen, 2006; Petralia et al., 2015). Overall, the complexity of the invaginations in the *Drosophila* brain rivals or surpasses those found in the vertebrate brain, yet these neuronal invaginations in insect synapses were overlooked or missed by electron microscopists for the past 60 years!

Invaginations from presynaptic terminals also are common at neuromotor junctions including neuromuscular (NMJ) and secretomotor (such as glands) junctions (Petralia et al., 2017). These invaginating structures can either partially or fully invaginate into the postsynaptic cell. Such invaginating structures are part of mechanisms mediating rapid responses of skeletal muscle fibers. Because these invaginating structures also are found in NMJs of some slower muscles and glands, they might facilitate maintaining an enclosed space for exchange of regulatory factors. This function is best understood for NMJs of larval *Drosophila* skeletal muscle (reviewed in Deshpande and Rodal, 2016; Van Vactor and Sigrist, 2017, Guangming et al., 2020). A hundred-fold increase in muscle area occurs during larval growth (Deshpande and Rodal, 2016) and this must be accompanied by an equally impressive and matching growth in the NMJ; thus, this enclosed invagination area is a special arrangement to allow for the exchange back and forth across the synapse of a large number of different growth and regulatory factors to maintain this organization through development. For example, Wg (wingless; a Wnt ligand) is one of several regulatory proteins transported from the presynaptic terminal membrane via release of exosomes, probably from multivesicular bodies into the invagination intercellular space, that affect postsynaptic differentiation; other factors move retrogradely to affect presynaptic differentiation (Deshpande and Rodal, 2016). Another curious example is the transport of Arc1, important for synaptic plasticity, in capsid-like structures of Arc1 protein + mRNA within exosomes probably derived from presynaptic multivesicular bodies (Ashley et al., 2018).

Invaginating Complexes of Processes (Figures 1I,J)

Some mechanoreceptor and photoreceptor cells in various invertebrates and vertebrates have large invaginations at their bases that contain a complex of both postsynaptic and presynaptic invaginating processes (Petralia et al., 2016, 2017). This is best known for the photoreceptor synapses of vertebrates (**Figures 1I,J**), in which the various processes are arranged within as well as subjacent to the invagination. Thus, they are in different positions and with different combinations of glutamate receptors within the area of glutamate spillover diffusion; GABA and ephaptic conduction are probably also involved here (Kramer and Davenport, 2015; Petralia et al., 2017). The main invaginating structures extend from bipolar and horizontal cells; their invagination and function are partly dependent on trans-synaptic complexes of proteins including calcium channel subunits and receptors (Kerschensteiner, 2017; Wang et al., 2017; Cao et al., 2020; Maddox et al., 2020; Tsukamoto et al., 2021). Invaginating horizontal cell processes form a type of reciprocal synapse including a feed-forward function along with negative feedback to provide lateral inhibition to help the brain modulate signals from groups of adjacent photoreceptor cells. The feedback mechanism from the horizontal cell processes to the photoreceptor cell may involve variable combinations of three different mechanisms: GABA (**Figure 1I**), proton (H^+), and ephaptic transmission (electrical coupling between nerve processes not involving direct synapses) (Liu et al., 2013; Gardner et al., 2015; Kramer and Davenport, 2015; Petralia et al., 2017; Barnes et al., 2020; Hirano et al., 2020).

Horizontal cell processes vary in structure among vertebrates, and often have large vesicles of unknown function. Human horizontal cell processes at the rod photoreceptor terminal form definitive synapses (**Figure 1J**; Linberg and Fisher, 1988). Many fish have unusual spinules that invaginate into the photoreceptor cell from the horizontal cell processes, and they have enlarged ends with internal densities (Popova, 2014). These structures are numerous in the day but mostly gone at night. Popova (2014) suggests that they mediate feedback activity essential for the coding of antagonistic color information. They possibly have some role in postsynaptic neurotransmission and retract when glutamate receptors are activated (Weiler and Schultz, 1993

Why Are Invaginating Structures So Important for Synapse Function?

We have discussed the various aspects of this question in greater detail in our previous reviews (Petralia et al., 2015, 2016, 2017, 2018). This is perhaps easier to answer for those invaginations with synaptic active zones containing presynaptic vesicles and postsynaptic densities. In these cases, the invagination creates a unique, isolated environment for biochemical exchange/activity between the presynaptic and postsynaptic structures. Depending on the structural arrangements, this can either improve the transmission of biochemical and/or electrical signals or sequester and isolate chemicals associated with plasticity between pre- and postsynaptic processes. One such example is the mossy terminal synapses of the hippocampus (Petralia et al., 2016, 2018). These large terminals are invaginated by large, modified compound spines called thorny excrescences, providing numerous active zones within the invagination (somewhat similar structures are found in the thalamus; Petralia et al., 2016; Pelzer et al., 2017). The cleft region is continuous and excludes glial processes. Overall, this specialized synapse is designed to have a higher net probability of release than typical cortical synapses (Henze et al., 2000). And as we have discussed, the invagination in the retinal photoreceptor synapses is highly organized with processes arranged at different distances and positions to take best advantage of neurotransmitter spillover and feedback mechanisms to affect the highly specialized visual responses. In some cases, an invaginating process without active zones is designed to modify neurotransmission, as we have discussed for presynaptic invaginating processes in inhibitory synapses in the mammalian forebrain and horizontal cell spinules in the fish retina. The *Drosophila* NMJ is the best studied example of a synaptic invagination providing an isolated and regulated local environment for chemical exchange to affect synaptic plasticity, as we discussed above. Finally, a large variety of small invaginating processes exists, and which are often broadly classified as "spinules," lacking active zones and originating from postsynaptic, presynaptic, or glial components of the synapse. Many lines of evidence support various functions for these spinules in nutrient exchange, modulation/mediation of synaptic activity, and interneuronal signaling. Most intriguing and least studied are possible electrical field/ephaptic signaling effects (Faber and Pereda, 2018) that are likely facilitated by the invaginating structures (Gardner et al., 2015).

DATA AVAILABILITY STATEMENT

The raw data supporting the conclusions of this article will be made available by the authors, without undue reservation.

AUTHOR CONTRIBUTIONS

RP and PY organized the manuscript and figures. RP wrote the main text. RP, PY, and Y-XW provided the research data for figures. PY and DK edited the manuscript. All authors reviewed the manuscript.

FUNDING

This study was supported by the Intramural Research Programs of NIH/NIDCD and NIH/NIA. The Advanced Imaging Core code is ZIC DC000081.

ACKNOWLEDGMENTS

We thank Harald F. Hess for providing the mouse nucleus accumbens FIB-SEM dataset, and Harald F. Hess and Shan C. Xu for providing the *Drosophila* protocerebral bridge and mushroom body FIB-SEM datasets. We also thank Inna Belyantseva and Katie Kindt for critical reading of the manuscript.

SUPPLEMENTARY MATERIAL

The Supplementary Material for this article can be found online at: https://www.frontiersin.org/articles/10.3389/fnsyn.2021.685052/full#supplementary-material

REFERENCES

Ashley, J., Cordy, B., Lucia, D., Fradkin, L. G., Budnik, V., and Thomson, T. (2018). Retrovirus-like gag protein Arc1 binds RNA and traffics across synaptic boutons. *Cell* 172, 262–274. doi: 10.1016/j.cell.2017.12.022

Bailey, C. H., and Thompson, E. B. (1979). Indented synapses in *Aplysia*. *Brain Res.* 173, 13–20. doi: 10.1016/0006-8993(79)91091-6

Bailey, C. H., Thompson, E. B., Castellucci, V. F., and Kandel, E. R. (1979). Ultrastructure of the synapses of sensory neurons that mediate the gill-withdrawal reflex in *Aplysia*. *J. Neurocytol.* 8, 415–444. doi: 10.1007/bf01214801

Barnes, S., Grove, J. C. R., McHugh, C. F., Hirano, A. A., and Brecha, N. C. (2020). Horizontal cell feedback to cone photoreceptors in mammalian retina: Novel insights from the GABA-pH hybrid model. *Front. Cell Neurosci.* 14:595064. doi: 10.3389/fncel.2020.595064

Bastiani, M. J., and Goodman, C. S. (1984). Neuronal growth cone: Specific interactions mediated by filopodial insertion and induction of coated vesicles. *P. Natl. Acad. Sci.* 81, 1849–1853. doi: 10.1073/pnas.81.6.1849

Boyne, A. F., and Mcleod, S. (1979). Ultrastructural plasticity in stimulated nerve-terminals - Pseudopodial invasions of abutted terminals in torpedine ray electric organ. *Neuroscience* 4, 615–624. doi: 10.1016/0306-4522(79)90138-6

Boyne, A. F., and Tarrant, S. B. (1982). Pseudopodial interdigitations between abutted nerve-terminals - Diffusion traps which occur in several nuclei of the rat limbic system. *J. Neurosci.* 2, 463–469. doi: 10.1523/jneurosci.02-04-00463.1982

Bumbarger, D. J., Riebesell, M., Rodelsperger, C., and Sommer, R. J. (2013). System-wide rewiring underlies behavioral differences in predatory and bacterial-feeding nematodes. *Cell* 152, 109–119. doi: 10.1016/j.cell.2012.12.013

Campbell, C., Lindhartsen, S., Knyaz, A., Erisir, A., and Nahmani, M. (2020). Cortical presynaptic boutons progressively engulf spinules as they mature. *Eneuro* 7:5. doi: 10.1523/ENEURO.0426-19.2020

Cao, Y., Wang, Y., Dunn, H. A., Orlandi, C., Shutlz, N., Kamasawa, N., et al. (2020). Interplay between cell-adhesion molecules governs synaptic wiring of cone photoreceptors. *P. Natl. Acad. Sci.* 117, 23914–23924. doi: 10.1073/pnas.2009940117

Case, N. M., Young, J. Z., and Gray, E. G. (1972). Ultrastructure and synaptic relations in optic lobe of brain of *Eledone* and *Octopus*. *J. Ultra Mol. Struct. R.* 39, 115–123. doi: 10.1016/s0022-5320(72)80012-1

Chang, F. L. F., and Greenough, W. T. (1984). Transient and enduring morphological correlates of synaptic activity and efficacy change in the rat hippocampal slice. *Brain Res.* 309, 35–46. doi: 10.1016/0006-8993(84)91008-4

Cohen, A. I. (1973). Ultrastructural analysis of photoreceptors of squid and their synaptic connections .3. Photoreceptor terminations in optic lobes. *J. Comp. Neurol.* 147, 399–425. doi: 10.1002/cne.901470306

Cuentas-Condori, A., Mulcahy, B., He, S. W., Palumbos, S., Zhen, M., and Miller, D. M. (2019). C. elegans neurons have functional dendritic spines. *Elife* 8:47918. doi: 10.7554/eLife.47918

Delgado, T., Petralia, R. S., Freeman, D. W., Sedlacek, M., Wang, Y. X., and Brenowitz, S. D. (2019). Comparing 3D ultrastructure of presynaptic and postsynaptic mitochondria. *Biol. Open* 8:044834. doi: 10.1242/bio.044834

Deshpande, M., and Rodal, A. A. (2016). The crossroads of synaptic growth signaling, membrane traffic and neurological disease: Insights from *Drosophila*. *Traffic* 17, 87–101. doi: 10.1111/tra.12345

Desmond, N. L., and Levy, W. B. (1983). Synaptic correlates of associative potentiation depression - an ultrastructural-study in the hippocampus. *Brain Res.* 265, 21–30. doi: 10.1016/0006-8993(83)91329-x

Dilly, P. N., Gray, E. G., and Young, J. Z. (1963). Electron microscopy of optic nerves and optic lobes of *Octopus* and *Eledone*. *Proc. R. Soc. Ser. B-Bio.* 158, 446–456. doi: 10.1098/rspb.1963.0057

Faber, D. S., and Pereda, A. E. (2018). Two forms of electrical transmission between neurons. *Front. Mol. Neurosci.* 11:00427. doi: 10.3389/fnmol.2018.00427

Frotscher, M., and Leranth, C. (1986). The cholinergic innervation of the rat fascia-dentata - identification of target structures on granule cells by combining choline-acetyltransferase immunocytochemistry and Golgi impregnation. *J. Comp. Neurol.* 243, 58–70. doi: 10.1002/cne.902430106

Ganeshina, O., Berry, R. W., Petralia, R. S., Nicholson, D. A., and Geinisman, Y. (2004a). Synapses with a segmented, completely partitioned postsynaptic density express more AMPA receptors than other axospinous synaptic junctions. *Neuroscience* 125, 615–623. doi: 10.1016/j.neuroscience.2004.02.025

Ganeshina, O., Berry, R. W., Petralia, R. S., Nicholson, D. A., and Geinisman, Y. (2004b). Differences in the expression of AMPA and NMDA receptors between axospinous perforated and nonperforated synapses are related to the configuration and size of postsynaptic densities. *J. Comp. Neurol.* 468, 86–95. doi: 10.1002/cne.10950

Gardner, C. L., Jones, J. R., Baer, S. M., and Crook, S. M. (2015). Drift-diffusion simulation of the ephaptic effect in the triad synapse of the retina. *J. Comput. Neurosci.* 38, 129–142. doi: 10.1007/s10827-014-0531-7

Gray, G. C., Martin, V. J., and Satterlie, R. A. (2009). Ultrastructure of the retinal synapses in cubozoans. *Biol. Bull.* 217, 35–49. doi: 10.1086/bblv217n1p35

Gruber, L., Rybak, J., Hansson, B. S., and Cantera, R. (2018). Synaptic spinules in the olfactory circuit of *Drosophila melanogaster*. *Front. Cell Neurosci.* 12:86. doi: 10.3389/fncel.2018.00086

Guangming, G., Junhua, G., Chenchen, Z., Yang, M., and Wei, X. (2020). Neurexin and neuroligins maintain the balance of ghost and satellite boutons at the *Drosophila* neuromuscular junction. *Front. Neuroanat.* 14:00019. doi: 10.3389/fnana.2020.00019

Haghighat, N., Cohen, R. S., and Pappas, G. D. (1984). Fine-structure of squid (*Loligo-pealei*) optic lobe synapses. *Neuroscience* 13, 527–546. doi: 10.1016/0306-4522(84)90246-x

Hall, D. H., and Russell, R. L. (1991). The posterior nervous-system of the nematode *Caenorhabditis elegans* - serial reconstruction of identified neurons and complete pattern of synaptic-interactions. *J. Neurosci.* 11, 1–22. doi: 10.1523/jneurosci.11-01-00001.1991

Henze, D. A., Urban, N. N., and Barrionuevo, G. (2000). The multifarious hippocampal mossy fiber pathway: a review. *Neuroscience* 98, 407–427. doi: 10.1016/s0306-4522(00)00146-9

Hirano, A. A., Vuong, H. E., Kornmann, H. L., Schietroma, C., Stella, S. L., Barnes, S., et al. (2020). Vesicular release of GABA by mammalian horizontal cells mediates inhibitory output to photoreceptors. *Front. Cell Neurosci.* 14:600777. doi: 10.3389/fncel.2020.600777

Kerschensteiner, D. (2017). Aligning a synapse. *Neuron* 93, 1241–1243. doi: 10.1016/j.neuron.2017.03.012

Kramer, R. H., and Davenport, C. M. (2015). Lateral inhibition in the vertebrate retina: The case of the missing neurotransmitter. *PLoS Biol.* 13:1002322. doi: 10.1371/journal.pbio.1002322

Linberg, K. A., and Fisher, S. K. (1988). Ultrastructural Evidence That horizontal cell axon terminals are presynaptic in the human retina. *J. Comp. Neurol.* 268, 281–297. doi: 10.1002/cne.902680211

Liu, X., Hirano, A. A., Sun, X. P., Brecha, N. C., and Barnes, S. (2013). Calcium channels in rat horizontal cells regulate feedback inhibition of photoreceptors through an unconventional GABA- and pH-sensitive mechanism. *J. Physiol-Lon.* 591, 3309–3324. doi: 10.1113/jphysiol.2012.248179

Maddox, J. W., Randall, K. I., Yadav, R. P., Williams, B., Hagen, J., and Derr, P. J. (2020). A dual role for $\mathrm{Ca}_v1.4$ Ca^{2+} channels in the molecular and structural organization of the rod photoreceptor synapse. *eLife* 9:62184. doi: 10.7554/eLife.62184

Mitchell, N., Petralia, R. S., Currier, D. G., Wang, Y. X., Kim, A., Mattson, M. P., et al. (2012). Sonic hedgehog regulates presynaptic terminal size, ultrastructure and function in hippocampal neurons. *J. Cell Sci.* 125, 4207–4213. doi: 10.1242/jcs.105080

Nagerl, U. V., Willig, K. I., Hein, B., Hell, S. W., and Bonhoeffer, T. (2008). Live-cell imaging of dendritic spines by STED microscopy. *P. Natl. Acad. Sci. USA* 105, 18982–18987. doi: 10.1073/pnas.0810028105

Nilsson, D. E., Gislen, L., Coates, M. M., Skogh, C., and Garm, A. (2005). Advanced optics in a jellyfish eye. *Nature* 435, 201–205. doi: 10.1038/nature03484

Omiya, Y., Uchigashima, M., Konno, K., Yamasaki, M., Miyazaki, T., Yoshida, T., et al. (2015). VGluT3-expressing CCK-positive basket cells construct invaginating synapses enriched with endocannabinoid signaling proteins in particular cortical and cortex-like amygdaloid regions of mouse brains. *J. Neurosci.* 35, 4215–4228. doi: 10.1523/jneurosci.4681-14.2015

Pelzer, P., Horstmann, H., and Kuner, T. (2017). Ultrastructural and functional properties of a giant synapse driving the piriform cortex to mediodorsal thalamus projection. *Front. Synaptic. Neurosci.* 9:3. doi: 10.3389/fnsyn.2017.00003

Petralia, R. S., Mattson, M. P., and Yao, P. J. (2014). Communication breakdown: The impact of ageing on synapse structure. *Ageing Res. Rev.* 14, 31–42. doi: 10.1016/j.arr.2014.01.003

Petralia, R. S., Wang, Y. X., Mattson, M. P., and Yao, P. J. (2015). Structure, distribution, and function of neuronal/synaptic spinules and related invaginating projections. *Neuromol. Med.* 17, 211–240. doi: 10.1007/s12017-015-8358-6

Petralia, R. S., Wang, Y. X., Mattson, M. P., and Yao, P. J. (2016). The Diversity of spine synapses in animals. *Neuromol. Med.* 18, 497–539. doi: 10.1007/s12017-016-8405-y

Petralia, R. S., Wang, Y. X., Mattson, M. P., and Yao, P. J. (2017). Invaginating presynaptic terminals in neuromuscular junctions, photoreceptor terminals, and other synapses of animals. *Neuromol. Med.* 19, 193–240. doi: 10.1007/s12017-017-8445-y

Petralia, R. S., Wang, Y. X., Mattson, M. P., and Yao, P. J. (2018). Invaginating structures in mammalian synapses. *Front. Synaptic. Neurosci.* 10:4. doi: 10.3389/fnsyn.2018.00004

Popova, E. (2014). Role of dopamine in distal retina. *J. Comp. Physiol. A* 200, 333–358. doi: 10.1007/s00359-014-0906-2

Prokop, A., and Meinertzhagen, I. A. (2006). Development and structure of synaptic contacts in *Drosophila*. *Semin. Cell Dev. Biol.* 17, 20–30. doi: 10.1016/j.semcdb.2005.11.010

Rigon, F., Gasparini, F., Shimeld, S. M., Candiani, S., and Manni, L. (2018). Developmental signature, synaptic connectivity and neurotransmission are conserved between vertebrate hair cells and tunicate coronal cells. *J. Comp. Neurol.* 526, 957–971. doi: 10.1002/cne.24382

Rodriguez-Moreno, J., Rollenhagen, A., Arlandis, J., Santuy, A., Merchan-Pérez, A., DeFelipe, J., et al. (2018). Quantitative 3D ultrastructure of thalamocortical synapses from the "lemniscal" ventral posteromedial nucleus in mouse barrel Cortex. *Cereb. Cortex* 28, 3159–3175. doi: 10.1093/cercor/bhx187

Rodriguez-Moreno, J., Porrero, C., Rollenhagen, A., Rubio-Teves, M., Casas-Torremocha, D., and Alonso-Nanclares, L. (2020). Area-specific synapse structure in branched posterior nucleus axons reveals a new level of complexity in thalamocortical networks. *J. Neurosci.* 40, 2663–2679. doi: 10.1523/jneurosci.2886-19.2020

Roelandse, M., Welman, A., Wagner, U., Hagmann, J., and Matus, A. (2003). Focal motility determines the geometry of dendritic spines. *Neuroscience* 121, 39–49. doi: 10.1016/s0306-4522(03)00405-6

Rollenhagen, A., Walkenfort, B., Yakoubi, R., Klauke, S. A., Schmuhl-Giesen, S. F., and Heinen-Weiler, J. (2020). Synaptic organization of the human temporal lobe neocortex as revealed by high-resolution transmission, focused ion beam scanning, and electron microscopic tomography. *Int. J. Mol. Sci.* 21:5558. doi: 10.3390/ijms21155558

Spacek, J., and Harris, K. M. (2004). Trans-endocytosis via spinules in adult rat hippocampus. *J. Neurosci.* 24, 4233–4241. doi: 10.1523/jneurosci.0287-04.2004

Stark, W. S., Sapp, R., and Carlson, S. D. (1989). Ultrastructure of the ocellar visual-system in normal and mutant *Drosophila melanogaster*. *J. Neurogenet.* 5, 127–153. doi: 10.3109/01677068909066203

Tao-Cheng, J. H., Dosemeci, A., Gallant, P. E., Miller, S., Galbraith, J. A., Winters, C. A., et al. (2009). Rapid turnover of spinules at synaptic terminals. *Neuroscience* 160, 42–50. doi: 10.1016/j.neuroscience.2009.02.031

Tsukamoto, Y., Iseki, K., and Omi, N. (2021). Helical fasciculation of bipolar and horizontal cell neurites for wiring with photoreceptors in macaque and mouse retinas. *Invest. Ophthalmol. Vis. Sci.* 62:31. doi: 10.1167/iovs.62.1.31

Ueda, Y., and Hayashi, Y. (2013). PIP_3 regulates spinule formationin dendritic spines during structured long-term potentiation. *J. Neurosci.* 33, 11040–11047. doi: 10.1523/jneurosci.3122-12.2013

Van Vactor, D., and Sigrist, S. J. (2017). Presynaptic morphogenesis, active zone organization and structural plasticity in *Drosophila*. *Curr. Opin. Neurobiol.* 43, 119–129. doi: 10.1016/j.conb.2017.03.003

Wang, Y. C., Fehlhaber, K. E., Sarria, I., Cao, Y., Ingram, N. T., and Guerrero-Given, D. (2017). The auxiliary calcium channel subunit alpha 2 delta 4 is required for axonal elaboration, synaptic transmission, and wiring of rod photoreceptors. *Neuron* 93, 1359–1374. doi: 10.1016/j.neuron.2017.02.021

Ware, R. W., Clark, D., Crossland, K., and Russell, R. L. (1975). Nerve ring of nematode *Caenorhabditis elegans* - Sensory input and motor output. *J. Comp. Neurol.* 162, 71–110. doi: 10.1002/cne.901620106

Weiler, R., and Schultz, K. (1993). Ionotropic Non-N-methyl-D-aspartate agonists induce retraction of dendritic spinules from retinal horizontal cells. *P. Natl. Acad. Sci. USA* 90, 6533–6537. doi: 10.1073/pnas.90.14.6533

Westrum, L. E., and Blackstad, T. W. (1962). Electron microscopic study of stratum radiatum of rat hippocampus (regio superior, Ca 1) with particular emphasis on synaptology. *J. Comp. Neurol.* 119, 281–309. doi: 10.1002/cne.901190303

White, J. G., Southgate, E., Thomson, J. N., and Brenner, S. (1986). The structure of the nervous-system of the nematode *Caenorhabditis elegans*. *Philos. T. Roy. Soc. B* 314, 1–340. doi: 10.1098/rstb.1986.0056

Wood, B. M., Baena, V., Huang, H., Jorgens, D. M., Terasaki, M., and Kornberg, T. B. (2021). Cytonemes with complex geometries and composition extend into invaginations of target cells. *J. Cell Biol.* 220:202101116. doi: 10.1083/jcb.202101116

Yao, P. J., Eren, E., Petralia, R. S., Gu, J. W., Wang, Y. X., and Kapogiannis, D. (2020). Mitochondrial protrusions in neuronal cells. *Iscience* 23:101514. doi: 10.1016/j.isci.2020.101514

Yao, P. J., Petralia, R. S., Bushlin, I., Wang, Y., and Furukawa, K. (2005). Synaptic distribution of the endocytic accessory proteins AP180 and CALM. *J. Comp. Neurol.* 481, 58–69. doi: 10.1002/cne.20362

Yoshida, T., Uchigashima, M., Yamasaki, M., Katona, I., Yamazaki, M., Sakimura, K., et al. (2011). Unique inhibitory synapse with particularly rich endocannabinoid signaling machinery on pyramidal neurons in basal amygdaloid nucleus. *P. Natl. Acad. Sci. USA* 108, 3059–3064. doi: 10.1073/pnas.1012875108

Zaccard, C. R., Shapiro, L., Martin-de-Saavedra, M. D., Pratt, C., Myczek, K., Song, A., et al. (2020). Rapid 3D enhanced resolution microscopy reveals diversity in dendritic spinule dynamics, regulation, and function. *Neuron* 107, 522–537. doi: 10.1016/j.neuron.2020.04.025

Conflict of Interest: The authors declare that the research was conducted in the absence of any commercial or financial relationships that could be construed as a potential conflict of interest.

frontiers
in Synaptic Neuroscience

ORIGINAL RESEARCH
published: 17 June 2021
doi: 10.3389/fnsyn.2021.671288

Visualizing Synaptic Multi-Protein Patterns of Neuronal Tissue With DNA-Assisted Single-Molecule Localization Microscopy

*Kaarjel K. Narayanasamy[1,2], Aleksandar Stojic[1], Yunqing Li[2], Steffen Sass[1], Marina R. Hesse[1], Nina S. Deussner-Helfmann[2], Marina S. Dietz[2], Thomas Kuner[1], Maja Klevanski[1] and Mike Heilemann[1,2]**

[1] Department of Functional Neuroanatomy, Institute for Anatomy and Cell Biology, Heidelberg University, Heidelberg, Germany, [2] Institute of Physical and Theoretical Chemistry, Goethe-University Frankfurt, Frankfurt, Germany

OPEN ACCESS

Edited by:
Thomas A. Blanpied,
University of Maryland, Baltimore,
United States

Reviewed by:
Paul R. Selvin,
University of Illinois
at Urbana-Champaign, United States
Aaron Levy,
University of Maryland, Baltimore,
United States
Yeoan Youn,
University of Illinois at
Urbana-Champaign, United States in
collaboration with reviewer PS

***Correspondence:**
Mike Heilemann
heileman@chemie.uni-frankfurt.de

Received: 23 February 2021
Accepted: 25 May 2021
Published: 17 June 2021

Citation:
Narayanasamy KK, Stojic A, Li Y, Sass S, Hesse MR, Deussner-Helfmann NS, Dietz MS, Kuner T, Klevanski M and Heilemann M (2021) Visualizing Synaptic Multi-Protein Patterns of Neuronal Tissue With DNA-Assisted Single-Molecule Localization Microscopy.
Front. Synaptic Neurosci. 13:671288.
doi: 10.3389/fnsyn.2021.671288

The development of super-resolution microscopy (SRM) has widened our understanding of biomolecular structure and function in biological materials. Imaging multiple targets within a single area would elucidate their spatial localization relative to the cell matrix and neighboring biomolecules, revealing multi-protein macromolecular structures and their functional co-dependencies. SRM methods are, however, limited to the number of suitable fluorophores that can be imaged during a single acquisition as well as the loss of antigens during antibody washing and restaining for organic dye multiplexing. We report the visualization of multiple protein targets within the pre- and postsynapse in 350–400 nm thick neuronal tissue sections using DNA-assisted single-molecule localization microscopy (SMLM). In a single labeling step, antibodies conjugated with short DNA oligonucleotides visualized multiple targets by sequential exchange of fluorophore-labeled complementary oligonucleotides present in the imaging buffer. This approach avoids potential effects on structural integrity when using multiple rounds of immunolabeling and eliminates chromatic aberration, because all targets are imaged using a single excitation laser wavelength. This method proved robust for multi-target imaging in semi-thin tissue sections with a lateral resolution better than 25 nm, paving the way toward structural cell biology with single-molecule SRM.

Keywords: single-molecule localization microscopy, super-resolution microscopy, DNA-PAINT, neuronal synapse, multiplexing, Exchange PAINT, semi-thin brain tissue sections, tissue imaging

INTRODUCTION

Super-resolution microscopy (SRM) has revolutionized our understanding of cell biology. Single-molecule localization microscopy (SMLM) is one branch of SRM, which employs photoswitchable or transiently binding fluorophore labels and has demonstrated a near-molecular spatial resolution (Sauer and Heilemann, 2017) allowing molecular quantification (Dietz and Heilemann, 2019). A further exciting development was the integration of short DNA oligonucleotides into the concept of SMLM, as realized in DNA point accumulation in nanoscale topography (DNA-PAINT)

(Jungmann et al., 2010). The short oligonucleotides act as transiently hybridizing pairs, with one coupled to a target protein (the "docking strand", attached to e.g., an antibody) and a second carrying a fluorophore (the "imager strand") suspended in the imaging buffer. The transient hybridization of both oligonucleotides generates a temporally short and spatially localized signal, which at low concentration of imager strands is recorded as a single-molecule emission event. A particular strength of DNA-PAINT is that multi-color imaging is not limited by the number of fluorophores that can be separated by their emission spectra, but instead the "color" is encoded into the DNA sequence of the pair of docking and imager strand utilized in consecutive imaging rounds. Implementing an experimental protocol that exchanges imager strands in the buffer solution allows for imaging of more targets than if discrimination occurs on the basis of emission spectra, a method termed Exchange PAINT (Jungmann et al., 2014). Multiplexing and the excellent spatial resolution achieved with DNA-PAINT is now beginning to evolve as a tool in cell biology (Harwardt et al., 2020; Schröder et al., 2020; Strauss and Jungmann, 2020).

The next important step in the application of SRM to cell biology is to visualize the nano-architecture of proteins in the functional context, which demands for super-resolution imaging in tissue and multiplexed imaging of many proteins in the same sample. SMLM imaging of 15 protein targets in cells and tissue was recently achieved using multiple rounds of antibody labeling and fluorophore staining (Klevanski et al., 2020). Here, we demonstrate the integration of DNA-PAINT for super-resolution imaging of structurally preserved neuronal brain tissue from rats, and we achieve a lateral spatial resolution of better than 25 nm. We demonstrate multiplexed imaging of four targets using only one excitation laser light source and the same fluorophore for all targets. This advantage further demonstrates the robustness of Exchange PAINT as multiple structures can be aligned without the need for chromatic correction. In addition, a single antibody labeling step minimizes sample damage that might occur with many repeated immunostainings. Furthermore, we integrate recent developments in DNA-PAINT labels that allow for faster imaging (Strauss and Jungmann, 2020). In short, we established an experimental pipeline for robust and fast super-resolution imaging of proteins in structurally preserved tissue that achieves near-molecular spatial resolution and enables the ultrastructural investigation of protein assemblies in their native environment.

RESULTS

We employed Exchange PAINT (Jungmann et al., 2014) for super-resolution imaging of multiple protein targets in neuronal tissue. Using this technique, four proteins were immunolabeled simultaneously, thereby maintaining low sample preparation time while obtaining an information-rich dataset. In a first experiment, α-tubulin, mitochondria (TOM20), microtubule-associated protein 2 (MAP2), and vesicular glutamate transporter (VGLUT1) were labeled with primary antibodies (Ab) and secondary Ab conjugated to DNA docking strands (P1, P5, R1, or R4; see section "Materials and Methods") (**Figure 1**). Docking and imager strand sequences and modifications are reported in **Table 1** and **Table 2**, respectively.

The protocol for sequential DNA-PAINT imaging started by adding P1 imager strands into the buffer and imaging α-tubulin in the first round, followed by washing away the strands and replacing them with P5 imager strands for mitochondrial imaging. This set of steps was repeated with R1 and R4 strands until all labeled proteins were imaged within the same region of interest (ROI). Each set of frames was rendered individually and merged together using fiducial markers to obtain an overlay of four protein targets organized within tissue (see section "Materials and Methods").

This method was implemented to study the structure and organization of proteins in semi-thin neuronal tissue sections, specifically within the medial nucleus of the trapezoid body (MNTB) region, which contains the calyx of Held (**Figure 2a**, inset), a giant presynaptic terminal (gray) partially enveloping the postsynaptic principal cell (purple) with finger-like protrusions. Each calyx contains hundreds of active zones (AZs) for glutamatergic synaptic transmission (Sätzler et al., 2002; Dondzillo et al., 2010). A transverse section of the calyx of Held reveals the soma of the principal cell and presynaptic endings distributed around the edges, exposing the AZs of the synaptic contact. α-tubulin, mitochondria, MAP2, and VGLUT1 were stained with the Ab-DNA conjugate and imaged with Exchange PAINT (**Figure 2a**). The image shows several principal cells enveloped by the presynaptic calyx of Held, two of them fully visible within the tissue matrix (stippled lines), with one sectioned across the nucleus, as well as axons and capillaries (dotted line). MAP2 is commonly used as a neuronal marker as it selectively labels neuronal cells, specifically the cytoplasm of the soma and dendrites (Sarnat, 2013). VGLUT1 is a marker for synaptic vesicles (SVs), which are concentrated in the presynaptic terminal of the calyx. Regions with interesting morphological and organizational protein distribution are magnified in **Figures 2i–iv**, representing the co-organization between tubulin (red) and mitochondria (cyan) within morphologically distinct structures. **Figures 2i,ii** represent the transverse- and cross-sections of axons, respectively, which show the parallel organization of tubulin filaments along the length of the axon or the circular arrangement of tubulin within an axon bundle. Mitochondria within the axons are thin, elongated structures sandwiched between tubulin filaments and are distributed randomly along and across the axon bundle. The protein organization seen here is in line with the fact that tubulin filaments (microtubules) play a role in mitochondrial transport along axons to the presynaptic terminals where they are needed to maintain continuous synaptic transmission (Verstreken et al., 2005; Zorgniotti et al., 2021).

Apart from axons, tubulin and mitochondria are also co-organized in other parts of the neural network. **Figure 2iii** shows the organization between tubulin and mitochondria within the soma of the principal cell. Here, tubulin filaments appear as short, thin fibrils without a distinct organizational pattern. Similarly, mitochondria show random arrangement within the soma. MAP2 clearly labels the soma of principal cells with larger and oval shaped mitochondria embedded within the

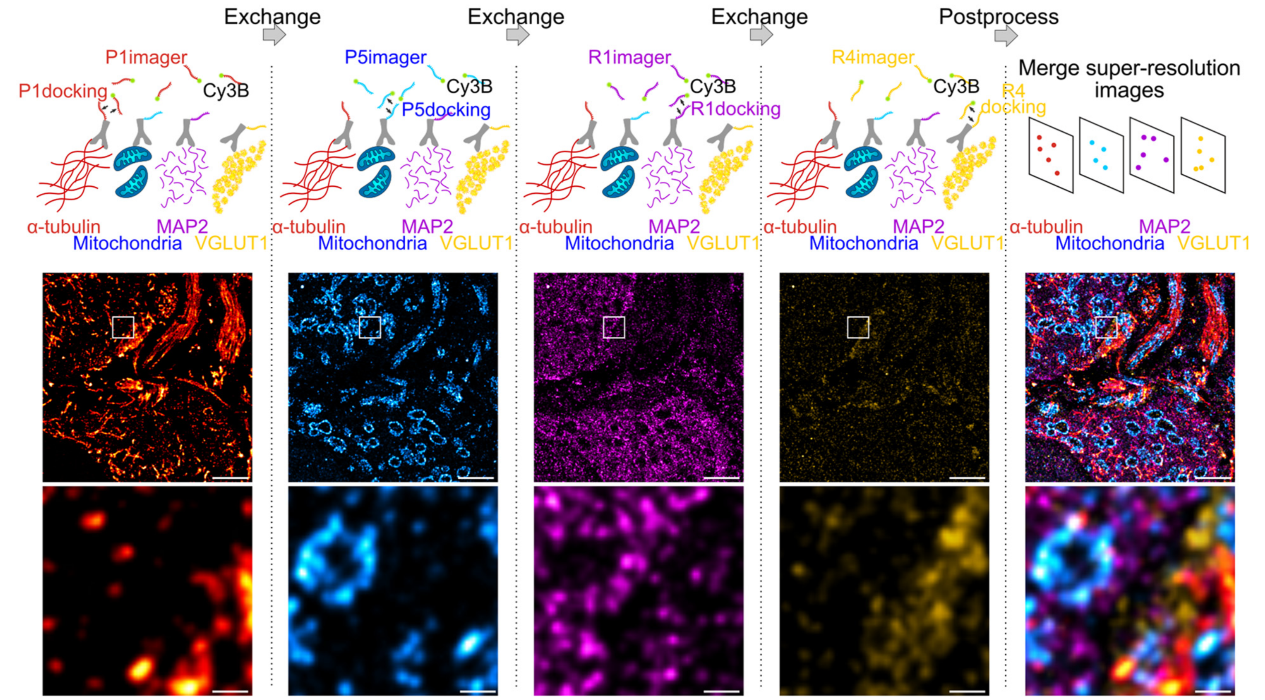

FIGURE 1 | Exchange DNA-PAINT of four targets imaged sequentially. Four protein targets in tissue were labeled with primary antibodies and their corresponding secondary antibody-docking strand conjugate (P1, P5, R1, or R4). The Cy3B labeled imager strands were imaged sequentially by strand type with wash steps between each imaging round. All SMLM rendered images depicting each target were merged to obtain a multi-protein super-resolved image. Scale bar 1 µm **(top)** and 0.1 µm **(bottom)**.

matrix (**Figure 2v**). Another morphologically distinct structure of tubulin is observed next to the smaller calyx synapse. Here, tubulin forms dense, small bundles and each bundle is organized tightly with 1–2 mitochondria (**Figure 2iv**).

Figures 2vi,vii show presynaptic compartments of the calyces containing SV clusters (yellow) next to the principal cell. A feature of interest is the proximity of SVs to tubulin, which can be found as punctate structures embedded in the synaptic site (**Figure 2vi**) or bordering the outer edge of the SV cluster (**Figure 2vii**). The close proximity of tubulin and SVs has been documented before (Piriya Ananda Babu et al., 2020) and function in the transport and regulation of SV precursors to the presynaptic terminal. Furthermore, mitochondria localized in between SVs in the presynapse are morphologically more compact and dense compared to those in the principal cell.

Next, we characterized the image quality using experimental parameters used for SMLM data (Sauer and Heilemann, 2017). We determined the localization precision and the spatial resolution achieved with the different imager strands used in the Exchange PAINT experiment, i.e., P1, P5, R1, and R4. The P1 and P5 strands were among the first DNA sequences used in DNA-PAINT and hybridized into a duplex of nine nucleotide base pairs (Schnitzbauer et al., 2017). The R1 and R4 docking strands contained repeated and concatenated sequences that allowed the hybridization of multiple imager strands onto one docking strand increasing the frequency of events (Strauss and Jungmann, 2020). The localization precision of events was calculated from the nearest neighbor value (Endesfelder et al., 2014; **Figure 3A**) and the lowest localization precision value obtained was 3 nm with P5 strands. Median values recorded for all four strands were below 5 nm. The spatial resolution obtained for the four imager strands was determined by a decorrelation analysis (Descloux et al., 2019) which reported median values around 25 nm, and the highest resolution achieved was 21 nm for the P5 strand (**Figure 3B**).

Although there was no apparent difference in the localization precision and resolution between the P strands and R strands, a marked advantage of the R strands was the shorter acquisition time required during imaging and increased frequency of binding between imager and docking strands, which was reported to reduce the imaging time (Strauss and Jungmann, 2020). We sought to quantify this using Fourier Ring Correlation (FRC) analysis (Nieuwenhuizen et al., 2013) by calculating the resolution of images formed over time. Each super-resolved image was reconstructed from 20,000 frames with an integration time of 150 ms (P1 and P5) or 100 ms (R1 and R4), respectively. **Figure 3C** shows that the FRC curve plateaued before imaging time was complete, therefore all images were able to achieve maximum resolution at 20 000 frames. Saturation of resolution was calculated at 95% of the lowest resolution value achieved for each image. Indeed, both R strands were able to achieve maximum resolution faster than P strands, with R1 and R4 at 17 and 20 min, and P1 and P5 at 37 and 34 min, respectively. The reduction in imaging time by 15–20 min, and comparable localization precision and resolution make

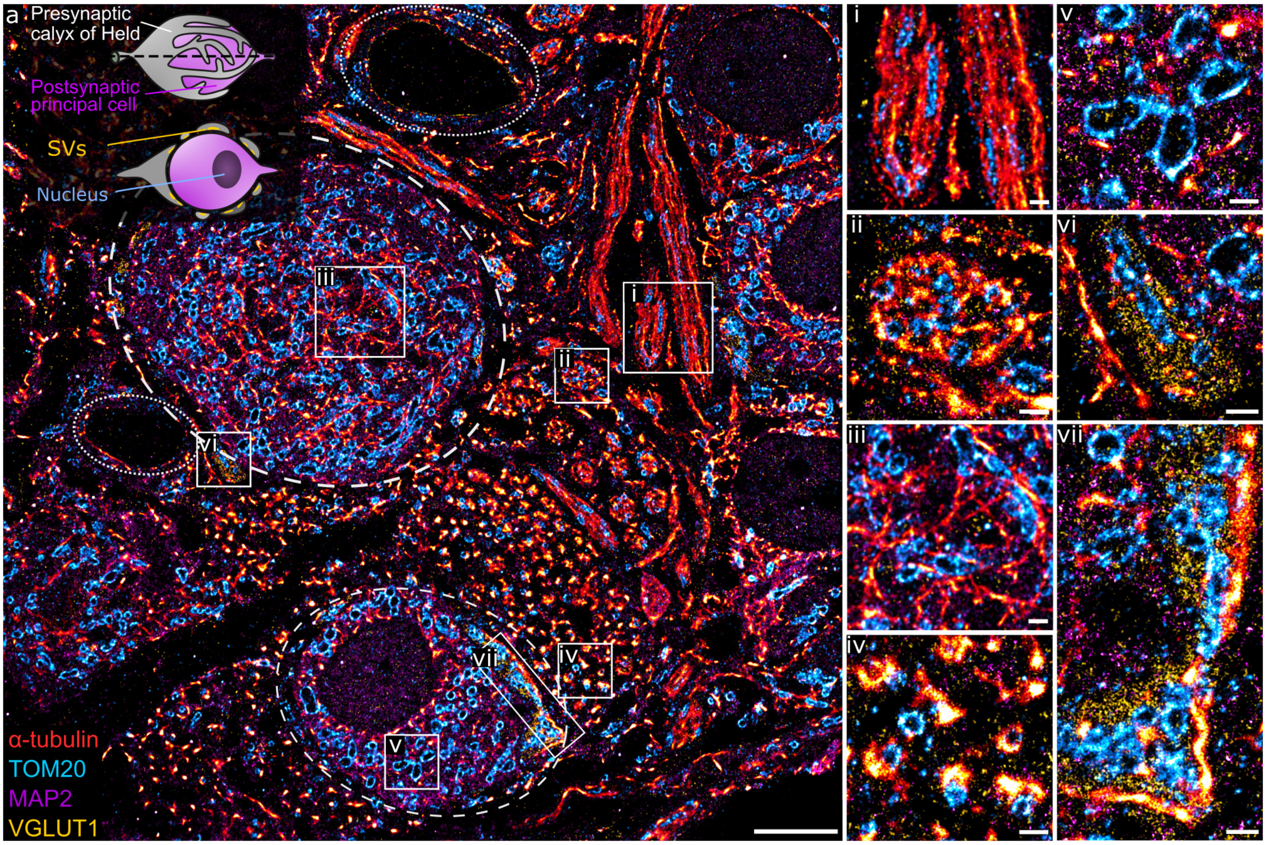

FIGURE 2 | (a) A four-target overlay DNA-PAINT image of MNTB tissue with two calyx synapses and corresponding postsynaptic principal cell (stippled lines), capillaries (dotted lines), and a graphical representation of the calyx of Held (inset). **(i–vii)** Magnification of regions within the primary image **(a)** showing different protein morphologies and organization of tubulin, mitochondria, MAP2, and VGLUT1 within the MNTB. Scale bar 5 μm **(a)** and 0.5 μm **(i–vii)**.

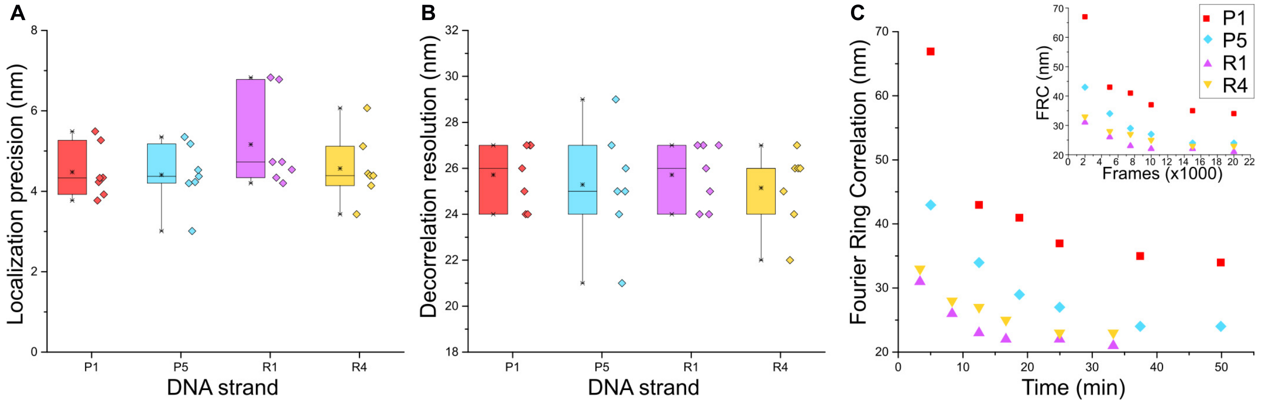

FIGURE 3 | Comparison between P1, P5, R1, and R4 DNA-PAINT strands for **(A)** localization precision by nearest neighbor analysis (Endesfelder et al., 2014) and **(B)** rendered image resolution by decorrelation analysis; n = 7. **(C)** Fourier Ring Correlation (FRC) resolution trend of the four strands over image acquisition time and FRC over number of frames (inset); *n* = 1.

the R strands suitable for faster Exchange PAINT imaging of multiple targets.

We next sought to apply Exchange PAINT to visualize a key component of the synaptic architecture – the AZ. Here, synaptic scaffold proteins Bassoon and Homer that delineate the active zone and postsynaptic density (PSD) were imaged in MNTB tissue to observe their distribution. The presynaptic region was identified using the SV marker VGLUT1 and the postsynaptic

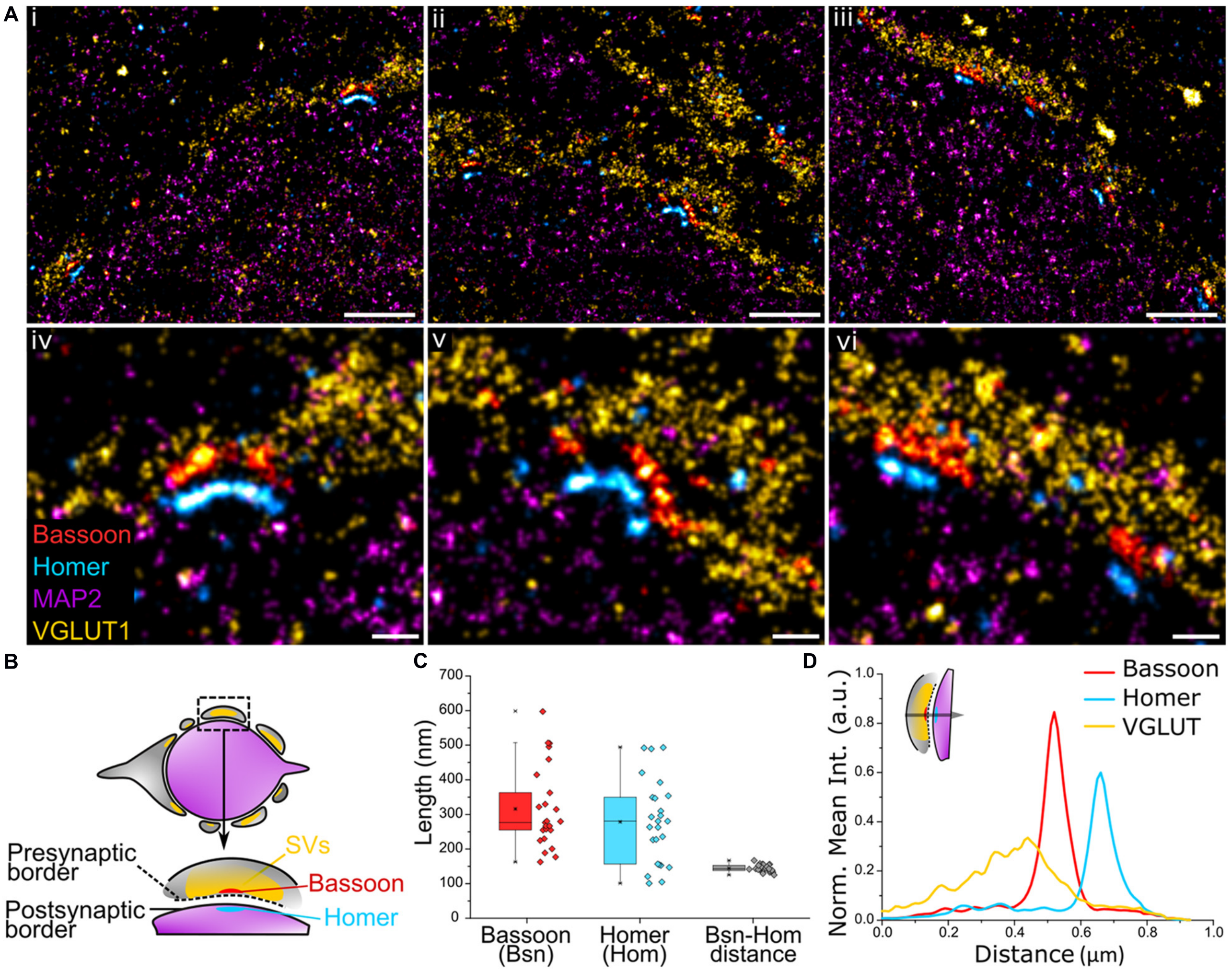

FIGURE 4 | (A) Four-target images of **(i–iii)** the organization of multiple Bassoon and Homer structures sandwiched between VGLUT1 (SV) and MAP2 (microtubules) along the presynaptic border of the calyx of Held and the postsynaptic border of the principal cell. **(iv–vi)** Magnification of the AZ-PSD interface with aligned Bassoon and Homer structures showing linear or curved morphologies. **(B)** Graphical representation of a trans-section of a calyx of Held principal cell (purple) surrounded by the presynaptic cell (gray) and the organization of Bassoon, Homer, and SVs. **(C)** Quantification of the length of Bassoon- or Homer-positive areas, and the distance between Bassoon and Homer; *n* = 25. **(D)** Line profile of 2D spatial organization of protein density based on fluorescence intensity from VGLUT1 to Bassoon to Homer; *n* = 16. Scale bar 1 µm **(i–iii)** and 0.2 µm **(iv–vi)**.

area using the neuronal marker MAP2. Multiple Bassoon (AZ) and Homer (PSD) structures represent synaptic contacts formed by the calyx and principal cell (**Figure 4Ai–iii**). Bassoon is located on the inner presynaptic border, defined here by the inner edge of the VGLUT1 band, and Homer is juxtaposed against Bassoon and found on the edge of the MAP2 signal (**Figures 4Aiv–vi,B**). Magnified images of Bassoon and Homer show highly resolved edges and a defined space in between, partially reflecting the presence of the synaptic cleft, as well as curved (**Figures 4Aiv,v**) or linear morphologies (**Figure 4Avi**) of the AZ and PSD.

The profile views of Bassoon and Homer were measured lengthwise (**Figure 4C**) and had a comparable median length of 277 and 281 nm, respectively (Bassoon mean = 316 nm, SD = 117; Homer mean = 278 nm, SD = 120). Of considerable interest in studies of synaptic specializations is the distance between Bassoon and Homer. These scaffold proteins are located below their respective synaptic plasma membranes, therefore, unlike the synaptic cleft which has a distance of only 28 ± 9 nm in the calyx (Sätzler et al., 2002), are spaced far enough apart to be easily resolved using super-resolution light microscopy. The Bassoon-Homer distance was found to fall into a narrow distribution range with median 143 nm (mean = 144 nm, SD = 10 nm; **Figure 4C**). This distance is reflected in the intensity line profiles of Bassoon and Homer (**Figure 4D**). This value is in good agreement with previous SMLM studies reporting values of ~150 ± 20 nm in brain tissue (Dani et al., 2010) and ~165 ± 9 nm in neuronal cultures (Glebov et al., 2016).

The relative localization of VGLUT1 and Homer to Bassoon was determined by measuring the fluorescence intensity profile of the corresponding proteins within the AZ from the presynaptic terminal toward the principal cell (**Figure 4D** and inset). The 2D line profile shows defined Bassoon and Homer peaks with respective widths of 82 nm and 85 nm at FWHM (Gaussian fitting). SVs are found to be anchored at higher density closer to Bassoon. SVs function in the release of neurotransmitters at the presynaptic AZ, hence are present in high density on the presynaptic membrane. While the exact function of Bassoon is still unknown, it was shown to play a role in short-term SV replenishment during neurotransmission (Dani et al., 2010; Hallermann et al., 2010; Parthier et al., 2018) and SV tethering to the AZ (Mukherjee et al., 2010), thus accounting for the colocalization of SVs and Bassoon.

DISCUSSION

Studies in structural biology require imaging in greater spatial resolution and to observe proteins in their native environment. One of the challenges in imaging neuronal structures is studying the precise organization of proteins within a dense spatial matrix as well as their relative localization to other neuronal proteins. To this end, SRM has been used as a tool due to its ability to resolve structures in the nanoscale and image multiple targets to obtain an overview of protein arrangement within neurons (Colnaghi et al., 2019; Kubo et al., 2019), and has shed light on disease pathologies within dense structures (Shahmoradian et al., 2019).

Single-molecule localization microscopy methods such as STORM and Bayesian blinking and bleaching (3B) have been used to study the organization of proteins in the AZ (Dani et al., 2010; Glebov et al., 2016). However, the number of spectrally distinct fluorophores that can be used for photoswitching and for which chromatic aberration can be corrected are limited, which prevents the imaging of more than three structures at a time. To overcome this, super-resolution imaging with dSTORM (Heilemann et al., 2008) was accomplished by sequential staining realized via bleaching, elution, and restaining using antibodies or other labels against 16 protein targets to obtain an overview of protein distribution within the calyx of Held (Klevanski et al., 2020). The signal density of a target protein can be enhanced by implementing multiple rounds of labeling and imaging (Venkataramani et al., 2018). An alternative solution to visualize protein targets in SRM is the integration of DNA-based protein labels (e.g., antibodies), such as in DNA-PAINT (Schnitzbauer et al., 2017), in which the specificity of a target is encoded in the DNA sequence attached to the protein label and probed by a sequence-complementary and fluorophore-labeled DNA oligonucleotide contained in the imaging buffer. This concept has the additional advantage of providing a nearly constant signal over time and being less prone to photobleaching, which has also been adapted to other super-resolution imaging techniques (Spahn et al., 2019a,b; Glogger et al., 2020).

DNA-PAINT can be extended to image multi-protein targets without requiring specialized optics in a concept termed Exchange PAINT (Jungmann et al., 2014). This method has previously been used to study multiple targets within primary neuronal cultures (Wang et al., 2017; Guo et al., 2019). However, to our knowledge DNA-PAINT has so far not been employed to study synaptic organization in neuronal tissue. Here, we have demonstrated the robustness of the Exchange PAINT method to image protein organization within the calyx of Held and principal cell in semi-thin MNTB tissue in super resolution. This method allows the imaging of multiple targets within a dense structure and is not limited by fluorophore type. Instead, the use of a single fluorophore type prevents chromatic aberration which allows the study of spatial arrangement of structures with better accuracy. Furthermore, Exchange PAINT does not require the use of harsh and time-consuming elution steps or bleaching methods. The single antibody labeling step for multiple target proteins reduces sample preparation time and is only limited by the availability of secondary antibody species. Further increasing the number of protein targets for multiplexing is also possible by using DNA docking strands directly conjugated to primary antibodies, extending the versatility of this method. In addition, we employed an imaging buffer with increased salinity that we reasoned stabilizes DNA duplex formation, which is in line with previous reports (Schueder et al., 2019). Using this buffer, we detected a higher number of binding events over time with the same imager strand concentration, which reduces acquisition time and maintains low background signal. At the same time, we verified that this imaging buffer does not alter the structural integrity of the tissue sample at the level of spatial resolution we attain with the imaging method. Furthermore, the use of R strands speeds up image acquisition and offers exemplary image resolution and localization precision. Indeed, the resolution achieved here surpasses that achieved in similar tissue sections with dSTORM imaging by ∼5 nm (Klevanski et al., 2020). Using Exchange PAINT, multiple dense nanostructures of the pre- and post-synapse can be super-resolved to study their nanoscale spatial patterns within structurally preserved tissue sections. A possible extension would be to incorporate quantitative DNA-PAINT into this workflow, which was recently used to determine the copy numbers of AMPA receptors (Böger et al., 2019).

In conclusion, the method presented here for multi-target imaging using Exchange PAINT in tissue represents an important step forward in studying the protein organization of synapses at the nanoscale. While studying synaptic organization in cultured cells using DNA-PAINT has been reported, it does not necessarily exemplify their native organization in tissue. Therefore, this workflow represents a means to advance the field of synaptic biology by studying structurally relevant neuronal organization *in situ* with near-molecular spatial resolution using optical SRM.

MATERIALS AND METHODS

Medial Nucleus of the Trapezoid Body Tissue Preparation

All experiments that involved the use of animals were performed in compliance with the relevant laws and institutional guidelines of Baden–Württemberg, Germany (protocol G-75/15). Animals were kept under environmentally controlled conditions in the absence of pathogens and *ad libitum* access to food and water. Preparation of brain sections containing the MNTB for

TABLE 1 | Sequences of docking strands.

Name	Sequence	Modification
P1 docking strand	TTATACATCTA	5′ – Thiol
P5 docking strand	TTTCAATGTAT	5′ – Thiol
R1 docking strand	TCCTCCTCCTCCTCCTCCT	5′ – Azide
R4 docking strand	ACACACACACACACACACA	5′ – Azide

TABLE 2 | Sequences of imager strands.

Name	Sequence	Modification
P1 imager strand	TAGATGTAT	3′ – Cy3B
P5 imager strand	CATACATTGA	3′ – Cy3B
R1 imager strand	AGGAGGA	3′ – Cy3B
R4 imager strand	TGTGTGT	3′ – Cy3B

Exchange PAINT was performed according to an established protocol (Klevanski et al., 2020) with slight modifications. Briefly, Sprague-Dawley rats (Charles River) at postnatal day 13 were anaesthetized and perfused transcardially with PBS followed by 4% PFA (Sigma). Brains were dissected and further fixed in 4% PFA overnight at 4°C. On the following day 200 μm thick vibratome (SLICER HR2, Sigmann-Elektronik) sections of the brainstem (containing MNTB) were prepared. MNTB were excised and infiltrated in 2.1 M sucrose (Sigma) in 0.1 M cacodylate buffer overnight at 4°C. Tissue was mounted on a holder, plunge-frozen in liquid nitrogen in 2.1 M sucrose and semi-thin sections (350 nm) were cut using the cryo-ultramicrotome (UC6, Leica). Sections were picked up with a custom made metal loop in a droplet of 1% methylcellulose and 1.15 M sucrose and transferred to 35 mm glass bottom dishes (MatTek) pre-coated with 30 μg/ml of fibronectin from human plasma (Sigma) and TetraSpeck fluorescent beads (1:500, Invitrogen). Dishes containing sections were stored at 4°C prior to their use.

Antibody-DNA Conjugation

Secondary antibodies of donkey anti-chicken (703-005-155), donkey anti-goat (705-005-147), donkey anti-mouse (715-005-151), and donkey anti-rabbit (711-005-152) were purchased from Jackson Immunoresearch. DNA strands were purchased from Metabion with a thiol modification on the 5′ end for each docking strand and a Cy3B dye on the 3′ end for the imager strands.

The secondary antibody to DNA docking strand conjugation was prepared using a maleimide linker as previously reported in detail (1). The thiolated DNA strands were reduced using 250 mM DTT (A39255, Thermo). The reduced DNA was purified using a Nap-5 column (17085301, GE Healthcare) to remove DTT and concentrated with a 3 kDa Amicon spin column (UFC500396, Merck Milipore).

Antibodies (>1.5 mg/mL) were reacted with the maleimide-PEG2-succinimidyl ester crosslinker in a 1:10 molar ratio and purified with 7K cutoff Zeba desalting spin columns (89882, Thermo Fisher Scientific) and concentrated to > 1.5 mg/mL. The DNA and antibody solutions were cross-reacted at a 10:1 molar ratio overnight and excess DNA was filtered through a 100 kDa Amicon spin column (UFC510096, Merck Milipore). The antibody-DNA solution was stored at 4°C.

Immunolabeling

Tissue samples were labeled with antibodies against α-tubulin-mouse (T6199, Sigma), TOM20-rabbit (sc-11415, Santa Cruz), MAP2-chicken (188006, SySy), VGLUT1-goat (135307, SySy), Homer1/2/3-rabbit (160103, SySy), and Bassoon-mouse (SAP7F407, Enzo Life Sciences). Tissue samples in dishes were washed with PBS three times for 10 min each to remove the sucrose-methylcellulose layer and blocked with 5% fetal calf serum (FCS) for 30 min. The primary antibodies were diluted in 0.5% FCS and applied to the tissue section for 1 h at room temperature (rt) and washed off three times with PBS. The conjugated secondary antibody-DNA docking strand in 0.5% FCS was applied onto tissue for 1 h at rt and washed 3 times with PBS. The tissue was then stained with Alexa Fluor 488-conjugated WGA (WGA-A488) (W11261, Thermo Fisher Scientific) in PBS for 10 min and washed off three times with PBS.

Image Acquisition

Single-molecule localization microscopy and widefield microscopy were performed on a modified Olympus IX81 inverted microscope setup with an Olympus 150x TIRF oil immersion objective (UIS2, 1.49NA) and the samples were illuminated in TIRF mode during acquisition. For imaging Cy3B DNA imager strands, a 561 nm laser line (Coherent Sapphire LP) was focused onto the sample at a density of 0.88 kW/cm^2 through a 4L TIRF filter (TRF89902-EM, Chroma) and ET605/70 M nm bandpass filter (Chroma) and signals were detected with an Andor iXon EM+ DU-897 EMCCD camera (Oxford Instruments). WGA-A488 widefield images were obtained using a 491 nm laser line (Olympus Digital Laser System). SMLM frames were acquired using the multi-dimensional acquisition (MDA) mode in Micro-Manager 2.0 (Edelstein et al., 2014).

Imaging Conditions

DNA-PAINT imaging was performed in 5× Buffer C (2.5 M NaCl; S7653, Sigma in 5x PBS; 14200-059, Gibco) supplemented with 1 mM ethylenediaminetetraacetic acid (EDTA; E6758, Sigma), 2.5 mM 3,4-dihydroxybenzoic acid (PCA; 03930590, Sigma), 10 nM protocatechuate 3,4-dioxygenase pseudomonas (PCD; P8279, Sigma), and 1 mM (±)-6-hydroxy-2,5,7,8-tetra-methylchromane-2-carboxylic acid (Trolox; 238813-5G, Sigma). P strands (P1 and P5) were imaged at an imager strand concentration of 0.5 nM and acquisition rate of 150 ms, and R strands (R1 and R4) at a concentration of 50 pM and acquisition rate of 100 ms. All images were acquired with 50 EM gain, for 10,000 to 20,000 frames. Exchange PAINT was performed manually by adding the imaging buffer to the sample chamber and acquiring camera images. The buffer was then removed and the sample washed five times with 1× PBS to remove all imager strands. The subsequent imaging buffer containing another imager strand was then added and the procedure repeated until all targets were imaged.

Image Processing

Frames containing single molecule events were processed and rendered using Picasso software (Schnitzbauer et al., 2017). Events in each frame were localized by fitting using the Maximum Likelihood Estimation for Integrated Gaussian parameters (Smith et al., 2010). The localized events were then filtered by their width and height of the Point Spread Function (sx. sy). The resulting localizations were drift corrected using redundant cross-correlation (RCC), rendered using the "One Pixel Blur" function and further processed using the "linked localizations" function to merge localizations that appeared in multiple consecutive frames. Images were merged in Fiji (Schindelin et al., 2012) using the "merge channels" tool and aligned by linear transformation using 0.1 μm Tetraspeck fiducial markers (2155302, Invitrogen) as registration reference. The individual channels were assigned pseudocolours. The localization precision was determined via a nearest neighbor analysis (NeNA) (Endesfelder et al., 2014) embedded into the Picasso software. The lateral spatial resolution was calculated for rendered SMLM images using an ImageJ plugin for decorrelation analysis (Descloux et al., 2019).

Image Analysis

The length of Bassoon and Homer were measured in ImageJ by creating a binary mask of the rendered image with the preset "moments" threshold. A line was drawn along the long axis of the AZ and PSD structure, respectively, and the length was measured. The distance between Bassoon and Homer was measured by drawing a line perpendicular to both structures and adjusting the spline fit to incorporate the linear length of the structures. The fluorescence intensity for each structure was plotted and fitted with a Gaussian function. The distance was calculated from the distance between the peak intensities of the two structures. Similarly, the line profile of Bassoon, Homer, and VGLUT1 was obtained by measuring their fluorescence intensity using the line tool with spline fit perpendicular to the structures. Fluorescence intensity against distance was averaged for all ROIs with Bassoon peak intensity as the reference point.

Fourier Ring Correlation analysis (Nieuwenhuizen et al., 2013) was performed by saving filtered and drift-corrected DNA-PAINT localizations from Picasso and opening the localizations in ThunderSTORM (Ovesný et al., 2014). Localizations were filtered according to frame length from 0 to 20,000 and each frame length was filtered into blocks of 100. Rendered images were saved and FRC values were calculated using the BIOP.FRC plugin in ImageJ with the Fixed 1/7 criteria.

DATA AVAILABILITY STATEMENT

The raw data supporting the conclusions of this article will be made available by the authors, without undue reservation.

ETHICS STATEMENT

The animal study was reviewed and approved by the Regierungspräsidium Karlsruhe.

AUTHOR CONTRIBUTIONS

MH conceptualized the study. KN, MH, MK, and TK conceived the experiments. MH, KN, SS, and MK done the optical instrument set up. KN, AS, YL, MD, ND-H, MK, and MRH performed the experiments. KN, ND-H, MD, MH, and MK performed the data analysis. All authors contributed to manuscript revision, read, and approved the final submitted version.

FUNDING

MH and TK acknowledge the funding by the Baden-Württemberg Foundation (Mult!Nano, Methods in life sciences program), in whose name this research was conducted. MH, ND-H, MD, and YL acknowledge the funding by the Deutsche Forschungsgemeinschaft (DFG, Grant SFB 902), and the Volkswagen Foundation (Grant 91067-9).

ACKNOWLEDGMENTS

We are grateful to Christoph Spahn for support with FRC analysis.

REFERENCES

Böger, C., Hafner, A. S., Schlichthärle, T., Strauss, M. T., Malkusch, S., Endesfelder, U., et al. (2019). Super-Resolution imaging and estimation of protein copy numbers at single synapses with DNA-point accumulation for imaging in nanoscale topography. *Neurophotonics* 6:035008.

Colnaghi, L., Russo, L., Natale, C., Restelli, E., Cagnotto, A., Salmona, M., et al. (2019). Super resolution microscopy of SUMO proteins in neurons. *Front. Cell. Neurosci.* 13:486. doi: 10.3389/fncel.2019.00486

Dani, A., Huang, B., Bergan, J., Dulac, C., and Zhuang, X. (2010). Superresolution imaging of chemical synapses in the brain. *Neuron* 68, 843–856. doi: 10.1016/j.neuron.2010.11.021

Descloux, A., Grußmayer, K. S., and Radenovic, A. (2019). Parameter-free image resolution estimation based on decorrelation analysis. *Nat. Methods* 16, 918–924. doi: 10.1038/s41592-019-0515-7

Dietz, M. S., and Heilemann, M. (2019). Optical super-resolution microscopy unravels the molecular composition of functional protein complexes. *Nanoscale* 11, 17981–17991. doi: 10.1039/c9nr06364a

Dondzillo, A., Sätzler, K., Horstmann, H., Altrock, W. D., Gundelfinger, E. D., and Kuner, T. (2010). Targeted three-dimensional immunohistochemistry reveals localization of presynaptic proteins bassoon and piccolo in the rat calyx of held before and after the onset of hearing. *J. Comp. Neurol.* 518, 1008–1029. doi: 10.1002/cne.22260

Edelstein, A. D., Tsuchida, M. A., Amodaj, N., Pinkard, H., Vale, R. D., and Stuurman, N. (2014). Advanced methods of microscope control using μManager software. *J. Biol. Methods* 1:e10. doi: 10.14440/jbm.2014.36

Endesfelder, U., Malkusch, S., Fricke, F., and Heilemann, M. (2014). A simple method to estimate the average localization precision of a single-molecule localization microscopy experiment. *Histochem. Cell Biol.* 141, 629–638. doi: 10.1007/s00418-014-1192-3

Glebov, O. O., Cox, S., Humphreys, L., and Burrone, J. (2016). Neuronal activity controls transsynaptic geometry. *Sci. Rep.* 6:22703. doi: 10.1038/srep22703

Glogger, M., Spahn, C., Enderlein, J., and Heilemann, M. (2020). Multicolor, bleaching-resistant super-resolution optical fluctuation imaging with oligonucleotide-based exchangeable fluorophores. *Angewandte Chemie* 60, 6310–6313. doi: 10.1002/anie.202013166

Guo, S. M., Veneziano, R., Gordonov, S., Li, L., Danielson, E., Perez de Arce, K., et al. (2019). Multiplexed and high-throughput neuronal fluorescence imaging with diffusible probes. *Nat. Commun.* 10:4377.

Hallermann, S., Fejtova, A., Schmidt, H., Weyhersmüller, A., Angus Silver, R., Gundelfinger, E. D., et al. (2010). Bassoon speeds vesicle reloading at a central excitatory synapse. *Neuron* 68, 710–723. doi: 10.1016/j.neuron.2010.10.026

Harwardt, M. L. I. E., Schröder, M. S., Li, Y., Malkusch, S., Freund, P., Gupta, S., et al. (2020). Single-molecule super-resolution microscopy reveals heteromeric complexes of MET and EGFR upon ligand activation. *Int. J. Mol. Sci.* 21:2803. doi: 10.3390/ijms21082803

Heilemann, M., van de Linde, S., Schüttpelz, M., Kasper, R., Seefeldt, B., Mukherjee, A., et al. (2008). Subdiffraction-resolution fluorescence imaging with conventional fluorescent probes. *Angewandte Chemie* 47, 6172–6176. doi: 10.1002/anie.200802376

Jungmann, R., Avendaño, M. S., Woehrstein, J. B., Dai, M., Shih, W. M., and Yin, P. (2014). Multiplexed 3D cellular super-resolution imaging with DNA-PAINT and exchange-PAINT. *Nat. Methods* 11, 313–318. doi: 10.1038/nmeth.2835

Jungmann, R., Steinhauer, C., Scheible, M., Kuzyk, A., Tinnefeld, P., and Simmel, F. C. (2010). Single-molecule kinetics and super-resolution microscopy by fluorescence imaging of transient binding on DNA origami. *Nano Lett.* 10, 4756–4761. doi: 10.1021/nl103427w

Klevanski, M., Herrmannsdoerfer, F., Sass, S., Venkataramani, V., Heilemann, M., and Kuner, T. (2020). Automated highly multiplexed super-resolution imaging of protein nano-architecture in cells and tissues. *Nat. Commun.* 11:1552.

Kubo, A., Misonou, H., Matsuyama, M., Nomori, A., Wada-Kakuda, S., Takashima, A., et al. (2019). Distribution of endogenous normal tau in the mouse brain. *J. Comp. Neurol.* 527, 985–998. doi: 10.1002/cne.24577

Mukherjee, K., Yang, X., Gerber, S. H., Kwon, H. B., Ho, A., Castillo, P. E., et al. (2010). Piccolo and bassoon maintain synaptic vesicle clustering without directly participating in vesicle exocytosis. *Proc. Natl. Acad. Sci. U.S.A.* 107, 6504–6509. doi: 10.1073/pnas.1002307107

Nieuwenhuizen, R. P. J., Lidke, K. A., Bates, M., Puig, D. L., Grünwald, D., Stallinga, S., et al. (2013). Measuring image resolution in optical nanoscopy. *Nat. Methods* 10, 557–562. doi: 10.1038/nmeth.2448

Ovesný, M., Křížek, P., Borkovec, J., Svindrych, Z., and Hagen, G. M. (2014). ThunderSTORM: a comprehensive imagej plug-in for PALM and STORM data analysis and super-resolution imaging. *Bioinformatics* 30, 2389–2390. doi: 10.1093/bioinformatics/btu202

Parthier, D., Kuner, T., and Körber, C. (2018). The presynaptic scaffolding protein piccolo organizes the readily releasable pool at the calyx of held. *J. Physiol.* 596, 1485–1499. doi: 10.1113/jp274885

Piriya Ananda Babu, L., Wang, H. Y., Eguchi, K., Guillaud, L., and Takahashi, T. (2020). Microtubule and actin differentially regulate synaptic vesicle cycling to maintain high-frequency neurotransmission. *J. Neurosci. Off. J. Soc. Neurosci.* 40, 131–142. doi: 10.1523/jneurosci.1571-19.2019

Sarnat, H. B. (2013). Clinical neuropathology practice guide 5-2013: markers of neuronal maturation. *Clin. Neuropathol.* 32, 340–369. doi: 10.5414/np300638

Sätzler, K., Söhl, L. F., Bollmann, J. H., Borst, J. G. G., Frotscher, M., Sakmann, B., et al. (2002). Three-dimensional reconstruction of a calyx of held and its postsynaptic principal neuron in the medial nucleus of the trapezoid body. *J. Neurosci. Off. J. Soc. Neurosci.* 22, 10567–10579. doi: 10.1523/jneurosci.22-24-10567.2002

Sauer, M., and Heilemann, M. (2017). Single-molecule localization microscopy in eukaryotes. *Chem. Rev.* 117, 7478–7509. doi: 10.1021/acs.chemrev.6b00667

Schindelin, J., Arganda-Carreras, I., Frise, E., Kaynig, V., Longair, M., Pietzsch, T., et al. (2012). Fiji: an open-source platform for biological-image analysis. *Nat. Methods* 9, 676–682. doi: 10.1038/nmeth.2019

Schnitzbauer, J., Strauss, M. T., Schlichthaerle, T., Schueder, F., and Jungmann, R. (2017). Super-resolution microscopy with DNA-PAINT. *Nat. Protoc.* 12, 1198–1228. doi: 10.1038/nprot.2017.024

Schröder, M. S., Harwardt, M. L. I. E., Rahm, J. V., Li, Y., Freund, P., Dietz, M. S., et al. (2020). Imaging the fibroblast growth factor receptor network on the plasma membrane with DNA-assisted single-molecule super-resolution microscopy. *Methods* S1046-2023, 30024–30024. doi: 10.1016/j.ymeth.2020.05.004

Schueder, F., Stein, J., Stehr, F., Auer, A., Sperl, B., Strauss, M. T., et al. (2019). An order of magnitude faster DNA-PAINT imaging by optimized sequence design and buffer conditions. *Nat. Methods* 16, 1101–1104. doi: 10.1038/s41592-019-0584-7

Shahmoradian, S. H., Lewis, A. J., Genoud, C., Hench, J., Moors, T. E., Navarro, P. P., et al. (2019). Lewy pathology in Parkinson's disease consists of crowded organelles and lipid membranes. *Nat. Neurosci.* 22, 1099–1109. doi: 10.1038/s41593-019-0423-2

Smith, C. S., Joseph, N., Rieger, B., and Lidke, K. A. (2010). Fast, single-molecule localization that achieves theoretically minimum uncertainty. *Nat. Methods* 7, 373–375. doi: 10.1038/nmeth.1449

Spahn, C., Grimm, J. B., Lavis, L. D., Lampe, M., and Heilemann, M. (2019a). Whole-cell, 3D, and multicolor STED imaging with exchangeable fluorophores. *Nano Lett.* 19, 500–505.

Spahn, C., Hurter, F., Glaesmann, M., Karathanasis, C., Lampe, M., and Heilemann, M. (2019b). Protein-specific, multicolor and 3D STED imaging in cells with DNA-labeled antibodies. *Angewandte Chemie* 58, 18835–18838. doi: 10.1002/anie.201910115

Strauss, S., and Jungmann, R. (2020). Up to 100-fold speed-up and multiplexing in optimized DNA-PAINT. *Nat. Methods* 17, 789–791. doi: 10.1038/s41592-020-0869-x

Venkataramani, V., Kardorff, M., Herrmannsdörfer, F., Wieneke, R., Klein, A., Tampé, R., et al. (2018). Enhanced labeling density and whole-cell 3D dSTORM imaging by repetitive labeling of target proteins. *Sci. Rep.* 8:5507.

Verstreken, P., Ly, C. V., Venken, K. J. T., Koh, T. W., Zhou, Y., and Bellen, H. J. (2005). Synaptic mitochondria are critical for mobilization of reserve pool vesicles at *Drosophila* neuromuscular junctions. *Neuron* 47, 365–378. doi: 10.1016/j.neuron.2005.06.018

Wang, Y., Woehrstein, J. B., Donoghue, N., Dai, M., Avendaño, M. S., Schackmann, R. C. J., et al. (2017). Rapid sequential in situ multiplexing with DNA exchange imaging in neuronal cells and tissues. *Nano Lett.* 17, 6131–6139. doi: 10.1021/acs.nanolett.7b02716

Zorgniotti, A., Ditamo, Y., Arce, C. A., and Bisig, C. G. (2021). Irreversible incorporation of L-Dopa into the C-Terminus of α-tubulin inhibits binding of molecular motor KIF5B to microtubules and alters mitochondrial traffic along the axon. *Neurobiol. Dis.* 147:105164. doi: 10.1016/j.nbd.2020.105164

Conflict of Interest: The authors declare that the research was conducted in the absence of any commercial or financial relationships that could be construed as a potential conflict of interest.

frontiers
in Synaptic Neuroscience

PERSPECTIVE
published: 22 October 2021
doi: 10.3389/fnsyn.2021.753462

A Quantitative Perspective of Alpha-Synuclein Dynamics – Why Numbers Matter

*Christian G. Specht**

Diseases and Hormones of the Nervous System (DHNS), Inserm, Université Paris-Saclay, Paris, France

The function of synapses depends on spatially and temporally controlled molecular interactions between synaptic components that can be described in terms of copy numbers, binding affinities, and diffusion properties. To understand the functional role of a given synaptic protein, it is therefore crucial to quantitatively characterise its biophysical behaviour in its native cellular environment. Single molecule localisation microscopy (SMLM) is ideally suited to obtain quantitative information about synaptic proteins on the nanometre scale. Molecule counting of recombinant proteins tagged with genetically encoded fluorophores offers a means to determine their absolute copy numbers at synapses due to the known stoichiometry of the labelling. As a consequence of its high spatial precision, SMLM also yields accurate quantitative measurements of molecule concentrations. In addition, live imaging of fluorescently tagged proteins at synapses can reveal diffusion dynamics and local binding properties of behaving proteins under normal conditions or during pathological processes. In this perspective, it is argued that the detailed structural information provided by super-resolution imaging can be harnessed to gain new quantitative information about the organisation and dynamics of synaptic components *in cellula*. To illustrate this point, I discuss the concentration-dependent aggregation of α-synuclein in the axon and the concomitant changes in the dynamic equilibrium of α-synuclein at synapses in quantitative terms.

Keywords: fluorescence recovery after photobleaching (FRAP), quantitative neurobiology, green fluorescent protein (GFP), gene dosage, liquid-liquid phase separation (LLPS), Parkinson's disease (PD), Lewy body (LB)

Edited by:
Thomas Kuner,
Heidelberg University, Germany

Reviewed by:
Janosch P. Heller,
Dublin City University, Ireland
Luís F. Ribeiro,
VIB-KU Leuven Center for Brain & Disease Research, Belgium

****Correspondence:***
Christian G. Specht
christian.specht@inserm.fr
orcid.org/0000-0001-6038-7735

Received: *04 August 2021*
Accepted: *30 September 2021*
Published: *22 October 2021*

Citation:
Specht CG (2021) A Quantitative Perspective of Alpha-Synuclein Dynamics – Why Numbers Matter. Front. Synaptic Neurosci. 13:753462. doi: 10.3389/fnsyn.2021.753462

INTRODUCTION

Fluorescence Imaging and Quantitative Neurobiology

The quantitation of neurobiological experiments relies heavily on fluorescence microscopy. The strength of this approach lies in the fact that fluorescent signals can be measured accurately across a wide range of intensities (**Figures 1A,B**). Arguably, the most decisive breakthrough in quantitative imaging came with the discovery of green fluorescent protein (GFP) as a versatile fluorescent marker [reviewed in Piston et al. (1999)]. Using genetically encoded fluorophores fused to a protein of interest has the advantage that the labelling is specific and quantitative, resulting in a linear detection over a wide dynamic range. Furthermore, GFP is quite small and relatively inert, meaning that in many instances the tagging of proteins does not interfere with their localisation and/or function (e.g., Wang and Hazelrigg, 1994; Marshall et al., 1995). These qualities have driven the development of a growing palette of fluorescent proteins for specific applications including photoactivatable fluorescent proteins for super-resolution imaging and biosensors for functional imaging in living cells (Kim et al., 2021).

Almost any kind of fluorescence intensity measurement can be used to illustrate and compare differences in protein concentration between and within neurons. To qualify as *quantitative*, however, the data should meet a number of criteria. The fluorescence signals must be sufficiently bright to be distinguished from the background noise. The dynamic range should cover both the weakest signals above background as well as the brightest signals without reaching saturation (0–255 in an 8-bit image). Moreover, the acquisition should be conducted in the linear range, where pixel intensities increase in the same way as the amount of fluorescent proteins. If these conditions are met, the data provide accurate information about the *relative quantities* of fluorophores and by extension target proteins within a given cellular compartment (**Figure 1C**).

There are limits to the applicability of conventional fluorescence microscopy for quantitative neurobiology when it comes to the demarcation of the observed space. Diffusely distributed fluorophores within large compartments such as neuronal somata or thick dendrites produce greater signals than those within thin structures such as dendritic spines or axons. While confocal microscopy can prevent this effect to some extent by collecting only the emitted light from the focal plane (**Figure 1A**), the problem persists as the compartments get smaller. The underlying reason is that the point spread functions (PSF) of closely spaced fluorophores overlap as a result of the diffraction of light. In other words, the measurement of areas or volumes becomes meaningless when their size approaches the diffraction limit, as is the case for synaptic boutons, axons, or dendritic spines. Neither the size of these structures (in pixels or voxels) nor the fluorophore concentrations (in arbitrary units of intensity) can be determined accurately. Ultimately, the apparent size and signal intensity become inextricably linked and cannot be measured independently (**Figure 1C**). The only meaningful quantitative information that can be extracted under these conditions is the integrated intensity that reflects the total quantity of fluorophores within a given compartment, independent of the space occupied by the fluorophores.

Single Molecule Localisation Microscopy and Absolute Quantification

Several super-resolution imaging approaches bypass the diffraction limit of fluorescence microscopy by essentially reducing the observed space and thus providing a more defined readout. Within the field of neurobiology, these approaches have begun to yield new structural insights that have changed our understanding of the internal organisation of neurons [reviewed in Werner et al. (2021)]. Some of the most remarkable discoveries to date are the identification of a periodic organisation of the actin cytoskeleton in axons and elsewhere in the neuron (Xu et al., 2013; Leterrier et al., 2015; Bär et al., 2016), or the *trans*-synaptic alignment of pre- and postsynaptic protein assemblies at excitatory and inhibitory synapses (Tang et al., 2016; Yang et al., 2021). Super-resolution imaging of Lewy bodies (LBs) has highlighted the presence of various organelles surrounding a crowded core containing α-synuclein, lipids, and fragmented membranes (Shahmoradian et al., 2019), which has led to a lively debate about the role of α-synuclein fibrillisation in the formation of LBs in Parkinson's disease (PD; Lashuel, 2020; Ericsson et al., 2021).

A previously overlooked consequence of the gain in spatial resolution is that fluorescence intensity measurements can now be applied to more restricted sub-cellular compartments such as specific organelles, cytoskeletal elements, or, in the case of neurobiology, the postsynaptic density (PSD), and the presynaptic active zone (AZ). Since the estimation of the occupied space is more precise in super-resolution imaging, the concentration of a target protein in a specific compartment (the integrated fluorescence intensity divided by the area or volume) can be calculated quite accurately. This value has actual biological significance as it describes the relative enrichment of a protein at a given location, which ultimately reflects its diffusion properties and/or the strength of its molecular interactions. Hence the power of super-resolution imaging can be exploited to obtain new types of quantitative information.

Single molecule localisation microscopy (SMLM) is particularly well suited for quantitative analysis, since it not only achieves a localisation precision on the order of 10–20 nm, but also provides an exact quantitative readout in the form of single molecule detections (Lelek et al., 2021). This makes SMLM an inherently quantitative approach. The technique relies on the use of photoactivatable fluorophores that can be imaged sequentially rather than all at once. In this way, single fluorophore signals are temporally separated, which makes it possible to calculate the positions (and numbers) of the emitting molecules with great precision. Clustering algorithms have been repurposed to allow grouping of the detections into spatially and/or temporally defined subsets for quantitative analysis, including Ripley's functions, DBSCAN, Voronoi tessellation and, more recently, graph-based approaches (Khater et al., 2020). The dynamic range of SMLM is theoretically unlimited from a true zero up to closely packed fluorophores. The sensitivity of SMLM is that of a single molecule (**Figure 1D**).

Single molecule localisation microscopy can even be used for *absolute quantification*, where the numbers of single molecule detections are converted into actual molecule numbers and packing densities (e.g., Maynard et al., 2021). Different approaches have been developed, generally involving some kind of internal calibration standard that can be extrapolated to clusters of detections arising from larger protein complexes or unknown structures (Wu et al., 2020). SMLM-based molecule counting is best performed with genetically encoded photoactivatable fluorophores, because this ensures the complete labelling of the target proteins, in particular when using a knock-in animal model. Quantitative SMLM analysis of endogenous proteins is also possible using immuno-labelling with reversibly blinking organic dyes (STORM). However, antibody labelling

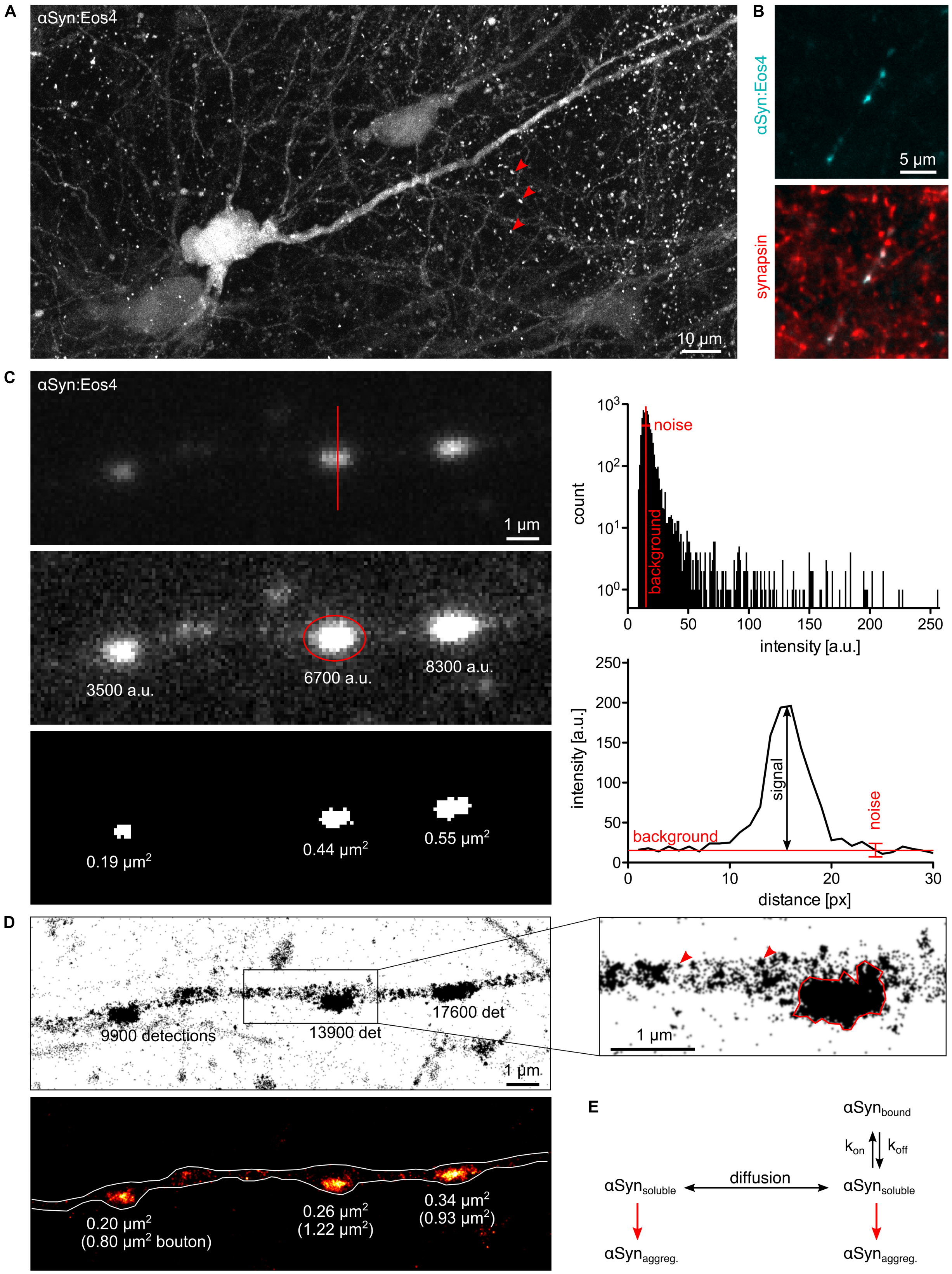

FIGURE 1 | (Continued)

FIGURE 1 | Quantitative fluorescence microscopy of α-synuclein. **(A)** Lentivirus-driven expression of αSyn:Eos4 in an organotypic hippocampal slice, visualised by confocal imaging using 488 nm illumination. The recombinant fusion protein is distributed throughout the somato-dendritic compartment of a pyramidal neuron and enriched in presynaptic terminals (red arrowheads). Scale: 10 μm. **(B)** Co-localisation of recombinant αSyn:Eos4 (low expressing construct, cyan) with endogenous synapsin I (immuno-labelling, red) at synapses in cultured cortical neurons. Scale: 5 μm. **(C)** Conventional fluorescence imaging of αSyn:Eos4 (low expressing construct) in a fixed cortical neuron (excitation 488 nm). Top panel: image with full dynamic intensity range (0–255 arbitrary units, a.u., frequency histogram). The red line denotes a trace through a synaptic bouton along which an intensity profile was measured. Middle panel: same image displayed with enhanced brightness for visibility. The values represent background-corrected integrated intensity readings of αSyn:Eos4 at individual boutons. Bottom panel: measurement of the apparent sizes of αSyn:Eos4 clusters in a binary image. Scale: 1 μm. **(D)** Single molecule super-resolution imaging of αSyn:Eos4 (561 nm laser excitation with photoconversion, 20,000 frames). Top: pointillist single molecule localisation microscopy (SMLM) image with the number of detections of each bouton. The zoom on the right shows that αSyn:Eos4 occupies a sub-region of the bouton, likely corresponding to the synaptic vesicle (SV) domain. Red arrowheads indicate clusters of detections arising from single mEos4b fluorophores. Bottom: rendered image showing that the high density domains of αSyn:Eos4 make up only 20–40% of the total area of the synapse. **(E)** Simplified model showing the dynamic equilibrium of α-synuclein at synapses. Increased expression or reduced synaptic binding at synapses raises the concentration of the soluble fraction of α-synuclein in the axon and promotes its aggregation throughout the neuron.

is notoriously non-linear, and these experiments are generally restricted to fixed samples (Lelek et al., 2021).

Why Numbers Matter: α-Synuclein Dosage and Parkinson's Disease

In many cases, a simple qualitative comparison of signal intensities may be sufficient to describe a biological effect. What then are the advantages of a fully quantitative approach? The strongest arguments for quantitative imaging are that (1) many biological phenomena are concentration dependent, (2) the relevance of a change in protein distribution is best evaluated on a linear scale, (3) quantitative data can be directly compared between different laboratories and experimental approaches, and (4) biophysical models rely on quantitative parameters to describe biological phenomena in mathematical terms. The need for quantitative information is exemplified by the presynaptic protein α-synuclein, because we do not yet fully understand many of the processes that underlie its dynamic behaviour within cells. In particular, the pathophysiology of α-synuclein is a uniquely quantitative problem.

Strongly enriched in presynaptic boutons (**Figures 1A,B**), α-synuclein is associated with synaptic vesicles (SV; Clayton and George, 1999) due to their lipid composition and curvature (Davidson et al., 1998). Other possible binding partners of α-synuclein include lipid rafts (Fortin et al., 2004), VAMP2 (Burré et al., 2010), as well as synapsin III (Zaltieri et al., 2015) and synapsin Ia (Atias et al., 2019). Based on the multiplicity of its molecular interactions hundreds of putative functions of α-synuclein have been proposed, as critically discussed by Vladimir Uversky (2017). Judging from the fact that the deficiency of α-synuclein and its paralogs β- and γ-synuclein does not result in overt phenotypes (Abeliovich et al., 2000; Chen et al., 2002; Connor-Robson et al., 2016), it is likely that α-synuclein plays a modulatory role in SV cycling that can be compensated by other presynaptic components. What makes α-synuclein one of the most studied macromolecules is that it plays a decisive role in PD and other neurodegenerative diseases referred to as synucleinopathies (Goedert and Spillantini, 1998). The first evidence linking α-synuclein to the pathophysiology of PD was the discovery of α-synuclein as the main protein component of LBs (Spillantini et al., 1997). Several point mutations in the *SNCA* gene that increase the propensity of α-synuclein to aggregate were identified in inherited cases of early onset PD (e.g., Polymeropoulos et al., 1997; Kruger et al., 1998). Certain conformations of wildtype and mutant α-synuclein produce β-sheeted fibrils (Iwai et al., 1995; Conway et al., 1998; El-Agnaf et al., 1998; Narhi et al., 1999) that first appear in the axons and eventually condensate as LBs in the somata of affected neurons (Volpicelli-Daley et al., 2011).

Overexpression of α-synuclein as a result of gene duplication or triplication is also associated with familial PD (Singleton et al., 2003; Chartier-Harlin et al., 2004; Ibáñez et al., 2004), indicating that the tendency of α-synuclein to aggregate is concentration dependent. It has recently been demonstrated that the formation of intracellular aggregates of α-synuclein in response to seeding of exogenous fibrils is more pronounced in cultured hippocampal neurons that express high endogenous levels of α-synuclein than in other neuronal populations (Courte et al., 2020). Since nucleation-dependent polymerisation processes are concentration and time-dependent and are strongly affected by the reaction conditions (temperature, pH, and buffer composition) (Hashimoto et al., 1998; Wood et al., 1999), understanding α-synuclein toxicity in neurons requires a quantitative in-cell approach.

A Quantitative Approach to α-Synuclein Dynamics

As argued above, fluorescence microscopy offers a direct, quantitative view of α-synuclein distribution both in fixed and live neurons (**Figure 1C**). GFP-tagged α-synuclein accumulates at presynaptic locations similarly to the endogenous protein, suggesting that the fluorophore does not interfere with lipid binding (Specht et al., 2005; Caputo et al., 2020). Since the fusion of a small protein of 140 amino acid residues with a fluorescent protein of 250 residues could impair its function, the development of alternative tagging strategies is desirable. Nonetheless, the fact that the subcellular distribution α-synuclein is preserved justifies the use of genetically encoded fluorophores to study the protein dynamics of α-synuclein in living neurons.

A defining feature of α-synuclein is its exceptional mobility. Fluorescence recovery after photobleaching (FRAP) shows that GFP-tagged α-synuclein moves rapidly in the soma and the axon (Spinelli et al., 2014), probably in the form of freely diffusing monomers. At least two dynamic states of α-synuclein were identified at synapses, a fast component similar to the one in the axon, as well as a slower component that exchanges with a time constant of 2–3 min, pointing to the transient interaction of α-synuclein with synaptic binding sites (Spinelli et al., 2014). Occupancy of these binding sites depends on the strength of the molecular interactions, the concentration of free (soluble) α-synuclein and its diffusion in the axon, which creates a dynamic equilibrium between free and reversibly bound proteins. Interestingly, the mobility of α-synuclein also shapes its likely functional behaviour at synapses. In response to presynaptic activity, α-synuclein dissociates from the synaptic binding sites and is temporarily dispersed in the neighbouring axon, a property that it shares with other vesicle associated proteins such as synapsin (Fortin et al., 2005).

Although time-lapse imaging accurately describes the diffusion of α-synuclein at steady state or out of equilibrium, the interpretation of the data is complicated by the low spatial resolution of conventional fluorescence microscopy. The small diameter of axons and the small volume of presynaptic terminals present morphological constraints on diffusion that need to be taken into account. This is shown by the difference in the effective exchange rates of soluble α-synuclein measured in the soma and in the axon (Spinelli et al., 2014). Another consequence of the low spatial resolution is that the diffusion properties of molecules in spatially separated sub-domains cannot be studied independently, making it difficult to attribute the different kinetic states in FRAP experiments (Reshetniak et al., 2020). In particular, there is a distinct lack of information about actual fluorophore numbers, concentrations, and molecule fluxes of α-synuclein between the axon and the synapse. In classical FRAP experiments, fluorescence intensities are usually normalised to correct for differences in the initial intensity of synaptic puncta. Normalisation and the calculation of averages means that information about absolute molecule quantities is often disregarded. Since the occupancy of synaptic binding sites is dependent on the concentration of free α-synuclein, overexpression can saturate the binding sites, which may be partly to blame for conflicting experimental results (Fortin et al., 2005; Spinelli et al., 2014; Reshetniak et al., 2020; Weston et al., 2021). Another problem is that FRAP can induce phototoxicity and/or crosslinking (Lippincott-Schwartz et al., 2003), as suggested by the fact that most synaptic proteins display a significant immobile fraction, irrespective of their dynamic properties (Reshetniak et al., 2020). The detection of a stable component does therefore not necessarily prove the existence of aggregated α-synuclein at the synapse as has been suggested (Spinelli et al., 2014; Weston et al., 2021).

In contrast, the high spatial resolution of SMLM makes it possible to measure detection densities within defined axonal compartments. Quantitative single molecule imaging can thus give access to several relevant biophysical parameters. For example, the number of available binding sites of α-synuclein at synapses probably scales with the number of SVs. Molecule counting can yield copy numbers and absolute concentrations of α-synuclein. According to previous estimates, α-synuclein is very abundant, with about of 20–70 copies per SV and about 6,500 copies per bouton (Wilhelm et al., 2014; Fakhree et al., 2016). These values are likely to vary sharply between different neuronal cells and types of synapses. The affinity of α-synuclein for its synaptic binding sites is reflected in the steep concentration gradient between the synaptic and extrasynaptic α-synuclein populations. Single molecule localisation microscopy images of cortical neurons expressing low levels of recombinant α-synuclein tagged with the photoconvertible fluorophore mEos4b (αSyn:Eos4) show the enrichment of α-synuclein in synaptic boutons (**Figure 1D**). Most αSyn:Eos4 detections are concentrated in a sub-region of the bouton that probably corresponds to the SV domain. The concentration elsewhere in the bouton is much lower, to the point that clusters of detections from single molecules are visible and the notion of concentration itself becomes ill defined. The fact that the concentration of α-synuclein outside the SV domain is similar to that in the axon shaft suggests that this volume contains freely diffusing α-synuclein as observed by FRAP (Spinelli et al., 2014). Single molecule tracking can provide further information about diffusion and binding of α-synuclein at synapses, taking into account the existence of different diffusive states (e.g., Laurent et al., 2019; Verdier et al., 2021). If the association of α-synuclein with SVs gives rise to oligomers as suggested by Burré and colleagues (Burré et al., 2014), a degree of cooperativity of binding may be expected. An alternative model suggests that α-synuclein is clustered together with synapsin and SVs in a liquid phase (Hoffmann et al., 2021), which would be governed by particular stoichiometries and modes of diffusion.

CONCLUSION

A Spatio-Temporal Model of α-Synuclein Aggregation

In addition to a possible functional role, the dynamic properties of α-synuclein have important implications for pathology. There is some debate about the toxicity of different species of α-synuclein. One theory has it that LBs themselves are relatively inert (Goldberg and Lansbury, 2000), and that intermediate, toxic species such as misfolded oligomers or proto-fibrils bind to different cellular targets, disrupting essential physiological processes [reviewed in Gracia et al. (2020)]. The existence of distinct fibrillar polymorphs that can trigger α-synuclein aggregation in neurons and exhibit different phenotypic profiles clearly demonstrates that fibrils play a central role in the prion-like propagation of α-synuclein toxicity (Peelaerts et al., 2015; Shrivastava et al., 2020). However, there is no consensus on the initial dysregulation of endogenous α-synuclein in the recipient neurons and whether the toxic aggregates are formed at the synapse itself as some studies suggest (e.g., Kramer and Schulz-Schaeffer, 2007; Spinelli et al., 2014) or elsewhere in the neuron. An alternative explanation is that the aggregation of α-synuclein in the axon leads to its depletion at synapses, and that the pathological process is initiated or at least exacerbated by a loss of function of α-synuclein (Collier et al., 2016; Ninkina et al., 2020).

Lipid binding of α-synuclein was shown to induce an α-helical conformation in the N-terminal two-thirds of the protein (Davidson et al., 1998). Interestingly, lipid binding and the stabilisation of the α-helical structure also reduces the tendency of α-synuclein to form fibrils *in vitro* (Zhu and Fink, 2003). Based on these findings it can be hypothesised that α-synuclein aggregation in neurons depends on the concentration of free α-synuclein rather than the bound fraction at synapses. If these considerations are correct, any condition that shifts the dynamic equilibrium towards free α-synuclein, such as overexpression or changes in the affinity for synaptic binding sites is expected to accelerate the aggregation process (**Figure 1E**). It may further be speculated that the aggregation can begin anywhere in the neuron, since the concentration of freely diffusing α-synuclein is probably uniform. This would also be true if α-synuclein aggregation is driven by liquid-liquid phase separation (LLPS; Ray et al., 2020). That said, nucleation probably depends on the transmission process of toxic α-synuclein aggregates between cells. If membrane binding and internalisation is a random process, most transmission events are likely to occur on axons, due to their large total surface area. If, on the other hand, the transmission of toxic forms of α-synuclein depends on a synapse-specific mechanism (e.g., Shrivastava et al., 2020), nucleation would preferentially occur at synapses.

Quantitative imaging can provide essential information that helps distinguish between these possibilities. The systematic quantification of α-synuclein expression can substantiate the relationship between protein concentrations in neurons and their susceptibility to pathogenic insults. Since the concentration of soluble α-synuclein can be measured in the soma, this could be easily accomplished with conventional fluorescence microscopy, using a recently developed knock-in mouse model expressing endogenous α-synuclein-GFP (Caputo et al., 2020). SMLM can add ultra-structural and quantitative information when it comes to the characterisation of small compartments such as axons and synaptic terminals, including absolute copy numbers and shifts in the occupancy of synaptic binding sites. Quantitative super-resolution imaging has thus an important role to play when concentration-dependent processes are investigated in diffraction limited domains, which could provide new insights into α-synuclein dynamics and toxicity.

DATA AVAILABILITY STATEMENT

The raw data supporting the conclusions of this article will be made available by the author without undue reservation.

AUTHOR CONTRIBUTIONS

CS: conception and writing.

ACKNOWLEDGMENTS

Ronald Melki (MIRCen), Jean-Baptiste Masson (Institut Pasteur), and Nadine Schibille (IRAMAT-CEB) are thanked for insightful discussions and critical reading of the manuscript.

REFERENCES

Abeliovich, A., Schmitz, Y., Farinas, I., Choi-Lundberg, D., Ho, W. H., Castillo, P. E., et al. (2000). Mice lacking alpha-synuclein display functional deficits in the nigrostriatal dopamine system. *Neuron* 25, 239–252. doi: 10.1016/s0896-6273(00)80886-7

Atias, M., Tevet, Y., Sun, J., Stavsky, A., Tal, S., Kahn, J., et al. (2019). Synapsins regulate alpha-synuclein functions. *Proc. Natl. Acad. Sci. U.S.A.* 116, 11116–11118. doi: 10.1073/pnas.1903054116

Bär, J., Kobler, O., van Bommel, B., and Mikhaylova, M. (2016). Periodic F-actin structures shape the neck of dendritic spines. *Sci. Rep.* 6:37136. doi: 10.1038/srep37136

Burré, J., Sharma, M., and Südhof, T. C. (2014). Alpha-synuclein assembles into higher-order multimers upon membrane binding to promote SNARE complex formation. *Proc. Natl. Acad. Sci. U.S.A.* 111, E4274–E4283. doi: 10.1073/pnas.1416598111

Burré, J., Sharma, M., Tsetsenis, T., Buchman, V., Etherton, M. R., and Südhof, T. C. (2010). Alpha-synuclein promotes SNARE-complex assembly in vivo and in vitro. *Science* 329, 1663–1667. doi: 10.1126/science.1195227

Caputo, A., Liang, Y., Raabe, T. D., Lo, A., Horvath, M., Zhang, B., et al. (2020). Snca-GFP knock-in mice reflect patterns of endogenous expression and pathological seeding. *eNeuro* 7:ENEURO.0007-20.2020. doi: 10.1523/eneuro.0007-20.2020

Chartier-Harlin, M. C., Kachergus, J., Roumier, C., Mouroux, V., Douay, X., Lincoln, S., et al. (2004). Alpha-synuclein locus duplication as a cause of familial Parkinson's disease. *Lancet* 364, 1167–1169. doi: 10.1016/s0140-6736(04)17103-1

Chen, P. E., Specht, C. G., Morris, R. G., and Schoepfer, R. (2002). Spatial learning is unimpaired in mice containing a deletion of the alpha-synuclein locus. *Eur. J. Neurosci.* 16, 154–158. doi: 10.1046/j.1460-9568.2002.02062.x

Clayton, D. F., and George, J. M. (1999). Synucleins in synaptic plasticity and neurodegenerative disorders. *J. Neurosci. Res.* 58, 120–129.

Collier, T. J., Redmond, D. E. Jr., Steece-Collier, K., Lipton, J. W., and Manfredsson, F. P. (2016). Is alpha-synuclein loss-of-function a contributor to Parkinsonian pathology? Evidence from non-human primates. *Front. Neurosci.* 10:12. doi: 10.3389/fnins.2016.00012

Connor-Robson, N., Peters, O. M., Millership, S., Ninkina, N., and Buchman, V. L. (2016). Combinational losses of synucleins reveal their differential requirements for compensating age-dependent alterations in motor behavior and dopamine metabolism. *Neurobiol. Aging* 46, 107–112. doi: 10.1016/j.neurobiolaging.2016.06.020

Conway, K. A., Harper, J. D., and Lansbury, P. T. (1998). Accelerated in vitro fibril formation by a mutant alpha-synuclein linked to early-onset Parkinson disease. *Nat. Med.* 4, 1318–1320.

Courte, J., Bousset, L., Boxberg, Y. V., Villard, C., Melki, R., and Peyrin, J. M. (2020). The expression level of alpha-synuclein in different neuronal populations is the primary determinant of its prion-like seeding. *Sci. Rep.* 10:4895. doi: 10.1038/s41598-020-61757-x

Davidson, W. S., Jonas, A., Clayton, D. F., and George, J. M. (1998). Stabilization of alpha-synuclein secondary structure upon binding to synthetic membranes. *J. Biol. Chem.* 273, 9443–9449.

El-Agnaf, O. M., Jakes, R., Curran, M. D., and Wallace, A. (1998). Effects of the mutations Ala30 to Pro and Ala53 to Thr on the physical and morphological properties of alpha-synuclein protein implicated in Parkinson's disease. *FEBS Lett.* 440, 67–70. doi: 10.1016/s0014-5793(98)01419-7

Ericsson, M., von Saucken, V., Newman, A. J., Doehr, L., Hoesch, C., Kim, T. E., et al. (2021). Crowded organelles, lipid accumulation, and abnormal membrane tubulation in cellular models of enhanced α-synuclein membrane interaction. *Brain Res.* 1758:147349. doi: 10.1016/j.brainres.2021.147349

Fakhree, M. A., Zijlstra, N., Raiss, C. C., Siero, C. J., Grabmayr, H., Bausch, A. R., et al. (2016). The number of α-synuclein proteins per vesicle gives insights into its physiological function. *Sci. Rep.* 6:30658. doi: 10.1038/srep30658

Fortin, D. L., Nemani, V. M., Voglmaier, S. M., Anthony, M. D., Ryan, T. A., and Edwards, R. H. (2005). Neural activity controls the synaptic accumulation of alpha-synuclein. *J. Neurosci.* 25, 10913–10921. doi: 10.1523/JNEUROSCI.2922-05.2005

Fortin, D. L., Troyer, M. D., Nakamura, K., Kubo, S., Anthony, M. D., and Edwards, R. H. (2004). Lipid rafts mediate the synaptic localization of alpha-synuclein. *J. Neurosci.* 24, 6715–6723. doi: 10.1523/JNEUROSCI.1594-04.2004

Goedert, M., and Spillantini, M. G. (1998). Lewy body diseases and multiple system atrophy as alpha-synucleinopathies. *Mol. Psychiatry* 3, 462–465. doi: 10.1038/sj.mp.4000458

Goldberg, M. S., and Lansbury, P. T. Jr. (2000). Is there a cause-and-effect relationship between alpha-synuclein fibrillization and Parkinson's disease? *Nat. Cell Biol.* 2, E115–E119. doi: 10.1038/35017124

Gracia, P., Camino, J. D., Volpicelli-Daley, L., and Cremades, N. (2020). Multiplicity of α-Synuclein aggregated species and their possible roles in disease. *Int. J. Mol. Sci.* 21:8043. doi: 10.3390/ijms21218043

Hashimoto, M., Hsu, L. J., Sisk, A., Xia, Y., Takeda, A., Sundsmo, M., et al. (1998). Human recombinant NACP/alpha-synuclein is aggregated and fibrillated in vitro: relevance for Lewy body disease. *Brain Res.* 799, 301–306. doi: 10.1016/s0006-8993(98)00514-9

Hoffmann, C., Sansevrino, R., Morabito, G., Logan, C., Vabulas, R. M., Ulusoy, A., et al. (2021). Synapsin condensates recruit alpha-synuclein. *J. Mol. Biol.* 433:166961. doi: 10.1016/j.jmb.2021.166961

Ibáñez, P., Bonnet, A. M., Débarges, B., Lohmann, E., Tison, F., Pollak, P., et al. (2004). Causal relation between alpha-synuclein gene duplication and familial Parkinson's disease. *Lancet* 364, 1169–1171. doi: 10.1016/s0140-6736(04)17104-3

Iwai, A., Yoshimoto, M., Masliah, E., and Saitoh, T. (1995). Non-A beta component of Alzheimer's disease amyloid (NAC) is amyloidogenic. *Biochemistry* 34, 10139–10145. doi: 10.1021/bi00032a006

Khater, I. M., Nabi, I. R., and Hamarneh, G. (2020). A review of super-resolution single-molecule localization microscopy cluster analysis and quantification methods. *Patterns (N Y)* 1:100038. doi: 10.1016/j.patter.2020.100038

Kim, H., Ju, J., Lee, H. N., Chun, H., and Seong, J. (2021). Genetically encoded biosensors based on fluorescent proteins. *Sensors (Basel)* 21:795. doi: 10.3390/s21030795

Kramer, M. L., and Schulz-Schaeffer, W. J. (2007). Presynaptic alpha-synuclein aggregates, not Lewy bodies, cause neurodegeneration in dementia with Lewy bodies. *J. Neurosci.* 27, 1405–1410.

Kruger, R., Kuhn, W., Muller, T., Woitalla, D., Graeber, M., Kosel, S., et al. (1998). Ala30Pro mutation in the gene encoding alpha-synuclein in Parkinson's disease. *Nat. Genet.* 18, 106–108.

Lashuel, H. A. (2020). Do Lewy bodies contain alpha-synuclein fibrils? and Does it matter? A brief history and critical analysis of recent reports. *Neurobiol. Dis.* 141:104876. doi: 10.1016/j.nbd.2020.104876

Laurent, F., Floderer, C., Favard, C., Muriaux, D., Masson, J. B., and Vestergaard, C. L. (2019). Mapping spatio-temporal dynamics of single biomolecules in living cells. *Phys. Biol.* 17:015003. doi: 10.1088/1478-3975/ab5167

Lelek, M., Gyparaki, M. T., Beliu, G., Schueder, F., Griffié, J., Manley, S., et al. (2021). Single-molecule localization microscopy. *Nat. Rev. Methods Primers* 1, 1–27.

Leterrier, C., Potier, J., Caillol, G., Debarnot, C., Rueda Boroni, F., and Dargent, B. (2015). Nanoscale architecture of the axon initial segment reveals an organized and robust scaffold. *Cell Rep.* 13, 2781–2793. doi: 10.1016/j.celrep.2015.11.051

Lippincott-Schwartz, J., Altan-Bonnet, N., and Patterson, G. H. (2003). Photobleaching and photoactivation: following protein dynamics in living cells. *Nat. Cell Biol.* 5, S7–S14.

Marshall, J., Molloy, R., Moss, G. W., Howe, J. R., and Hughes, T. E. (1995). The jellyfish green fluorescent protein: a new tool for studying ion channel expression and function. *Neuron* 14, 211–215. doi: 10.1016/0896-6273(95)90279-1

Maynard, S. A., Rostaing, P., Schaefer, N., Gemin, O., Candat, A., Dumoulin, A., et al. (2021). Identification of a stereotypic molecular arrangement of endogenous glycine receptors at spinal cord synapses. *bioRxiv* [Preprint]. doi: 10.1101/2021.09.09.459599

Narhi, L., Wood, S. J., Steavenson, S., Jiang, Y., Wu, G. M., Anafi, D., et al. (1999). Both familial Parkinson's disease mutations accelerate alpha-synuclein aggregation. *J. Biol. Chem.* 274, 9843–9846.

Ninkina, N., Tarasova, T. V., Chaprov, K. D., Roman, A. Y., Kukharsky, M. S., Kolik, L. G., et al. (2020). Alterations in the nigrostriatal system following conditional inactivation of α-synuclein in neurons of adult and aging mice. *Neurobiol. Aging* 91, 76–87. doi: 10.1016/j.neurobiolaging.2020.02.026

Peelaerts, W., Bousset, L., Van der Perren, A., Moskalyuk, A., Pulizzi, R., Giugliano, M., et al. (2015). α-Synuclein strains cause distinct synucleinopathies after local and systemic administration. *Nature* 522, 340–344. doi: 10.1038/nature14547

Piston, D. W., Patterson, G. H., and Knobel, S. M. (1999). Quantitative imaging of the green fluorescent protein (GFP). *Methods Cell Biol.* 58, 31–48. doi: 10.1016/s0091-679x(08)61947-0

Polymeropoulos, M. H., Lavedan, C., Leroy, E., Ide, S. E., Dehejia, A., Dutra, A., et al. (1997). Mutation in the alpha-synuclein gene identified in families with Parkinson's disease. *Science* 276, 2045–2047.

Ray, S., Singh, N., Kumar, R., Patel, K., Pandey, S., Datta, D., et al. (2020). α-Synuclein aggregation nucleates through liquid-liquid phase separation. *Nat. Chem.* 12, 705–716. doi: 10.1038/s41557-020-0465-9

Reshetniak, S., Ußling, J. E., Perego, E., Rammner, B., Schikorski, T., Fornasiero, E. F., et al. (2020). A comparative analysis of the mobility of 45 proteins in the synaptic bouton. *EMBO J.* 39:e104596. doi: 10.15252/embj.2020104596

Shahmoradian, S. H., Lewis, A. J., Genoud, C., Hench, J., Moors, T. E., Navarro, P. P., et al. (2019). Lewy pathology in Parkinson's disease consists of crowded organelles and lipid membranes. *Nat. Neurosci.* 22, 1099–1109. doi: 10.1038/s41593-019-0423-2

Shrivastava, A. N., Bousset, L., Renner, M., Redeker, V., Savistchenko, J., Triller, A., et al. (2020). Differential membrane binding and seeding of distinct α-synuclein fibrillar polymorphs. *Biophys. J.* 118, 1301–1320. doi: 10.1016/j.bpj.2020.01.022

Singleton, A. B., Farrer, M., Johnson, J., Singleton, A., Hague, S., Kachergus, J., et al. (2003). alpha-Synuclein locus triplication causes Parkinson's disease. *Science* 302:841.

Specht, C. G., Tigaret, C. M., Rast, G. F., Thalhammer, A., Rudhard, Y., and Schoepfer, R. (2005). Subcellular localisation of recombinant alpha- and gamma-synuclein. *Mol. Cell. Neurosci.* 28, 326–334. doi: 10.1016/j.mcn.2004.09.017

Spillantini, M. G., Schmidt, M. L., Lee, V. M., Trojanowski, J. Q., Jakes, R., and Goedert, M. (1997). Alpha-synuclein in Lewy bodies. *Nature* 388, 839–840.

Spinelli, K. J., Taylor, J. K., Osterberg, V. R., Churchill, M. J., Pollock, E., Moore, C., et al. (2014). Presynaptic alpha-synuclein aggregation in a mouse model of Parkinson's disease. *J. Neurosci.* 34, 2037–2050. doi: 10.1523/JNEUROSCI.2581-13.2014

Tang, A. H., Chen, H., Li, T. P., Metzbower, S. R., MacGillavry, H. D., and Blanpied, T. A. (2016). A trans-synaptic nanocolumn aligns neurotransmitter release to receptors. *Nature* 536, 210–214. doi: 10.1038/nature19058

Uversky, V. N. (2017). Looking at the recent advances in understanding alpha-synuclein and its aggregation through the proteoform prism. *F1000Res* 6:525. doi: 10.12688/f1000research.10536.1

Verdier, H., Duval, M., Laurent, F., Cassé, A., Vestergaard, C. L., and Masson, J.-B. (2021). Learning physical properties of anomalous random walks using graph neural networks. *J. Phys. A Math. Theor.* 54:234001.

Volpicelli-Daley, L. A., Luk, K. C., Patel, T. P., Tanik, S. A., Riddle, D. M., Stieber, A., et al. (2011). Exogenous α-synuclein fibrils induce Lewy body pathology leading to synaptic dysfunction and neuron death. *Neuron* 72, 57–71. doi: 10.1016/j.neuron.2011.08.033

Wang, S., and Hazelrigg, T. (1994). Implications for bcd mRNA localization from spatial distribution of exu protein in *Drosophila oogenesis*. *Nature* 369, 400–403. doi: 10.1038/369400a0

Werner, C., Sauer, M., and Geis, C. (2021). Super-resolving microscopy in neuroscience. *Chem. Rev.* doi: 10.1021/acs.chemrev.0c01174

Weston, L. J., Cook, Z. T., Stackhouse, T. L., Sal, M. K., Schultz, B. I., Tobias, Z. J. C., et al. (2021). In vivo aggregation of presynaptic alpha-synuclein is not influenced by its phosphorylation at serine-129. *Neurobiol. Dis.* 152:105291. doi: 10.1016/j.nbd.2021.105291

Wilhelm, B. G., Mandad, S., Truckenbrodt, S., Krohnert, K., Schafer, C., Rammner, B., et al. (2014). Composition of isolated synaptic boutons reveals the amounts of vesicle trafficking proteins. *Science* 344, 1023–1028. doi: 10.1126/science.1252884

Wood, S. J., Wypych, J., Steavenson, S., Louis, J. C., Citron, M., and Biere, A. L. (1999). alpha-synuclein fibrillogenesis is nucleation-dependent. Implications for the pathogenesis of Parkinson's disease. *J. Biol. Chem.* 274, 19509–19512. doi: 10.1074/jbc.274.28.19509

Wu, Y. L., Tschanz, A., Krupnik, L., and Ries, J. (2020). Quantitative data analysis in single-molecule localization microscopy. *Trends Cell Biol.* 30, 837–851. doi: 10.1016/j.tcb.2020.07.005

Xu, K., Zhong, G., and Zhuang, X. (2013). Actin, spectrin, and associated proteins form a periodic cytoskeletal structure in axons. *Science* 339, 452–456. doi: 10.1126/science.1232251

Yang, X., Le Corronc, H., Legendre, P., Triller, A., and Specht, C. G. (2021). Differential regulation of glycinergic and GABAergic nanocolumns at mixed inhibitory synapses. *EMBO Rep.* 22:e52154. doi: 10.15252/embr.202052154

Zaltieri, M., Grigoletto, J., Longhena, F., Navarria, L., Favero, G., Castrezzati, S., et al. (2015). Alpha-synuclein and synapsin III cooperatively regulate synaptic function in dopamine neurons. *J. Cell Sci.* 128, 2231–2243. doi: 10.1242/jcs.157867

Zhu, M., and Fink, A. L. (2003). Lipid binding inhibits alpha-synuclein fibril formation. *J. Biol. Chem.* 278, 16873–16877. doi: 10.1074/jbc.M210136200

Conflict of Interest: The author declares that the research was conducted in the absence of any commercial or financial relationships that could be construed as a potential conflict of interest.

frontiers
in Synaptic Neuroscience

REVIEW
published: 23 November 2021
doi: 10.3389/fnsyn.2021.790773

Contribution of Membrane Lipids to Postsynaptic Protein Organization

Manon Westra†, Yolanda Gutierrez† and Harold D. MacGillavry*

Cell Biology, Neurobiology and Biophysics, Department of Biology, Faculty of Science, Utrecht University, Utrecht, Netherlands

The precise subsynaptic organization of proteins at the postsynaptic membrane controls synaptic transmission. In particular, postsynaptic receptor complexes are concentrated in distinct membrane nanodomains to optimize synaptic signaling. However, despite the clear functional relevance of subsynaptic receptor organization to synaptic transmission and plasticity, the mechanisms that underlie the nanoscale organization of the postsynaptic membrane remain elusive. Over the last decades, the field has predominantly focused on the role of protein-protein interactions in receptor trafficking and positioning in the synaptic membrane. In contrast, the contribution of lipids, the principal constituents of the membrane, to receptor positioning at the synapse remains poorly understood. Nevertheless, there is compelling evidence that the synaptic membrane is enriched in specific lipid species and that deregulation of lipid homeostasis in neurons severely affects synaptic functioning. In this review we focus on how lipids are organized at the synaptic membrane, with special emphasis on how current models of membrane organization could contribute to protein distribution at the synapse and synaptic transmission. Finally, we will present an outlook on how novel technical developments could be applied to study the dynamic interplay between lipids and proteins at the postsynaptic membrane.

Keywords: synapse, membrane, lipid, membrane organization, synaptic plasiticity, synaptic plasma membrane

OPEN ACCESS

Edited by:
Xiaobing Chen,
National Institutes of Health (NIH),
United States

Reviewed by:
Masaki Fukata,
National Institute for Physiological Sciences (NIPS), Japan
Bernardo Moreno-López,
University of Cádiz, Spain

****Correspondence:***
Harold D. MacGillavry
h.d.macgillavry@uu.nl

†These authors have contributed equally to this work

Received: *07 October 2021*
Accepted: *02 November 2021*
Published: *23 November 2021*

Citation:
Westra M, Gutierrez Y and MacGillavry HD (2021) Contribution of Membrane Lipids to Postsynaptic Protein Organization.
Front. Synaptic Neurosci. 13:790773.
doi: 10.3389/fnsyn.2021.790773

INTRODUCTION

Experience-dependent modulation of synaptic connections in the brain underlies complex cognitive processes such as learning and memory. In particular, activity-dependent changes in the postsynaptic organization are thought to be essential for the expression of the long-term changes in the efficiency of synaptic transmission that underlie memory formation (Martin et al., 2000; Takeuchi et al., 2014). Indeed, recent super-resolution microscopy studies demonstrated that the positioning of synaptic scaffolding molecules and receptors anchored at the postsynaptic density (PSD) is tightly controlled at the nanoscale and is adjusted by synaptic activity (Fukata et al., 2013; MacGillavry et al., 2013; Nair et al., 2013; Tang et al., 2016; Goncalves et al., 2020). Specifically, subsynaptic clusters of receptors, or nanodomains, in the synaptic membrane enriched in AMPA- or NMDA-type glutamate receptors (AMPARs and NMDARs) and scaffolding molecules were found to be aligned with the presynaptic glutamate release site to optimize synaptic transmission (Tang et al., 2016; Li et al., 2021). However, how these nanodomains are formed and modulated during synaptic plasticity remains unknown.

Despite synaptic receptors being integral membrane proteins that are embedded in the lipid bilayer, the contribution of lipids to synaptic organization and functioning remains poorly understood. Nevertheless, lipids are the most abundant components of the brain and lipid dysregulation is thought to underlie several cognitive disorders (Kanungo et al., 2013; Martín et al., 2014; Pérez-Cañamás et al., 2017; van der Kant et al., 2019). Interestingly, synapses are enriched in specific lipid species such as cholesterol and sphingolipids (Breckenridge et al., 1972) and other less abundant components, such as phosphoinositides. This unique lipid composition can have various important consequences for synapse organization and functioning. For instance, lipids can control compartmentalization and proper positioning or activation of critical synaptic protein complexes (Haucke and Di Paolo, 2007; Arendt et al., 2010; Dotti et al., 2014; Brachet et al., 2015). Moreover, changes in lipid composition determine membrane viscosity, thereby directly controlling the mobility and lateral diffusion of membrane molecules. Indeed, the particular composition of the lipid bilayer strongly favors the maintenance of a heterogeneous spatial organization of membrane lipids and associated proteins (Ingólfsson et al., 2017; Fitzner et al., 2020). The unique composition and structure of the synaptic membrane is therefore predicted to directly impact the activity-dependent changes in protein organization at synapses, ultimately controlling synaptic physiology and brain function.

In this review we will focus on the contribution of the postsynaptic plasma membrane to synapse organization and neuronal function. We will discuss our current understanding of the lipid composition of the synaptic membrane, consider intrinsic and extrinsic factors that influence membrane organization and lastly, we will highlight technical advances that can be used to further study the role of the membrane in postsynaptic organization.

THE NEURONAL AND SYNAPTIC LIPIDOME

The composition of the plasma membrane is significantly different between cell types, is adjusted during developmental stages and can adapt in response to environmental changes. We are only beginning to understand how this dynamic diversity in lipid composition influences cellular functions but it is becoming clear that the heterogeneity in lipid composition directly determines physical properties of the membrane and is important for key cellular processes.

Cellular membrane lipids are amphipathic molecules with a characteristic polar headgroup and long hydrophobic fatty acid tails causing them to spontaneously form a thin lipid bilayer (**Figure 1**). Lipids can be categorized based on their head groups, fatty acid chain lengths and degree of saturation. The three major classes of membrane lipids are phospholipids, glycolipids, and sterol (**Figure 1A**). Phospholipids form the vast majority of lipids in plasma membranes (>50%), with a small contribution of glycolipids (<5%). Cholesterol constitutes 25–35% of the membrane lipids and provides rigidity to the plasma membrane. Together, the phospholipids phosphatidylethanolamine (PE), phosphatidylcholine (PC), phosphatidylserine (PS), and sphingomyelin constitute more than half the mass of lipids in most mammalian membranes.

Advances in lipidomic profiling have enabled the precise identification and quantification of lipid species in tissues. These approaches revealed that lipid composition of the brain is highly distinct from other tissues with relatively high levels of cholesterol and polyunsaturated fatty acids (PUFAs; Bozek et al., 2015; Fitzner et al., 2020). Interestingly, comparison between species revealed that this diversity rapidly expanded in primates, linking brain lipidome complexity to the evolution of higher cognitive brain functions (Bozek et al., 2015). Further analysis of cell-type specific lipid profiles revealed that neurons are particularly enriched in cholesterol and ceramide (Fitzner et al., 2020).

Several studies have investigated the lipid composition of synaptic plasma membranes isolated using zonal centrifugation from adult rat brain (Cotman et al., 1969; Breckenridge et al., 1972; Igbavboa et al., 2002; Tulodziecka et al., 2016). The major lipid types in synaptic membranes are cholesterol, phospholipids and gangliosides, with PE and PC as the most abundant phospholipids (Cotman et al., 1969; Igbavboa et al., 2002). Compared to the whole brain, the fraction of glycolipids in synaptic membranes seems lower while sphingomyelin seems more abundant (Cotman et al., 1969). Interestingly, although sphingomyelin is detected at low levels, in contrast to other membranes, in synapses sphingomyelin is composed of almost exclusively stearic (18:0) acid (Breckenridge et al., 1972). When looking more closely at the fatty acid composition, it was found that the synaptic plasma membrane is particularly enriched in PUFAs (Cotman et al., 1969; Breckenridge et al., 1972; Igbavboa et al., 2002). Particularly high levels of docosahexaenoic acid (DHA) in PE and PS phospholipids were detected, which is a striking difference compared to the plasma membrane composition of other tissues. A recent comprehensive lipidomic study showed that the lipid composition of the PSD membrane evolves with development (Tulodziecka et al., 2016), with key species such as cholesterol progressively increasing during development. Additionally, glycosphingolipid levels are developmentally regulated and increase throughout postnatal life (Ngamukote et al., 2007).

It is worth noting, however, that several technical limitations prevent forming a comprehensive characterization of the absolute synaptic plasma membrane lipidome with existing biochemical approaches. Whereas synaptosomal preparations contain a mixture of presynaptic membranes, like synaptic vesicles, and other organellar membranes, isolation of PSD plasma membrane relies on the use of non-ionic detergents that can influence the extracted lipid content. Nevertheless, despite differences in absolute numbers of certain lipid species, namely cholesterol and glycosphingolipids, relative compositional changes in response to specific conditions can reliably be detected (Tulodziecka et al., 2016).

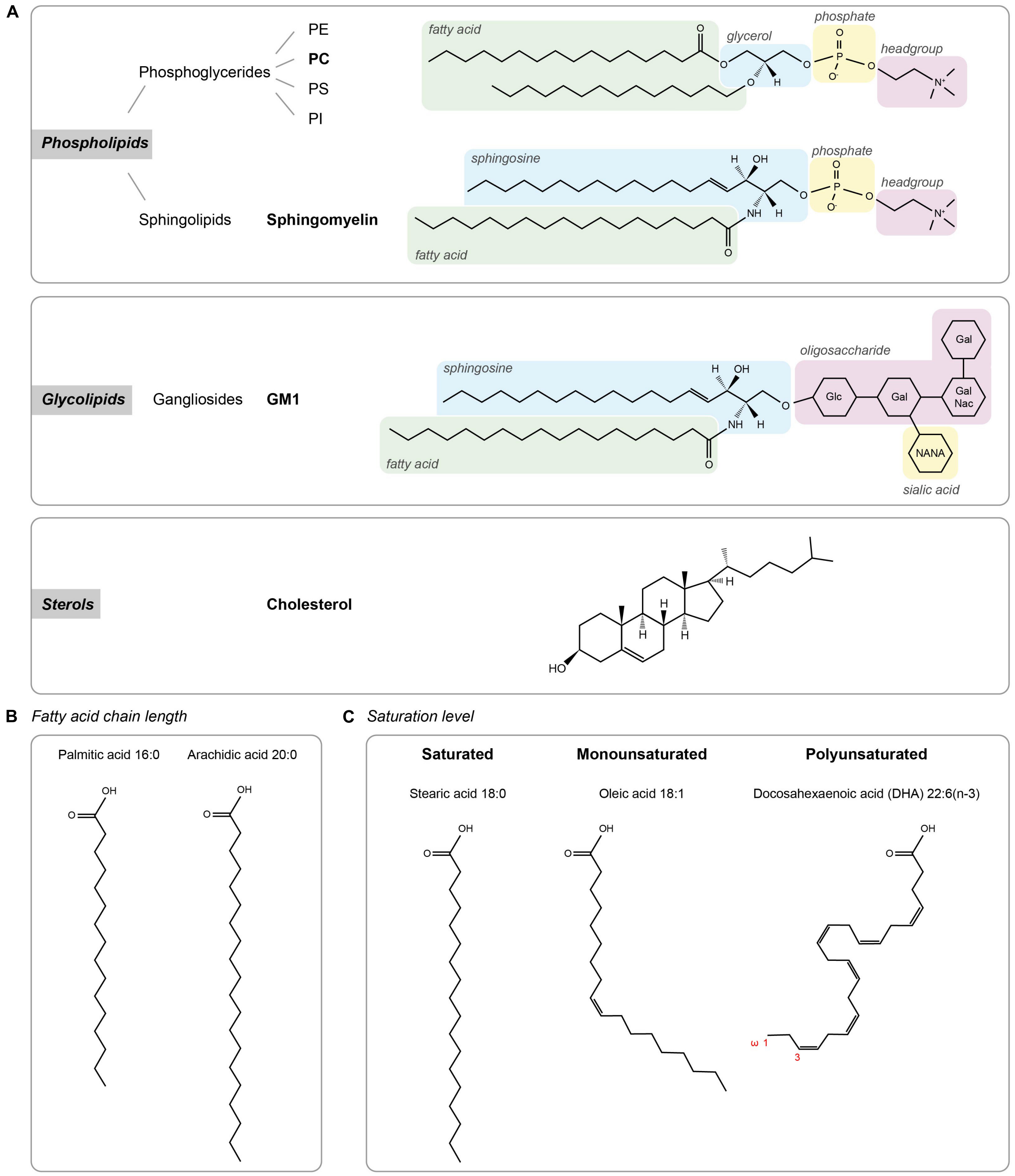

FIGURE 1 | Lipid types. **(A)** The three major classes of membrane lipids (phospholipids, glycolipids, and sterols) with an example lipid structure (bold) for each. Glc – D-glucose, Gal – D-galactose, NANA – N-actylneuraminic acid, and GalNac – *N*-acetyl-D-galactoseamine. **(B,C)** Acyl chain composition. **(B)** Fatty acid chain length for palmitic acid and arachidic acid. **(C)** Lipid structures of lipids with different saturation levels (stearic acid, oleic acid, and docosahexaenoic acid).

MEMBRANE COMPOSITION DICTATES ITS ORGANIZATION: INTRINSIC FACTORS

The distinct lipidomic profile of neuronal membranes is likely to influence key neuronal functions. Particularly at synapses, the specific lipid composition could contribute to the heterogeneous nanodomain organization of receptors. However, testing the precise contribution of individual lipids to membrane organization and function in neurons remains technically challenging. Nevertheless, pioneering studies in model membrane systems have characterized the unique biophysical properties of individual lipid species and revealed that these intrinsic properties determine important organizational properties of membranes. We will first provide a brief overview of the general concepts and models of membrane organization and then discuss how these could be incorporated in our current understanding of synapse organization. For more extensive reviews on membrane organization, we refer to a few excellent recent reviews (Sezgin et al., 2017; Jacobson et al., 2019; van Deventer et al., 2021).

Contribution of Biophysical Properties of Lipids to Membrane Organization

The classic fluid mosaic model (Singer and Nicolson, 1972) was the first to conceptualize and explain experimental observations on the fluidic nature of the plasma membrane. It emphasized that the two-dimensional lipid bilayer is liquid, and that membrane fluidity is the key driver that allows the heterogeneous mixing of lipids and membrane proteins. Almost 50 years later, this model is still valid and has clear relevance for our current thinking on membrane organization. The fluidity of membranes is a key determinant of the diffusion rate of lipids and transmembrane proteins in the membrane as formalized in the hydrodynamic model proposed by Saffman and Delbrück (1975). Membrane fluidity is largely determined by acyl chain composition of membrane lipids (**Figures 1B,C**). First, longer acyl chains have a larger surface area available for Van der Waals interactions with neighboring acyl chains, reducing membrane fluidity. Second, while straight saturated acyl chains can be efficiently packed closely together, the kink in the hydrocarbon chain of unsaturated acyl chains prevents efficient packing and thus helps to maintain membrane fluidity. Another important determinant of fluidity is cholesterol, which generally promotes packing of lipids.

Driven by their intrinsic biophysical properties, long saturated acyl chains and cholesterol tend to segregate into tightly packed, liquid-ordered (Lo) phases, whereas unsaturated acyl chains preferentially accumulate in liquid-disordered (Ld) phases. This phase behavior has been studied extensively in synthetic model membranes and has also been observed in giant plasma membrane vesicles (GPMVs) derived from living cells (Baumgart et al., 2007). These observations have greatly influenced the lipid raft theory proposing the existence of ordered lipid domains enriched in cholesterol and glycosphingolipids that facilitate the clustering of specific membrane proteins and associated signaling complexes to form dynamic signaling platforms (Simons and Ikonen, 1997; **Figure 2**). This theory has been investigated vigorously by biochemical methods that extract detergent-resistant membranes (DRMs) enriched in glycosphingolipids and cholesterol (Brown and Rose, 1992). However, because of technical caveats associated with these biochemical approaches and the absence of direct visualization of lipid rafts in living cells, this theory has gained considerable criticism (Pike, 2009; Levental et al., 2020). Nevertheless, in general, rafts are considered to constitute rather small (20–200 nm) and transient membrane domains (Pike, 2006; Eggeling et al., 2009) and considerable attention has been devoted to characterize raft-promoting lipids such as cholesterol and glycosphingolipids in different cellular systems. In contrast, the role of (poly-) unsaturated fatty acids in membrane organization is less well understood. However, these lipids are increasingly recognized as drivers of membrane domain formation (Wassall and Stillwell, 2009). Particularly, studies using GPMVs indicate that polyunsaturated lipids (especially DHA) promote the formation and stabilization of ordered membrane domains by increasing the phase difference in ordering (Levental et al., 2016, 2017).

Variations in membrane thickness can also have profound consequences for the organization of transmembrane proteins. The thickness of the membrane is primarily determined by the acyl chain properties of the lipids, with longer, saturated chains forming thicker membranes. When the hydrophobic transmembrane segment of a protein does not match the hydrophobic thickness of the membrane, a so-called hydrophobic mismatch will occur. To compensate for such hydrophobic mismatches, lipids with matching chain lengths will preferentially surround the transmembrane segment causing local variations in the lateral distribution of lipids. Also, the protein can adapt its orientation or conformation to match the thickness (de Planque et al., 2001), or even undergo aggregation to minimize the mismatch. Hydrophobic matching has therefore been proposed as a mechanism that drives self-assembly of domains consisting of transmembrane proteins and lipids with similar hydrophobic length (Mouritsen and Bloom, 1984; Anderson and Jacobson, 2002). Indeed, computational simulations and experimental analysis in model membranes and cells indicate that hydrophobic matching could promote the lateral segregation of proteins and lipids which is further modulated by cholesterol (Kaiser et al., 2011; Diaz-Rohrer et al., 2014). The mattress model by Mouritsen and Bloom (1984) proposes that hydrophobic mismatch promotes lateral segregation in the membrane such that lipids and proteins self-organize in domains of similar hydrophobic thickness. This has for instance been found to underlie the segregation into functionally distinct membrane domains of two related SNARE proteins, Syntaxin-1 and -4 (Milovanovic et al., 2015). Whether such mechanisms underlie the compartmentalization of postsynaptic transmembrane proteins has not been studied yet.

The concepts and models discussed here conceptualized many of the observations on membrane organization in synthetic and cellular membrane models. However, it is becoming increasingly clear that these models are not universal and the factors determining membrane heterogeneity are highly interdependent (Bernardino de la Serna et al., 2016). Both fluidity

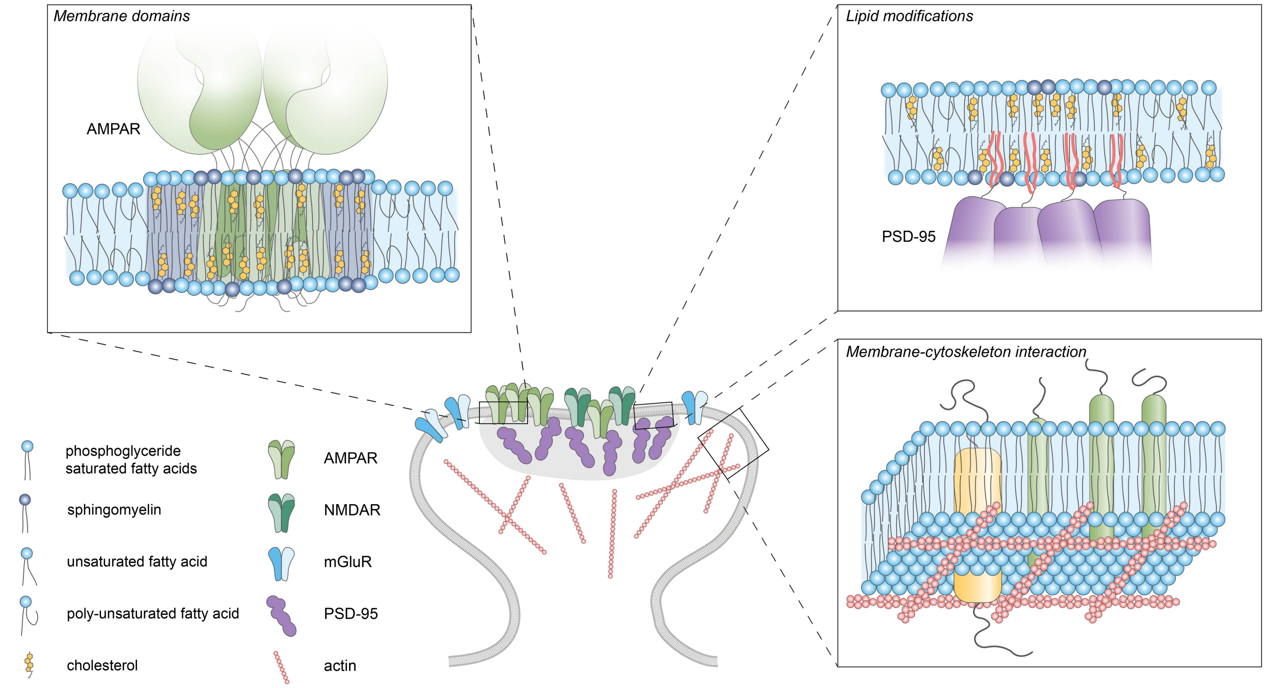

FIGURE 2 | Lipid-protein interactions. Schematic diagram of the different lipid-protein interactions within the postsynaptic plasma membrane. Membrane domains enriched in cholesterol, glycosphingolipids and saturated lipids can facilitate clustering of membrane proteins by influencing fluidity and thickness of the membrane. Reversible palmitoylation can translocate proteins to the plasma membrane. Actin-linked transmembrane proteins can act as "pickets" and hinder the diffusion of lipids and proteins within the membrane.

and membrane thickness can lead to lateral heterogeneity in the membrane. Particularly, in cellular membranes interactions between lipids and membrane proteins seem dominant in determining membrane domain formation. Thus, the nature of membrane domains, i.e., their spatial dimensions and lifetimes are likely to be highly dependent on the specific subcellular composition of the membrane. Indeed, the current goal of the field is to understand how the interplay between the biophysical properties of lipids and membrane proteins orchestrates membrane organization.

INTRINSIC DETERMINANTS OF POSTSYNAPTIC MEMBRANE ORGANIZATION

At excitatory synapses, the density of glutamate receptors is a direct determinant of synaptic strength. Mechanisms that control the retention and positioning of receptors have therefore gained tremendous interest. Scaffold proteins in the PSD form a structural platform that anchor receptors via intricate networks of protein-protein interactions. Nevertheless, concepts in membrane biology pose a central role for the intrinsic capacity of lipids to self-organize and form functional membrane domains. In the following sections we discuss how the unique composition of the postsynaptic membrane suggests that synapses actively maintain and perhaps adjust this composition to instruct the organization and function of synaptic protein components.

Fluidity Controls Receptor Diffusion

Lipidomics studies consistently point out that the brain and particularly synaptic membranes are enriched in both cholesterol and PUFAs. How does this specific composition, with high concentrations of lipids that have opposing effects on lipid ordering and membrane fluidity, influence fluidity at the postsynaptic membrane? Commonly, quantification of the mobility of transmembrane proteins using fluorescence recovery after photobleaching or single-molecule tracking approaches is taken as an estimate of membrane fluidity. However, synaptic membrane proteins are mostly either directly anchored to scaffold proteins or are slowed down in their diffusion due to the relative high density of proteins at the synapse (Li and Blanpied, 2016; Li et al., 2016). In fact, the diffusion of even small transmembrane proteins that are unable to bind synaptic scaffolds is severely influenced by local, subsynaptic variations in cytoplasmic protein density (Li and Blanpied, 2016). Measures of protein mobility do therefore not directly report on the fluidity or ordering of lipids within the membrane itself but are the result of a complex interplay of many different factors. Nevertheless, single-molecule tracking studies showed that even the diffusion rates of fluorescently labeled lipids that are not specifically enriched at synaptic sites are significantly reduced in the postsynaptic membranes compared to extrasynaptic regions (Renner M. L. et al., 2009). However, more direct measures of membrane fluidity using for instance environment-sensitive dyes would be of interest. As an alternative, recently developed computational approaches now allow investigation of the dynamic interplay between lipids and membrane proteins at high spatiotemporal resolution (Ingólfsson et al., 2016). In particular, coarse-grained molecular dynamics simulations allow accurate predictions of how mixtures of lipid species are organized. In a recently developed model of a "brain-like plasma membrane" it was found that while the high concentration of cholesterol leads to an overall increase in acyl chain ordering, the fluidizing effect of high levels of tail unsaturation appears to balance this out (Ingólfsson et al., 2017). Interestingly, however, the extent of ordering in the case of brain membranes was unequally divided over the inner and outer membrane leaflets, with the brain membrane showing distinctively more ordering in the outer leaflet. Also, diffusion rates of lipids were on average 40% lower in brain membranes. Comparable to earlier models of cellular membranes, considerable heterogeneity in the lateral distribution of lipids was found, with more but smaller and more transient cholesterol domains in the brain membrane. These simulations thus provide an unprecedented high-resolution snapshot of how the plasma membrane of neurons could be organized, and it will be of interest to expand these models to test how the high molecular density of integral and membrane-associated proteins at the synapse will influence and interact with this specific composition of lipids.

Synapses Have Raft Properties

The enrichment of cholesterol and sphingolipids at synaptic membranes and the computational simulations suggest that the postsynaptic membrane could have confined regions reminiscent of lipid rafts. Indeed, DRMs isolated from whole brain contain key components of excitatory synapses, most notably PSD-95, as well as glutamate receptors and interacting proteins (Perez and Bredt, 1998; Brückner et al., 1999; Suzuki et al., 2001, 2011; Hering et al., 2003; Ma et al., 2003; Besshoh et al., 2005; Hou et al., 2008; Delint-Ramirez et al., 2010). Moreover, rafts can be isolated from synaptic membrane fractions (Suzuki et al., 2001, 2011; Besshoh et al., 2005) and ChTx (cholera toxin) labeling overlaps with PSD-95 staining, indicating the presence of raft-like structures at the PSD (Perez and Bredt, 1998; Brückner et al., 1999; Suzuki et al., 2001; Hering et al., 2003; Hou et al., 2008). At the ultrastructural level, electron cryotomography showed that GM1-positive raft-like membranes were frequently found associated, preferentially with adult PSDs (Suzuki et al., 2001; Besshoh et al., 2005; Swulius et al., 2012), consistent with the developmental increase in raft-promoting lipids at synaptic membranes (Tulodziecka et al., 2016). Further, immuno-EM studies demonstrated the presence of raft markers such as flotilins at the PSD (Suzuki, 2002; Hering et al., 2003), that were also shown to interact with NMDAR subunits (Swanwick et al., 2009). All these data thus suggest that raft-like domains exist within the postsynaptic membrane, perhaps compartmentalizing specific receptor complexes (Perez and Bredt, 1998; Brückner et al., 1999; Suzuki et al., 2001; Hering et al., 2003; Allen et al., 2007; Hou et al., 2008). Indeed, PSD-95-NMDAR complexes isolated from raft fractions were enriched in a different complement of signaling molecules than those isolated from PSD or soluble fractions (Delint-Ramirez et al., 2010). The association of NMDARs with raft vs. non-raft domains has been shown to be regulated for instance during spatial memory formation (Delint-Ramírez et al., 2008) and ischemia (Besshoh et al., 2005) indicating that the association of synaptic receptors with specific membrane domains can be dynamic and regulated by synaptic activity.

Thus, although lipid raft characterization relies on biochemical procedures that may occlude investigation of more complex membrane dynamics, evidence gathered through these and other experimental means clearly points toward the existence of a heterogeneous distribution of different components in the postsynaptic membrane. However, it remains difficult to assess how individual lipid types contribute to this heterogeneity. In large part this is difficult because the behavior of individual lipids is highly dependent on the environment. For example, while PUFAs might form disordered membrane domains, they could also contribute to stabilize ordered membrane domains (Wassall and Stillwell, 2009; Levental et al., 2016). Additionally, the interactions of lipids with proteins provide an extra layer of complexity that could underlie the lateral distribution of postsynaptic membrane components.

Lipids Modulate Synaptic Transmission

Consistent with the notion that lipid rafts are important for regulating NMDAR function, interfering with membrane cholesterol levels was shown to perturb NMDAR-dependent calcium responses as well as LTP (Koudinov and Koudinova, 2001; Frank et al., 2004, 2008; Kotti et al., 2006; Maggo and Ashton, 2014; Guo et al., 2021). More specifically, cholesterol depletion was reported to decrease the open probability of NMDARs and reduce the fraction of synaptic immobile NMDARs (Korinek et al., 2015, 2020). Furthermore, cholesterol reduction increased basal internalization of AMPARs (Hering et al., 2003) and the mobility of slow diffusing molecules within the synapse (Renner M. et al., 2009). In addition, treatment with statins (inhibitors of cholesterol synthesis) impaired recognition and working memory (Maggo and Ashton, 2014; Guo et al., 2021). Cholesterol replenishment could rescue impaired LTD resulting from cholesterol loss in aged mice, also improving hippocampal learning and memory (Ledesma et al., 2012; Martin et al., 2014). On the contrary, other studies reported enhancement of LTP and hippocampal-dependent learning and memory after cholesterol reduction, while adding cholesterol impaired LTP (Li et al., 2006; Mans et al., 2010; Brachet et al., 2015). These conflicting results could be explained by a dose-dependent effect of cholesterol (Baytan et al., 2008; Wang and Zheng, 2015). To untangle these effects, several studies have looked at it from a different perspective: what influence does glutamatergic synaptic transmission have on cholesterol levels? Stimulation of glutamatergic transmission was found to induce a loss of cholesterol from synaptic membranes and recruitment of CYP46A1 – an enzyme responsible for cholesterol removal – to the synaptic plasma membrane (Sodero et al., 2012; Brachet et al., 2015; Mitroi et al., 2019). Taken together, these findings highlight the dynamic interplay between cholesterol levels and glutamatergic transmission.

Long-chain PUFAs, particularly DHA, are also found to be enriched in synapses and could play an important role in compartmentalizing the membrane and thereby influencing synaptic transmission. The addition of exogenous DHA to dissociated neuronal cultures was found to enhance spontaneous glutamatergic synaptic activity and promote NMDAR function (Nishikawa et al., 1994; Cao et al., 2009). Furthermore, the protein levels of both AMPAR and NMDAR subunits were higher in the DHA-supplemented cultures (Cao et al., 2009). However, DHA-treatment has been linked to variable effects on synaptic plasticity on brain slices. Exogenous DHA supplementation leads to facilitated LTP in the corticostriatal pathway (Mazzocchi-Jones, 2015) whereas LTP and LTD in the CA1 region were found to be impaired (Young et al., 1998; Mirnikjoo et al., 2001) or unaffected (Fujita et al., 2001; Mazzocchi-Jones, 2015). Some of the discrepancies might arise from region-dependent effects of DHA on synaptic plasticity. In the CA1 region LTP was inhibited whereas in the dentate gyrus there was no effect on LTP after intracerebroventricular injection of DHA (Itokazu et al., 2000). Interestingly, dietary supplementation or deprivation has proven to be an effective method of manipulating DHA levels. The importance of DHA for synaptic plasticity has been found both in young mice, where maternal dietary deprivation of DHA leads to inhibited induction of LTP (Cao et al., 2009), as well as in old rats, where the age-related impairment of LTP is restored by a DHA-supplemented diet (McGahon et al., 1999). Although the variety of results found could be a result of the different experimental paradigms used, it is apparent that DHA plays an important role in modulating cognitive functions. This is highlighted also from the finding that DHA deficiency results in affected spatial learning whereas the *fat-1* transgenic mouse, producing high DHA levels, shows improved spatial learning (Fedorova et al., 2007; He et al., 2009). Lastly, it is important to note that apart from the structural role these lipids can play in membranes, cholesterol (through its metabolites) and PUFAs also have roles as signaling intermediates (Bazinet and Layé, 2014; Petrov et al., 2016). Therefore, although it cannot be concluded from these studies that modulating either cholesterol or PUFA levels solely influences membrane organization, these findings underscore the importance of synaptic membrane composition for neuronal function.

ADDITIONAL LAYERS CONTRIBUTING TO MEMBRANE ORGANIZATION: EXTRINSIC FACTORS

The intrinsic properties of lipids are likely to contribute to membrane organization, but in cellular membranes extrinsic factors add an additional layer of complexity. For instance, interactions with the underlying actin cytoskeleton, oligomerization of membrane proteins or immobilized, membrane-associated protein scaffolds can greatly impact domain formation in the membrane (Kusumi et al., 1993; Fujiwara et al., 2002; Tulodziecka et al., 2016). Particularly at the PSD, that contains a high density of transmembrane and membrane-associated proteins, reciprocal interactions between lipid species and proteins are likely to influence postsynaptic membrane organization.

Post-translational Lipid Modifications

In addition to hydrophobic structures in proteins, covalent binding of lipidic moieties can mediate the membrane association of proteins (**Figure 2**). These lipid modifications can be irreversibly added during translation or can be reversibly attached post-translationally by several enzymes [reviewed in detail in Magee and Seabra (2005), Hentschel et al. (2016), Resh (2016)]. Examples of irreversible lipid modifications include myristoylation and prenylation where myristoyl and prenyl groups are attached, respectively. On the other hand, the binding of a GPI anchor or palmitate group are reversible modifications that allow dynamic regulation of protein localization. Many proteins located in the PSD (either transmembrane or membrane-bound) present reversible lipid modifications that can be regulated by activity, incorporating another layer of control of synaptic function. The role of protein palmitoylation in synaptic plasticity is covered more extensively in the following reviews: Fukata et al. (2016), Ji and Skup (2021).

The saturated nature of the lipophilic palmitate group is thought to contribute to the association of palmitoylated proteins with ordered membrane domains. In fact, it has been shown that palmitoylation is essential for partitioning of transmembrane proteins to the ordered domain of GPMVs (Levental et al., 2010; Lorent et al., 2017). Several synaptic receptors are palmitoylated. For instance, different AMPAR subunits are palmitoylated at specific sites (Hayashi et al., 2005). Beyond establishing a quality check-point for protein surface expression, this lipid modification is shown to be a regulated activity-dependent process that controls AMPAR trafficking and recycling (Greaves and Chamberlain, 2007; Yang et al., 2009). Also, NMDAR subunits undergo palmitoylation, influencing their trafficking and stabilization at the synaptic plasma membrane (Hayashi et al., 2009). Nevertheless, it is worth noting that while palmitoylation generally promotes the partitioning of transmembrane proteins into ordered membrane regions, it is not strictly necessary nor sufficient in all cases. For example, the transferrin receptor, a canonical non-raft marker, is palmitoylated at two residues, and the raft reporter caveolin is present in detergent resistant fractions even when its palmitoylation residues are mutated (Alvarez et al., 1990; Dietzen et al., 1995).

For cytosolic proteins, palmitoylation mediates the efficient and dynamic translocation to the membrane. A prominent example is the protein AKAP79, which undergoes dynamic, activity-regulated palmitoylation (Keith et al., 2012; Woolfrey et al., 2015). Interestingly, palmitoylation of AKAP79 is required for its recruitment to dendritic spines and contributes to its stabilization in membranes through association with lipid rafts, which occurs only when it is palmitoylated (Delint-Ramirez et al., 2011; Keith et al., 2012; Purkey et al., 2018). Additionally, the main organizer of PSD architecture, PSD-95, is also anchored to the membrane through palmitoylation of two residues (Topinka and Bredt, 1998; Craven et al., 1999; El-Husseini et al., 2000). Interestingly, Tulodziecka et al. (2016), using biochemical approaches and lipidome analysis of synaptosomal membrane fractions, revealed a developmentally regulated increase in PSD-95 palmitoylation, which is accompanied by an enrichment of domain-promoting lipid species. Thus, while it is clear that palmitoylation controls membrane targeting of key synaptic components, it is plausible that palmitoylation also serves as a nucleation platform for defined lipids. As such, insertion of palmitoylated proteins such as PSD-95, could facilitate the segregation of protein/lipid nanodomains that contribute to the subsynaptic organization of the PSD. In line with this notion, the use of a specific intrabody recognizing palmitoylated PSD-95 in combination with STED microscopy revealed subsynaptic nanodomains of palmitoylated PSD-95 (Fukata et al., 2013). Additionally, PSD-95 palmitoylation regulates its conformation and orientation at the PSD, subsynaptic organization, as well as AMPAR clustering and surface expression at synapses (El-Husseini et al., 2002; Tsutsumi et al., 2008; Fukata et al., 2013; Jeyifous et al., 2016; Yokoi et al., 2016), ultimately controlling synaptic strength.

Although palmitoylation regulates trafficking and membrane targeting of synaptic proteins, its dynamic nature could thus also contribute to regulate the nanoscale distribution of synaptic proteins. Although further experiments are required to elucidate this point, it is tempting to speculate that palmitoyl residues contribute to this subsynaptic organization through interactions with defined membrane regions.

Protein-Lipid Interactions

Several models of membrane organization include the role of cortical actin in membrane organization (Kusumi et al., 1993; Fujiwara et al., 2002). In particular, the picket-fence model poses that certain actin-linked transmembrane proteins act as “pickets” and hinder diffusion of phospholipids to the next compartment (**Figure 2**). Even though the actin cytoskeleton is absent from the PSD, it is still one of the major constituents of spines and greatly influences spine morphogenesis and architecture, having a crucial role in neuronal function (Sidenstein et al., 2016; Basu and Lamprecht, 2018). Using single-molecule tracking of a lipid-bound protein Renner M. L. et al. (2009) revealed that actin depolymerization increases diffusion rates of the probe indicating that the actin cytoskeleton could hinder the diffusion of membrane proteins in spines.

Interestingly, several receptors have been reported to contain specific recognition domains for cholesterol and sphingolipids that could be involved in concentrating these receptors in specific lipid domains (Hanson et al., 2008; Jafurulla et al., 2017). For example, mGluR1 is recruited to lipid rafts through a cholesterol recognition/interaction amino acid consensus (CRAC) motif. This recruitment is enhanced upon agonist activation of the receptor, and mutations that reduce mGluR1 affinity for lipid rafts as well as alterations in cholesterol content have a direct effect in the regulation of the agonist-dependent activation of downstream pathways (Kumari et al., 2013). Nevertheless, it is worth noting that although these motifs are present in integral membrane proteins, there is inconclusive evidence to support their necessity or sufficiency for cholesterol binding. Although later efforts have focused on defining a structure-based cholesterol-binding pocket consensus (Marlow et al., 2021), cholesterol and sphingolipids can also interact with membrane-associated proteins and receptors that lack such specific binding motifs. Such lipid-protein interactions could then form a so-called “lipid shell,” allowing proteins to segregate into defined domains (Anderson and Jacobson, 2002; Fantini and Barrantes, 2009). Interestingly, recent structural studies of AMPARs in complex with CNIH2, but not with CNIH3, presented the acyl chains of two lipids penetrating the CNIH-binding site. Therefore, by extending the hydrophobic network and preventing a closer CNIH2-AMPAR interaction, membrane lipids could contribute to regulate receptor function (Zhang et al., 2021). In addition to binding to their specific scaffold proteins, these receptor-specific properties and their interaction with defined PSD membrane regions could also contribute to the segregation of AMPA- and NMDARs on distinct nanodomains within the PSD (Goncalves et al., 2020; Li et al., 2021).

TECHNICAL ADVANCES AND CHALLENGES TO STUDY LIPID ORGANIZATION IN THE SYNAPTIC PLASMA MEMBRANE

The precise organization of different lipid species within the postsynaptic membrane remains largely elusive. This lack of understanding predominantly arises from the lack of adequate tools to study the integrity and lateral heterogeneity of biological membranes in their native state (Jacobson et al., 2007). Nevertheless, new tools continue to be developed to bridge this knowledge gap (Muro et al., 2014; Sezgin et al., 2017) and it will be exciting to see the application of these tools to study the synaptic membrane.

Recent advances in lipidomics methods allow studying the composition of different neuronal compartments in greater detail, including the synaptic plasma membrane (Iuliano et al., 2021). However, while detailed lipidomic characterization provides a general picture of membrane composition (Aureli et al., 2015; Fitzner et al., 2020), it does not reveal the heterogeneity and dynamics of the lateral order of lipids in the membrane. Nevertheless, these studies provide important insights and can be currently combined with *in silico* analysis and databases to analyze protein-membrane interactions to provide further insights into the molecular dynamics at specific membranes (Ingólfsson et al., 2017; Mohamed et al., 2019; Hernández-Adame et al., 2021).

Major advances and efforts have been developed in recent years to directly visualize different lipid species and determine their precise localization and organization. For an in-depth review and overview of fluorescent lipid probes, we refer to Klymchenko and Kreder (2014). A major difficulty in visualizing lipids with fluorescence microscopy arises from the fact that fluorophores are often almost the size of the lipid molecule itself. The addition of such fluorophores could therefore influence the behavior of the lipid and alter its specific amphiphilic properties thereby changing its dynamics. One strategy to circumvent this caveat is to label the head group of the lipid with a fluorophore through the addition of a linker to prevent interaction with the surrounding headgroups (Kinoshita et al., 2017; Mobarak et al., 2018). Such newly developed fluorescent lipid analogs combined with super-resolution imaging (e.g., STED-FCS), single-molecule tracking, and expansion microscopy allow the study of membrane organization at high spatial resolution (Lenne et al., 2006; Eggeling et al., 2009; Mizuno et al., 2011; Klymchenko and Kreder, 2014; Komura et al., 2016; Götz et al., 2020; Sun et al., 2021). Alternatively, reporters that bind to specific lipids can also be used. However, such probes can influence the native membrane organization. For example ChTx, that can bind up to five GM1 gangliosides and thereby could induce cluster formation (Day and Kenworthy, 2015). In the case of cholesterol, filipin is widely used for visualization, but requires fixation because the dye permeabilizes membranes (Behnke et al., 1984). An alternative solution relies on the use of a single domain (D4) from a cholesterol-binding toxin, being sufficient for the binding of cholesterol and use as a sensor for cholesterol in live cells without perturbing its native behavior (Maekawa, 2017).

Single-molecule tracking studies have proven to be a powerful approach in studying the dynamic behavior of lipids and transmembrane proteins in synapses (Choquet and Triller, 2013) and revealed for instance the dynamic exchange of receptors in and out of synapses. Single-molecule trajectories also provide spatial information on the local, temporal confinement of transmembrane proteins, defined as regions where molecules are retained longer than expected from a Brownian moving molecule (Saxton, 1993; Simson et al., 1995), that could indicate the presence of membrane domains. A particularly powerful approach to study the dynamic behavior of lipids is high-speed (up to 25-μs intervals) single-molecule tracking of lipids coupled to photostable dyes. This can reveal temporal subdiffusive behavior and confinement of lipids and membrane proteins that are not observed at typical, slower frame rates (20–30-ms intervals; Fujiwara et al., 2002). Such studies revealed for instance that at these time scales most lipid species and transmembrane proteins undergo short-term confinement in nanoscale compartments and longer-term "hop" movements to adjacent compartments, a phenomenon referred to as "hop diffusion" (Fujiwara et al., 2002; Kusumi et al., 2010). These compartments have been related to the picket-fence model where lipids and transmembrane proteins "hop" from compartments fenced by cortical actin segments (Fujiwara et al., 2016).

The use of environment-sensitive dyes (Danylchuk et al., 2020) allows the study of membrane ordering. These lipophilic dyes have a different emission spectrum dependent on their localization in a more ordered or disordered phase of the membrane. Interestingly, a recent study made it even possible to image lipid order at the nanoscale using the photoswitchable solvatochromic probe NR4A in combination with super-resolution microscopy (Danylchuk et al., 2019). However, some of these probes are derived from voltage-sensitive probes, and could thus behave differently in the excitable membranes of neurons (Obaid et al., 2004).

Finally, a direct test of how individual lipids contribute to membrane organization or functioning in living cells is still lacking. Specific modulation of the composition of cellular membranes cannot be achieved with common pharmacological treatments. Therefore, there is still a void in molecular tools to locally and temporally manipulate membrane composition without affecting downstream pathways. Optical manipulation of lipid biosynthesis might be an interesting future direction to manipulate lipid levels with high spatiotemporal precision (Kol et al., 2019).

Altogether, it is increasingly clear that although recent technical developments provide great insight, a combination of tools and approaches is still required to define the precise lipid composition and organization at the nanoscale in the synaptic membrane.

CONCLUSION AND FUTURE DIRECTIONS

The lateral distribution of lipids and proteins in the plasma membrane is highly heterogeneous and is organized as a dynamic patchwork with specific components concentrated in domains that vary largely in size and lifetime. The unique intrinsic composition of the synaptic membrane, as well as the specific spatial distribution of lipids, is predicted to contribute to the formation of specialized nanodomains within the postsynaptic membrane. It will thus be important to understand how lipid and protein components of the postsynaptic plasma membrane interact to contribute to the organization and function of synapses.

Different approaches have been used to characterize the lipid composition of the synaptic plasma membrane. Through isolation of enriched synaptic plasma membrane fractions important observations have been made. In particular, it is evident that the synaptic membrane is enriched in cholesterol and PUFAs and that its composition evolves during development. However, the dynamic nature and lateral heterogeneity of the membrane precludes drawing the complete picture. Therefore, development of new tools is required to provide a better understanding of the organization of the synaptic plasma membrane and how it is modulated by neuronal activity. Importantly, information can be gathered not only on a descriptive level, but also through finer tools to manipulate membrane composition in a spatial and temporally regulated manner.

Another interesting notion is the cooperative nature of protein-lipid interactions. Although synapses have raft properties and general concepts for membrane organization seem to be true for the synaptic membrane, the high abundance of proteins within the synapse makes it a unique structure. Thus, generalizing models of membrane organization and imposing these on how synapses are organized is not straightforward. Nevertheless, while protein-protein domain nucleation undoubtedly plays an important instructive role in shaping the nanoscale architecture of synapses, the interaction of proteins with lipids in the surrounding membrane is likely modulating this nanoarchitecture. This is particularly relevant for proteins containing lipid interacting domains as well as post-translational lipid modifications. The challenge is thus to not only consider protein- and lipid-driven lateral organization as mutually exclusive mechanisms, but to investigate the concerted actions of proteins and lipids in generating the functional heterogeneity of the postsynaptic membrane. However, determining the contribution of lipids to synaptic organization remains a considerable challenge. One important consideration is that lipids can have a dual role, both as structural organizers of membrane domains and as signaling molecules. In fact, lipid signaling greatly contributes to neuronal function (Dotti et al., 2014), directing both intracellular transport of vesicles as well as controlling targeting or activation of key enzymes. For example, lysophospholipid-triggered signaling controls excitatory and inhibitory postsynaptic currents through defined presynaptic and postsynaptic mechanisms, respectively (García-Morales et al., 2015). Thus, altered synaptic function as a result of experimental lipid composition manipulations, could arise from effects on membrane organization, but could also be an indirect effect of disrupted signaling. Designing novel experimental tools to specifically delineate these entangled functions of lipids in synaptic signaling is a formidable task. Nevertheless, the rapid progress in the field of membrane biology and the ongoing efforts in developing novel, specific experimental tools to study membrane organization, are likely to stimulate studies on postsynaptic membrane organization. Such studies are critical to move the field toward a more comprehensive model that integrates both nanoscale protein organization as well as the heterogeneity of the synaptic lipidome.

AUTHOR CONTRIBUTIONS

MW, YG, and HM wrote the manuscript. All authors contributed to the article and approved the submitted version.

FUNDING

This work was supported by Netherlands Organization for Scientific Research (016.Vidi.171.029 to HM).

ACKNOWLEDGMENTS

We want to thank all members of the MacGillavry Lab for discussions.

REFERENCES

Allen, J. A., Halverson-Tamboli, R. A., and Rasenick, M. M. (2007). Lipid raft microdomains and neurotransmitter signalling. *Nat. Rev. Neurosci.* 8, 128–140. doi: 10.1038/nrn2059

Alvarez, E., Girones, N., and Davis, R. J. (1990). Inhibition of the receptor-mediated endocytosis of diferric transferrin is associated with the covalent modification of the transferrin receptor with palmitic acid. *J. Biol. Chem.* 265, 16644–16655. doi: 10.1016/s0021-9258(17)46270-3

Anderson, R. G. W., and Jacobson, K. (2002). A role for lipid shells in targeting proteins to caveolae, rafts, and other lipid domains. *Science* 296, 1821–1825. doi: 10.1126/science.1068886

Arendt, K. L., Royo, M., Fernández-Monreal, M., Knafo, S., Petrok, C. N., Martens, J. R., et al. (2010). PIP 3 controls synaptic function by maintaining AMPA receptor clustering at the postsynaptic membrane. *Nat. Neurosci.* 13, 36–44. doi: 10.1038/nn.2462

Aureli, M., Grassi, S., Prioni, S., Sonnino, S., and Prinetti, A. (2015). Lipid membrane domains in the brain. *Biochim. Biophys. Acta - Mol. Cell Biol. Lipids* 1851, 1006–1016. doi: 10.1016/j.bbalip.2015.02.001

Basu, S., and Lamprecht, R. (2018). The Role of Actin Cytoskeleton in Dendritic Spines in the Maintenance of Long-Term Memory. *Front. Mol. Neurosci.* 11:143. doi: 10.3389/fnmol.2018.00143

Baumgart, T., Hammond, A. T., Sengupta, P., Hess, S. T., Holowka, D. A., Baird, B. A., et al. (2007). Large-scale fluid/fluid phase separation of proteins and lipids in giant plasma membrane vesicles. *Proc. Natl. Acad. Sci. U. S. A.* 104, 3165–3170. doi: 10.1073/pnas.0611357104

Baytan, S. H., Alkanat, M., Okuyan, M., Ekinci, M., Gedikli, E., Ozeren, M., et al. (2008). Simvastatin impairs spatial memory in rats at a specific dose level. *Tohoku J. Exp. Med.* 214, 341–349. doi: 10.1620/tjem.214.341

Bazinet, R. P., and Layé, S. (2014). Polyunsaturated fatty acids and their metabolites in brain function and disease. *Nat. Rev. Neurosci.* 15, 771–785. doi: 10.1038/nrn3820

Behnke, O., Tranum-Jensen, J., and Van Deurs, B. (1984). Filipin as a cholesterol probe. II. Filipin-cholesterol interaction in red blood cell membranes. *Eur. J. Cell Biol.* 35, 200–215.

Bernardino de la Serna, J., Schütz, G. J., Eggeling, C., and Cebecauer, M. (2016). There Is No Simple Model of the Plasma Membrane Organization. *Front. Cell Dev. Biol.* 4, 1–17. doi: 10.3389/fcell.2016.00106

Besshoh, S., Bawa, D., Teves, L., Wallace, M. C., and Gurd, J. W. (2005). Increased phosphorylation and redistribution of NMDA receptors between synaptic lipid rafts and post-synaptic densities following transient global ischemia in the rat brain. *J. Neurochem.* 93, 186–194. doi: 10.1111/j.1471-4159.2004.03009.x

Bozek, K., Wei, Y., Yan, Z., Liu, X., Xiong, J., Sugimoto, M., et al. (2015). Organization and Evolution of Brain Lipidome Revealed by Large-Scale Analysis of Human, Chimpanzee, Macaque, and Mouse Tissues. *Neuron* 85, 695–702. doi: 10.1016/j.neuron.2015.01.003

Brachet, A., Norwood, S., Brouwers, J. F., Palomer, E., Helms, J. B., Dotti, C. G., et al. (2015). LTP-triggered cholesterol redistribution activates Cdc42 and drives AMPA receptor synaptic delivery. *J. Cell Biol.* 208, 791–806. doi: 10.1083/jcb.201407122

Breckenridge, W. C., Gombos, G., and Morgan, I. G. (1972). The lipid composition of adult rat brain synaptosomal plasma membranes. *Biochim. Biophys. Acta - Biomembr.* 266, 695–707. doi: 10.1016/0005-2736(72)90365-3

Brown, D. A., and Rose, J. K. (1992). Sorting of GPI-anchored proteins to glycolipid-enriched membrane subdomains during transport to the apical cell surface. *Cell* 68, 533–544. doi: 10.1016/0092-8674(92)90189-J

Brückner, K., Labrador, J. P., Scheiffele, P., Herb, A., Seeburg, P. H., and Klein, R. (1999). EphrinB ligands recruit GRIP family PDZ adaptor proteins into raft membrane microdomains. *Neuron* 22, 511–524. doi: 10.1016/S0896-6273(00)80706-0

Cao, D., Kevala, K., Kim, J., Moon, H.-S. S., Jun, S. B., Lovinger, D., et al. (2009). Docosahexaenoic acid promotes hippocampal neuronal development and synaptic function. *J. Neurochem.* 111, 510–521. doi: 10.1111/j.1471-4159.2009.06335.x

Choquet, D., and Triller, A. (2013). The Dynamic Synapse. *Neuron* 80, 691–703. doi: 10.1016/j.neuron.2013.10.013

Cotman, C., Blank, M. L., Moehl, A., and Snyder, F. (1969). Lipid Composition of Synaptic Plasma Membranes Isolated from Rat Brain by Zonal Centrifugation. *Biochemistry* 8, 4606–4612. doi: 10.1021/bi00839a056

Craven, S. E., El-Husseini, A. E., and Bredt, D. S. (1999). Synaptic targeting of the postsynaptic density protein PSD-95 mediated by lipid and protein motifs. *Neuron* 22, 497–509. doi: 10.1074/jbc.M910153199

Danylchuk, D. I., Moon, S., Xu, K., and Klymchenko, A. S. (2019). Switchable Solvatochromic Probes for Live−Cell Super−resolution Imaging of Plasma Membrane Organization. *Angew. Chemie* 131, 15062–15066. doi: 10.1002/ange.201907690

Danylchuk, D. I., Sezgin, E., Chabert, P., and Klymchenko, A. S. (2020). Redesigning Solvatochromic Probe Laurdan for Imaging Lipid Order Selectively in Cell Plasma Membranes. *Anal. Chem.* 92, 14798–14805. doi: 10.1021/acs.analchem.0c03559

Day, C. A., and Kenworthy, A. K. (2015). Functions of cholera toxin B-subunit as a raft cross-linker. *Essays Biochem.* 57, 135–145. doi: 10.1042/bse0570135

de Planque, M. R. R., Goormaghtigh, E., Greathouse, D. V., Koeppe, R. E., Kruijtzer, J. A. W., Liskamp, R. M. J., et al. (2001). Sensitivity of Single Membrane-Spanning α-Helical Peptides to Hydrophobic Mismatch with a Lipid Bilayer: Effects on Backbone Structure, Orientation, and Extent of Membrane Incorporation. *Biochemistry* 40, 5000–5010. doi: 10.1021/bi000804r

Delint-Ramirez, I., Fernández, E., Bayés, A., Kicsi, E., Komiyama, N. H., and Grant, S. G. N. (2010). In vivo composition of NMDA receptor signaling complexes differs between membrane subdomains and is modulated by PSD-95 and PSD-93. *J. Neurosci.* 30, 8162–8170. doi: 10.1523/JNEUROSCI.1792-10.2010

Delint-Ramírez, I., Salcedo-Tello, P., and Bermudez-Rattoni, F. (2008). Spatial memory formation induces recruitment of NMDA receptor and PSD-95 to synaptic lipid rafts. *J. Neurochem.* 106, 1658–1668. doi: 10.1111/j.1471-4159.2008.05523.x

Delint-Ramirez, I., Willoughby, D., Hammond, G. V. R., Ayling, L. J., and Cooper, D. M. F. (2011). Palmitoylation targets AKAP79 protein to lipid rafts and promotes its regulation of calcium-sensitive adenylyl cyclase type 8. *J. Biol. Chem.* 286, 32962–32975. doi: 10.1074/jbc.M111.243899

Diaz-Rohrer, B. B., Levental, K. R., Simons, K., and Levental, I. (2014). Membrane raft association is a determinant of plasma membrane localization. *Proc. Natl. Acad. Sci.* 111, 8500–8505. doi: 10.1073/pnas.1404582111

Dietzen, D. J., Hastings, W. R., and Lublin, D. M. (1995). Caveolin is palmitoylated on multiple cysteine residues. Palmitoylation is not necessary for localization of caveolin to caveolae. *J. Biol. Chem.* 270, 6838–6842. doi: 10.1074/jbc.270.12.6838

Dotti, C. G., Esteban, J. A., and Ledesma, M. D. (2014). Lipid dynamics at dendritic spines. *Front. Neuroanat.* 8, 1–11. doi: 10.3389/fnana.2014.00076

Eggeling, C., Ringemann, C., Medda, R., Schwarzmann, G., Sandhoff, K., Polyakova, S., et al. (2009). Direct observation of the nanoscale dynamics of membrane lipids in a living cell. *Nature* 457, 1159–1162. doi: 10.1038/nature07596

El-Husseini, A. E., Craven, S. E., Chetkovich, D. M., Firestein, B. L., Schnell, E., Aoki, C., et al. (2000). Dual palmitoylation of PSD-95 mediates its vesiculotubular sorting, postsynaptic targeting, and ion channel clustering. *J. Cell Biol.* 148, 159–171. doi: 10.1083/jcb.148.1.159

El-Husseini, A. E. D., Schnell, E., Dakoji, S., Sweeney, N., Zhou, Q., Prange, O., et al. (2002). Synaptic strength regulated by palmitate cycling on PSD-95. *Cell* 108, 849–863. doi: 10.1016/S0092-8674(02)00683-9

Fantini, J., and Barrantes, F. J. (2009). Sphingolipid/cholesterol regulation of neurotransmitter receptor conformation and function. *Biochim. Biophys. Acta - Biomembr.* 1788, 2345–2361. doi: 10.1016/j.bbamem.2009.08.016

Fedorova, I., Hussein, N., Di Martino, C., Moriguchi, T., Hoshiba, J., Majchrzak, S., et al. (2007). An n-3 fatty acid deficient diet affects mouse spatial learning in the Barnes circular maze. *Prostaglandins Leukot. Essent. Fat. Acids* 77, 269–277. doi: 10.1016/j.plefa.2007.10.013

Fitzner, D., Bader, J. M., Penkert, H., Bergner, C. G., Su, M., Weil, M.-T., et al. (2020). Cell-Type- and Brain-Region-Resolved Mouse Brain Lipidome. *Cell Rep.* 32:108132. doi: 10.1016/j.celrep.2020.108132

Frank, C., Giammarioli, A. M., Pepponi, R., Fiorentini, C., and Rufini, S. (2004). Cholesterol perturbing agents inhibit NMDA-dependent calcium influx in rat hippocampal primary culture. *FEBS Lett.* 566, 25–29. doi: 10.1016/j.febslet.2004.03.113

Frank, C., Rufini, S., Tancredi, V., Forcina, R., Grossi, D., and D'Arcangelo, G. (2008). Cholesterol depletion inhibits synaptic transmission and synaptic plasticity in rat hippocampus. *Exp. Neurol.* 212, 407–414. doi: 10.1016/j.expneurol.2008.04.019

Fujita, S., Ikegaya, Y., Nishikawa, M., Nishiyama, N., and Matsuki, N. (2001). Docosahexaenoic acid improves long-term potentiation attenuated by phospholipase A2 inhibitor in rat hippocampal slices. *Br. J. Pharmacol.* 132, 1417–1422. doi: 10.1038/sj.bjp.0703970

Fujiwara, T., Ritchie, K., Murakoshi, H., Jacobson, K., and Kusumi, A. (2002). Phospholipids undergo hop diffusion in compartmentalized cell membrane. *J. Cell Biol.* 157, 1071–1081. doi: 10.1083/jcb.200202050

Fujiwara, T. K., Iwasawa, K., Kalay, Z., Tsunoyama, T. A., Watanabe, Y., Umemura, Y. M., et al. (2016). Confined diffusion of transmembrane proteins and lipids induced by the same actin meshwork lining the plasma membrane. *Mol. Biol. Cell* 27, 1101–1119. doi: 10.1091/mbc.E15-04-0186

Fukata, Y., Dimitrov, A., Boncompain, G., Vielemeyer, O., Perez, F., and Fukata, M. (2013). Local palmitoylation cycles define activity-regulated postsynaptic subdomains. *J. Cell Biol.* 202, 145–161. doi: 10.1083/jcb.201302071

Fukata, Y., Murakami, T., Yokoi, N., and Fukata, M. (2016). Local Palmitoylation Cycles and Specialized Membrane Domain Organization. *Curr. Top. Membr.* 2016, 97–141. doi: 10.1016/bs.ctm.2015.10.003

García-Morales, V., Montero, F., González-Forero, D., Rodríguez-Bey, G., Gómez-Pérez, L., Medialdea-Wandossell, M. J., et al. (2015). Membrane-Derived Phospholipids Control Synaptic Neurotransmission and Plasticity. *PLoS Biol.* 13:1002153. doi: 10.1371/journal.pbio.1002153

Goncalves, J., Bartol, T. M., Camus, C., Levet, F., Menegolla, A. P., Sejnowski, T. J., et al. (2020). Nanoscale co-organization and coactivation of AMPAR, NMDAR, and mGluR at excitatory synapses. *Proc. Natl. Acad. Sci. U. S. A.* 117:14503. doi: 10.1073/PNAS.1922563117

Götz, R., Kunz, T. C., Fink, J., Solger, F., Schlegel, J., Seibel, J., et al. (2020). Nanoscale imaging of bacterial infections by sphingolipid expansion microscopy. *Nat. Commun.* 11:6173. doi: 10.1038/s41467-020-19897-1

Greaves, J., and Chamberlain, L. H. (2007). Palmitoylation-dependent protein sorting. *J. Cell Biol.* 176, 249–254. doi: 10.1083/jcb.200610151

Guo, Y., Zou, G., Qi, K., Jin, J., Yao, L., Pan, Y., et al. (2021). Simvastatin impairs hippocampal synaptic plasticity and cognitive function in mice. *Mol. Brain* 14:41. doi: 10.1186/s13041-021-00758-x

Hanson, M. A., Cherezov, V., Griffith, M. T., Roth, C. B., Jaakola, V.-P., Chien, E. Y. T., et al. (2008). A Specific Cholesterol Binding Site Is Established by the 2.8 Å Structure of the Human β2-Adrenergic Receptor. *Structure* 16, 897–905. doi: 10.1016/j.str.2008.05.001

Haucke, V., and Di Paolo, G. (2007). Lipids and lipid modifications in the regulation of membrane traffic. *Curr. Opin. Cell Biol.* 19, 426–435. doi: 10.1016/j.ceb.2007.06.003

Hayashi, T., Rumbaugh, G., and Huganir, R. L. (2005). Differential Regulation of AMPA Receptor Subunit Trafficking by Palmitoylation of Two Distinct Sites. *Neuron* 47, 709–723. doi: 10.1016/j.neuron.2005.06.035

Hayashi, T., Thomas, G. M., and Huganir, R. L. (2009). Dual Palmitoylation of NR2 Subunits Regulates NMDA Receptor Trafficking. *Neuron* 64, 213–226. doi: 10.1016/j.neuron.2009.08.017

He, C., Qu, X., Cui, L., Wang, J., and Kang, J. X. (2009). Improved spatial learning performance of fat-1 mice is associated with enhanced neurogenesis and neuritogenesis by docosahexaenoic acid. *Proc. Natl. Acad. Sci. U. S. A.* 106, 11370–11375. doi: 10.1073/pnas.0904835106

Hentschel, A., Zahedi, R. P., and Ahrends, R. (2016). Protein lipid modifications - More than just a greasy ballast. *Proteomics* 16, 759–782. doi: 10.1002/pmic.201500353

Hering, H., Lin, C., and Sheng, M. (2003). Lipid Rafts in the Maintenance of Synapses, Dendritic Spines, and Surface AMPA Receptor Stability. *J. Neurosci.* 23, 3262–3271. doi: 10.1523/JNEUROSCI.23-08-03262.2003

Hernández-Adame, P. L., Meza, U., Rodríguez-Menchaca, A. A., Sánchez-Armass, S., Ruiz-García, J., and Gomez, E. (2021). Determination of the size of lipid rafts studied through single-molecule FRET simulations. *Biophys. J.* 2021:003. doi: 10.1016/j.bpj.2021.04.003

Hou, Q., Huang, Y., Amato, S., Snyder, S. H., Huganir, R. L., and Man, H.-Y. (2008). Regulation of AMPA receptor localization in lipid rafts. *Mol. Cell. Neurosci.* 38, 213–223. doi: 10.1016/j.mcn.2008.02.010

Igbavboa, U., Hamilton, J., Kim, H. Y., Sun, G. Y., and Wood, W. G. (2002). A new role for apolipoprotein E: Modulating transport of polyunsaturated phospholipid molecular species in synaptic plasma membranes. *J. Neurochem.* 80, 255–261. doi: 10.1046/j.0022-3042.2001.00688.x

Ingólfsson, H. I., Arnarez, C., Periole, X., and Marrink, S. J. (2016). Computational 'microscopy' of cellular membranes. *J. Cell Sci.* 129, 257–268. doi: 10.1242/jcs.176040

Ingólfsson, H. I., Carpenter, T. S., Bhatia, H., Bremer, P. T., Marrink, S. J., and Lightstone, F. C. (2017). Computational Lipidomics of the Neuronal Plasma Membrane. *Biophys. J.* 113, 2271–2280. doi: 10.1016/j.bpj.2017.10.017

Itokazu, N., Ikegaya, Y., Nishikawa, M., and Matsuki, N. (2000). Bidirectional actions of docosahexaenoic acid on hippocampal neurotransmissions in vivo. *Brain Res.* 862, 211–216. doi: 10.1016/S0006-8993(00)02129-6

Iuliano, M., Seeley, C., Sapp, E., Jones, E. L., Martin, C., Li, X., et al. (2021). Disposition of Proteins and Lipids in Synaptic Membrane Compartments Is Altered in Q175/Q7 Huntington's Disease Mouse Striatum. *Front. Synaptic Neurosci.* 13:618391. doi: 10.3389/fnsyn.2021.618391

Jacobson, K., Liu, P., and Lagerholm, B. C. (2019). The Lateral Organization and Mobility of Plasma Membrane Components. *Cell* 177, 806–819. doi: 10.1016/j.cell.2019.04.018

Jacobson, K., Mouritsen, O. G., and Anderson, R. G. W. (2007). Lipid rafts: at a crossroad between cell biology and physics. *Nat. Cell Biol.* 9, 7–14. doi: 10.1038/ncb0107-7

Jafurulla, M., Bandari, S., Pucadyil, T. J., and Chattopadhyay, A. (2017). Sphingolipids modulate the function of human serotonin 1A receptors: Insights from sphingolipid-deficient cells. *Biochim. Biophys. Acta - Biomembr.* 1859, 598–604. doi: 10.1016/j.bbamem.2016.10.016

Jeyifous, O., Lin, E. I., Chen, X., Antinone, S. E., Mastro, R., Drisdel, R., et al. (2016). Palmitoylation regulates glutamate receptor distributions in Postsynaptic densities through control of PSD95 conformation and orientation. *Proc. Natl. Acad. Sci. U. S. A.* 113, E8482–E8491. doi: 10.1073/pnas.1612963113

Ji, B., and Skup, M. (2021). Roles of palmitoylation in structural long-term synaptic plasticity. *Mol. Brain* 14:8. doi: 10.1186/s13041-020-00717-y

Kaiser, H. J., Orłowski, A., Róg, T., Nyholm, T. K. M., Chai, W., Feizi, T., et al. (2011). Lateral sorting in model membranes by cholesterol-mediated hydrophobic matching. *Proc. Natl. Acad. Sci. U. S. A.* 108, 16628–16633. doi: 10.1073/pnas.1103742108

Kanungo, S., Soares, N., He, M., and Steiner, R. D. (2013). Sterol metabolism disorders and neurodevelopment-an update. *Dev. Disabil. Res. Rev.* 17, 197–210. doi: 10.1002/ddrr.1114

Keith, D. J., Sanderson, J. L., Gibson, E. S., Woolfrey, K. M., Robertson, H. R., Olszewski, K., et al. (2012). Palmitoylation of A-Kinase anchoring protein 79/150 regulates dendritic endosomal targeting and synaptic plasticity mechanisms. *J. Neurosci.* 32, 7119–7136. doi: 10.1523/JNEUROSCI.0784-12.2012

Kinoshita, M., Suzuki, K. G. N., Matsumori, N., Takada, M., Ano, H., Morigaki, K., et al. (2017). Raft-based sphingomyelin interactions revealed by new fluorescent sphingomyelin analogs. *J. Cell Biol.* 216, 1183–1204. doi: 10.1083/jcb.201607086

Klymchenko, A. S., and Kreder, R. (2014). Fluorescent Probes for Lipid Rafts: From Model Membranes to Living Cells. *Chem. Biol.* 21, 97–113. doi: 10.1016/j.chembiol.2013.11.009

Kol, M., Williams, B., Toombs-Ruane, H., Franquelim, H. G., Korneev, S., Schroeer, C., et al. (2019). Optical manipulation of sphingolipid biosynthesis using photoswitchable ceramides. *Elife* 8:43230. doi: 10.7554/eLife.43230

Komura, N., Suzuki, K. G. N., Ando, H., Konishi, M., Koikeda, M., Imamura, A., et al. (2016). Raft-based interactions of gangliosides with a GPI-anchored receptor. *Nat. Chem. Biol.* 12, 402–410. doi: 10.1038/nchembio.2059

Korinek, M., Gonzalez-Gonzalez, I. M., Smejkalova, T., Hajdukovic, D., Skrenkova, K., Krusek, J., et al. (2020). Cholesterol modulates presynaptic and postsynaptic properties of excitatory synaptic transmission. *Sci. Rep.* 10:12651. doi: 10.1038/s41598-020-69454-5

Korinek, M., Vyklicky, V., Borovska, J., Lichnerova, K., Kaniakova, M., Krausova, B., et al. (2015). Cholesterol modulates open probability and desensitization of NMDA receptors. *J. Physiol.* 593, 2279–2293. doi: 10.1113/jphysiol.2014.288209

Kotti, T. J., Ramirez, D. M. O., Pfeiffer, B. E., Huber, K. M., and Russell, D. W. (2006). Brain cholesterol turnover required for geranylgeraniol production and learning in mice. *Proc. Natl. Acad. Sci. U. S. A.* 103, 3869–3874. doi: 10.1073/pnas.0600316103

Koudinov, A. R., and Koudinova, N. V. (2001). Essential role for cholesterol in synaptic plasticity and neuronal degeneration. *FASEB J.* 15, 1858–1860. doi: 10.1096/fj.00-0815fje

Kumari, R., Castillo, C., and Francesconi, A. (2013). Agonist-dependent signaling by group I metabotropic glutamate receptors is regulated by association with lipid domains. *J. Biol. Chem.* 288, 32004–32019. doi: 10.1074/jbc.M113.475863

Kusumi, A., Sako, Y., and Yamamoto, M. (1993). Confined lateral diffusion of membrane receptors as studied by single particle tracking (nanovid microscopy). Effects of calcium-induced differentiation in cultured epithelial cells. *Biophys. J.* 65, 2021–2040. doi: 10.1016/S0006-3495(93)81253-0

Kusumi, A., Shirai, Y. M., Koyama-Honda, I., Suzuki, K. G. N., and Fujiwara, T. K. (2010). Hierarchical organization of the plasma membrane: Investigations by single-molecule tracking vs. fluorescence correlation spectroscopy. *FEBS Lett.* 584, 1814–1823. doi: 10.1016/j.febslet.2010.02.047

Ledesma, M. D., Martin, M. G., and Dotti, C. G. (2012). Lipid changes in the aged brain: Effect on synaptic function and neuronal survival. *Prog. Lipid Res.* 51, 23–35. doi: 10.1016/j.plipres.2011.11.004

Lenne, P.-F., Wawrezinieck, L., Conchonaud, F., Wurtz, O., Boned, A., Guo, X.-J., et al. (2006). Dynamic molecular confinement in the plasma membrane by microdomains and the cytoskeleton meshwork. *EMBO J.* 25, 3245–3256. doi: 10.1038/sj.emboj.7601214

Levental, I., Levental, K. R., and Heberle, F. A. (2020). Lipid Rafts: Controversies Resolved, Mysteries Remain. *Trends Cell Biol.* 30, 341–353. doi: 10.1016/j.tcb.2020.01.009

Levental, I., Lingwood, D., Grzybek, M., Coskun, U., and Simons, K. (2010). Palmitoylation regulates raft affinity for the majority of integral raft proteins. *Proc. Natl. Acad. Sci.* 107, 22050–22054. doi: 10.1073/pnas.1016184107

Levental, K. R., Lorent, J. H., Lin, X., Skinkle, A. D., Surma, M. A., Stockenbojer, E. A., et al. (2016). Polyunsaturated Lipids Regulate Membrane Domain Stability by Tuning Membrane Order. *Biophys. J.* 110, 1800–1810. doi: 10.1016/j.bpj.2016.03.012

Levental, K. R., Surma, M. A., Skinkle, A. D., Lorent, J. H., Zhou, Y., Klose, C., et al. (2017). ω-3 polyunsaturated fatty acids direct differentiation of the membrane phenotype in mesenchymal stem cells to potentiate osteogenesis. *Sci. Adv.* 3:eaao1193. doi: 10.1126/sciadv.aao1193

Li, L., Cao, D., Kim, H., Lester, R., and Fukuchi, K. I. (2006). Simvastatin enhances learning and memory independent of amyloid load in mice. *Ann. Neurol.* 60, 729–739. doi: 10.1002/ana.21053

Li, S., Raychaudhuri, S., Lee, S. A., Brockmann, M. M., Wang, J., Kusick, G., et al. (2021). Asynchronous release sites align with NMDA receptors in mouse hippocampal synapses. *Nat. Commun.* 12:21004. doi: 10.1038/s41467-021-21004-x

Li, T. P., and Blanpied, T. A. (2016). Control of Transmembrane Protein Diffusion within the Postsynaptic Density Assessed by Simultaneous Single-Molecule Tracking and Localization Microscopy. *Front. Synaptic Neurosci.* 8, 1–14. doi: 10.3389/fnsyn.2016.00019

Li, T. P., Song, Y., MacGillavry, H. D., Blanpied, T. A., and Raghavachari, S. (2016). Protein Crowding within the Postsynaptic Density Can Impede the Escape of Membrane Proteins. *J. Neurosci.* 36, 4276–4295. doi: 10.1523/JNEUROSCI.3154-15.2016

Lorent, J. H., Diaz-Rohrer, B., Lin, X., Spring, K., Gorfe, A. A., Levental, K. R., et al. (2017). Structural determinants and functional consequences of protein affinity for membrane rafts. *Nat. Commun.* 8:1219. doi: 10.1038/s41467-017-01328-3

Ma, L., Huang, Y. Z., Pitcher, G. M., Valtschanoff, J. G., Ma, Y. H., Feng, L. Y., et al. (2003). Ligand-dependent recruitment of the ErbB4 signaling complex into neuronal lipid rafts. *J. Neurosci.* 23, 3164–3175. doi: 10.1523/jneurosci.23-08-03164.2003

MacGillavry, H. D., Song, Y., Raghavachari, S., and Blanpied, T. A. (2013). Nanoscale Scaffolding Domains within the Postsynaptic Density Concentrate Synaptic AMPA Receptors. *Neuron* 78, 615–622. doi: 10.1016/j.neuron.2013.03.009

Maekawa, M. (2017). Domain 4 (D4) of Perfringolysin O to Visualize Cholesterol in Cellular Membranes—The Update. *Sensors* 17:504. doi: 10.3390/s17030504

Magee, T., and Seabra, M. C. (2005). Fatty acylation and prenylation of proteins: what's hot in fat. *Curr. Opin. Cell Biol.* 17, 190–196. doi: 10.1016/j.ceb.2005.02.003

Maggo, S., and Ashton, J. C. (2014). Effects of HMG-CoA reductase inhibitors on learning and memory in the guinea pig. *Eur. J. Pharmacol.* 723, 294–304. doi: 10.1016/j.ejphar.2013.11.018

Mans, R. A., Chowdhury, N., Cao, D., Mcmahon, L. L., and Li, L. (2010). Simvastatin enhances hippocampal long-term potentiation in C57BL/6 mice. *Neuroscience* 166, 435–444. doi: 10.1016/j.neuroscience.2009.12.062

Marlow, B., Kuenze, G., Li, B., Sanders, C. R., and Meiler, J. (2021). Structural determinants of cholesterol recognition in helical integral membrane proteins. *Biophys. J.* 120, 1592–1604. doi: 10.1016/j.bpj.2021.02.028

Martin, M. G., Ahmed, T., Korovaichuk, A., Venero, C., Menchón, S. A., Salas, I., et al. (2014). Constitutive hippocampal cholesterol loss underlies poor cognition in old rodents. *EMBO Mol. Med.* 6, 902–917. doi: 10.15252/emmm.201303711

Martín, M. G., Pfrieger, F., and Dotti, C. G. (2014). Cholesterol in brain disease: sometimes determinant and frequently implicated. *EMBO Rep.* 15, 1036–1052. doi: 10.15252/embr.201439225

Martin, S. J., Grimwood, P. D., and Morris, R. G. M. (2000). Synaptic plasticity and memory: an evaluation of the hypothesis. *Neurosci.* 23, 649–711.

Mazzocchi-Jones, D. (2015). Impaired corticostriatal LTP and depotentiation following iPLA2 inhibition is restored following acute application of DHA. *Brain Res. Bull.* 111, 69–75. doi: 10.1016/j.brainresbull.2014.12.010

McGahon, B., Martin, D. S., Horrobin, D., and Lynch, M. (1999). Age-related changes in synaptic function: analysis of the effect of dietary supplementation with ω-3 fatty acids. *Neuroscience* 94, 305–314. doi: 10.1016/S0306-4522(99)00219-5

Milovanovic, D., Honigmann, A., Koike, S., Göttfert, F., Pähler, G., Junius, M., et al. (2015). Hydrophobic mismatch sorts SNARE proteins into distinct membrane domains. *Nat. Commun.* 6, 1–10. doi: 10.1038/ncomms6984

Mirnikjoo, B., Brown, S. E., Kim, H. F. S., Marangell, L. B., Sweatt, J. D., and Weeber, E. J. (2001). Protein Kinase Inhibition by ω-3 Fatty Acid. *J. Biol. Chem.* 276, 10888–10896. doi: 10.1074/jbc.M008150200

Mitroi, D. N., Pereyra-Gómez, G., Soto-Huelin, B., Senovilla, F., Kobayashi, T., Esteban, J. A., et al. (2019). NPC1 enables cholesterol mobilization during long-term potentiation that can be restored in Niemann-Pick disease type C by CYP46A1 activation. *EMBO Rep.* 20:e48143. doi: 10.15252/embr.201948143

Mizuno, H., Abe, M., Dedecker, P., Makino, A., Rocha, S., Ohno-Iwashita, Y., et al. (2011). Fluorescent probes for superresolution imaging of lipid domains on the plasma membrane. *Chem. Sci.* 2:1548. doi: 10.1039/c1sc00169h

Mobarak, E., Javanainen, M., Kulig, W., Honigmann, A., Sezgin, E., Aho, N., et al. (2018). How to minimize dye-induced perturbations while studying biomembrane structure and dynamics: PEG linkers as a rational alternative. *Biochim. Biophys. Acta - Biomembr.* 1860, 2436–2445. doi: 10.1016/j.bbamem.2018.07.003

Mohamed, A., Shah, A. D., Chen, D., and Hill, M. M. (2019). RaftProt V2: understanding membrane microdomain function through lipid raft proteomes. *Nucleic Acids Res.* 47, D459–D463. doi: 10.1093/nar/gky948

Mouritsen, O. G., and Bloom, M. (1984). Mattress model of lipid-protein interactions in membranes. *Biophys. J.* 46, 141–153. doi: 10.1016/S0006-3495(84)84007-2

Muro, E., Atilla-Gokcumen, G. E., and Eggert, U. S. (2014). Lipids in cell biology: how can we understand them better? *Mol. Biol. Cell* 25, 1819–1823. doi: 10.1091/mbc.e13-09-0516

Nair, D., Hosy, E., Petersen, J. D., Constals, A., Giannone, G., Choquet, D., et al. (2013). Super-Resolution Imaging Reveals That AMPA Receptors Inside Synapses Are Dynamically Organized in Nanodomains Regulated by PSD95. *J. Neurosci.* 33, 13204–13224. doi: 10.1523/JNEUROSCI.2381-12.2013

Ngamukote, S., Yanagisawa, M., Ariga, T., Ando, S., and Yu, R. K. (2007). Developmental changes of glycosphingolipids and expression of glycogenes in mouse brains. *J. Neurochem.* 103, 2327–2341. doi: 10.1111/j.1471-4159.2007.04910.x

Nishikawa, M., Kimura, S., and Akaike, N. (1994). Facilitatory effect of docosahexaenoic acid on N-methyl-D-aspartate response in pyramidal neurones of rat cerebral cortex. *J. Physiol.* 475, 83–93. doi: 10.1113/jphysiol.1994.sp020051

Obaid, A. L., Loew, L. M., Wuskell, J. P., and Salzberg, B. M. (2004). Novel naphthylstyryl-pyridinium potentiometric dyes offer advantages for neural network analysis. *J. Neurosci. Methods* 134, 179–190. doi: 10.1016/j.jneumeth.2003.11.011

Perez, A.-S., and Bredt, D. S. (1998). The N-terminal PDZ-containing region of postsynatpic density-95 mediates association with caveolar-like lipid domains. *Neurosci. Lett.* 258, 121–123. doi: 10.1016/S0304-3940(98)00846-5

Pérez-Cañamás, A., Benvegnù, S., Rueda, C. B., Rábano, A., Satrústegui, J., and Ledesma, M. D. (2017). Sphingomyelin-induced inhibition of the plasma membrane calcium ATPase causes neurodegeneration in type A Niemann–Pick disease. *Mol. Psychiatry* 22, 711–723. doi: 10.1038/mp.2016.148

Petrov, A. M., Kasimov, M. R., and Zefirov, A. L. (2016). Brain cholesterol metabolism and its defects: Linkage to neurodegenerative diseases and synaptic dysfunction. *Acta Naturae* 8, 58–73. doi: 10.32607/20758251-2016-8-1-58-73

Pike, L. J. (2006). Rafts defined: a report on the Keystone symposium on lipid rafts and cell function. *J. Lipid Res.* 47, 1597–1598. doi: 10.1194/jlr.E600002-JLR200

Pike, L. J. (2009). The challenge of lipid rafts. *J. Lipid Res.* 50, S323–S328. doi: 10.1194/jlr.R800040-JLR200

Purkey, A. M., Woolfrey, K. M., Crosby, K. C., Stich, D. G., Chick, W. S., Aoto, J., et al. (2018). AKAP150 Palmitoylation Regulates Synaptic Incorporation of Ca2+-Permeable AMPA Receptors to Control LTP. *Cell Rep.* 25, 974.e–987.e. doi: 10.1016/j.celrep.2018.09.085

Renner, M., Choquet, D., and Triller, A. (2009). Control of the Postsynaptic Membrane Viscosity. *J. Neurosci.* 29, 2926–2937. doi: 10.1523/JNEUROSCI.4445-08.2009

Renner, M. L., Cognet, L., Lounis, B., Triller, A., and Choquet, D. (2009). The excitatory postsynaptic density is a size exclusion diffusion environment. *Neuropharmacology* 56, 30–36. doi: 10.1016/j.neuropharm.2008.07.022

Resh, M. D. (2016). *Lipid Modification of Proteins in Biochemistry of Lipids, Lipoproteins and Membranes*. Amsterdam: Elsevier, 391–414. doi: 10.1016/B978-0-444-63438-2.00013-4

Saffman, P. G., and Delbrück, M. (1975). Brownian motion in biological membranes. *Proc. Natl. Acad. Sci. U. S. A.* 72, 3111–3113. doi: 10.1073/pnas.72.8.3111

Saxton, M. J. (1993). Lateral diffusion in an archipelago. Single-particle diffusion. *Biophys. J.* 64, 1766–1780. doi: 10.1016/S0006-3495(93)81548-0

Sezgin, E., Levental, I., Mayor, S., and Eggeling, C. (2017). The mystery of membrane organization: Composition, regulation and roles of lipid rafts. *Nat. Rev. Mol. Cell Biol.* 18, 361–374. doi: 10.1038/nrm.2017.16

Sidenstein, S. C., D'Este, E., Böhm, M. J., Danzl, J. G., Belov, V. N., and Hell, S. W. (2016). Multicolour Multilevel STED nanoscopy of Actin/Spectrin Organization at Synapses. *Sci. Rep.* 6:26725. doi: 10.1038/srep26725

Simons, K., and Ikonen, E. (1997). Functional rafts in cell membranes. *Nature* 387, 569–572. doi: 10.1038/42408

Simson, R., Sheets, E. D., and Jacobson, K. (1995). Detection of temporary lateral confinement of membrane proteins using single-particle tracking analysis. *Biophys. J.* 69, 989–993. doi: 10.1016/S0006-3495(95)79972-6

Singer, S. J., and Nicolson, G. L. (1972). The Fluid Mosaic Model of the Structure of Cell Membranes. *Science* 175, 720–731. doi: 10.1126/science.175.4023.720

Sodero, A. O., Vriens, J., Ghosh, D., Stegner, D., Brachet, A., Pallotto, M., et al. (2012). Cholesterol loss during glutamate-mediated excitotoxicity. *EMBO J.* 31, 1764–1773. doi: 10.1038/emboj.2012.31

Sun, D., Fan, X., Shi, Y., Zhang, H., Huang, Z., Cheng, B., et al. (2021). Click-ExM enables expansion microscopy for all biomolecules. *Nat. Methods* 18, 107–113. doi: 10.1038/s41592-020-01005-2

Suzuki, T. (2002). Lipid rafts at postsynaptic sites: distribution, function and linkage to postsynaptic density. *Neurosci. Res.* 44, 1–9. doi: 10.1016/S0168-0102(02)00080-9

Suzuki, T., Ito, J. I., Takagi, H., Saitoh, F., Nawa, H., and Shimizu, H. (2001). Biochemical evidence for localization of AMPA-type glutamate receptor subunits in the dendritic raft. *Mol. Brain Res.* 89, 20–28. doi: 10.1016/S0169-328X(01)00051-1

Suzuki, T., Zhang, J., Miyazawa, S., Liu, Q., Farzan, M. R., and Yao, W.-D. (2011). Association of membrane rafts and postsynaptic density: proteomics, biochemical, and ultrastructural analyses. *J. Neurochem.* 119, 64–77. doi: 10.1111/j.1471-4159.2011.07404.x

Swanwick, C. C., Shapiro, M. E., Yi, Z., Chang, K., and Wenthold, R. J. (2009). NMDA receptors interact with flotillin-1 and -2, lipid raft-associated proteins. *FEBS Lett.* 583, 1226–1230. doi: 10.1016/j.febslet.2009.03.017

Swulius, M. T., Farley, M. M., Bryant, M. A., and Waxham, M. N. (2012). Electron cryotomography of postsynaptic densities during development reveals a mechanism of assembly. *Neuroscience* 212, 19–29. doi: 10.1016/j.neuroscience.2012.03.042

Takeuchi, T., Duszkiewicz, A. J., and Morris, R. G. M. (2014). The synaptic plasticity and memory hypothesis: Encoding, storage and persistence. *Philos. Trans. R. Soc. B Biol. Sci.* 369:288. doi: 10.1098/rstb.2013.0288

Tang, A.-H., Chen, H., Li, T. P., Metzbower, S. R., MacGillavry, H. D., and Blanpied, T. A. (2016). A trans-synaptic nanocolumn aligns neurotransmitter release to receptors. *Nature* 536, 210–214. doi: 10.1038/nature19058

Topinka, J. R., and Bredt, D. S. (1998). N-terminal palmitoylation of PSD-95 regulates association with cell membranes and interaction with K+ channel K(v)1.4. *Neuron* 20, 125–134. doi: 10.1016/S0896-6273(00)80440-7

Tsutsumi, R., Fukata, Y., and Fukata, M. (2008). Discovery of protein-palmitoylating enzymes. *Pflügers Arch. - Eur. J. Physiol.* 456, 1199–1206. doi: 10.1007/s00424-008-0465-x

Tulodziecka, K., Diaz-Rohrer, B. B., Farley, M. M., Chan, R. B., Di Paolo, G., Levental, K. R., et al. (2016). Remodeling of the postsynaptic plasma membrane during neural development. *Mol. Biol. Cell* 27, 3480–3489. doi: 10.1091/mbc.E16-06-0420

van der Kant, R., Langness, V. F., Herrera, C. M., Williams, D. A., Fong, L. K., Leestemaker, Y., et al. (2019). Cholesterol Metabolism Is a Druggable Axis that Independently Regulates Tau and Amyloid-β in iPSC-Derived Alzheimer's Disease Neurons. *Cell Stem Cell* 24, 363.e–375.e. doi: 10.1016/j.stem.2018.12.013

van Deventer, S., Arp, A. B., and van Spriel, A. B. (2021). Dynamic Plasma Membrane Organization: A Complex Symphony. *Trends Cell Biol.* 31, 119–129. doi: 10.1016/j.tcb.2020.11.004

Wang, D., and Zheng, W. (2015). Dietary cholesterol concentration affects synaptic plasticity and dendrite spine morphology of rabbit hippocampal neurons. *Brain Res.* 1622, 350–360. doi: 10.1016/j.brainres.2015.06.049

Wassall, S. R., and Stillwell, W. (2009). Polyunsaturated fatty acid–cholesterol interactions: Domain formation in membranes. *Biochim. Biophys. Acta - Biomembr.* 1788, 24–32. doi: 10.1016/j.bbamem.2008.10.011

Woolfrey, K. M., Sanderson, J. L., and Dell'Acqua, M. L. (2015). The palmitoyl acyltransferase DHHC2 regulates recycling endosome exocytosis and synaptic potentiation through palmitoylation of AKAP79/150. *J. Neurosci.* 35, 442–456. doi: 10.1523/JNEUROSCI.2243-14.2015

Yang, G., Xiong, W., Kojic, L., and Cynader, M. S. (2009). Subunit-selective palmitoylation regulates the intracellular trafficking of AMPA receptor. *Eur. J. Neurosci.* 30, 35–46. doi: 10.1111/j.1460-9568.2009.06788.x

Yokoi, N., Fukata, Y., Sekiya, A., Murakami, T., Kobayashi, K., and Fukata, M. (2016). Identification of PSD-95 depalmitoylating enzymes. *J. Neurosci.* 36, 6431–6444. doi: 10.1523/JNEUROSCI.0419-16.2016

Young, C., Gean, P. W., Wu, S. P., Lin, C. H., and Shen, Y. Z. (1998). Cancellation of low-frequency stimulation-induced long-term depression by docosahexaenoic acid in the rat hippocampus. *Neurosci. Lett.* 247, 198–200. doi: 10.1016/S0304-3940(98)00272-9

Zhang, D., Watson, J. F., Matthews, P. M., Cais, O., and Greger, I. H. (2021). Gating and modulation of a hetero-octameric AMPA glutamate receptor. *Nature* 594, 454–458. doi: 10.1038/s41586-021-03613-0

Conflict of Interest: The authors declare that the research was conducted in the absence of any commercial or financial relationships that could be construed as a potential conflict of interest.

frontiers
in Synaptic Neuroscience

REVIEW
published: 24 November 2021
doi: 10.3389/fnsyn.2021.761530

Light Sheet Illumination for 3D Single-Molecule Super-Resolution Imaging of Neuronal Synapses

Gabriella Gagliano[1,2,3†], *Tyler Nelson*[1,2,3†], *Nahima Saliba*[1†], *Sofía Vargas-Hernández*[1,4,5†] *and Anna-Karin Gustavsson*[1,3,5,6,7*]

[1]Department of Chemistry, Rice University, Houston, TX, United States, [2]Applied Physics Program, Rice University, Houston, TX, United States, [3]Smalley-Curl Institute, Rice University, Houston, TX, United States, [4]Systems, Synthetic, and Physical Biology Program, Rice University, Houston, TX, United States, [5]Institute of Biosciences & Bioengineering, Rice University, Houston, TX, United States, [6]Department of Biosciences, Rice University, Houston, TX, United States, [7]Laboratory for Nanophotonics, Rice University, Houston, TX, United States

The function of the neuronal synapse depends on the dynamics and interactions of individual molecules at the nanoscale. With the development of single-molecule super-resolution microscopy over the last decades, researchers now have a powerful and versatile imaging tool for mapping the molecular mechanisms behind the biological function. However, imaging of thicker samples, such as mammalian cells and tissue, in all three dimensions is still challenging due to increased fluorescence background and imaging volumes. The combination of single-molecule imaging with light sheet illumination is an emerging approach that allows for imaging of biological samples with reduced fluorescence background, photobleaching, and photodamage. In this review, we first present a brief overview of light sheet illumination and previous super-resolution techniques used for imaging of neurons and synapses. We then provide an in-depth technical review of the fundamental concepts and the current state of the art in the fields of three-dimensional single-molecule tracking and super-resolution imaging with light sheet illumination. We review how light sheet illumination can improve single-molecule tracking and super-resolution imaging in individual neurons and synapses, and we discuss emerging perspectives and new innovations that have the potential to enable and improve single-molecule imaging in brain tissue.

Keywords: 3D single-molecule imaging, super-resolution microscopy, light sheet illumination, point spread function engineering, neuronal synapses

Edited by:
Thomas Kuner,
Heidelberg University, Germany

Reviewed by:
Shigeki Watanabe,
Johns Hopkins University, United States
Jason D. Shepherd,
The University of Utah, United States

****Correspondence:***
Anna-Karin Gustavsson
anna-karin.gustavsson@rice.edu

†These authors have contributed equally to this work and share first authorship

Received: *20 August 2021*
Accepted: *27 October 2021*
Published: *24 November 2021*

Citation:
Gagliano G, Nelson T, Saliba N, Vargas-Hernández S and Gustavsson A-K (2021) Light Sheet Illumination for 3D Single-Molecule Super-Resolution Imaging of Neuronal Synapses. Front. Synaptic Neurosci. 13:761530. doi: 10.3389/fnsyn.2021.761530

INTRODUCTION

Neurons are the specialized units of the nervous system that communicate *via* the release of chemical neurotransmitters at the junctions, or synapses, between them (for reviews, see e.g., Guillery, 2005; Yuste, 2015; **Figure 1**). Given that neurons and synapses are intricate and that the width of the synaptic cleft is on the order of tens of nanometers, advanced techniques are needed to image and understand their architecture and molecular dynamics at the nanoscale.

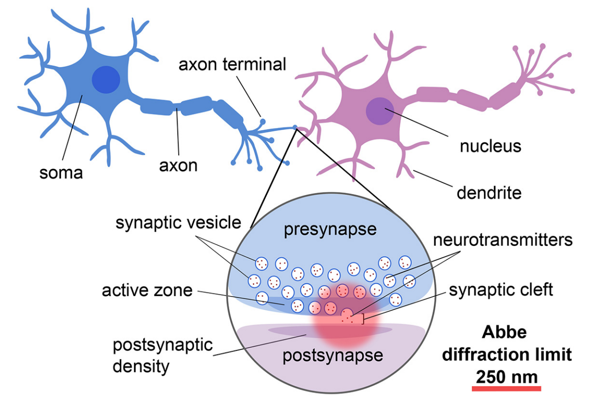

FIGURE 1 | Schematic showing the different components and length scales involved in neuronal and synaptic imaging demonstrating the importance of super-resolution techniques for resolving these structures.

Early methods of studying neuronal tissues include electron microscopy (EM), which was used to directly visualize the synapse. EM studies allowed measurements of the synaptic cleft (De Robertis and Bennett, 1955; Palay and Palade, 1955), and discoveries of other distinct features of neuronal communication, such as the accumulation of synaptic vesicles (SVs) at presynaptic terminals (De Robertis and Bennett, 1954; Palade, 1954). This discovery in combination with the hypothesis of neurotransmitter release (Del Castillo and Katz, 1954) eventually led to the conclusion that synaptic vesicles were the mechanism by which neurotransmitters were stored and released across the synapse (De Robertis et al., 1963). Hence, with the dawn of EM came the ability to investigate the sub-cellular organization of synapses at exquisite spatial resolution (for reviews, see e.g., Siksou et al., 2009; Harris and Weinberg, 2012). However, EM is limited in its ability to study molecular assembly and mechanisms because of restricted labeling specificity, poor temporal resolution, and the necessity to work with dead samples.

Fluorescence microscopy, on the other hand, offers the benefits of very specific labeling, excellent temporal resolution, and the ability to study live samples. However, due to the diffraction limit imposed by the finite wavelength of light, conventional optical microscopy has been inherently limited in its ability to resolve cellular nanoscale structures (Abbe, 1873). This issue was overcome by the invention of super-resolution (SR) fluorescence microscopy over a decade ago and marked an important milestone in imaging technology, which was recognized with the Nobel Prize in Chemistry 2014 to W. E. Moerner (Moerner, 2015), Eric Betzig (Betzig, 2015), and Stefan Hell (Hell, 2015). Since its invention, SR microscopy has paved the way for detailed studies of synaptic architecture and its molecular mechanisms and dynamics. An emerging approach that shows great promise for imaging in biological samples and has recently been implemented for single-molecule tracking and SR imaging is light sheet illumination (for reviews, see e.g., Power and Huisken, 2017; Gustavsson et al., 2018b). After introducing light sheet illumination and a comparison with other conventional illumination strategies, we will briefly review the history and application of deterministic optical SR techniques for neuronal imaging, as well as the fundamentals and applications of single-molecule tracking and SR imaging in 2D and 3D. We will then discuss light sheet illumination's impact on the improvement of these techniques and its relevance to studies of neurons and synapses. We will conclude with some emerging perspectives that have the possibility to further improve these methods and lead to new discoveries about the function of synapses at the molecular level.

LIGHT SHEET ILLUMINATION FOR OPTICAL SECTIONING IN THICK SAMPLES

Light sheet fluorescence microscopy (LSFM), also known as selective plane illumination microscopy (SPIM), is a wide-field method where the sample is illuminated with a thin sheet of light introduced perpendicular to the detection axis (Huisken et al., 2004). This method optically sections the sample and excites fluorophores only in a thin slice around the image plane. This results in reduced fluorescence background, photobleaching, and photodamage, which makes LSFM a great option for imaging of thick and sensitive samples.

The idea of implementing a sheet of light as an illumination mechanism was initially presented in 1902 (Siedentopf and Zsigmondy, 1902), where sunlight projected through a slit aperture was utilized to observe gold nanoparticles. Light sheet illumination then became a powerful contribution to the scientific community in the 1990s when it was combined with fluorescence microscopy, as it allowed researchers to image biological processes in 3D. Specifically, a form of LSFM called orthogonal-plane fluorescence optical sectioning (OPFOS; Voie et al., 1993) was the first to use a cylindrical lens to create a light sheet and was developed to image the internal 3D architecture of the cochlea. Another form of LSFM, a thin light-sheet microscope (TLSM), was developed to aid oceanographers in observing aquatic microbes (Fuchs et al., 2002) before the subsequent development of the updated design SPIM (Huisken et al., 2004). SPIM was originally developed to allow for non-invasive imaging of live embryos where the sample could be rotated for the sequential acquisition of multiple views (Huisken et al., 2004). Since then, light sheet technologies have advanced rapidly to achieve enhanced image quality, axial resolution, field-of-view (FOV) size, and acquisition rates (for a review, see e.g., Gustavsson et al., 2018b), and LSFM has become the gold standard for 3D and 4D imaging of developmental processes and live species behavior (for reviews, see e.g., Huisken and Stainier, 2009; Santi, 2011; Power and Huisken, 2017).

Light sheet illumination has several benefits over more conventional illumination strategies. One of the most commonly used illumination strategies for fluorescence imaging is wide-field epi-illumination, where the entire sample is illuminated at once and the fluorescence light is detected through the same objective as is used for illuminating the sample. Although straightforward to implement, this approach results in increased fluorescence background due to excitation of fluorophores away from the image plane, greater risk of premature photobleaching of fluorophores, and increased risk of photodamaging sensitive live samples. These factors are also critical when it comes to single-molecule imaging: the increased background leads to reduced precision in localizing single molecules, and the premature photobleaching of fluorophores outside of the current detection volume reduces the density of localizations, which effectively reduces the achievable resolution in the reconstruction. We will discuss these considerations in more detail in later sections.

Confocal microscopy is another commonly used approach for fluorescence imaging that provides background reduction through the use of a pinhole that blocks light originating from planes away from the image plane. However, its point-scanning nature makes it a much slower approach than wide-field alternatives. The speed of the acquisition can be improved using spinning disk confocal imaging, where the confocal concept is parallelized using an array of pinholes on a rotating disk. This approach has been used together with single-molecule imaging (Hosny et al., 2013; Chen X. et al., 2015). Even though the light is only detected near the image plane, the excitation light still passes through the entire sample both in conventional confocal and spinning disk confocal microscopy, which increases the risk of photobleaching and photodamage. The issue with premature photobleaching of fluorophores outside of the current detection volume has been mitigated by pairing spinning disk confocal imaging with DNA-PAINT (Schueder et al., 2017), where fluorophores are continuously replenished from a large, diffusing pool. However, both the excitation intensity and the detection efficiency can be limited by the disk, which reduces the localization precision for single-molecule imaging.

Total internal reflection fluorescence (TIRF) microscopy, also known as evanescent wave microscopy, is a wide-field approach that exploits the evanescent wave resulting from a laser beam that is totally internally reflected at the interface between the coverslip and the sample (Axelrod, 2001). The evanescent wave reaches a few hundred nanometers into the sample and thus TIRF provides exquisite optical sectioning with very low fluorescence background, photobleaching, and photodamage. TIRF has therefore been used extensively for single-molecule imaging (Bates et al., 2007; Shroff et al., 2007). However, it is limited to imaging very close to the coverslip and cannot be used for imaging deeper into the sample. In comparison, the optical sectioning capability of LSFM efficiently reduces the issues of high background fluorescence, photobleaching, and photodamage that are problematic in the other illumination strategies. LSFM is also a wide-field technique that is compatible with volumetric imaging of thick samples away from the coverslip.

For these reasons, LSFM has successfully been used for numerous applications in large-scale imaging, including imaging of the brain (for a review, see e.g., Corsetti et al., 2019). Specifically, LSFM has been applied to large neuronal populations such as those of the vomeronasal organ of the mouse (Holekamp et al., 2008) and to whole-brain imaging in mice (Dodt et al., 2007; Mertz and Kim, 2010), rats (Stefaniuk et al., 2016), songbirds (Rocha et al., 2019), and in zebrafish larvae to detect rapid changes in neural activity (Ahrens et al., 2013; Panier et al., 2013; Vladimirov et al., 2014; Park et al., 2015; Quirin et al., 2016; Greer and Holy, 2019). LSFM has also been improved to enable fast imaging of transient events in rat dendritic tissue (Haslehurst et al., 2018), to investigate the arrangement of human neural aggregates and their Ca^{2+} oscillations (Gualda et al., 2014), to study the interaction between sensory neurons and Schwann cells during neurotrauma (Xiao et al., 2015), and for functional volumetric imaging of hippocampal neurons in a 3D culture system (Chen et al., 2019). LSFM has also been paired with deep neural networks for imaging neurons in transgenic mouse brains (Zhao et al., 2020).

Overall, LSFM serves a very important role in imaging the brain as our understanding of the interactions among large neural networks depends upon the communication of multiple neurons across vast areas. Furthermore, LSFM provides the gentle illumination required for live-cell imaging and therefore, when combined with single-particle tracking (SPT) and single-molecule SR methods, offers great potential to study structures and interactions in synapses at the nanoscale. In the following sections, different SPT and SR methods will be described, in addition to the ways in which they can be improved by pairing with LSFM.

DETERMINISTIC SUPER-RESOLUTION TECHNIQUES AND THEIR APPLICATIONS IN NEURONAL AND SYNAPTIC IMAGING

There are two major groups of optical SR methods: stochastic and deterministic. We will discuss stochastic methods relying on single-molecule localization in some detail in the later sections. In deterministic SR imaging, knowledge of the spatial distribution of the excitation light is utilized in combination with the non-linear response of fluorophores to excitation as a means to circumvent the diffraction limit.

Stimulated emission depletion (STED) microscopy is an SR technique that utilizes a doughnut-shaped depletion laser overlaid atop a confocal excitation spot to deplete fluorophores in the periphery of the target region, effectively reducing the extent of the confocal spot by stimulating transitions of fluorophores from an excited singlet to the ground singlet state (Hell and Wichmann, 1994; Sahl et al., 2017). For more detailed information on STED microscopy, see e.g., Eggeling et al. (2013), Hell (2015), and Blom and Widengren (2017). STED has been used successfully for live-cell imaging, as demonstrated in *S. cerevisiae* and *E. coli* over two decades ago (Klar et al., 2000). STED has also been applied extensively to study neurons and synapses. In one example, STED was used to resolve individual vesicles in the synapse and confirm that the vesicle membrane protein synaptotagmin I clusters in patches on the presynaptic membrane independently of nerve terminal stimulation (Willig et al., 2006). Furthermore, two-color STED live-cell imaging was used to investigate the ultrastructure of endogenous F-actin in hippocampal neurons and revealed a subcortical periodic actin lattice in both axons and dendrites (D'Este et al., 2015). Live-cell STED imaging was also used to image the structure and morphological plasticity of dendritic spines in hippocampal samples and brain slices (Nägerl et al., 2008; Tønnesen et al., 2011; Urban et al., 2011). More recently, STED microscopy has been utilized to reveal activity-dependent enlargement in presynaptic boutons and axon shafts (Chéreau et al., 2017). However, despite its contributions to the field, STED is limited by its point-scanning nature, which makes it non-ideal for imaging over larger fields of view or for tracking of single-molecule dynamics. Given the high-power densities needed, there is also an increased risk for premature photobleaching and phototoxicity, which potentially limits its use for live-cell imaging of sensitive samples. Because absorption of biological material is minimal in the far-red region, far-red emitting fluorescent proteins have been used to mitigate the risk of photodamaging samples during STED imaging of dendritic spines (Wegner et al., 2017). However, such fluorescent proteins typically display lower photostability and quantum yield relative to shorter wavelength fluorescent proteins. The use of novel far-red synthetic dyes, such as silicon rhodamines (SiR; Lukinavičius et al., 2013, 2014; D'Este et al., 2015), in combination with Halo- or SNAP-tag labeling is another approach that holds great promise to further improve imaging in live cells in future STED studies. The issue of photobleaching was mitigated with the development of a technique called super-resolution shadow imaging (SUSHI; Tønnesen et al., 2018). In this method, extracellular fluid in the brain is fluorescently labeled and imaged using 3D-STED, creating a negative image of the structures to be studied and thus reducing the impact of photobleaching. SUSHI is well-suited for visualizing the structure of synapses since the synaptic clefts are full of fluorescently labeled extracellular fluid (Hrabetova et al., 2018). Even though SUSHI is limited in that it cannot resolve single-molecule mechanisms or be used to study specific structures, it can be combined with single-molecule localization approaches to correlate structural context with molecular specificity (Inavalli et al., 2019).

Reversible saturable optical fluorescence transitions (RESOLFT) microscopy is a more general term for techniques which make use of photoswitchable molecules and various types of on and off states together with inhomogeneous illumination (Schwentker et al., 2007). STED is one example within the RESOLFT concept, but other RESOLFT methods utilize switching between other types of states, such as an excited singlet and dark triplet states, where lower laser intensities are sufficient for switching. These other methods within the RESOLFT concept can thus be gentler for live-cell imaging. For example, RESOLFT has been used to image dendritic spines with low light intensities in 2D in living brain slices (Testa et al., 2012) and in 3D together with the imaging of the postsynaptic protein Homer1 in cultured neurons (Bodén et al., 2021). A variation of RESOLFT called molecular nanoscale live imaging with sectioning ability (MoNaLISA) allows intrinsic optical sectioning of large samples and has been demonstrated for imaging in living neurons and brain tissue (Masullo et al., 2018).

Another method that utilizes knowledge of the spatial distribution of the excitation illumination to circumvent the diffraction limit is structured illumination microscopy (SIM), where the effective lateral resolution is improved over the classical diffraction limit by a factor of two (Gustafsson, 2000). Because SIM requires relatively low excitation intensities, it is gentle and thus favorable for live-cell imaging. It is also compatible with multi-color imaging. Since it is a wide-field technique, in contrast to STED, SIM allows for imaging of large fields of view with good temporal resolution. For more detailed reviews, see e.g., Hirano et al. (2015), Heintzmann and Huser (2017), and Zheng et al. (2021). SIM has been used to image many different challenging cell types, including neurons. For example, it was used to study the plasticity of dendritic spines in mice hippocampal neurons (Guo et al., 2018). SIM was also used to reveal that PDZD8, an ER protein, was localized at ER-mitochondria contact sites in mammalian neurons and regulated synaptically-evoked Ca^{2+} dynamics (Hirabayashi et al., 2017). SIM studies in neuronal growth cones also aided in the discovery of a distinct form of endocytosis at the leading edge responsible for coordinated vesicle and actin-bundling generation during axon growth (Nozumi et al., 2017). Additionally, SIM was used to determine the spatial distributions of the presynaptic protein synapsin and the postsynaptic proteins Homer1 and PSD-95 through imaging of thousands of synapses (Lagache et al., 2018). SIM can be generalized to 3D by generating a pattern along both the lateral and axial directions (Gustafsson et al., 2008). 3D SIM revealed complex actin structures in the neuron growth cone and was used to observe the dynamics of cortical actin in hippocampal neurons and glia (Fiolka et al., 2012). While classical SIM most definitely continues to prove itself useful for neuronal imaging, it presents limitations in that the technique only offers a two-fold improvement in resolution. Non-linear SIM (NL-SIM), or saturated SIM (SSIM), however, exceeds this limit by making use of saturating excitation intensities (Gustafsson, 2005). Theoretically, this non-linear method can achieve infinite resolution and, like classical SIM, it can be expanded to 3D, but in practice, the resolution achieved is typically limited to around 50 nm (Gustafsson, 2005). While such a technique is advantageous in that it allows for improved resolution in 3D, it requires high laser intensities to nearly reach saturation conditions, which increases the rate of photobleaching. Hence, SSIM requires samples to be labeled with bright and photostable fluorophores (Gustafsson, 2005). SSIM also requires acquisition with multiple patterns, which limits the temporal resolution.

Deterministic SR techniques each offer their own unique advantages and will continue to provide important contributions to our understanding of neuronal and synaptic function. However, they are not single-molecule techniques, and they are limited to studies of molecular mechanisms and interactions. In the rest of this review, we will focus on techniques that allow for the fundamental goal of detecting single molecules in 2D and 3D, and how these techniques further benefit from the combination with light sheet illumination for imaging of neurons and synapses.

SINGLE-MOLECULE LOCALIZATION MICROSCOPY

In this review we will consider two applications of single-molecule localization microscopy: SPT of the motion of individual molecules to acquire information about their dynamics and interactions, and single-molecule SR microscopy for resolving static extended structures (for reviews, see e.g., von Diezmann et al., 2017; Möckl and Moerner, 2020; **Figure 2**). Both of these applications rely on the detection of the position of single molecules and can be coupled with light sheet illumination to better understand structures at the nanoscale. In localization microscopy, a single fluorophore is localized by detecting a sufficient number of photons from the fluorophore on a camera and then analyzing the diffraction-limited spatial distribution of photons, known as the point spread function (PSF). Each photon in the measured PSF can be treated as a sample of the probability distribution centered on the true position of the fluorophore, and an estimator of the center of the PSF can then be used to localize the fluorophore position in 2D with a precision that is much finer than the width of the intensity distribution of the PSF. In the following sections, we will describe methods for SPT and single-molecule SR imaging and showcase some examples of their applications for imaging of neurons and synapses. For extensive reviews of applications of these techniques in neuroscience, see e.g., Kim et al. (2010), Maglione and Sigrist (2013), Tønnesen and Nägerl (2013), Bannai (2018), Nosov et al. (2020), Carvalhais et al. (2021), Werner et al. (2021), and Zieger and Choquet (2021).

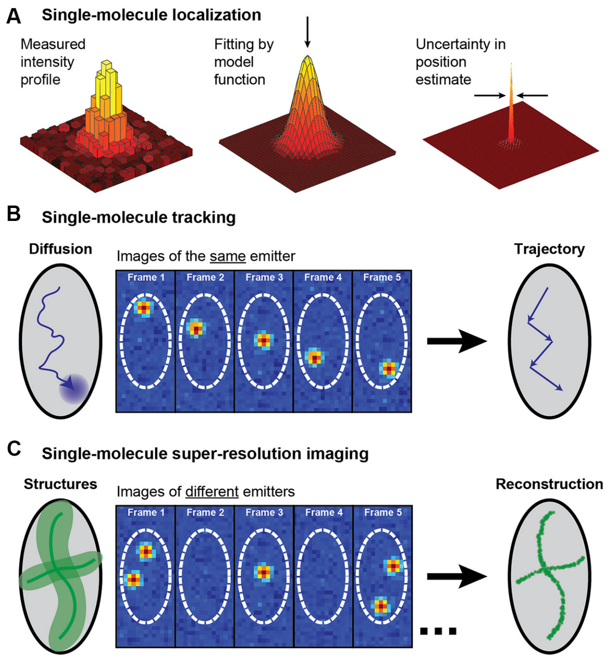

FIGURE 2 | Schematic illustrating single-molecule super-localization, tracking, and super-resolution imaging. **(A)** The noisy diffraction-limited pattern of an isolated fluorophore's intensity profile on the camera can be fit with a model function, such as a 2D Gaussian, to estimate the position of the fluorophore with a precision that is better than the diffraction limit. **(B)** In single-molecule tracking, the same single fluorophore is super-localized over multiple frames to create a trajectory that yields information about the fluorophore dynamics. **(C)** A diffraction-limited image with all molecules fluorescing simultaneously can be super-resolved by sequentially super-localizing many different spatially isolated molecules. This approach requires some active control to allow just a small fraction of the fluorophores to emit in each camera frame. Figure reprinted with permission from von Diezmann et al. (2017). Copyright (2017) American Chemical Society.

SINGLE-PARTICLE TRACKING IN 2D REVEALS INFORMATION ABOUT MOLECULAR DYNAMICS AND INTERACTIONS

SPT is a method used to observe the dynamics and intermolecular interactions of individual particles and molecules at high spatial and temporal resolution (for a review, see e.g., Shen et al., 2017). In SPT, the same particle is localized and tracked over time, providing information on nanoscale dynamics and interactions beyond the optical diffraction limit. With the ability to directly monitor individual particles, one can obtain information about heterogeneous systems and unique events that would have otherwise been lost in averaged measurements. SPT can therefore provide a more complete understanding of the behavior of individual molecules in complex systems and of the mechanisms behind various biological processes.

For this reason, SPT has been used extensively to study nanoscale dynamics in neurons and synapses. Quantum dot (QD)-SPT is a commonly used technique for observing the molecular membrane dynamics of neurons, and has led to insights into the functions of neurotransmitter transporters (Thal et al., 2019) and receptors (Ehrensperger et al., 2007; Bürli et al., 2010; Arizono et al., 2012). Despite the discoveries QD-SPT has contributed to neuroscience, there are drawbacks associated with using QDs. The large size of QDs compared to organic dyes or fluorescent proteins limits the mobility of the molecule in narrow areas such as the synaptic cleft (Groc et al., 2007; Alcor et al., 2009). Additionally, QDs have to be tagged to the proteins of interest and blink erratically between on and off states which complicates their use in SPT (Groc et al., 2007; Alcor et al., 2009).

SptPALM is a method that overcomes some of the challenges presented by QD-SPT by combining SPT with (fluorescence) PhotoActivation Localization Microscopy [(f)PALM], where photoactivatable fluorophores are activated and then tracked until they photobleach (Manley et al., 2008). SptPALM utilizes smaller labels that also typically lessen the issues with blinking and are well suited for live-cell imaging. Thousands of these photoactivated fluorophores, most commonly fluorescent proteins, can be tracked simultaneously in live cells by single-molecule localization followed by trajectory reconstruction, allowing for studies of high-density dynamics of single molecules (Manley et al., 2008, 2010). SptPALM in neurons has provided insight into the organization and dynamics of individual actin molecules within dendritic spines (Tatavarty et al., 2009; Frost et al., 2010), revealing their heterogenous distribution and role in supporting diverse processes in the synapse. SptPALM has also revealed a heterogeneous distribution of CaMKII in dendritic spines in non-stimulated and stimulated rat hippocampal neurons, suggesting that CaMKII fulfills multiple functions both inside and outside of the postsynaptic density (Lu et al., 2014). Another study has also revealed that CaMKII has both a kinase- and structure-dependent role for actin remodeling in the spine (Kim et al., 2015). In addition, sptPALM has been used to track the dynamics of the transcription factor NF-κB p65 (Widera et al., 2016), which is transported from the synapse to the nucleus upon glutamate activation. Another study using sptPALM investigated the mobility of syntaxin1A, a protein involved in synaptic vesicle docking, and it was found that the mobility increased in response to opto- and thermo-genetic neuronal stimulation and that diffusion and trapping of syntaxin1A in nanoclusters regulated neurotransmitter release (Bademosi et al., 2016; **Figure 3A**). Additionally, sptPALM was used to investigate the effect of Shank knockdown on the mobility of cortactin and revealed that Shank proteins are key intermediates between the synapse and the spine actin cytoskeleton *via* cortactin (MacGillavry et al., 2016). Furthermore, sptPALM has been used to explore the mechanisms connecting voltage-gated calcium channels with short-term plasticity (Heck et al., 2019), as well as the spatiotemporal distribution of postsynaptic AMPA receptors (Hoze et al., 2012; Nair et al., 2013). SptPALM has also been used to map how the membrane dynamics of GABAA receptors are altered with mutations associated with epilepsy (Bouthour et al., 2012). These examples of SPT in neurons and synapses highlight the versatility and strength of SPT for improving our understanding of the function of synapses at the molecular level. However, as we will discuss further in later sections, such methods for neuronal imaging can be further improved upon with the incorporation of LSFM.

SINGLE-MOLECULE SUPER-RESOLUTION MICROSCOPY IN 2D UNVEILS STRUCTURES AT THE NANOSCALE

The second application of single-molecule localization microscopy, single-molecule SR imaging, strives to map nanoscale extended structures that are densely labeled with fluorophores. In addition to being able to localize the positions of the single molecules, localization-based SR imaging also requires some form of control of the density of the fluorophores that emit in each camera frame. Various methods have been developed using some photophysical, photochemical, or binding and unbinding mechanism to keep most of the fluorophores in an off state to ensure that just a small, non-overlapping subset of the fluorophores fluoresce simultaneously. By localizing different fluorophores in many subsequent frames, a point-by-point reconstruction of the underlying structure can be created. Methods that utilize single-molecule localization microscopy to achieve SR include (f)PALM (Betzig et al., 2006; Hess et al., 2006), (direct) Stochastic Optical Reconstruction Microscopy (d STORM; Rust et al., 2006; Heilemann et al., 2008), and various methods based on Point Accumulation for Imaging in Nanoscale Topography (PAINT; Sharonov and Hochstrasser, 2006). For more detailed reviews about these stochastic SR methods, please see e.g., von Diezmann et al. (2017), Möckl and Moerner (2020), and Lelek et al. (2021).

These stochastic SR methods have been used for numerous 2D studies of the neuronal synapse. For example, PALM has been used to study the spatial distribution of perisynaptic actin and its correlation with the postsynaptic density proteins GKAP and PSD-95 (Frost et al., 2010), to quantify the morphology of dendritic spines (Izeddin et al., 2011), and to reveal that nanoscale scaffolding domains within the postsynaptic density concentrate synaptic AMPA receptors (MacGillavry et al., 2013).

Two- or three-color STORM has been applied in conjunction with large-volume, automated, ultrathin sectioning to image ganglion cells (Sigal et al., 2015), to image parvalbumin-positive interneurons and their associated extracellular matrix, called perineural nets, in mouse primary visual cortices (Sigal et al., 2019), to discover a spatial correlation between AMPA receptor nanodomains and the post-synaptic adhesion protein neuroligin-1 (Haas et al., 2018), and to determine the nanoscale co-organization of AMPA receptors, NMDA receptors, and mGluR at excitatory synapses (Goncalves et al., 2020). DSTORM has also been combined with PALM to enable two-color imaging for studies of the spatial relation between actin in dendritic spines and the postsynaptic density protein Shank2 (Izeddin et al., 2011), with sptPALM to map the plasma membrane in primary hippocampal rat neurons (Ries et al., 2012), and with confocal approaches to investigate NMDA-receptor activation at single synapses (Metzbower et al., 2019).

DNA-PAINT (Jungmann et al., 2010) is a powerful implementation of PAINT where short single-stranded DNA oligonucleotides tagged with a fluorophore transiently bind to complementary oligonucleotides which are bound to a target molecule, such as an antibody to a protein of interest. DNA-PAINT overcomes PAINT's limitations of target selectivity and specificity and, like PAINT, is not limited by photobleaching since the binding is reversible and bleached fluorophores can be replaced by an excess of unbleached ones. Since the on/off switching is controlled by the choice of oligonucleotide sequences rather than by the photophysical or photochemical properties of the fluorophore, DNA-PAINT also allows for a wider selection of fluorophores than (f)PALM and (d)STORM. An additional benefit is that multiplexing can be done through the use of multiple different oligonucleotide pairs imaged sequentially using the same fluorophore—a method called Exchange-PAINT (Jungmann et al., 2014). Exchange-PAINT mitigates the issue of chromatic-aberration induced offsets between different color channels that arise when using other techniques where different fluorophores are used. A tradeoff is that DNA- and Exchange-PAINT imaging are typically much slower than the other single-molecule SR methods. The recently developed Peptide-PAINT (Eklund et al., 2020) makes use of small, programmable peptide pairs instead of the single-stranded DNA oligonucleotides used in DNA-PAINT. In addition to their smaller size, these peptides can produce more favorable kinetics than their oligonucleotide counterparts and can, in that way, improve the imaging speed. DNA-PAINT conventionally requires the target cell to be fixed and permeabilized, meaning

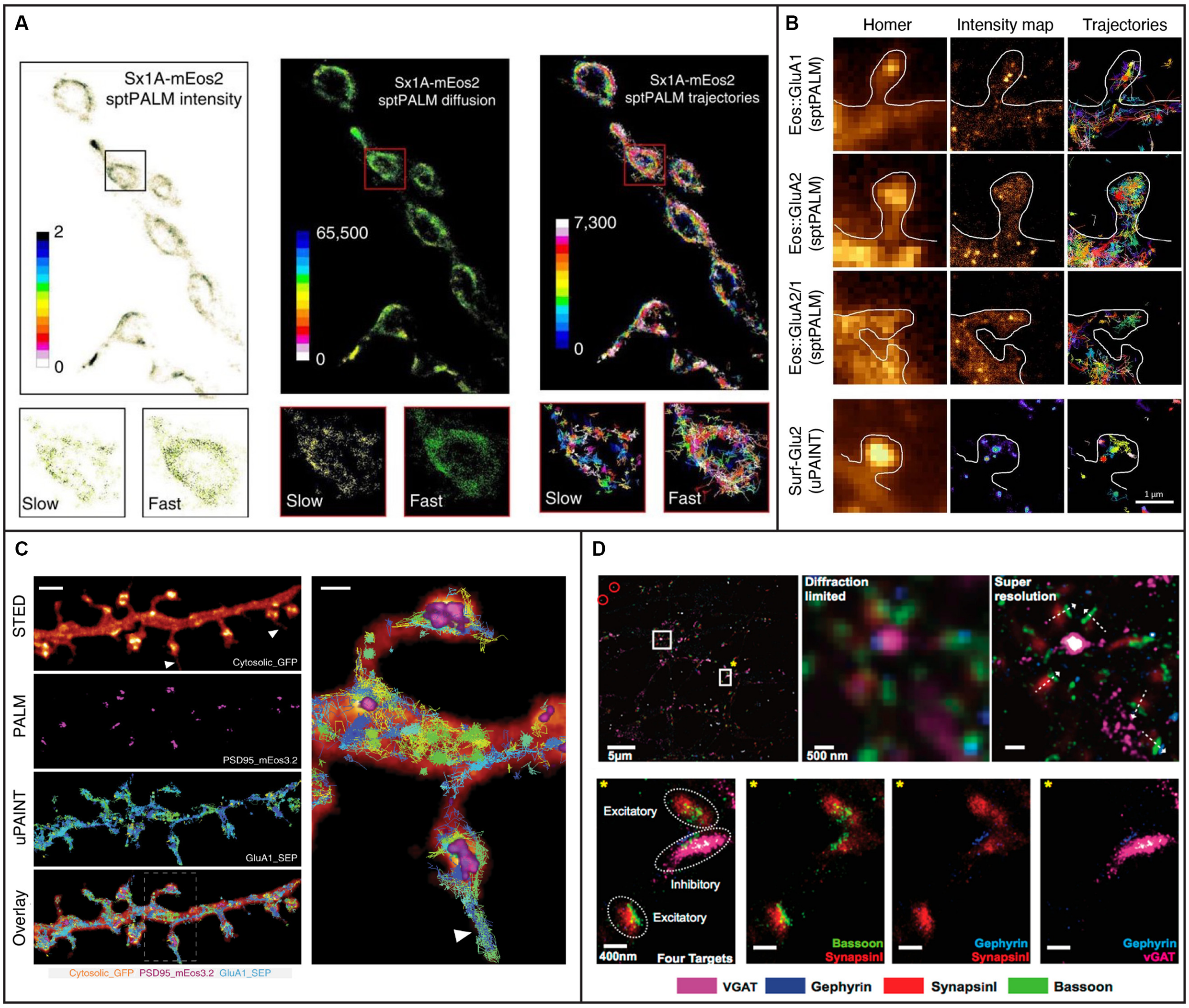

FIGURE 3 | Examples of 2D single-molecule tracking and 2D super-resolution imaging in neurons and synapses. **(A)** sptPALM was used to image the distribution and mobility of attachment receptor protein syntaxin1A fused with photoconvertible fluorescent protein mEos2 in the motor nerve terminal of *Drosophila* larvae. Insets demonstrate average intensity, diffusion coefficient, and trajectory map showing slow and fast populations of syntaxin1A on a synaptic bouton. Figure reprinted from Bademosi et al. (2016). Reprinted with permission from Springer, under Creative Commons Attribution 4.0 International License. **(B)** The organization of AMPA receptors into nanodomains inside the spines of live hippocampal neurons demonstrated with single-molecule tracking techniques sptPALM and uPAINT. The first column shows diffraction-limited images of Homer1c and the following two columns show intensity maps and trajectories from measurements using sptPALM (top three rows) or uPAINT (bottom row). The scale bar is 1 μm. Adapted from Nair et al. (2013) (https://www.jneurosci.org/content/33/32/13204). **(C)** Combining deterministic approaches STED and SUSHI with stochastic techniques PALM and uPAINT enabled correlative super-resolution imaging of neuron morphology and analysis of the distribution and dynamics of synaptic proteins in live hippocampal neurons. The right panel is a close up of the area marked with a rectangle in the overlay. The scale bar is 2 μm in the left panel and 500 nm in the close up. Reprinted by permission from Springer Nature: Springer Nature, Nature Methods, (Inavalli et al., 2019), copyright 2019. **(D)** The four synaptic proteins vGAT, Gephyrin, SynapsinI, and Bassoon imaged sequentially with Exchange-PAINT. The top left panel shows a merged image of the synaptic proteins, where gold nanoparticles were used as fiducials for registration (circled in red). The scale bar is 5 μm. The top middle and top left panels show diffraction-limited and super-resolved images, respectively, of the region in the top left panel marked with a white square without a star. The super-resolved image allows distinction of the orientation of individual synapses as shown with white arrows. The scale bar is 500 nm. The bottom panels show the region marked with a white square and yellow star in the top left panel. The four targeted synaptic proteins are first shown together and then pair-wise. The scale bars are 400 nm. Reprinted with permission from Wang et al. (2017). Copyright (2017) American Chemical Society.

this method is typically not compatible with live-cell imaging. LIVE-PAINT (Oi et al., 2020) addresses this issue by combining peptides for labeling with fluorescent proteins which are coded for and expressed within the target cell. Quantitative DNA-PAINT (qPAINT) is a PAINT approach that allows for counting of the number of targets (Jungmann et al., 2016), and it has been utilized e.g., to image and estimate copy numbers of surface AMPA-type receptors at synapses of rat hippocampal neurons (Böger et al., 2019). In another study, Universal (u)PAINT (Giannone et al., 2010), which utilizes the PAINT concept for tracking of dynamics in membranes, was used together with sptPALM, dSTORM, STED, and EM to investigate the correlation between the dynamics and distribution of AMPA receptors with the position of clusters of the postsynaptic density protein PSD-95 (Nair et al., 2013; **Figure 3B**). Another recent study combined uPAINT with STED and PALM, and SUSHI with sptPALM and PALM, to study the position and movements of synaptic proteins within the morphological context of growth cones and dendritic spines (Inavalli et al., 2019; **Figure 3C**). UPAINT has also been combined with PALM for tracking of transmembrane proteins over postsynaptic densities whose internal structures were simultaneously super-resolved. The results provided important experimental confirmation that the density of scaffold proteins in the postsynaptic density strongly influences the mobility of transmembrane proteins (Li and Blanpied, 2016). Furthermore, uPAINT was combined with sptPALM to investigate the degree to which the mobility of AMPA receptors depends on protein crowding in the synapse (Li et al., 2016). Exchange-PAINT has also been demonstrated for up to eight-target imaging in primary neurons and included the co-localization of the four synaptic proteins Bassoon, Synapsin1, Gephyrin, and vGAT (Wang et al., 2017; **Figure 3D**).

All these stochastic SR techniques can be improved upon further by the combination with LSFM for optical sectioning. Some important technical considerations on improving both SPT and single-molecule SR imaging will be described in the next section.

CONSIDERATIONS FOR IMPROVING SINGLE-MOLECULE TRACKING AND SUPER-RESOLUTION IMAGING

In this section, we will provide some technical details on how to improve the achievable localization precision which may prove helpful for the user. These considerations will also highlight the benefits of using LSFM for SPT and stochastic SR imaging.

The precision that can be achieved from single-molecule localization microscopy depends on multiple parameters, such as the number of the detected signal and background photons, the effective pixel size of the images, and the choice of position estimator. The simplest position estimator is the centroid or average photon position, but superior estimators are preferable. A simple 2D function such as a Gaussian or Airy function may be used as a model of the PSF, in combination with a fitting criterion such as a least squares or maximum likelihood estimator (MLE). MLE can provide improved localization precision compared to least-squares Gaussian fitting, especially for low background levels, but at the cost of computational complexity (Rieger and Stallinga, 2014). A common choice that balances analysis speed and acceptable precision is to fit using a 2D Gaussian with a constant background offset and an unweighted least squares estimator (Mortensen et al., 2010). For extensive reviews on the merits of different analysis approaches, see e.g., Abraham et al. (2009), Deschout et al. (2014), and Small and Stahlheber (2014).

Two other ways to improve the localization precision are to increase the signal photons from the target fluorophores and to reduce the background fluorescence coming from the rest of the sample. The first steps to achieve a reduction of background from the rest of the sample are to ensure proper filtering of Rayleigh and Raman scattered light, shield from light from other sources in the room, use specific labels, and work with far-red fluorophores where the autofluorescence from the sample is lower. However, even the background coming from the labeled structure itself, or from diffusing PAINT probes, can be problematic. This is especially true when imaging thicker samples and when imaging in 3D using long-range PSFs (as will be discussed in more detail in the "Single-Molecule Tracking and Super-Resolution Imaging in 3d" section). Therefore, reducing this background is critical to enable and improve imaging in these situations. For DNA-PAINT imaging, important recent advances, such as the development of fluorogenic probes (Chung et al., 2020), have been made to reduce the background coming from the diffusing unbound fluorophores. An additional and complementary approach to mitigate the issue with high fluorescence background is to use LSFM to optically section the sample and in that way improve the localization precision.

Improving the signal can be done by selecting fluorophores that are bright and yield many photons. For SPT, the fluorophore should also be small enough to not obstruct the motion of the tracked molecule and photostable to allow for long track lengths. In addition, it should be live-cell compatible and either genetically encoded or cell-membrane permeable unless tracking is done in membranes. The labeling should also be specific to the target. Fluorescent proteins fulfill many of these criteria and have revolutionized live-cell imaging (Chalfie, 2009; Shimomura, 2009; Tsien, 2009; Kremers et al., 2011). However, they are typically not as bright or photostable as synthetic dyes, which reduces the localization precision. Fluorescent proteins also require transfection and the expression of fluorescent proteins may perturb cell function. Synthetic dyes are generally brighter and more photostable than fluorescent proteins, but they can yield higher background due to unspecific binding. They also often require fixation and permeabilization for labeling of structures inside cells, and the labeling efficiency can be limited. Quantum dots provide bright labels, but their size and complex blinking behavior can limit their applicability. For SR imaging, the fluorophores should also be bright to improve the localization precision, but they must allow for control of the on/off state. In PAINT approaches, the on/off fraction is controlled *via* binding kinetics and fluorophore concentration rather than by the photophysics of the fluorophore, which is why the requirements on the fluorophores for PAINT imaging are less stringent than for the other techniques. Here, bright fluorophores can be imaged over longer exposure times to increase the number of photons collected and yield excellent localization precision, at the cost of increased imaging time. Many SR applications do not require live samples, so here fluorophores that are not cell membrane permeable could be used if the cell is permeabilized before labeling. Large efforts are continuously being made to improve parameters of fluorophores for SPT and SR imaging such as brightness, photostability, excitation and emission wavelengths, blinking and activation properties, cell permeability, and labeling specificity (Dempsey et al., 2011; Chozinski et al., 2014; Grimm et al., 2015, 2016a,b), so researchers should carefully select optimal fluorophore and imaging conditions for their specific applications.

SINGLE-MOLECULE TRACKING AND SUPER-RESOLUTION IMAGING IN 3D

Given that 3D information is crucial for a complete understanding of biological specimens, modes of imaging that enable the acquisition of both lateral and axial information are invaluable. Confocal microscopy can provide excellent contrast and can generate 3D images through stacking of multiple z-planes, but it is inherently diffraction limited in all dimensions. Because of its confocal scanning nature, it also suffers from a limited temporal resolution on the order of seconds, and high peak powers increase the risk of photobleaching and photodamaging the sample. Fast 3D SPT has been achieved using confocal active-feedback approaches, such as orbital imaging (Levi et al., 2005; Katayama et al., 2009) and TSUNAMI (Perillo et al., 2015), where multiple confocal laser beams trace orbits around the tracked particle. An alternative active-feedback approach is based on a fast-scanning single confocal spot combined with a nanopositioner to keep the molecule within the 3D scanning region (Hou et al., 2019). The extension of this method to single molecules has historically been limited by piezoelectric response time and the number of photons detected from the single molecules. However, a recently developed method termed 3D Single Molecule Active Real-time Tracking (3D-SMART) has optimized these parameters to yield 3D tracking of single molecules with excellent temporal resolution over extended times (Hou et al., 2020). MINFLUX (Balzarotti et al., 2017), is another scanning approach that has recently been extended for 3D tracking and SR imaging. In MINFLUX, a fluorophore targeted by a doughnut-shaped beam will fluoresce more intensely the further it is from the center of the doughnut beam, which can be used to precisely determine the position of the fluorophore. MINFLUX has been used for SR imaging of the post-synaptic protein PSD-95 with essentially isotropic 3D resolution of 2–3 nm (Gwosch et al., 2020). This method facilitates work with very low photon counts and can achieve better spatial precision than other single-molecule localization techniques, which opens up possibilities for very detailed studies of synaptic structures and dynamics in the future. However, all these scanning methods have limitations when it comes to the number of particles that can be tracked or imaged in parallel.

Biplane (Toprak et al., 2007; Juette et al., 2008; Ram et al., 2008) and multiplane (Ram et al., 2012; Abrahamsson et al., 2013; Chen J. et al., 2014; Knight et al., 2015; Smith et al., 2015) imaging are wide-field approaches based on splitting the detected light into two or more light paths with different optical path lengths before they are imaged on a camera. This allows for the detection of the 3D position of many individual molecules in parallel. However, care has to be taken to balance the axial range used and the required spatial or temporal resolution, as the signal is weakened by splitting the light into multiple planes. Two-color biplane imaging combined with spectral demixing has been used to image nanostructures in 3D in hippocampal neurons, including β-tubulin, β2-spectrin, β4-spectrin, and AnkG in axons and Homer1 and Bassoon at the synapse (Winterflood et al., 2015). Biplane imaging has also been paired with advanced statistical analysis to determine the stoichiometry of and distance between the synaptic vesicle proteins synapsin and vesicular glutamate transporters (Lagache et al., 2018).

An alternative wide-field approach is to use engineered PSFs (for a review, see e.g., von Diezmann et al., 2017), where the axial (z) position of the emitter is encoded directly in the shape of the PSF on the camera (**Figure 4**). This is accomplished by modifying the phase pattern of the emitted light in the Fourier plane of the microscope and allows for scan-free wide-field 3D detection of emitters with excellent precision by the addition of a small number of optical elements to a standard fluorescence microscope. A common approach is to introduce a weak cylindrical lens in the emission light path to create an astigmatic PSF (Kao and Verkman, 1994; Huang et al., 2008a; Spille et al., 2012; Li et al., 2013; Izeddin et al., 2014). An early use of astigmatic PSFs for 3D SR imaging of the synapse involved STORM imaging of the architecture and distance between 10 protein components of the presynaptic active zone and the postsynaptic density in brain tissues (Dani et al., 2010; **Figure 5A**). Astigmatism in combination with STORM was also used to discover that axons are wrapped in evenly-spaced periodic structures called the membrane-associated periodic skeleton, composed of actin, spectrin, and other related proteins (Xu et al., 2013; **Figure 5B**). These studies have also been extended to map the membrane-associated periodic skeleton in axons, dendrites, and soma of neurons at different developmental stages (Zhong et al., 2014; Han et al., 2017). Astigmatism and dSTORM have also been used to determine the location of the transmembrane protein assembly γ-secretase, an enzyme linked to Alzheimer's disease (Schedin-Weiss et al., 2016), as well as to identify a mechanism for controlling synaptic weight through imaging of Munc13-1 supramolecular assemblies (Sakamoto et al., 2018; **Figure 5C**). More recently, astigmatism was employed to map protein distributions and arrangements within a calyx of Held synapse through multiplexed dSTORM imaging (Klevanski et al., 2020). Astigmatism has also been combined with PALM and STORM for two-color 3D SR imaging to characterize the ultrastructure of inhibitory synapses and to count scaffold proteins and receptor binding sites (Specht et al., 2013). In addition, astigmatism has been used with two-color STORM for 3D SR imaging together with EM and STED to determine the spatial distribution of proteins EphB2 and SynCAM in relation to the postsynaptic density, which revealed that SynCAM 1 shapes the cleft edge, while EphB2 is enriched deeper into the postsynapse (Perez de Arce et al., 2015), as well as for imaging of the distribution of presynaptic proteins in relation to the postsynaptic scaffolding protein PSD-95, which revealed trans-synaptic alignment of the distributions (Tang et al., 2016; **Figure 5D**).

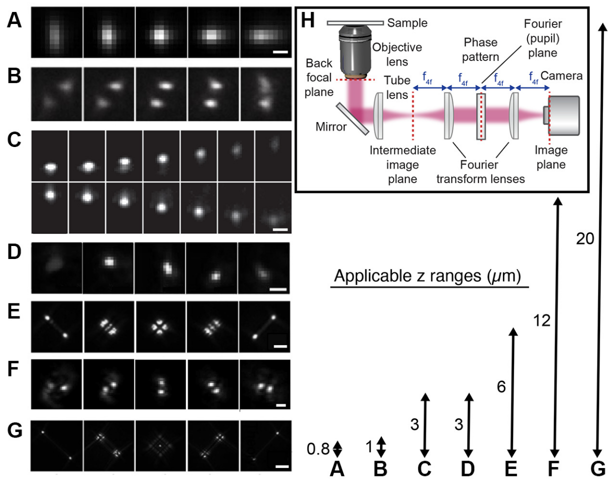

FIGURE 4 | Engineered point spread functions (PSFs) for single-molecule localization allowing tracking and super-resolution imaging in 3D. The arrows (right) represent both the available axial ranges and the range over which the different PSFs were imaged, except in the case of the DH PSF that was imaged over a 3 μm axial range. **(A)** Astigmatic (Huang et al., 2008b). The scale bar is 0.5 μm. Reprinted from Huang et al. (2008b). Reprinted with permission from AAAS. **(B)** Phase ramp (Baddeley et al., 2011). Figure reprinted by permission from Springer Nature: Springer Nature, Nano Research (Baddeley et al., 2011), copyright 2011. **(C)** Accelerating beam (Jia et al., 2014). The scale bar is 1 μm. Figure reprinted by permission from Springer Nature: Springer Nature, Nature Photonics (Jia et al., 2014), copyright 2014. **(D)** Corkscrew (Lew et al., 2011). Reprinted with permission from Lew et al. (2011) © The Optical Society. **(E)** Tetrapod (Shechtman et al., 2015). The scale bar is 2 μm. Reprinted from Shechtman et al. (2015) with permission from the American Chemical Society (https://pubs.acs.org/doi/10.1021/acs.nanolett.5b01396). Further permissions related to the material excerpted should be directed to the ACS. **(F)** Double-helix (DH; Pavani et al., 2009). The scale bar is 2 μm. Reprinted with permission from Pavani et al. (2009). **(G)** Tetrapod (Shechtman et al., 2015). The scale bar is 5 μm. Reprinted from Shechtman et al. (2015) with permission from the American Chemical Society (https://pubs.acs.org/doi/10.1021/acs.nanolett.5b01396). Further permissions related to the material excerpted should be directed to the ACS. **(H)** The optical design used for PSF engineering was implemented with a transmissive dielectric phase mask to modulate the shape of the PSF.

PSF engineering has also been used to create more complex PSFs with various axial ranges between 0.8 and 20 μm, including the bisected pupil (Backer et al., 2014), self-bending (Jia et al., 2014), corkscrew (Lew et al., 2011), double helix (DH; Pavani et al., 2009; Thompson et al., 2010; Backlund et al., 2014; Gustavsson et al., 2018a; Bennett et al., 2020), and tetrapod PSFs (Shechtman et al., 2014, 2015, 2017; Weiss et al., 2020). The desired phase pattern can be implemented using transmissive dielectric phase masks, a liquid crystal spatial light modulator (SLM), or a deformable mirror. Transmissive dielectric masks allow for the implementation of any type of phase pattern with excellent photon efficiency. However, one mask is required for each type of PSF, axial range, and wavelength range used. An SLM also allows for the implementation of any type of phase pattern; the choice of pattern is flexible and can be easily and rapidly updated. However, an SLM can only modulate one polarization direction of the emitted light, which means that either half of the light has to be discarded, at the cost of reduced localization precision, or more elaborate optical designs have to be implemented to recover the other polarization direction (Backlund et al., 2012). The deformable mirror consists of a continuous membrane and is therefore only suited for smoothly varying phase patterns. For these types of phase patterns, the deformable mirror can be easily and rapidly updated to facilitate various axial ranges and wavelengths and offers excellent photon efficiency.

Longer-range engineered PSFs have not yet been extensively implemented for imaging in cultured neurons or in brain tissues, but they hold great promise for addressing questions about 3D molecular dynamics and nanoscale morphology in these types of samples. Just like in the case of localization microscopy in 2D, the spatiotemporal resolution that can be achieved for 3D localization using engineered PSFs depends on the signal-to-background ratio between the signal from the fluorophore and the background fluorescence from the rest of the cell. The footprint of engineered PSFs on the camera is larger, which means that the signal photons are spread over more pixels. Since imaging in thick samples, such as entire cells or tissues, typically results in high fluorescence background, methods to improve the signal-to-background ratio are critical to enable and improve 3D single-molecule imaging in these situations. Combining engineered PSFs with LSFM for optical sectioning of thick samples is thus a promising route to solve these problems which can pave the way for new discoveries in neuroscience.

LIGHT SHEET ILLUMINATION STRATEGIES FOR IMPROVED WIDE-FIELD DETECTION OF SINGLE MOLECULES IN 3D

LSFM has revolutionized large-scale imaging of brain tissue and neural networks, but its optical sectioning capability also greatly benefits SPT and single-molecule SR imaging (for more extensive reviews on the marriage of single-molecule approaches with LSFM, see e.g., Power and Huisken, 2017; Gustavsson et al., 2018b). When merging single-molecule approaches with LSFM, a high numerical aperture (NA) detection objective is ideal to capture as many photons as possible emitted from the individual fluorophores to improve the detected signal, as well as a high-NA illumination objective to create a thin light sheet to reduce out-of-focus background fluorescence, photobleaching, and photodamage. However, high-NA objectives have short working distances and large physical profiles, which prevent concomitant use in most LSFM designs. For whole-cell or tissue imaging, it is desirable that fluorophores can be excited all the way down to the coverslip, but this is difficult to achieve using SPIM-like approaches with high-NA objectives. Several different approaches have therefore been designed to address these challenges.

An early implementation for single-molecule imaging utilized the conventional SPIM approach with a cylindrical lens and a long working distance illumination objective to achieve high contrast for SPT in *C. tentans* larvae (Ritter et al., 2010). However, due to the use of a cylindrical lens which forms a light sheet with a Gaussian profile that diverges away from the focus, this

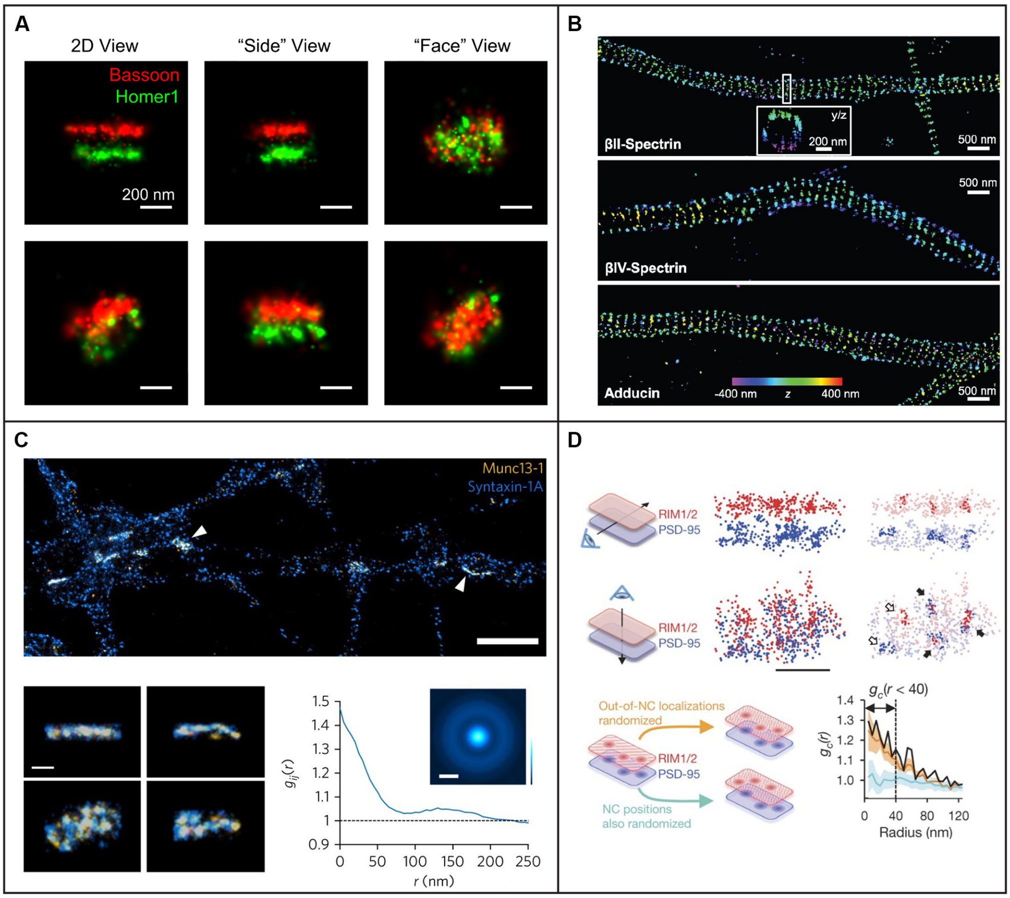

FIGURE 5 | Examples of 3D single-molecule super-resolution imaging in neurons and synapses. **(A)** STORM with astigmatism was used to image pre- and postsynaptic scaffolding proteins Bassoon and Homer1 in 3D, providing information about the shape of the presynaptic active zone and postsynaptic density from different angles for two different pre- and postsynaptic pairs in the top and bottom row, respectively. The scale bars are 200 nm. Figure reprinted with permission from Dani et al. (2010). **(B)** STORM with astigmatism was used to image and analyze the 3D organization of cytoskeletal protein spectrin and actin-capping protein adducin, revealing their periodic axon-surrounding structure. The scale bars are 500 nm. Figure reprinted from Xu et al. (2013). Reprinted with permission from AAAS. **(C)** STORM with astigmatism was used to image multiple views of Munc13-1 (yellow) assemblies and syntaxin-1A (blue) at the active zone. The graph illustrates pair correlation analysis of the STORM datasets, demonstrating nanoscale co-clustering of Munc13-1 and syntaxin-1A. The scale bar is 2 μm in the top panel and 200 nm in the bottom panel. Reprinted by permission from Springer Nature: Springer Nature, Nature Neuroscience, (Sakamoto et al., 2018), copyright 2018. Reprinted with kind permission from Springer. **(D)** Light sheet illumination combined with two-color 3D-STORM was used for imaging of synaptic RIM1/2 and PSD-95. The trans-synaptic alignment of protein nanoclusters in the active zone and the PSD are shown both with top and side views. Closed arrows indicate the trans-synaptic alignment and open arrows correspond to non-aligned nanoclusters. In the lower panels a paired cross-correlation function is shown for RIM1/2 and PSD-95 distributions in two different simulated conditions: first, for randomly distributed nanoclusters (light blue trend), and second, for a random selection of molecules outside the originally measured nanocluster positions (orange trend). The scale bar is 200 nm. Reprinted by permission from Springer Nature: Springer Nature, Nature, (Tang et al., 2016), copyright 2016.

light sheet could not be used to excite fluorophores all the way down to the coverslip because of aberrations in the light sheet at the interface between the sample chamber wall and the coverslip would have been introduced. This method was thus limited to imaging 100–200 μm above the coverslip, which prevents imaging of individual adherent mammalian cells or tissues.

One convenient way to circumvent the issue of steric hindrance between two high-NA objectives is to use a single high-NA objective for both fluorescence detection and the formation of an oblique light sheet for excitation. Multiple different implementations of this type of pseudo-TIRF illumination have been developed, including highly inclined and laminated optical sheet (HILO; Tokunaga et al., 2008), variable-angle epifluorescence microscopy (VAEM; Konopka and Bednarek, 2008), and methods that address the resulting angle mismatch between the light sheet plane and the image plane by rotating the image plane (Dunsby, 2008; Bouchard et al., 2015; Maioli et al., 2016) or by adding a second detection objective perpendicular to the light sheet plane (Theer et al., 2016; **Figure 6**). However, the latter methods come at the cost of increased complexity and a lower effective NA in the detection path, which reduces the detected signal. Overall, single-objective oblique light sheet methods offer a convenient approach for optical sectioning using a conventional epi-fluorescence microscope. However, these light sheets are generally relatively thick, the thickness and intensity of the light sheet depend on the incident angle, and the FOV is limited due to the non-planarity between the light sheet and image planes unless one of the approaches above is implemented to address this issue.

Another approach termed light-sheet Bayesian microscopy (LSBM) resembles the single-objective oblique methods, but here a separate illumination objective is used together with a Pellin-Boca prism to direct the light sheet along the image plane (Hu et al., 2013, 2016). In this design, the entire sample is angled instead of the illumination and image planes, which circumvents the issue with non-planarity between the light sheet and image planes. Since the resulting light sheet is still relatively thick, the authors paired this illumination scheme with Bayesian bleach-and-blink (3B) image reconstruction of PALM/STORM data (Cox et al., 2012; Rosten et al., 2013) to better localize molecules in dense regions. This design also utilizes a somewhat lower-NA detection objective of NA 1.0, which reduces the achievable localization precision. Furthermore, the addition of the prism pathway and the custom-made sample holder adds complexity and prevents direct addition to a conventional microscope.

The first approach that utilized SPIM for single-molecule SR imaging is termed individual molecule localization with selective plane illumination (IML-SPIM; Cella Zanacchi et al., 2011). Here the thickness of the light sheet can be tuned depending on the illumination objective and the light sheet parameters are not coupled with the light sheet position. Using this approach together with PALM and astigmatism, the authors demonstrated 3D single-molecule SR imaging in up to 150 μm thick samples. Because the method relies on conventional SPIM, the sample must be mounted in an agarose gel away from the coverslip, which is not compatible with studies of adherent, mammalian cells or samples positioned on conventional coverslips. However, this method demonstrates that 3D single-molecule imaging can be achieved even far away from the coverslip with a relatively simple setup and a NA 1.1 detection objective.

Multiple different methods have then been developed to circumvent the restrictions posed by SPIM and oblique light sheet approaches for SPT and SR imaging. In reflected light sheet microscopy (RLSM), a second illumination objective is mounted vertically and used to form a light sheet that is then redirected parallel with the image plane by reflection off of a polished atomic force microscopy (AFM) cantilever positioned directly adjacent to the sample (Gebhardt et al., 2013). A similar approach has also been developed that uses micro-prisms on the coverslip rather than an AFM cantilever for reflection (Greiss et al., 2016). These methods utilize high-NA objectives for both illumination and detection, which allows for the formation of very thin light sheets and excellent detection efficiency. However, they suffer from a gap of about 2 μm just above the coverslip that is inaccessible to the light sheet due to the Gaussian beam profile.

Similar approaches based on reflection to redirect the light sheet to overlap with the image plane have also been developed using only a single objective. In single-objective SPIM (soSPIM), the light sheet exits the objective lens vertically and offset from the center of the FOV, and is then reflected using a micro-mirror mounted at 45° in a custom-made sample chamber, similar to an inverted RLSM design (Galland et al., 2015). In single-objective light-sheet microscopy (SO-LSM), the light sheet is instead directed along the image plane using a microfluidic chamber with reflective side walls angled at 45° (Meddens et al., 2016). Both of these methods allow for the formation of very thin light sheets and detection with high efficiency using a high-NA objective on a conventional epi-illumination microscope. In these designs, the illumination and detection optics are coupled, so axial scanning requires synchronous translation of the objective lens or sample stage, translation of the light sheet beam at the mirror, and defocusing of the light sheet beam to keep the beam waist in the center of the FOV. This has been achieved using a beam-steering unit and an electrically tunable lens to translate the light sheet axially and along the optical axis in the image plane. In soSPIM, the sample is placed in raised wells and in SO-LSM the sample is mounted in agarose gel to suspend the sample above the coverslip to allow for imaging throughout the sample. Although these optical and electronic designs are relatively complex compared to some other light sheet designs and the custom-made sample chambers require sophisticated fabrication approaches, they have successfully been implemented for 3D SPT and SR imaging using astigmatism.

Conventional Gaussian light sheets are inherently limited by the diffraction-based trade-off between the thickness of the light sheet at its beam waist and the depth-of-focus over which it remains thin. Bessel and Airy beams are examples of invariant beams that have the useful property of staying focused over a long distance along the propagation direction (Durnin et al., 1987; Fahrbach and Rohrbach, 2010; Vettenburg et al., 2014; Yang et al., 2014), meaning a narrow 1D beam can be scanned to form a thin plane of excitation light. These beams are also self-healing (Bouchal et al., 1998; Fahrbach and Rohrbach, 2010; Fahrbach et al., 2010; Nylk et al., 2016; Zhang et al., 2016), which is valuable when propagating through scattering media such as neuronal tissue (Fahrbach and Rohrbach, 2012; Nylk et al., 2016). One issue with Bessel and Airy beams is that they have prominent side lobes which excite fluorophores outside of the light sheet plane. A solution to this problem was developed with the invention of lattice light sheet (LLS) microscopy (Chen B.-C. et al., 2014), where Bessel beams in a linear array are spaced with a specific periodicity such that the beams interfere constructively in the main lobes and destructively elsewhere to greatly reduce the contributions from the side lobes. This design can be used either in an SR-SIM mode due to its structured illumination, or it can be dithered to create a very thin and uniform light sheet. LLS has been demonstrated for 3D SPT and single-molecule SR microscopy through pairing with astigmatism for e.g., PALM imaging of the entire nuclear lamina (Chen B.-C. et al., 2014), PAINT imaging of ER structures (Nixon-Abell et al., 2016), and multicolor PALM and PAINT imaging of DNA, the nuclear lamina, and intracellular membranes (Legant et al., 2016). LLS provides a powerful tool for SPT and single-molecule SR imaging and it can be used for imaging of entire adherent mammalian cells as well as larger samples. However, steric hindrance between the objectives and between the detection objective and the coverslip prevent the use of commercially available higher-NA detection objectives.

In the original study, the illumination objective was custom-designed and the NA of the detection objective was limited to 1.1. The optical and electronic complexity and cost might also prevent implementation in many laboratories.

More recently, our group developed a method that combines a tilted light sheet with engineered PSFs (TILT3D; Gustavsson et al., 2018a). Here the light sheet is formed by a cylindrical lens, focused by a long working distance illumination objective, and reflected into the sample at an angle by a prism or mirror. This approach requires only simple optics to form the light sheet and the tilt allows for imaging of entire adherent samples all the way down to the coverslip. By pairing this tilted light sheet illumination with long-range PSFs, there is no need to create a very thin light sheet using complicated optics and electronics, since the 3D position of individual molecules will be detected throughout the entire volume excited by the light sheet and determined by the shape of the PSFs on the camera. TILT3D allows for flexible yet simple 3D SPT and single-molecule SR imaging in 3D over a user-defined axial range using conventional coverslips, a conventional epi-fluorescence microscope, and a high-NA detection objective. In the original implementation, a 2.1 μm thick light sheet was used together with an NA 1.4 detection objective and a two-channel detection module where a DH PSF was used for single-molecule imaging with high precision and a tetrapod PSF was used for detection of fiducial beads for drift correction over a large axial range (Gustavsson et al., 2018a). This design has allowed for 3D dSTORM imaging of e.g., mitochondria (Gustavsson et al., 2018a), the entire nuclear lamina (Gustavsson et al., 2018a), and sugars in the glycocalyx in cancer cells (Möckl et al., 2019a). The optical sectioning would be improved further by using thinner light sheets, and the design is compatible with the implementation of Bessel beam light sheets, but at the cost of increased complexity. Nevertheless, even the original design improved the signal-to-background ratio up to five-fold throughout the mammalian cells compared to epi-illumination. By matching the axial range of the used PSF to the thickness and tilt of the light sheet over the used FOV, TILT3D provides a very simple and effective platform for 3D SPT and single-molecule SR imaging with high precision, and it has great potential to be a useful tool for improved imaging in neurons and neuronal tissues in the future.

APPLICATIONS OF LIGHT SHEET SINGLE-MOLECULE IMAGING IN NEURONS AND SYNAPSES

Combining SPT and SR techniques with LSFM allows for improved investigation of the dynamics and organization of single molecules in neurons. Oblique LSFM was combined with sptPALM to improve the localization precision and live-cell compatibility when studying actin within dendritic spines (Frost et al., 2010). It was also used with sptPALM for tracking and classification of the dynamics of CaMKII in different regions of dendritic spines (Lu et al., 2014), and for tracking of cortactin in the investigation of the role of Shank proteins as links between the synapse and the actin cytoskeleton (MacGillavry et al., 2016). Oblique LSFM illumination has also been combined with live-cell PALM for imaging of the subsynaptic distribution of PSD-95 in rat hippocampal neurons (MacGillavry et al., 2013). In addition, oblique LSFM has been implemented for two-color dSTORM and PALM with astigmatism for pairwise 3D SR imaging of the synaptic proteins RIM1/2, PSD-95, GKAP, and Shank to reveal trans-synaptic nanocolumns that aligned neurotransmitter release to receptors (Tang et al., 2016; **Figure 5D**). Bessel light sheets combined with the spontaneously blinking fluorophores HMSiR (Uno et al., 2014) have been used to super-resolve the structure of dopaminergic neurons in the adult *Drosophila* brain (Chu et al., 2019). More recently, a Bessel light sheet together with astigmatism was used to obtain 3D super-resolved reconstructions of microtubule networks in the primary neurons of rat pups for large FOVs (Lu et al., 2019).

Moreover, LSFM has been combined with Super-resolution Optical Fluctuation Imaging (SOFI; Dertinger et al., 2009) and Super-Resolution Radial Fluctuations (SRRF; Gustafsson et al., 2016), which utilize computational analysis of temporal (SOFI and SRRF) and radial (SSRF) intensity fluctuations of fluorophores in acquired image series to generate a super-resolved reconstruction. Although these methods do not technically localize individual molecules and generally do not achieve the same resolution as single-molecule localization techniques, they can be useful because of their simplicity, ability to image densely labeled samples rapidly, and their low-excitation intensity requirements. Recently, LSFM has been successfully combined with SRRF and 3B analysis to image neurons in the *Drosophila* brain (Chen et al., 2020). High-contrast imaging was achieved using a 700 nm thin Bessel light sheet, and reconstructions from these slices were combined to form a 3D rendering. In a very recent study, the combination of LSFM with SOFI (LS-SOFI) achieved rapid SR analysis of neuronal structures and synaptic proteins (Mizrachi et al., 2020).

3D single-molecule LSFM is a comprehensive method that maintains the benefits of conventional fluorescence microscopy while improving precision, resolution, and live-cell compatibility. This allows for high-contrast gentle SPT in living cells and nanoscale visualization of synaptic structures in neurons which offers numerous opportunities for future discoveries in cell biology and biomedical research. Extending single-molecule LSFM for imaging over large areas may also provide insights into how single-molecule interactions affect the brain as a whole.

DISCUSSION

The inherent optical sectioning capability of LSFM that offers reduced fluorescence background, photobleaching, and photodamage is particularly well-suited for single-molecule imaging in thick or sensitive samples. Since the developments of single-molecule SR imaging and LSFM over a decade ago, there have been continuous developments in both these techniques to improve the speed, sensitivity, accuracy, imaging depth, and live-cell compatibility.

One LSFM approach that allows for both excellent sectioning and imaging deeper into the sample is to use light sheets

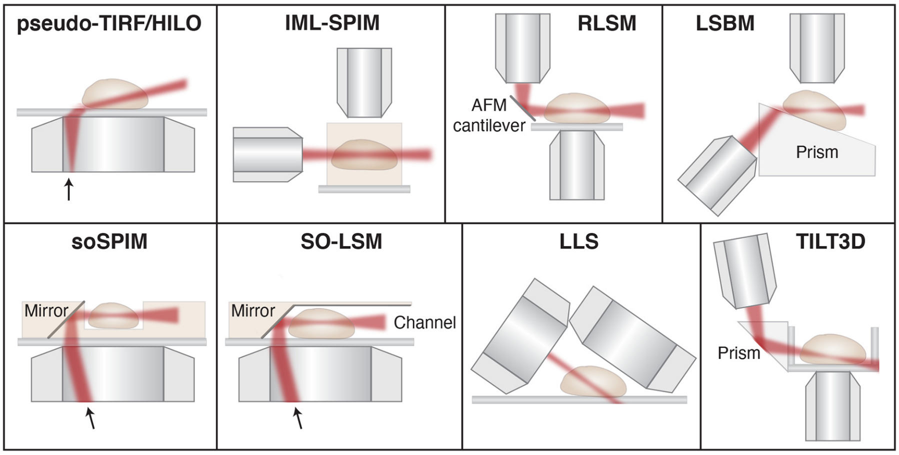

FIGURE 6 | Schematic showing different light sheet approaches developed for improved single-molecule tracking and super-resolution imaging. Pseudo-TIRF/HILO, highly inclined and laminated optical sheet (Tokunaga et al., 2008); IML-SPIM, individual molecule localization with selective-plane illumination microscopy (Cella Zanacchi et al., 2011); RLSM, reflected light sheet microscopy (Gebhardt et al., 2013); LSBM, light-sheet Bayesian microscopy (Hu et al., 2013); soSPIM, single-objective SPIM (Galland et al., 2015); SO-LSM, single-objective light-sheet microscopy (Meddens et al., 2016); LLS, lattice light-sheet (Chen B.-C. et al., 2014); TILT3D, tilted light sheet microscopy with 3D PSFs (Gustavsson et al., 2018a). Illustrations are not to scale. Figure adapted with permission from Gustavsson et al. (2018b) © The Optical Society.

based on propagation invariant beams, such as Bessel and Airy beams. Their non-diffractive (Durnin et al., 1987) and self-healing (Bouchal et al., 1998) properties, as well as their larger depth of field when compared to regular Gaussian light sheets, which diverge quickly after focusing, make them particularly useful for imaging in thick, scattering samples, such as neuronal tissue (for a review, see e.g., Corsetti et al., 2019). The choice of light sheet approach should be made considering both the needed optical sectioning ability and the experimental implementation requirements, where invariant beams allow for thinner light sheets, but at the price of increased complexity and cost compared to Gaussian light sheets.

Neurons and neuronal tissues cause aberrations and scattering of the light that affects both the illumination and detection pathways. These aberrations will reduce the optical sectioning and penetration depth for LSFM and reduce the collection efficiency and the quality of the PSF for single-molecule localization. Adaptive optics (AO) is an approach that can be used to counteract the effects of optics- and sample-induced aberrations to improve the characteristics of both the light sheet in the illumination pathway and the PSF in the detection pathway (Burke et al., 2015; Wang et al., 2015; Wilding et al., 2016; Ji, 2017). AO can be implemented using deformable mirrors or SLMs. AO thus has the possibility to improve the precision, accuracy, and useful imaging depth for single-molecule LSFM imaging.

SPT and SR LSFM in neurons and synapses will also benefit from the ongoing developments of fluorophores with improved photostability, brightness, excitation and emission wavelengths, blinking and activation properties, labeling specificity, cell membrane permeability, and live-cell compatibility. Such developments include far-red fluorophores that can be actively controlled in live-cell compatible conditions (Lukinavičius et al., 2013, 2014; Grimm et al., 2016a,b, 2017; Bucevičius et al., 2020), as well as fluorogenic DNA-PAINT probes (Chung et al., 2020) and improvements to DNA-PAINT docking strands and imaging buffer (Civitci et al., 2020) for faster imaging with improved signal-to-background ratio.

As previously mentioned, MINFLUX is an emerging method that allows for imaging with nanometer precision (Balzarotti et al., 2017; Gwosch et al., 2020). Although the widespread application has so far been limited due to the technical complexity of the method, it has the potential to address a range of questions related to synaptic nanoscale structure and dynamics in the future.

Expansion microscopy (ExM) is a method of physically increasing the size of cells and tissues using an isotropically expandable gel (Chen F. et al., 2015; Wassie et al., 2019). ExM has proven useful for nanoscale imaging of neuronal samples, including imaging of the synaptic proteins Homer and Bassoon (Chozinski et al., 2016), actin filament organizations in dendrites and postsynaptic spines (Park et al., 2020), the morphology of gonadotropin-releasing hormone neurons (Wang et al., 2020), and the neuronal cytoskeleton (Jurriens et al., 2021). ExM has been paired with LLS to achieve a nanoscale resolution to uncover the organization of proteins and neural circuits in mouse brain samples and in the entire *Drosophila* brain (Bürgers et al., 2019; Gao et al., 2019). ExM has also been combined with single-molecule SR approaches like dSTORM (Xu et al., 2019) and 3D dSTORM using astigmatism (Zwettler et al., 2020), but so far such applications for neuronal or synaptic imaging are limited. In ExM-dSTORM, care must be taken as the fluorophores can be degraded if labeling is done before the sample preparation, and conventional blinking buffers can shrink the gel if it is not stabilized. Another option is to use fluorophores that will spontaneously blink in a gel-compatible buffer, such as silicon rhodamines (Zwettler et al., 2020). ExM has the potential to be combined with both LSFM and 3D single-molecule SR approaches for future studies of neuronal samples and synapses. However, the researcher must be careful to ensure that the chemical linking to the gel does not cause distortions of the structure of interest. ExM is also limited to imaging of fixed samples and cannot be used for live-cell studies.

Recently, important advances have also been made to improve SPT and single-molecule SR imaging in densely labeled samples using deep learning (for a review, see e.g., Möckl et al., 2020a). These developments include using neural nets to optimize and localize engineered PSFs faster and for overlapping emitters (Nehme et al., 2018, 2020; Zhang et al., 2018), phase retrieval of aberrations, and background correction (Paine and Fienup, 2018; Möckl et al., 2019b, 2020b; Saha et al., 2020). The next steps in this field are to standardize controls to ensure the validity of the analysis, as well as to make these approaches more easily accessible and comparable for a wide range of users. The combination of LSFM with 3D single-molecule localization microscopy provides a powerful tool for tracking single-molecule dynamics and imaging of nanoscale structures in neuronal synapses. Continued developments in these fields will further improve not only the achievable precision and resolution but also the live-cell compatibility and the ease of implementation of the methods. In the future, this will hopefully lead to improved understanding and new discoveries about the molecular mechanisms at work all the way from within individual synapses to the entire brain.

AUTHOR CONTRIBUTIONS

GG, TN, NS, SV-H, and A-KG wrote the manuscript. All authors contributed to the article and approved the submitted version.

FUNDING

This work was funded by grants to A-KG from the Welch Foundation (C-2064-20210327), the National Institute of General Medical Sciences (R00GM134187), and startup funds from the Cancer Prevention and Research Institute of Texas (RR200025). A-KG is a Cancer Prevention and Research Institute of Texas (CPRIT) Scholar in Cancer Research.

REFERENCES

Abbe, E. (1873). Contributions to the theory of the microscope and microscopic detection (Translated from German). *Arch. Mikrosk. Anat.* 9, 413–468. doi: 10.1007/BF02956173

Abraham, A. V., Ram, S., Chao, J., Ward, E. S., and Ober, R. J. (2009). Quantitative study of single molecule location estimation techniques. *Opt. Express* 17, 23352–23373. doi: 10.1364/OE.17.023352

Abrahamsson, S., Chen, J., Hajj, B., Stallinga, S., Katsov, A. Y., Wisniewski, J., et al. (2013). Fast multicolor 3D imaging using aberration-corrected multifocus microscopy. *Nat. Methods* 10, 60–63. doi: 10.1038/nmeth.2277

Ahrens, M. B., Orger, M. B., Robson, D. N., Li, J. M., and Keller, P. J. (2013). Whole-brain functional imaging at cellular resolution using light-sheet microscopy. *Nat. Methods* 10, 413–420. doi: 10.1038/nmeth.2434

Alcor, D., Gouzer, G., and Triller, A. (2009). Single-particle tracking methods for the study of membrane receptors dynamics. *Eur. J. Neurosci.* 30, 987–997. doi: 10.1111/j.1460-9568.2009.06927.x

Arizono, M., Bannai, H., Nakamura, K., Niwa, F., Enomoto, M., Matsu-ura, T., et al. (2012). Receptor-selective diffusion barrier enhances sensitivity of astrocytic processes to metabotropic glutamate receptor stimulation. *Sci. Signal.* 5:ra27. doi: 10.1126/scisignal.2002498

Axelrod, D. (2001). Total internal reflection fluorescence microscopy in cell biology. *Traffic* 2, 764–774. doi: 10.1034/j.1600-0854.2001.21104.x

Backer, A. S., Backlund, M. P., von Diezmann, A. R., Sahl, S. J., and Moerner, W. E. (2014). A bisected pupil for studying single-molecule orientational dynamics and its application to three-dimensional super-resolution microscopy. *Appl. Phys. Lett.* 104:193701. doi: 10.1063/1.4876440

Backlund, M. P., Joyner, R., Weis, K., and Moerner, W. E. (2014). Correlations of three-dimensional motion of chromosomal loci in yeast revealed by the double-helix point spread function microscope. *Mol. Biol. Cell* 25, 3619–3629. doi: 10.1091/mbc.E14-06-1127

Backlund, M. P., Lew, M. D., Backer, A. S., Sahl, S. J., Grover, G., Agrawal, A., et al. (2012). Simultaneous, accurate measurement of the 3D position and orientation of single molecules. *Proc. Natl. Acad. Sci. U S A* 109, 19087–19092. doi: 10.1073/pnas.1216687109

Baddeley, D., Cannell, M. B., and Soeller, C. (2011). Three-dimensional sub-100 nm super-resolution imaging of biological samples using a phase ramp in the objective pupil. *Nano Res.* 4, 589–598. doi: 10.1007/s12274-011-0115-z

Bademosi, A. T., Lauwers, E., Padmanabhan, P., Odierna, L., Chai, Y. J., Papadopulos, A., et al. (2016). *in vivo* single-molecule imaging of syntaxin1A reveals polyphosphoinositide- and activity-dependent trapping in presynaptic nanoclusters. *Nat. Commun.* 7:13660. doi: 10.1038/ncomms13660

Balzarotti, F., Eilers, Y., Gwosch, K. C., Gynnå, A. H., Westphal, V., Stefani, F. D., et al. (2017). Nanometer resolution imaging and tracking of fluorescent molecules with minimal photon fluxes. *Science* 355, 606–612. doi: 10.1126/science.aak9913

Bannai, H. (2018). Molecular membrane dynamics: insights into synaptic function and neuropathological disease. *Neurosci. Res.* 129, 47–56. doi: 10.1016/j.neures.2017.07.007

Bates, M., Huang, B., Dempsey, G. T., and Zhuang, X. (2007). Multicolor super-resolution imaging with photo-switchable fluorescent probes. *Science* 317, 1749–1753. doi: 10.1126/science.1146598

Bennett, H. W., Gustavsson, A.-K., Bayas, C. A., Petrov, P. N., Mooney, N., Moerner, W. E., et al. (2020). Novel fibrillar structure in the inversin compartment of primary cilia revealed by 3D single-molecule superresolution microscopy. *Mol. Biol. Cell* 31, 619–639. doi: 10.1091/mbc.E19-09-0499

Betzig, E. (2015). Single molecules, cells and super-resolution optics (Nobel Lecture). *Angew. Chem. Int. Ed. Engl.* 54, 8034–8053. doi: 10.1002/anie.201501003

Betzig, E., Patterson, G. H., Sougrat, R., Lindwasser, O. W., Olenych, S., Bonifacino, J. S., et al. (2006). Imaging intracellular fluorescent proteins at nanometer resolution. *Science* 313, 1642–1645. doi: 10.1126/science.1127344

Blom, H., and Widengren, J. (2017). Stimulated emission depletion microscopy. *Chem. Rev.* 117, 7377–7427. doi: 10.1021/acs.chemrev.6b00653

Bodén, A., Pennacchietti, F., Coceano, G., Damenti, M., Ratz, M., and Testa, I. (2021). Volumetric live cell imaging with three-dimensional parallelized RESOLFT microscopy. *Nat. Biotechnol.* 39, 609–618. doi: 10.1038/s41587-020-00779-2

Böger, C., Hafner, A.-S., Schlichthärle, T., Strauss, M. T., Malkusch, S., Endesfelder, U., et al. (2019). Super-resolution imaging and estimation of protein copy numbers at single synapses with DNA-point accumulation for imaging in nanoscale topography. *Neurophotonics* 6:035008. doi: 10.1117/1.NPh.6.3.035008

Bouchal, Z., Wagner, J., and Chlup, M. (1998). Self-reconstruction of a distorted nondiffracting beam. *Opt. Commun.* 151, 207–211. doi: 10.1016/S0030-4018(98)00085-6

Bouchard, M. B., Voleti, V., Mendes, C. S., Lacefield, C., Grueber, W. B., Mann, R. S., et al. (2015). Swept confocally-aligned planar excitation (SCAPE) microscopy for high-speed volumetric imaging of behaving organisms. *Nat. Photonics* 9, 113–119. doi: 10.1038/nphoton.2014.323

Bouthour, W., Leroy, F., Emmanuelli, C., Carnaud, M., Dahan, M., Poncer, J. C., et al. (2012). A human mutation in Gabrg2 associated with generalized epilepsy alters the membrane dynamics of GABAA receptors. *Cereb. Cortex* 22, 1542–1553. doi: 10.1093/cercor/bhr225

Bucevicius, J., Gilat, T., and Lukinavičius, G. (2020). Far-red switching DNA probes for live cell nanoscopy. *Chem. Commun.* 56, 14797–14800. doi: 10.1039/d0cc06759h

Bürgers, J., Pavlova, I., Rodriguez-Gatica, J. E., Henneberger, C., Oeller, M., Ruland, J. A., et al. (2019). Light-sheet fluorescence expansion microscopy: fast mapping of neural circuits at super resolution. *Neurophotonics* 6:015005. doi: 10.1117/1.NPh.6.1.015005

Burke, D., Patton, B., Huang, F., Bewersdorf, J., and Booth, M. J. (2015). Adaptive optics correction of specimen-induced aberrations in single-molecule switching microscopy. *Optica* 2:177. doi: 10.1364/OPTICA.2.000177

Bürli, T., Baer, K., Ewers, H., Sidler, C., Fuhrer, C., and Fritschy, J.-M. (2010). Single particle tracking of α7 nicotinic AChR in hippocampal neurons reveals regulated confinement at glutamatergic and GABAergic perisynaptic sites. *PLoS One* 5:e11507. doi: 10.1371/journal.pone.0011507

Carvalhais, L. G., Martinho, V. C., Ferreiro, E., and Pinheiro, P. S. (2021). Unraveling the nanoscopic organization and function of central mammalian presynapses with super-resolution microscopy. *Front. Neurosci.* 14:578409. doi: 10.3389/fnins.2020.578409

Cella Zanacchi, F., Lavagnino, Z., Perrone Donnorso, M., Del Bue, A., Furia, L., Faretta, M., et al. (2011). Live-cell 3D super-resolution imaging in thick biological samples. *Nat. Methods* 8, 1047–1049. doi: 10.1038/nmeth.1744

Chalfie, M. (2009). GFP: lighting up life (Nobel Lecture). *Angew. Chem. Int. Ed. Engl.* 48, 5603–5611. doi: 10.1002/anie.200902040

Chen, B.-C., Legant, W. R., Wang, K., Shao, L., Milkie, D. E., Davidson, M. W., et al. (2014). Lattice light-sheet microscopy: imaging molecules to embryos at high spatiotemporal resolution. *Science* 346:1257998. doi: 10.1126/science.1257998

Chen, J., Zhang, Z., Li, L., Chen, B.-C., Revyakin, A., Hajj, B., et al. (2014). Single-molecule dynamics of enhanceosome assembly in embryonic stem cells. *Cell* 156, 1274–1285. doi: 10.1016/j.cell.2014.01.062

Chen, F., Tillberg, P. W., and Boyden, E. S. (2015). Expansion microscopy. *Science* 347, 543–548. doi: 10.1126/science.1260088

Chen, X., Zeng, Z., Wang, H., and Xi, P. (2015). Three-dimensional multimodal sub-diffraction imaging with spinning-disk confocal microscopy using blinking/fluctuating probes. *Nano Res.* 8, 2251–2260. doi: 10.1007/s12274-015-0736-8

Chen, C.-Y., Liu, Y.-T., Lu, C.-H., Lee, P.-Y., Tsai, Y.-C., Wu, J.-S., et al. (2019). The applications of lattice light-sheet microscopy for functional volumetric imaging of hippocampal neurons in a three-dimensional culture system. *Micromachines (Basel)* 10:599. doi: 10.3390/mi10090599

Chen, R., Zhao, Y., Li, M., Wang, Y., Zhang, L., and Fei, P. (2020). Efficient super-resolution volumetric imaging by radial fluctuation Bayesian analysis light-sheet microscopy. *J. Biophotonics* 13:e201960242. doi: 10.1002/jbio.201960242

Chéreau, R., Saraceno, G. E., Angibaud, J., Cattaert, D., and Nägerl, U. V. (2017). Superresolution imaging reveals activity-dependent plasticity of axon morphology linked to changes in action potential conduction velocity. *Proc. Natl. Acad. Sci. U S A* 114, 1401–1406. doi: 10.1073/pnas.1607541114

Chozinski, T. J., Gagnon, L. A., and Vaughan, J. C. (2014). Twinkle, twinkle little star: photoswitchable fluorophores for super-resolution imaging. *FEBS Lett.* 588, 3603–3612. doi: 10.1016/j.febslet.2014.06.043

Chozinski, T. J., Halpern, A. R., Okawa, H., Kim, H.-J., Tremel, G. J., Wong, R. O. L., et al. (2016). Expansion microscopy with conventional antibodies and fluorescent proteins. *Nat. Methods* 13, 485–488. doi: 10.1038/nmeth.3833

Chu, L.-A., Lu, C.-H., Yang, S.-M., Liu, Y.-T., Feng, K.-L., Tsai, Y.-C., et al. (2019). Rapid single-wavelength lightsheet localization microscopy for clarified tissue. *Nat. Commun.* 10:4762. doi: 10.1038/s41467-019-12715-3

Chung, K. K., Zhang, Z., Kidd, P., Zhang, Y., Williams, N. D., Rollins, B., et al. (2020). Fluorogenic probe for fast 3D whole-cell DNA-PAINT. *bioRxiv* [Preprint]. doi: 10.1101/2020.04.29.066886

Civitci, F., Shangguan, J., Zheng, T., Tao, K., Rames, M., Kenison, J., et al. (2020). Fast and multiplexed superresolution imaging with DNA-PAINT-ERS. *Nat. Commun.* 11:4339. doi: 10.1038/s41467-020-18181-6

Corsetti, S., Gunn-Moore, F., and Dholakia, K. (2019). Light sheet fluorescence microscopy for neuroscience. *J. Neurosci. Methods* 319, 16–27. doi: 10.1016/j.jneumeth.2018.07.011

Cox, S., Rosten, E., Monypenny, J., Jovanovic-Talisman, T., Burnette, D. T., Lippincott-Schwartz, J., et al. (2012). Bayesian localization microscopy reveals nanoscale podosome dynamics. *Nat. Methods* 9, 195–200. doi: 10.1038/nmeth.1812

Dani, A., Huang, B., Bergan, J., Dulac, C., and Zhuang, X. (2010). Superresolution imaging of chemical synapses in the brain. *Neuron* 68, 843–856. doi: 10.1016/j.neuron.2010.11.021

D'Este, E., Kamin, D., Göttfert, F., El-Hady, A., and Hell, S. W. (2015). STED nanoscopy reveals the ubiquity of subcortical cytoskeleton periodicity in living neurons. *Cell Rep.* 10, 1246–1251. doi: 10.1016/j.celrep.2015.02.007

De Robertis, E., Arnaiz, G. R. D. L., Salganicoff, L., Iraldi, A. P. D., and Zieher, L. M. (1963). Isolation of synaptic vesicles and structural organization of the acetycholine system within brain nerve endings. *J. Neurochem.* 10, 225–235. doi: 10.1111/j.1471-4159.1963.tb05038.x

De Robertis, E. D., and Bennett, H. S. (1954). A submicroscopic vesicular component of Schwann cells and nerve satellite cells. *Exp. Cell Res.* 6, 543–545. doi: 10.1016/0014-4827(54)90209-8

De Robertis, E. D., and Bennett, H. S. (1955). Some features of the submicroscopic morphology of synapses in frog and earthworm. *J. Biophys. Biochem. Cytol.* 1, 47–58. doi: 10.1083/jcb.1.1.47

Del Castillo, J., and Katz, B. (1954). Quantal components of the end-plate potential. *J. Physiol.* 124, 560–573. doi: 10.1113/jphysiol.1954.sp005129

Dempsey, G. T., Vaughan, J. C., Chen, K. H., Bates, M., and Zhuang, X. (2011). Evaluation of fluorophores for optimal performance in localization-based super-resolution imaging. *Nat. Methods* 8, 1027–1036. doi: 10.1038/nmeth.1768

Dertinger, T., Colyer, R., Iyer, G., Weiss, S., and Enderlein, J. (2009). Fast, background-free, 3D super-resolution optical fluctuation imaging (SOFI). *Proc. Natl. Acad. Sci. U S A* 106, 22287–22292. doi: 10.1038/nmeth.1768

Deschout, H., Zanacchi, F. C., Mlodzianoski, M., Diaspro, A., Bewersdorf, J., Hess, S. T., et al. (2014). Precisely and accurately localizing single emitters in fluorescence microscopy. *Nat. Methods* 11, 253–266. doi: 10.1038/nmeth.2843

Dodt, H.-U., Leischner, U., Schierloh, A., Jährling, N., Mauch, C. P., Deininger, K., et al. (2007). Ultramicroscopy: three-dimensional visualization of neuronal networks in the whole mouse brain. *Nat. Methods* 4, 331–336. doi: 10.1038/nmeth1036

Dunsby, C. (2008). Optically sectioned imaging by oblique plane microscopy. *Opt. Express* 16, 20306–20316. doi: 10.1364/oe.16.020306

Durnin, J., Miceli, J. J., and Eberly, J. H. (1987). Diffraction-free beams. *Phys. Rev. Lett.* 58, 1499–1501. doi: 10.1103/PhysRevLett.58.1499

Eggeling, C., Willig, K. I., and Barrantes, F. J. (2013). STED microscopy of living cells - new frontiers in membrane and neurobiology. *J. Neurochem.* 126, 203–212. doi: 10.1111/jnc.12243

Ehrensperger, M.-V., Hanus, C., Vannier, C., Triller, A., and Dahan, M. (2007). Multiple association states between glycine receptors and gephyrin identified by SPT analysis. *Biophys. J.* 92, 3706–3718. doi: 10.1529/biophysj.106.095596

Eklund, A. S., Ganji, M., Gavins, G., Seitz, O., and Jungmann, R. (2020). Peptide-PAINT super-resolution imaging using transient coiled coil interactions. *Nano Lett.* 20, 6732–6737. doi: 10.1021/acs.nanolett.0c02620

Fahrbach, F. O., and Rohrbach, A. (2010). A line scanned light-sheet microscope with phase shaped self-reconstructing beams. *Opt. Express* 18, 24229–24244. doi: 10.1364/OE.18.024229

Fahrbach, F. O., and Rohrbach, A. (2012). Propagation stability of self-reconstructing Bessel beams enables contrast-enhanced imaging in thick media. *Nat. Commun.* 3:632. doi: 10.1038/ncomms1646

Fahrbach, F. O., Simon, P., and Rohrbach, A. (2010). Microscopy with self-reconstructing beams. *Nat. Photonics* 4, 780–785. doi: 10.1038/nphoton.2010.204

Fiolka, R., Shao, L., Rego, E. H., Davidson, M. W., and Gustafsson, M. G. L. (2012). Time-lapse two-color 3D imaging of live cells with doubled resolution using structured illumination. *Proc. Natl. Acad. Sci. U S A* 109, 5311–5315. doi: 10.1073/pnas.1119262109

Frost, N. A., Shroff, H., Kong, H., Betzig, E., and Blanpied, T. A. (2010). Single-molecule discrimination of discrete perisynaptic and distributed sites of actin filament assembly within dendritic spines. *Neuron* 67, 86–99. doi: 10.1016/j.neuron.2010.05.026

Fuchs, E., Jaffe, J. S., Long, R. A., and Azam, F. (2002). Thin laser light sheet microscope for microbial oceanography. *Opt. Express* 10, 145–154. doi: 10.1364/oe.10.000145

Galland, R., Grenci, G., Aravind, A., Viasnoff, V., Studer, V., and Sibarita, J.-B. (2015). 3D high- and super-resolution imaging using single-objective SPIM. *Nat. Methods* 12, 641–644. doi: 10.1038/nmeth.3402

Gao, R., Asano, S. M., Upadhyayula, S., Pisarev, I., Milkie, D. E., Liu, T.-L., et al. (2019). Cortical column and whole-brain imaging with molecular contrast and nanoscale resolution. *Science* 363:eaau8302. doi: 10.1126/science.aau8302

Gebhardt, J. C. M., Suter, D. M., Roy, R., Zhao, Z. W., Chapman, A. R., Basu, S., et al. (2013). Single-molecule imaging of transcription factor binding to DNA in live mammalian cells. *Nat. Methods* 10, 421–426. doi: 10.1038/nmeth.2411

Giannone, G., Hosy, E., Levet, F., Constals, A., Schulze, K., Sobolevsky, A. I., et al. (2010). Dynamic superresolution imaging of endogenous proteins on living cells at ultra-high density. *Biophys. J.* 99, 1303–1310. doi: 10.1016/j.bpj.2010.06.005

Goncalves, J., Bartol, T. M., Camus, C., Levet, F., Menegolla, A. P., Sejnowski, T. J., et al. (2020). Nanoscale co-organization and coactivation of AMPAR, NMDAR and mGluR at excitatory synapses. *Proc. Natl. Acad. Sci. U S A* 117, 14503–14511. doi: 10.1073/pnas.1922563117

Greer, C. J., and Holy, T. E. (2019). Fast objective coupled planar illumination microscopy. *Nat. Commun.* 10:4483. doi: 10.1038/s41467-019-12340-0

Greiss, F., Deligiannaki, M., Jung, C., Gaul, U., and Braun, D. (2016). Single-molecule imaging in living drosophila embryos with reflected light-sheet microscopy. *Biophys. J.* 110, 939–946. doi: 10.1016/j.bpj.2015.12.035

Grimm, J. B., English, B. P., Chen, J., Slaughter, J. P., Zhang, Z., Revyakin, A., et al. (2015). A general method to improve fluorophores for live-cell and single-molecule microscopy. *Nat. Methods* 12, 244–250. doi: 10.1038/nmeth.3256

Grimm, J. B., English, B. P., Choi, H., Muthusamy, A. K., Mehl, B. P., Dong, P., et al. (2016a). Bright photoactivatable fluorophores for single-molecule imaging. *Nat. Methods* 13, 985–988. doi: 10.1038/nmeth.4034

Grimm, J. B., Klein, T., Kopek, B. G., Shtengel, G., Hess, H. F., Sauer, M., et al. (2016b). Synthesis of a far-red photoactivatable silicon-containing rhodamine for super-resolution microscopy. *Angew. Chem. Int. Ed. Engl.* 55, 1723–1727. doi: 10.1002/anie.201509649

Grimm, J. B., Muthusamy, A. K., Liang, Y., Brown, T. A., Lemon, W. C., Patel, R., et al. (2017). A general method to fine-tune fluorophores for live-cell and *in vivo* imaging. *Nat. Methods* 14, 987–994. doi: 10.1038/nmeth.4403

Groc, L., Lafourcade, M., Heine, M., Renner, M., Racine, V., Sibarita, J.-B., et al. (2007). Surface trafficking of neurotransmitter receptor: comparison between single-molecule/quantum dot strategies. *J. Neurosci.* 27, 12433–12437. doi: 10.1523/JNEUROSCI.3349-07.2007

Gualda, E. J., Simão, D., Pinto, C., Alves, P. M., and Brito, C. (2014). Imaging of human differentiated 3D neural aggregates using light sheet fluorescence microscopy. *Front. Cell. Neurosci.* 8:221. doi: 10.3389/fncel.2014.00221

Guillery, R. W. (2005). Observations of synaptic structures: origins of the neuron doctrine and its current status. *Phil. Trans. R. Soc. B Biol. Sci.* 360, 1281–1307. doi: 10.1098/rstb.2003.1459

Guo, Y., Li, D., Zhang, S., Yang, Y., Liu, J.-J., Wang, X., et al. (2018). Visualizing intracellular organelle and cytoskeletal interactions at nanoscale resolution on millisecond timescales. *Cell* 175, 1430–1442.e17. doi: 10.1016/j.cell.2018.09.057

Gustafsson, M. G. L. (2000). Surpassing the lateral resolution limit by a factor of two using structured illumination microscopy. *J. Microsc.* 198, 82–87. doi: 10.1046/j.1365-2818.2000.00710.x

Gustafsson, M. G. L. (2005). Nonlinear structured-illumination microscopy: Wide-field fluorescence imaging with theoretically unlimited resolution. *Proc. Natl. Acad. Sci. U S A* 102, 13081–13086. doi: 10.1073/pnas.0406877102

Gustafsson, N., Culley, S., Ashdown, G., Owen, D. M., Pereira, P. M., and Henriques, R. (2016). Fast live-cell conventional fluorophore nanoscopy with ImageJ through super-resolution radial fluctuations. *Nat. Commun.* 7:12471. doi: 10.1038/ncomms12471

Gustavsson, A.-K., Petrov, P. N., Lee, M. Y., Shechtman, Y., and Moerner, W. E. (2018a). 3D single-molecule super-resolution microscopy with a tilted light sheet. *Nat. Commun.* 9:123. doi: 10.1038/s41467-017-02563-4

Gustavsson, A.-K., Petrov, P. N., and Moerner, W. E. (2018b). Light sheet approaches for improved precision in 3D localization-based super-resolution imaging in mammalian cells [Invited]. *Opt. Express* 26, 13122–13147. doi: 10.1364/OE.26.013122

Gustafsson, M. G. L., Shao, L., Carlton, P. M., Wang, C. J. R., Golubovskaya, I. N., Cande, W. Z., et al. (2008). Three-dimensional resolution doubling in wide-field fluorescence microscopy by structured illumination. *Biophys. J.* 94, 4957–4970. doi: 10.1529/biophysj.107.120345

Gwosch, K. C., Pape, J. K., Balzarotti, F., Hoess, P., Ellenberg, J., Ries, J., et al. (2020). MINFLUX nanoscopy delivers 3D multicolor nanometer resolution in cells. *Nat. Methods* 17, 217–224. doi: 10.1038/s41592-019-0688-0

Haas, K. T., Compans, B., Letellier, M., Bartol, T. M., Grillo-Bosch, D., Sejnowski, T. J., et al. (2018). Pre-post synaptic alignment through neuroligin-1 tunes synaptic transmission efficiency. *eLife* 7:e31755. doi: 10.7554/eLife.31755

Han, B., Zhou, R., Xia, C., and Zhuang, X. (2017). Structural organization of the actin-spectrin-based membrane skeleton in dendrites and soma of neurons. *Proc. Natl. Acad. Sci. U S A* 114, E6678–E6685. doi: 10.1073/pnas.1705043114

Harris, K. M., and Weinberg, R. J. (2012). Ultrastructure of synapses in the mammalian brain. *Cold Spring Harb. Perspect. Biol.* 4:a005587. doi: 10.1101/cshperspect.a005587

Haslehurst, P., Yang, Z., Dholakia, K., and Emptage, N. (2018). Fast volume-scanning light sheet microscopy reveals transient neuronal events. *Biomed. Opt. Express* 9, 2154–2167. doi: 10.1364/BOE.9.002154

Heck, J., Parutto, P., Ciuraszkiewicz, A., Bikbaev, A., Freund, R., Mitlöhner, J., et al. (2019). Transient confinement of CaV2.1 Ca2+-channel splice variants shapes synaptic short-term plasticity. *Neuron* 103, 66–79.e12. doi: 10.1016/j.neuron.2019.04.030

Heilemann, M., vane Linde, S., Schüttpelz, M., Kasper, R., Seefeldt, B., Mukherjee, A., et al. (2008). Subdiffraction-resolution fluorescence imaging with conventional fluorescent probes. *Angew. Chem. Int. Ed. Engl.* 47, 6172–6176. doi: 10.1002/anie.200802376

Heintzmann, R., and Huser, T. (2017). Super-resolution structured illumination microscopy. *Chem. Rev.* 117, 13890–13908. doi: 10.1021/acs.chemrev.7b00218

Hell, S. W. (2015). Nanoscopy with focused light (Nobel Lecture). *Angew. Chem. Int. Ed. Engl.* 54, 8054–8066. doi: 10.1002/anie.201504181

Hell, S. W., and Wichmann, J. (1994). Breaking the diffraction resolution limit by stimulated emission: stimulated-emission-depletion fluorescence microscopy. *Opt. Lett.* 19, 780–782. doi: 10.1364/ol.19.000780

Hess, S. T., Girirajan, T. P. K., and Mason, M. D. (2006). Ultra-high resolution imaging by fluorescence photoactivation localization microscopy. *Biophys. J.* 91, 4258–4272. doi: 10.1529/biophysj.106.091116

Hirabayashi, Y., Kwon, S.-K., Paek, H., Pernice, W. M., Paul, M. A., Lee, J., et al. (2017). ER-mitochondria tethering by PDZD8 regulates Ca $^{2+}$ dynamics in mammalian neurons. *Science* 358, 623–630. doi: 10.1126/science.aan6009

Hirano, Y., Matsuda, A., and Hiraoka, Y. (2015). Recent advancements in structured-illumination microscopy toward live-cell imaging. *Microscopy (Oxf)* 64, 237–249. doi: 10.1093/jmicro/dfv034

Holekamp, T. F., Turaga, D., and Holy, T. E. (2008). Fast three-dimensional fluorescence imaging of activity in neural populations by objective-coupled planar illumination microscopy. *Neuron* 57, 661–672. doi: 10.1016/j.neuron.2008.01.011

Hosny, N. A., Song, M., Connelly, J. T., Ameer-Beg, S., Knight, M. M., and Wheeler, A. P. (2013). Super-resolution imaging strategies for cell biologists using a spinning disk microscope. *PLoS One* 8:e74604. doi: 10.1371/journal.pone.0074604

Hou, S., Exell, J., and Welsher, K. (2020). Real-time 3D single molecule tracking. *Nat. Commun.* 11:3607. doi: 10.1038/s41467-020-17444-6

Hou, S., Johnson, C., and Welsher, K. (2019). Real-time 3D single particle tracking: towards active feedback single molecule spectroscopy in live cells. *Molecules* 24:2826. doi: 10.3390/molecules24152826

Hoze, N., Nair, D., Hosy, E., Sieben, C., Manley, S., Herrmann, A., et al. (2012). Heterogeneity of AMPA receptor trafficking and molecular interactions revealed by superresolution analysis of live cell imaging. *Proc. Natl. Acad. Sci. U S A* 109, 17052–17057. doi: 10.1073/pnas.1204589109

Hrabetova, S., Cognet, L., Rusakov, D. A., and Nägerl, U. V. (2018). Unveiling the extracellular space of the brain: from super-resolved microstructure to *in vivo* function. *J. Neurosci.* 38, 9355–9363. doi: 10.1523/JNEUROSCI.1664-18.2018

Hu, Y. S., Cang, H., and Lillemeier, B. F. (2016). Hu. *Proc. Natl. Acad. Sci. U S A* 113, 7201–7206. doi: 10.1073/pnas.1512331113

Hu, Y. S., Zhu, Q., Elkins, K., Tse, K., Li, Y., Fitzpatrick, J. A. J., et al. (2013). Light-sheet Bayesian microscopy enables deep-cell super-resolution imaging of heterochromatin in live human embryonic stem cells. *Opt. Nanoscopy* 2:7. doi: 10.1186/2192-2853-2-7

Huang, B., Jones, S. A., Brandenburg, B., and Zhuang, X. (2008a). Whole-cell 3D STORM reveals interactions between cellular structures with nanometer-scale resolution. *Nat. Methods* 5, 1047–1052. doi: 10.1038/nmeth.1274

Huang, B., Wang, W., Bates, M., and Zhuang, X. (2008b). Three-dimensional super-resolution imaging by stochastic optical reconstruction microscopy. *Science* 319, 810–813. doi: 10.1126/science.1153529

Huisken, J., and Stainier, D. Y. R. (2009). Selective plane illumination microscopy techniques in developmental biology. *Development* 136, 1963–1975. doi: 10.1242/dev.022426

Huisken, J., Swoger, J., Del Bene, F., Wittbrodt, J., and Stelzer, E. H. K. (2004). Optical sectioning deep inside live embryos by selective plane illumination microscopy. *Science* 305, 1007–1009. doi: 10.1126/science.1100035

Inavalli, V. V. G. K., Lenz, M. O., Butler, C., Angibaud, J., Compans, B., Levet, F., et al. (2019). A super-resolution platform for correlative live single-molecule imaging and STED microscopy. *Nat. Methods* 16, 1263–1268. doi: 10.1038/s41592-019-0611-8

Izeddin, I., Récamier, V., Bosanac, L., Cissé, I. I., Boudarene, L., Dugast-Darzacq, C., et al. (2014). Single-molecule tracking in live cells reveals distinct target-search strategies of transcription factors in the nucleus. *eLife* 3:e02230. doi: 10.7554/eLife.02230

Izeddin, I., Specht, C. G., Lelek, M., Darzacq, X., Triller, A., Zimmer, C., et al. (2011). Super-resolution dynamic imaging of dendritic spines using a low-affinity photoconvertible actin probe. *PLoS One* 6:e15611. doi: 10.1371/journal.pone.0015611

Ji, N. (2017). Adaptive optical fluorescence microscopy. *Nat. Methods* 14, 374–380. doi: 10.1038/nmeth.4218

Jia, S., Vaughan, J. C., and Zhuang, X. (2014). Isotropic three-dimensional super-resolution imaging with a self-bending point spread function. *Nat. Photonics* 8, 302–306. doi: 10.1038/nphoton.2014.13

Juette, M. F., Gould, T. J., Lessard, M. D., Mlodzianoski, M. J., Nagpure, B. S., Bennett, B. T., et al. (2008). Three-dimensional sub-100 nm resolution fluorescence microscopy of thick samples. *Nat. Methods* 5, 527–529. doi: 10.1038/nmeth.1211

Jungmann, R., Avendaño, M. S., Dai, M., Woehrstein, J. B., Agasti, S. S., Feiger, Z., et al. (2016). Quantitative super-resolution imaging with qPAINT. *Nat. Methods* 13, 439–442. doi: 10.1038/nmeth.3804

Jungmann, R., Avendaño, M. S., Woehrstein, J. B., Dai, M., Shih, W. M., and Yin, P. (2014). Multiplexed 3D cellular super-resolution imaging with DNA-PAINT and Exchange-PAINT. *Nat. Methods* 11, 313–318. doi: 10.1038/nmeth.2835

Jungmann, R., Steinhauer, C., Scheible, M., Kuzyk, A., Tinnefeld, P., and Simmel, F. C. (2010). Single-molecule kinetics and super-resolution microscopy by fluorescence imaging of transient binding on DNA origami. *Nano Lett.* 10, 4756–4761. doi: 10.1021/nl103427w

Jurriens, D., van Batenburg, V., Katrukha, E. A., and Kapitein, L. C. (2021). "Chapter 6 - Mapping the neuronal cytoskeleton using expansion microscopy," in *Methods in Cell Biology*, eds P. Guichard and V. Hamel (Cambridge, MA: Academic Press), 105–124.

Kao, H. P., and Verkman, A. S. (1994). Tracking of single fluorescent particles in three dimensions: use of cylindrical optics to encode particle position. *Biophys. J.* 67, 1291–1300. doi: 10.1016/S0006-3495(94)80601-0

Katayama, Y., Burkacky, O., Meyer, M., Bräuchle, C., Gratton, E., and Lamb, D. C. (2009). Real-time nanomicroscopy *via* three-dimensional single-particle tracking. *ChemPhysChem.* 10, 2458–2464. doi: 10.1002/cphc.200900436

Kim, K., Lakhanpal, G., Lu, H. E., Khan, M., Suzuki, A., Kato Hayashi, M., et al. (2015). A temporary gating of actin remodeling during synaptic plasticity consists of the interplay between the kinase and structural functions of CaMKII. *Neuron* 87, 813–826. doi: 10.1016/j.neuron.2015.07.023

Kim, S. A., Sanabria, H., Digman, M. A., Gratton, E., Schwille, P., Zipfel, W. R., et al. (2010). Quantifying Translational mobility in neurons: comparison between current optical techniques. *J. Neurosci.* 30, 16409–16416. doi: 10.1523/JNEUROSCI.3063-10.2010

Klar, T. A., Jakobs, S., Dyba, M., Egner, A., and Hell, S. W. (2000). Fluorescence microscopy with diffraction resolution barrier broken by stimulated emission. *Proc. Natl. Acad. Sci. U S A* 97, 8206–8210. doi: 10.1073/pnas.97.15.8206

Klevanski, M., Herrmannsdoerfer, F., Sass, S., Venkataramani, V., Heilemann, M., and Kuner, T. (2020). Automated highly multiplexed super-resolution imaging of protein nano-architecture in cells and tissues. *Nat. Commun.* 11:1552. doi: 10.1038/s41467-020-15362-1

Knight, S. C., Xie, L., Deng, W., Guglielmi, B., Witkowsky, L. B., Bosanac, L., et al. (2015). Dynamics of CRISPR-Cas9 genome interrogation in living cells. *Science* 350, 823–826. doi: 10.1126/science.aac6572

Konopka, C. A., and Bednarek, S. Y. (2008). Variable-angle epifluorescence microscopy: a new way to look at protein dynamics in the plant cell cortex. *Plant J.* 53, 186–196. doi: 10.1111/j.1365-313X.2007.03306.x

Kremers, G.-J., Gilbert, S. G., Cranfill, P. J., Davidson, M. W., and Piston, D. W. (2011). Fluorescent proteins at a glance. *J. Cell Sci.* 124, 157–160. doi: 10.1242/jcs.072744

Lagache, T., Grassart, A., Dallongeville, S., Faklaris, O., Sauvonnet, N., Dufour, A., et al. (2018). Mapping molecular assemblies with fluorescence microscopy and object-based spatial statistics. *Nat. Commun.* 9:698. doi: 10.1038/s41467-018-03053-x

Legant, W. R., Shao, L., Grimm, J. B., Brown, T. A., Milkie, D. E., Avants, B. B., et al. (2016). High-density three-dimensional localization microscopy across large volumes. *Nat. Methods* 13, 359–365. doi: 10.1038/nmeth.3797

Lelek, M., Gyparaki, M. T., Beliu, G., Schueder, F., Griffié, J., Manley, S., et al. (2021). Single-molecule localization microscopy. *Nat. Rev. Methods Primers* 1:39. doi: 10.1038/s43586-021-00038-x

Levi, V., Ruan, Q., and Gratton, E. (2005). 3-D particle tracking in a two-photon microscope: application to the study of molecular dynamics in cells. *Biophys. J.* 88, 2919–2928. doi: 10.1529/biophysj.104.044230

Lew, M. D., Lee, S. F., Badieirostami, M., and Moerner, W. E. (2011). Corkscrew point spread function for far-field three-dimensional nanoscale localization of pointlike objects. *Opt. Lett.* 36, 202–204. doi: 10.1364/OL.36.000202

Li, T. P., and Blanpied, T. A. (2016). Control of transmembrane protein diffusion within the postsynaptic density assessed by simultaneous single-molecule tracking and localization microscopy. *Front. Synaptic Neurosci.* 8:19. doi: 10.3389/fnsyn.2016.00019

Li, Y., Hu, Y., and Cang, H. (2013). Light sheet microscopy for tracking single molecules on the apical surface of living cells. *J. Phys. Chem. B* 117, 15503–15511. doi: 10.1021/jp405380g

Li, T. P., Song, Y., MacGillavry, H. D., Blanpied, T. A., and Raghavachari, S. (2016). Protein crowding within the postsynaptic density can impede the escape of membrane proteins. *J. Neurosci.* 36, 4276–4295. doi: 10.1523/JNEUROSCI.3154-15.2016

Lu, H. E., MacGillavry, H. D., Frost, N. A., and Blanpied, T. A. (2014). Multiple spatial and kinetic subpopulations of CaMKII in spines and dendrites as resolved by single-molecule tracking PALM. *J. Neurosci.* 34, 7600–7610. doi: 10.1523/JNEUROSCI.4364-13.2014

Lu, C.-H., Tang, W.-C., Liu, Y.-T., Chang, S.-W., Wu, F. C. M., Chen, C.-Y., et al. (2019). Lightsheet localization microscopy enables fast, large-scale and three-dimensional super-resolution imaging. *Commun. Biol.* 2:177. doi: 10.1038/s42003-019-0403-9

Lukinavičius, G., Reymond, L., D'Este, E., Masharina, A., Göttfert, F., Ta, H., et al. (2014). Fluorogenic probes for live-cell imaging of the cytoskeleton. *Nat. Methods* 11, 731–733. doi: 10.1038/nmeth.2972

Lukinavičius, G., Umezawa, K., Olivier, N., Honigmann, A., Yang, G., Plass, T., et al. (2013). A near-infrared fluorophore for live-cell super-resolution microscopy of cellular proteins. *Nat. Chem.* 5, 132–139. doi: 10.1038/nchem.1546

MacGillavry, H. D., Kerr, J. M., Kassner, J., Frost, N. A., and Blanpied, T. A. (2016). Shank-cortactin interactions control actin dynamics to maintain flexibility of neuronal spines and synapses. *Eur. J. Neurosci.* 43, 179–193. doi: 10.1111/ejn.13129

MacGillavry, H. D., Song, Y., Raghavachari, S., and Blanpied, T. A. (2013). Nanoscale scaffolding domains within the postsynaptic density concentrate synaptic AMPA receptors. *Neuron* 78, 615–622. doi: 10.1016/j.neuron.2013.03.009

Maglione, M., and Sigrist, S. J. (2013). Seeing the forest tree by tree: super-resolution light microscopy meets the neurosciences. *Nat. Neurosci.* 16, 790–797. doi: 10.1038/nn.3403

Maioli, V., Chennell, G., Sparks, H., Lana, T., Kumar, S., Carling, D., et al. (2016). Time-lapse 3-D measurements of a glucose biosensor in multicellular spheroids by light sheet fluorescence microscopy in commercial 96-well plates. *Sci. Rep.* 6:37777. doi: 10.1038/srep37777

Manley, S., Gillette, J. M., and Lippincott-Schwartz, J. (2010). Single-particle tracking photoactivated localization microscopy for mapping single-molecule dynamics. *Methods Enzymol.* 475, 109–120. doi: 10.1016/S0076-6879(10)75005-9

Manley, S., Gillette, J. M., Patterson, G. H., Shroff, H., Hess, H. F., Betzig, E., et al. (2008). High-density mapping of single-molecule trajectories with photoactivated localization microscopy. *Nat. Methods* 5, 155–157. doi: 10.1038/nmeth.1176

Masullo, Luciano A., Bodén, A., Pennacchietti, F., Coceano, G., Ratz, M., and Testa, I. (2018). Enhanced photon collection enables four dimensional fluorescence nanoscopy of living systems. *Nat. Commun.* 9:3281. doi: 10.1038/s41467-018-05799-w

Meddens, M. B. M., Liu, S., Finnegan, P. S., Edwards, T. L., James, C. D., and Lidke, K. A. (2016). Single objective light-sheet microscopy for high-speed whole-cell 3D super-resolution. *Biomed. Opt. Express* 7, 2219–2236. doi: 10.1364/BOE.7.002219

Mertz, J., and Kim, J. (2010). Scanning light-sheet microscopy in the whole mouse brain with HiLo background rejection. *J. Biomed. Opt.* 15:016027. doi: 10.1117/1.3324890

Metzbower, S. R., Joo, Y., Benavides, D. R., and Blanpied, T. A. (2019). Properties of individual hippocampal synapses influencing NMDA-receptor activation by spontaneous neurotransmission. *eNeuro* 6:ENEURO.0419-18.2019. doi: 10.1523/ENEURO.0419-18.2019

Mizrachi, J., Narasimhan, A., Qi, X., Drewes, R., Palaniswamy, R., Wu, Z., et al. (2020). Super-resolution light-sheet fluorescence microscopy by SOFI. *bioRxiv* [Preprint]. doi: 10.1101/2020.08.17.254797

Möckl, L., and Moerner, W. E. (2020). Super-resolution microscopy with single molecules in biology and beyond-essentials, current trends and future challenges. *J. Am. Chem. Soc.* 142, 17828–17844. doi: 10.1021/jacs.0c08178

Möckl, L., Pedram, K., Roy, A. R., Krishnan, V., Gustavsson, A.-K., Dorigo, O., et al. (2019a). Quantitative super-resolution microscopy of the mammalian glycocalyx. *Dev. Cell* 50, 57–72. doi: 10.1016/j.devcel.2019.04.035

Möckl, L., Petrov, P. N., and Moerner, W. E. (2019b). Accurate phase retrieval of complex 3D point spread functions with deep residual neural networks. *Appl. Phys. Lett.* 115:251106. doi: 10.1063/1.5125252

Möckl, L., Roy, A. R., and Moerner, W. E. (2020a). Deep learning in single-molecule microscopy: fundamentals, caveats and recent developments [Invited]. *Biomed. Opt. Express* 11, 1633–1661. doi: 10.1364/BOE.386361

Möckl, L., Roy, A. R., Petrov, P. N., and Moerner, W. E. (2020b). Accurate and rapid background estimation in single-molecule localization microscopy using the deep neural network BGnet. *Proc. Natl. Acad. Sci. U S A* 117, 60–67. doi: 10.1073/pnas.1916219117

Moerner, W. E. W. E. (2015). Single-molecule spectroscopy, imaging and photocontrol: foundations for super-resolution microscopy (Nobel Lecture). *Angew. Chem. Int. Ed. Engl.* 54, 8067–8093. doi: 10.1002/anie.201501949

Mortensen, K. I., Churchman, L. S., Spudich, J. A., and Flyvbjerg, H. (2010). Optimized localization analysis for single-molecule tracking and super-resolution microscopy. *Nat. Methods* 7, 377–381. doi: 10.1038/nmeth.1447

Nägerl, U. V., Willig, K. I., Hein, B., Hell, S. W., and Bonhoeffer, T. (2008). Live-cell imaging of dendritic spines by STED microscopy. *Proc. Natl. Acad. Sci. U S A* 105, 18982–18987. doi: 10.1073/pnas.0810028105

Nair, D., Hosy, E., Petersen, J. D., Constals, A., Giannone, G., Choquet, D., et al. (2013). Super-resolution imaging reveals that AMPA receptors inside synapses are dynamically organized in nanodomains regulated by PSD95. *J. Neurosci.* 33, 13204–13224. doi: 10.1523/JNEUROSCI.2381-12.2013

Nehme, E., Freedman, D., Gordon, R., Ferdman, B., Weiss, L. E., Alalouf, O., et al. (2020). DeepSTORM3D: dense 3D localization microscopy and PSF design by deep learning. *Nat. Methods* 17, 734–740. doi: 10.1038/s41592-020-0853-5

Nehme, E., Weiss, L. E., Michaeli, T., and Shechtman, Y. (2018). Deep-STORM: super-resolution single-molecule microscopy by deep learning. *Optica* 5:458. doi: 10.1364/OPTICA.5.000458

Nixon-Abell, J., Obara, C. J., Weigel, A. V., Li, D., Legant, W. R., Xu, C. S., et al. (2016). Increased spatiotemporal resolution reveals highly dynamic dense tubular matrices in the peripheral ER. *Science* 354:aaf3928. doi: 10.1126/science.aaf3928

Nosov, G., Kahms, M., and Klingauf, J. (2020). The decade of super-resolution microscopy of the presynapse. *Front. Synaptic Neurosci.* 12:32. doi: 10.3389/fnsyn.2020.00032

Nozumi, M., Nakatsu, F., Katoh, K., and Igarashi, M. (2017). Coordinated movement of vesicles and actin bundles during nerve growth revealed by superresolution microscopy. *Cell Rep.* 18, 2203–2216. doi: 10.1016/j.celrep.2017.02.008

Nylk, J., McCluskey, K., Aggarwal, S., Tello, J. A., and Dholakia, K. (2016). Enhancement of image quality and imaging depth with Airy light-sheet microscopy in cleared and non-cleared neural tissue. *Biomed. Opt. Express* 7, 4021–4033. doi: 10.1364/BOE.7.004021

Oi, C., Gidden, Z., Holyoake, L., Kantelberg, O., Mochrie, S., Horrocks, M. H., et al. (2020). LIVE-PAINT allows super-resolution microscopy inside living cells using reversible peptide-protein interactions. *Commun. Biol.* 3:458. doi: 10.1038/s42003-020-01188-6

Paine, S. W., and Fienup, J. R. (2018). Machine learning for improved image-based wavefront sensing. *Opt. Lett.* 43, 1235–1238. doi: 10.1364/OL.43.001235

Palade, G. E. (1954). Electron microscope observations of interneuronal and neuromuscular synapses. *Anat. Rec.* 118, 335–336.

Palay, S. L., and Palade, G. E. (1955). The fine structure of neurons. *J. Biophys. Biochem. Cytol.* 1, 69–88. doi: 10.1083/jcb.1.1.69

Panier, T., Romano, S., Olive, R., Pietri, T., Sumbre, G., Candelier, R., et al. (2013). Fast functional imaging of multiple brain regions in intact zebrafish larvae using selective plane illumination microscopy. *Front. Neural Circuits* 7:65. doi: 10.3389/fncir.2013.00065

Park, C. E., Cho, Y., Cho, I., Jung, H., Kim, B., Shin, J. H., et al. (2020). Super-resolution three-dimensional imaging of actin filaments in cultured cells and the brain *via* expansion microscopy. *ACS Nano* 14, 14999–15010. doi: 10.1021/acsnano.0c04915

Park, O. K., Kwak, J., Jung, Y. J., Kim, Y. H., Hong, H.-S., Hwang, B. J., et al. (2015). 3D light-sheet fluorescence microscopy of cranial neurons and vasculature during zebrafish embryogenesis. *Mol. Cells* 38, 975–981. doi: 10.14348/molcells.2015.0160

Pavani, S. R. P., Thompson, M. A., Biteen, J. S., Lord, S. J., Liu, N., Twieg, R. J., et al. (2009). Three-dimensional, single-molecule fluorescence imaging beyond the diffraction limit by using a double-helix point spread function. *Proc. Natl. Acad. Sci. U S A* 106, 2995–2999. doi: 10.1073/pnas.0900245106

Perez de Arce, K., Schrod, N., Metzbower, S. W. R., Allgeyer, E., Kong, G. K.-W., Tang, A.-H., et al. (2015). Topographic Mapping of the Synaptic Cleft into Adhesive Nanodomains. *Neuron* 88, 1165–1172. doi: 10.1016/j.neuron.2015.11.011

Perillo, E. P., Liu, Y.-L., Huynh, K., Liu, C., Chou, C.-K., Hung, M.-C., et al. (2015). Deep and high-resolution three-dimensional tracking of single particles using nonlinear and multiplexed illumination. *Nat. Commun.* 6:7874. doi: 10.1038/ncomms8874

Power, R. M., and Huisken, J. (2017). A guide to light-sheet fluorescence microscopy for multiscale imaging. *Nat. Methods* 14, 360–373. doi: 10.1038/nmeth.4224

Quirin, S., Vladimirov, N., Yang, C.-T., Peterka, D. S., Yuste, R., and Ahrens, M. B. (2016). Calcium imaging of neural circuits with extended depth-of-field light-sheet microscopy. *Opt. Lett.* 41, 855–858. doi: 10.1364/OL.41.000855

Ram, S., Kim, D., Ober, R. J., and Ward, E. S. (2012). 3D single molecule tracking with multifocal plane microscopy reveals rapid intercellular transferrin transport at epithelial cell barriers. *Biophys. J.* 103, 1594–1603. doi: 10.1016/j.bpj.2012.08.054

Ram, S., Prabhat, P., Chao, J., Sally Ward, E., and Ober, R. J. (2008). High accuracy 3D quantum dot tracking with multifocal plane microscopy for the study of fast intracellular dynamics in live cells. *Biophys. J.* 95, 6025–6043. doi: 10.1529/biophysj.108.140392

Rieger, B., and Stallinga, S. (2014). The lateral and axial localization uncertainty in super-resolution light microscopy. *ChemPhysChem* 15, 664–670. doi: 10.1002/cphc.201300711

Ries, J., Kaplan, C., Platonova, E., Eghlidi, H., and Ewers, H. (2012). A simple, versatile method for GFP-based super-resolution microscopy *via* nanobodies. *Nat. Methods* 9, 582–584. doi: 10.1038/nmeth.1991

Ritter, J. G., Veith, R., Veenendaal, A., Siebrasse, J. P., and Kubitscheck, U. (2010). Light sheet microscopy for single molecule tracking in living tissue. *PLoS One* 5:e11639. doi: 10.1371/journal.pone.0011639

Rocha, M. D., Düring, D. N., Bethge, P., Voigt, F. F., Hildebrand, S., Helmchen, F., et al. (2019). Tissue clearing and light sheet microscopy: imaging the unsectioned adult zebra finch brain at cellular resolution. *Front. Neuroanat.* 13:13. doi: 10.3389/fnana.2019.00013

Rosten, E., Jones, G. E., and Cox, S. (2013). ImageJ plug-in for Bayesian analysis of blinking and bleaching. *Nat. Methods* 10, 97–98. doi: 10.1038/nmeth.2342

Rust, M. J., Bates, M., and Zhuang, X. (2006). Sub-diffraction-limit imaging by stochastic optical reconstruction microscopy (STORM). *Nat. Methods* 3, 793–795. doi: 10.1038/nmeth929

Saha, D., Schmidt, U., Zhang, Q., Barbotin, A., Hu, Q., Ji, N., et al. (2020). Practical sensorless aberration estimation for 3D microscopy with deep learning. *Opt. Express* 28, 29044–29053. doi: 10.1364/OE.401933

Sahl, S. J., Hell, S. W., and Jakobs, S. (2017). Fluorescence nanoscopy in cell biology. *Nat. Rev. Mol. Cell Biol.* 18, 685–701. doi: 10.1038/nrm.2017.71

Sakamoto, H., Ariyoshi, T., Kimpara, N., Sugao, K., Taiko, I., Takikawa, K., et al. (2018). Synaptic weight set by Munc13-1 supramolecular assemblies. *Nat. Neurosci.* 21, 41–49. doi: 10.1038/s41593-017-0041-9

Santi, P. A. (2011). Light sheet fluorescence microscopy: a review. *J. Histochem. Cytochem.* 59, 129–138. doi: 10.1369/0022155410394857

Schedin-Weiss, S., Caesar, I., Winblad, B., Blom, H., and Tjernberg, L. O. (2016). Super-resolution microscopy reveals γ- secretase at both sides of the neuronal synapse. *Acta Neuropathol. Commun.* 4:29. doi: 10.1186/s40478-016-0296-5

Schueder, F., Lara-Gutiérrez, J., Beliveau, B. J., Saka, S. K., Sasaki, H. M., Woehrstein, J. B., et al. (2017). Multiplexed 3D super-resolution imaging of whole cells using spinning disk confocal microscopy and DNA-PAINT. *Nat. Commun.* 8:2090. doi: 10.1038/s41467-017-02028-8

Schwentker, M. A., Bock, H., Hofmann, M., Jakobs, S., Bewersdorf, J., Eggeling, C., et al. (2007). Wide-field subdiffraction RESOLFT microscopy using fluorescent protein photoswitching. *Microsc. Res. Tech.* 70, 269–280. doi: 10.1002/jemt.20443

Sharonov, A., and Hochstrasser, R. M. (2006). Wide-field subdiffraction imaging by accumulated binding of diffusing probes. *Proc. Natl. Acad. Sci. U S A* 103, 18911–18916. doi: 10.1073/pnas.0609643104

Shechtman, Y., Gustavsson, A.-K., Petrov, P. N., Dultz, E., Lee, M. Y., Weis, K., et al. (2017). Observation of live chromatin dynamics in cells *via* 3D localization microscopy using Tetrapod point spread functions. *Biomed. Opt. Express* 8, 5735–5748. doi: 10.1364/BOE.8.005735

Shechtman, Y., Sahl, S. J., Backer, A. S., and Moerner, W. E. (2014). Optimal point spread function design for 3D imaging. *Phys. Rev. Lett.* 113:133902. doi: 10.1103/PhysRevLett.113.133902

Shechtman, Y., Weiss, L. E., Backer, A. S., Sahl, S. J., and Moerner, W. E. (2015). Precise three-dimensional scan-free multiple-particle tracking over large axial ranges with tetrapod point spread functions. *Nano Lett.* 15, 4194–4199. doi: 10.1021/acs.nanolett.5b01396

Shen, H., Tauzin, L. J., Baiyasi, R., Wang, W., Moringo, N., Shuang, B., et al. (2017). Single particle tracking: from theory to biophysical applications. *Chem. Rev.* 117, 7331–7376. doi: 10.1021/acs.chemrev.6b00815

Shimomura, O. (2009). Discovery of green fluorescent protein (GFP; Nobel Lecture). *Angew. Chem. Int. Ed. Engl.* 48, 5590–5602. doi: 10.1002/anie.200902240

Shroff, H., Galbraith, C. G., Galbraith, J. A., White, H., Gillette, J., Olenych, S., et al. (2007). Dual-color superresolution imaging of genetically expressed probes within individual adhesion complexes. *Proc. Natl. Acad. Sci. U S A* 104, 20308–20313. doi: 10.1073/pnas.0710517105

Siedentopf, H., and Zsigmondy, R. (1902). Uber Sichtbarmachung und Größenbestimmung ultramikoskopischer Teilchen, mit besonderer Anwendung auf Goldrubingläser. *Ann. Phys.* 315, 1–39. doi: 10.1002/andp.19023150102

Sigal, Y. M., Bae, H., Bogart, L. J., Hensch, T. K., and Zhuang, X. (2019). Structural maturation of cortical perineuronal nets and their perforating synapses revealed by superresolution imaging. *Proc. Natl. Acad. Sci. U S A* 116, 7071–7076. doi: 10.1073/pnas.1817222116

Sigal, Y. M., Speer, C. M., Babcock, H. P., and Zhuang, X. (2015). Mapping synaptic input fields of neurons with super-resolution imaging. *Cell* 163, 493–505. doi: 10.1016/j.cell.2015.08.033

Siksou, L., Triller, A., and Marty, S. (2009). An emerging view of presynaptic structure from electron microscopic studies. *J. Neurochem.* 108, 1336–1342. doi: 10.1111/j.1471-4159.2009.05888.x

Small, A., and Stahlheber, S. (2014). Fluorophore localization algorithms for super-resolution microscopy. *Nat. Methods* 11, 267–279. doi: 10.1038/nmeth.2844

Smith, C. S., Preibisch, S., Joseph, A., Abrahamsson, S., Rieger, B., Myers, E., et al. (2015). Nuclear accessibility of β-actin mRNA is measured by 3D single-molecule real-time tracking. *J. Cell Biol.* 209, 609–619. doi: 10.1083/jcb.201411032

Specht, C. G., Izeddin, I., Rodriguez, P. C., El Beheiry, M., Rostaing, P., Darzacq, X., et al. (2013). Quantitative nanoscopy of inhibitory synapses: counting gephyrin molecules and receptor binding sites. *Neuron* 79, 308–321. doi: 10.1016/j.neuron.2013.05.013

Spille, J.-H., Kaminski, T., Königshoven, H.-P., and Kubitscheck, U. (2012). Dynamic three-dimensional tracking of single fluorescent nanoparticles deep inside living tissue. *Opt. Express* 20, 19697–19707. doi: 10.1364/OE.20.019697

Stefaniuk, M., Gualda, E. J., Pawlowska, M., Legutko, D., Matryba, P., Koza, P., et al. (2016). Light-sheet microscopy imaging of a whole cleared rat brain with Thy1-GFP transgene. *Sci. Rep.* 6:28209. doi: 10.1038/srep28209

Tang, A.-H., Chen, H., Li, T. P., Metzbower, S. R., MacGillavry, H. D., and Blanpied, T. A. (2016). A trans-synaptic nanocolumn aligns neurotransmitter release to receptors. *Nature* 536, 210–214. doi: 10.1038/nature19058

Tatavarty, V., Kim, E.-J., Rodionov, V., and Yu, J. (2009). Investigating sub-spine actin dynamics in rat hippocampal neurons with super-resolution optical imaging. *PLoS One* 4:e7724. doi: 10.1371/journal.pone.0007724

Testa, I., Urban, N. T., Jakobs, S., Eggeling, C., Willig, K. I., and Hell, S. W. (2012). Nanoscopy of living brain slices with low light levels. *Neuron* 75, 992–1000. doi: 10.1016/j.neuron.2012.07.028

Thal, L. B., Tomlinson, I. D., Quinlan, M. A., Kovtun, O., Blakely, R. D., and Rosenthal, S. J. (2019). Single quantum dot imaging reveals PKCβ-dependent alterations in membrane diffusion and clustering of an attention-deficit hyperactivity disorder/autism/bipolar disorder-associated dopamine transporter variant. *ACS Chem. Neurosci.* 10, 460–471. doi: 10.1021/acschemneuro.8b00350

Theer, P., Dragneva, D., and Knop, M. (2016). πSPIM: High NA high resolution isotropic light-sheet imaging in cell culture dishes. *Sci. Rep.* 6:32880. doi: 10.1038/srep32880

Thompson, M. A., Casolari, J. M., Badieirostami, M., Brown, P. O., and Moerner, W. E. (2010). Three-dimensional tracking of single mRNA particles in Saccharomyces cerevisiae using a double-helix point spread function. *Proc. Natl. Acad. Sci. U S A* 107, 17864–17871. doi: 10.1073/pnas.1012868107

Tokunaga, M., Imamoto, N., and Sakata-Sogawa, K. (2008). Highly inclined thin illumination enables clear single-molecule imaging in cells. *Nat. Methods* 5, 159–161. doi: 10.1038/nmeth1171

Tønnesen, J., Inavalli, V. V. G. K., and Nägerl, U. V. (2018). Super-resolution imaging of the extracellular space in living brain tissue. *Cell* 172, 1108–1121.e15. doi: 10.1016/j.cell.2018.02.007

Tønnesen, J., Nadrigny, F., Willig, K. I., Wedlich-Söldner, R., and Nägerl, U. V. (2011). Two-color STED microscopy of living synapses using a single laser-beam pair. *Biophys. J.* 101, 2545–2552. doi: 10.1016/j.bpj.2011.10.011

Tønnesen, J., and Nägerl, U. V. (2013). Superresolution imaging for neuroscience. *Exp. Neurol.* 242, 33–40. doi: 10.1016/j.expneurol.2012.10.004

Toprak, E., Balci, H., Blehm, B. H., and Selvin, P. R. (2007). Three-dimensional particle tracking *via* bifocal imaging. *Nano Lett.* 7, 2043–2045. doi: 10.1021/nl0709120

Tsien, R. Y. (2009). Constructing and exploiting the fluorescent protein paintbox (Nobel Lecture). *Angew. Chem. Int. Ed. Engl.* 48, 5612–5626. doi: 10.1002/anie.200901916

Uno, S., Kamiya, M., Yoshihara, T., Sugawara, K., Okabe, K., Tarhan, M. C., et al. (2014). A spontaneously blinking fluorophore based on intramolecular spirocyclization for live-cell super-resolution imaging. *Nat. Chem.* 6, 681–689. doi: 10.1038/nchem.2002

Urban, N. T., Willig, K. I., Hell, S. W., and Nägerl, U. V. (2011). STED nanoscopy of actin dynamics in synapses deep inside living brain slices. *Biophys. J.* 101, 1277–1284. doi: 10.1016/j.bpj.2011.07.027

Vettenburg, T., Dalgarno, H. I. C., Nylk, J., Coll-Lladó, C., Ferrier, D. E. K., Čižmár, T., et al. (2014). Light-sheet microscopy using an Airy beam. *Nat. Methods* 11, 541–544. doi: 10.1038/nmeth.2922

Vladimirov, N., Mu, Y., Kawashima, T., Bennett, D. V., Yang, C.-T., Looger, L. L., et al. (2014). Light-sheet functional imaging in fictively behaving zebrafish. *Nat. Methods* 11, 883–884. doi: 10.1038/nmeth.3040

Voie, A. H., Burns, D. H., and Spelman, F. A. (1993). Orthogonal-plane fluorescence optical sectioning: Three-dimensional imaging of macroscopic biological specimens. *J. Microsc.* 170, 229–236. doi: 10.1111/j.1365-2818.1993.tb03346.x

von Diezmann, L., Shechtman, Y., and Moerner, W. E. (2017). Three-dimensional localization of single molecules for super-resolution imaging and single-particle tracking. *Chem. Rev.* 117, 7244–7275. doi: 10.1021/acs.chemrev.6b00629

Wang, L., Guo, W., Shen, X., Yeo, S., Long, H., Wang, Z., et al. (2020). Different dendritic domains of the GnRH neuron underlie the pulse and surge modes of GnRH secretion in female mice. *eLife* 9:e53945. doi: 10.7554/eLife.53945

Wang, K., Sun, W., Richie, C. T., Harvey, B. K., Betzig, E., and Ji, N. (2015). Direct wavefront sensing for high-resolution *in vivo* imaging in scattering tissue. *Nat. Commun.* 6:7276. doi: 10.1038/ncomms8276

Wang, Y., Woehrstein, J. B., Donoghue, N., Dai, M., Avendaño, M. S., Schackmann, R. C. J., et al. (2017). Rapid sequential in situ multiplexing with dna exchange imaging in neuronal cells and tissues. *Nano Lett.* 17, 6131–6139. doi: 10.1021/acs.nanolett.7b02716

Wassie, A. T., Zhao, Y., and Boyden, E. S. (2019). Expansion microscopy: principles and uses in biological research. *Nat. Methods* 16, 33–41. doi: 10.1038/s41592-018-0219-4

Wegner, W., Ilgen, P., Gregor, C., van Dort, J., Mott, A. C., Steffens, H., et al. (2017). *in vivo* mouse and live cell STED microscopy of neuronal actin plasticity using far-red emitting fluorescent proteins. *Sci. Rep.* 7:11781. doi: 10.1038/s41598-017-11827-4

Weiss, L. E., Shalev Ezra, Y., Goldberg, S., Ferdman, B., Adir, O., Schroeder, A., et al. (2020). Three-dimensional localization microscopy in live flowing cells. *Nat. Nanotechnol.* 15, 500–506. doi: 10.1038/s41565-020-0662-0

Werner, C., Sauer, M., and Geis, C. (2021). Super-resolving microscopy in neuroscience. *Chem. Rev.* 121, 11971–12015. doi: 10.1021/acs.chemrev.0c01174

Widera, D., Klenke, C., Nair, D., Heidbreder, M., Malkusch, S., Sibarita, J.-B., et al. (2016). Single-particle tracking uncovers dynamics of glutamate-induced retrograde transport of NF-κB p65 in living neurons. *Neurophotonics* 3:041804. doi: 10.1117/1.NPh.3.4.041804

Wilding, D., Pozzi, P., Soloviev, O., Vdovin, G., and Verhaegen, M. (2016). Adaptive illumination based on direct wavefront sensing in a light-sheet fluorescence microscope. *Opt. Express* 24, 24896–24906. doi: 10.1364/OE.24.024896

Willig, K. I., Rizzoli, S. O., Westphal, V., Jahn, R., and Hell, S. W. (2006). STED microscopy reveals that synaptotagmin remains clustered after synaptic vesicle exocytosis. *Nature* 440, 935–939. doi: 10.1038/nature04592

Winterflood, C. M., Platonova, E., Albrecht, D., and Ewers, H. (2015). Dual-color 3D superresolution microscopy by combined spectral-demixing and biplane imaging. *Biophys. J.* 109, 3–6. doi: 10.1016/j.bpj.2015.05.026

Xiao, Y., Faucherre, A., Pola-Morell, L., Heddleston, J. M., Liu, T.-L., Chew, T.-L., et al. (2015). High-resolution live imaging reveals axon-glia interactions during peripheral nerve injury and repair in zebrafish. *Dis. Model. Mech.* 8, 553–564. doi: 10.1242/dmm.018184

Xu, H., Tong, Z., Ye, Q., Sun, T., Hong, Z., Zhang, L., et al. (2019). Molecular organization of mammalian meiotic chromosome axis revealed by expansion STORM microscopy. *Proc. Natl. Acad. Sci. U S A* 116, 18423–18428. doi: 10.1073/pnas.1902440116

Xu, K., Zhong, G., and Zhuang, X. (2013). Actin, spectrin and associated proteins form a periodic cytoskeletal structure in axons. *Science* 339, 452–456. doi: 10.1126/science.1232251

Yang, Z., Prokopas, M., Nylk, J., Coll-Lladó, C., Gunn-Moore, F. J., Ferrier, D. E. K., et al. (2014). A compact Airy beam light sheet microscope with a tilted cylindrical lens. *Biomed. Opt. Express BOE* 5, 3434–3442. doi: 10.1364/BOE.5.003434

Yuste, R. (2015). From the neuron doctrine to neural networks. *Nat. Rev. Neurosci.* 16, 487–497. doi: 10.1038/nrn3962

Zhang, P., Liu, S., Chaurasia, A., Ma, D., Mlodzianoski, M. J., Culurciello, E., et al. (2018). Analyzing complex single-molecule emission patterns with deep learning. *Nat. Methods* 15, 913–916. doi: 10.1038/s41592-018-0153-5

Zhang, P., Phipps, M. E., Goodwin, P. M., and Werner, J. H. (2016). Light-sheet microscopy by confocal line scanning of dual-Bessel beams. *J. Biomed. Opt* 21:100502. doi: 10.1117/1.JBO.21.10.100502

Zhao, F., Zhu, L., Fang, C., Yu, T., Zhu, D., Fei, P., et al. (2020). Deep-learning super-resolution light-sheet add-on microscopy (Deep-SLAM) for easy isotropic volumetric imaging of large biological specimens. *Biomed. Opt. Express* 11, 7273–7285. doi: 10.1364/BOE.409732

Zheng, X., Zhou, J., Wang, L., Wang, M., Wu, W., Chen, J., et al. (2021). Current challenges and solutions of super-resolution structured illumination microscopy. *APL Photonics* 6:020901. doi: 10.1063/5.0038065

Zhong, G., He, J., Zhou, R., Lorenzo, D., Babcock, H. P., Bennett, V., et al. (2014). Developmental mechanism of the periodic membrane skeleton in axons. *eLife* 3:e04581. doi: 10.7554/eLife.04581

Zieger, H. L., and Choquet, D. (2021). Nanoscale synapse organization and dysfunction in neurodevelopmental disorders. *Neurobiol. Dis.* 158:105453. doi: 10.1016/j.nbd.2021.105453

Zwettler, F. U., Reinhard, S., Gambarotto, D., Bell, T. D. M., Hamel, V., Guichard, P., et al. (2020). Molecular resolution imaging by post-labeling expansion single-molecule localization microscopy (Ex-SMLM). *Nat. Commun.* 11:3388. doi: 10.1038/s41467-020-17086-8

Conflict of Interest: The authors declare that the research was conducted in the absence of any commercial or financial relationships that could be construed as a potential conflict of interest.

frontiers in Synaptic Neuroscience

ORIGINAL RESEARCH
published: 26 November 2021
doi: 10.3389/fnsyn.2021.727406

Genetic Code Expansion and Click-Chemistry Labeling to Visualize GABA-A Receptors by Super-Resolution Microscopy

Alexander Kuhlemann[1]†, Gerti Beliu[1,2]†, Dieter Janzen[3], Enrica Maria Petrini[4], Danush Taban[1], Dominic A. Helmerich[1], Sören Doose[1], Martina Bruno[4], Andrea Barberis[4], Carmen Villmann[3], Markus Sauer[1] and Christian Werner[1]*

[1] Department of Biotechnology and Biophysics, University of Würzburg, Biocenter, Würzburg, Germany, [2] Rudolf Virchow Center for Integrative and Translational Bioimaging, University of Wuerzburg, Würzburg, Germany, [3] Institute of Clinical Neurobiology, University of Würzburg, Würzburg, Germany, [4] Neuroscience and Brain Technologies Department, Istituto Italiano Di Tecnologia, Genova, Italy

Fluorescence labeling of difficult to access protein sites, e.g., in confined compartments, requires small fluorescent labels that can be covalently tethered at well-defined positions with high efficiency. Here, we report site-specific labeling of the extracellular domain of γ-aminobutyric acid type A (GABA-A) receptor subunits by genetic code expansion (GCE) with unnatural amino acids (ncAA) combined with bioorthogonal click-chemistry labeling with tetrazine dyes in HEK-293-T cells and primary cultured neurons. After optimization of GABA-A receptor expression and labeling efficiency, most effective variants were selected for super-resolution microscopy and functionality testing by whole-cell patch clamp. Our results show that GCE with ncAA and bioorthogonal click labeling with small tetrazine dyes represents a versatile method for highly efficient site-specific fluorescence labeling of proteins in a crowded environment, e.g., extracellular protein domains in confined compartments such as the synaptic cleft.

Keywords: super-resolution microscopy (SRM), click-chemistry, *d*STORM, GABA-A receptor, genetic code expansion

Edited by:
Thomas A. Blanpied,
University of Maryland, Baltimore,
United States

Reviewed by:
Tija Carey Jacob,
University of Pittsburgh, United States
Katharine R. Smith,
University of Colorado Denver,
United States

****Correspondence:***
Christian Werner
christian.werner@uni-wuerzburg.de

†These authors have contributed equally to this work

Received: *18 June 2021*
Accepted: *02 November 2021*
Published: *26 November 2021*

Citation:
Kuhlemann A, Beliu G, Janzen D, Petrini EM, Taban D, Helmerich DA, Doose S, Bruno M, Barberis A, Villmann C, Sauer M and Werner C (2021) Genetic Code Expansion and Click-Chemistry Labeling to Visualize GABA-A Receptors by Super-Resolution Microscopy. Front. Synaptic Neurosci. 13:727406. doi: 10.3389/fnsyn.2021.727406

INTRODUCTION

In the central nervous system, phasic and tonic inhibition is dominantly controlled by γ-aminobutyric acid type A (GABA-A) receptors. These hetero-pentameric, ligand-gated, ionotropic receptors can arrange in different subunit compositions from 19 different subunits to allow high diversity of gating properties, pharmacology, and expression patterns in both specific brain regions and distinct subcellular domains (Wisden and Seeburg, 1992; Barnard et al., 1998; Mody and Pearce, 2004; Olsen and Sieghart, 2008, 2009). Defective GABA-A receptor-mediated inhibition can result in neurodevelopmental and neuropsychiatric disorders, Alzheimer's disease, and stroke (Vien et al., 2015; de Jonge et al., 2017; Govindpani et al., 2017; Ali Rodriguez et al., 2018; Wang et al., 2018). Surface GABA-A receptors laterally diffuse between synaptic and extrasynaptic sites, an activity-dependent feature that depends on receptor interaction with inhibitory scaffolding molecules like gephyrin (Petrini et al., 2014). So far, super-resolution microscopy of GABA-A receptor subcellular distributions relied on immunolabeling or genetic fluorophore fusions (de Luca et al., 2017; Crosby et al., 2019). However, fluorescent proteins exhibit a size of ∼5 nm and can impede native receptor function. Antibodies can induce crosslinking and internalization and due to their larger size of ∼10 nm introduce a substantial linkage error and impact diffusion of receptors (Weber et al., 1978; Schnell et al., 2012; Dalmau et al., 2017). Linkage error describes the distance between the fluorophore and the binding site of the targeted protein and is calculated by adding the distances of handles needed for the respective labeling procedure. Furthermore, efficient labeling of proteins in a crowded environment or at sterically demanding sites, e.g., in postsynaptic compartments of neurons or at the basal plasma membrane of adherent cells remains challenging because of reduced epitope accessibility (Gray, 1969; Lee et al., 2017; Waldchen et al., 2020). In addition, larger fluorescent labels can likely affect the mobility of proteins, e.g., receptors inside narrow synaptic clefts of 20–30 nm (Beghein and Gettemans, 2017; de Luca et al., 2017).

To reduce the size and linkage error, smaller fluorescent labels such as nanobodies, affimers, aptamers, genetically encoded tags, and superbinding peptides have been developed (Opazo et al., 2012; Nikic et al., 2015; Maric et al., 2017; Thorn, 2017; Schlichthaerle et al., 2018). However, the most direct and less-invasive method to label a protein of interest at a well-defined position with a small fluorophore uses genetic code expansion (GCE) by incorporation of unnatural amino acids (ncAA) that can be labeled by a strain-promoted inverse electron demanding Diels Alder cycloaddition (SPIEDAC) reaction with tetrazine dyes (Beliu et al., 2019). GCE and bioorthogonal click labeling with tetrazine dyes have been used advantageously for site-specific labeling, FRET imaging, and high-end fluorescence imaging of extra- and intracellular protein targets in different model organisms (Ramil and Lin, 2013; Chin, 2014; Uttamapinant et al., 2015; Neubert et al., 2018; Wang et al., 2018; Waterhouse et al., 2018; Serfling et al., 2019; Nikic-Spiegel, 2020; Beliu et al., 2021; Liauw et al., 2021). Although there are reports on the integration of light-activatable potassium channels in rat hippocampal networks *in vivo* and implementation of GCE in living mouse brain was also reported recently, the successful fusion of this method with click chemistry labeling and super-resolution fluorescence microscopy of synaptic receptors in neurons remain challenging (Kang et al., 2013; Ernst et al., 2016). In our recent report, we already could provide evidence that click-chemistry labeling of GCE modified NR1 subunits of the NMDA receptor complex yields functional receptors and can outperform antibody binding in sterically demanding environments (Neubert et al., 2018). In a following report, super-resolution imaging was applied to GCE modified AMPA receptor auxiliary subunits to address masked epitopes in primary neurons and organotypic brain slices (Bessa-Neto et al., 2021). However, a validation of click-chemistry labeling of GCE modified receptor subunits forming multimeric membrane receptors in primary neurons is still missing.

Here, we set out to introduce ncAA in extracellular domains of GABA-A receptor subunits by GCE in HEK-293-T cells and primary cultured neurons followed by site-specific labeling with tetrazine dyes and visualization by *direct* stochastic optical reconstruction microscopy (*d*STORM) and structured illumination microscopy (SIM) (Gustafsson, 2000; Heilemann et al., 2008; van de Linde et al., 2011).

RESULTS

We first introduced the AMBER stop codon (TAG) by exchanging lysine or serine codons at different unstructured regions of the extracellular domain of the GABA-A receptor α2 subunit for site-specific labeling (**Figure 1** and **Supplementary Figure 1**). Each Amber mutant construct of GABA-A receptor α2 subunit was co-transfected with β1 and γ2 subunits in HEK-293-T cells to ensure proper surface delivery of α2 subunits, along with an orthogonal tRNA/tRNA-synthetase pair (Nikic et al., 2016). Immediately after transfection, the clickable ncAA trans-Cyclooct-2-en-L-lysine (TCO*) was fed to cells for ncAA incorporation. After bioorthogonal click-labeling of TCO* with the tetrazine-dye H-tet-Cy5, the labeling efficiency of the different mutants was evaluated by confocal laser scanning microscopy in HEK-293-T cells. Here, Amber mutants S181TAG and S201TAG showed the most efficient labeling demonstrated by a continuous fluorescence signal visible along the cell membrane (**Figure 2** and **Supplementary Figure 2**).

To verify signal specificity, Amber mutants without supplied TCO* were also investigated but showed negligible staining after the addition of H-tet-Cy5 (**Figure 2**, middle). Furthermore, α2 wildtype (WT) receptors carrying an HA tag showed neglectable non-specific H-tet-Cy5 signal (**Figure 2**, lower panel). With a similar approach, we also modified conserved regions of α1 subunits of GABA-A R by GCE. Fluorescence imaging showed that the S181TAG mutant of the α1 subunits can be efficiently labeled with H-Tet-Cy5. In parallel, negative controls demonstrated the specificity of bioorthogonal click-labeling of α1 subunits (**Supplementary Figure 3**).

Next, we performed patch-clamp experiments in HEK-293 cells expressing the mutant α2 S181TAG, which showed the highest labeling efficiency on the equatorial cell membrane (**Figure 2**), to demonstrate that the chosen ncAA incorporation site preserves physiological GABA-A receptor function (**Figure 3**).

Here, patch-clamp recordings revealed similar current amplitudes and *I*–*V* curves for the S181TAG mutant and α2 WT indicating native receptor function (**Figures 3A–D**). This was further confirmed by the similar block exerted by Zn^{2+}-ions (WT 4.3 ± 0.47 nA at 30 μM GABA and 3.7 ± 0.46 nA for GABA + Zn^{2+}; $p = 0.0009$; mutant 3.2 ± 0.6 nA for GABA and 2.7 ± 0.5 nA for GABA + Zn^{2+}, $p = 0.0134$, two-tailed paired *t*-test) and the comparable sensitivity of currents to picrotoxinin (WT 4.3 ± 0.47 nA at 30 μM GABA and 1.3 ± 0.35 nA for GABA+picrotoxinin, $p = 0.0124$; mutant 2.7 ± 0.5 nA for GABA and 1.1 ± 0.3 nA for GABA+picrotoxinin, $p = 0.0013$, two-tailed paired *t*-test) obtained for α2β1γ2 WT and the mutant α2S181TAG combined with β1γ2. Note there were no significant differences when α2β1γ2 WT was compared to the mutant S181TAG co-transfected with β1γ2 ($p = 0.157$ for GABA, $p = 0.168$ for GABA + Zn^{2+}, $p = 0.644$ for GABA + picrotoxinin;

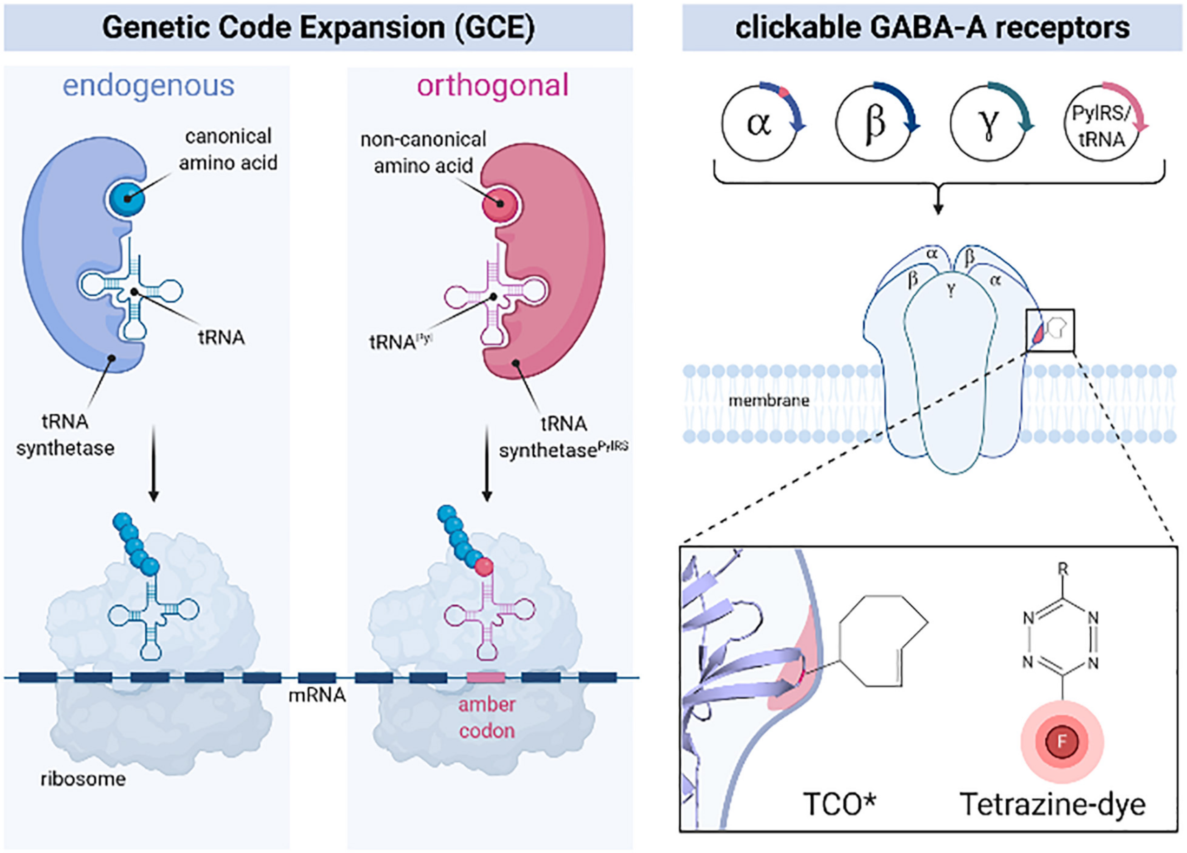

FIGURE 1 | Principle of genetic code expansion (GCE) using amber codon suppression for site-directed labeling of GABA-A receptors with tetrazine-dyes. Introduction of an orthogonal tRNA-synthetase/tRNA pair (red) to the endogenous expression machinery (blue) of mammalian cells allows site-specific incorporation of ncAA in α2 subunits of GABA-A receptors during translation, resulting in full-length GABA-A receptors equipped with a clickable ncAA (here: TCO*) (left). The mutation site is located in the extracellular domain (ATD) of GABA-A receptor α2 subunit (right) and labeled by bioorthogonal click chemistry with a tetrazine-dye (inset) to visualize functional, pentameric GABA-A receptors with unprecedented small linkage error in primary neurons (right).

unpaired *t*-test; **Figure 3A**), revealing that functional γ subunit-containing α2 WT and S181TAG GABA-A receptors are in the receptor complex and expressed at the surface membrane of HEK293 cells with similar efficiency. Co-application of GABA and the positive allosteric modulator diazepam demonstrated increased current responses, indicating that the mutation S181 does not affect the benzodiazepine binding site located at the α/γ interface (**Figure 3D**). The residue S181 is localized in the β8–β9 loop, which has been suggested to enable structural transitions following ligand binding into ion channel opening (Du et al., 2015). As these structural transitions are a prerequisite for ion channel opening and subsequent picrotoxinin binding, the mutation does not affect the overall β8–β9 loop flexibility and thus ion channel function of the mutated GABA-A receptor complex, respectively.

Next, we investigated the influence of ncAA incorporation and click-labeling on the diffusion of receptors by fluorescence recovery after photobleaching (FRAP) experiments with GABA-A α2 wt subunit and the click-labeled S181TAG mutant, carrying HA upstream of the GABA-A α2 sequence. FRAP analysis revealed similar fluorescence recovery times on equatorial membranes of HEK-293T cells for both labeling methods demonstrating the negligible impact of ncAA insertion on receptor trafficking and lateral diffusion (**Figure 3E**).

Overall, these data demonstrate that the small footprint of tetrazine dyes combined with the site-specific introduction of ncAAs preserves the functionality of GABA-A receptors. To visualize the distribution of GABA-A receptors in the plasma membrane of HEK-293-T cells, we used single-molecule sensitive super-resolution imaging by *d*STORM of immunolabeled and tetrazine-dye labeled receptors (S181TAG) in TIRF mode (Haselmann et al., 2018; Siddig et al., 2020). *d*STORM images revealed a homogeneous distribution of GABA-A receptors on the basal plasma membrane independent of the used labeling method. However, DBSCAN cluster analysis (applied to combine repeated localizations from identical fluorophores) detected more localization clusters per μm^2 for H-Tet-Cy5 click-labeling compared to anti-HA CF568 antibody labeling of the N-terminal HA-tag (**Figure 4**). The increased number of detected clusters in click labeling compared to conventional antibody staining is fluorophore-independent, since swapping of the fluorescent dyes resulted in similar cluster localizations

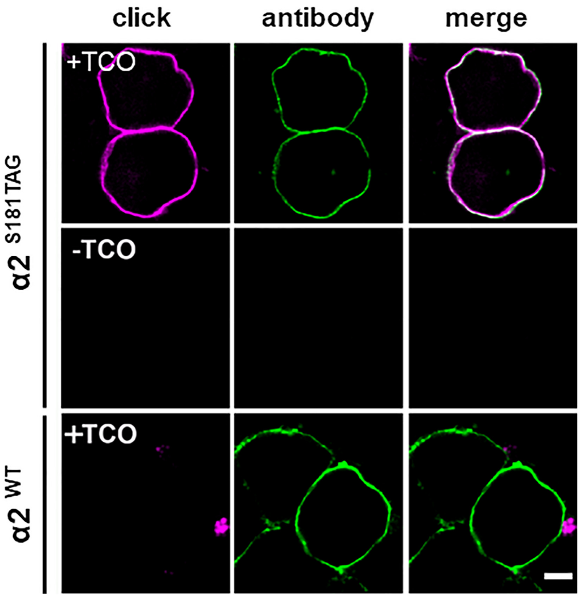

FIGURE 2 | Specificity of bioorthogonal labeling of α2 click-mutant S181TAG of GABA-A receptor α2 subunits. Confocal microscopy of membrane-targeted GABA-A receptor α2 subunits in HEK-293-T cells with coexpression of β1 and γ2 subunits to ensure bonafide membrane delivery of receptors. The ncAA TCO* was click-labeled with the tetrazine-dye H-tet-Cy5 (magenta). Antibody labeling of HA-tag (green) serves as positive control for GCE as the HA tag is located at the n-terminal part of the protein and expression of HA-tag is only feasible after successful ncAA incorporation. The lower panels show negative controls with omission of ncAA feeding (-TCO) after transfection of the S181TAG mutant and low unspecific background signal of H-tet-Cy5 (magenta) on WT α2 receptors (green) supplied with ncAA (+TCO). Scale bar, 5 μm.

preserving better labeling efficiency of the click labeling. Moreover, these experiments rule out an effect of photophysical features of the different dye combinations on the detection of clusters (**Supplementary Figure 4**). Localization clusters result from multiple blinking events of single dyes and dye-labeled antibodies in photoswitching buffer. This result corroborates recent findings that plasma membrane molecules on the basal membrane of adherent cells are more difficult to access by IgG antibodies (Gray, 1969). Thus, GCE with ncAA and bioorthogonal click labeling with substantially smaller tetrazine dyes offers a useful alternative for high-efficient labeling of masked protein epitopes difficult to access by immunolabeling.

As chemical synapses represent high-density crowded regions where small fluorescent probes can be used advantageously for tracking and localization of postsynaptic receptors, we tested our approach in cultured primary neurons. We used our S181TAG construct that enables incorporation of the click-α2 subunit along with endogenous GABA-A receptor subunits into complete GABA-A heteropentamers expressed at the neuronal surface. Therefore, we transfected day *in vitro* (DIV) 14 primary neurons with S181TAG and the tRNA/tRNA synthetase pair applying low DNA concentrations and fed neurons with TCO*. After 24 h, we applied Pyrimidyl-Tet-ATTO-643 (Pyr-Tet-ATTO643, **Supplementary Figure 5**) to target clickable α2 subunits at the surface membrane and concomitantly immunolabeled vesicular GABA transporter (vGAT) to visualize presynaptic GABAergic terminals with a specific primary antibody and secondary goat anti-mouse Alexa Fluor 568 (AF568) labeled antibodies. SIM images of primary neurons revealed specific localization of clickable GABA-A receptors on the neuronal surface that accumulated at synaptic sites juxtaposing the presynaptic vGAT signal demonstrating the successful translation of the method for labeling of postsynaptic receptors (**Figure 5**).

Of note, the tRNA/tRNA-synthetase plasmid is not optimized for neuronal transfection with lipofection thus leading to low transfection rates. However, the transfection efficiency might be well increased by designing codon-optimized plasmids along with DNA delivery to neurons via nucleofection or AAV and lentivirus-mediated transduction, respectively. Interestingly, the combination of our GCE and click labeling approach with Crispr-Cas mediated knock-in techniques is a promising future perspective for quantification synaptic proteins (Willems et al., 2020). Genetically modified click receptors form functional GABA-A recombinant receptor channels that express at the cell surface and exhibit normal diffusion behavior. Furthermore, when expressed in neurons, genetically modified α2 subunits are incorporated into endogenous receptors and can be targeted to GABAergic synapses. The new GCE labeling approach for GABA-A receptors can be used to unravel nanoscopic changes in receptor distribution at GABAergic synapses during synaptic plasticity. In addition, it might be a valuable tool to study pathological mechanisms in limbic encephalitis associated with GABA-A receptor autoantibodies (Guo et al., 2020). Here, the impact of pathogenic autoantibodies on GABA-A receptor mobility inside and outside of synaptic compartments and the arrangement of receptors at synaptic sites could be documented in pathologic conditions with so far unmatched precision (Spatola et al., 2017).

To conclude, we have shown that GCE with ncAA and bioorthogonal labeling with small tetrazine dyes can be used advantageously for site-specific labeling of difficult-to-access proteins in neurons with minimal linkage error. The method thus provides advantageous labeling of synaptic proteins for super-resolution microscopy and receptor trafficking studies in crowded or sterically demanding nanoenvironments, e.g., small compartments in the synaptic cleft.

MATERIALS AND METHODS

Molecular Biology

The plasmid for expressing the modified α2 subunit of the GABA-A receptor in mammalian cells was obtained from Addgene (Addgene # 49169) (Tretter et al., 2008). The superecliptic pHluorin tag was removed by introducing an XhoI restriction site upstream of the GABA-A coding sequence and subsequent cutting with XhoI-XhoI. The α2-TAG amber stop mutants were produced by introducing a TAG stop codon via PCR-based site-directed mutagenesis of the α2 vector using custom-designed primers (Sigma) and Q5

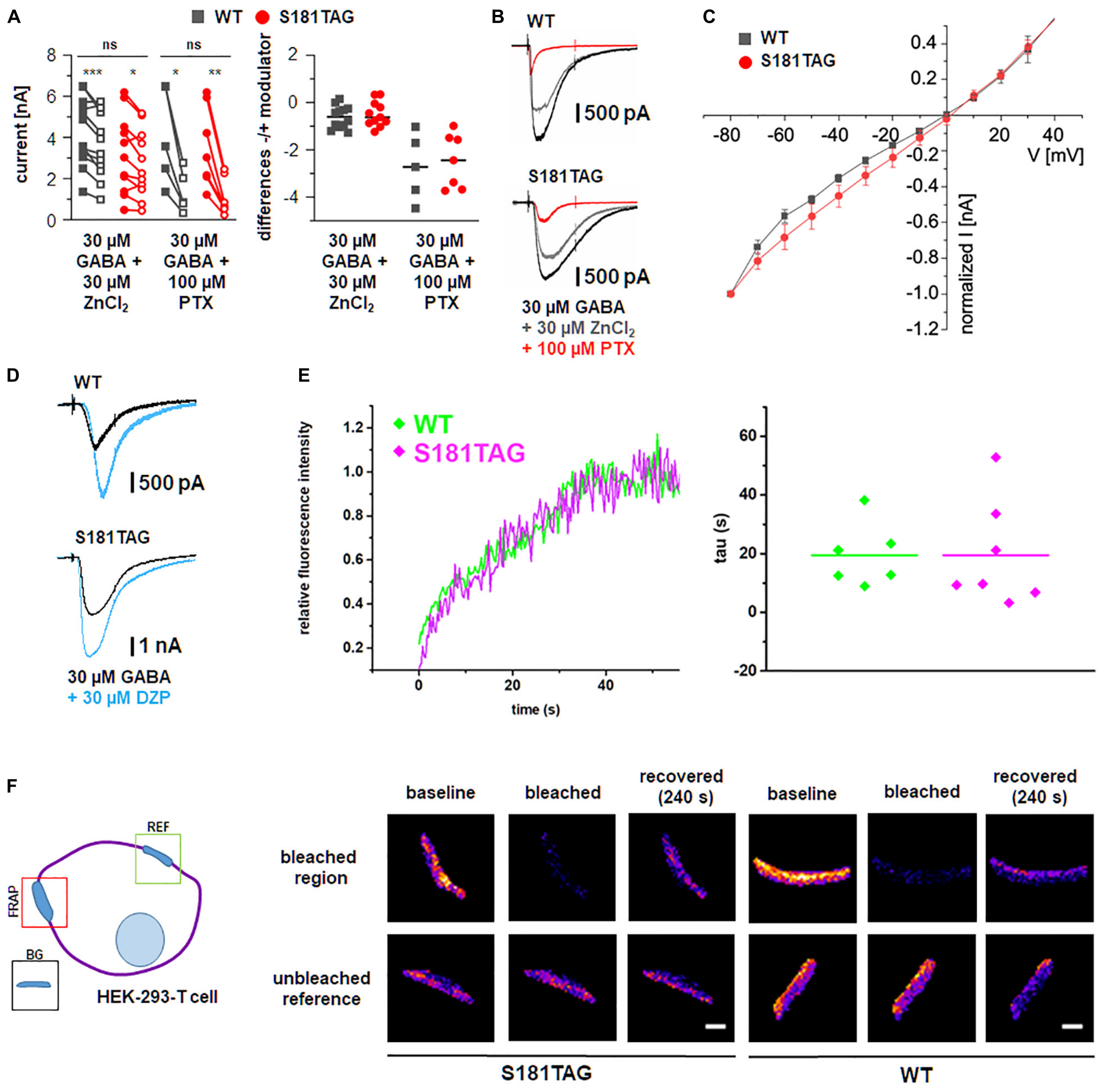

FIGURE 3 | Physiological channel function and diffusion behavior of surface GCE modified GABA-A receptors. **(A)** Validation of physiological function of modified GABA-A receptors by patch-clamp electrophysiology of HEK-293 cells. Left: Amplitude of GABA-evoked currents elicited from WT (gray) and click receptors (red) in control conditions (filled symbol) and upon the application of Zn^{2+} or picrotoxinin (PTX, open symbol). Each pair of symbols represents one patched cell. The number of recorded cells varied between 5 and 12 ($n = 5$–12). Significance level $^{*}p \leq 0.05$, $^{**}p \leq 0.01$, and $^{***}p \leq 0.001$. Right: Differences between each current pair shown left. **(B)** Representative current traces for data shown in **(A)**. Black traces: 30 μM GABA; gray traces: 30 μM GABA + 30 μM $ZnCl_2$; red traces: 30 μM GABA + 100 μM (PTX). **(C)** Comparison of IV curves of WT and click mutant S181TAG applying voltage steps of 10 mV starting at –80 mV. S181TAG modified α2 subunits coexpressed with β1 and γ2 subunits show similar *I–V* curves compared to WT receptors. **(D)** Representative current traces of diazepam (DZP) modulation from WT and click receptors. Black traces: 3 μM GABA (WT), 30 μM GABA (S181TAG); blue traces: 3 μM GABA + 3 μM DZP (WT), 30 μM GABA + 30 μM DZP (S181TAG). **(E)** Diffusion behavior of click-mutant S181TAG vs WT in HEK-293-T cell membranes. Impact of amber mutation S181TAG on GABA-A receptor diffusion determined by FRAP experiments. HEK-293-T cells expressing WT (green) and click S181TAG (magenta) GABA-A receptor α2 subunits labeled with anti-HA AF488. Both constructs show similar fluorescence recovery after photo bleaching of selected regions on equatorial membrane. Right: Evaluation of time constant tau (s), defined as the diffusion time necessary to reach 50% of the fluorescence intensity of the recovered state, shows similar values for click-mutant and the WT (WT: 19.50 ± 4.38 vs. S181TAG: 19.51 ± 6.78, mean ± SEM; $p = 0.617$, Mann–Whitney *U* test). This might indicate that the amber mutant is not hindering the diffusion of functional GABA-A receptors. Lines denote mean and single data points are depicted. **(F)** Scheme for FRAP recordings. FRAP recordings taken from selected regions of interest (blue) on anti-HA immunolabeled HEK293-T cell membranes (magenta). Reference regions (REF) on cell membrane without strong photobleaching and background signal (BG) from extracellular signal entering the equation. Exemplary FRAP images of S181TAG mutant and WT labeled with anti-HA AlexaFluor 488 antibodies. Images display baseline, photobleached, and recovered signal after 240 s inside respective regions of interest for photobleached (FRAP) and reference (REF) regions. Scale bar = 1 μm.

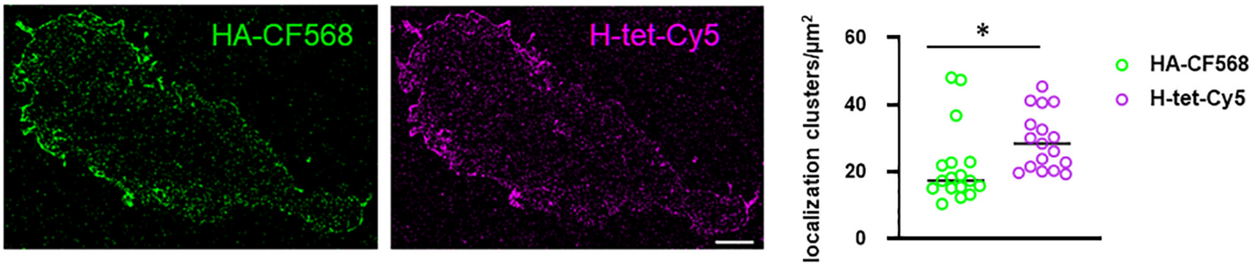

FIGURE 4 | *d*STORM images of immunolabeled HA-tag modified (HA-CF568) and click-chemistry labeled S181TAG GABA-A receptor α2 subunits (H-tet-Cy5) in the same HEK-293-T cell. Cluster analysis applying a DBSCAN algorithm demonstrates that H-tet-Cy5 labeling (magenta) exhibits a higher labeling density (localization clusters/μm^2) than immunolabeling with anti-HA-CF568 antibodies (green); lines represent median, $p = 0.005$ ($n = 17$, non-parametric Mann–Whitney U test). Scale bar: 2 µm. Significance level $^*p \leq 0.05$.

High-Fidelity DNA Polymerase (New England BioLabs). The plasmid pCMV NES-PylRSAF/tRNAPyl plasmid was a kind gift of Edward Lemke (EMBL, Heidelberg). Plasmids were amplified after transformation to *Escherichia coli* XL1 – Blue followed by MIDI-prep DNA isolation and sequenced (Nucleobond®, Xtra Midi, Macherey & Nagel, #740410). GABA-A receptor β1 and γ2 subunits were described previously (Petrini et al., 2011).

Cell Culture

Labteks were coated with poly-D-lysine (Sigma-Aldrich, #P6407, 0.5 mg/ml) for 1 h at room temperature for adherence of HEK-293-T cells; 1 × 10^5 HEK-293-T cells were seeded at least 4 h before transfection on four-well Lab-Tek II chambered cover slides (Nunc, cat. no. 155409) and cultured at a 5% CO_2 atmosphere at 37°C.

HEK-293-T cells (German Collection of Microorganisms and Cell Cultures, Braunschweig, Germany; #ACC635) were maintained in T25-culture flasks (Thermo Fisher, Cat. Nr. 156340) in Dulbecco's Modified Eagle's Medium (DMEM, Sigma-Aldrich, #D5796) supplemented with 10% FCS (Sigma-Aldrich, #F7524), and 1% Pen-Strep (Sigma-Aldrich, #P4333).

All experiments with primary neuronal cultures carried out in accordance with the guidelines established by the European Communities Council (Directive 2010/63/EU of September 22, 2010) were permitted by the Italian Ministry of Health and followed the rules approved by the Italian Institute of Technology. Primary cultures of hippocampal neurons were prepared from P0-P1 C57BL/6J mice as previously published (Polenghi et al., 2020). Neurons were plated at a density of 70 × 10^3 cells/cm^2 on poly-D-lysine pre-coated coverslips and kept in Neurobasal-A medium (Thermo Fisher, Italy) supplemented with B-27 (Thermo Fisher, Italy) 2%, Glutamax 1% (Thermo Fisher, Italy), and gentamycin 5 mg/ml (Sigma) at 37°C in 7.4% CO_2.

Transfection

At 60–80% confluency HEK-293-T cells were transfected using Jetprime (JetPrime, Polyplus) applying a 2:1 DNA/Jetprime ratio. GABA-A receptor subunits were transfected at the following ratio with a total amount of 1750 ng DNA per well: 500 ng α2 subunit, 500 ng β1 subunit, 250 ng γ2 subunit, and 500 ng pCMV NES-PylRSAF/tRNAPyl.

TCO* (SiChem, SC-8008, Bremen, Germany) was fed separately (250 µM final), diluted in 1M HEPES (one part of 100 mM TCO-A was added to three parts of 1M HEPES, and added in the corner of a single well of four-well Labtek chamber). After 24 h, the medium was exchanged to fresh cell growth medium. The cells were incubated approx. 48 h before labeling and fixation.

Hippocampal neurons were transfected at DIV 14 with the clickable α2 subunit and pCMV NES-PylRSAF/tRNAPyl in 1:2 ratio along with EGFP using Effectene (#301425, Qiagen, Germany) following the manufacturer's protocol. The following day (DIV 15) each coverslip was supplemented with TCO 250 µM.

Labeling

Transfected HEK-293-T cells fed with unnatural amino acids were reacted with 1.5 µM tetrazine dye H-tet-Cy5 (#CLK-015-05, Jena Bioscience, Germany) in cell growth medium for 30 min on ice (60 min for *d*STORM experiments). Alternatively, cells were incubated with an anti-HA Alexa Fluor 488, anti-HA Alexa Fluor 555, and anti-HA Alexa Fluor 647 (A21287, 26183-A555, and 26183-A647, Thermo Scientific, concentration: 2 µg/ml), respectively, for 30 min on ice or anti-HA CF568 antibody (5 µg/ml) for 60 min on ice (*d*STORM experiments) to reveal successful incorporation and membrane targeting of GABA-A receptor subunit α 2.

For dual-color dSTORM experiments in **Supplementary Figure 4**, cells were labeled either with Me-tet-Cy5 (3 µM, Jena Biosciences, CLK-1019-1) along with anti-HA CF568 antibody (5 µg/ml, DOL 3.3) or with Me-tet-CF568 (3 µM) together with anti-HA Cy5 antibody (5 µg/ml, DOL 2.2) for 60 min on ice to reveal successful incorporation and membrane targeting of GABA-A receptor subunit α2. Anti-HA CF568 and anti-HA Cy5 were custom-labeled by reacting unconjugated anti-HA antibody (26183, Thermo Scientific) with fivefold excess of CF568 succinimidyl ester (Sigma, SCJ4600027) or Cy5 succinimidyl ester (GE Healthcare, PA15101) for 3 h at room temperature in 100 mM sodium hydrogen carbonate buffer and subsequent removal of unconjugated CF568 or Cy5 fluorophores using Zeba Spin Desalting Columns (Thermo Scientific) following the manufacturer's instructions.

Me-tet-CF568 was custom-conjugated by reacting 10-fold molar excess of Me-tetrazine-amine (14 mM, Jena Biosciences, CLK-A138-10) with 100 μg of NHS-CF568 (1.4 mM) in anhydrous dimethylsulfoxide (DMSO) (Invitrogen, D12345), containing 0.1% N,N-diisopropylethylamine (DIPEA) (Sigma, 496219-100ML), respectively. Reactions took place at room temperature overnight. Resulting tetrazine conjugates were purified by HPLC on a Kinetex biphenyl column (150 × 4.6 mm) consisting of 2.6 μm particles at 100-Å pore size (Phenomenex, 00F-4622-E0) with a flow rate of 1 ml/min. Solvent A consisted of 0.1% aqueous formic acid (Merck, 33015-1L-M) and solvent B was 95% acetonitrile (ChemSolute, 2697.2500) in 0.1% aqueous formic acid (Merck, 33015-1L-M). Purification was done using a linear gradient of 0% B to 60% B over 30 min. The resulting elution peaks were collected and dried with a speed-vac consisting of a centrifuge (ThermoFisher, SPD111V), a refrigerated vapor trap (ThermoFisher, RVT400), and a vacuum pump (ThermoFisher, VLP80). The pellets were resuspended in double-distilled water, and the final concentration was determined by UV–VIS absorption spectrometry (Jasco V-650). Prior to fixation in 4% formaldehyde and 0.25% glutaraldehyde for 15 min for *d*STORM imaging cells were washed twice in HBSS. For conventional fluorescence microscopy, 4% formaldehyde was used for cell fixation. Following fixation, cells were again washed three times with PBS. Live imaging of clickable GABA-A receptors was performed in the respective medium.

Transfected neurons, supplemented with TCO* at DIV 15, were fixed at DIV16 with PFA 4% and probed by immunocytochemistry. After blocking with BSA 1% for 10 min, surface labeling of α2 click subunits was performed by incubating neurons with 0.75 μM Pyr-Tet-ATTO643 (#CLK-101, Jena Bioscience, Germany) for 10 min at 37°C. Next, after generous washing in BSA 1%, in order to immunolabel presynaptic GABAergic terminals, neurons were permeabilized (0.2% Triton X-100 for 10 min) and incubated with primary anti-vGAT antibody (SYSY #131 011) followed by goat anti-mouse AF568 secondary antibody (Thermo Fisher). Coverslips were mounted in DAKO fluorescent mounting medium.

Confocal Microscopy

Confocal microscopy was performed on an LSM700 (Zeiss) using a 63x/1.4 oil immersion objective. 488, 555, and 641 nm laser lines were used for excitation of anti-HA-AF488, anti-HA-AF555, and anti-HA-AF647 antibodies or H-tet-Cy5, respectively. Acquisitions used a pixel size of 100 nm. For comparisons of applied reagents, experimental settings and image postprocessing procedures were kept constant. Images were processed in FIJI by linear adjustment of brightness and contrast only.

Fluorescence Recovery After Photobleaching

Fluorescence recovery after photobleaching was applied on HA-antibody labeled (using anti-HA AF488, Thermo Scientific no.: A21287, applied at a final concentration of 2 μg/ml for 20 min) control and mutant constructs expressed in HEK-293-T cells. Fluorescent signal was bleached by applying maximal laser output of the 641 and 561 nm DPSS laser lines and signal recovery (240 cycles, 300 ms interval, 2 μs dwell time) was fitted in ZEN software with a mono-exponential function to yield t_{rel}: $I(t) = I_i - (I_f - I_0) * \exp(-t/t_{rel})$.

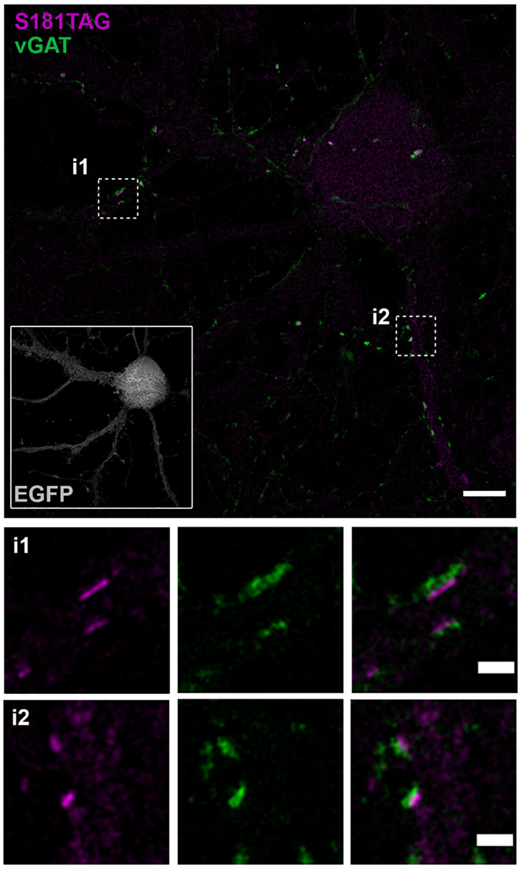

FIGURE 5 | Structured illumination microscopy (SIM) of clickable GABA-A receptor α2 subunits transfected in primary neurons (DIV 14) by effectene. SIM image depicting neuronal morphology by co-expression of cytosolic EGFP (gray, inset, lower left). Postsynaptic S181TAG α2 subunits clicked by Pyrimidyl-tet-ATTO643 (magenta) and immunolabeling of GABAergic presynapses by primary vGAT antibody and goat anti-mouse AF568 secondary antibody (green). Insets provide higher detail images of localization of S181TAG α2 subunits next to presynaptic compartments of GABAergic synapses. Scale bar: 5 μm (overview image), 1 μm (zoomed images).

Patch-Clamp Electrophysiology

Whole cell patch-clamp analysis was performed with a setup as described recently (Schaefer et al., 2019). Recording pipettes had resistances of 3–4 MΩ. Voltage steps reaching from −80 to +40 mV were applied before agonist application and resulting currents were low-pass filtered at 2.9 kHz, and digitized at a sampling rate of 20 kHz with the software Patchmaster Next (HEKA). Data analysis was performed in OriginPro 2020 (OriginLab).

For electrophysiological characterization of the GABA-A receptors, HEK-293 cells were used (CRL-1573; ATCC). Heterologous expression of the respective receptor construct was verified by HA-tag labeling using an anti-HA AF488 antibody (Thermo Fisher, A-21287, 1 μg per 500 μl cell culture medium) applied for 15 min at room temperature and excited via a Zeiss HXP 120 C lamp coupled into the fluorescence beam path of a Zeiss Axio Observer D1 inverse microscope.

The extracellular solution contained (in mM) 137 NaCl, 5.4 KCl, 1.8 $CaCl_2$, 1 $MgCl_2$, and 5 HEPES; pH 7.3, adjusted with NaOH; 330 ± 1.5 mOsm/L. To activate the receptor, the extracellular solution was supplemented with 30 μM GABA (Sigma Aldrich, A2129) and applied for 50 ms with a pressure of 1 bar using an Octaflow II applications system (ALA Scientific Instruments). For testing the membrane insertion of γ2 subunit, 30 μM $ZnCl_2$ or 30 μM diazepam was co-applied together with 30 μM GABA. The pipette solution was composed of (in mM) 120 CsCl, 20 $N(Et)_4Cl$, 1 $CaCl_2$, 2 $MgCl_2$, 11 EGTA, and 10 HEPES; pH 7.2, adjusted with CsOH; 315 ± 1.5 mOsm/L. GABA-A receptor currents were blocked using 100 μM picrotoxin (Sigma Aldrich, P8390). GraphPad Prism 9.0.0 (GraphPad Software, San Diego, CA, United States) was used to calculate mean values, standard error of the mean, and statistical significance. Two-tailed paired (current pairs) and unpaired (WT vs. S181TAG) *t*-tests were used to estimate significance values with $^{*}p < 0.05$, $^{**}p < 0.01$, and $^{***}p < 0.001$.

Structured Illumination Microscopy

For SIM, immunolabeled primary hippocampal neurons were embedded in DAKO and recorded on a commercial SIM Zeiss ELYRA S.1 system with a Plan-Apochromat 63x/1.40 oil immersion objective; 488 nm and 561 nm OPSL laser, and a 642 nm diode laser were used as excitation lasers with respective filter sets for GFP, AF568, and Pyrimidyl-tet-ATTO643 fluorophores. Recording of image stacks was performed by applying structured illumination using five rotational and five phase variations and the image was reconstructed in ZEN software (ZEN 2.3, Carl Zeiss Microscopy GmbH, Jena, Germany). Chromatic aberration was corrected in ZEN software by applying affine transformations generated from stacks of embedded TetraspeckTM beads (Z7279, Thermo Fisher Scientific, Waltham, MA, United States). Brightness and contrast of reconstructed images were adjusted linearly in FIJI (Schindelin et al., 2012).

Spectral Characteristics of Dyes and Turn-On Ratios

H-tet-Cy5 was purchased from Jena Bioscience, Jena, Germany # CLK-015-05. Absorbance and emission spectra of Pyr-tet-ATTO643 were recorded in quartz glass cuvettes using an FP-6500 spectrofluorometer (Jasco). Excitation wavelength was positioned over absorption maxima, and spectra were recorded at constant 25°C stabilized via Peltier thermocouple. Time-dependent fluorescence intensities were measured in quartz glass cuvettes using an FP-6500 spectrofluorometer (Jasco). An increase in relative fluorescence for determining the turn-on ratio was measured after performing a click-reaction in cuvette applying 25 μM TCO* and 1 μM dye solutions.

Direct Stochastic Optical Reconstruction Microscopy

Direct stochastic optical reconstruction microscopy imaging was performed on a customized Olympus IX-71 inverted wide-field fluorescence microscope. CF568 and Cy5 were excited using 558- or 640-nm optically pumped semiconductor lasers (OPSL) applying 4 kW/cm^2 irradiation intensity (Genesis MX561-500 STM, Genesis MX639-1000 STM, Coherent), passing a laser clean-up filter 567/15 (Semrock), respective 640/10 (Chroma) and focused into an oil-immersion objective (60×, NA 1.45; Olympus). Emission was filtered by a dichroic mirror (FF 410/504/582/669 Brightline, Semrock) and spectrally filtered by a bandpass filter (679/41 BrightLine HC, 607/70 Brightline HC, Semrock). The emitted signal was collected in 15.000 frames at 15 ms exposure time on two electron-multiplying CCD cameras (Andor Ixon DU 897). Additional lenses in the emission path yielded a final pixel size of 129 nm for the camera detecting Cy5 and 131 nm for the camera acquiring CF568. Total internal reflection (TIRF) was applied for imaging of basal HEK cell membranes. Photoswitching buffer was PBS stabilized and contained 100 mM cysteamine hydrochloride (Sigma-Aldrich) adjusted to pH 7.4 by addition of potassium hydroxide. Reconstruction of super-resolution images was performed in Thunderstorm (Ovesny et al., 2014) or rapidSTORM 3.3 (Wolter et al., 2012). Localizations were filtered using a detection threshold of 6500 counts, and drift correction was applied by Thunderstorm's built-in cross-correlation-based algorithm. Chromatic aberration was corrected in FIJI using the plugin BunwarpJ[1] (Sorzano et al., 2005) by applying elastic transformations generated from stacks of embedded TetraspeckTM beads (Z7279, Thermo Fisher Scientific, Waltham, MA, United States).

Cluster Analysis of *Direct* Stochastic Optical Reconstruction Microscopy Data

For cluster analysis, a custom-written python script applying the DBSCAN algorithm on the localization data was used. It identified GABA-A receptor α2 clusters by applying the parameters "epsilon" of 20 nm and "minPoints" of 3. Cluster densities were calculated from the number of clusters detected by DBSCAN divided by the area of the region of interest. Non-parametric Mann–Whitney *U* test was applied in Origin for testing statistical significance.

DATA AVAILABILITY STATEMENT

The raw data supporting the conclusions of this article will be made available by the authors, without undue reservation.

---

[1] https://imagej.net/BUnwarpJ

ETHICS STATEMENT

The animal study was reviewed and approved by Regierung von Unterfranken, Approval # 55.2.2-2532-2-811.

AUTHOR CONTRIBUTIONS

AK and GB: investigation (lead), visualization (equal) writing–original draft (equal), and writing–review and editing (equal). DJ: investigation (supporting), visualization (equal), writing–original draft (equal), and writing–review and editing (equal). EP, MB, DT, and DAH: investigation (supporting). SD: investigation (supporting), visualization (supporting), and funding acquisition (supporting). CV and AB: supervision (supporting). MS: conceptualization (supporting), funding acquisition (equal), supervision (equal), visualization (supporting), writing–original draft (supporting), and writing–review and editing (lead). CW: conceptualization (lead), funding acquisition (equal), supervision (equal), investigation (supporting), visualization (supporting), writing–original draft (lead), and writing–review and editing (lead). All authors contributed to the article and approved the submitted version.

FUNDING

This work was supported by the Deutsche Forschungsgemein schaft (DFG) FOR3004 SYNABS to CV and MS, VI586 to CV, DO1257/4-1 to SD, and SA829/19-1 to MS. DJ was supported by the Graduate School of Life Sciences Würzburg.

ACKNOWLEDGMENTS

We thank Elke Maier und Ivan Simeonov for technical assistance in cell culture work. We thank Edward Lemke (European Molecular Biology Laboratory, Heidelberg) for the gift of the pCMV NES-PylRSAF/tRNAPyl plasmid. **Figure 1** is created with biorender.com.

SUPPLEMENTARY MATERIAL

The Supplementary Material for this article can be found online at: https://www.frontiersin.org/articles/10.3389/fnsyn.2021.727406/full#supplementary-material

Supplementary Figure 1 | Click sites of GABA-A receptor α2 subunit (green) SWISS modeled on α1 subunit template (PDB code: 6HUG). Amber sites (magenta and cyan) were introduced using PCR-based site-directed mutagenesis. The two mutants S181TAG and S201TAG (magenta) showed efficient incorporation of the unnatural amino acid TCO*A, when expressed in HEK-293-T cells and labeled with H-tet-Cy5 (**Figure 2**). In contrast, the two mutants K73TAG and K274TAG (cyan) showed significantly lower fluorescence labeling.

Supplementary Figure 2 | Confocal microscopy of GABA-A receptor S201TAG mutant. Top row: α2 click-mutant S201TAG shows similar performance as S181TAG for labeling surface α2 GABA-A receptor subunits by click-chemistry labeling. Modified α2 subunits are targeted by H-tet-Cy3, and anti-HA antibody labeling is applied to verify incorporation of TCO*. Negative controls omit ncAA application and show minor signal for both tetrazine and HA-tag labeling (-TCO). Scale bar = 5 μm.

Supplementary Figure 3 | Confocal microscopy testing the specific labeling of GABA-A receptor α1 subunits.GABA-A receptor subunits imaged on the equatorial membrane HEK-293-T cells with coexpression of β1 and γ2 subunits to ensure proper surface delivery of receptors using a confocal laser scanning microscope. First row: α1 click-mutant S181TAG shows slightly lower performance compared to S181TAG in α2 subunits, click-chemistry labeling of incorporated ncAA TCO* using H-tet-Cy5 (magenta) and HA-Tag labeling (green) serving as positive control for incorporation of the unnatural amino acid. Negative controls include omission of the ncAA after transfection of the S181TAG mutant (middle) and barely no H-tet-Cy5 signal (magenta) on WT α2 receptors (green) (bottom). Scale bar = 10 μm.

Supplementary Figure 4 | Evaluating effect of fluorophore selection on cluster detection. *d*STORM images of immunolabeled HA-tag modified (HA-Cy5, magenta) and click-chemistry labeled S181TAG GABA-A receptor α2 subunits (tet-CF568, green) on identical HEK-293-T cell membranes. Right, DBSCAN cluster analysis shows similar trends toward higher labeling density using click-chemistry labeling (tet, filled symbols) compared to anti-HA (HA, open symbols) antibody labeling, independent of conjugated fluorophore. Scale bar = 2 μm.

Supplementary Figure 5 | Absorption (black), emission (magenta) spectra, and turn-on ratios of Pyr-tet-ATTO643 applied in this study. **(a)** Absorption and corresponding fluorescence spectrum of Pyr-tet-ATTO643. **(b)** Relative fluorescence increase of Pyr-tet-ATTO643 normalized on initial fluorescence before the addition of 25 μM TCO*.

REFERENCES

Ali Rodriguez, R., Joya, C., and Hines, R. M. (2018). Common ribs of inhibitory synaptic dysfunction in the umbrella of neurodevelopmental disorders. *Front. Mol. Neurosci.* 11:132. doi: 10.3389/fnmol.2018.00132

Barnard, E. A., Skolnick, P., Olsen, R. W., Mohler, H., Sieghart, W., Biggio, G., et al. (1998). International union of pharmacology. XV. subtypes of gamma-aminobutyric acid(a) receptors: classification on the basis of subunit structure and receptor function. *Pharmacol. Rev.* 50, 291–313.

Beghein, E., and Gettemans, J. (2017). Nanobody technology: a versatile toolkit for microscopic imaging, protein-protein interaction analysis, and protein function exploration. *Front. Immunol.* 8:771. doi: 10.3389/fimmu.2017.00771

Beliu, G., Altrichter, S., Guixa-Gonzalez, R., Hemberger, M., Brauer, I., Dahse, A. K., et al. (2021). Tethered agonist exposure in intact adhesion/class B2 GPCRs through intrinsic structural flexibility of the GAIN domain. *Mol. Cell* 81, 905–921e5. doi: 10.1016/j.molcel.2020.12.042

Beliu, G., Kurz, A. J., Kuhlemann, A. C., Behringer-Pliess, L., Meub, M., Wolf, N., et al. (2019). Bioorthogonal labeling with tetrazine-dyes for super-resolution microscopy. *Commun. Biol.* 2:261. doi: 10.1038/s42003-019-0518-z

Bessa-Neto, D., Kuhlemann, A., Beliu, G., Pecoraro, V., Doose, S., Retailleau, N., et al. (2021). Bioorthogonal labeling of transmembrane proteins with non-canonical amino acids allows access to masked epitopes in live neurons. *bioRxiv* [Preprint] doi: 10.1101/2021.02.27.433189

Chin, J. W. (2014). Expanding and reprogramming the genetic code of cells and animals. *Annu. Rev. Biochem.* 83, 379–408.

Crosby, K. C., Gookin, S. E., Garcia, J. D., Hahm, K. M., Dell'Acqua, M. L., and Smith, K. R. (2019). Nanoscale subsynaptic domains underlie the organization of the inhibitory synapse. *Cell Rep.* 26, 3284–3297.e3. doi: 10.1016/j.celrep.2019.02.070

Dalmau, J., Geis, C., and Graus, F. (2017). Autoantibodies to synaptic receptors and neuronal cell surface proteins in autoimmune diseases of the central nervous system. *Physiol. Rev.* 97, 839–887.

de Jonge, J. C., Vinkers, C. H., Hulshoff Pol, H. E., and Marsman, A. (2017). GABAergic mechanisms in schizophrenia: linking postmortem and in vivo studies. *Front. Psychiatry* 8:118. doi: 10.3389/fpsyt.2017.00118

de Luca, E., Ravasenga, T., Petrini, E. M., Polenghi, A., Nieus, T., Guazzi, S., et al. (2017). Inter-synaptic lateral diffusion of GABAA receptors shapes inhibitory synaptic currents. *Neuron* 95, 63–69.e5. doi: 10.1016/j.neuron.2017.06.022

Du, J., Lu, W., Wu, S., Cheng, Y., and Gouaux, E. (2015). Glycine receptor mechanism elucidated by electron cryo-microscopy. *Nature* 526, 224–229. doi: 10.1038/nature14853

Ernst, R. J., Krogager, T. P., Maywood, E. S., Zanchi, R., Beranek, V., Elliott, T. S., et al. (2016). Genetic code expansion in the mouse brain. *Nat. Chem. Biol.* 12, 776–778.

Govindpani, K., Calvo-Flores Guzman, B., Vinnakota, C., Waldvogel, H. J., Faull, R. L., and Kwakowsky, A. (2017). Towards a better understanding of GABAergic remodeling in Alzheimer's disease. *Int. J. Mol. Sci* 18:1813. doi: 10.3390/ijms18081813

Gray, E. G. (1969). Electron microscopy of excitatory and inhibitory synapses: a brief review. *Prog. Brain Res.* 31, 141–155.

Guo, C. Y., Gelfand, J. M., and Geschwind, M. D. (2020). Anti-gamma-aminobutyric acid receptor type A encephalitis: a review. *Curr. Opin. Neurol.* 33, 372–380. doi: 10.1097/WCO.0000000000000814

Gustafsson, M. G. (2000). Surpassing the lateral resolution limit by a factor of two using structured illumination microscopy. *J. Microsci.* 198, 82–87. doi: 10.1046/j.1365-2818.2000.00710.x

Haselmann, H., Mannara, F., Werner, C., Planaguma, J., Miguez-Cabello, F., Schmidl, L., et al. (2018). Human autoantibodies against the AMPA receptor subunit GluA2 induce receptor reorganization and memory dysfunction. *Neuron* 100, 91–105e9. doi: 10.1016/j.neuron.2018.07.048

Heilemann, M., van de Linde, S., Schuttpelz, M., Kasper, R., Seefeldt, B., Mukherjee, A., et al. (2008). Subdiffraction-resolution fluorescence imaging with conventional fluorescent probes. *Angew. Chem. Int. Ed. Engl.* 47, 6172–6176. doi: 10.1002/anie.200802376

Kang, J. Y., Kawaguchi, D., Coin, I., Xiang, Z., O'Leary, D. D., Slesinger, P. A., et al. (2013). In vivo expression of a light-activatable potassium channel using unnatural amino acids. *Neuron* 80, 358–370. doi: 10.1016/j.neuron.2013.08.016

Lee, S. H., Jin, C., Cai, E., Ge, P., Ishitsuka, Y., Teng, K. W., et al. (2017). Super-resolution imaging of synaptic and extra-synaptic AMPA receptors with different-sized fluorescent probes. *Elife* 6:e27744.

Liauw, B. W., Afsari, H. S., and Vafabakhsh, R. (2021). Conformational rearrangement during activation of a metabotropic glutamate receptor. *Nat. Chem. Biol.* 17, 291–297. doi: 10.1038/s41589-020-00702-5

Maric, H. M., Hausrat, T. J., Neubert, F., Dalby, N. O., Doose, S., Sauer, M., et al. (2017). Gephyrin-binding peptides visualize postsynaptic sites and modulate neurotransmission. *Nat. Chem. Biol.* 13, 153–160. doi: 10.1038/nchembio.2246

Mody, I., and Pearce, R. A. (2004). Diversity of inhibitory neurotransmission through GABA(A) receptors. *Trends Neurosci.* 27, 569–575. doi: 10.1016/j.tins.2004.07.002

Neubert, F., Beliu, G., Terpitz, U., Werner, C., Geis, C., Sauer, M., et al. (2018). Bioorthogonal click chemistry enables site-specific fluorescence labeling of functional NMDA receptors for super-resolution imaging. *Angew. Chem. Int. Ed. Engl.* 57, 16364–16369. doi: 10.1002/anie.201808951

Nikic, I., Estrada Girona, G., Kang, J. H., Paci, G., Mikhaleva, S., Koehler, C., et al. (2016). Debugging eukaryotic genetic code expansion for site-specific click-PAINT super-resolution microscopy. *Angew. Chem. Int. Ed. Engl.* 55, 16172–16176. doi: 10.1002/anie.201608284

Nikic, I., Kang, J. H., Girona, G. E., Aramburu, I. V., and Lemke, E. A. (2015). Labeling proteins on live mammalian cells using click chemistry. *Nat. Protoc.* 10, 780–791. doi: 10.1038/nprot.2015.045

Nikic-Spiegel, I. (2020). Expanding the genetic code for neuronal studies. *Chembiochem* 21, 3169–3179. doi: 10.1002/cbic.202000300

Olsen, R. W., and Sieghart, W. (2008). International union of pharmacology. LXX. Subtypes of gamma-aminobutyric Acid(A) receptors: classification on the basis of subunit composition, pharmacology, and function. update. *Pharmacol. Rev.* 60, 243–260. doi: 10.1124/pr.108.00505

Olsen, R. W., and Sieghart, W. (2009). GABA A receptors: subtypes provide diversity of function and pharmacology. *Neuropharmacology* 56, 141–148. doi: 10.1016/j.neuropharm.2008.07.045

Opazo, F., Levy, M., Byrom, M., Schafer, C., Geisler, C., Groemer, T. W., et al. (2012). Aptamers as potential tools for super-resolution microscopy. *Nat. Methods* 9, 938–939. doi: 10.1038/nmeth.2179

Ovesny, M., Krizek, P., Borkovec, J., Svindrych, Z., and Hagen, G. M. (2014). ThunderSTORM: a comprehensive ImageJ plug-in for PALM and STORM data analysis and super-resolution imaging. *Bioinformatics* 30, 2389–2390. doi: 10.1093/bioinformatics/btu202

Petrini, E. M., Nieus, T., Ravasenga, T., Succol, F., Guazzi, S., Benfenati, F., et al. (2011). Influence of GABAAR monoliganded states on GABAergic responses. *J. Neurosci.* 31, 1752–1761. doi: 10.1523/JNEUROSCI.1453-10.2011

Petrini, E. M., Ravasenga, T., Hausrat, T. J., Iurilli, G., Olcese, U., Racine, V., et al. (2014). Synaptic recruitment of gephyrin regulates surface GABAA receptor dynamics for the expression of inhibitory LTP. *Nat. Commun.* 5:3921. doi: 10.1038/ncomms4921

Polenghi, A., Nieus, T., Guazzi, S., Gorostiza, P., Petrini, E. M., and Barberis, A. (2020). Kainate receptor activation shapes short-term synaptic plasticity by controlling receptor lateral mobility at glutamatergic synapses. *Cell Rep.* 31:107735. doi: 10.1016/j.celrep.2020.107735

Ramil, C. P., and Lin, Q. (2013). Bioorthogonal chemistry: strategies and recent developments. *Chem. Commun.* 49, 11007–11022. doi: 10.1039/c3cc44272a

Schaefer, N., Janzen, D., Bakirci, E., Hrynevich, A., Dalton, P. D., and Villmann, C. (2019). 3D Electrophysiological measurements on cells embedded within fiber-reinforced matrigel. *Adv. Healthcare Mater.* 8:1801226. doi: 10.1002/adhm.201801226

Schindelin, J., Arganda-Carreras, I., Frise, E., Kaynig, V., Longair, M., Pietzsch, T., et al. (2012). Fiji: an open-source platform for biological-image analysis. *Nat. Methods* 9, 676–682. doi: 10.1038/nmeth.2019

Schlichthaerle, T., Eklund, A. S., Schueder, F., Strauss, M. T., Tiede, C., Curd, A., et al. (2018). Site-specific labeling of affimers for DNA-PAINT microscopy. *Angew. Chem. Int. Ed. Engl.* 57, 11060–11063. doi: 10.1002/anie.201804020

Schnell, U., Dijk, F., Sjollema, K. A., and Giepmans, B. N. (2012). Immunolabeling artifacts and the need for live-cell imaging. *Nat. Methods* 9, 152–158.

Serfling, R., Seidel, L., Bock, A., Lohse, M. J., Annibale, P., and Coin, I. (2019). Quantitative single-residue bioorthogonal labeling of G protein-coupled receptors in live cells. *ACS Chem. Biol.* 14, 1141–1149. doi: 10.1021/acschembio.8b01115

Siddig, S., Aufmkolk, S., Doose, S., Jobin, M. L., Werner, C., Sauer, M., et al. (2020). Super-resolution imaging reveals the nanoscale organization of metabotropic glutamate receptors at presynaptic active zones. *Sci. Adv.* 6:eaay7193. doi: 10.1126/sciadv.aay7193

Sorzano, C. O., Thevenaz, P., and Unser, M. (2005). Elastic registration of biological images using vector-spline regularization. *IEEE Trans. Biomed. Eng.* 52, 652–663. doi: 10.1109/TBME.2005.844030

Spatola, M., Petit-Pedrol, M., Simabukuro, M. M., Armangue, T., Castro, F. J., Barcelo Artigues, M. I., et al. (2017). Investigations in GABAA receptor antibody-associated encephalitis. *Neurology* 88, 1012–1020. doi: 10.1212/WNL.0000000000003713

Thorn, K. (2017). Genetically encoded fluorescent tags. *Mol. Biol. Cell* 28, 848–857. doi: 10.1091/mbc.e16-07-0504

Tretter, V., Jacob, T. C., Mukherjee, J., Fritschy, J. M., Pangalos, M. N., and Moss, S. J. (2008). The clustering of GABA(A) receptor subtypes at inhibitory synapses is facilitated via the direct binding of receptor alpha 2 subunits to gephyrin. *J. Neurosci.* 28, 1356–1365. doi: 10.1523/JNEUROSCI.5050-07.2008

Uttamapinant, C., Howe, J. D., Lang, K., Beranek, V., Davis, L., Mahesh, M., et al. (2015). Genetic code expansion enables live-cell and super-resolution imaging of site-specifically labeled cellular proteins. *J. Am. Chem. Soc.* 137, 4602–4605.

van de Linde, S., Loschberger, A., Klein, T., Heidbreder, M., Wolter, S., Heilemann, M., et al. (2011). Direct stochastic optical reconstruction microscopy with standard fluorescent probes. *Nat. Protoc.* 6, 991–1009. doi: 10.1038/nprot.2011.336

Vien, T. N., Modgil, A., Abramian, A. M., Jurd, R., Walker, J., Brandon, N. J., et al. (2015). Compromising the phosphodependent regulation of the GABAAR beta3 subunit reproduces the core phenotypes of autism spectrum disorders. *Proc. Natl. Acad. Sci. U.S.A.* 112, 14805–14810. doi: 10.1073/pnas.1514657112

Waldchen, F., Schlegel, J., Gotz, R., Luciano, M., Schnermann, M., Doose, S., et al. (2020). Whole-cell imaging of plasma membrane receptors by 3D lattice light-sheet dSTORM. *Nat. Commun.* 11:887. doi: 10.1038/s41467-020-14731-0

Wang, Y. C., Dzyubenko, E., Sanchez-Mendoza, E. H., Sardari, M., Silva de Carvalho, T., Doeppner, T. R., et al. (2018). Postacute delivery of GABAA alpha5 antagonist promotes postischemic neurological recovery and peri-infarct brain remodeling. *Stroke* 49, 2495–2503. doi: 10.1161/STROKEAHA.118.021378

Waterhouse, A., Bertoni, M., Bienert, S., Studer, G., Tauriello, G., Gumienny, R., et al. (2018). SWISS-MODEL: homology modelling of protein structures and complexes. *Nucleic Acids Res.* 46, W296–W303.

Weber, K., Rathke, P. C., and Osborn, M. (1978). Cytoplasmic microtubular images in glutaraldehyde-fixed tissue culture cells by electron microscopy and by immunofluorescence microscopy. *Proc. Natl. Acad. Sci. U.S.A.* 75, 1820–1824. doi: 10.1073/pnas.75.4.1820

Willems, J., de Jong, A. P. H., Scheefhals, N., Mertens, E., Catsburg, L. A. E., Poorthuis, R. B., et al. (2020). ORANGE: a CRISPR/Cas9-based genome editing toolbox for epitope tagging of endogenous proteins in neurons. *PLoS Biol.* 18:e3000665. doi: 10.1371/journal.pbio.3000665

Wisden, W., and Seeburg, P. H. (1992). GABAA receptor channels: from subunits to functional entities. *Curr. Opin. Neurobiol.* 2, 263–269. doi: 10.1016/0959-4388(92)90113-y

,

Wolter, S., Loschberger, A., Holm, T., Aufmkolk, S., Dabauvalle, M. C., van de Linde, S., et al. (2012). Rapidstorm: accurate, fast open-source software for localization microscopy. *Nat. Methods* 9, 1040–1041. doi: 10.1038/nmeth.2224

Conflict of Interest: The authors declare that the research was conducted in the absence of any commercial or financial relationships that could be construed as a potential conflict of interest.

frontiers in Synaptic Neuroscience

MINI REVIEW
published: 03 January 2022
doi: 10.3389/fnsyn.2021.798204

(M)Unc13s in Active Zone Diversity: A *Drosophila* Perspective

Chengji Piao [1,2] ***and Stephan J. Sigrist*** [1,2*]

[1] *Institute for Biology/Genetics, Freie Universität Berlin, Berlin, Germany,* [2] *NeuroCure Cluster of Excellence, Charité Universitätsmedizin, Berlin, Germany*

The so-called active zones at pre-synaptic terminals are the ultimate filtering devices, which couple between action potential frequency and shape, and the information transferred to the post-synaptic neurons, finally tuning behaviors. Within active zones, the release of the synaptic vesicle operates from specialized "release sites." The (M)Unc13 class of proteins is meant to define release sites topologically and biochemically, and diversity between Unc13-type release factor isoforms is suspected to steer diversity at active zones. The two major Unc13-type isoforms, namely, Unc13A and Unc13B, have recently been described from the molecular to the behavioral level, exploiting *Drosophila* being uniquely suited to causally link between these levels. The exact nanoscale distribution of voltage-gated Ca^{2+} channels relative to release sites ("coupling") at pre-synaptic active zones fundamentally steers the release of the synaptic vesicle. Unc13A and B were found to be either tightly or loosely coupled across *Drosophila* synapses. In this review, we reported recent findings on diverse aspects of *Drosophila* Unc13A and B, importantly, their nano-topological distribution at active zones and their roles in release site generation, active zone assembly, and pre-synaptic homeostatic plasticity. We compared their stoichiometric composition at different synapse types, reviewing the correlation between nanoscale distribution of these two isoforms and release physiology and, finally, discuss how isoform-specific release components might drive the functional heterogeneity of synapses and encode discrete behavior.

Keywords: active zone diversity, pre-synaptic plasticity, active zone ultrastructure, release sites, synaptic transmission

Edited by:
Thomas A. Blanpied,
University of Maryland, United States

Reviewed by:
J. Troy Littleton,
Massachusetts Institute of Technology, United States
Tobias Moser,
University Medical Center Göttingen, Germany

****Correspondence:***
Stephan J. Sigrist
stephan.sigrist@fu-berlin.de

Received: *19 October 2021*
Accepted: *29 November 2021*
Published: *03 January 2022*

Citation:
Piao C and Sigrist SJ (2022) (M)Unc13s in Active Zone Diversity: A Drosophila Perspective.
Front. Synaptic Neurosci. 13:798204.
doi: 10.3389/fnsyn.2021.798204

INTRODUCTION

Upon the arrival of action potentials at the pre-synaptic terminal, neurotransmitters stored at synaptic vesicles (SVs) are released from a specialized region of the plasma membrane called active zones (AZs). Although AZs largely share the same complement of proteins, the probability of SV release varies tremendously across different neurons and even between AZs formed by the same neuron (Akbergenova et al., 2018), resulting, *inter alia*, in differences in the short-term plasticity of SV release. While short-term facilitation is typical for synapses with a high initial release probability, short-term depression is often observed at ones with a low initial release probability (Fioravante and Regehr, 2011). Importantly, synapses with different adaptive behaviors might convey signals in defined frequency ranges.

Aspects of functional diversity have previously been attributed to various AZ sizes and shapes (Atwood and Karunanithi, 2002; Moser et al., 2020; Wichmann and Kuner, 2022). The number, density, and distribution of Ca^{2+} channels in or near the AZ area account for AZ heterogeneity as well (Holderith et al., 2012; Eltes et al., 2017). The functional differentiation of AZs can also be achieved by building synapses from distinct molecules or isoforms or varied quantities, densities, and nanoscale arrangements of the very same molecule (Nusser, 2018; Karlocai et al., 2021). The Unc13 protein family is of particular relevance here. A recent enlightening review by Jeremy Dittman highlighted Unc13s as the hubs of AZs, coordinating diverse aspects of synaptic transmission (Dittman, 2019). The roles of Unc13 are fulfilled by different isoforms. Mammals contain three brain-specific Munc13 isoforms, namely, Munc13-1, bMunc13-2, and Munc13-3. Munc13-1 is the dominant isoform expressed throughout the brain, while Munc13-2 and Munc13-3 display strikingly distinct expression patterns. Munc13-2 is preferentially present in the rostral brain regions, and Munc13-3 is almost exclusively present in the cerebellum of rats (Augustin et al., 1999). Synapses employing different Unc13 isoforms as priming factors exhibit different forms of short-term plasticity (Rosenmund et al., 2002). However, the neonatal lethality of Munc13-1/2 double mutants makes it difficult to decipher how their distinct release attributes contribute differently to information coding and behavior. Luckily, recent studies of two Unc13 isoforms in *Drosophila* have linked their molecular functions to discrete behavioral components (**Table 1**), making the protein a great candidate to unveil the design principles tuning functional diversity over a spectrum of synapse types.

THE FLY UNC13 ISFORMS: UNC13A VS. UNC13B

The (only) fly *Unc13* locus was identified in 1999 (Aravamudan et al., 1999). In line with the function of its *Caenorhabditis elegans* and mammalian homologs, characterizing a *Drosophila unc13* null mutant revealed its essential role for SV exocytosis *per se*. The locus generates two isoforms, namely, Unc13A and Unc13B, which differ in their extended N-termini. The identical C-terminal region encompasses a C1 domain, a regulatory C2B domain, followed by a large catalytic Munc homology (MUN) domain and a C2C domain (**Figure 1A**). This arrangement shared by the isoforms is highly conserved across evolution, suggesting conserved functions of the C-terminal fragment in SV priming and molecularly defining vesicle release sites. Reconstitution data suggest that the entire C1-C2B-MUN-C2C complex can bridge the plasma and vesicle membranes; the very C-terminal part C2C domain is thought to be critical for this ability (Liu et al., 2016; Quade et al., 2019). The central extent of the homologous region, known as the MUN domain (Xu et al., 2017), is key for the Unc13 SV priming function and is the minimal Unc13 protein domain required to carry out the priming activity (Basu et al., 2005). However, how the MUN domain is involved in the SNARE assembly exactly remains largely elusive. It has been suggested that its weak interaction with the SNARE syntaxin-1 catalyzes the transition of closed syntaxin-1 to an open conformation, thus enabling the SNARE assembly (Ma et al., 2011; Magdziarek et al., 2020). In mammals, a member of the extended (M)Unc13 family, CAPS, shares only the Unc13 MUN domain (Koch et al., 2000) and is essential for dense-core vesicle exocytosis (Berwin et al., 1998; Rupnik et al., 2000; Liu et al., 2008). A CAPS homolog with a related function is also found in *Drosophila* (Renden et al., 2001). The MUN domain may also interact with synaptobrevin-2 and recruit vesicles. Other recent studies have proposed a role of the (M)unc13-1 MUN domain cooperating with (M)unc18-1 in orchestrating the SNARE assembly by stabilizing the template complex formed by Unc18, syntaxin-1, and synaptobrevin-2 (Wang et al., 2019; Shu et al., 2020). The C2B domain, which can bind to Ca^{2+} and phosphatidylinositolphosphate, likely acts here as a release probability and short-term plasticity modulator (Shin et al., 2010); the C1 domain, positioned next to the C2B domain, is meant to regulate diacylglycerol-dependent release augmentation (Basu et al., 2007). In addition to these two signaling domains, Unc13A harbors a calmodulin-binding sequence (CAM) that has been shown to be essential for regulating the priming activity and short-term plasticity (Lipstein et al., 2012, 2013; Piotrowski et al., 2020), whereas it does not exist in the N-terminal part of the B isoform (Xu et al., 1998). The N-terminus of Unc13A also comprises a proline-rich motif (PxxP) binding to the SH3 domains of Rim-binding protein *in vitro* (Bohme et al., 2016). The very similar domain structure mode is shared by all mammalian Unc13 members: Munc13-1, ubMunc13-2, bMunc13-2 and Munc13-3, and Unc13-L and Unc13-S in *C. elegans*. The canonical C-terminal CAM-C1-C2B-MUN-C2C complex presents in all Munc13 isoforms, and the N-terminal regions of Munc13-1 and ubMunc13-2 contain an additional C2A domain, which is absent in fly. The calmodulin-interacting motif and C2A domain also exist in nematode Unc13-L.

DISTINCT NANOSCOPIC DISTRIBUTIONS OF UNC13A AND UNC13B IN ACTIVE ZONES

To couple the SV release to electrical stimulation by action potentials, calcium ions entering the cell through voltage-gated Ca^{2+} channels activate the Ca^{2+} sensor synaptotagmin on the SVs to trigger fusion. The efficacy of synaptic transmission depends largely on the distance between SVs and voltage-gated Ca^{2+} channels. The two major fly isoforms of Unc13, Unc13A, and Unc13B are found co-expressed within individual AZs but astonishingly with different nanoscopic patterns. The nano-topology was first mapped at the peripheral neuromuscular junctions (NMJs) of *Drosophila* larvae using dual-color super-resolution-stimulated emission depletion (STED) microscopy (Bohme et al., 2016). The pre-synaptic voltage-gated Ca^{2+} channel α 1 subunit encoded by *Cacophony* forms a cluster in the center of AZ labeled by Bruchpilot (BRP) in *Drosophila* (Kawasaki et al., 2004; Fouquet et al., 2009). Unc13A was localized closer to the Cacophony cluster. Unc13B, in contrast, was found at a greater distance (**Figure 1B**). The average

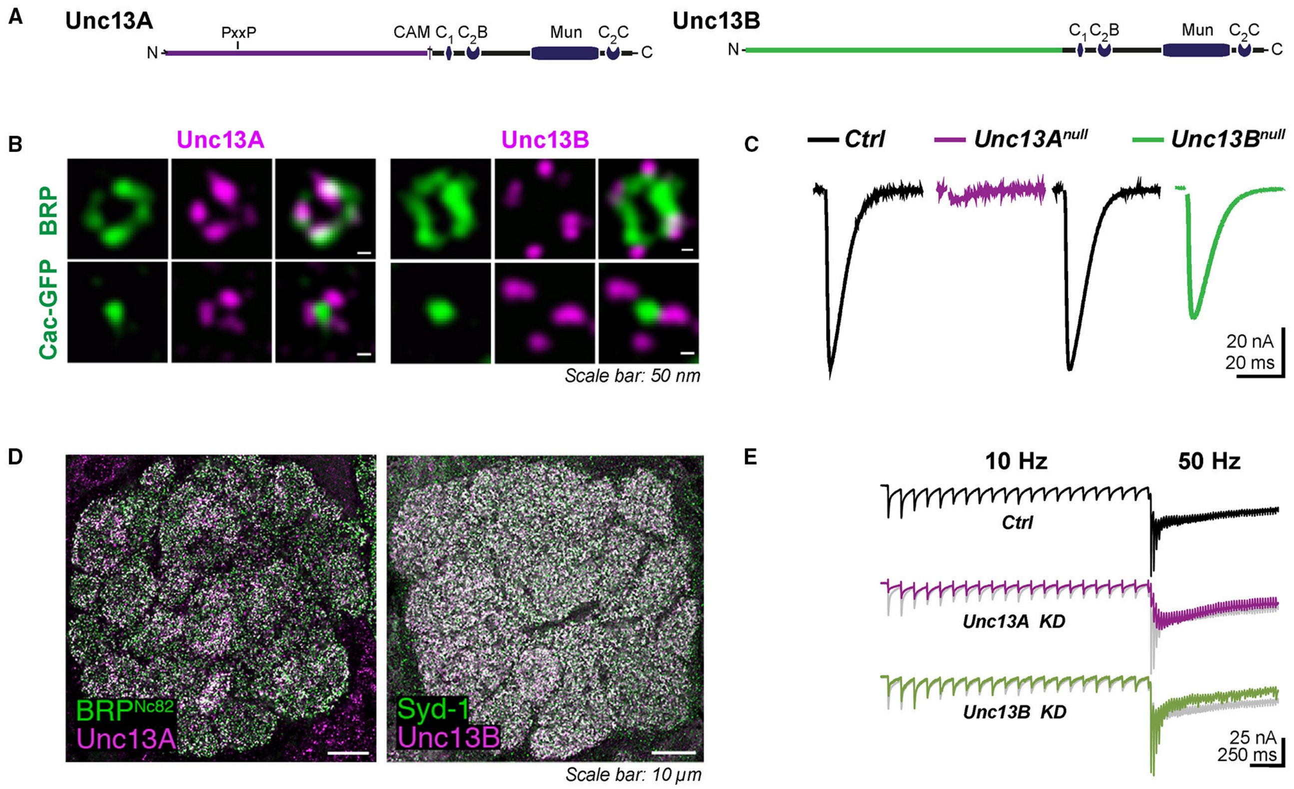

FIGURE 1 | (A) Domain structures of Unc13A and Unc13B. **(B)** Nano-topology of Unc13A and B at active zone (AZ) and their coupling distance to Ca^{2+} channels at *Drosophila* neuromuscular junctions (NMJs) shown by super-resolution-stimulated emission depletion microscopy (STED) images. Synaptic transmission at NMJ is dominantly controlled by Unc13A. Null mutants of *Unc13B* only showed a mild reduction in the response evoked, recording traces shown in **(C)**. **(D)** Expression pattern of Unc13A and Unc13B in the antennal lobe of *Drosophila*. **(E)** Synaptic currents evoked recorded at fast-depressed olfactory receptor neuron (ORN)-to-projection neuron (PN) synapses. **(A–C)** are modified from Bohme et al. (2016) and **(D,E)** are modified from Fulterer et al. (2018).

distances from the AZ center defined by the center of the BRP signal (overlaying the AZ-central Cacophony cluster) for Unc13A and Unc13B were measured to be about 70 nm and 120 nm at NMJ, respectively. This "design rule" of distinctly patterned nanodomain spacing of the two components relative to the Ca^{2+} channels was subsequently found to apply to all synapses studied so far in the central nervous system (CNS) of *Drosophila*. Concretely, the A isoform was found at 74–83 nm from the center of AZ, while the B isoform was, with a distance of 102–115 nm, at different relay synapses within the *Drosophila* olfactory system, including olfactory receptor neuron (ORN), projection neuron (PN), and Kenyon cell (KC) output synapses (Fulterer et al., 2018; Woitkuhn et al., 2020). Moreover, this principle of Ca^{2+} channel coupling distance for the two isoforms applies to not only excitatory but also inhibitory synapses. A three-channel two-dimensional time-gated STED (gSTED) imaging on PN-derived AZs in the lateral horn (LH) showed that Unc13A localized at about 60 nm relative to the AZ center, and the B isoform spots were still found at further distances at inhibitory PN (iPN) output synapses. These were the same as the coupling distances at the terminals of cholinergic excitatory PN (ePN) in the LH (Pooryasin et al., 2021).

Which molecular scenario might underlie this astonishing degree of release site nanoscale patterning? In addition to the release sites proper, an evolutionarily conserved set of AZ scaffold proteins has been suggested to function in the spatial organization of synapse nano-topology, including RIM, Rim-binding protein (RimBP), Liprin-α, and the glutamate (E), leucine (L), lysine (K), and serine (S) rich protein (ELKS)-family BRP. The Unc13A/B nano-topology design present across *Drosophila* synapses is seemingly tuned by two clusters of AZ scaffold proteins, namely, BRP/RimBP and Syd-1/Liprin-α complex. Syd-1 and Liprin-α, according to intravital live imaging, arrive early at nascent AZs and initiate the AZ assembly (Owald et al., 2010). Together with this complex, Unc13B clusters appear before the emergence of Unc13A along the AZ maturation trajectory and, finally (after synapse maturation is completed), colocalize with them at the outer edge of matured AZs at NMJ. Syd-1 and Liprin-α may recruit Unc13B by interacting with its N-terminus, which normally plays a role in the localization of Unc13 protein. The Unc13B accumulation at NMJ AZs depends genetically on the Syd-1/Liprin-α complex. Its expression was dramatically reduced at the NMJs of *liprin-α* and *syd-1* mutants, whereas *brp* knockdown or *Rimbp* deletion had no effect on Unc13B levels. In contrast, the A isoform is recruited via the

AZ scaffold BRP/RimBP complex. The N-terminus is essential here for the AZ anchoring of Unc13A and interacts directly with the SH3 domain of RimBP and the N-terminal region of BRP (Bohme et al., 2016). Unc13A levels at both the larval NMJ and adult brain of *Drosophila* are tightly regulated by BRP levels. An additional gene copy number of BRP drives the upscaling of Unc13A, whereas pan-neural *brp* knockdown results in the almost complete loss of Unc13A (Huang et al., 2020; Huang and Sigrist, 2021).

Importantly, though both isoforms in the *Drosophila* brain are expressed in all neuropile areas, their relative abundance varies greatly among different types of synapses. Within the antennal lobe, the first processing center of the fly olfactory system, ORN-derived AZs display a high release probability (Kazama and Wilson, 2008) and are enriched for Unc13A, shown by STED to be tightly coupled to the Ca^{2+} channels. In contrast, the slow and facilitating local interneuron (LN) output synapses appear as Unc13B-dominated (**Figure 1D**). The second-order neurons of the olfactory circuit, called PNs, convey information from the antennal lobes to both the mushroom body calyx and LH. The PN terminals synapse onto KC dendrites in the calyx and PN-output synapses here are strongly enriched for Unc13B (Fulterer et al., 2018). Interestingly, the ratio of Unc13A/B in the higher memory center, known as the mushroom body, in turn, shows differences between specific bundles of axons ("lobes") of mushroom body intrinsic neurons. The A isoform here is enriched in the two prime (α' and β') lobes and the γ lobe, while Unc13B exhibits higher levels in the α and β lobes (Woitkuhn et al., 2020). Additionally, the two isoforms are recruited to the AZ via the AZ master proteins BRP and Syd-1, respectively, across the synapses of the *Drosophila* brain (Fulterer et al., 2018; Huang et al., 2020). Hereby, the relative levels of two Unc13 isoforms at different synapses correlate strongly with the BRP/Syd-1 ratio. The AZs rich in Unc13A or B show likely contrasting release characteristics, which will be discussed later. The molecular abundance differences of two isoforms across the CNS probably produce functional differentiation, which is important for the information transfer within neuron networks.

UNC13A AND UNC13B CONTROL PHASIC VS. TONIC RELEASE ACROSS *DROSOPHILA* BRAIN SYNAPSES

As has been said above, analyzing the two isoforms unmasked drastic differences in their nanoscopic distribution at the level of the individual AZ. Subsequent work across several synapses showed consistently that the two isoforms, as suggested by their either tight or loose nanoscale coupling to the central Ca^{2+} channel cluster, promote distinct release features concerning short-term synaptic plasticity: Unc13A mediates fast phasic and Unc13B slow tonic release. We sketch these findings in the following.

Synaptic transmission at the larval NMJ seems to be dominantly controlled by Unc13A, as Unc13A deletion at NMJs decreased the evoked neurotransmitter release by almost 90% (**Figure 1C**) and greatly reduced the number of docked SVs close to the Ca^{2+} source (Bohme et al., 2016). On the single AZ level, the evoked SV release correlated strongly with the local BRP and Unc13A level (Peled et al., 2014; Reddy-Alla et al., 2017). The relation between evoked release and BRP was shown to be mediated by Unc13A, which, in turn, is stoichiometrically recruited by BRP. Indeed, the discrete clusters of Unc13A within individual AZs, at NMJ AZs typically 4–5, might well represent discrete SV release sites (Reddy-Alla et al., 2017). Here, the functional aspect of Unc13A generating "release sites" is obviously executed by the conserved C-terminal part of Unc13A, while the topological aspect of stable anchoring in defined nanoscopic positions depends on the Unc13A N-terminus. Expressing only the C-terminal part of it generates release sites at atypical locations (Reddy-Alla et al., 2017). This concept of Unc13 clusters forming release sites was independently described for central mammalian synapses (Sakamoto et al., 2018).

Tight and loose coupling to the Ca^{2+} channels of the two isoforms, sharing the very same C-terminal part, is thus associated with distinct release features and short-term synaptic plasticity, as best described at the first relay synapses of the fly olfactory circuit due to ideal electrophysiology recording conditions here. These ORN-to-PN synapses are cholinergic. Notably, in terms of post-synaptic signal reception, two components with distinct signaling kinetics were described pharmacologically at ORN-to-PN synapses, as a fast and a slow excitatory post-synaptic current (EPSC) component could be isolated when applying the nicotinic agonist imidacloprid or curare. The fast curare-sensitive component depressed more rapidly than the imidacloprid-sensitive component, presumably mediated by distinct types of acetylcholine receptors or distinct states of the same receptor (Nagel et al., 2015; Nagel and Wilson, 2016). As has been mentioned above, when knocking down the dominant Unc13A isoform at the ORN terminals, the fast, phasic response recorded at the PN was almost absent, indicated by a drastic reduction in peak amplitude and a delay in the time to peak. By contrast, Unc13B has a rather modest contribution to the signal transduction at ORN-to-PN synapses here, probably contributing to the tonic release component (**Figure 1E**). Taken together, these findings suggest the attractive idea that a specific release component, mediated by either Unc13A or B, might be "matched" to a specific post-synaptic neurotransmitter receptor, resulting in the establishment of two parallel "information channels" across one synapse.

The ORN terminals exhibit high release probability and feature a robust short-term depression upon repetitive stimulation. The loss of Unc13A at ORN-derived AZs results in a drastic shift toward short-term facilitation, suggesting that Unc13A dominates the SV release probability here (Fulterer et al., 2018). In line with this, transmission and short-term synaptic plasticity at KC-to-mushroom body output neuron γ1pedc> α/β synapses operate with a high SV release probability, which is promoted by Unc13A as well (Woitkuhn et al., 2020).

Although the Unc13B isoform seems to be somewhat dispensable at these synapses with a high release probability, it is clearly not just a functionally redundant "minor" member of

TABLE 1 | Unc13A vs. Unc13B in Ca^{2+} channel coupling distance and functions in *Drosophila*.

	Synapse type	**Unc13A**	**Unc13B**	**Method**	**References**
Average distance to Ca^{2+} channel/AZ center	NMJ	70 nm	120 nm	STED	Bohme et al., 2016
		76.8 nm	145 nm	Simulation	
	ORN-derived AZs at AL	83 ± 6 nm	115 ± 8 nm	STED	Fulterer et al., 2018
	LN-derived AZs at AL	74 ± 2 nm	102 ± 3 nm		
	PN-to-KC	74 ± 4 nm	102 ± 1 nm		
	ePN-to-LHN	61 ± 1 nm	101 ± 4 nm	gSTED	Pooryasin et al., 2021
	iPN-to-LHN	60 ± 2 nm	102 ± 4 nm		
	KC-derived AZs at MB lobes	100–150 nm	150–250 nm		Woitkuhn et al., 2020
SV release	NMJ	eEJC amplitude ↓↓↓ mEJC amplitude ↑ mEJC frequency ↑ PPR ↑ Time to peak ↑	eEJC amplitude ↓ mEJC amplitude ↔ mEJC frequency ↔ PPR ↔ (L3 stage)/↑ (L2 stage) Time to peak ↔	Two-electrode voltage clamp Current clamp	Bohme et al., 2016; Ramesh et al., 2021
	ORN-to-PN	EPSC amplitude ↓ PPR ↑ Time to peak ↑	EPSC amplitude ↔ (↓) PPR ↔ Time to peak ↔	*In vivo* whole-cell patch clamp	Fulterer et al., 2018
	LN-to-LN	Peak amplitude ↔ Time to peak ↔	Peak amplitude ↓ Time to peak ↔		
	KC-to-MBON γ1pedc> α/β	EPSC amplitude ↓ Short-term depression ↓	/		Woitkuhn et al., 2020
	ePN-to-KC	MaxΔF/F$_0$ ↓ Time to peak ↑	MaxΔF/F$_0$ ↓ Time to peak ↔	*In vivo* calcium imaging	Pooryasin et al., 2021
		MaxΔF/F$_0$ ↓ ↓ Time to peak ↑			
Innate behavior	Heterozygous mutants	Ethanol preference ↑		CAFÉ assay	Das et al., 2013
		Ethanol sensitivity ↓		Ethanol LOR assay	Xu et al., 2018
	Kenyon cell	Odor avoidance ↔		T-maze	Bohme et al., 2019;
		Shock avoidance ↔			Woitkuhn et al., 2020
	ePN	Odor attraction ↓	Odor attraction ↑		Pooryasin et al., 2021
		Odor avoidance ↓	Odor avoidance ↓		
	iPN	Odor attraction ↔	Odor attraction ↔		
		Odor avoidance ↔	Odor avoidance ↔		
Memory	Kenyon cell	STM ↓↓	STM ↓		Bohme et al., 2019;
		MTM ↓↓	MTM ↓		Woitkuhn et al., 2020
		ASM ↓↓	ASM↔		
		ARM ↓	ARM↔		

AL, antennal lobe; ARM, anesthesia-resistant memory; ASM, anesthesia-sensitive memory; AZ, active zone; eEJC, evoked excitatory junction current; ePN, excitatory projection neuron; EPSC, excitatory postsynaptic current; gSTED, time-gated super-resolution stimulated emission depletion microscopy; iPN, inhibitory projection neuron; KC, Kenyon cell; LHN, lateral horn neuron; LN, local interneuron; MB, mushroom body; MBON, mushroom body output neuron; mEJC, miniature excitatory junction current; MTM, mid-term memory; NMJ, neuromuscular junction; ORN, olfactory receptor neuron; PN, projection neuron; PPR, paired pulse ratio; STED, super-resolution-stimulated emission depletion microscopy; STM, short-term memory.

the Unc13 family in the *Drosophila* CNS. As has been mentioned previously, the distribution of Unc13B is rather homogeneous over the antennal lobes of the fly brain, which matches the pattern of LN-derived AZs (Ng et al., 2002; Mosca and Luo, 2014). These inhibitory interneurons, unlike PNs, respond transiently to odor stimuli (Nagel et al., 2015). This attribute enables the activities of LNs to signal the onset/offset or concentration fluctuations of odor. The LNs receive diverse synaptic inputs, including excitatory synapses from ORN and PN, and inhibition from other LNs (Yaksi and Wilson, 2010). The LN-to-LN synapses are slow and facilitating (Nagel and Wilson, 2016). Intriguingly, Unc13B is the dominant isoform at these synapses. Knocking down of Unc13B at LN terminals greatly reduced the inhibitory transmission between LN and LN (Fulterer et al., 2018). The A isoform, though it coexists with Unc13B at this synapse type, has only an insignificant effect on synaptic transmission, implying that the B isoform functionality dictates the slow release character at these synapses.

In addition to these electrophysiological findings at different synapses, Ca^{2+} imaging conveyed a similar idea that Unc13A promotes a fast, transient release component, whereas Unc13B contributes to a slow and tonic component at the very same ePN-to-KC synapses in the mushroom body calyx (Pooryasin et al., 2021). Importantly, different Unc13 isoforms promoting distinct SV release components is not a unique phenomenon restricted to *Drosophila* or insects. Indeed, the nematode *C. elegans* also expresses two isoforms of Unc13, namely, a long form, Unc13-L, and a short one, Unc13-S, again differing in their N-termini. Unc13-L harbors a C2A domain, which is missing in the Unc13-S N-terminus. The long form localizes in the close proximity to the calcium entry site of *C. elegans* NMJ, while Unc13-S displays a more diffuse distribution. Unc13-L missing the N-terminal part also displayed diffuse axonal localization, suggesting the precise AZ location of the protein defined by its N-terminus as in *Drosophila*. The long form near the Ca^{2+} source promotes fast vesicular release, while the slow component is apparently mediated by both isoforms (Hu et al., 2013, 2015). Finally, different Munc13 isoforms were also found to mediate distinct components of short-term plasticity in mammals. Synapses employing bMunc13-2 get potentiated, while those relying on Munc13-1 get depressed upon repetitive stimulation (Rosenmund et al., 2002; Zhou et al., 2013; Kawabe et al., 2017). Thus, different Unc13 isoforms, obviously across evolution, endow synapses with different release kinetics and favor different forms of short-term plasticity, acting as different temporal filters of signal transduction (Mukunda and Narayanan, 2017) and contributing to the heterogeneity of information coding.

DISTINCT ROLES OF UNC13A AND B IN INFORMATION DECODING TO STEER OLFACTORY BEHAVIOR

Short-term plasticity imposes a filtering function on synaptic information transmission (Fortune and Rose, 2001); therefore, depressed A-component and B-mediated facilitated components probably contribute differently to tuning sensory coding. The *Drosophila* olfactory system generating olfactory smell behavior is a particularly well-studied system. Here, odor information sensed by ORN is further transmitted to two higher processing centers, namely, the mushroom body and the LH. The latter structure mediates innate olfactory behavior, receiving not only the excitatory input via ePNs but also the inhibitory input from iPNs (Tanaka et al., 2012). The iPNs thereby were suggested to act as a high-pass filter of transmitter release from ePNs (Parnas et al., 2013). The ORN-to-PN connections follow a nearly one-to-one manner, yet PNs are more broadly tuned by odor than ORNs owing to signal transmission being carried by two kinetically distinct EPSC components on different time scales and dynamic inhibition from LNs (Kazama and Wilson, 2008; Nagel et al., 2015). Unlike the probably largely random PN-to-KC inputs, olfactory inputs to LH neurons (LHNs) are rather stereotyped and biased to certain overrepresented PN glomeruli. Different morphological types of LHNs exhibit distinct information computation features that depend on their specific connectivity patterns. The LHNs receiving pooled excitatory coactivated PN inputs are broadly tuned to odors. By contrast, neurons combining excitation and inhibition from coactivated PNs are narrowly tuned (Fisek and Wilson, 2014; Jeanne and Wilson, 2015; Jeanne et al., 2018). In this regard, Unc13A at the ePN AZs was found to be required for the proper sensation of odor and their valence (appetitive or aversive). By contrast, the B isoform here seemingly encodes a more generic aversive valence of inputs captured (Pooryasin et al., 2021). In addition, the Unc13B-mediated release component of the iPNs acts as an antagonistic signal to that of ePNs, which can reset the attraction-shifted innate smell responses caused by Unc13B downregulation at ePNs. The behavioral alterations are imputed to the loss of isoform-specific release components rather than developmental deficits or a complete destruction of AZ structure, as experiments employing temporally restricted downregulation of either isoform or interfering with the AZ nano-topology by expression of only the C-terminal fragments that generate ectopic release sites (Reddy-Alla et al., 2017) converged to very similar conclusions.

In another context, Unc13A and Unc13B, as said above, enriched in different mushroom body lobes, are also probably of importance for circuits encoding and storing discrete memory components. Short-term associative aversive olfactory memory was found impaired when either isoform was knocked down in KCs (Bohme et al., 2019; Woitkuhn et al., 2020). The short-term memory deficit caused by Unc13A downregulation could not be restored by re-expressing the C-terminal part of it, which generates release sites at atypical locations as mentioned above (Bohme et al., 2019). Mid-term memory performances were impaired in both Unc13A and B downregulated conditions as well, though to a much lesser extent when knocking down only the B isoform in KCs (Woitkuhn et al., 2020). The mid-term memory is composed of an anesthesia-sensitive and an anesthesia-resistant memory (ARM) component (Quinn and Dudai, 1976). Notably, the anesthesia-sensitive memory component measured 3 h after training was completely abolished in Unc13A knocked-down flies. Meanwhile, ARM performance was deteriorated in the A isoform deletion scenario but remained unaffected in Unc13B knocked-down animals. These distinct memory phases and components rely on different subsets of KCs. The Unc13A-rich γ lobe particularly encodes short-term memory and is recruited during retrieval of the ARM component (Bouzaiane et al., 2015). In addition, the early memory trace after training is found in the α' and β' lobes whose AZs are also enriched in Unc13A (Wang et al., 2008). Outputs from these two lobes are required for forming a solid mid-term memory (Krashes et al., 2007) and retrieval of a long-term ARM (Bouzaiane et al., 2015). In contrast, the α and β lobes with a relatively high Unc13B/Unc13A ratio are involved in anesthesia-sensitive memory and a short-term ARM retrieval. Thus, memory form-specific impairment caused by isoform A or B downregulation might, to some extent, be attributable to the stoichiometric differences in the levels of the two isoforms across mushroom body lobes. How exactly Unc13 isoform-specific release components interact and differentially filter KC activity patterns instrumental for forming distinct memory components is an issue now warranting research.

The *Drosophila Unc13* locus has also been linked to behavioral responses to ethanol exposure. At a sedating concentration, ethanol decreased the release of the pre-synaptic vesicle from ORNs elicited by odor presentation, and, surprisingly, this reduction was less pronounced in *Unc13* heterozygous loss-of-function mutants based on measurements using synapto-pHluorin. The heterozygotes were also less sensitive to the sedative effects of ethanol measured by the loss of righting reflex assay (Xu et al., 2018) and, at the same time, showed an increased preference for ethanol in the so-called CAFÉ assay (Das et al., 2013). Ethanol interacts with the C1 domain at a conserved Glu-residue, which is shared by both isoforms (Das et al., 2013). A low concentration of ethanol could already inhibit the interaction between diacylglycerol and the C1 domain *in vitro* (Xu et al., 2018), which lowers the energy barrier for SV fusion and influences the probability of the vesicle release (Basu et al., 2007). However, the behavioral regulation does not seem to be conserved in heterozygous *munc13-1* mice, potentially due to a compensatory effect by other Munc13 isoforms (Wooden et al., 2020). Here again, its accessibility to the genetic analysis makes *Drosophila* an attractive model for investigating the role of synaptic plasticity in ethanol intoxication and addiction.

DIFFERENT ROLES OF UNC13 A AND B IN THE PLASTIC REMODELING OF ACTIVE ZONES

Memory formation is accompanied and mediated by the synaptic growth and structural remodeling. Are Unc13A and Unc13B, which contribute to varied forms of learning behaviors, involved in this process as well? As has been said, synaptic transmission seems dominantly controlled by Unc13A at CNS fast synapses and the peripheral larval NMJs. Notably, Unc13A, which predicts single AZ release activity by controlling its SV release probability, has just been found to be involved in pre-synaptic homeostatic plasticity. The latter can be triggered at the NMJ of *Drosophila* larvae by the application of a glutamate receptor blocker Philanthotoxin, resulting in a compensatory enhancement of pre-synaptic neurotransmitter release by upregulation of both the SV-release probability at existing release sites and the number of functional release sites (Muller et al., 2012; Lazarevic et al., 2013; Li et al., 2018). When resolved by STED, the number of BRP/Unc13A clusters at a single AZ, probably corresponding to the release sites per AZ, varied greatly, but mostly ranged from two to six clusters. Within minutes after Philanthotoxin treatment, seemingly new BRP/Unc13A nanomodules were incorporated into remodeling AZs, resulting in a right shifting of the distribution of the cluster number per AZ. This rapid remodeling process, which is essential to consolidate release potentiation, is lost in *unc13A* mutants, indicating its indispensable role in the plastic augmentation of SV release. The incorporation of nanomodules depends on the stable and precise location of Unc13A at the AZ via the N-terminus. As has been described above, the Unc13A C-terminal fragments, which are incapable of pre-synaptic homeostatic plasticity, could not recover the short-term memory impairment provoked by the Unc13A downregulation in the memory center of *Drosophila*, linking its plasticity regulation function to memory formation (Bohme et al., 2019).

The early onset of the Unc13B during the AZ assembly may indicate its involvement in development. Synaptic release probabilities at mature NMJs are dominantly defined by Unc13A. Null mutants of *Unc13B* only showed a mild reduction in the response evoked (Bohme et al., 2016). However, Unc13B deletion during the early developmental stage could also result in an altered release probability. A recent study by Ramesh et al. (2021) revealed that the release component meditated by Unc13B at nascent AZs facilitated glutamate receptor incorporation at opposing post-synapses. The knocking down of Unc13B in motoneurons suppressed the GluRIIA accumulation at the NMJ, while gain-of-function *Unc13B* mutation with enhanced glutamate releasement (Lipstein et al., 2017) drastically promoted GluRIIA accumulation (Ramesh et al., 2021). This operation is again partially mediated by its interaction with Syd-1.

OUTLOOK

Drosophila Unc13 isoforms are nano-clustered by distinct AZ scaffolding proteins and thus form release sites that are either tightly or loosely coupled to Ca^{2+} channels. They change the AZ release characteristics, probably as a direct consequence, providing functional diversity to *Drosophila* synapses and obviously beyond. The stoichiometric mixing of Unc13A and B likely evolved to endow synapses with a dynamic range of optimal frequencies for transmission, accordingly, tuning specific activity patterns in support of specific behavioral components. These relations in *Drosophila*, with its unique possibilities for behavioral genetics, as well as in mammals, should be investigated for deepening our understanding of how AZ-based information filtering contributes to information processing and, consequently, behavior.

AUTHOR CONTRIBUTIONS

CP wrote the first draft of the manuscript. SS and CP reviewed and edited the manuscript. Both authors contributed to the article and approved the submitted version.

FUNDING

This work was supported by the OpenAccess Publication Fund of Freie Universität Berlin. The support of the Deutsche Forschungsgemeinschaft (DFG) (FOR2705 [Project-ID: 365082554], FOR5228 [Project-ID: 447288260], SFB1315 [Project-ID: 327654276], and SI 849/14-1 [Project-ID: 445178831]) was gratefully acknowledged.

REFERENCES

Akbergenova, Y., Cunningham, K. L., Zhang, Y. V., Weiss, S., and Littleton, J. T. (2018). Characterization of developmental and molecular factors underlying release heterogeneity at *Drosophila* synapses. *Elife* 7:e38268. doi: 10.7554/eLife.38268.030

Aravamudan, B., Fergestad, T., Davis, W. S., Rodesch, C. K., and Broadie, K. (1999). *Drosophila* Unc-13 is essential for synaptic transmission. *Nat. Neurosci.* 2, 965–971. doi: 10.1038/14764

Atwood, H. L., and Karunanithi, S. (2002). Diversification of synaptic strength: presynaptic elements. *Nat. Rev. Neurosci.* 3, 497–516. doi: 10.1038/nrn876

Augustin, I., Betz, A., Herrmann, C., Jo, T., and Brose, N. (1999). Differential expression of two novel Munc13 proteins in rat brain. *Biochem. J.* 337(Pt 3), 363–371. doi: 10.1042/bj3370363

Basu, J., Betz, A., Brose, N., and Rosenmund, C. (2007). Munc13-1 C1 domain activation lowers the energy barrier for synaptic vesicle fusion. *J. Neurosci.* 27, 1200–1210. doi: 10.1523/JNEUROSCI.4908-06.2007

Basu, J., Shen, N., Dulubova, I., Lu, J., Guan, R., Guryev, O., et al. (2005). A minimal domain responsible for Munc13 activity. *Nat. Struct. Mol. Biol.* 12, 1017–1018. doi: 10.1038/nsmb1001

Berwin, B., Floor, E., and Martin, T. F. (1998). CAPS (mammalian UNC-31) protein localizes to membranes involved in dense-core vesicle exocytosis. *Neuron* 21, 137–145. doi: 10.1016/S0896-6273(00)80521-8

Bohme, M. A., Beis, C., Reddy-Alla, S., Reynolds, E., Mampell, M. M., Grasskamp, A. T., et al. (2016). Active zone scaffolds differentially accumulate Unc13 isoforms to tune Ca(2+) channel-vesicle coupling. *Nat. Neurosci.* 19, 1311–1320. doi: 10.1038/nn.4364

Bohme, M. A., Mccarthy, A. W., Grasskamp, A. T., Beuschel, C. B., Goel, P., Jusyte, M., et al. (2019). Rapid active zone remodeling consolidates presynaptic potentiation. *Nat. Commun.* 10:1085. doi: 10.1038/s41467-019-08977-6

Bouzaiane, E., Trannoy, S., Scheunemann, L., Placais, P. Y., and Preat, T. (2015). Two independent mushroom body output circuits retrieve the six discrete components of *Drosophila* aversive memory. *Cell Rep.* 11, 1280–1292. doi: 10.1016/j.celrep.2015.04.044

Das, J., Xu, S. Y., Pany, S., Guillory, A., Shah, V., and Roman, G. W. (2013). The pre-synaptic Munc13-1 binds alcohol and modulates alcohol self-administration in *Drosophila*. *J. Neurochem.* 126, 715–726. doi: 10.1111/jnc.12315

Dittman, J. S. (2019). Unc13: a multifunctional synaptic marvel. *Curr. Opin. Neurobiol.* 57, 17–25. doi: 10.1016/j.conb.2018.12.011

Eltes, T., Kirizs, T., Nusser, Z., and Holderith, N. (2017). Target cell type-dependent differences in Ca(2+) channel function underlie distinct release probabilities at hippocampal glutamatergic terminals. *J. Neurosci.* 37, 1910–1924. doi: 10.1523/JNEUROSCI.2024-16.2017

Fioravante, D., and Regehr, W. G. (2011). Short-term forms of presynaptic plasticity. *Curr. Opin. Neurobiol.* 21, 269–274. doi: 10.1016/j.conb.2011.02.003

Fisek, M., and Wilson, R. I. (2014). Stereotyped connectivity and computations in higher-order olfactory neurons. *Nat. Neurosci.* 17, 280–288. doi: 10.1038/nn.3613

Fortune, E. S., and Rose, G. J. (2001). Short-term synaptic plasticity as a temporal filter. *Trends Neurosci.* 24, 381–385. doi: 10.1016/S0166-2236(00)01835-X

Fouquet, W., Owald, D., Wichmann, C., Mertel, S., Depner, H., Dyba, M., et al. (2009). Maturation of active zone assembly by *Drosophila* Bruchpilot. *J. Cell Biol.* 186, 129–145. doi: 10.1083/jcb.2008 12150

Fulterer, A., Andlauer, T. F. M., Ender, A., Maglione, M., Eyring, K., Woitkuhn, J., et al. (2018). Active zone scaffold protein ratios tune functional diversity across brain synapses. *Cell Rep.* 23, 1259–1274. doi: 10.1016/j.celrep.2018.03.126

Holderith, N., Lorincz, A., Katona, G., Rozsa, B., Kulik, A., Watanabe, M., et al. (2012). Release probability of hippocampal glutamatergic terminals scales with the size of the active zone. *Nat. Neurosci.* 15, 988–997. doi: 10.1038/nn.3137

Hu, Z., Tong, X. J., and Kaplan, J. M. (2013). UNC-13L, UNC-13S, and Tomosyn form a protein code for fast and slow neurotransmitter release in Caenorhabditis elegans. *Elife* 2:e00967. doi: 10.7554/eLife.00967.020

Hu, Z., Vashlishan-Murray, A. B., and Kaplan, J. M. (2015). NLP-12 engages different UNC-13 proteins to potentiate tonic and evoked release. *J. Neurosci.* 35, 1038–1042. doi: 10.1523/JNEUROSCI.2825-14.2015

Huang, S., Piao, C., Beuschel, C. B., Gotz, T., and Sigrist, S. J. (2020). Presynaptic active zone plasticity encodes sleep need in *Drosophila*. *Curr. Biol.* 30, 1077–1091.e1075. doi: 10.1016/j.cub.2020.01.019

Huang, S., and Sigrist, S. J. (2021). Presynaptic and postsynaptic long-term plasticity in sleep homeostasis. *Curr. Opin. Neurobiol.* 69, 1–10. doi: 10.1016/j.conb.2020.11.010

Jeanne, J. M., Fisek, M., and Wilson, R. I. (2018). The organization of projections from olfactory glomeruli onto higher-order neurons. *Neuron 98* 1198–1213.e1196. doi: 10.1016/j.neuron.2018.05.011

Jeanne, J. M., and Wilson, R. I. (2015). Convergence, divergence, and reconvergence in a feedforward network improves neural speed and accuracy. *Neuron* 88, 1014–1026. doi: 10.1016/j.neuron.2015.10.018

Karlocai, M. R., Heredi, J., Benedek, T., Holderith, N., Lorincz, A., and Nusser, Z. (2021). Variability in the Munc13-1 content of excitatory release sites. *Elife* 10:e67468. doi: 10.7554/eLife.67468.sa2

Kawabe, H., Mitkovski, M., Kaeser, P. S., Hirrlinger, J., Opazo, F., Nestvogel, D., et al. (2017). ELKS1 localizes the synaptic vesicle priming protein bMunc13-2 to a specific subset of active zones. *J. Cell. Biol.* 216, 1143–1161. doi: 10.1083/jcb.201606086

Kawasaki, F., Zou, B., Xu, X., and Ordway, R. W. (2004). Active zone localization of presynaptic calcium channels encoded by the cacophony locus of *Drosophila*. *J. Neurosci.* 24, 282–285. doi: 10.1523/JNEUROSCI.3553-03.2004

Kazama, H., and Wilson, R. I. (2008). Homeostatic matching and nonlinear amplification at identified central synapses. *Neuron* 58, 401–413. doi: 10.1016/j.neuron.2008.02.030

Koch, H., Hofmann, K., and Brose, N. (2000). Definition of Munc13-homology-domains and characterization of a novel ubiquitously expressed Munc13 isoform. *Biochem. J.* 349, 247–253. doi: 10.1042/bj3490247

Krashes, M. J., Keene, A. C., Leung, B., Armstrong, J. D., and Waddell, S. (2007). Sequential use of mushroom body neuron subsets during *Drosophila* odor memory processing. *Neuron* 53, 103–115. doi: 10.1016/j.neuron.2006.11.021

Lazarevic, V., Pothula, S., Andres-Alonso, M., and Fejtova, A. (2013). Molecular mechanisms driving homeostatic plasticity of neurotransmitter release. *Front. Cell Neurosci.* 7:244. doi: 10.3389/fncel.2013.00244

Li, X., Goel, P., Chen, C., Angajala, V., Chen, X., and Dickman, D. K. (2018). Synapse-specific and compartmentalized expression of presynaptic homeostatic potentiation. *Elife* 7:e34338. doi: 10.7554/eLife.34338

Lipstein, N., Sakaba, T., Cooper, B. H., Lin, K. H., Strenzke, N., Ashery, U., et al. (2013). Dynamic control of synaptic vesicle replenishment and short-term plasticity by Ca(2+)-calmodulin-Munc13-1 signaling. *Neuron* 79, 82–96. doi: 10.1016/j.neuron.2013.05.011

Lipstein, N., Schaks, S., Dimova, K., Kalkhof, S., Ihling, C., Kolbel, K., et al. (2012). Nonconserved Ca(2+)/calmodulin binding sites in Munc13s differentially control synaptic short-term plasticity. *Mol. Cell Biol.* 32, 4628–4641. doi: 10.1128/MCB.00933-12

Lipstein, N., Verhoeven-Duif, N. M., Michelassi, F. E., Calloway, N., Van Hasselt, P. M., Pienkowska, K., et al. (2017). Synaptic UNC13A protein variant causes increased neurotransmission and dyskinetic movement disorder. *J. Clin. Invest.* 127, 1005–1018. doi: 10.1172/JCI90259

Liu, X., Seven, A. B., Camacho, M., Esser, V., Xu, J., Trimbuch, T., et al. (2016). Functional synergy between the Munc13 C-terminal C1 and C2 domains. *Elife* 5:e13696. doi: 10.7554/eLife.13696

Liu, Y., Schirra, C., Stevens, D. R., Matti, U., Speidel, D., Hof, D., et al. (2008). CAPS facilitates filling of the rapidly releasable pool of large dense-core vesicles. *J. Neurosci.* 28, 5594–5601. doi: 10.1523/JNEUROSCI.5672-07.2008

Ma, C., Li, W., Xu, Y., and Rizo, J. (2011). Munc13 mediates the transition from the closed syntaxin-Munc18 complex to the SNARE complex. *Nat. Struct. Mol. Biol.* 18, 542–549. doi: 10.1038/nsmb.2047

Magdziarek, M., Bolembach, A. A., Stepien, K. P., Quade, B., Liu, X., and Rizo, J. (2020). Re-examining how Munc13-1 facilitates opening of syntaxin-1. *Protein Sci.* 29, 1440–1458. doi: 10.1002/pro.3844

Mosca, T. J., and Luo, L. (2014). Synaptic organization of the *Drosophila* antennal lobe and its regulation by the Teneurins. *Elife* 3:e03726. doi: 10.7554/eLife.03726.023

Moser, T., Grabner, C. P., and Schmitz, F. (2020). Sensory processing at ribbon synapses in the retina and the cochlea. *Physiol. Rev.* 100, 103–144. doi: 10.1152/physrev.00026.2018

Mukunda, C. L., and Narayanan, R. (2017). Degeneracy in the regulation of short-term plasticity and synaptic filtering by presynaptic mechanisms. *J. Physiol.* 595, 2611–2637. doi: 10.1113/JP273482

Muller, M., Liu, K. S., Sigrist, S. J., and Davis, G. W. (2012). RIM controls homeostatic plasticity through modulation of the readily-releasable vesicle pool. *J. Neurosci.* 32, 16574–16585. doi: 10.1523/JNEUROSCI.0981-12.2012

Nagel, K. I., Hong, E. J., and Wilson, R. I. (2015). Synaptic and circuit mechanisms promoting broadband transmission of olfactory stimulus dynamics. *Nat. Neurosci.* 18, 56–65. doi: 10.1038/nn.3895

Nagel, K. I., and Wilson, R. I. (2016). Mechanisms underlying population response dynamics in inhibitory interneurons of the *Drosophila* antennal lobe. *J. Neurosci.* 36, 4325–4338. doi: 10.1523/JNEUROSCI.3887-15.2016

Ng, M., Roorda, R. D., Lima, S. Q., Zemelman, B. V., Morcillo, P., and Miesenböck, G. (2002). Transmission of olfactory information between three populations of neurons in the antennal lobe of the fly. *Neuron* 36, 463–474. doi: 10.1016/S0896-6273(02)00975-3

Nusser, Z. (2018). Creating diverse synapses from the same molecules. *Curr. Opin. Neurobiol.* 51, 8–15. doi: 10.1016/j.conb.2018.01.001

Owald, D., Fouquet, W., Schmidt, M., Wichmann, C., Mertel, S., Depner, H., et al. (2010). A Syd-1 homologue regulates pre- and postsynaptic maturation in *Drosophila*. *J. Cell Biol.* 188, 565–579. doi: 10.1083/jcb.200908055

Parnas, M., Lin, A. C., Huetteroth, W., and Miesenbock, G. (2013). Odor discrimination in *Drosophila*: from neural population codes to behavior. *Neuron* 79, 932–944. doi: 10.1016/j.neuron.2013.08.006

Peled, E. S., Newman, Z. L., and Isacoff, E. Y. (2014). Evoked and spontaneous transmission favored by distinct sets of synapses. *Curr. Biol.* 24, 484–493. doi: 10.1016/j.cub.2014.01.022

Piotrowski, C., Moretti, R., Ihling, C. H., Haedicke, A., Liepold, T., Lipstein, N., et al. (2020). Delineating the molecular basis of the CalmodulinbMunc13-2 interaction by cross-linking/mass spectrometry-evidence for a novel CaM binding Motif in bMunc13-2. *Cells* 9:136. doi: 10.3390/cells9010136

Pooryasin, A., Maglione, M., Schubert, M., Matkovic-Rachid, T., Hasheminasab, S. M., Pech, U., et al. (2021). Unc13A and Unc13B contribute to the decoding of distinct sensory information in *Drosophila*. *Nat. Commun.* 12:1932. doi: 10.1038/s41467-021-22180-6

Quade, B., Camacho, M., Zhao, X., Orlando, M., Trimbuch, T., Xu, J., et al. (2019). Membrane bridging by Munc13-1 is crucial for neurotransmitter release. *Elife* 8:e42806. doi: 10.7554/eLife.42806.025

Quinn, W. G., and Dudai, Y. (1976). Memory phases in *Drosophila*. *Nature* 262, 576–577. doi: 10.1038/262576a0

Ramesh, N., Escher, M. J. F., Mampell, M. M., Bohme, M. A., Gotz, T. W. B., Goel, P., et al. (2021). Antagonistic interactions between two Neuroligins coordinate pre- and postsynaptic assembly. *Curr. Biol.* 31, 1711–1725.e1715. doi: 10.1016/j.cub.2021.01.093

Reddy-Alla, S., Bohme, M. A., Reynolds, E., Beis, C., Grasskamp, A. T., Mampell, M. M., et al. (2017). Stable positioning of Unc13 restricts synaptic vesicle fusion to defined release sites to promote synchronous neurotransmission. *Neuron* 95, 1350–1364.e1312. doi: 10.1016/j.neuron.2017.08.016

Renden, R., Berwin, B., Davis, W., Ann, K., Chin, C. T., Kreber, R., et al. (2001). *Drosophila* CAPS is an essential gene that regulates dense-core vesicle release and synaptic vesicle fusion. *Neuron* 31, 421–437. doi: 10.1016/S0896-6273(01)00382-8

Rosenmund, C., Sigler, A., Augustin, I., Reim, K., Brose, N., and Rhee, J. S. (2002). Differential control of vesicle priming and short-term plasticity by Munc13 isoforms. *Neuron* 33, 411–424. doi: 10.1016/S0896-6273(02)00568-8

Rupnik, M., Kreft, M., Sikdar, S. K., Grilc, S., Romih, R., Zupancic, G., et al. (2000). Rapid regulated dense-core vesicle exocytosis requires the CAPS protein. *Proc. Natl. Acad. Sci. U. S. A.* 97, 5627–5632. doi: 10.1073/pnas.090359097

Sakamoto, H., Ariyoshi, T., Kimpara, N., Sugao, K., Taiko, I., Takikawa, K., et al. (2018). Synaptic weight set by Munc13-1 supramolecular assemblies. *Nat. Neurosci.* 21, 41–49. doi: 10.1038/s41593-017-0041-9

Shin, O. H., Lu, J., Rhee, J. S., Tomchick, D. R., Pang, Z. P., Wojcik, S. M., et al. (2010). Munc13 C2B domain is an activity-dependent Ca2+ regulator of synaptic exocytosis. *Nat. Struct. Mol. Biol.* 17, 280–288. doi: 10.1038/nsmb.1758

Shu, T., Jin, H., Rothman, J. E., and Zhang, Y. (2020). Munc13-1 MUN domain and Munc18-1 cooperatively chaperone SNARE assembly through a tetrameric complex. *Proc. Natl. Acad. Sci. U. S. A.* 117, 1036–1041. doi: 10.1073/pnas.1914361117

Tanaka, N. K., Endo, K., and Ito, K. (2012). Organization of antennal lobe-associated neurons in adult *Drosophila* melanogaster brain. *J. Comp. Neurol.* 520, 4067–4130. doi: 10.1002/cne.23142

Wang, S., Li, Y., Gong, J., Ye, S., Yang, X., Zhang, R., et al. (2019). Munc18 and Munc13 serve as a functional template to orchestrate neuronal SNARE complex assembly. *Nat. Commun.* 10:69. doi: 10.1038/s41467-018-08028-6

Wang, Y., Mamiya, A., Chiang, A. S., and Zhong, Y. (2008). Imaging of an early memory trace in the *Drosophila* mushroom body. *J. Neurosci.* 28, 4368–4376. doi: 10.1523/JNEUROSCI.2958-07.2008

Wichmann, C., and Kuner, T. (2022). Heterogeneity of glutamatergic synapses: cellular mechanisms and network consequences. *Physiol. Rev.* 102, 269–318. doi: 10.1152/physrev.00039.2020

Woitkuhn, J., Ender, A., Beuschel, C. B., Maglione, M., Matkovic-Rachid, T., Huang, S., et al. (2020). The Unc13A isoform is important for phasic release and olfactory memory formation at mushroom body synapses. *J. Neurogenet* 34, 106–114. doi: 10.1080/01677063.2019.1710146

Wooden, J. I., Schuller, K., Roman, G., Das, J., and Leasure, J. L. (2020). MUNC13-1 heterozygosity does not alter voluntary ethanol consumption or sensitivity in mice. *Alcohol* 83, 89–97. doi: 10.1016/j.alcohol.2019.06.007

Xu, J., Camacho, M., Xu, Y., Esser, V., Liu, X., Trimbuch, T., et al. (2017). Mechanistic insights into neurotransmitter release and presynaptic plasticity from the crystal structure of Munc13-1 C1C2BMUN. *Elife* 6:e22567. doi: 10.7554/eLife.22567.040

Xu, S., Pany, S., Benny, K., Tarique, K., Al-Hatem, O., Gajewski, K., et al. (2018). Ethanol regulates presynaptic activity and sedation through presynaptic Unc13 proteins in *Drosophila*. *eNeuro* 5:ENEURO.0125-18.2018. doi: 10.1523/ENEURO.0125-18.2018

Xu, X. Z., Wes, P. D., Chen, H., Li, H. S., Yu, M., Morgan, S., et al. (1998). Retinal targets for calmodulin include proteins implicated in synaptic transmission. *J. Biol. Chem.* 273, 31297–31307. doi: 10.1074/jbc.273.47.31297

Yaksi, E., and Wilson, R. I. (2010). Electrical coupling between olfactory glomeruli. *Neuron* 67, 1034–1047. doi: 10.1016/j.neuron.2010.08.041

Zhou, K., Stawicki, T. M., Goncharov, A., and Jin, Y. (2013). Position of UNC-13 in the active zone regulates synaptic vesicle release probability and release kinetics. *Elife* 2:e01180. doi: 10.7554/eLife.01180.026

Conflict of Interest: The authors declare that the research was conducted in the absence of any commercial or financial relationships that could be construed as a potential conflict of interest.

frontiers
in Synaptic Neuroscience

HYPOTHESIS AND THEORY
published: 05 January 2022
doi: 10.3389/fnsyn.2021.798225

Hypothesis Relating the Structure, Biochemistry and Function of Active Zone Material Macromolecules at a Neuromuscular Junction

Joseph A. Szule*

Department of Veterinary Pathobiology, Texas A&M University, College Station, TX, United States

This report integrates knowledge of *in situ* macromolecular structures and synaptic protein biochemistry to propose a unified hypothesis for the regulation of certain vesicle trafficking events (i.e., docking, priming, Ca^{2+}-triggering, and membrane fusion) that lead to neurotransmitter secretion from specialized "active zones" of presynaptic axon terminals. Advancements in electron tomography, to image tissue sections in 3D at nanometer scale resolution, have led to structural characterizations of a network of different classes of macromolecules at the active zone, called "Active Zone Material'. At frog neuromuscular junctions, the classes of Active Zone Material macromolecules "top-masts", "booms", "spars", "ribs" and "pins" direct synaptic vesicle docking while "pins", "ribs" and "pegs" regulate priming to influence Ca^{2+}-triggering and membrane fusion. Other classes, "beams", "steps", "masts", and "synaptic vesicle luminal filaments' likely help organize and maintain the structural integrity of active zones. Extensive studies on the biochemistry that regulates secretion have led to comprehensive characterizations of the many conserved proteins universally involved in these trafficking events. Here, a hypothesis including a partial proteomic atlas of Active Zone Material is presented which considers the common roles, binding partners, physical features/structure, and relative positioning in the axon terminal of both the proteins and classes of macromolecules involved in the vesicle trafficking events. The hypothesis designates voltage-gated Ca^{2+} channels and Ca^{2+}-gated K^+ channels to ribs and pegs that are connected to macromolecules that span the presynaptic membrane at the active zone. SNARE proteins (Syntaxin, SNAP25, and Synaptobrevin), SNARE-interacting proteins Synaptotagmin, Munc13, Munc18, Complexin, and NSF are designated to ribs and/or pins. Rab3A and Rabphillin-3A are designated to top-masts and/or booms and/or spars. RIM, Bassoon, and Piccolo are designated to beams, steps, masts, ribs, spars, booms, and top-masts. Spectrin is designated to beams. Lastly, the luminal portions of SV2 are

Edited by:
Xiaobing Chen,
National Institutes of Health (NIH),
United States

Reviewed by:
Vladan Lucic,
Max Planck Institute of Biochemistry,
Germany
Noreen Reist,
Colorado State University,
United States
Hiroshi Nishimune,
Tokyo Metropolitan Institute of
Gerontology, Japan

***Correspondence:**
Joseph A. Szule
jszule@cvm.tamu.edu

Received: 19 October 2021
Accepted: 14 December 2021
Published: 05 January 2022

Citation:
Szule JA (2022) Hypothesis Relating the Structure, Biochemistry and Function of Active Zone Material Macromolecules at a Neuromuscular Junction.
Front. Synaptic Neurosci. 13:798225.
doi: 10.3389/fnsyn.2021.798225

Abbreviations: NMJ, Neuromuscular junction; AZM, Active zone material; PM, Presynaptic membrane; SV, Synaptic vesicle.

thought to form the bulk of the observed synaptic vesicle luminal filaments. The goal here is to help direct future studies that aim to bridge Active Zone Material structure, biochemistry, and function to ultimately determine how it regulates the trafficking events *in vivo* that lead to neurotransmitter secretion.

Keywords: synapse, neuromuscular junction, active zone, active zone material, neurotransmitter secretion, synaptic vesicle, vesicle trafficking, electron tomography

INTRODUCTION

At chemical synapses, the electrical activity of neuronal axon terminals increases the probability that neurotransmitter molecules in synaptic vesicles (SVs) will be secreted from specialized regions along the presynaptic plasma membrane (PM) called active zones (Katz, 1969; Couteaux and Pecot-Dechavassine, 1970). Prior to secretion, SVs undergo several transient trafficking events (i.e., "docking", "priming", "Ca^{2+}-triggering" and "membrane fusion") at active zones that are each necessary for secretion to occur. However, the definition and criteria of these trafficking events are often dependent on the experimental approach, and this has led to many variations of the morphological and biochemical criteria used to define each step (Slater, 2015). For the purpose of this report, docking is described as the directed movement of an SV towards the PM at the active zone, where the SV membrane will be held in direct contact with the PM to become docked. Once an SV is docked, priming influences the probability that the membranes will fuse, as only a small subset of the docked SVs will be triggered to secrete their contents when an electrical impulse arrives (Katz and Miledi, 1979; Heuser and Reese, 1981). Ca^{2+}-triggering occurs when Ca^{2+} ions bind specific SV proteins at sufficient concentrations to increase the probability that a docked SV and the PM will undergo membrane fusion, where the two distinct lipid bilayers from each membrane will undergo rearrangements and form a pore that is continuous from the vesicle lumen to the extracellular synaptic cleft (Chernomordik et al., 1995). It is important to note that disruption in the molecular mechanisms of any of these events, either through genetic mutations or pharmacological intervention, will also disrupt the end result of neurotransmitter secretion.

Based on techniques that involve transmission electron microscopy of either tissue sections or freeze-fracture replicas, active zones in presynaptic terminals are generally characterized by the presence of docked SVs held at the PM, a network of macromolecules attached to both the docked SV membranes and the PM called active zone material (AZM), and many large macromolecules that span the PM (Palade, 1954; Palay, 1954; Couteaux and Pecot-Dechavassine, 1970; Heuser et al., 1974, 1979; Propst and Ko, 1987; Harlow et al., 2001). Electron tomography has been used to characterize the fine structure of AZM macromolecules in 3D at nanometer scale resolution *in situ* to provide insights into their direct roles in these trafficking events (Harlow et al., 2001, 2013; Ress et al., 2004; Nagwaney et al., 2009; Fernandez-Busnadiego et al., 2010; Stigloher et al., 2011; Szule et al., 2012, 2015; Matkovic et al., 2013; Imig et al., 2014; Perkins et al., 2015; Cole et al., 2016; Jung et al., 2016, 2018).

Extensive biochemistry studies have also led to a comprehensive characterization of the many conserved protein families universally involved in these trafficking events [reviewed by Rizo and Rosenmund (2008), Sudhof and Rizo (2011), Rizo and Sudhof (2012), and Rizo and Xu (2015)]. Each trafficking event requires specific biochemical interactions between proteins of SVs, AZM macromolecules, and the PM to proceed (Takamori et al., 2006; Südhof and Rothman, 2009; Südhof, 2012, 2013; Snead and Eliezer, 2019), although the mechanistic details of each event are under considerable debate (Hanson et al., 1997; Jahn and Sudhof, 1999; Klenchin and Martin, 2000; Price et al., 2000; Jahn et al., 2003; Szule and Coorssen, 2003; Han et al., 2004; Südhof, 2004; Jackson and Chapman, 2008; Neher and Sakaba, 2008; Chua et al., 2010; Gundersen and Umbach, 2013; Szule et al., 2015). A hypothesized proteomic atlas will be provided here to describe how these conserved proteins are thought to be assembled and function in their AZM macromolecular complexes *in situ* to regulate SV docking, priming, Ca^{2+}-triggering, and membrane fusion that ultimately control the regulation of triggered neurotransmitter secretion.

The basic mechanisms for the events that lead to triggered secretion are thought to be conserved across neuron-types due to the homology of the proteins involved, the consistent presence of docked SVs connected to AZM at various active zones, and the universality of Ca^{2+} as the trigger for neurotransmitter secretion (Südhof, 2012; Ackermann et al., 2015). However, there are also well-described differences in protein isoforms and the architecture of AZM which are likely to accommodate synapse-specific physiologies (Palade, 1954; Palay, 1954; Gray, 1963; Zhai and Bellen, 2004; Nagwaney et al., 2009; Ehmann et al., 2014; Ackermann et al., 2015; Slater, 2015). The frog NMJ is a historically established model system of chemical synaptic transmission (Bennett, 1999; Homan and Meriney, 2018); its physiology is well understood (Fatt and Katz, 1952; Kuffler and Vaughan Williams, 1953; Katz and Miledi, 1967, 1979), the organization of axon terminals is known (Couteaux and Pecot-Dechavassine, 1970; McMahan et al., 1972; Heuser et al., 1974, 1979; Ceccarelli and Hurlbut, 1980; Slater, 2003, 2015; Rizzoli and Betz, 2004), and the molecular architecture of its AZM has been quantitatively characterized in 3D by electron tomography at rest and while undergoing SV docking, priming and membrane fusion (Harlow et al., 2001, 2013; Ress et al., 2004; Szule et al., 2012, 2015; Jung et al., 2016). It should be noted that potential artifacts caused by aldehyde fixation and heavy metal staining were addressed using high-pressure freezing and freeze-substitution methods. It was determined that there were no significant differences in the positions and dimensions of the AZM macromolecules (Jung et al., 2016), however, future studies using cryoelectron tomography without the use of heavy metal stains may help refine their unstained dimensions. Thus, AZM at frog NMJs will be used here as a model system to link various conserved proteins involved in neurotransmitter secretion to the macromolecules involved in SV docking, priming, Ca^{2+}-triggering, and membrane fusion.

OVERVIEW OF ACTIVE ZONES AT FROG NEUROMUSCULAR JUNCTIONS

Active zones in a motor neuron axon terminal at frog NMJs are situated immediately across the synaptic cleft from a junctional fold in the post-synaptic muscle cell membrane (Couteaux and Pecot-Dechavassine, 1970). The main body of AZM is a band that is ~1 µm long, ~50 nm wide, and extending ~75 nm into the cytoplasm. It is flanked on each side by ~10–20 docked SVs, a small portion of which (1–3%) will secrete their neurotransmitter cargo when the axon terminal is stimulated by an electrical impulse (Couteaux and Pecot-Dechavassine, 1970; Heuser et al., 1974). Further, the macromolecules that span the PM at the active zone are organized in a parallel double row array (Heuser et al., 1974, 1979; Ceccarelli et al., 1979a,b; Fesce et al., 1980; Stanley et al., 2003). Transmission electron tomography has shown that AZM is highly ordered. It is composed of morphologically distinct classes of macromolecules that are categorized based on their relative positions, their dimensions, and their connectivity to the SVs, the PM, and the other AZM macromolecules (**Figure 1**; **Table 1**; Harlow et al., 2001, 2013; Szule et al., 2012). Although AZM macromolecules are defined as morphologically distinct structures, their extensive connection to each other, the SVs (both docked and undocked) and the PM make it likely that different domains of individual proteins are components of more than one AZM macromolecule. Further, the dimensions of each AZM macromolecule are also sufficient to accommodate multiple proteins. These results have been described (Harlow et al., 2001, 2013; Ress et al., 2004; Szule et al., 2012; Jung et al., 2016), and reviewed (Szule et al., 2015), but a brief description will be provided here.

The superficial layer of AZM, ≤15 nm from the PM, consists of beams, ribs, pegs, and pins (**Figure 1**; **Table 1**). Beams are situated adjacent to the PM and their long axis runs parallel to the long axis of the active zone. Ribs, which are also situated adjacent to the PM but perpendicular to beams, connect to beams and docked SV membrane. Pegs are short filaments that connect ribs to the PM-spanning macromolecules that are arranged in the distinguishing parallel double row array (Heuser et al., 1974; Pumplin et al., 1981; Harlow et al., 2001). Pins connect to the SV membrane and the PM and are situated around the region of contact between these membranes.

The intermediate layer of AZM, ~15–30 nm from the PM, consists of steps and spars (**Figure 1**; **Table 1**). Steps are situated periodically along the midline of the AZM band deeper into the cytoplasm compared to beams. Spars connect to steps near the midline of the band and to docked SVs at the periphery of the band.

The deep layer of AZM, ~30–75 nm from the PM, consists of masts, booms, and top-masts (**Figure 1**; **Table 1**). Masts extend from the steps perpendicular to the plane of the PM and consist of four to nine thinner fibers. Booms connect to masts and to docked SVs. Top-masts connect to masts and to the membrane of nearby undocked SVs. Booms and top-masts have a comparable mean diameter thickness, both classes of structures connect to the masts in similar positions, and top-masts occur in variable angular orientations. Thus, it is conceivable that booms and top-masts are the same macromolecular complexes and that their differences described here are based upon whether the SV that they connect at a resting active zone is docked or undocked.

SV luminal filaments can be visualized by transmission electron microscopy in frog NMJs that had been fixed and stained by high pressure freezing and freeze-substitution, but not when aldehyde fixed and heavy metal stained at room temperature (Harlow et al., 2013). Interestingly, cryoelectron tomography on cultured CNS neurons revealed that the lumen of some SVs also contained filamentous material (Schrod et al., 2018). The SV luminal filaments at frog NMJs, found in both docked and undocked SVs, occupies ~10% of the luminal volume and forms a chiral structure that radiates from the center of the lumen to provide each SV a distinguishable orientation (Harlow et al., 2013; **Figure 1**). The filaments connect to the luminal surface of an SV membrane by ~25 nub connection sites, which are also stereotypically arranged, and link to the different classes of AZM and non-AZM macromolecules by transmembrane macromolecules. The many different SV transmembrane proteins, that have variously sized luminal domains (Takamori et al., 2006; Burré and Volknandt, 2007), have been proposed to link in the SV lumen in a specified configuration so as to predefine where the proteins of the AZM macromolecules connect to the cytosolic surface of the SV membrane, i.e., the so-called AZM-binding domain (Harlow et al., 2013).

SV Trafficking Events at Active Zones of Frog Neuromuscular Junctions

SV Docking

To test the involvement of AZM in the SV trafficking events at frog NMJs, the axon terminals of motor neurons were chemically fixed during high-frequency electrical stimulation. Fixation-stabilized "snapshots" of undocked SVs were captured during their transition to becoming docked while interacting with the different classes of AZM macromolecules to discern the morphological interactions and steps during SV docking (**Figure 2**-Top; Szule et al., 2012). During step 1 of docking, the full complement of ~7 booms stably connects with the undocked SV when it is 30–40 nm from the PM which may function to draw the SV to the PM and/or orient the SV so that it is able to interact with other AZM macromolecules. During step 2 of docking, the SV stably connects with the full complement of ~2 spars when it is 17–24 nm from the PM, in addition to the previous connections with booms, which may also draw the SV to the PM and stabilize its orientation to facilitate interaction with other AZM macromolecules. During step 3 of docking, undocked SVs interact with the full complement of ~4 ribs and ~4 pins when it is less than 16 nm from the PM, in addition to the previous connections with spars and booms, which may function

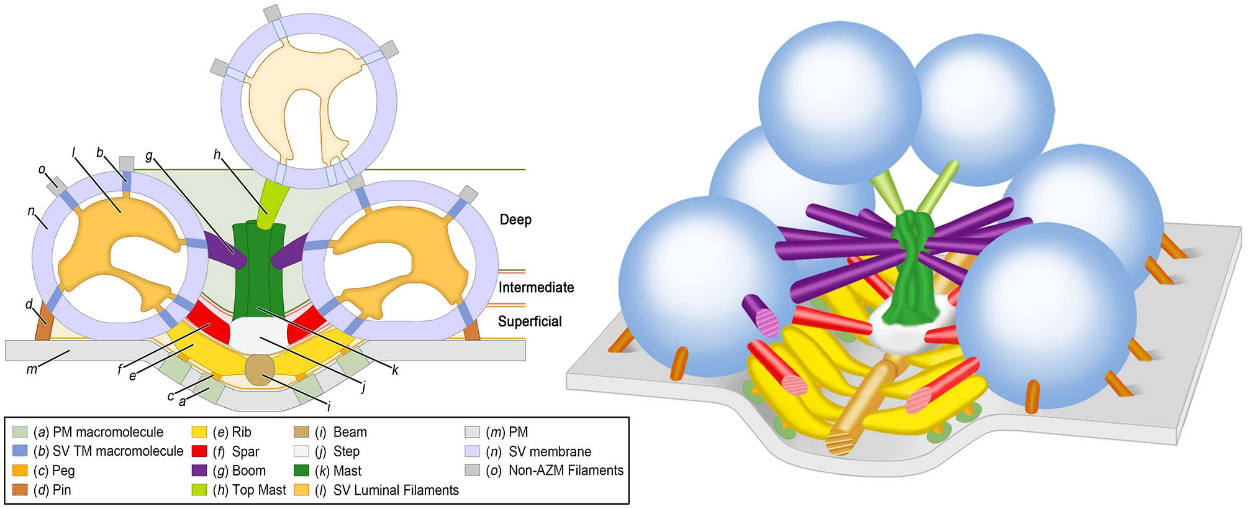

FIGURE 1 | Organization of AZM and SVs at an active zone of a frog NMJ. 2D (Left) and 3D (Right) schematic diagrams derived from electron tomography analysis of active zones showing the positions, dimensions, and connectivity of AZM macromolecules to SV membranes and the PM (see legend for color codes). Docked SVs are in direct contact with the PM whereas undocked SVs are not. The SV luminal filaments and SV transmembrane (TM) macromolecules are ghosted in the undocked SV because their orientations and spatial relationships to AZM and non-AZM macromolecules have not been observed directly. The AZM band is ∼1 mm long and is composed of 5–10 repeats of the unit shown in the 3D schematic diagram on the right. Adapted from Harlow et al. (2001), Szule et al. (2012), and Harlow et al. (2013). NMJ, Neuromuscular junction; AZM, Active zone material; PM, Presynaptic membrane; SV, Synaptic vesicle.

TABLE 1 | Dimensions of active zone material (AZM) macromolecules.

	Mean ± S.D. nm *(n)*		
AZM macromolecule	**Length**	**Diameter**	**Reference**
Ribs	∼28	∼9	Szule et al. (2012)
Proximal portion of ribs	∼17		Jung et al. (2016)
Pegs	≤7		Harlow et al. (2001)
Pins	∼13	∼5	Jung et al. (2016)
Spars	∼18	∼7	Szule et al. (2012)
Booms	∼16	∼7	Szule et al. (2012)
Top-Masts	∼25	∼7	Szule et al. (2012)
Steps	∼28 × ∼22	∼14	Szule et al. (2012)
Mast bundle of filaments	∼32	∼22	Szule et al. (2012)
Mast filaments	∼32	∼9	Szule et al. (2012)
Beams	∼75	∼11	Harlow et al. (2001) and Szule et al. (2012)

to fine-tune the alignment of the SV prior to becoming docked on a predefined, specialized position of the PM. Once the SV has interacted with the full complement of AZM macromolecules, force is likely applied between the SV membrane and PM to overcome the repulsive and hydration forces that are present upon their close apposition (Rand and Parsegian, 1989), bringing the SV membrane into direct contact with the PM where it becomes docked.

SV Priming

Electron tomography was also used to study the structural role of AZM macromolecules during docked SV priming at active zones from frog NMJs. It was determined that there are correlations between several structural parameters with the probability that the SV will fuse when the terminal is electrically stimulated, including the area of SV-PM contact, the length of ribs and pins, and the positions of pegs (Jung et al., 2016; **Figure 2**-Middle). Further, electron microscopy of frog NMJ freeze-fracture replicas led to the conclusion that the positions of transmembrane macromolecules, and consequently their associated pegs, are dynamic during exocytosis (Stanley et al., 2003). Thus, it was hypothesized that priming for each docked SV is continuously changing (**Figure 2**-Middle). The area of SV-PM contact and the position of the pegs and their associated PM-spanning macromolecules is thought to be due to force being applied by the shortening ribs and pins, which resulted in increased membrane destabilization and movement of the putative voltage-gated Ca^{2+}-channels closer to the Ca^{2+}-sensor protein at the SV-PM interface (Jung et al., 2016).

Ca^{2+}-Triggering and Membrane Fusion

Ca^{2+} ions that enter the axon terminal through voltage-gated Ca^{2+}-channels when an electrical impulse depolarizes the PM bind to Ca^{2+}-sensor proteins embedded on the SV membrane. At sufficient concentrations, Ca^{2+} binding to the sensor protein changes its interactions with the PM (Chapman

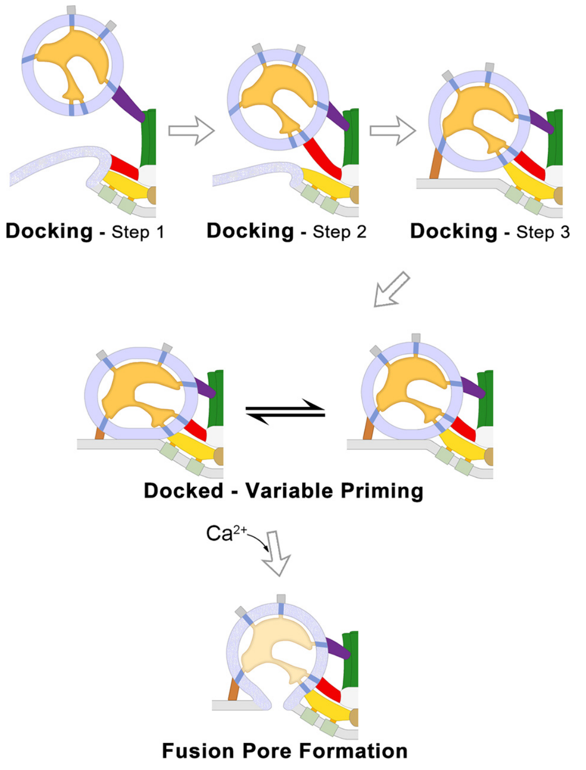

FIGURE 2 | SV trafficking events that lead to neurotransmitter secretion at frog NMJs. 2D schematic diagrams of the SV trafficking events at frog NMJs derived from electrically stimulated terminals and analyzed by electron tomography. The three steps of SV docking are characterized by the distance between the undocked SV to the PM and their connections to specific AZM macromolecules (Top). After an SV is docked it undergoes priming which determines the probability that it will fuse when an electrical impulse arrives; the variable priming model states that priming is regulated by forces exerted by AZM macromolecules, which are variable and in dynamic equilibrium, to destabilize the SV membrane–PM contact site and change the positioning of voltage-gated Ca^{2+}-channels in relation to the Ca^{2+}-sensor protein embedded in the docked SV membrane (Middle). When sufficient concentrations of cytosolic Ca^{2+} bind the sensor protein Synaptotagmin, the SV membrane and PM undergo lipidic membrane fusion to form a pore through which neurotransmitter molecules are secreted to the synaptic cleft (Bottom). Adapted from Szule et al. (2012) and Jung et al. (2016).

and Davis, 1998; Hui et al., 2009; Paddock et al., 2011; Bowers and Reist, 2020). These changes are thought to overcome an energy barrier and initiate membrane lipid rearrangements that ultimately result in the formation of a fusion pore between the SV membrane and PM, as described by the stalk-pore hypothesis (Chernomordik et al., 1995; Kozlov et al., 2010). At frog NMJs, fused SVs undergo full fusion (**Figure 2**-Bottom) and the SV membrane then flattens into the PM and moves to a lateral position where it is endocytosed (Heuser and Reese, 1973). There is little evidence for "Kiss-and-Run" fusion at frog NMJs (Rizzoli and Jahn, 2007), as compared to other synapses throughout the nervous system (Alabi and Tsien, 2013), and the proteins involved in endocytosis and SV recycling are beyond the scope of this report, but see Doherty and McMahon (2009). SVs that had fused and vacated the docking sites are replaced at the active zone by a nearby undocked SV from the recycling pool (Rizzoli and Betz, 2005), presumably by one that is connected to a top-mast (Szule et al., 2012).

The AZM macromolecules that connect to SV membranes are likely formed through specific interactions between proteins of a base AZM complex attached to the PM and proteins bound to SV membranes. The functions and interacting domains of various proteins that contribute to AZM structures at different synapses have been comprehensively reviewed elsewhere (Südhof, 2004; Schoch and Gundelfinger, 2006; Takamori et al., 2006; Rizo and Rosenmund, 2008; Chua et al., 2010), although it is important to note that not all of these proteins have been specifically identified at active zones of frog NMJs. Here, a hypothesis is presented that relates the contributions of several proteins that have been implicated in AZM regulated vesicle trafficking events to the different classes of AZM macromolecules. The hypothesis considers the common roles, binding partners, physical features/structure, and relative positioning in the axon terminal of both the proteins and classes of macromolecules involved in the vesicle trafficking events. The structures of several proteins listed below have been determined by x-ray crystallography, single particle cryo-electron microscopy, or NMR spectroscopy in solution and deposited in the Protein Data Bank (PDB[1]). The length, width, and depth of several protein structures, at their greatest distance in each dimension, were measured here unless otherwise stated using the "Measurements" tool from the Mol* Viewer software package (Sehnal et al., 2021).

HYPOTHESIS: PROTEINS THAT CONSTITUTE "ACTIVE ZONE MATERIAL" MACROMOLECULES

Cation Channels

N-type Ca^{2+}-channels (Ca$_V$2.2; Catterall, 2000–2013), the prominent type of voltage-gated Ca^{2+}-channels present at active zones of frog NMJs (Robitaille et al., 1990; Cohen et al., 1991), allow the influx of Ca^{2+} into the cytosol in response to membrane depolarization to trigger membrane fusion. The channel consists of the α_{1B} pore-forming subunit, β subunit, and α_2/β_1 subunits. α_{1B} also has a large cytoplasmic domain that includes the 87 amino acid "synprint" region in the II-III linker that interacts with a cytosolic region of the SNARE protein syntaxin and influences channel gating (Sheng et al., 1994; Bezprozvanny et al., 1995; Jarvis et al., 2002). The single particle cryo-electron microscopy-derived structure of the α_{1B} subunit [PDB accession code: 7MIY (Gao et al., 2021)] has an expected diameter in the plane of the PM of $\sim$11 nm (**Table 2**).

Ca^{2+}-gated K$^+$-channels found at active zones of frog NMJs regulate the efflux of K$^+$ to repolarize the membrane potential in preparation for subsequent rounds of triggered secretion (Robitaille and Charlton, 1992; Robitaille et al., 1993a,b). From the x-ray diffraction-derived structure of Ca^{2+}-gated K$^+$-channels [PDB accession code: 1LNQ (Jiang et al., 2002)], the

---

[1] http://www.wwpdb.org

TABLE 2 | Hypothesis of protein contributions to the classes of AZM macromolecules.

Protein	Putative function	PDB accession	Dimensions, nm (LxWxD)	AZM structure
N-type Ca^{2+}-channel	Cation regulation	7MIY	11 × 11 × 22	Pegs, Ribs
Ca^{2+}-gated K^{+} channels	Cation regulation	1LNQ	13 × 13 × 13	Pegs, Ribs
Syntaxin	Late stage of secretion	1N7S	10 × 1 × 1	Ribs/Pegs, Pins
SNAP25	Late stage of secretion	1N7S	12 × 2 × 2	Ribs, Pins
Synaptobrevin	Late stage of secretion	1N7S	9 × 1 × 1	Ribs, Pins
SNARE complex	Late stage of secretion	1N7S	12 × 3 × 3	Ribs, Pins
Synaptotagmin	Ca^{2+}-sensor for secretion	5CCG	8 × 5 × 5	Ribs, Pins
Munc13	SNARE complex regulation			Ribs, pins
Munc18	SNARE complex regulation	6LPC	8 × 8 × 5	Ribs
Complexin	SNARE complex regulation	3RK3	8 × 1 × 1	Ribs
NSF	SNARE complex regulation	3J95	13 × 13 × 9	Ribs
Rab3A	SV Tethering and Docking	1ZBD	5 × 4 × 3	Top-Masts, Booms, Spars
Rabphilin-3A	SV Tethering and Docking	1ZBD	8 × 3 × 2	Top-Masts, Booms, Spars
Rab3A-Rabphilin-3A	SV Tethering and Docking	1ZBD	8 × 5 × 3	Top-Masts, Booms, Spars
RIM	Scaffolding			Beams, Steps, Masts, Ribs, Spars, Booms, Top-Masts
Bassoon/piccolo	Scaffolding		80 × 10 × 10	Beams, Steps, Masts, Ribs, Spars, Booms, Top-Masts
Spectrin	Scaffolding			Beams
SV2	Vesicle Scaffolding			SV luminal filaments

diameter in the plane of the PM is expected to range from ∼8 to 13 nm (**Table 2**).

The freeze-fracture replicas of macromolecules that span the PM at active zones each have diameters that range from 9 to 13 nm (Fesce et al., 1980) which includes a thin coating of platinum/carbon.

Thus, based on the requirement for cation flux through the PM at active zones to mediate neurotransmitter secretion and similarities in the dimensions of the cation channels and the PM-spanning macromolecules observed by freeze-fracture techniques at active zones of frog NMJs, it is hypothesized that the N-type Ca^{2+}-channels and Ca^{2+}-gated K^{+} channels are included in the macromolecules that span the PM, and their large cytoplasmic domains, including the synprint region, are included in pegs and ribs (**Table 2**). However, the specific composition and arrangements of the channel types in relation to each other and the docked SVs are under investigation. Through computational modeling, it has been estimated that on average two, but as few as one, active N-type Ca^{2+}-channels associated with a docked SV are required to trigger membrane fusion (Dittrich et al., 2013; Homan et al., 2018). Further, it has also been proposed that the N-type Ca^{2+}-channels are included in the rows that are proximal to the docked SVs (Jung et al., 2016).

The SNARE Proteins

Syntaxin, SNAP25 with Synaptobrevin together referred to as SNARE proteins (Soluble NSF-Attachment Protein Receptor) assemble to form the SNARE complex, and several models have implicated the complex as essential for membrane fusion (Sollner et al., 1993b; Weber et al., 1998; Melia et al., 2002; Han et al., 2004; Südhof and Rothman, 2009; Jackson, 2010; Karatekin et al., 2010). Additionally, other models suggest the roles of the SNARE complex to be upstream to membrane fusion, such as during docking and priming (Coorssen et al., 1998; Tahara et al., 1998; Price et al., 2000; Harlow et al., 2001, 2013; Szule and Coorssen, 2003, 2004; Szule et al., 2003, 2012; Gundersen and Umbach, 2013; Imig et al., 2014; Meriney et al., 2014; Jung et al., 2016).

Syntaxin has a transmembrane domain that spans the PM associated with N-type Ca^{2+} channels through the synprint domain (Bennett et al., 1992b; Sheng et al., 1994; Bezprozvanny et al., 1995; Rettig et al., 1997; Jarvis et al., 2002). *SNAP25* has been post-translationally modified with palmitoyl lipid moieties so that it associates with and is anchored in the hydrophobic core of the PM (Veit et al., 1996). *Synaptobrevin*, also referred to as VAMP (Vesicle-Associated Membrane Protein), has a transmembrane domain that is integral to the SV membrane. The PM-associated proteins Syntaxin and SNAP25 interact with the SV membrane-associated protein Synaptobrevin to form a SNARE core complex through associations of their so-called SNARE coiled-coil domains. The SNARE core complex forms a four-helix bundle with contribution of one coiled-coil domain (i.e., a characteristic 65 amino acid stretch) from Syntaxin, two from SNAP25, and one from Synaptobrevin [reviewed by Sudhof and Rizo (2011) and Rizo (2018)]. Syntaxin1, SNAP25, and VAMP2 are neuronal isoforms, and are present at active zones of frog NMJs (Boudier et al., 1996). From x-ray crystallography [PDB accession code: 1SFC (Sutton et al., 1998); PDB accession code: 1N7S (Ernst and Brunger, 2003)] and cryo-electron microscopy [PDB accession code: 6MTI (Grushin et al., 2019)], the SNARE core complex is ∼12 nm in length and ∼3 nm in diameter (**Table 2**). Further, it has been estimated that multiple SNARE core complexes, at least three in cultured PC12 cells, are associated with each docked vesicle for biological secretion to proceed (Hua and Scheller, 2001). Once assembled, the SNARE core complex is variable in length and it is proposed to zipper, and effectively shorten, to exert force between the two opposing membranes (Weber et al., 1998; Melia et al., 2002).

Pins and ribs/pegs are connected to both the PM and SV membranes, in agreement with the assignment of the SNARE core complex to these AZM macromolecules. The physical dimensions of the SNARE core complex can be accommodated by pins (∼13 nm in length and 5 nm in diameter; **Table 1**), and the proximal portion of ribs between the peg proximal to the docked SV and the SV membrane (∼17 nm in length and

~9 nm in diameter; **Table 1**). It was concluded that pins and proximal portions of ribs change the length to exert variable amounts of force between the SV membrane and PM during the final stage of docking and during priming, as would be expected if SNARE complexes were included in these structures (Szule et al., 2012; Jung et al., 2016). However, further scrutiny suggests that the proximal portions of ribs are associated with pegs that are associated with large macromolecules transmembrane to the PM likely to include voltage-gated Ca^{2+}-channels (Harlow et al., 2001), whereas pins have not been documented to be associated with any such large macromolecules that span the PM. Therefore, while it is plausible that SNARE core complexes are components of both pins and ribs, either only a subset of SNARE core complexes associate with the voltage-gated Ca^{2+}-channels or they are only components of the proximal portions of ribs (**Table 2**).

Synaptotagmin

Synaptotagmin is the putative Ca^{2+}-sensor protein to trigger neurotransmitter secretion (Perin et al., 1990; Mackler et al., 2002). There are 17 isoforms of Synaptotagmin that impart different Ca^{2+}-sensitive cellular functions, and Synaptotagmin 1 has been shown to be present at active zones of frog NMJs (Boudier et al., 1999). For a review of the different isoforms of Synaptotagmin, see Südhof (2002) and Wolfes and Dean (2020). Synaptotagmin has a short SV luminal domain, a transmembrane domain that is integral to the SV membrane, SNARE-interacting domains, and two cytoplasmic Ca^{2+}-binding C_2 domains (C_2A and C_2B) that interact with the plasma membrane (Rizo and Sudhof, 1998; Groffen et al., 2010; Grushin et al., 2019). The SNARE interacting domain consists of multiple binding sites between the C_2 domains and the SNARE core complex, with the primary interface between C_2B and the Syntaxin-SNAP25 complex suggested to be involved triggered secretion that occurs at motoneuron active zones (Zhou et al., 2015). Ca^{2+}-binding to Synaptotagmin changes its interactions with the plasma membrane by masking repulsive electrostatic charges and inducing insertion of hydrophobic residues of the C_2 domains into the hydrophobic region of lipid bilayers to lower the energy barrier of membrane fusion (Chernomordik et al., 1995; Chapman and Davis, 1998; Hui et al., 2009; Kozlov et al., 2010; Paddock et al., 2011; Bowers and Reist, 2020). Further, in the absence of Ca^{2+}-binding, Synaptotagin 1 and 2 form oligomeric rings that are 20–40 nm in diameter (Wang et al., 2014; Zanetti et al., 2016).

The x-ray crystallography-derived structure of Synaptotagmin 2 [PDB accession code: 5CCG (Zhou et al., 2015)] is ~8 nm × ~5 nm × ~5 nm (**Table 2**).

Pins and ribs/pegs are connected to both the PM and SV membranes, and their ~8 connections form a ring around the SV-PM contact area that has been measured to have an average diameter of 20–25 nm (Szule et al., 2012; Jung et al., 2016). This arrangement agrees with the assignment of Synaptotagmin in the proximal portions of ribs and pins. Synaptotagmin is transmembrane to the SV membrane and the SNARE interacting domains are situated with, and bound to, SNARE core complexes, which are proposed to be included in the proximal portions of ribs and pins. The C_2 domains interact with the PM, and the connection sites of ribs/pegs and pins with the PM are closest to the SV membrane—PM contact site when the SV is most primed. And, the rings formed by oligomers of Synaptotagmin are similar in dimension to the rings formed by ribs/pegs and pins around the SV membrane—PM contact site. Further, these AZM macromolecules are of sufficient size to accommodate Synaptotagmin. Thus, it is proposed that Synaptotagmin is included in the proximal portions of ribs and/or pins (**Table 2**).

SNARE Auxiliary Proteins

Munc13 is a large protein (~200 kD) that is thought to be involved in SV priming (Augustin et al., 1999), operating through interactions with membrane lipids including diacylglycerols (Basu et al., 2007), and SNARE proteins (Betz et al., 1997). It has been proposed that Munc13 interactions with Syntaxin regulate the associations between Syntaxin and SNAP25, thereby providing an acceptor complex for Synaptobrevin (Guan et al., 2008). There are several domains of Munc13 including C_2A domain, CaMb (Calmodulin-binding sequence), C1 (membrane diacylglycerol lipid-binding), C_2B, MUN, and C_2C, however, the structure-function relationship of several of these domains remain unclear. Further, the structure of Munc13 in its entirety has not yet been solved, but rather only certain domains have been characterized including a fraction of the MUN-CD domain which has been proposed to be structurally similar to other membrane tethering domains (Li et al., 2011). A fragment of Munc13, that includes the C1, C_2B, and MUN domains, is elongated and reported to be 19.5 nm in length (Xu et al., 2017). It has also been proposed that the C1-C_2B-MUN-C_2C domains bridge the SV membrane to the PM (Quade et al., 2019).

Munc18 is a member of the Sec1/Munc18 (SM) family of proteins that are conserved and critical for different types of membrane trafficking (Carr and Rizo, 2010). Munc18 is thought to be involved in SV priming by controlling the formation of the SNARE complex through direct interactions with the closed conformation of Syntaxin, thereby stabilizing it and hindering the assembly of the SNARE core complex (Dulubova et al., 1999, 2003; Rizo and Sudhof, 2002; Burkhardt et al., 2008; Gerber et al., 2008). It has further been proposed that Munc13 and Munc18 cooperatively chaperone SNARE complex assembly prior to zippering (Shu et al., 2020). The x-ray crystallography-derived structure of Munc18 [PDB accession code: 6LPC (Wang et al., 2020)] is ~8 nm × ~8 nm × ~5 nm (**Table 2**).

Complexin is a cytosolic protein that interacts with the SNARE complex (Chen et al., 2002) at a position that also binds Synaptotagmin (Tang et al., 2006) and has been proposed to act as a clamp that inhibits membrane fusion by inhibiting the complete zippering of the SNARE complex (Giraudo et al., 2006). In this model, Complexin is dislodged from the SNARE complex in a Ca^{2+}-dependent manner to allow membrane fusion to proceed. In an alternate and contradictory model, Complexin has been proposed to facilitate secretion because deletion of Complexin results in reduced Ca^{2+}-triggered neurotransmitter release in synapses of the mouse central nervous system (Xue et al., 2008). Regardless of its physiological role in secretion, it is established that Complexin interacts with the SNARE complex. The x-ray crystallography-derived structure of Complexin [PDB accession code: 3RK3 (Kummel et al., 2011)] is ∼8 nm × ∼1 nm × ∼1 nm (**Table 2**).

NSF (N-ethylmaleimide Sensitive Factor) is an ATPase that, together with SNAP (Soluble NSF Attachment Protein), has been proposed to disassemble the SNARE complex after membrane fusion has occurred so that Syntaxin and SNAP25 can interact with Synaptobrevin of an incoming SV and form a new SNARE complex (Sollner et al., 1993a). NSF binds a subcomplex of SNAP protein and cis-SNARE complex, i.e., Syntaxin, SNAP25, and Synaptobrevin are anchored in the same membrane after fusion, to form a so-called 20S super-complex. ATP hydrolysis initiates NSF to exert torque to unwind the highly stable four-helix SNARE complex bundle (Zhao et al., 2015), and is present in active zones of frog NMJs (Boudier et al., 1996). The single particle cryo-electron microscopy-derived structure of NSF [PDB accession code: 3J95 (Zhao et al., 2015)] is ∼13 nm × ∼13 nm × ∼9 nm (**Table 2**).

Munc13, Munc18, Complexin, NSF each directly associate with the SNARE proteins, that are designated above to be included in the ribs and/or pins. The diameter of the SNARE complex, Munc18, and Complexin (not including Munc13 because its dimensions are unknown) is 9 nm if they were bound together, and less if their binding positions with the SNARE complex were staggered, which can be accommodated by the average diameter of the ribs (9 nm; **Table 1**). Further, the average full length of ribs (29 nm; **Table 1**) or just the proximal portion of ribs (17 nm; **Table 1**) are sufficient to accommodate this complex if their binding to the SNARE complex were staggered. However, it is unlikely that the diameter of the pins (5 nm; **Table 1**) can accommodate this large complex but it is plausible that pins accommodate fewer proteins bound with the SNARE complex or possibly the Munc13 bridge between the SV membrane and the PM. It is also established that NSF binds the cis-SNARE complex, i.e., they are anchored in the same membrane after the SV and PM had fused, which presents the possibility that it is a component of AZM at rest while the SNARE complex is in a trans configuration, i.e., Syntaxin and SNAP25 anchored in the PM and Synaptobrevin anchored in the SV membrane. However, it is also plausible that NSF is recruited from the cytosol by the presence of the cis-SNARE complex after membrane fusion had occurred. Thus, it is hypothesized here that Munc13 is localized to ribs and/or pins, Munc18, and Complexin, are localized to ribs, and NSF is either a component of ribs at rest or binds ribs and/or pins after membrane fusion had occurred (**Table 2**).

Rab3A and Rabphilin-3A

Rab proteins constitute a large family of low molecular mass GTP-binding proteins that are involved in multiple stages of membrane trafficking throughout the cell (Grosshans et al., 2006; Hutagalung and Novick, 2011). They interact with effectors preferentially while in a GTP-bound state through a Switch domain (Pfeffer, 2005). Rab3 proteins are a sub-family that associate with SVs during the late stages of membrane trafficking (Matteoli et al., 1991; Geppert et al., 1997), however, there are multiple isoforms of Rab3 which may have multiple functions, making interpretations of knock-out and over-expression studies difficult (Schluter et al., 2002). *Rab3A* is the most abundant Rab3 protein in the nervous system and in its GTP-bound state translocates from the cytosol to interact with the hydrophobic region of the SV membrane and its effector *Rabphilin-3A* (Stahl et al., 1996). Rabphilin-3A possesses 2 tandem C_2 domains that bind to SV membranes in a Ca^{2+}-dependent manner (Chung et al., 1998). SV redistribution within axon terminals of *C. elegans* and mouse motor-neurons has been demonstrated in Rab3 and Rab3A mutant animals, respectively, with a reduced proportion of SVs at active zones within <50–150 nm of the PM (Nonet et al., 1997; Coleman et al., 2007). It was concluded that Rab3A is not essential for SV fusion with the PM, but rather is required to maintain a normal reserve of SVs during repetitive stimulation by directing them to the active zones (Südhof, 1995; Nonet et al., 1997; Coleman et al., 2007). From the x-ray crystallography-derived structure of Rab3A/Rabphilin-3A complex [PDB accession code: 1ZBD (Ostermeier and Brunger, 1999)] Rab3A is ∼5 nm × ∼4 nm × ∼3 nm, Rabphilin-3A is ∼8 nm × ∼3 nm × ∼2 nm, and the overall Rab3A/Rabphilin-3A complex is ∼8 nm × ∼5 nm × ∼3 nm (**Table 2**).

Rab3A-Rabphilin-3A are directly involved in the interactions between the AZM and the SV membranes at an active zone. The interactions between AZM and the membranes of undocked and docking SVs involve the top masts, booms, spars, ribs and pins, and the dimensions of each are sufficient to accommodate the inclusion of Rab3A and Rabphilin-3A. However, as outlined above, it is likely that the rib connections to docking SV membranes involve the SNARE proteins to form a SNARE core complex to exert force between the docking SV membrane and the PM to bring them into direct contact. Further, pin-SV membrane connections are not likely to involve Rab3A-Rabphilin-3A interactions because pins are directly involved in step 3 of docking once the SV is 15 nm from the PM and in regulating priming for Ca^{2+}-triggered membrane fusion once the SV is docked on the PM (**Figure 2**; Szule et al., 2012; Jung et al., 2016). Also, the pin-SV interactions are not likely involved in maintaining a normal reserve of undocked SVs during stimulation or affecting the movement/state/positioning of undocked SVs during the early steps of docking when it is >15 nm from the PM. Top-masts are likely to be involved in maintaining a normal reserve of undocked SVs at the active zone during stimulation, and the booms and spars are likely to affect the positioning of undocked SV when they are further than 15 nm from the PM. Therefore, it is hypothesized that Rab3A and Rabphilin-3A are localized to the interface of SV membranes with the top-masts, and/or booms, and/or spars (**Table 2**).

AZM Scaffolding Proteins

The AZM consists of several multidomain scaffolding proteins that interact with other proteins enriched at active zones (Schoch and Gundelfinger, 2006; Mittelstaedt et al., 2010).

RIM (Rab3-Interacting Molecules) protein is generally thought to be a critical active zone organizer that recruits voltage-gated Ca^{2+}-channels and is involved in SV docking and priming (Zarebidaki et al., 2020). There are seven members of the RIM protein family, encoded by four genes, with RIM1α likely involved in neurotransmission. RIM1α has a zinc-finger, PDZ, C_2A, and C_2B domains. RIMs have been reported to bind with Rab3A in a GTP-dependent manner (Wang et al., 1997), with Munc13 to form a Rab3-RIM-Munc13 tripartite complex (Dulubova et al., 2005), directly with voltage-gated Ca^{2+}-channels (Kiyonaka et al., 2007; Picher et al., 2017), and with other scaffolding proteins such as liprin-α and ELKS (Schoch et al., 2002; Wang et al., 2002; Lu et al., 2005). Although the structure of RIM in its entirety has not yet been solved, the structures of individual domains have been derived by solution NMR or x-ray crystallography. The structures of the zinc-finger domain [PDB accession code: 2A20 (Dulubova et al., 2005)] is ∼4 nm × ∼3 nm × ∼2 nm, the PDZ domain [PDB accession code: 1ZUB (Lu et al., 2005)] is ∼4 nm × ∼4 nm × ∼2 nm, the C_2A domain [PDB accession code: 2BWQ (Dai et al., 2005)], and the C_2B domain [PDB accession code: 2Q3X (Guan et al., 2007)] is ∼5 nm × ∼4 nm × ∼3 nm (**Table 2**).

Bassoon and *Piccolo* are scaffolding proteins that are enriched at the synaptic active zone, they share high sequence similarity, and have several similar protein interacting domains (Cases-Langhoff et al., 1996; tom Dieck et al., 1998); reviewed by Gundelfinger et al. (2016). Both Basoon and Piccolo are thought to be vertebrate-specific and have been found at active zones of synapses from both the central and peripheral nervous systems. They are also thought to perform multiple presynaptic functions including assembly of active zones, organization of neurotransmitter release machinery, endocytosis, and synapse maintenance. Bassoon and Piccolo have two zinc-finger, three coiled-coil, PDZ, C_2A, and C_2B domains that perform the various functions and bind with other active zone proteins. These proteins include, but are not limited to, Munc13, CAST (CAZ-Associated Structural Protein; an active zone scaffolding protein that is structurally related to ELKS), RIM, and voltage-gated Ca^{2+}-channels (Takao-Rikitsu et al., 2004; Wang et al., 2009; Chen et al., 2011; Gundelfinger et al., 2016). Using immunohistochemistry and super-resolution STED microscopy on active zones at mouse NMJs (Nishimune et al., 2016), Bassoon and Piccolo were shown to be localized to AZM in the vicinity of the voltage-gated Ca^{2+}-channels. Although the structures of Bassoon and Piccolo in their entirety have not yet been solved, silica modeling has predicted their structures based on x-ray crystallography and solution NMR of the multiple domains (Gundelfinger et al., 2016). Overall, Bassoon and Piccolo have an elongated length of ∼80 nm that generally appears filamentous with interspersed globular domains that are estimated to be less than ∼10 nm in diameter (**Table 2**).

Spectrins are a family of cytoskeletal proteins separated into α-Spectrins (αI, αII) and β-Spectrins (βI, βII, βIII, βIV, βV), which are each composed of 2 α and 2 β subunits. Spectrins contain a Calponin Homology (CH) domain, SRC Homology 3 (SH3) domain, Pleckstrin Homology (PH) domain, EF hand domain, and spectrin repeats, and there are binding sites for other proteins including ankyrin, actin, synapsin, among others, and membranes containing PIP_2, phosphatidylserine, and phosphatidylethanolamine lipids (reviewed by Machnicka et al., 2014). Spectrins generally create membrane scaffolds at Golgi, endoplasmic reticulum, and plasma membrane with various functions during cellular trafficking (reviewed by De Matteis and Morrow, 2000). Brain-derived Spectrins have been shown to interact with the presynaptic protein Synapsin I (Sikorski et al., 1991), and β-Spectrin has been shown to interact either directly or indirectly with several active zone proteins including Munc13 in rat brain (Sakaguchi et al., 1998), and voltage-gated Ca^{2+} channels at active zones of the torpedo electric organ synapse which is a modified NMJ (Sunderland et al., 2000). The x-ray crystallography-derived structure of the Spectrin repeat region of β-Spectrin [PDB accession code: 6M3P (Li et al., 2020)] is ∼15 nm × ∼3 nm × ∼2 nm, which link to form elongated filaments.

RIM likely interacts with Rab3A in the top-masts and/or booms and/or spars, Munc13 in the ribs, and voltage-gated Ca^{2+}-channels in ribs/pegs, as outlined above. However, for RIM to simultaneously interact with Rab3A, Munc13, and voltage-gated Ca^{2+}-channels, it is also likely to be a component of beams, steps, and masts. Bassoon and Piccolo function by inducing the assembly and organization of AZM, they possess several protein-binding domains, and their lengths can extend across the depth of AZM. It is likely that their interactions with voltage-gated Ca^{2+}-channels, Munc13 and RIM are localized to pegs, ribs, spars/booms/top-masts. Further, the other scaffolding interactions between Bassoon/Piccolo, RIM, Liprin-α, and CAST/ELKS are likely to occur in the central regions of the AZM (i.e., in the beams, steps, and masts). Spectrin is an elongated filamentous cytoskeletal protein at the interface with the PM, and it possesses several domains that bind other AZM proteins proposed to be at or near the PM including voltage-gated Ca^{2+} channels and Munc13. Beams are also elongated (∼75 nm; **Table 1**) filamentous AZM macromolecules at the interface with the PM that are connected to ∼10–12 ribs, which are thought to include voltage-gated Ca^{2+} channels and Munc13. Thus, it is hypothesized here that Spectrin is a component of beams.

Vesicle Scaffolding

The protein backbone of the luminal filaments is thought to be glycosylated, which forms a carbohydrate matrix that helps bind the soluble content of the SVs (Rahamimoff and Fernandez, 1997; Reigada et al., 2003). It was further hypothesized that the SV luminal filaments organize the locations of AZM macromolecule connections on the external membrane surface and impart the SV with a distinct orientation (Harlow et al., 2013).

SV2 (Synaptic Vesicle protein 2) is an ∼80 kD, highly glycosylated protein that is common to SVs throughout vertebrate nervous systems, and there are three isoforms (SV2A, SV2B, and SV2C) that have differing expression patterns through development. SV2 has 12 transmembrane domains that traverse the SV membrane, seven cytoplasmic domains of varying lengths with phosphorylation sites, and six luminal domains of varying lengths with at least three glycosylation sites (Bajjalieh et al., 1994; Bartholome et al., 2017). SV2 is present at frog NMJs (Dunaevsky and Connor, 2000). At mouse NMJs, SV2A is down-regulated in motor nerve terminals on fast-twitch muscle fibers after birth whereas SV2B and SV2C are retained at nearly all NMJs into adulthood (Chakkalakal et al., 2010). SV2 binds active zone proteins including Synaptotagmin, Synaptophysin, Synaptobrevin, and Rab3A (Bennett et al., 1992a), and it was also proposed that there are ∼2 copies of SV2 per SV (Takamori et al., 2006). The structure of SV2 isolated from its native tissue has not been determined but based on its primary and secondary structures, the large luminal domains are able to traverse the SV lumen several times. Thus, it is likely that the luminal portions of SV2 form the bulk of the luminal assembly of macromolecules detected in SVs at frog NMJs processed by the high-pressure freezing and freeze-substitution methods of fixation and staining (**Figure 1**; Harlow et al., 2013). The large cytoplasmic domains are likely components of AZM macromolecules that connect to SV membranes, such as ribs, pins, spars, booms, and top-masts, and/or non-AZM macromolecules that link SVs to other undocked SVs (**Figure 1**; Szule et al., 2012; Harlow et al., 2013). The nubs linking the luminal assembly to the luminal surface of the SV membrane are also likely composed of a combination of SV2 at the transitions to transmembrane regions and also the luminal portions of other SV membrane proteins, such as synaptotagmin, synaptophysin, synaptobrevin, and Rab3A, that link to SV2.

SUMMARY

The current report, although not exhaustive, provides a hypothesis that incorporates cellular and morphological features of synaptic active zones with biochemical mechanisms of the transient SV trafficking events that lead to neurotransmitter secretion. These events include recruiting and tethering undocked SVs to the active zone, SV docking as a directed approach to the PM, SV priming after it has docked, Ca^{2+}-triggering initiated by an electrical impulse, and fusion between the SV membrane and PM to secrete neurotransmitters. Due to the quantitative characterization of AZM at frog NMJs, both at rest and during impulse-evoked synaptic activity, it is an appropriate model system for which to propose a hypothesis relating to structure, biochemistry, and function. AZM is composed of several morphologically distinct macromolecules that each play a role in the transient stages of membrane trafficking and active zone assembly/organization. In summary (see **Table 2**), the cation channels are proposed to be included in pegs and ribs, the SNARE proteins and SNARE auxiliary proteins are proposed to be included in ribs and pins, Rab3A and Rabphillin-3A are proposed to be included in spars and/or booms and/or top-masts, the scaffolding proteins are proposed to be included in steps and masts, and SV2 is proposed to compose the bulk of SV luminal filaments. It would be of great interest to test this model so that the function of AZM at presynaptic terminals can be understood at the molecular level.

DATA AVAILABILITY STATEMENT

The original contributions presented in the study are included in the article, further inquiries can be directed to the corresponding author.

AUTHOR CONTRIBUTIONS

The author confirms being the sole contributor of this work and has approved it for publication.

FUNDING

This work was funded by the National Institutes of Neurological Disorders and Stroke of the National Institutes of Health, award number R03NS106327.

ACKNOWLEDGMENTS

I am thankful to Dr. R. Burghardt and Dr. Young il Lee for their suggestions with the manuscript. I would also like to acknowledge my Father, Joseph L. Szule (1949–2021), for his life-long support.

REFERENCES

Ackermann, F., Waites, C. L., and Garner, C. C. (2015). Presynaptic active zones in invertebrates and vertebrates. *EMBO Rep.* 16, 923–938. doi: 10.15252/embr.201540434

Alabi, A. A., and Tsien, R. W. (2013). Perspectives on kiss-and-run: role in exocytosis, endocytosis and neurotransmission. *Annu. Rev. Physiol.* 75, 393–422. doi: 10.1146/annurev-physiol-020911-153305

Augustin, I., Rosenmund, C., Sudhof, T. C., and Brose, N. (1999). Munc13-1 is essential for fusion competence of glutamatergic synaptic vesicles. *Nature* 400, 457–461. doi: 10.1038/22768

Bajjalieh, S. M., Frantz, G. D., Weimann, J. M., McConnell, S. K., and Scheller, R. H. (1994). Differential expression of synaptic vesicle protein 2 (SV2) isoforms. *J. Neurosci.* 14, 5223–5235. doi: 10.1523/JNEUROSCI.14-09-05223.1994

Bartholome, O., Van den Ackerveken, P., Sanchez Gil, J., de la Brassinne Bonardeaux, O., Leprince, P., Franzen, R., et al. (2017). Puzzling out synaptic vesicle 2 family members functions. *Front. Mol. Neurosci.* 10:148. doi: 10.3389/fnmol.2017.00148

Basu, J., Betz, A., Brose, N., and Rosenmund, C. (2007). Munc13-1 C1 domain activation lowers the energy barrier for synaptic vesicle fusion. *J. Neurosci.* 27, 1200–1210. doi: 10.1523/JNEUROSCI.4908-06.2007

Bennett, M. R. (1999). The early history of the synapse: from Plato to Sherrington. *Brain Res. Bull.* 50, 95–118. doi: 10.1016/s0361-9230(99)00094-5

Bennett, M. K., Calakos, N., Kreiner, T., and Scheller, R. H. (1992a). Synaptic vesicle membrane proteins interact to form a multimeric complex. *J. Cell. Biol.* 116, 761–775. doi: 10.1083/jcb.116.3.761

Bennett, M. K., Calakos, N., and Scheller, R. H. (1992b). Syntaxin: a synaptic protein implicated in docking of synaptic vesicles at presynaptic active zones. *Science* 257, 255–259. doi: 10.1126/science.1321498

Betz, A., Okamoto, M., Benseler, F., and Brose, N. (1997). Direct interaction of the rat unc-13 homologue Munc13-1 with the N terminus of syntaxin. *J. Biol. Chem.* 272, 2520–2526. doi: 10.1074/jbc.272.4.2520

Bezprozvanny, I., Scheller, R. H., and Tsien, R. W. (1995). Functional impact of syntaxin on gating of N-type and Q-type calcium channels. *Nature* 378, 623–626. doi: 10.1038/378623a0

Boudier, J. A., Charvin, N., Boudier, J. L., Fathallah, M., Tagaya, M., Takahashi, M., et al. (1996). Distribution of components of the SNARE complex in relation to transmitter release sites at the frog neuromuscular junction. *Eur. J. Neurosci.* 8, 545–552. doi: 10.1111/j.1460-9568.1996.tb01239.x

Boudier, J. A., Martin-Moutot, N., Boudier, J. L., Iborra, C., Takahashi, M., and Seagar, M. J. (1999). Redistribution of presynaptic proteins during alpha-latrotoxin-induced release of neurotransmitter and membrane retrieval at the frog neuromuscular junction. *Eur. J. Neurosci.* 11, 3449–3456. doi: 10.1046/j.1460-9568.1999.00778.x

Bowers, M. R., and Reist, N. E. (2020). The C2A domain of synaptotagmin is an essential component of the calcium sensor for synaptic transmission. *PLoS One* 15:e0228348. doi: 10.1371/journal.pone.0228348

Burkhardt, P., Hattendorf, D. A., Weis, W. I., and Fasshauer, D. (2008). Munc18a controls SNARE assembly through its interaction with the syntaxin N-peptide. *EMBO J.* 27, 923–933. doi: 10.1038/emboj.2008.37

Burré, J., and Volknandt, W. (2007). The synaptic vesicle proteome. *J. Neurochem.* 101, 1448–1462. doi: 10.1111/j.1471-4159.2007.04453.x

Carr, C. M., and Rizo, J. (2010). At the junction of SNARE and SM protein function. *Curr. Opin. Cell Biol.* 22, 488–495. doi: 10.1016/j.ceb.2010.04.006

Cases-Langhoff, C., Voss, B., Garner, A. M., Appeltauer, U., Takei, K., Kindler, S., et al. (1996). Piccolo, a novel 420 kDa protein associated with the presynaptic cytomatrix. *Eur. J. Cell Biol.* 69, 214–223.

Catterall, W. A. (2000–2013). "Biochemical Studies of Voltage-Gated Ca^{2+} Channels," in *Madame Curie Bioscience Database [Internet]*, (Austin, TX: Landes Bioscience).

Ceccarelli, B., Grohovaz, F., and Hurlbut, W. P. (1979a). Freeze-fracture studies of frog neuromuscular junctions during intense release of neurotransmitter. I. Effects of black widow spider venom and Ca2+-free solutions on the structure of the active zone. *J. Cell Biol.* 81, 163–177. doi: 10.1083/jcb.81.1.163

Ceccarelli, B., Grohovaz, F., and Hurlbut, W. P. (1979b). Freeze-fracture studies of frog neuromuscular junctions during intense release of neurotransmitter. II. Effects of electrical stimulation and high potassium. *J. Cell Biol.* 81, 178–192. doi: 10.1083/jcb.81.1.178

Ceccarelli, B., and Hurlbut, W. P. (1980). Vesicle hypothesis of the release of quanta of acetylcholine. *Physiol. Rev.* 60, 396–441. doi: 10.1152/physrev.1980.60.2.396

Chakkalakal, J. V., Nishimune, H., Ruas, J. L., Spiegelman, B. M., and Sanes, J. R. (2010). Retrograde influence of muscle fibers on their innervation revealed by a novel marker for slow motoneurons. *Development* 137, 3489–3499. doi: 10.1242/dev.053348

Chapman, E. R., and Davis, A. F. (1998). Direct interaction of a Ca2+-binding loop of synaptotagmin with lipid bilayers. *J. Biol. Chem.* 273, 13995–14001. doi: 10.1074/jbc.273.22.13995

Chen, J., Billings, S. E., and Nishimune, H. (2011). Calcium channels link the muscle-derived synapse organizer laminin β2 to Bassoon and CAST/Erc2 to organize presynaptic active zones. *J. Neurosci.* 31, 512–525. doi: 10.1523/JNEUROSCI.3771-10.2011

Chen, X., Tomchick, D. R., Kovrigin, E., Arac, D., Machius, M., Sudhof, T. C., et al. (2002). Three-dimensional structure of the complexin/SNARE complex. *Neuron* 33, 397–409. doi: 10.1016/s0896-6273(02)00583-4

Chernomordik, L., Kozlov, M. M., and Zimmerberg, J. (1995). Lipids in biological membrane fusion. *J. Membr. Biol.* 146, 1–14. doi: 10.1007/BF00232676

Chua, J. J., Kindler, S., Boyken, J., and Jahn, R. (2010). The architecture of an excitatory synapse. *J. Cell Sci.* 123, 819–823. doi: 10.1242/jcs.052696

Chung, S. H., Song, W. J., Kim, K., Bednarski, J. J., Chen, J., Prestwich, G. D., et al. (1998). The C2 domains of Rabphilin3A specifically bind phosphatidylinositol 4,5-bisphosphate containing vesicles in a Ca2+-dependent manner. *in vitro* characteristics and possible significance. *J. Biol. Chem.* 273, 10240–10248. doi: 10.1074/jbc.273.17.10240

Cohen, M. W., Jones, O. T., and Angelides, K. J. (1991). Distribution of Ca2+ channels on frog motor nerve terminals revealed by fluorescent omega-conotoxin. *J. Neurosci.* 11, 1032–1039. doi: 10.1523/JNEUROSCI.11-04-01032.1991

Cole, A. A., Chen, X., and Reese, T. S. (2016). A network of three types of filaments organizes synaptic vesicles for storage, mobilization and docking. *J. Neurosci.* 36, 3222–3230. doi: 10.1523/JNEUROSCI.2939-15.2016

Coleman, W. L., Bill, C. A., and Bykhovskaia, M. (2007). Rab3a deletion reduces vesicle docking and transmitter release at the mouse diaphragm synapse. *J. Neurosci.* 148, 1–6. doi: 10.1016/j.neuroscience.2007.06.011

Coorssen, J. R., Blank, P. S., Tahara, M., and Zimmerberg, J. (1998). Biochemical and functional studies of cortical vesicle fusion: the SNARE complex and Ca2+ sensitivity. *J. Cell Biol.* 143, 1845–1857. doi: 10.1083/jcb.143.7.1845

Couteaux, R., and Pecot-Dechavassine, M. (1970). [Synaptic vesicles and pouches at the level of "active zones" of the neuromuscular junction]. *C. R. Acad. Sci. Hebd. Seances Acad. Sci. D.* 271, 2346–2349.

Dai, H., Tomchick, D. R., Garcia, J., Sudhof, T. C., Machius, M., and Rizo, J. (2005). Crystal structure of the RIM2 C2A-domain at 1.4 A resolution. *Biochemistry* 44, 13533–13542. doi: 10.1021/bi0513608

De Matteis, M. A., and Morrow, J. S. (2000). Spectrin tethers and mesh in the biosynthetic pathway. *J. Cell Sci.* 113, 2331–2343. doi: 10.1242/jcs.113.13.2331

Dittrich, M., Pattillo, J. M., King, J. D., Cho, S., Stiles, J. R., and Meriney, S. D. (2013). An excess-calcium-binding-site model predicts neurotransmitter release at the neuromuscular junction. *Biophys. J.* 104, 2751–2763. doi: 10.1016/j.bpj.2013.05.023

Doherty, G. J., and McMahon, H. T. (2009). Mechanisms of endocytosis. *Annu. Rev. Biochem.* 78, 857–902. doi: 10.1146/annurev.biochem.78.081307.110540

Dulubova, I., Lou, X., Lu, J., Huryeva, I., Alam, A., Schneggenburger, R., et al. (2005). A Munc13/RIM/Rab3 tripartite complex: from priming to plasticity? *EMBO J.* 24, 2839–2850. doi: 10.1038/sj.emboj.7600753

Dulubova, I., Sugita, S., Hill, S., Hosaka, M., Fernandez, I., Sudhof, T. C., et al. (1999). A conformational switch in syntaxin during exocytosis: role of munc18. *EMBO J.* 18, 4372–4382. doi: 10.1093/emboj/18.16.4372

Dulubova, I., Yamaguchi, T., Arac, D., Li, H., Huryeva, I., Min, S. W., et al. (2003). Convergence and divergence in the mechanism of SNARE binding by Sec1/Munc18-like proteins. *Proc. Natl. Acad. Sci. U S A* 100, 32–37. doi: 10.1073/pnas.232701299

Dunaevsky, A., and Connor, E. A. (2000). F-actin is concentrated in nonrelease domains at frog neuromuscular junctions. *J. Neurosci.* 20, 6007–6012. doi: 10.1523/JNEUROSCI.20-16-06007.2000

Ehmann, N., van de Linde, S., Alon, A., Ljaschenko, D., Keung, X. Z., Holm, T., et al. (2014). Quantitative super-resolution imaging of Bruchpilot distinguishes active zone states. *Nat. Commun.* 5:4650. doi: 10.1038/ncomms5650

Ernst, J. A., and Brunger, A. T. (2003). High resolution structure, stability and synaptotagmin binding of a truncated neuronal SNARE complex. *J. Biol. Chem.* 278, 8630–8636. doi: 10.1074/jbc.M211889200

Fatt, P., and Katz, B. (1952). Spontaneous subthreshold activity at motor nerve endings. *J. Physiol.* 117, 109–128. doi: 10.1113/jphysiol.1952.sp004735

Fernandez-Busnadiego, R., Zuber, B., Maurer, U. E., Cyrklaff, M., Baumeister, W., and Lucic, V. (2010). Quantitative analysis of the native presynaptic cytomatrix by cryoelectron tomography. *J. Cell Biol.* 188, 145–156. doi: 10.1083/jcb.200908082

Fesce, R., Grohovaz, F., Hurlbut, W. P., and Ceccarelli, B. (1980). Freeze-fracture studies of frog neuromuscular junctions during intense release of neurotransmitter. III. A morphometric analysis of the number and diameter of intramembrane particles. *J. Cell Biol.* 85, 337–345. doi: 10.1083/jcb.85.2.337

Gao, S., Yao, X., and Yan, N. (2021). Structure of human Cav2.2 channel blocked by the painkiller ziconotide. *Nature* 596, 143–147. doi: 10.1038/s41586-021-03699-6

Geppert, M., Goda, Y., Stevens, C. F., and Sudhof, T. C. (1997). The small GTP-binding protein Rab3A regulates a late step in synaptic vesicle fusion. *Nature* 387, 810–814. doi: 10.1038/42954

Gerber, S. H., Rah, J. C., Min, S. W., Liu, X., de Wit, H., Dulubova, I., et al. (2008). Conformational switch of syntaxin-1 controls synaptic vesicle fusion. *Science* 321, 1507–1510. doi: 10.1126/science.1163174

Giraudo, C. G., Eng, W. S., Melia, T. J., and Rothman, J. E. (2006). A clamping mechanism involved in SNARE-dependent exocytosis. *Science* 313, 676–680. doi: 10.1126/science.1129450

Gray, E. G. (1963). Electron microscopy of presynaptic organelles of the spinal cord. *J. Anat.* 97, 101–106.

Groffen, A. J., Martens, S., Diez Arazola, R., Cornelisse, L. N., Lozovaya, N., de Jong, A. P., et al. (2010). Doc2b is a high-affinity Ca2+ sensor for spontaneous neurotransmitter release. *Science* 327, 1614–1618. doi: 10.1126/science.1183765

Grosshans, B. L., Ortiz, D., and Novick, P. (2006). Rabs and their effectors: achieving specificity in membrane traffic. *Proc. Natl. Acad. Sci. U S A* 103, 11821–11827. doi: 10.1073/pnas.0601617103

Grushin, K., Wang, J., Coleman, J., Rothman, J. E., Sindelar, C. V., and Krishnakumar, S. S. (2019). Structural basis for the clamping and Ca(2+) activation of SNARE-mediated fusion by synaptotagmin. *Nat. Commun.* 10:2413. doi: 10.1038/s41467-019-10391-x

Guan, R., Dai, H., and Rizo, J. (2008). Binding of the Munc13-1 MUN domain to membrane-anchored SNARE complexes. *Biochemistry* 47, 1474–1481. doi: 10.1021/bi702345m

Guan, R., Dai, H., Tomchick, D. R., Dulubova, I., Machius, M., Sudhof, T. C., et al. (2007). Crystal structure of the RIM1alpha C2B domain at 1.7 A resolution. *Biochemistry* 46, 8988–8998. doi: 10.1021/bi700698a

Gundelfinger, E. D., Reissner, C., and Garner, C. C. (2016). Role of bassoon and piccolo in assembly and molecular organization of the active zone. *Front. Synaptic Neurosci.* 7:19. doi: 10.3389/fnsyn.2015.00019

Gundersen, C. B., and Umbach, J. A. (2013). Synaptotagmins 1 and 2 as mediators of rapid exocytosis at nerve terminals: the dyad hypothesis. *J. Theor. Biol.* 332, 149–160. doi: 10.1016/j.jtbi.2013.04.029

Han, X., Wang, C. T., Bai, J., Chapman, E. R., and Jackson, M. B. (2004). Transmembrane segments of syntaxin line the fusion pore of Ca2+-triggered exocytosis. *Science* 304, 289–292. doi: 10.1126/science.1095801

Hanson, P. I., Heuser, J. E., and Jahn, R. (1997). Neurotransmitter release - four years of SNARE complexes. *Curr. Opin. Neurobiol.* 7, 310–315. doi: 10.1016/s0959-4388(97)80057-8

Harlow, M. L., Ress, D., Stoschek, A., Marshall, R. M., and McMahan, U. J. (2001). The architecture of active zone material at the frog's neuromuscular junction. *Nature* 409, 479–484. doi: 10.1038/35054000

Harlow, M. L., Szule, J. A., Xu, J., Jung, J. H., Marshall, R. M., and McMahan, U. J. (2013). Alignment of synaptic vesicle macromolecules with the macromolecules in active zone material that direct vesicle docking. *PLoS One* 8:e69410. doi: 10.1371/journal.pone.0069410

Heuser, J. E., and Reese, T. S. (1973). Evidence for recycling of synaptic vesicle membrane during transmitter release at the frog neuromuscular junction. *J. Cell Biol.* 57, 315–344. doi: 10.1083/jcb.57.2.315

Heuser, J. E., and Reese, T. S. (1981). Structural changes after transmitter release at the frog neuromuscular junction. *J. Cell Biol.* 88, 564–580. doi: 10.1083/jcb.88.3.564

Heuser, J. E., Reese, T. S., Dennis, M. J., Jan, Y., Jan, L., and Evans, L. (1979). Synaptic vesicle exocytosis captured by quick freezing and correlated with quantal transmitter release. *J. Cell Biol.* 81, 275–300. doi: 10.1083/jcb.81.2.275

Heuser, J. E., Reese, T. S., and Landis, D. M. (1974). Functional changes in frog neuromuscular junctions studied with freeze-fracture. *J. Neurocytol.* 3, 109–131. doi: 10.1007/BF01111936

Homan, A. E., Laghaei, R., Dittrich, M., and Meriney, S. D. (2018). Impact of spatiotemporal calcium dynamics within presynaptic active zones on synaptic delay at the frog neuromuscular junction. *J. Neurophysiol.* 119, 688–699. doi: 10.1152/jn.00510.2017

Homan, A. E., and Meriney, S. D. (2018). Active zone structure-function relationships at the neuromuscular junction. *Synapse* 72:e22057. doi: 10.1002/syn.22057

Hua, Y., and Scheller, R. H. (2001). Three SNARE complexes cooperate to mediate membrane fusion. *Proc. Natl. Acad. Sci. U S A* 98, 8065–8070. doi: 10.1073/pnas.131214798

Hui, E., Johnson, C. P., Yao, J., Dunning, F. M., and Chapman, E. R. (2009). Synaptotagmin-mediated bending of the target membrane is a critical step in Ca(2+)-regulated fusion. *Cell* 138, 709–721. doi: 10.1016/j.cell.2009.05.049

Hutagalung, A. H., and Novick, P. J. (2011). Role of Rab GTPases in membrane traffic and cell physiology. *Physiol. Rev.* 91, 119–149. doi: 10.1152/physrev.00059.2009

Imig, C., Min, S. W., Krinner, S., Arancillo, M., Rosenmund, C., Sudhof, T. C., et al. (2014). The morphological and molecular nature of synaptic vesicle priming at presynaptic active zones. *Neuron* 84, 416–431. doi: 10.1016/j.neuron.2014.10.009

Jackson, M. B. (2010). SNARE complex zipping as a driving force in the dilation of proteinaceous fusion pores. *J. Membr. Biol.* 235, 89–100. doi: 10.1007/s00232-010-9258-1

Jackson, M. B., and Chapman, E. R. (2008). The fusion pores of Ca2+ -triggered exocytosis. *Nat. Struct. Mol. Biol.* 15, 684–689. doi: 10.1038/nsmb.1449

Jahn, R., Lang, T., and Sudhof, T. C. (2003). Membrane fusion. *Cell* 112, 519–533. doi: 10.1016/s0092-8674(03)00112-0

Jahn, R., and Sudhof, T. C. (1999). Membrane fusion and exocytosis. *Annu. Rev. Biochem.* 68, 863–911. doi: 10.1146/annurev.biochem.68.1.863

Jarvis, S. E., Barr, W., Feng, Z. P., Hamid, J., and Zamponi, G. W. (2002). Molecular determinants of syntaxin 1 modulation of N-type calcium channels. *J. Biol. Chem.* 277, 44399–44407. doi: 10.1074/jbc.M206902200

Jiang, Y., Lee, A., Chen, J., Cadene, M., Chait, B. T., and MacKinnon, R. (2002). Crystal structure and mechanism of a calcium-gated potassium channel. *Nature* 417, 515–522. doi: 10.1038/417515a

Jung, J. H., Szule, J. A., Marshall, R. M., and McMahan, U. J. (2016). Variable priming of a docked synaptic vesicle. *Proc. Natl. Acad. Sci. U S A* 113, E1098–E1107. doi: 10.1073/pnas.1523054113

Jung, J. H., Szule, J. A., Stouder, K., Marshall, R. M., and McMahan, U. J. (2018). Active zone material-directed orientation, docking and fusion of dense core vesicles alongside synaptic vesicles at neuromuscular junctions. *Front. Neuroanat.* 12:72. doi: 10.3389/fnana.2018.00072

Karatekin, E., Di Giovanni, J., Iborra, C., Coleman, J., O'Shaughnessy, B., Seagar, M., et al. (2010). A fast, single-vesicle fusion assay mimics physiological SNARE requirements. *Proc. Natl. Acad. Sci. U S A* 107, 3517–3521. doi: 10.1073/pnas.0914723107

Katz, B. (1969). *The Release of Neural Transmitter Substances.* Springfield, IL: Thomas.

Katz, B., and Miledi, R. (1967). The timing of calcium action during neuromuscular transmission. *J. Physiol.* 189, 535–544. doi: 10.1113/jphysiol.1967.sp008183

Katz, B., and Miledi, R. (1979). Estimates of quantal content during 'chemical potentiation' of transmitter release. *Proc. R. Soc. Lond. B. Biol. Sci.* 205, 369–378. doi: 10.1098/rspb.1979.0070

Kiyonaka, S., Wakamori, M., Miki, T., Uriu, Y., Nonaka, M., Bito, H., et al. (2007). RIM1 confers sustained activity and neurotransmitter vesicle anchoring to presynaptic Ca2+ channels. *Nat. Neurosci.* 10, 691–701. doi: 10.1038/nn1904

Klenchin, V. A., and Martin, T. F. (2000). Priming in exocytosis: attaining fusion-competence after vesicle docking. *Biochimie* 82, 399–407. doi: 10.1016/s0300-9084(00)00208-x

Kozlov, M. M., McMahon, H. T., and Chernomordik, L. V. (2010). Protein-driven membrane stresses in fusion and fission. *Trends Biochem. Sci.* 35, 699–706. doi: 10.1016/j.tibs.2010.06.003

Kuffler, S. W., and Vaughan Williams, E. M. (1953). Small-nerve junctional potentials; the distribution of small motor nerves to frog skeletal muscle and the membrane characteristics of the fibres they innervate. *J. Physiol.* 121, 289–317. doi: 10.1113/jphysiol.1953.sp004948

Kummel, D., Krishnakumar, S. S., Radoff, D. T., Li, F., Giraudo, C. G., Pincet, F., et al. (2011). Complexin cross-links prefusion SNAREs into a zigzag array. *Nat. Struct. Mol. Biol.* 18, 927–933. doi: 10.1038/nsmb.2101

Li, J., Chen, K., Zhu, R., and Zhang, M. (2020). Structural basis underlying strong interactions between ankyrins and spectrins. *J. Mol. Biol.* 432, 3838–3850. doi: 10.1016/j.jmb.2020.04.023

Li, W., Ma, C., Guan, R., Xu, Y., Tomchick, D. R., and Rizo, J. (2011). The crystal structure of a Munc13 C-terminal module exhibits a remarkable similarity to vesicle tethering factors. *Structure* 19, 1443–1455. doi: 10.1016/j.str.2011.07.012

Lu, J., Li, H., Wang, Y., Sudhof, T. C., and Rizo, J. (2005). Solution structure of the RIM1alpha PDZ domain in complex with an ELKS1b C-terminal peptide. *J. Mol. Biol.* 352, 455–466. doi: 10.1016/j.jmb.2005.07.047

Machnicka, B., Czogalla, A., Hryniewicz-Jankowska, A., Boguslawska, D. M., Grochowalska, R., Heger, E., et al. (2014). Spectrins: a structural platform for stabilization and activation of membrane channels, receptors and transporters. *Biochim. Biophys. Acta* 1838, 620–634. doi: 10.1016/j.bbamem.2013.05.002

Mackler, J. M., Drummond, J. A., Loewen, C. A., Robinson, I. M., and Reist, N. E. (2002). The C(2)B Ca(2+)-binding motif of synaptotagmin is required for synaptic transmission *in vivo*. *Nature* 418, 340–344. doi: 10.1038/nature00846

Matkovic, T., Siebert, M., Knoche, E., Depner, H., Mertel, S., Owald, D., et al. (2013). The Bruchpilot cytomatrix determines the size of the readily releasable pool of synaptic vesicles. *J. Cell Biol.* 202, 667–683. doi: 10.1083/jcb.201301072

Matteoli, M., Takei, K., Cameron, R., Hurlbut, P., Johnston, P. A., Sudhof, T. C., et al. (1991). Association of Rab3A with synaptic vesicles at late stages of the secretory pathway. *J. Cell Biol.* 115, 625–633. doi: 10.1083/jcb.115.3.625

McMahan, U. J., Peper, K., and Spitzer, N. C. (1972). Visual identification of nerve terminals in living isolated skeletal-muscle. *Proc. Royal Soc. Lond. Series B. Biol. Sci.* 181, 421–430. doi: 10.1098/rspb.1972.0059

Melia, T. J., Weber, T., McNew, J. A., Fisher, L. E., Johnston, R. J., Parlati, F., et al. (2002). Regulation of membrane fusion by the membrane-proximal coil of the t-SNARE during zippering of SNAREpins. *J. Cell Biol.* 158, 929–940. doi: 10.1083/jcb.200112081

Meriney, S. D., Umbach, J. A., and Gundersen, C. B. (2014). Fast, Ca-dependent exocytosis at nerve terminals: shortcomings of SNARE-based models. *Prog. Neurobiol.* 121, 55–90. doi: 10.1016/j.pneurobio.2014.07.001

Mittelstaedt, T., Alvarez-Baron, E., and Schoch, S. (2010). RIM proteins and their role in synapse function. *Biol. Chem.* 391, 599–606. doi: 10.1515/BC.2010.064

Nagwaney, S., Harlow, M. L., Jung, J. H., Szule, J. A., Ress, D., Xu, J., et al. (2009). Macromolecular connections of active zone material to docked synaptic vesicles and presynaptic membrane at neuromuscular junctions of mouse. *J. Comp. Neurol.* 513, 457–468. doi: 10.1002/cne.21975

Neher, E., and Sakaba, T. (2008). Multiple roles of calcium ions in the regulation of neurotransmitter release. *Neuron* 59, 861–872. doi: 10.1016/j.neuron.2008.08.019

Nishimune, H., Badawi, Y., Mori, S., and Shigemoto, K. (2016). Dual-color STED microscopy reveals a sandwich structure of bassoon and piccolo in active zones of adult and aged mice. *Sci. Rep.* 6:27935. doi: 10.1038/srep27935

Nonet, M. L., Staunton, J. E., Kilgard, M. P., Fergestad, T., Hartwieg, E., Horvitz, H. R., et al. (1997). *Caenorhabditis elegans* rab-3 mutant synapses exhibit impaired function and are partially depleted of vesicles. *J. Neurosci.* 17, 8061–8073. doi: 10.1523/JNEUROSCI.17-21-08061.1997

Ostermeier, C., and Brunger, A. T. (1999). Structural basis of rab effector specificity: crystal structure of the small G protein Rab3A complexed with the effector domain of rabphilin-3A. *Cell* 96, 363–374. doi: 10.1016/s0092-8674(00)80549-8

Paddock, B. E., Wang, Z., Biela, L. M., Chen, K., Getzy, M. D., Striegel, A., et al. (2011). Membrane penetration by synaptotagmin is required for coupling calcium binding to vesicle fusion *in vivo*. *J. Neurosci.* 31, 2248–2257. doi: 10.1523/JNEUROSCI.3153-09.2011

Palade, G. E. (1954). Electron microscope observations of interneuronal and neuromuscular synapses. *Anat. Rec.* 118, 335–336.

Palay, S. L. (1954). Electron microscope study of the cytoplasm of neurons. *Anat. Rec.* 118:335.

Perin, M. S., Fried, V. A., Mignery, G. A., Jahn, R., and Sudhof, T. C. (1990). Phospholipid binding by a synaptic vesicle protein homologous to the regulatory region of protein kinase C. *Nature* 345, 260–263. doi: 10.1038/345260a0

Perkins, G. A., Jackson, D. R., and Spirou, G. A. (2015). Resolving presynaptic structure by electron tomography. *Synapse* 69, 268–282. doi: 10.1002/syn.21813

Pfeffer, S. R. (2005). Structural clues to Rab GTPase functional diversity. *J. Biol. Chem.* 280, 15485–15488. doi: 10.1074/jbc.R500003200

Picher, M. M., Oprisoreanu, A. M., Jung, S., Michel, K., Schoch, S., and Moser, T. (2017). Rab interacting molecules 2 and 3 directly Interact with the pore-forming CaV1.3 Ca(2+) channel subunit and promote its membrane expression. *Front. Cell. Neurosci.* 11:160. doi: 10.3389/fncel.2017.00160

Price, A., Seals, D., Wickner, W., and Ungermann, C. (2000). The docking stage of yeast vacuole fusion requires the transfer of proteins from a cis-SNARE complex to a Rab/Ypt protein. *J. Cell Biol.* 148, 1231–1238. doi: 10.1083/jcb.148.6.1231

Propst, J. W., and Ko, C. P. (1987). Correlations between active zone ultrastructure and synaptic function studied with freeze-fracture of physiologically identified neuromuscular junctions. *J. Neurosci.* 7, 3654–3664. doi: 10.1523/JNEUROSCI.07-11-03654.1987

Pumplin, D. W., Reese, T. S., and Llinas, R. (1981). Are the presynaptic membrane particles the calcium channels?. *Proc. Natl. Acad. Sci. U S A* 78, 7210–7213. doi: 10.1073/pnas.78.11.7210

Quade, B., Camacho, M., Zhao, X., Orlando, M., Trimbuch, T., Xu, J., et al. (2019). Membrane bridging by Munc13–1 is crucial for neurotransmitter release. *eLife* 8:e42806. doi: 10.7554/eLife.42806

Rahamimoff, R., and Fernandez, J. M. (1997). Pre- and postfusion regulation of transmitter release. *Neuron* 18, 17–27. doi: 10.1016/s0896-6273(01)80043-x

Rand, R. P., and Parsegian, V. A. (1989). Hydration forces between phospholipid bilayers. *Biochim. Biophys. Acta* 988, 351–376. doi: 10.1016/0304-4157(89)90010-5

Reigada, D., Diez-Perez, I., Gorostiza, P., Verdaguer, A., Gomez de Aranda, I., Pineda, O., et al. (2003). Control of neurotransmitter release by an internal gel matrix in synaptic vesicles. *Proc. Natl. Acad. Sci. U S A* 100, 3485–3490. doi: 10.1073/pnas.0336914100

Ress, D. B., Harlow, M. L., Marshall, R. M., and McMahan, U. J. (2004). Methods for generating high-resolution structural models from electron microscope tomography data. *Structure* 12, 1763–1774. doi: 10.1016/j.str.2004.07.022

Rettig, J., Heinemann, C., Ashery, U., Sheng, Z. H., Yokoyama, C. T., Catterall, W. A., et al. (1997). Alteration of Ca2+ dependence of neurotransmitter release by disruption of Ca2+ channel/syntaxin interaction. *J. Neurosci.* 17, 6647–6656. doi: 10.1523/JNEUROSCI.17-17-06647.1997

Rizo, J. (2018). Mechanism of neurotransmitter release coming into focus. *Protein Sci.* 27, 1364–1391. doi: 10.1002/pro.3445

Rizo, J., and Rosenmund, C. (2008). Synaptic vesicle fusion. *Nat. Struct. Mol. Biol.* 15, 665–674. doi: 10.1038/nsmb.1450

Rizo, J., and Sudhof, T. C. (1998). C2-domains, structure and function of a universal Ca2+-binding domain. *J. Biol. Chem.* 273, 15879–15882. doi: 10.1074/jbc.273.26.15879

Rizo, J., and Sudhof, T. C. (2002). Snares and Munc18 in synaptic vesicle fusion. *Nat. Rev. Neurosci.* 3, 641–653. doi: 10.1038/nrn898

Rizo, J., and Sudhof, T. C. (2012). The membrane fusion enigma: SNAREs, Sec1/Munc18 proteins and their accomplices—guilty as charged? *Annu. Rev. Cell Dev. Biol.* 28, 279–308. doi: 10.1146/annurev-cellbio-101011-155818

Rizo, J., and Xu, J. (2015). The synaptic vesicle release machinery. *Annu. Rev. Biophys.* 44, 339–367. doi: 10.1146/annurev-biophys-060414-034057

Rizzoli, S. O., and Betz, W. J. (2004). The structural organization of the readily releasable pool of synaptic vesicles. *Science* 303, 2037–2039. doi: 10.1126/science.1094682

Rizzoli, S. O., and Betz, W. J. (2005). Synaptic vesicle pools. *Nat. Rev. Neurosci.* 6, 57–69. doi: 10.1038/nrn1583

Rizzoli, S. O., and Jahn, R. (2007). Kiss-and-run, collapse and 'readily retrievable' vesicles. *Traffic* 8, 1137–1144. doi: 10.1111/j.1600-0854.2007.00614.x

Robitaille, R., Adler, E. M., and Charlton, M. P. (1990). Strategic location of calcium channels at transmitter release sites of frog neuromuscular synapses. *Neuron* 5, 773–779. doi: 10.1016/0896-6273(90)90336-e

Robitaille, R., Adler, E. M., and Charlton, M. P. (1993a). Calcium channels and calcium-gated potassium channels at the frog neuromuscular junction. *J. Physiol. Paris* 87, 15–24. doi: 10.1016/0928-4257(93)90020-t

Robitaille, R., Garcia, M. L., Kaczorowski, G. J., and Charlton, M. P. (1993b). Functional colocalization of calcium and calcium-gated potassium channels in control of transmitter release. *Neuron* 11, 645–655. doi: 10.1016/0896-6273(93)90076-4

Robitaille, R., and Charlton, M. P. (1992). Presynaptic calcium signals and transmitter release are modulated by calcium-activated potassium channels. *J. Neurosci.* 12, 297–305. doi: 10.1523/JNEUROSCI.12-01-00297.1992

Sakaguchi, G., Orita, S., Naito, A., Maeda, M., Igarashi, H., Sasaki, T., et al. (1998). A novel brain-specific isoform of beta spectrin: isolation and its interaction with Munc13. *Biochem. Biophys. Res. Commun.* 248, 846–851. doi: 10.1006/bbrc.1998.9067

Schluter, O. M., Khvotchev, M., Jahn, R., and Sudhof, T. C. (2002). Localization versus function of Rab3 proteins. Evidence for a common regulatory role in controlling fusion. *J. Biol. Chem.* 277, 40919–40929. doi: 10.1074/jbc.M203704200

Schoch, S., Castillo, P. E., Jo, T., Mukherjee, K., Geppert, M., Wang, Y., et al. (2002). RIM1alpha forms a protein scaffold for regulating neurotransmitter release at the active zone. *Nature* 415, 321–326. doi: 10.1038/415321a

Schoch, S., and Gundelfinger, E. D. (2006). Molecular organization of the presynaptic active zone. *Cell Tissue Res.* 326, 379–391. doi: 10.1007/s00441-006-0244-y

Schrod, N., Vanhecke, D., Laugks, U., Stein, V., Fukuda, Y., Schaffer, M., et al. (2018). Pleomorphic linkers as ubiquitous structural organizers of vesicles in axons. *PLoS One* 13:e0197886. doi: 10.1371/journal.pone.0197886

Sehnal, D., Bittrich, S., Deshpande, M., Svobodova, R., Berka, K., Bazgier, V., et al. (2021). Mol* viewer: modern web app for 3D visualization and analysis of large biomolecular structures. *Nucleic Acids Res.* 49, W431–W437. doi: 10.1093/nar/gkab314

Sheng, Z. H., Rettig, J., Takahashi, M., and Catterall, W. A. (1994). Identification of a syntaxin-binding site on N-type calcium channels. *Neuron* 13, 1303–1313. doi: 10.1016/0896-6273(94)90417-0

Shu, T., Jin, H., Rothman, J. E., and Zhang, Y. (2020). Munc13–1 MUN domain and Munc18-1 cooperatively chaperone SNARE assembly through a tetrameric complex. *Proc. Natl. Acad. Sci. U S A* 117, 1036–1041. doi: 10.1073/pnas.1914361117

Sikorski, A. F., Terlecki, G., Zagon, I. S., and Goodman, S. R. (1991). Synapsin I-mediated interaction of brain spectrin with synaptic vesicles. *J. Cell Biol.* 114, 313–318. doi: 10.1083/jcb.114.2.313

Slater, C. R. (2003). Structural determinants of the reliability of synaptic transmission at the vertebrate neuromuscular junction. *J. Neurocytol.* 32, 505–522. doi: 10.1023/B:NEUR.0000020607.17881.9b

Slater, C. R. (2015). The functional organization of motor nerve terminals. *Prog. Neurobiol.* 134, 55–103. doi: 10.1016/j.pneurobio.2015.09.004

Snead, D., and Eliezer, D. (2019). Intrinsically disordered proteins in synaptic vesicle trafficking and release. *J. Biol. Chem.* 294, 3325–3342. doi: 10.1074/jbc.REV118.006493

Sollner, T., Bennett, M. K., Whiteheart, S. W., Scheller, R. H., and Rothman, J. E. (1993a). A protein assembly-disassembly pathway *in vitro* that may correspond to sequential steps of synaptic vesicle docking, activation and fusion. *Cell* 75, 409–418. doi: 10.1016/0092-8674(93)90376-2

Sollner, T., Whiteheart, S. W., Brunner, M., Erdjument-Bromage, H., Geromanos, S., Tempst, P., et al. (1993b). SNAP receptors implicated in vesicle targeting and fusion. *Nature* 362, 318–324. doi: 10.1038/362318a0

Stahl, B., Chou, J. H., Li, C., Sudhof, T. C., and Jahn, R. (1996). Rab3 reversibly recruits rabphilin to synaptic vesicles by a mechanism analogous to raf recruitment by ras. *EMBO J.* 15, 1799–1809.

Stanley, E. F., Reese, T. S., and Wang, G. Z. (2003). Molecular scaffold reorganization at the transmitter release site with vesicle exocytosis or botulinum toxin C1. *Eur. J. Neurosci.* 18, 2403–2407. doi: 10.1046/j.1460-9568.2003.02948.x

Stigloher, C., Zhan, H., Zhen, M., Richmond, J., and Bessereau, J. L. (2011). The presynaptic dense projection of the *Caenorhabditis elegans* cholinergic neuromuscular junction localizes synaptic vesicles at the active zone through SYD-2/liprin and UNC-10/RIM-dependent interactions. *J. Neurosci.* 31, 4388–4396. doi: 10.1523/JNEUROSCI.6164-10.2011

Südhof, T. C. (1995). The synaptic vesicle cycle: a cascade of protein-protein interactions. *Nature* 375, 645–653. doi: 10.1038/375645a0

Südhof, T. C. (2002). Synaptotagmins: why so many?. *J. Biol. Chem.* 277, 7629–7632. doi: 10.1074/jbc.R100052200

Südhof, T. C. (2004). The synaptic vesicle cycle. *Annu. Rev. Neurosci.* 27, 509–547. doi: 10.1146/annurev.neuro.26.041002.131412

Südhof, T. C. (2012). The presynaptic active zone. *Neuron* 75, 11–25. doi: 10.1016/j.neuron.2012.06.012

Südhof, T. C. (2013). Neurotransmitter release: the last millisecond in the life of a synaptic vesicle. *Neuron* 80, 675–690. doi: 10.1016/j.neuron.2013.10.022

Sudhof, T. C., and Rizo, J. (2011). Synaptic vesicle exocytosis. *Cold Spring Harb. Perspect. Biol.* 3:a005637. doi: 10.1101/cshperspect.a005637

Südhof, T. C., and Rothman, J. E. (2009). Membrane fusion: grappling with SNARE and SM proteins. *Science* 323, 474–477. doi: 10.1126/science.1161748

Sunderland, W. J., Son, Y. J., Miner, J. H., Sanes, J. R., and Carlson, S. S. (2000). The presynaptic calcium channel is part of a transmembrane complex linking a synaptic laminin (alpha4beta2gamma1) with non-erythroid spectrin. *J. Neurosci.* 20, 1009–1019. doi: 10.1523/JNEUROSCI.20-03-01009.2000

Sutton, R. B., Fasshauer, D., Jahn, R., and Brunger, A. T. (1998). Crystal structure of a SNARE complex involved in synaptic exocytosis at 2.4 A resolution. *Nature* 395, 347–353. doi: 10.1038/26412

Szule, J. A., and Coorssen, J. R. (2003). Revisiting the role of SNAREs in exocytosis and membrane fusion. *Biochim. Biophys. Acta* 1641, 121–135. doi: 10.1016/s0167-4889(03)00095-8

Szule, J. A., and Coorssen, J. R. (2004). Comment on "transmembrane segments of syntaxin line the fusion pore of Ca2+-triggered exocytosis". *Science* 306:813. doi: 10.1126/science.1101572

Szule, J. A., Harlow, M. L., Jung, J. H., De-Miguel, F. F., Marshall, R. M., and McMahan, U. J. (2012). Regulation of synaptic vesicle docking by different classes of macromolecules in active zone material. *PLoS One* 7:e33333. doi: 10.1371/journal.pone.0033333

Szule, J. A., Jarvis, S. E., Hibbert, J. E., Spafford, J. D., Braun, J. E., Zamponi, G. W., et al. (2003). Calcium-triggered membrane fusion proceeds independently of specific presynaptic proteins. *J. Biol. Chem.* 278, 24251–24254. doi: 10.1074/jbc.C300197200

Szule, J. A., Jung, J. H., and McMahan, U. J. (2015). The structure and function of 'active zone material' at synapses. *Philos. Trans. R. Soc. Lond. B. Biol. Sci.* 370:20140189. doi: 10.1098/rstb.2014.0189

Tahara, M., Coorssen, J. R., Timmers, K., Blank, P. S., Whalley, T., Scheller, R., et al. (1998). Calcium can disrupt the SNARE protein complex on sea urchin egg secretory vesicles without irreversibly blocking fusion. *J. Biol. Chem.* 273, 33667–33673. doi: 10.1074/jbc.273.50.33667

Takamori, S., Holt, M., Stenius, K., Lemke, E. A., Gronborg, M., Riedel, D., et al. (2006). Molecular anatomy of a trafficking organelle. *Cell* 127, 831–846. doi: 10.1016/j.cell.2006.10.030

Takao-Rikitsu, E., Mochida, S., Inoue, E., Deguchi-Tawarada, M., Inoue, M., Ohtsuka, T., et al. (2004). Physical and functional interaction of the active zone proteins, CAST, RIM1 and bassoon, in neurotransmitter release. *J. Cell Biol.* 164, 301–311. doi: 10.1083/jcb.200307101

Tang, J., Maximov, A., Shin, O. H., Dai, H., Rizo, J., and Sudhof, T. C. (2006). A complexin/synaptotagmin 1 switch controls fast synaptic vesicle exocytosis. *Cell* 126, 1175–1187. doi: 10.1016/j.cell.2006.08.030

tom Dieck, S., Sanmarti-Vila, L., Langnaese, K., Richter, K., Kindler, S., Soyke, A., et al. (1998). Bassoon, a novel zinc-finger CAG/glutamine-repeat protein selectively localized at the active zone of presynaptic nerve terminals. *J. Cell Biol.* 142, 499–509. doi: 10.1083/jcb.142.2.499

Veit, M., Sollner, T. H., and Rothman, J. E. (1996). Multiple palmitoylation of synaptotagmin and the t-SNARE SNAP-25. *FEBS Lett.* 385, 119–123. doi: 10.1016/0014-5793(96)00362-6

Wang, J., Bello, O., Auclair, S. M., Wang, J., Coleman, J., Pincet, F., et al. (2014). Calcium sensitive ring-like oligomers formed by synaptotagmin. *Proc. Natl. Acad. Sci. U S A* 111, 13966–13971. doi: 10.1073/pnas.1415849111

Wang, X., Gong, J., Zhu, L., Wang, S., Yang, X., Xu, Y., et al. (2020). Munc13 activates the Munc18–1/syntaxin-1 complex and enables Munc18-1 to prime SNARE assembly. *EMBO J.* 39:e103631. doi: 10.15252/embj.2019103631

Wang, X., Hu, B., Zieba, A., Neumann, N. G., Kasper-Sonnenberg, M., Honsbein, A., et al. (2009). A protein interaction node at the neurotransmitter release site: domains of aczonin/piccolo, bassoon, CAST and rim converge on the N-terminal domain of Munc13–1. *J. Neurosci.* 29, 12584–12596. doi: 10.1523/JNEUROSCI.1255-09.2009

Wang, Y., Liu, X., Biederer, T., and Sudhof, T. C. (2002). A family of RIM-binding proteins regulated by alternative splicing: implications for the genesis of synaptic active zones. *Proc. Natl. Acad. Sci. U S A* 99, 14464–14469. doi: 10.1073/pnas.182532999

Wang, Y., Okamoto, M., Schmitz, F., Hofmann, K., and Sudhof, T. C. (1997). Rim is a putative Rab3 effector in regulating synaptic-vesicle fusion. *Nature* 388, 593–598. doi: 10.1038/41580

Weber, T., Zemelman, B. V., McNew, J. A., Westermann, B., Gmachl, M., Parlati, F., et al. (1998). SNAREpins: minimal machinery for membrane fusion. *Cell* 92, 759–772. doi: 10.1016/s0092-8674(00)81404-x

Wolfes, A. C., and Dean, C. (2020). The diversity of synaptotagmin isoforms. *Curr. Opin. Neurobiol.* 63, 198–209. doi: 10.1016/j.conb.2020.04.006

Xu, J., Camacho, M., Xu, Y., Esser, V., Liu, X., Trimbuch, T., et al. (2017). Mechanistic insights into neurotransmitter release and presynaptic plasticity from the crystal structure of Munc13–1 C1C2BMUN. *eLife* 6:e22567. doi: 10.7554/eLife.22567

Xue, M., Stradomska, A., Chen, H., Brose, N., Zhang, W., Rosenmund, C., et al. (2008). Complexins facilitate neurotransmitter release at excitatory and inhibitory synapses in mammalian central nervous system. *Proc. Natl. Acad. Sci. U S A* 105, 7875–7880. doi: 10.1073/pnas.0803012105

Zanetti, M. N., Bello, O. D., Wang, J., Coleman, J., Cai, Y., Sindelar, C. V., et al. (2016). Ring-like oligomers of synaptotagmins and related C2 domain proteins. *eLife* 5:e17262. doi: 10.7554/eLife.17262

Zarebidaki, F., Camacho, M., Brockmann, M. M., Trimbuch, T., Herman, M. A., and Rosenmund, C. (2020). Disentangling the roles of RIM and Munc13 in synaptic vesicle localization and neurotransmission. *J. Neurosci.* 40, 9372–9385. doi: 10.1523/JNEUROSCI.1922-20.2020

Zhai, R. G., and Bellen, H. J. (2004). The architecture of the active zone in the presynaptic nerve terminal. *Physiology (Bethesda)* 19, 262–270. doi: 10.1152/physiol.00014.2004

Zhao, M., Wu, S., Zhou, Q., Vivona, S., Cipriano, D. J., Cheng, Y., et al. (2015). Mechanistic insights into the recycling machine of the SNARE complex. *Nature* 518, 61–67. doi: 10.1038/nature14148

Zhou, Q., Lai, Y., Bacaj, T., Zhao, M., Lyubimov, A. Y., Uervirojnangkoorn, M., et al. (2015). Architecture of the synaptotagmin-SNARE machinery for neuronal exocytosis. *Nature* 525, 62–67. doi: 10.1038/nature14975

Conflict of Interest: The author declares that the research was conducted in the absence of any commercial or financial relationships that could be construed as a potential conflict of interest.

frontiers
in Synaptic Neuroscience

REVIEW
published: 18 January 2022
doi: 10.3389/fnsyn.2021.754814

Towards a Comprehensive Optical Connectome at Single Synapse Resolution *via* Expansion Microscopy

Madison A. Sneve[1] *and Kiryl D. Piatkevich*[2,3,4]*

[1]*Department of Brain and Cognitive Sciences, MIT, Cambridge, MA, United States,* [2]*School of Life Sciences, Westlake University, Hangzhou, China,* [3]*Westlake Laboratory of Life Sciences and Biomedicine, Westlake University, Hangzhou, China,* [4]*Institute of Basic Medical Sciences, Westlake Institute for Advanced Study, Hangzhou, China*

Mapping and determining the molecular identity of individual synapses is a crucial step towards the comprehensive reconstruction of neuronal circuits. Throughout the history of neuroscience, microscopy has been a key technology for mapping brain circuits. However, subdiffraction size and high density of synapses in brain tissue make this process extremely challenging. Electron microscopy (EM), with its nanoscale resolution, offers one approach to this challenge yet comes with many practical limitations, and to date has only been used in very small samples such as *C. elegans*, tadpole larvae, fruit fly brain, or very small pieces of mammalian brain tissue. Moreover, EM datasets require tedious data tracing. Light microscopy in combination with tissue expansion *via* physical magnification—known as expansion microscopy (ExM)—offers an alternative approach to this problem. ExM enables nanoscale imaging of large biological samples, which in combination with multicolor neuronal and synaptic labeling offers the unprecedented capability to trace and map entire neuronal circuits in fully automated mode. Recent advances in new methods for synaptic staining as well as new types of optical molecular probes with superior stability, specificity, and brightness provide new modalities for studying brain circuits. Here we review advanced methods and molecular probes for fluorescence staining of the synapses in the brain that are compatible with currently available expansion microscopy techniques. In particular, we will describe genetically encoded probes for synaptic labeling in mice, zebrafish, *Drosophila* fruit flies, and *C. elegans*, which enable the visualization of post-synaptic scaffolds and receptors, presynaptic terminals and vesicles, and even a snapshot of the synaptic activity itself. We will address current methods for applying these probes in ExM experiments, as well as appropriate vectors for the delivery of these molecular constructs. In addition, we offer experimental considerations and limitations for using each of these tools as well as our perspective on emerging tools.

Keywords: expansion microscopy, optical connectome, super-resolution, electron miscroscopy, synaptic labeling

Edited by:
Thomas A. Blanpied,
University of Maryland, United States

Reviewed by:
Kristina D. Micheva,
Stanford University, United States
Joachim H. R. Lübke,
Helmholtz Association of German Research Centres (HZ), Germany

Correspondence:
Kiryl D. Piatkevich
kiryl.piatkevich@westlake.edu.cn

Received: *07 August 2021*
Accepted: *17 December 2021*
Published: *18 January 2022*

Citation:
Sneve MA and Piatkevich KD (2022) Towards a Comprehensive Optical Connectome at Single Synapse Resolution via Expansion Microscopy.
Front. Synaptic Neurosci. 13:754814.
doi: 10.3389/fnsyn.2021.754814

INTRODUCTION

Historical Perspective of Connectomics

Embedded in the concept of the "neuron doctrine" is the principle that neurons communicate through synapses, a striking assumption first made by Ramon y Cajal over a century ago (Ramón y Cajal, 1909). Cajal, in his now-famous illustrations of the silver-stained neurons, was the first person to predict the unique way that neurons are both spatially separated yet connected *via* the synapse (Llinás, 2003; Dhawale and Bhalla, 2008). Cajal was the first to dream of the form of the synapse, but he and his contemporaries were hindered from directly visualizing them by the limitations of the light microscope. The invention of the electron microscope provided researchers with the first toolkit to truly peer at the synapse (Palay, 1956; Wells, 2005). Quickly after its invention, electron microscopy (EM) produced the first high-resolution images of synaptic vesicles, providing key structural evidence for Cajal's vision of the way in which neurons connect (Robertson, 1953; De Robertis and Bennett, 1955; Palay and Palade, 1955). Sanford Palay, one of the early pioneers of using EM to study the brain, defined the form of the synapse by two common factors: close proximity of the postsynaptic and presynaptic cells divided by a gap of around 200 Å(20 nm), and the presence of mitochondria and vesicles at the presynaptic terminal (Palay, 1956). As microscopy technology advanced, so did the understanding of the structure and form of the synapse.

The modern neuroscientist has the privilege of access to a great deal more knowledge about the structure and function of the synapse than Cajal and his contemporaries would have had. Synapses can be broadly categorized by which of the two distinct mechanisms of synaptic transmission they use—chemical or electrical (Pereda, 2014). Chemical synapses are those which were first visualized through EM and are the more well-studied of the two varieties (Palay, 1956). In chemical synapses, vesicles from the presynaptic neuron release neurotransmitters into the synaptic cleft, which are then recognized by the postsynaptic cell, and thus specific signal defined by a particular neurotransmitter is transmitted. Electrical synapses, on the other hand, transmit information through a fundamentally different means. At an electrical synapse, the communicating cells are physically connected *via* gap junctions, allowing ions, and thus voltage, to be transmitted in most cases bidirectionally between neurons (Pereda, 2014). Electrical synapses were discovered through electrophysiological experiments several years after the first confirmation of the existence of chemical synapses through EM (Watanabe, 1958; Furshpan and Potter, 1959), and their role in the central nervous system (CNS) has only relatively recently been of widespread interest (Gibson et al., 1999; Galarreta and Hestrin, 2001; Hormuzdi et al., 2004). The focus of this review will primarily be on chemical synapses, particularly due to their relative abundance compared to electrical synapses in existing connectomes, although the importance of electrical synapses for brain function should not be underestimated.

Broadly, chemical synapses exist as one of two types—inhibitory or excitatory—based on whether they promote or impede an action potential in the postsynaptic neuron, respectively. In the mammalian CNS, the postsynaptic component of most excitatory synapses and of some inhibitory synapses is located on small protrusions known as dendritic spines (Gray, 1959; Chen et al., 2012; Berry and Nedivi, 2017). Synapses can be further characterized by what neurotransmitter the presynaptic neuron releases, as well as what receptors and scaffold proteins exist in the postsynaptic density (PSD) of spines. For example, the postsynaptic scaffold protein PSD-95, which is expressed only at glutamatergic synapses, is strongly associated with excitatory synapses, and the postsynaptic scaffold protein gephyrin, which interacts with GABA and glycine receptors, is strongly associated with inhibitory synapses (El-Husseini et al., 2000; Prange et al., 2004; Sheng and Kim, 2011). Recent studies have shown that mammalian neurons frequently remodel their spine architecture, assembling and removing excitatory and inhibitory postsynaptic sites in a coordinated manner in response to experience (Chen et al., 2012; Villa et al., 2016). Some individual spines are highly dynamic, appearing and disappearing in a manner of days, while others are more persistent (Berry and Nedivi, 2017).

As the wealth of knowledge surrounding the synapse expands further, there is a need for new technologies that can visualize synapses at high resolution and at high-throughputs. One particularly promising area of study that exemplifies this pressing need is connectomics, the study of wiring of neurons at the resolution of the single synapse. Mapping connectomes in model organisms such as *C. elegans*, *Drosophila melanogaster*, zebrafish, and mice is an immensely difficult and time-consuming endeavor, historically relying on EM. The colossal density of synapses—as many as 1 trillion synapses per cm^3 of cortex in human brains—combined with the extremely precise resolution needed to visualize single synapses makes the mapping of a connectome a herculean endeavor (Tang et al., 2001; Drachman, 2005). The first whole-organism connectome ever produced was of *C. elegans* hermaphrodite's 302 neurons and several thousand synapses, which was the result of many years of work from multiple labs and was expanded over time (Albertson et al., 1976; White et al., 1986; Hall and Russell, 1991; Jarrell et al., 2012; Cook S. J. et al., 2019). Recently, the whole-animal synaptic connectome of *Platynereis dumerilii* larva (Verasztó et al., 2020), the partial adult and larvae *Drosophila* connectomes (Ohyama et al., 2015; Scheffer et al., 2020; Hulse et al., 2021), the sea squirt *Ciona intestinalis* connectome (Ryan et al., 2016), a 0.13 mm^3 volume of the somatosensory cortex of a young adult mouse (Kasthuri et al., 2015), around 1 mm^3 of mouse visual cortex connectome (MICrONS Consortium et al., 2021), and 1 mm^3 of the human cerebral cortex (Shapson-Coe et al., 2021) have also been painstakingly reconstructed with EM. Though improvements in EM, such as serial block-face scanning EM, focused ion beam scanning EM, high-throughput serial section scanning EM, and transmission EM, complemented by advanced methods for connectome reconstruction, have facilitated and hastened this process, the imaging of even a partial connectome remains prohibitively demanding of time and resources for most researchers to perform (Xu et al., 2017; Motta et al., 2019; Hubbard et al., 2020; Witvliet et al., 2020). Several ambitious connectomics projects are currently underway, such as the IARPA MICrONS program and the FlyEM project, a multi-lab, multi-year effort which has produced one of the largest and most complete connectomes to date (Dorkenwald et al., 2019; Scheffer et al., 2020; Schneider-Mizell et al., 2020). However, due to the incredible challenge of producing a high-fidelity connectome, only limited volumes of the brain have been mapped so far. This demonstrates the ongoing challenge of imaging synapses at the nanoscale resolution and the need for vast improvements in imaging techniques and technology before connectome reconstruction reaches its full potential.

The speed and resource limitations of traditional methods of connectome reconstruction have significant drawbacks for the usefulness of the connectomes generated. The brain is a highly dynamic structure, and although some synapses and spines are relatively stable, others frequently reassemble, sometimes on the scale of hours (Berry and Nedivi, 2017). A connectome merely represents a snapshot of a brain in a moment in time, and to truly understand the connectivity of an organism, a single connectome will not suffice. Moreover, the connectomes of individual organisms may differ greatly and sometimes unexpectedly (Bergmann et al., 2020; Witvliet et al., 2020). Furthermore, merely knowing the number of synapses that connect two neurons does not provide all of the necessary information for understanding the function of the synapse. The molecular identity of the synapse is incredibly diverse and reveals essential information such as synaptic type and strength, without which a full vision of connectivity cannot be developed, and unfortunately, EM preparation techniques are largely incapable of preserving molecular identity (O'Rourke et al., 2012). On the other hand, optical microscopy is well suited for imaging large samples at high-throughput and compatible with multiplexed imaging required for revealing the molecular identity of synapses. Indeed, high-throughput optical imaging approaches, such as FAST, MOST, and tiling light sheet microscopy, have been already used for whole-brain imaging (Gong et al., 2016; Seiriki et al., 2017; Motta et al., 2019; Winnubst et al., 2019; Chen et al., 2020; Zhong et al., 2021). However, in this case, the resolution is limited by the diffraction of light and thus not sufficient for mapping synaptic connections. Super-resolution microscopy can break the diffraction limit of light but at the cost of greatly reduced throughput and the need for thin sample slicing to maintain point spread function (Sahl et al., 2017; Schermelleh et al., 2019). Expansion Microscopy (ExM), a recently developed tissue processing technique, allows for the imaging of biological specimens at the voxel rates of a diffraction-limited microscope, but with the voxel sizes of a super-resolution microscope (Chen F. et al., 2015; Tillberg et al., 2016). This makes ExM a form of super-resolution microscopy, which relies on swellable polymers to physically expand tissues before imaging (Chen F. et al., 2015). Physical magnification of the specimen occurs at the nanoscale by separating biomolecules, thus enabling subdiffraction limit resolution under a conventional microscope (Tillberg et al., 2016). Here, the authors would like to note that the first method that resulted in brain tissue expansion was reported by Miyawaki and colleagues in 2011 (Hama et al., 2011). However, it was not realized as a way to improve the spatial resolution of imaging until 2015 when Boyden and colleagues introduced the concept of ExM.

ExM has several crucial advantages over EM that make it particularly well suited for visualizing the synapse, particularly for large-scale projects like connectome mapping. For example, the time, labor, equipment, and skill demands of an ExM experiment are substantially less than that of an EM experiment (Wassie et al., 2019). ExM also is compatible with conventional molecular labeling tools and maintains optical microscopy's ability to image in color, allowing for the use of several fluorescent probes at once or sequentially, thus enabling multiplexing as well as revealing the molecular identity of the synapse *in situ* (Chen F. et al., 2015; Ku et al., 2016; Wassie et al., 2019; Alon et al., 2021; Payne et al., 2021). ExM is compatible with a wide variety of tissue types and has been used to image brain tissue in many of neuroscience's most widely used model organisms (Freifeld et al., 2017; Gao R. et al., 2019; Yu et al., 2020) and in monkey specimens (Zhao et al., 2017). ExM has already been successfully utilized to image neural connectivity at the resolution of the single synapse. For example, Gao R. et al. (2019) used ExM in tandem with lattice light-sheet microscopy to visualize synaptic proteins and neuronal morphology at nanoscale resolution in the mouse cortex and *Drosophila* brain. Shen et al. (2020) also recently used ExM combined with fluorescent labeling and antibody staining to trace likely synaptic connections in neurons while preserving cell-type specific molecular information. There is tremendous potential for ExM to revolutionize the way synapses are imaged and studied. The technology has produced visually stunning results of brain tissue in a variety of model organisms, and most ExM protocols are substantially more compatible with the high-throughput approach needed to tackle the problems of connectomics and beyond in the future.

We start by reviewing the ExM methods that have been already applied for synaptic mapping and imaging using immunostaining and fluorescent protein-based neuronal labeling and tracing, which facilitates assigning synapses to their parent neurons. We also discuss major challenges and limitations of the currently available ExM methods regarding the comprehensive optical connectome. We then summarize some major molecular strategies for visualizing the synapse at high resolution that can be used in combination with ExM for optical connectome. The first strategy involves fusing synaptic scaffold proteins, such as PSD-95, gephyrin, and synaptophysin, with fluorescent markers. Many tools are variations of this general technique and are widely used both for live imaging and for fixed sample preps, and we feature the most commonly used and the most promising for ExM below. The second strategy involves the use of intrabody-based probes known as FingRs, which bind to synaptic scaffold proteins. Although FingRs are a much newer and less established technology than tagged scaffold proteins, they have several key features that make them more suitable for certain applications. We finalize the review by providing experimental considerations and perspectives on ExM technology.

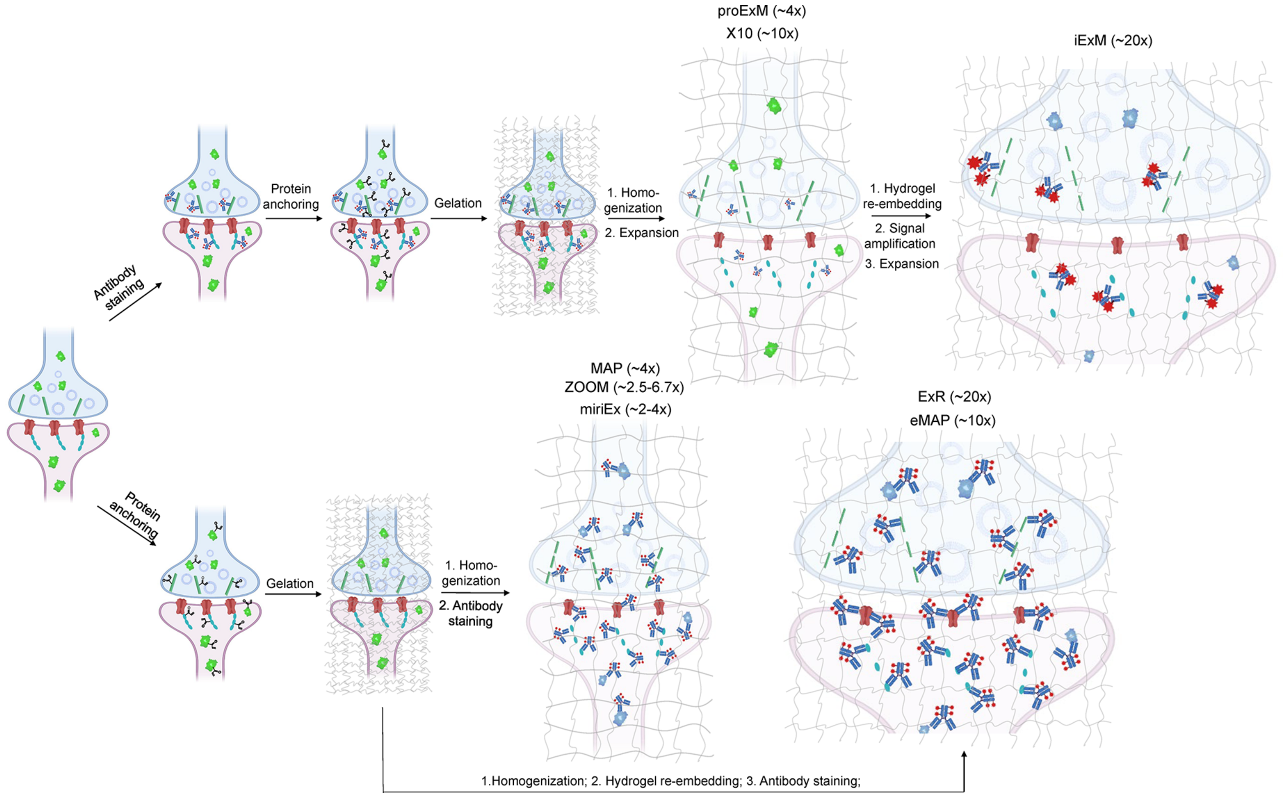

FIGURE 1 | Schematic representations of the ExM workflows with protein retention. Created with Biorender.com.

State-of-the-Art ExM Methods for the Optical Connectome

All ExM methods are based on physical magnification of biological sample *via* hydrogel embedding followed by mechanical homogenization to disrupt intermolecular complexes (so as to remove mechanical resistance to expanding) and subsequent hydrogel swelling usually in water or low salt buffers. To retain proteins in the expanded state, the sample is treated with a reagent to modify amino acid side chains (usually lysine) with a chemical anchor that participates in radical polymerization to covalently bound proteins into polymer mesh. For a more detailed overview of ExM protocols, we refer readers to recent reviews covering the basic principles of hydrogel-based tissue transformation (Wassie et al., 2019; Choi et al., 2021). As ExM employs optical microscopy for imaging it is heavily reliant on fluorescent probes for targeted biomolecule labeling. Immunohistochemistry (IHC), a fixed tissue staining procedure based on antibody labeling, is a widely used technique within neuroscience (Magaki et al., 2019) and at present, it is the most well-validated approach for synaptic protein visualization using ExM. Since the introduction of the ExM concept in 2014, a large diversity of tissue expansion protocols and methods have been developed for various applications and biological samples. The optimization of ExM was focused on three major aspects: (i) improving fluorescent labeling; (ii) increasing spatial resolution; and (iii) diversifying samples (*i.e.*, whole organs and organisms). We briefly review these aspects in the context of the optical connectome.

Depending on the ExM method, antibody staining can be performed either before tissue expansion or after hydrogel embedding and homogenization (**Figure 1**). In the earlier versions of ExM, fixed tissue is stained with antibodies before it is gelled and expanded, and several particularly useful antibodies for synaptic visualization were demonstrated to be compatible with subsequent tissue expansion (Chen F. et al., 2015; Chozinski et al., 2016). Among the most commonly used antibodies with ExM of brain tissue are Homer and Bassoon (Chen F. et al., 2015; Chozinski et al., 2016; Chang et al., 2017). Staining with antibodies against Homer1 allows for visualization of the post-synaptic components of excitatory synapses in fixed mammalian brain tissue (Gutierrez-Mecinas et al., 2016; Gao R. et al., 2019; Park et al., 2020). Antibodies against Bassoon stain the pre-synaptic components of synapses, and thus are useful to combine with post-synaptic markers like Homer1 (Micheva et al., 2010; Bürgers et al., 2019; Gao R. et al., 2019). Several other important synaptic proteins targeted by immunolabeling with ExM includes glutamate receptor 1, gephyrin, gamma-aminobutyric acid receptor Aα1/Aα2, vesicular glutamate transporter 1, vesicular GABA transporter (vGAT), Rab3A-binding protein (RIM), Shank2, and PSD95 (Chang et al., 2017;

Truckenbrodt et al., 2018; Bürgers et al., 2019; Hafner et al., 2019). However, immunostaining of synaptic complexes usually has low efficiency due to the limited accessibility of antibodies to densely packed synapses, where inter-protein distances are smaller than the size of conventional antibodies (Sarkar et al., 2020).

To overcome this limitation, much effort has been focused on the development of ExM methods that allow antibody staining to be performed after sample homogenization (**Figure 1**). By utilizing mild chemical treatment with the detergent-containing buffer it was possible to preserve antigens for immunostaining in the expanded samples (Ku et al., 2016; Park et al., 2019). In addition, it was demonstrated that tissue expansion provides better access for antibodies to epitopes of the synaptic proteins, which otherwise might be masked in the dense synaptic protein complexes (Sarkar et al., 2020). Molecular de-crowding *via* sample expansion significantly increased the efficiency of immunolabeling, which in turn not only improved visualization of synaptic connections but also expanded the list of commercially available antibodies for synaptic proteins compatible with ExM workflow. For example, the recently developed Expansion Revealing (ExR) method was successfully applied to image 7 synaptic proteins important for neural architecture and transmission including the presynaptic proteins Bassoon, RIM1/2, and the P/Q-type Calcium channel Cav2.1 alpha 1A subunit, and the postsynaptic proteins Homer1, Shank3, SynGAP, and PSD95 (Sarkar et al., 2020). This study also allowed us to gain new insights into the nanoscale alignment of presynaptic calcium channels with postsynaptic machinery in intact brain circuits (Sarkar et al., 2020). Earlier Ku et al. (2016) performed systematic screening of commercially available antibodies for synaptic proteins using ExM modification, called magnified analysis of the proteome (MAP). The screening has further extended the list of synaptic proteins present in different types of synapses (*e.g.*, VGluT1 vs. VGluT2, $GABA_BR1$, mGluR5, or different receptors) that can allow detection of synapses coming from different neuron types or brain regions with ExM. The very recent modification of MAP, denoted epitope-preserving MAP or eMAP, was optimized to achieve maximal preservation of antigenicity in mouse and marmoset brain tissue, thus increasing success rates of staining with synaptic antibodies to more than 94% (Park et al., 2021).

Another advantage of post-expansion immunostaining is the ability to carry out multiple rounds of labeling and imaging, providing an unprecedent degree of multiplexed super-resolution synaptic proteomic profiling. When expanded tissue samples are imaged in between rounds of immunostaining and antibody stripping, a variety of antibody signals can be converged into a single composite image, allowing for several synaptic proteins to be stained for and imaged at once. For example, the MAP and eMAP protocols were demonstrated to be suitable for highly multiplexed super-resolution imaging *via* repeated staining and destaining using antibodies for synaptic proteins including Homer1, Bassoon, PSD95, vGluT1, vGluT2, and $GABA_BR1$ (Ku et al., 2016). A similar approach was implemented in multi-round immunostaining Expansion Microscopy (miriEX) that involves tissue expansion followed by several iterations of antibody staining and stripping (Shen et al., 2020). The miriEX method was originally applied for iterative immunostaining endogenous synaptic proteins, such as Cannabinoid type 1 receptor, calbindin, and serotonin transporter, in mouse neurons that expressed Brainbow constructs (Shen et al., 2020). While iterative immunolabeling is proven to be a valid approach for multiplexed ExM imaging, it might not be a very practical one due to the need for extremely precise image co-registration between staining steps. Furthermore, this procedure involves buffer exchange and thus it can slightly alter the expansion factor due to osmolarity mismatch. Co-registration of images with varying expansion factors significantly complicates image processing and analysis steps (Alon et al., 2021). Alternatively, multiplexing can be achieved *via* blind unmixing without reference spectral measurements, allowing up to 15 color imaging (Seo et al., 2021). Seo at el. utilized spectral unmixing on expanded brain samples although only combing four labels for NeuN, GFAP, calretinin, NF-H. The multiplexing approach can significantly increase the utility of ExM for molecular profiling of synapses, however, it still needs to be carefully validated for a large variety of synaptic proteins.

In addition to 3D mapping and molecular profiling of synaptic connections, ExM methods with increased expansion factors can be used to visualize the nanoarchitecture of synapses (**Figure 2**). The resolution power of ExM is defined by the expansion factor. The majority of the ExM methods enable about four-fold sample expansion in linear dimension, which results in ∼70–80 nm of lateral resolution under conventional diffraction-limited microscopes (Tillberg et al., 2016). One strategy to increase the expansion factor is based on the iterative expansion through gel re-embedding, i.e., synthesis of new hydrogel network within an already expanded sample. This strategy was first employed in iterative ExM, or iExM, to achieve ∼16–22-fold linear expansion (Chang et al., 2017). The iExM method was carefully validated and characterized by imaging tubulin structures in cultured cells demonstrating isotropic expansion and about 25 nm of effective resolution. The achieved resolution was sufficient to clearly separate post- and pre-synaptic density proteins, such as Homer1, Bassoon, and Gephyrin, from neurotransmitter receptors GluR1 and GABAARα1/α2 in excitatory and inhibitory synapses, respectively (Chang et al., 2017). However, in iExM the proteins are not retained in the expanded state and the staining relies on custom oligonucleotide conjugated antibodies in combination with signal amplification *via* locked nucleic acid probes. Requirements for customized reagents prevented wide adaptation of iExM. Protein retention with the iterative expansion concept was realized in ExR (Sarkar et al., 2020), tetra-gel-based ExM (Gao et al., 2021), and eMAP (Park et al., 2021). For example, ExR, exhibiting effective resolution comparable to that of iExM, is compatible with commercially available antibodies applied to the expanded samples. Visualizing Cav2.1, PSD95, and RIM1/2 in mouse brain tissue revealed how calcium channel distributions participate in transsynaptic nanoarchitecture. Gel re-embedding complicates and extends sample preparation and treatment steps.

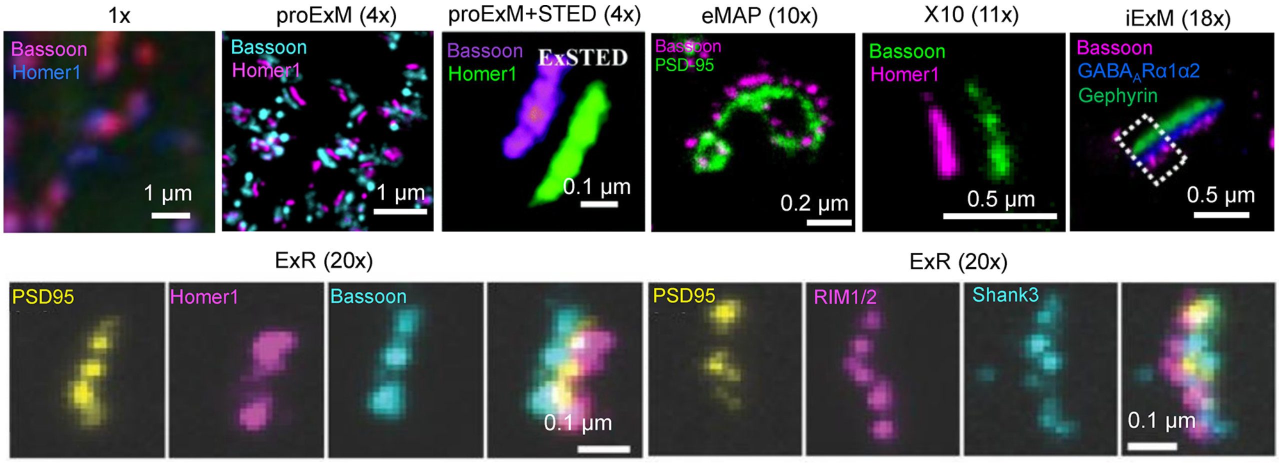

FIGURE 2 | Visualization of synapses in mouse brain tissue using different ExM protocol modifications. The values in parenthesis represent the linear expansion factor for the corresponding image. Adapted from Chen F. et al. (2015), Chang et al. (2017), Li et al. (2018), Truckenbrodt et al. (2018), Gao R. et al. (2019), Sarkar et al. (2020), and Park et al. (2021).

Alternatively, the higher expansion factors (>4-fold) can be achieved by modifying hydrogel chemical composition. For example, by utilizing new hydrogel monomers, Truckenbrodt et al. (2018) developed the X10 ExM method characterized by up to ∼11-fold expansion in a single expansion step and compatibility with conventional antibodies. The X10 procedure was used for multi-color imaging of the pre-synaptic active zones and the post-synaptic densities *via* Homer1, Bassoon, PSD95, and synaptophysin staining with an estimated effective resolution of about 25 nm. While X10 provides the convenience of single step expansion, the hydrogel it uses has poor mechanical properties in the expanded state and its polymerization requires special conditions. The expansion factor of the common ExM hydrogel can be also enhanced by adjusting the cross-linker molar ratio and monomer concentration (Park et al., 2019; Hu et al., 2020; Damstra et al., 2021). For example, the ZOOM and TREx protocols, characterized by the expansion factor of six-10-fold, were used for synaptic visualization using Homer and Bassoon antibodies (Park et al., 2019; Damstra et al., 2021), although the staining of other synaptic proteins still remains to be tested with these methods. It should be also noted that enhancement of resolution can be achieved by combining sample expansion with traditional super-resolution imaging techniques. For example, ExM was combined with stimulated emission depletion microscopy (STED), stochastic optical reconstruction microscopy (STORM), super-resolution optical fluctuation imaging (SOFI) to gain additional improvement in resolution (Gao et al., 2018; Li et al., 2018; Xu et al., 2019; Zwettler et al., 2020; Shi et al., 2021). However, to date, only ExSTED, a combination of ExM with STED, has been applied for synaptic imaging in mouse brain tissue (Li et al., 2018). The proof-of-principle applications of the ExM protocols with increased expansion factor clearly demonstrated the advantages of enhanced resolving power for synaptic nanoarchitecture imaging. However, further validation and characterization are required for establishing the new protocols for routine use in neuroscience research. In particular, it is important to confirm the distortion-free expansion of synaptic complexes, which are known to be very densely packed with proteins and tight proteins complexes.

The ExM methods reviewed above were mostly optimized for cultured cells or thin brain tissue sections. However, neural processes project to local and distal areas throughout the brain, reaching more than 78 cm in total length in the mouse brain (Winnubst et al., 2019). Therefore, imaging of small brain tissue volumes would have limited utility for complete connectome imaging and reconstructions, as registration of neuronal processes from independently expanded and imaged tissue sections from the same brain may not be feasible. It would be ideal if one could expand and image the intact brain with appropriate synaptic and neuron labeling as well as resolution to form a comprehensive connectome. However, this task meets several technical challenges on multiple fronts—expansion procedure, labeling, and imaging itself, which still remain to be fully addressed in practice. For example, four-fold expanded mouse brain with dimensions of 4 × 3 × 6 cm is impossible to image with nanoscale resolution in intact form due to the limited working distances of available objectives. One way to deal with this is to slice the expanded brain upon imaging, a solution already implemented in fMOST technology (Zhong et al., 2021) and in the MouseLight project (Winnubst et al., 2019).

Reducing the expansion factor of the original ExM protocol can facilitate entire brain imaging. For example, two-fold expanded mouse brain using the CUBIC-X protocol can be imaged under a custom light-sheet microscope, albeit with the cost of greatly reduced spatial resolution (Murakami et al., 2018). On the other hand, expansion of small model organisms such as *C. elegans*, *Drosophila*, and zebrafish, could be more feasible at present, as expanded samples can be imaged in an intact state using conventional imaging setups. ExM methods were already adopted for super-resolution imaging of *Drosophila* brain explant (Mosca et al., 2017; Jiang et al., 2018), enabling the mapping of presynaptic sites in the entire brain with lattice light sheet microscopy (Gao R. et al., 2019; Lillvis et al., 2021). It was also demonstrated that zebrafish brain explants (Freifeld et al., 2017) and even whole zebrafish larvae (up to 6 days post-fertilization; Sim et al., 2021) can be expanded and imaged using conventional imaging setups. Similarly to whole zebrafish expansion (Sim et al., 2021), the ExCel method can expand an entire *C. elegans* specimen using an extensive chemical treatment to ensure isotropic expansion (Yu et al., 2020). However, this treatment reduces the fluorescence of fluorescent proteins and antibodies, requiring a larger amount of antibodies and extended staining time (Yu et al., 2020). To facilitate antibody penetration into expanded samples, stochastic electrotransport (Kim et al., 2015) was shown to speed up antibody diffusion into thick (>5 mm) expanded mouse brain samples (Ku et al., 2016). Immunostaining of magnified samples extends the timeline and increases the cost of sample preparation.

In addition to identifying the synapse itself, an important part of connectomics is tracing synaptic connections to the originating neuron. From this perspective, the expression of fluorescent proteins might be a good alternative to antibodies, as the visualization of genetically encoded fluorescent probes does not require an additional staining step and they can be evenly expressed throughout the plasma membrane and/or cytoplasm. Protein-retention ExM (proExM) was demonstrated to retain native fluorescence of multiple fluorescent proteins in expanded samples, including mouse and monkey brain tissue (Tillberg et al., 2016). Owing to its high brightness and chemical stability, yellow fluorescent protein (YFP) has high performance in ExM and was used for neuronal tracing in mouse tissue (Gao R. et al., 2019). Indeed, cytoplasmic or membranal expression of fluorescent proteins is perhaps one of the most widely used approaches for neuronal tracing using optical microscopy. Fluorescent protein-based technology for neuronal tracing, such as Brainbow, has been already used in combination with ExM (Tillberg et al., 2016; Chang et al., 2017). Brainbow is a transgenic strategy for distinguishing individual cells from their neighbors, due to stochastic fluorescent protein expression that provides individual cells a unique fluorescent signature (Livet et al., 2007; Cai et al., 2013; Weissman and Pan, 2015; Shen et al., 2020). Brainbow allowed for individual neurons to be distinguished from the neighbors in mouse brain slices (Tillberg et al., 2016), while antibodies against gephyrin, Homer1, and Bassoon allowed those synapses to be characterized as excitatory or inhibitory (Shen et al., 2020). Improved versions of Brainbow, such as Tetbow (Sakaguchi et al., 2018), and Bitbow (Li et al., 2021), have been demonstrated to enable highly efficient neuronal morphology reconstruction. Applying proExM to the Bitbow-expressing *Drosophila* brain made it possible to reconstruct all 21 ventral nerve cord serotonergic neurons out of 26 estimated total. However, the fluorescent signal was amplified using immunostaining (Li et al., 2021). In addition, the expression of fluorescent proteins using the rabies virus is a powerful transneuronal tracing technology (Ugolini, 2011; Kim et al., 2016).

Fluorescent Synaptic Scaffold Proteins

Among the most established strategies we discuss is the fusion of synaptic scaffold proteins with fluorescent markers, which has launched many variations upon the theme of fusing a prominent biologically relevant synaptic protein with a fluorescent protein such as eGFP. The most widely used post-synaptic scaffold proteins involved are PSD-95 (Gray et al., 2006; Cane et al., 2014; Isshiki et al., 2014; Villa et al., 2016) and gephyrin (Craig et al., 1996; Villa et al., 2016), and the most widely used pre-synaptic scaffold protein is synaptophysin (Antonova et al., 2009; Li et al., 2010), and variants of these proteins have been imaged in many of the relevant model organisms used by neuroscientists.

Many of the following tools were developed with *in vivo* imaging in mind, but they are likely also compatible *post-vivo* with ExM in fixed tissue. It is our belief that complementing *in vivo* functional imaging of the synapse with ExM of the fixed tissue presents a powerful opportunity to study the structure and function of the synapse in tandem. Structural and connectomic data are significantly more useful when complemented by functional data: for example, a connectome alone would not reveal the strength of an individual synapse, but a connectome supplemented with functional data would present a much clearer picture of the synapse in question (Turner et al., 2020). ExM is uniquely situated to synergize structural and functional imaging and produce connectomes that are supplemented with custom functional data.

Probes to Visualize Post-synaptic Connections

We begin by describing tools to visualize the postsynaptic scaffold proteins. These approaches enable investigations of structural dynamics in live brains and provide fluorescent markers of synapses for post-fixed tissue expansion. In many researched vertebrate systems, commonly used proteins for fluorescence tagging are postsynaptic density protein 95 (PSD-95), also known as synapse-associated protein 90 (SAP-90), and gephyrin. These particular proteins are found at the postsynaptic density, a dense protein complex found in both excitatory and inhibitory synapses (Sheng and Kim, 2011; Dosemeci et al., 2016). The postsynaptic density of an excitatory neuron can contain several hundred PSD-95 molecules, and the postsynaptic density of an inhibitory synapse can contain tens or even hundreds of gephyrin molecules (Chen X. et al., 2005; Chen et al., 2011; Choii and Ko, 2015). While PSD-95 and gephyrin are among the most common postsynaptic density proteins studied in vertebrates, the postsynaptic density is full of many other proteins which could alternatively be labeled to provide insight into the structure of synapses (Helm et al., 2021).

PSD-95 plays a variety of roles in the postsynaptic density, most notably binding to key excitatory glutamate receptors and promoting the maturation and strengthening of dendritic spines and excitatory synapses (Chen et al., 2011; Cane et al., 2014; Taft and Turrigiano, 2014; Chen X. et al., 2015). This makes PSD-95 a faithful structural surrogate for excitatory synapses in vertebrate synapses. Genetically tagging PSD-95 with exogenous fluorescent proteins permits *in vivo* tracking of excitatory synapse structural dynamics (Gray et al., 2006; Cane et al., 2014; Isshiki et al., 2014;

Villa et al., 2016; Subramanian et al., 2019; **Figure 3A**). Some of the first experiments to fluorescently label the postsynaptic density in mammalian and zebrafish neurons used a PSD-95-GFP fusion (Craven et al., 1999; Niell et al., 2004). More recently, PSD-95 has been fused to mCherry for imaging of synaptic spines in live mice. For example, using a CPG15/Netrin knock-out mouse and PSD95-mCherry labeling *in vivo*, Subramanian et al. recently found that GPI-anchored CPG15 interacts with AMPA

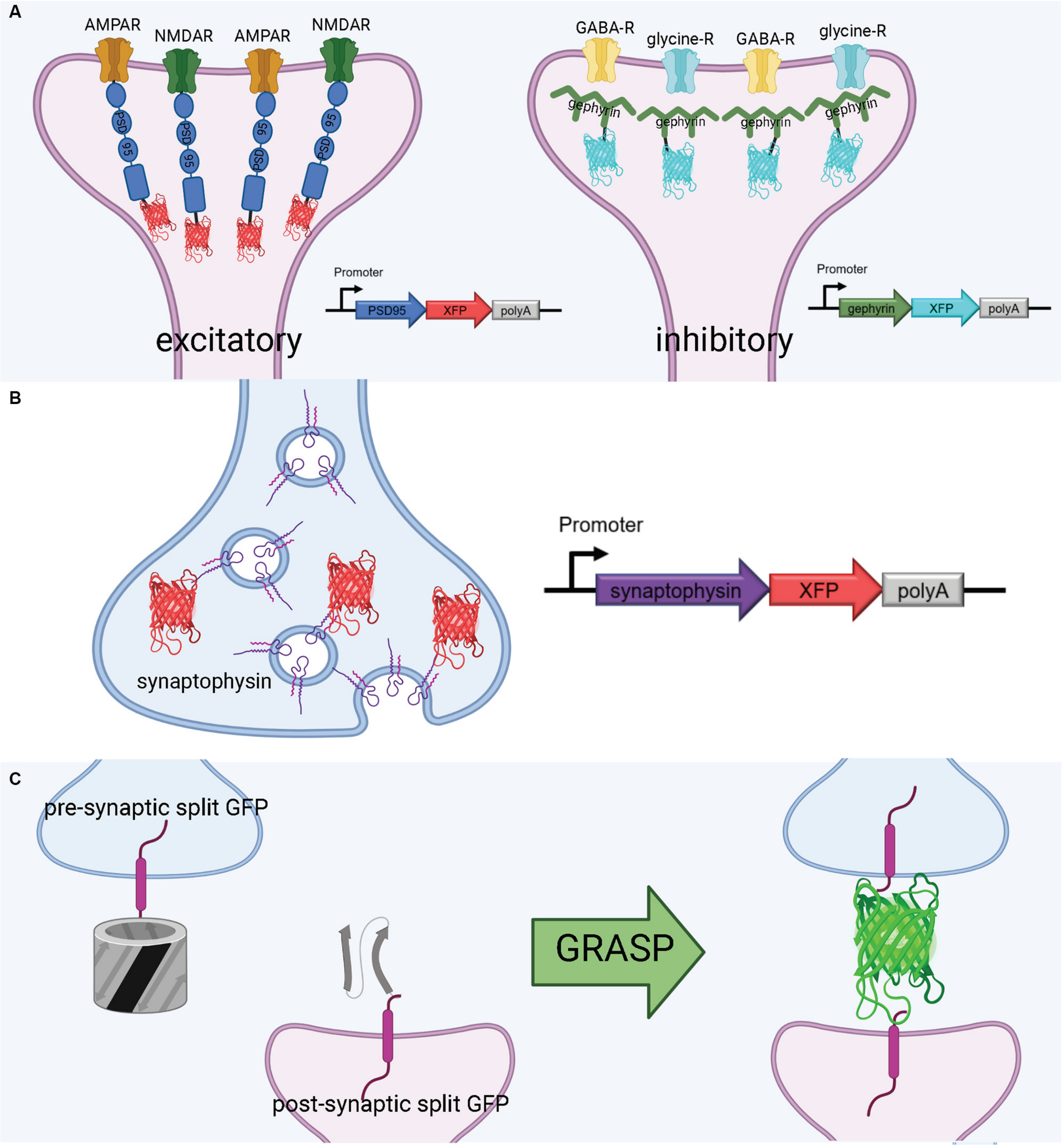

FIGURE 3 | Tools to visualize post-synaptic and pre-synaptic connections. **(A)** Schematic diagram of post-synaptic labeling of excitatory synapses with exogenous PSD-95-fluorescent protein hybrids and inhibitory synapses with exogenous gephyrin-fluorescent protein hybrids. **(B)** Schematic diagram of pre-synaptic labeling off synapses with exogenous synaptophysin-fluorescent protein hybrids. **(C)** Proximate synapse labeling with GFP Recombination Across Synaptic Partners (GRASP). Created with Biorender.com.

receptors and recruits PSD-95 to transient, unstable spines, leading to stable long-term synapses (Subramanian et al., 2019). This discovery would have been impossible without a structural marker of PSD-95, underscoring the importance of tools to visualize sub-synaptic structures *in vivo*. PSD-95 has been imaged in expanded mouse brain slices using antibodies (Sarkar et al., 2020); applying a similar technique to PSD-95-mCherry may even increase brightness in the expanded slice. Importantly, the coupling of live PSD-95 fusion imaging with later tissue expansion creates new possibilities for interrogating function and connectivity side-by-side. PSD-95 fusions such as PSD-95-mCherry allow for the structural dynamics and function of synapses to be interrogated in live brains and are then compatible with tissue expansion and microscopy to resolve the fine details of synaptic connections in fixed brains.

Gephyrin is a central postsynaptic scaffold found in the vertebrate CNS exclusively at glycinergic and GABAergic synapses (Craig et al., 1996; Tyagarajan and Fritschy, 2014). Gephyrin tagging with fluorescence proteins has been shown to be a reliable method to mark inhibitory synapses *in vitro* (Meier and Grantyn, 2004; Vlachos et al., 2013; Dejanovic et al., 2014) and *in vivo* (Oh et al., 2016; Villa et al., 2016; **Figure 3A**). The development of a teal-gephyrin as a morphological surrogate for inhibitory synapses revealed that one-third of inhibitory synapses reside on dendritic spines and that inhibitory synapses are clustered and persistently disassemble and reassemble at persistent sites *in vivo* (Villa et al., 2016). It should be noted that the inhibitory synapses on spines appear to be the most dynamic and plastic inhibitory synapses. Three-color imaging using PSD-95, Gephyrin, and a cell-filling fluorophore resolves three spine types: spines without PSD-95, spines with only PSD-95, and spines with both PSD-95 and gephyrin (Villa et al., 2016; Subramanian et al., 2019). Hence, gephyrin is an effective strategy for labeling inhibitory synapses and can be combined with other fluorescent markers.

In smaller brains, such as that of *Drosophila*, anterograde synaptic tracing is another option for mapping neural connections. For example, trans-Tango has been used to trace synaptic connections in neurons in several *Drosophila* brain regions, such as the olfactory and gustatory systems (Talay et al., 2017) and mushroom body (Scaplen et al., 2021). Trans-Tango relies on the Tango assay (Barnea et al., 2008), which is activated when a pan-neuronally expressed presynaptic fusion protein meets a postsynaptic fusion protein (Talay et al., 2017). Trans-Tango exhibits a high signal-to-noise ratio and can be applied to any genetically defined subset of neurons (Talay et al., 2017).

The expression of exogenous synaptic proteins poses the risk of interfering with the normal function of synapses. For example, overexpression of PSD-95 significantly enhances the amplitude of the excitatory postsynaptic current and increases the number of the synapse (El-Husseini et al., 2000; Béïque and Andrade, 2003). To minimize overexpression, the fusion proteins are usually expressed under weak promoters, e.g., the promoter of the polyubiquitin C gene (UBC; Subramanian et al., 2019). An even safer way to label synaptic proteins can be appending the gene of endogenous protein of interest in the genome with the gene of a tag. One approach for labeling synapses without the consequences of relying on exogenous protein expression is Synaptic Tagging with Recombination (STaR; Chen et al., 2014). STaR is a genetic approach which utilizes recombination in Bacterial Artificial Chromosomes to induce the expression of presynaptic and postsynaptic markers. Importantly, these markers can be targeted to specific neurons and are under the control of their endogenous regulatory mechanisms. In *Drosophila*, Chen et al. (2014) were able to concurrently label both presynaptic and postsynaptic markers by taking advantage of different recombination systems, allowing for visualization of synaptic pairs. The authors used this method to successfully visualize synapses in the *Drosophila* visual system, although there is potential for the method to be used in other model organisms and their appropriate recombination systems (such as Cre-Lox in mice; Chen et al., 2014). STaR is compatible with fixed brain preparations and thus holds potential for higher resolution usage in combination with ExM.

Just as STaR allows for synaptic protein tagging in *Drosophila*, there are *in vivo* genome editing strategies based on the CRISPR-Cas9 technology for mice that have been used to tag cellular proteins with epitopes without interfering with endogenous protein expression (Mikuni et al., 2016; Nishiyama et al., 2017). One such high-throughput option for monitoring endogenous synaptic proteins in live mice at single-cell resolution is SLENDR (Mikuni et al., 2016; Nishiyama et al., 2017). This method involves the delivery of the gene-editing machinery of CRISPR-Cas9 to neural progenitors in developing mouse embryos, traditionally through *in utero* electroporation. The CRISPR-Cas9 technology allows the user to label proteins of interest with small epitope tags, such as human influenza hemagglutinin (HA), Myc, and V5, as well as large payloads like monomeric EGFP and spaghetti monster fluorescent proteins (smFP; Viswanathan et al., 2015). Alternatively, Suzuki et al. developed a homology-independent targeted integration (HITI) strategy based on CRISPR-Cas9, which enables robust DNA knock-in in neurons of postnatal mammals *in vivo* (Suzuki et al., 2016). The HITI approach can be implemented using AAV-mediated gene delivery, reaching about 11% of infected neurons in adult mice. More recently, Gao Y. et al. (2019) introduced the homology-independent universal genome engineering (HiUGE) method, characterized by higher efficiency (>20%) and throughput than HITI. The HiUGE method was successfully utilized in neurons in mice to visualize inhibitory postsynaptic density (iPSD) proteome including inhibitory synaptic protein 1 (Insyn1), inhibitory synaptic protein 2 (Insyn2), and Rho GTPase activating protein 32 (Arhgap32; Uezu et al., 2016). Furthermore, by combining HiUGE with retrograde-transported AAV2-retro serotype (Tervo et al., 2016), in the same study Gao et al. performed neural circuit-selective protein manipulations in the well-defined cortico-striatal circuit and the thalamocortical circuit. Alternative CRISPR-Cas9 methods for targeted genomic integration of epitope tags, such as ORANGE (Open Resource for the Application of Neuronal Genome Editing) and TKIT (Targeted Knock-In with Two), were used for targeting PSD95, GluA1, and GluA2 with short epitope tags *in vivo* in mice with an efficiency of 10–16% (Willems et al., 2020; Fang et al., 2021). The ORANGE system was also validated *in vitro* for a variety of synaptic proteins, including voltage-dependent Ca^{2+}-channels, Rab3-interacting molecules, Bassoon, Glutamate receptor NMDA 1, etc. Another option for labeling endogenous synaptic proteins is endogenous labeling *via* exon duplication (ENABLED), which has been utilized specifically to label endogenous PSD-95 in mice. This genetic strategy is particularly notable for connectomics because it minimizes protein overexpression and can label a large subset of neurons (Fortin et al., 2014). These techniques and other similar strategies have the potential to be used to label synaptic proteins, image their dynamics in live mice, and then image synaptic connectivity in expanded brain slices.

Probes to Visualize Pre-synaptic Connections

Much as with postsynaptic proteins, pre-synaptic proteins can be fluorescently labeled to map synaptic connections. A well-established presynaptic protein for labeling synapses, particularly in vertebrates, is synaptophysin, a synaptic vesicle glycoprotein that interacts with the essential synaptic vesicle protein synaptobrevin and is thought to participate in synaptic vesicle release (Wiedenmann and Franke, 1985; Becher et al., 1999). Synaptophysin fused to a fluorescent protein has been used in many circumstances, such as in mice, rat hippocampal neurons, and zebrafish, as a faithful indicator of presynaptic machinery (Meyer and Smith, 2006; Antonova et al., 2009; Li et al., 2010; **Figure 3B**). Synaptophysin can also be used in tandem with postsynaptic markers, such as PSD-95, to label synaptic connections. Using this approach, Subramanian et al. (2019) could selectively visualize the dynamics of postsynaptic dendritic spines receiving contact from Synaptophysin-labeled presynaptic terminals. In a similar vein, it is also possible to label a postsynaptic marker such as PSD-95 *in vivo*, and later stain the tissue for a presynaptic marker such as synaptophysin to visualize synaptic connections (Broadhead et al., 2016).

A flexible approach to unambiguously map synaptic connectivity is based on GFP Reconstitution Across Synaptic Partners (GRASP; Feinberg et al., 2008; **Figure 3C**). Here, two nonfluorescent split-GFP fragments (GFP1–10 corresponding to the first 10 β-strands and GFP11 corresponding to the 11th β-strand of the GFP β-barrel) are tethered to pre- and post-synaptic membranes. Fluorescent GFP is reconstituted only when two neurons, each expressing one of the fragments, are tightly opposed through a synaptic cleft. GRASP, though originally developed in *C. elegans*, has utility in many model organisms (Feinberg et al., 2008). GRASP first was used in *Drosophila* in 2009 and has since been widely used and iterated upon (Gordon and Scott, 2009). For example, one of the first enhanced GRASP variants in *Drosophila* was specifically targeted to synapses by fusion of the presynaptic GFP fragment with Neurexin, a presynaptic cell adhesion protein (Fan et al., 2013). A later variant combines synaptobrevin and GRASP. The syb:GRASP fly chimera allows for *in vivo* activity-dependent circuit mapping, in contrast with the activity-independent neurexin variant (Macpherson et al., 2015). The same team behind the syb:GRASP fly also developed yellow and cyan GRASP variants for *Drosophila*, offering the advantages of multicolor labeling. A further enhancement of GRASP in *Drosophila* is t-GRASP, an activity-independent label which boasts greater signal specificity to the synapse (Shearin et al., 2018).

A mammalian version of GRASP (mGRASP) has had similar success in mapping synaptic connections in mouse brains (Kim et al., 2012; Song et al., 2018). Several variants and enhancements exist, such as CRASP, a cyan fluorescent protein-based variant (Li et al., 2016). Choi et al. (2018) have developed an enhanced GRASP construct, known as eGRASP, which has greater signal intensity than its predecessor. Furthermore, eGRASP expresses either a yellow or cyan fluorescent protein in presynaptic neurons, which allows for visualization of two distinct presynaptic populations which converge on the same postsynaptic neuron.

Neurexin, the presynaptic protein which was targeted in some GRASP variants (Fan et al., 2013), is another synaptic marker of interest, particularly in invertebrate systems (Kim and Emmons, 2017). For example, in *C. elegans*, neurexin located in the presynapse was shown to have an essential role in the development of the morphology of postsynaptic GABAergic neurons (Philbrook et al., 2018). In particular, neurexin is critical for the development of the spine-like protrusions that appear in *C. elegans* neurons (Philbrook et al., 2018). Presynaptic neurexin, in conjunction with the postsynaptic marker neuroligin, can be labeled to define synapses in a directional manner, as was demonstrated in live worms in the iBLINC system (Desbois et al., 2015). iBLINC fuses a recombinant biotin ligase with presynaptic neurexin and a small acceptor peptide with postsynaptic neuroligin. In an iBLINC synapse, biotin is transferred from the presynaptic biotin ligase to the postsynaptic acceptor peptide, and when streptavidin fused with fluorescent protein enters the space surrounding the synapse, it fluorescently labels the postsynaptic biotin, and thus the directional connection between the synapses can be observed (Desbois et al., 2015). Although this system was designed with *in vivo* use in mind, it represents a potential strategy to map synaptic connections in expanded animals, as protein retention expansion microscopy is compatible with streptavidin detection (Tillberg et al., 2016).

Another presynaptic marker used specifically in *C. elegans* is SYD-2, which has been shown to localize exclusively at the presynaptic active zone of worm neurons (Yeh et al., 2005). A fusion protein of SYD-2 and GFP allowed presynaptic puncta to be labeled in live *C. elegans* (Yeh et al., 2005). Furthermore, synaptic protein-protein interactions can now be probed in worms with Turbo ID, an enzyme-based proximity labeling strategy (Branon et al., 2018; Artan et al., 2021). TurboID was used to identify protein-protein interactions that a presynaptic protein, ELKS-1, was involved in Artan et al. (2021), representing a blueprint for a potential strategy for synaptic proximity labeling in *C. elegans*.

An alternative method of visualizing synaptic connections involves genetically-encoded fluorescence-based synapse labeling reagents (Kuljis et al., 2019). Kuljis et al. (2019) recently developed a system which utilizes neuroligin-1, a postsynaptic tag, to target fluorogen-activating protein (FAP) to postsynaptic sites (FAPpost). FAPpost emits a far-red signal upon binding of a small molecule fluorogen, which is applied to brain slices to induce fluorescence. The authors were able to identify synapses belonging to identifiable cell types in the mouse somatosensory cortex. Notably, unlike other constructs for visualizing synapses, FAPpost did not alter synaptic density or neuron firing properties. However, the sparse labeling shown with this technique may not be ideal for assembling complete connectomes.

FingRs

An alternative approach for visualizing synaptic proteins is the use of Fibronectin intrabodies generated with mRNA display (FingRs). These are intrabodies fused to fluorescent proteins which bind to the target endogenous protein and allow for precise visualization of the target's localization and density (Gross et al., 2013; **Figure 4A**). FingRs are a newer and less established technology than hybrid fluorescent proteins, and they hold great potential for imaging the synapse despite their recency and lack of widespread use. Unlike many other tools, there has been evidence to show that FingRs do not significantly affect endogenous protein expression, the number and strength of synapses, and synaptic transmission in brain slice (Gross et al., 2013; Bensussen et al., 2020). FingRs are expressed in behaving animals and then quantified using post-mortem histology, and must be expressed in living animals for weeks before they are visualized (Gross et al., 2013; Bensussen et al., 2020). This approach can easily be synthesized with existing ExM protocols. However, unlike standard fluorescent protein techniques, FingRs are not compatible with live imaging.

FingRs for PSD-95 and gephyrin were the first-ever developed (Gross et al., 2013), and have since proven useful for visualizing changes in synaptic strength in model organisms. Son et al. (2016) used FingRs in live zebrafish and found that FingR expression did not hinder protein expression at the synapse, number of synapses, and synapse function. Additionally, they used FingRs for PSD-95 and gephyrin to show that chronic hypoxia decreases the number of dopaminergic synapses (Son et al., 2016). Cook S. G. et al. (2019) used FingRs to simultaneously image PSD-95, gephyrin, and CaMKII in the hippocampal neural culture and found that amyloid beta (Aβ) interferes with CaMKII activation in stimulus-induced LTP, but not LTD. Xue Han's group has recently developed further FingR variants, including a red variant which can be used in conjunction with green variants (Bensussen et al., 2020).

A promising tool for understanding the relationship between structure and function in neural circuits is the recently-developed SynTagMA, a genetically encoded sensor for synaptic activity. SynTagMA is a fusion of a modified version of CAMPARI2, an established indicator of active neurons, with FingRs for either PSD-95 or synaptophysin (Moeyaert et al., 2018; Perez-Alvarez et al., 2020; **Figures 4B,C**). The PSD-95 SynTagMA construct targets post-synaptic terminals, and the synaptophysin SynTagMA construct targets pre-synaptic terminals (Perez-Alvarez et al., 2020). SynTagMA can detect synaptic activity by irreversibly changing from green fluorescence to red in the presence of calcium upon photoactivation by 395–405 nm illumination, generating a snapshot of synaptic activity at a user-defined time (Perez-Alvarez et al., 2020). SynTagMA can simultaneously tag thousands of active synapses. PSD-95-fused SynTagMA has successfully been used in awake head-fixed mice to visualize active synapses, and future experiments using this synaptically localized, photoconvertible calcium sensor will enable further study on the synaptic basis of complex brain function in health and disease. SynTagMA, if used in conjunction with other tools that map connectivity more directly, could be a crucial tool for understanding functional connectivity.

Experimental Considerations

The tools described in this article are all hypothetically compatible with standard ExM protocols and represent a mere subset of the possible ways to image the synapse at nanoscale resolution. Any imaging or staining done pre-expansion, including live imaging, will proceed normally (**Figure 5**). Afterward, the tissue intended for expansion can be chemically treated according to your ExM protocol of choice (Karagiannis and Boyden, 2018; Wassie et al., 2019). Though some troubleshooting may be involved to receive optimal results, combining previously established synaptic markers with ExM represents exciting possibilities for synaptic mapping in a variety of model organisms. There are, however, a few caveats to be noted about ExM. For example, while the isotropy of the tissue is generally very well preserved in various tissue types, it is important for new ExM users to validate that their tissues expanded in an isotropic manner (Wassie et al., 2019). However, if the protocol is executed correctly, there is no significant rearrangement of the synapse shown when expanded: the relative position of synaptic proteins stays the same after expansion (Zhao et al., 2017; Sarkar et al., 2020). Although the ExM process can degrade some proteins, fortunately, fluorescent proteins are relatively resistant to degradation during the protocol and maintain their brightness (Wassie et al., 2019). Brightness can be improved by processing the tissue with antibodies prior to expansion and choosing ExM protocols that are best equipped to preserve protein integrity suited for individual project needs (Parra-Damas and Saura, 2020). Another important consideration, specifically when the nanoarchitecture of synapses is studied, is the possible distortion upon expansion that may happen at the nanoscale, which is to be validated for every newly developed ExM method or protocol. The gold standard in the field for synapse identification is EM, but ExM views of synapses cannot be correlated with the ultrastructure as seen in EM, as ExM techniques are not compatible with the staining and sample processing done for EM.

The choice of gene delivery vector is an important consideration for mapping synaptic connections. One important limitation of many of the tools above, especially several of the sensors designed for use in mammalian brains such as mGRASP and SynTagMA, is that they are typically delivered to live mouse brains *via* AAV injection. Although AAVs are the favored gene delivery vector for many experiments, this strategy does not guarantee that every single neuron in the target area is labeled

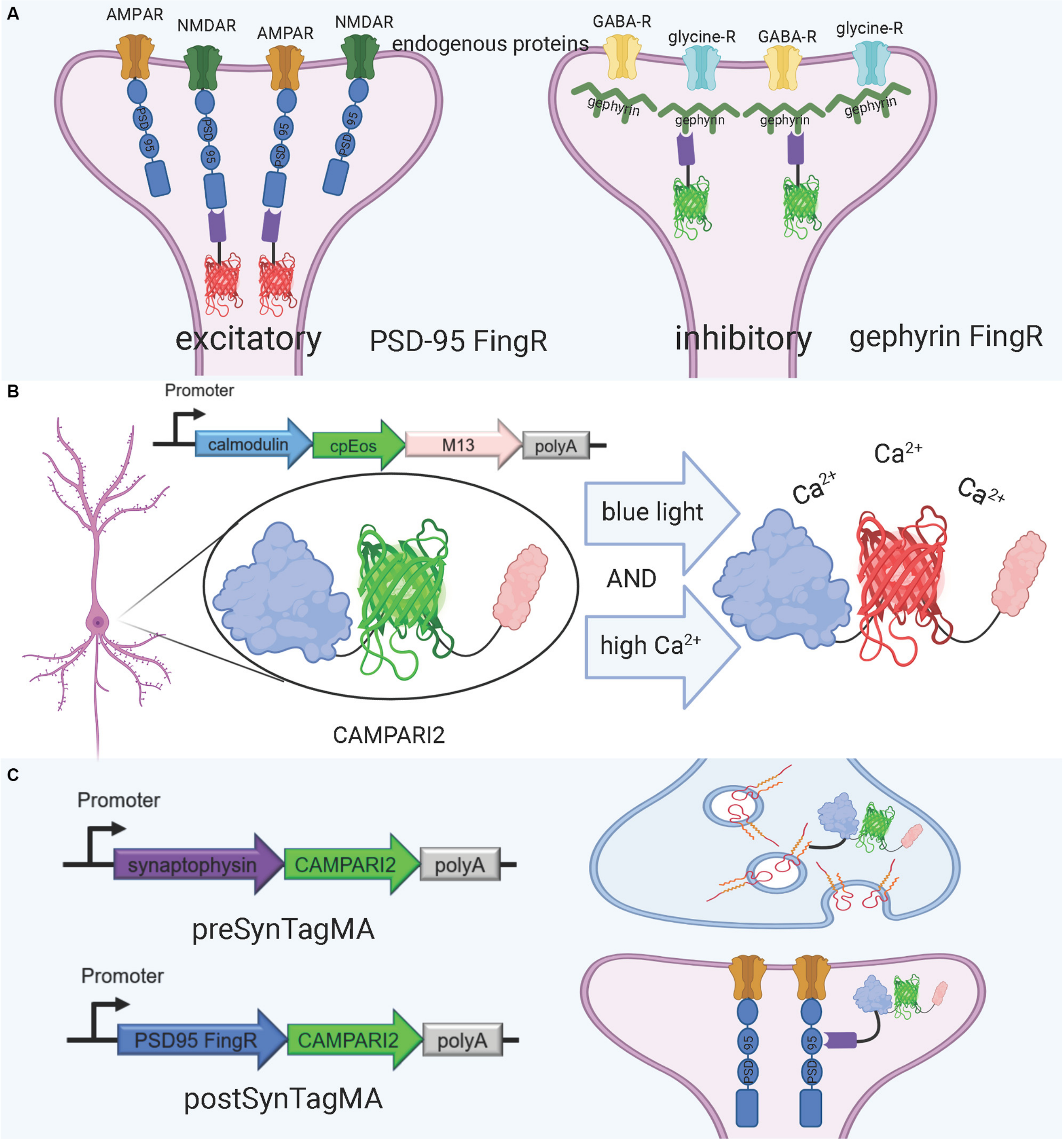

FIGURE 4 | FingRs and related tools. **(A)** Schematic diagram of FingRs for post-synaptic labeling of excitatory and inhibitory synapses, using endogenous PSD-95 and gephyrin, respectively. **(B)** Schematic diagram of CAMPARI2, a genetically encoded calcium indicator, which changes fluorescent wavelength in response to combined blue light and high calcium ion levels. CAMPARI2 forms the fluorescent component of SynTagMA. **(C)** Schematic diagram of pre-SynTagMA, which marks synaptophysin, and post-SynTagMA, which marks endogenous PSD-95 with the aid of a PSD-95-specific FingR. Created with Biorender.com.

(Chan et al., 2017; Wang et al., 2018). For example, when tracing synaptic connectivity in a small volume of the mouse brain, AAVs delivering Brainbow transgenes were not able to label every neuron for connectivity tracing, and the percent of neurons labeled varied widely based on cell type (Shen et al., 2020). For most applications, it is usually not necessary to label every single neuron, but when assembling complete connectomes, it is essential that as many neurons as possible be labeled. Thus, gene delivery strategies must be applied carefully and cautiously to avoid leaving out unlabelled neurons, particularly

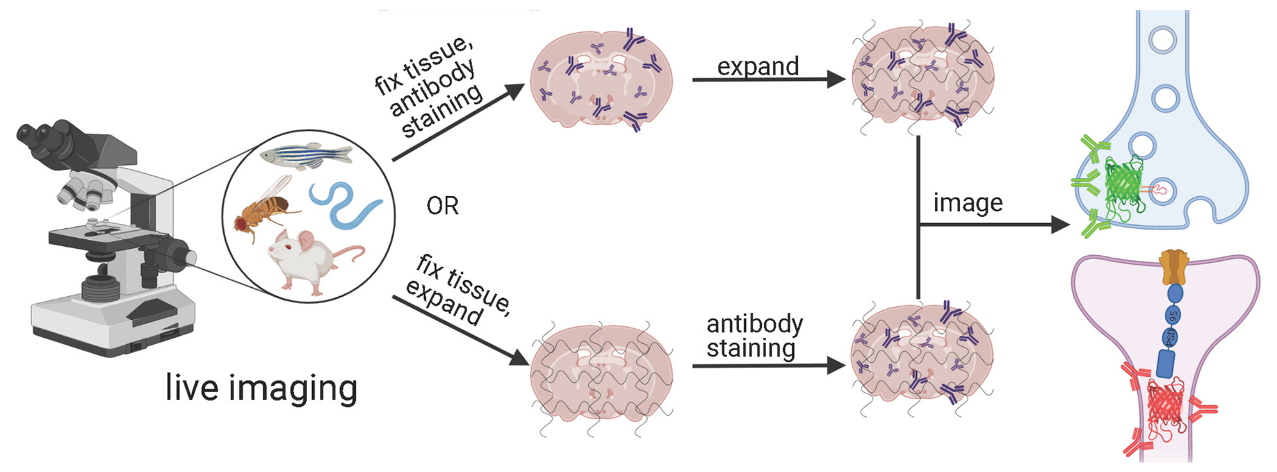

FIGURE 5 | Generalized workflow for combining tools to exogenously label post-synaptic and pre-synaptic neurons in a variety of model organisms with expansion microscopy. Created with Biorender.com.

in mammalian systems. Alternate gene delivery methods for mice, such as the generation of transgenic mouse lines or herpes simplex virus vectors, which have genomic integration rates much closer to 100%, should be considered for connectome-specific applications.

Conclusion/Perspective

There is a great need for the generation of connectomes. The first-ever complete connectome of an organism, the *C. elegans* connectome, has been indispensable for studying the worm brain. For example, the worm connectome has been combined with ablation experiments to generate circuit maps and has provided the basis for a number of computational models. Taking inspiration from connectomes has also led to biologically-informed innovations in machine learning (Hasani et al., 2020). However, much of the potential of the connectome has remained locked away, particularly because a single connectome cannot possibly represent the full range of connectivities in even a simple nervous system. Connectomes will be most useful when there are multiple, even hundreds, for a single species, let alone for different sexes, developmental stages, and mutants. Furthermore, many of the most commonly used model organisms, particularly zebrafish, mice, and rats, lack anything resembling a complete connectome, and current endeavors to generate these connectomes, though heroic, are incredibly expensive and time-consuming.

ExM has the potential to represent a paradigm shift in connectomics so that any lab with standard microscopy equipment can contribute to the endeavor to map synaptic connections. Rapid advances in synaptic imaging tools and in ExM protocols have paved the way for a powerful synergy: now all that is left is to turn the hypothetical into reality.

AUTHOR CONTRIBUTIONS

KP: conceptualization, supervision, and funding acquisition. MS: writing—original draft preparation. KP and MS: writing—review and editing, visualization. All authors contributed to the article and approved the submitted version.

FUNDING

This work was supported by start-up funding from the Foundation of Westlake University, Foundation for Innovative Research Groups of the National Natural Science Foundation of China grant 32050410298 and 32171093, 2020 BBRF Young Investigator Grant number 28961, and MRIC Funding 103536022023 to KP.

ACKNOWLEDGMENTS

We thank Ed Boyden, Mitch Murdock, Yangning Lu, and Orhan Celiker for their helpful comments. We especially thank Mitch Murdock for his support at the beginning of the writing process and Ed Boyden for his support throughout this process. Figures were created with Biorender.com.

REFERENCES

Albertson, D. G., Thompson, J. N., and Brenner, S. (1976). The pharynx of *Caenorhabditis elegans*. *Philos. Trans. R. Soc. Lond. B Biol. Sci.* 275, 299–325. doi: 10.1098/rstb.1976.0085

Alon, S., Goodwin, D. R., Sinha, A., Wassie, A. T., Chen, F., Daugharthy, E. R., et al. (2021). Expansion sequencing: spatially precise in situ transcriptomics in intact biological systems. *Science* 371:eaax2656. doi: 10.1126/science.aax2656

Antonova, I., Lu, F.-M., Zablow, L., Udo, H., and Hawkins, R. D. (2009). Rapid and long-lasting increase in sites for synapse assembly during late-phase potentiation in rat hippocampal neurons. *PLoS One* 4:e7690. doi: 10.1371/journal.pone.0007690

Artan, M., Barratt, S., Flynn, S. M., Begum, F., Skehel, M., Nicolas, A., et al. (2021). Interactome analysis of *C. elegans* synapses by TurboID-based proximity labeling. *bioRxiv* [Preprint]. doi: 10.1016/j.jbc.2021.101094

Barnea, G., Strapps, W., Herrada, G., Berman, Y., Ong, J., Kloss, B., et al. (2008). The genetic design of signaling cascades to record receptor activation. *Proc. Natl. Acad. Sci. U S A* 105, 64–69. doi: 10.1073/pnas.0710487105

Becher, A., Drenckhahn, A., Pahner, I., Margittai, M., Jahn, R., and Ahnert-Hilger, G. (1999). The synaptophysin-synaptobrevin complex: a hallmark of synaptic vesicle maturation. *J. Neurosci.* 19, 1922–1931. doi: 10.1523/JNEUROSCI.19-06-01922.1999

Bé̈ique, J.-C., and Andrade, R. (2003). PSD-95 regulates synaptic transmission and plasticity in rat cerebral cortex. *J. Physiol.* 546, 859–867. doi: 10.1113/jphysiol.2002.031369

Bensussen, S., Shankar, S., Ching, K. H., Zemel, D., Ta, T. L., Mount, R. A., et al. (2020). A viral toolbox of genetically encoded fluorescent synaptic tags. *iScience* 23:101330. doi: 10.1016/j.isci.2020.101330

Bergmann, E., Gofman, X., Kavushansky, A., and Kahn, I. (2020). Individual variability in functional connectivity architecture of the mouse brain. *Commun. Biol.* 3:738. doi: 10.1038/s42003-020-01472-5

Berry, K. P., and Nedivi, E. (2017). Spine dynamics: are they all the same. *Neuron* 96, 43–55. doi: 10.1016/j.neuron.2017.08.008

Branon, T. C., Bosch, J. A., Sanchez, A. D., Udeshi, N. D., Svinkina, T., Carr, S. A., et al. (2018). Efficient proximity labeling in living cells and organisms with TurboID. *Nat. Biotechnol.* 36, 880–887. doi: 10.1038/nbt.4201

Broadhead, M. J., Horrocks, M. H., Zhu, F., Muresan, L., Benavides-Piccione, R., DeFelipe, J., et al. (2016). PSD95 nanoclusters are postsynaptic building blocks in hippocampus circuits. *Sci. Rep.* 6:24626. doi: 10.1038/srep24626

Bürgers, J., Pavlova, I., Rodriguez-Gatica, J. E., Henneberger, C., Oeller, M., Ruland, J. A., et al. (2019). Light-sheet fluorescence expansion microscopy: fast mapping of neural circuits at super resolution. *Neurophotonics* 6:015005. doi: 10.1117/1.NPh.6.1.015005

Cai, D., Cohen, K. B., Luo, T., Lichtman, J. W., and Sanes, J. R. (2013). Improved tools for the brainbow toolbox. *Nat. Methods* 10, 540–547. doi: 10.1038/nmeth.2450

Cane, M., Maco, B., Knott, G., and Holtmaat, A. (2014). The relationship between PSD-95 clustering and spine stability *in vivo*. *J. Neurosci.* 34, 2075–2086. doi: 10.1523/JNEUROSCI.3353-13.2014

Chan, K. Y., Jang, M. J., Yoo, B. B., Greenbaum, A., Ravi, N., Wu, W.-L., et al. (2017). Engineered AAVs for efficient noninvasive gene delivery to the central and peripheral nervous systems. *Nat. Neurosci.* 20, 1172–1179. doi: 10.1038/nn.4593

Chang, J.-B., Chen, F., Yoon, Y.-G., Jung, E. E., Babcock, H., Kang, J. S., et al. (2017). Iterative expansion microscopy. *Nat. Methods* 14, 593–599. doi: 10.1038/nmeth.4261

Chen, Y., Akin, O., Nern, A., Tsui, C. Y. K., Pecot, M. Y., and Zipursky, S. L. (2014). Cell-type specific labeling of synapses *in vivo* through synaptic tagging with recombination (STaR). *Neuron* 81, 280–293. doi: 10.1016/j.neuron.2013.12.021

Chen, X., Levy, J. M., Hou, A., Winters, C., Azzam, R., Sousa, A. A., et al. (2015). PSD-95 family MAGUKs are essential for anchoring AMPA and NMDA receptor complexes at the postsynaptic density. *Proc. Natl. Acad. Sci. U S A* 112, E6983–E6992. doi: 10.1073/pnas.1517045112

Chen, Y., Li, X., Zhang, D., Wang, C., Feng, R., Li, X., et al. (2020). A versatile tiling light sheet microscope for imaging of cleared tissues. *Cell Rep.* 33:108349. doi: 10.1016/j.celrep.2020.108349

Chen, X., Nelson, C. D., Li, X., Winters, C. A., Azzam, R., Sousa, A. A., et al. (2011). PSD-95 is required to sustain the molecular organization of the postsynaptic density. *J. Neurosci.* 31, 6329–6338. doi: 10.1523/JNEUROSCI.5968-10.2011

Chen, F., Tillberg, P. W., and Boyden, E. S. (2015). Expansion microscopy. *Science* 347, 543–548. doi: 10.1126/science.1260088

Chen, J. L., Villa, K. L., Cha, J. W., So, P. T. C., Kubota, Y., and Nedivi, E. (2012). Clustered dynamics of inhibitory synapses and dendritic spines in the adult neocortex. *Neuron* 74, 361–373. doi: 10.1016/j.neuron.2012.02.030

Chen, X., Vinade, L., Leapman, R. D., Petersen, J. D., Nakagawa, T., Phillips, T. M., et al. (2005). Mass of the postsynaptic density and enumeration of three key molecules. *Proc. Natl. Acad. Sci. U S A* 102, 11551–11556. doi: 10.1073/pnas.0505359102

Choi, S. W., Guan, W., and Chung, K. (2021). Basic principles of hydrogel-based tissue transformation technologies and their applications. *Cell* 184, 4115–4136. doi: 10.1016/j.cell.2021.07.009

Choi, J.-H., Sim, S.-E., Kim, J., Choi, D. I., Oh, J., Ye, S., et al. (2018). Interregional synaptic maps among engram cells underlie memory formation. *Science* 360, 430–435. doi: 10.1126/science.aas9204

Choii, G., and Ko, J. (2015). Gephyrin: a central GABAergic synapse organizer. *Exp. Mol. Med.* 47:e158. doi: 10.1038/emm.2015.5

Chozinski, T. J., Halpern, A. R., Okawa, H., Kim, H.-J., Tremel, G. J., Wong, R. O. L., et al. (2016). Expansion microscopy with conventional antibodies and fluorescent proteins. *Nat. Methods* 13, 485–488. doi: 10.1038/nmeth.3833

Cook, S. G., Goodell, D. J., Restrepo, S., Arnold, D. B., and Bayer, K. U. (2019). Simultaneous live imaging of multiple endogenous proteins reveals a mechanism for Alzheimer's-related plasticity impairment. *Cell Rep.* 27, 658–665.e4. doi: 10.1016/j.celrep.2019.03.041

Cook, S. J., Jarrell, T. A., Brittin, C. A., Wang, Y., Bloniarz, A. E., Yakovlev, M. A., et al. (2019). Whole-animal connectomes of both *Caenorhabditis elegans* sexes. *Nature* 571, 63–71. doi: 10.1038/s41586-019-1352-7

Craig, A. M., Banker, G., Chang, W., McGrath, M. E., and Serpinskaya, A. S. (1996). Clustering of gephyrin at GABAergic but not glutamatergic synapses in cultured rat hippocampal neurons. *J. Neurosci.* 16, 3166–3177. doi: 10.1523/JNEUROSCI.16-10-03166.1996

Craven, S. E., El-Husseini, A. E., and Bredt, D. S. (1999). Synaptic targeting of the postsynaptic density protein PSD-95 mediated by lipid and protein motifs. *Neuron* 22, 497–509. doi: 10.1016/s0896-6273(00)80705-9

Damstra, H. G. J., Mohar, B., Eddison, M., Akhmanova, A., Kapitein, L. C., and Tillberg, P. W. (2021). Visualizing cellular and tissue ultrastructure using ten-fold robust expansion microscopy (TREx). *bioRxiv* [Preprint]. doi: 10.1101/2021.02.03.428837

De Robertis, E. D. P., and Bennett, H. S. (1955). Some features of the submicroscopic morphology of synapses in frog and earthworm. *J. Biophys. Biochem. Cytol.* 1, 47–58. doi: 10.1083/jcb.1.1.47

Dejanovic, B., Semtner, M., Ebert, S., Lamkemeyer, T., Neuser, F., Lüscher, B., et al. (2014). Palmitoylation of gephyrin controls receptor clustering and plasticity of GABAergic synapses. *PLoS Biol.* 12:e1001908. doi: 10.1371/journal.pbio.1001908

Desbois, M., Cook, S. J., Emmons, S. W., and Bülow, H. E. (2015). Directional trans-synaptic labeling of specific neuronal connections in live animals. *Genetics* 200, 697–705. doi: 10.1534/genetics.115.177006

Dhawale, A., and Bhalla, U. S. (2008). The network and the synapse: 100 years after cajal. *HFSP J.* 2, 12–16. doi: 10.2976/1.2835214

Dorkenwald, S., Turner, N. L., Macrina, T., Lee, K., Lu, R., Wu, J., et al. (2019). Binary and analog variation of synapses between cortical pyramidal neurons. *bioRxiv* [Preprint]. doi: 10.1101/2019.12.29.890319

Dosemeci, A., Weinberg, R. J., Reese, T. S., and Tao-Cheng, J.-H. (2016). The postsynaptic density: there is more than meets the eye. *Front. Synaptic Neurosci.* 8:23. doi: 10.3389/fnsyn.2016.00023

Drachman, D. A. (2005). Do we have brain to spare. *Neurology* 64, 2004–2005. doi: 10.1212/01.WNL.0000166914.38327.BB

El-Husseini, A. E.-D., Schnell, E., Chetkovich, D. M., Nicoll, R. A., and Bredt, D. S. (2000). PSD-95 involvement in maturation of excitatory synapses. *Science* 290, 1364–1368. doi: 10.1126/science.290.5495.1364

Fan, P., Manoli, D. S., Ahmed, O. M., Chen, Y., Agarwal, N., Kwong, S., et al. (2013). Genetic and neural mechanisms that inhibit *Drosophila* from mating with other species. *Cell* 154, 89–102. doi: 10.1016/j.cell.2013.06.008

Fang, H., Bygrave, A. M., Roth, R. H., Johnson, R. C., and Huganir, R. L. (2021). An optimized CRISPR/Cas9 approach for precise genome editing in neurons. *eLife* 10:e65202. doi: 10.7554/eLife.65202

Feinberg, E. H., VanHoven, M. K., Bendesky, A., Wang, G., Fetter, R. D., Shen, K., et al. (2008). GFP reconstitution across synaptic partners (GRASP) defines cell contacts and synapses in living nervous systems. *Neuron* 57, 353–363. doi: 10.1016/j.neuron.2007.11.030

Fortin, D. A., Tillo, S. E., Yang, G., Rah, J.-C., Melander, J. B., Bai, S., et al. (2014). live imaging of endogenous PSD-95 using ENABLED: a conditional strategy to fluorescently label endogenous proteins. *J. Neurosci.* 34, 16698–16712. doi: 10.1523/JNEUROSCI.3888-14.2014

Freifeld, L., Odstrcil, I., Förster, D., Ramirez, A., Gagnon, J. A., Randlett, O., et al. (2017). Expansion microscopy of zebrafish for neuroscience and developmental biology studies. *Proc. Natl. Acad. Sci. U S A* 114, E10799–E10808. doi: 10.1073/pnas.1706281114

Furshpan, E. J., and Potter, D. D. (1959). Transmission at the giant motor synapses of the crayfish. *J. Physiol.* 145, 289–325. doi: 10.1113/jphysiol.1959.sp006143

Galarreta, M., and Hestrin, S. (2001). Electrical synapses between Gaba-Releasing interneurons. *Nat. Rev. Neurosci.* 2, 425–433. doi: 10.1038/35077566

Gao, R., Asano, S. M., Upadhyayula, S., Pisarev, I., Milkie, D. E., Liu, T.-L., et al. (2019). Cortical column and whole-brain imaging with molecular contrast and nanoscale resolution. *Science* 363:eaau8302. doi: 10.1126/science.aau8302

Gao, Y., Hisey, E., Bradshaw, T. W. A., Erata, E., Brown, W. E., Courtland, J. L., et al. (2019). Plug-and-play protein modification using homology-independent universal genome engineering. *Neuron* 103, 583–597.e8. doi: 10.1016/j.neuron.2019.05.047

Gao, M., Maraspini, R., Beutel, O., Zehtabian, A., Eickholt, B., Honigmann, A., et al. (2018). Expansion stimulated emission depletion microscopy (ExSTED). *ACS Nano* 12, 4178–4185. doi: 10.1021/acsnano.8b00776

Gao, R., Yu, C.-C., Gao, L., Piatkevich, K. D., Neve, R. L., Munro, J. B., et al. (2021). A highly homogeneous polymer composed of tetrahedron-like monomers for high-isotropy expansion microscopy. *Nat. Nanotechnol.* 16, 698–707. doi: 10.1038/s41565-021-00875-7

Gibson, J. R., Beierlein, M., and Connors, B. W. (1999). Two networks of electrically coupled inhibitory neurons in neocortex. *Nature* 402, 75–79. doi: 10.1038/47035

Gong, H., Xu, D., Yuan, J., Li, X., Guo, C., Peng, J., et al. (2016). High-throughput dual-colour precision imaging for brain-wide connectome with cytoarchitectonic landmarks at the cellular level. *Nat. Commun.* 7:12142. doi: 10.1038/ncomms12142

Gordon, M. D., and Scott, K. (2009). Motor control in a *Drosophila* taste circuit. *Neuron* 61, 373–384. doi: 10.1016/j.neuron.2008.12.033

Gray, E. G. (1959). Electron microscopy of synaptic contacts on dendrite spines of the cerebral cortex. *Nature* 183, 1592–1593. doi: 10.1038/1831592a0

Gray, N. W., Weimer, R. M., Bureau, I., and Svoboda, K. (2006). Rapid redistribution of synaptic PSD-95 in the neocortex *in vivo*. *PLoS Biol.* 4:e370. doi: 10.1371/journal.pbio.0040370

Gross, G. G., Junge, J. A., Mora, R. J., Kwon, H.-B., Olson, C. A., Takahashi, T. T., et al. (2013). Recombinant probes for visualizing endogenous synaptic proteins in living neurons. *Neuron* 78, 971–985. doi: 10.1016/j.neuron.2013.04.017

Gutierrez-Mecinas, M., Kuehn, E. D., Abraira, V. E., Polgár, E., Watanabe, M., and Todd, A. J. (2016). Immunostaining for Homer reveals the majority of excitatory synapses in laminae I-III of the mouse spinal dorsal horn. *Neuroscience* 329, 171–181. doi: 10.1016/j.neuroscience.2016.05.009

Hafner, A.-S., Donlin-Asp, P. G., Leitch, B., Herzog, E., and Schuman, E. M. (2019). Local protein synthesis is a ubiquitous feature of neuronal pre- and postsynaptic compartments. *Science* 364:eaau3644. doi: 10.1126/science.aau3644

Hall, D. H., and Russell, R. L. (1991). The posterior nervous system of the nematode *Caenorhabditis elegans*: serial reconstruction of identified neurons and complete pattern of synaptic interactions. *J. Neurosci.* 11, 1–22. doi: 10.1523/JNEUROSCI.11-01-00001.1991

Hama, H., Kurokawa, H., Kawano, H., Ando, R., Shimogori, T., Noda, H., et al. (2011). Scale: a chemical approach for fluorescence imaging and reconstruction of transparent mouse brain. *Nat. Neurosci.* 14, 1481–1488. doi: 10.1038/nn.2928

Hasani, R., Lechner, M., Amini, A., Rus, D., and Grosu, R. (2020). Liquid time-constant networks. *arXiv* [Preprint]. Available online at: http://arxiv.org/abs/2006.04439. Accessed March 13, 2021.

Helm, M. S., Dankovich, T. M., Mandad, S., Rammner, B., Jähne, S., Salimi, V., et al. (2021). A large-scale nanoscopy and biochemistry analysis of postsynaptic dendritic spines. *Nat. Neurosci.* 24, 1151–1162. doi: 10.1038/s41593-021-00874-w

Hormuzdi, S. G., Filippov, M. A., Mitropoulou, G., Monyer, H., and Bruzzone, R. (2004). Electrical synapses: a dynamic signaling system that shapes the activity of neuronal networks. *Biochim. Biophys. Acta* 1662, 113–137. doi: 10.1016/j.bbamem.2003.10.023

Hu, Y., Chu, X., Chen, T., Pan, Q., Liu, C., Yi, J., et al. (2020). Improving resolving ability of expansion microscopy by varying crosslinker concentration. *Chem. Commun.* 56, 4176–4179. doi: 10.1039/d0cc00052c

Hubbard, P. M., Berg, S., Zhao, T., Olbris, D. J., Umayam, L., Maitin-Shepard, J., et al. (2020). Accelerated EM connectome reconstruction using 3D visualization and segmentation graphs. *bioRxiv* [Preprint]. doi: 10.1101/2020.01.17.909572

Hulse, B. K., Haberkern, H., Franconville, R., Turner-Evans, D. B., Takemura, S., Wolff, T., et al. (2021). A connectome of the *Drosophila* central complex reveals network motifs suitable for flexible navigation and context-dependent action selection. *eLife* 10:e66039. doi: 10.7554/eLife.66039

Isshiki, M., Tanaka, S., Kuriu, T., Tabuchi, K., Takumi, T., and Okabe, S. (2014). Enhanced synapse remodelling as a common phenotype in mouse models of autism. *Nat. Commun.* 5:4742. doi: 10.1038/ncomms5742

Jarrell, T. A., Wang, Y., Bloniarz, A. E., Brittin, C. A., Xu, M., Thomson, J. N., et al. (2012). The connectome of a decision-making neural network. *Science* 337, 437–444. doi: 10.1126/science.1221762

Jiang, N., Kim, H.-J., Chozinski, T. J., Azpurua, J. E., Eaton, B. A., Vaughan, J. C., et al. (2018). Superresolution imaging of *Drosophila* tissues using expansion microscopy. *Mol. Biol. Cell* 29, 1413–1421. doi: 10.1091/mbc.E17-10-0583

Karagiannis, E. D., and Boyden, E. S. (2018). Expansion microscopy: development and neuroscience applications. *Curr. Opin. Neurobiol.* 50, 56–63. doi: 10.1016/j.conb.2017.12.012

Kasthuri, N., Hayworth, K. J., Berger, D. R., Schalek, R. L., Conchello, J. A., Knowles-Barley, S., et al. (2015). Saturated reconstruction of a volume of neocortex. *Cell* 162, 648–661. doi: 10.1016/j.cell.2015.06.054

Kim, S.-Y., Cho, J. H., Murray, E., Bakh, N., Choi, H., Ohn, K., et al. (2015). Stochastic electrotransport selectively enhances the transport of highly electromobile molecules. *Proc. Natl. Acad. Sci. U S A* 112, E6274–E6283. doi: 10.1073/pnas.1510133112

Kim, B., and Emmons, S. W. (2017). Multiple conserved cell adhesion protein interactions mediate neural wiring of a sensory circuit in *C. elegans*. *eLife* 6:e29257. doi: 10.7554/eLife.29257

Kim, E. J., Jacobs, M. W., Ito-Cole, T., and Callaway, E. M. (2016). Improved monosynaptic neural circuit tracing using engineered rabies virus glycoproteins. *Cell Rep.* 15, 692–699. doi: 10.1016/j.celrep.2016.03.067

Kim, J., Zhao, T., Petralia, R. S., Yu, Y., Peng, H., Myers, E., et al. (2012). mGRASP enables mapping mammalian synaptic connectivity with light microscopy. *Nat. Methods* 9, 96–102. doi: 10.1038/nmeth.1784

Ku, T., Swaney, J., Park, J.-Y., Albanese, A., Murray, E., Cho, J. H., et al. (2016). Multiplexed and scalable super-resolution imaging of three-dimensional protein localization in size-adjustable tissues. *Nat. Biotechnol.* 34, 973–981. doi: 10.1038/nbt.3641

Kuljis, D. A., Park, E., Telmer, C. A., Lee, J., Ackerman, D. S., Bruchez, M. P., et al. (2019). Fluorescence-based quantitative synapse analysis for cell type-specific connectomics. *eNeuro* 6:ENEURO.0193-19.2019. doi: 10.1523/ENEURO.0193-19.2019

Li, R., Chen, X., Lin, Z., Wang, Y., and Sun, Y. (2018). Expansion enhanced nanoscopy. *Nanoscale* 10, 17552–17556. doi: 10.1039/c8nr04267e

Li, Y., Guo, A., and Li, H. (2016). CRASP: CFP reconstitution across synaptic partners. *Biochem. Biophys. Res. Commun.* 469, 352–356. doi: 10.1016/j.bbrc.2015.12.011

Li, L., Tasic, B., Micheva, K. D., Ivanov, V. M., Spletter, M. L., Smith, S. J., et al. (2010). Visualizing the distribution of synapses from individual neurons in the mouse brain. *PLoS One* 5:e11503. doi: 10.1371/journal.pone.0011503

Li, Y., Walker, L. A., Zhao, Y., Edwards, E. M., Michki, N. S., Cheng, H. P. J., et al. (2021). Bitbow enables highly efficient neuronal lineage tracing and morphology reconstruction in single *Drosophila* brains. *Front. Neural Circuits* 15:105. doi: 10.3389/fncir.2021.732183

Lillvis, J. L., Otsuna, H., Ding, X., Pisarev, I., Kawase, T., Colonell, J., et al. (2021). Rapid reconstruction of neural circuits using tissue expansion and lattice light sheet microscopy. *bioRxiv* [Preprint]. doi: 10.1101/2021.11.14.468535

Livet, J., Weissman, T. A., Kang, H., Draft, R. W., Lu, J., Bennis, R. A., et al. (2007). Transgenic strategies for combinatorial expression of fluorescent proteins in the nervous system. *Nature* 450, 56–62. doi: 10.1038/nature06293

Llinás, R. R. (2003). The contribution of santiago ramon y cajal to functional neuroscience. *Nat. Rev. Neurosci.* 4, 77–80. doi: 10.1038/nrn1011

Macpherson, L. J., Zaharieva, E. E., Kearney, P. J., Alpert, M. H., Lin, T.-Y., Turan, Z., et al. (2015). Dynamic labelling of neural connections in multiple colours by trans-synaptic fluorescence complementation. *Nat. Commun.* 6:10024. doi: 10.1038/ncomms10024

Magaki, S., Hojat, S. A., Wei, B., So, A., and Yong, W. H. (2019). "An introduction to the performance of immunohistochemistry," in *Biobanking: Methods and Protocols Methods in Molecular Biology*, eds W. H. Yong (New York, NY: Springer), 289–298.

Meier, J., and Grantyn, R. (2004). A gephyrin-related mechanism restraining glycine receptor anchoring at GABAergic synapses. *J. Neurosci.* 24, 1398–1405. doi: 10.1523/JNEUROSCI.4260-03.2004

Meyer, M. P., and Smith, S. J. (2006). Evidence from *in vivo* imaging that synaptogenesis guides the growth and branching of axonal arbors by two distinct mechanisms. *J. Neurosci.* 26, 3604–3614. doi: 10.1523/JNEUROSCI.0223-06.2006

Micheva, K. D., Busse, B., Weiler, N. C., O'Rourke, N., and Smith, S. J. (2010). Single-synapse analysis of a diverse synapse population: proteomic imaging methods and markers. *Neuron* 68, 639–653. doi: 10.1016/j.neuron.2010.09.024

MICrONS Consortium, M., Bae, J. A., Baptiste, M., Bodor, A. L., Brittain, D., Buchanan, J., et al. (2021). Functional connectomics spanning multiple areas of mouse visual cortex. *bioRxiv* [Preprint]. doi: 10.1101/2021.07.28.454025

Mikuni, T., Nishiyama, J., Sun, Y., Kamasawa, N., and Yasuda, R. (2016). High-throughput, high-resolution mapping of protein localization in mammalian brain by *in vivo* genome editing. *Cell* 165, 1803–1817. doi: 10.1016/j.cell.2016.04.044

Moeyaert, B., Holt, G., Madangopal, R., Perez-Alvarez, A., Fearey, B. C., Trojanowski, N. F., et al. (2018). Improved methods for marking active neuron populations. *Nat. Commun.* 9:4440. doi: 10.1038/s41467-018-06935-2

Mosca, T. J., Luginbuhl, D. J., Wang, I. E., and Luo, L. (2017). Presynaptic LRP4 promotes synapse number and function of excitatory CNS neurons. *eLife* 6:e27347. doi: 10.7554/eLife.27347

Motta, A., Berning, M., Boergens, K. M., Staffler, B., Beining, M., Loomba, S., et al. (2019). Dense connectomic reconstruction in layer 4 of the somatosensory cortex. *Science* 366:eaay3134. doi: 10.1126/science.aay3134

Murakami, T. C., Mano, T., Saikawa, S., Horiguchi, S. A., Shigeta, D., Baba, K., et al. (2018). A three-dimensional single-cell-resolution whole-brain atlas using CUBIC-X expansion microscopy and tissue clearing. *Nat. Neurosci.* 21, 625–637. doi: 10.1038/s41593-018-0109-1

Niell, C. M., Meyer, M. P., and Smith, S. J. (2004). in vivo imaging of synapse formation on a growing dendritic arbor. *Nat. Neurosci.* 7, 254–260. doi: 10.1038/nn1191

Nishiyama, J., Mikuni, T., and Yasuda, R. (2017). Virus-mediated genome editing *via* homology-directed repair in mitotic and postmitotic cells in mammalian brain. *Neuron* 96, 755–768.e5. doi: 10.1016/j.neuron.2017.10.004

Oh, W. C., Lutzu, S., Castillo, P. E., and Kwon, H.-B. (2016). *De novo* synaptogenesis induced by GABA in the developing mouse cortex. *Science* 353, 1037–1040. doi: 10.1126/science.aaf5206

Ohyama, T., Schneider-Mizell, C. M., Fetter, R. D., Aleman, J. V., Franconville, R., Rivera-Alba, M., et al. (2015). A multilevel multimodal circuit enhances action selection in *Drosophila*. *Nature* 520, 633–639. doi: 10.1038/nature14297

O'Rourke, N. A., Weiler, N. C., Micheva, K. D., and Smith, S. J. (2012). Deep molecular diversity of mammalian synapses: why it matters and how to measure it. *Nat. Rev. Neurosci.* 13, 365–379. doi: 10.1038/nrn3170

Palay, S. L. (1956). Synapses in the central nervous system. *J. Biophys. Biochem. Cytol.* 2, 193–202. doi: 10.1083/jcb.2.4.193

Palay, S. L., and Palade, G. E. (1955). The fine structure of neurons. *J. Biophys. Biochem. Cytol.* 1, 69–88. doi: 10.1083/jcb.1.1.69

Park, C. E., Cho, Y., Cho, I., Jung, H., Kim, B., Shin, J. H., et al. (2020). Super-resolution three-dimensional imaging of actin filaments in cultured cells and the brain *via* expansion microscopy. *ACS Nano* 14, 14999–15010. doi: 10.1021/acsnano.0c04915

Park, H.-E., Choi, D., Park, J. S., Sim, C., Park, S., Kang, S., et al. (2019). Scalable and isotropic expansion of tissues with simply tunable expansion ratio. *Adv. Sci. (Weinh)* 6:1901673. doi: 10.1002/advs.201901673

Park, J., Khan, S., Yun, D. H., Ku, T., Villa, K. L., Lee, J. E., et al (2021). Epitope-preserving magnified analysis of proteome (eMAP). *Sci. Adv.* 7: eabf6589. doi: 10.1126/sciadv.abf6589.

Parra-Damas, A., and Saura, C. A. (2020). Tissue clearing and expansion methods for imaging brain pathology in neurodegeneration: from circuits to synapses and beyond. *Front. Neurosci.* 14:914. doi: 10.3389/fnins.2020.00914

Payne, A. C., Chiang, Z. D., Reginato, P. L., Mangiameli, S. M., Murray, E. M., Yao, C.-C., et al. (2021). in situ genome sequencing resolves DNA sequence and structure in intact biological samples. *Science* 371:eaay3446. doi: 10.1126/science.aay3446

Pereda, A. E. (2014). Electrical synapses and their functional interactions with chemical synapses. *Nat. Rev. Neurosci.* 15, 250–263. doi: 10.1038/nrn3708

Perez-Alvarez, A., Fearey, B. C., O'Toole, R. J., Yang, W., Arganda-Carreras, I., Lamothe-Molina, P. J., et al. (2020). Freeze-frame imaging of synaptic activity using SynTagMA. *Nat. Commun.* 11:2464. doi: 10.1038/s41467-020-16315-4

Philbrook, A., Ramachandran, S., Lambert, C. M., Oliver, D., Florman, J., Alkema, M. J., et al. (2018). Neurexin directs partner-specific synaptic connectivity in *C. elegans*. *eLife* 7:e35692. doi: 10.7554/eLife.35692

Prange, O., Wong, T. P., Gerrow, K., Wang, Y. T., and El-Husseini, A. (2004). A balance between excitatory and inhibitory synapses is controlled by PSD-95 and neuroligin. *Proc. Natl. Acad. Sci. U S A* 101, 13915–13920. doi: 10.1073/pnas.0405939101

Ramón y Cajal, S. (1852–1934) A. du texte (1909). Histologie du système nerveux de l'homme et des vertébrés. Cervelet, cerveau moyen, rétine, couche optique, corps strié, écorce cérébrale générale et régionale, grand sympathique / par S. Ramon Cajal. Available online at: https://gallica.bnf.fr/ark:/12148/bpt6k6213192g. Accessed February 25, 2021.

Robertson, J. D. (1953). Ultrastructure of two invertebrate synapses. *Proc. Soc. Exp. Biol. Med.* 82, 219–223. doi: 10.3181/00379727-82-20071

Ryan, K., Lu, Z., and Meinertzhagen, I. A. (2016). The CNS connectome of a tadpole larva of Ciona intestinalis (L.) highlights sidedness in the brain of a chordate sibling. *eLife* 5:e16962. doi: 10.7554/eLife.16962

Sahl, S. J., Hell, S. W., and Jakobs, S. (2017). Fluorescence nanoscopy in cell biology. *Nat. Rev. Mol. Cell Biol.* 18, 685–701. doi: 10.1038/nrm.2017.71

Sakaguchi, R., Leiwe, M. N., and Imai, T. (2018). Bright multicolor labeling of neuronal circuits with fluorescent proteins and chemical tags. *eLife* 7:e40350. doi: 10.7554/eLife.40350

Sarkar, D., Kang, J., Wassie, A. T., Schroeder, M. E., Peng, Z., Tarr, T. B., et al. (2020). Expansion revealing: decrowding proteins to unmask invisible brain nanostructures. *bioRxiv* [Preprint]. doi: 10.1101/2020.08.29.273540.

Scaplen, K. M., Talay, M., Fisher, J. D., Cohn, R., Sorkaç, A., Aso, Y., et al. (2021). Transsynaptic mapping of *Drosophila* mushroom body output neurons. *eLife* 10:e63379. doi: 10.7554/eLife.63379

Scheffer, L. K., Xu, C. S., Januszewski, M., Lu, Z., Takemura, S., Hayworth, K. J., et al. (2020). A connectome and analysis of the adult *Drosophila* central brain. *eLife* 9:e57443. doi: 10.7554/eLife.57443

Schermelleh, L., Ferrand, A., Huser, T., Eggeling, C., Sauer, M., Biehlmaier, O., et al. (2019). Super-resolution microscopy demystified. *Nat. Cell Biol.* 21, 72–84. doi: 10.1038/s41556-018-0251-8

Schneider-Mizell, C. M., Bodor, A. L., Collman, F., Brittain, D., Bleckert, A. A., Dorkenwald, S., et al. (2020). Chandelier cell anatomy and function reveal a variably distributed but common signal. *bioRxiv* [Preprint]. doi: 10.1101/2020.03.31.018952

Seiriki, K., Kasai, A., Hashimoto, T., Schulze, W., Niu, M., Yamaguchi, S., et al. (2017). High-speed and scalable whole-brain imaging in rodents and primates. *Neuron* 94, 1085–1100.e6. doi: 10.1016/j.neuron.2017.05.017

Seo, J., Sim, Y., Kim, J., Kim, H., Cho, I., Yoon, Y.-G., et al. (2021). PICASSO: ultra-multiplexed fluorescence imaging of biomolecules through single-round imaging and blind source unmixing. *bioRxiv* [Preprint]. doi: 10.1101/2021.01.27.428247

Shapson-Coe, A., Januszewski, M., Berger, D. R., Pope, A., Wu, Y., Blakely, T., et al. (2021). A connectomic study of a petascale fragment of human cerebral cortex. *bioRxiv* [Preprint]. doi: 10.1101/2021.05.29.446289

Shearin, H. K., Quinn, C. D., Mackin, R. D., Macdonald, I. S., and Stowers, R. S. (2018). t-GRASP, a targeted GRASP for assessing neuronal connectivity. *J. Neurosci. Methods* 306, 94–102. doi: 10.1016/j.jneumeth.2018.05.014

Shen, F. Y., Harrington, M. M., Walker, L. A., Cheng, H. P. J., Boyden, E. S., and Cai, D. (2020). Light microscopy based approach for mapping connectivity with molecular specificity. *Nat. Commun.* 11:4632. doi: 10.1038/s41467-020-18422-8

Sheng, M., and Kim, E. (2011). The postsynaptic organization of synapses. *Cold Spring Harb. Perspect. Biol.* 3:a005678. doi: 10.1101/cshperspect.a005678

Shi, X., Li, Q., Dai, Z., Tran, A. A., Feng, S., Ramirez, A. D., et al. (2021). Label-retention expansion microscopy. *J. Cell Biol.* 220:e202105067. doi: 10.1083/jcb.202105067

Sim, J., Park, C. E., Cho, I., Min, K., Lee, J.-S., Chong, Y., et al. (2021). Whole-ExM: expansion microscopy imaging of all anatomical structures of whole larval zebrafish. *bioRxiv* [Preprint]. doi: 10.1101/2021.05.18.443629

Son, J.-H., Keefe, M. D., Stevenson, T. J., Barrios, J. P., Anjewierden, S., Newton, J. B., et al. (2016). Transgenic FingRs for live mapping of synaptic dynamics in genetically-defined neurons. *Sci. Rep.* 6:18734. doi: 10.1038/srep18734

Song, J. H., Lucaci, D., Calangiu, I., Brown, M. T. C., Park, J. S., Kim, J., et al. (2018). Combining mGRASP and optogenetics enables high-resolution functional mapping of descending cortical projections. *Cell Rep.* 24, 1071–1080. doi: 10.1016/j.celrep.2018.06.076

Subramanian, J., Michel, K., Benoit, M., and Nedivi, E. (2019). CPG15/neuritin mimics experience in selecting excitatory synapses for stabilization by facilitating PSD95 recruitment. *Cell Rep.* 28, 1584–1595.e5. doi: 10.1016/j.celrep.2019.07.012

Suzuki, K., Tsunekawa, Y., Hernandez-Benitez, R., Wu, J., Zhu, J., Kim, E. J., et al. (2016). *In vivo* genome editing via CRISPR/Cas9 mediated homology-independent targeted integration. *Nature* 540, 144–149. doi: 10.1038/nature20565

Taft, C. E., and Turrigiano, G. G. (2014). PSD-95 promotes the stabilization of young synaptic contacts. *Philos. Trans. R. Soc. B Biol. Sci.* 369:20130134. doi: 10.1098/rstb.2013.0134

Talay, M., Richman, E. B., Snell, N. J., Hartmann, G. G., Fisher, J. D., Sorkaç, A., et al. (2017). Transsynaptic mapping of second-order taste neurons in flies by trans-tango. *Neuron* 96, 783–795.e4. doi: 10.1016/j.neuron.2017.10.011

Tang, Y., Nyengaard, J. R., De Groot, D. M., and Gundersen, H. J. (2001). Total regional and global number of synapses in the human brain neocortex. *Synapse* 41, 258–273. doi: 10.1002/syn.1083

Tervo, D. G. R., Hwang, B.-Y., Viswanathan, S., Gaj, T., Lavzin, M., Ritola, K. D., et al. (2016). A designer AAV variant permits efficient retrograde access to projection neurons. *Neuron* 92, 372–382. doi: 10.1016/j.neuron.2016.09.021

Tillberg, P. W., Chen, F., Piatkevich, K. D., Zhao, Y., Yu, C.-C. J., English, B. P., et al (2016). Protein-retention expansion microscopy of cells and tissues labeled using standard fluorescent proteins and antibodies. *Nat. Biotechnol.* 34, 987–992. doi: 10.1038/nbt.3625

Truckenbrodt, S., Maidorn, M., Crzan, D., Wildhagen, H., Kabatas, S., and Rizzoli, S. O. (2018). X10 expansion microscopy enables 25-nm resolution on conventional microscopes. *EMBO Rep.* 19:e45836. doi: 10.15252/embr.201845836

Turner, N. L., Macrina, T., Bae, J. A., Yang, R., Wilson, A. M., Schneider-Mizell, C., et al. (2020). Multiscale and multimodal reconstruction of cortical structure and function. *bioRxiv* [Preprint]. doi: 10.1101/2020.10.14.338681

Tyagarajan, S. K., and Fritschy, J.-M. (2014). Gephyrin: a master regulator of neuronal function. *Nat. Rev. Neurosci.* 15, 141–156. doi: 10.1038/nrn3670

Uezu, A., Kanak, D. J., Bradshaw, T. W. A., Soderblom, E. J., Catavero, C. M., Burette, A. C., et al. (2016). Identification of an elaborate complex mediating postsynaptic inhibition. *Science* 353, 1123–1129. doi: 10.1126/science.aag0821

Ugolini, G. (2011). "Chapter 10 - Rabies Virus as a Transneuronal Tracer of Neuronal Connections," in *Advances in Virus Research Research Advances in Rabies*, ed A. C. Jackson (New York: Academic Press), 165–202.

Verasztó, C., Jasek, S., Gühmann, M., Shahidi, R., Ueda, N., Beard, J. D., et al. (2020). Whole-animal connectome and cell-type complement of the three-segmented Platynereis dumerilii larva. *bioRxiv* [Preprint]. doi: 10.1101/2020.08.21.260984

Villa, K. L., Berry, K. P., Subramanian, J., Cha, J. W., Oh, W. C., Kwon, H.-B., et al. (2016). Inhibitory synapses are repeatedly assembled and removed at persistent sites *in vivo*. *Neuron* 89, 756–769. doi: 10.1016/j.neuron.2016.01.010

Viswanathan, S., Williams, M. E., Bloss, E. B., Stasevich, T. J., Speer, C. M., Nern, A., et al. (2015). High-performance probes for light and electron microscopy. *Nat. Methods* 12, 568–576. doi: 10.1038/nmeth.3365

Vlachos, A., Reddy-Alla, S., Papadopoulos, T., Deller, T., and Betz, H. (2013). Homeostatic regulation of gephyrin scaffolds and synaptic strength at mature hippocampal gabaergic postsynapses†. *Cereb. Cortex* 23, 2700–2711. doi: 10.1093/cercor/bhs260

Wang, Y., Hu, Z., Ju, P., Yin, S., Wang, F., Pan, O., et al. (2018). Viral vectors as a novel tool for clinical and neuropsychiatric research applications. *Gen. Psychiatry* 31:e000015. doi: 10.1136/gpsych-2018-000015

Wassie, A. T., Zhao, Y., and Boyden, E. S. (2019). Expansion microscopy: principles and uses in biological research. *Nat. Methods* 16, 33–41. doi: 10.1038/s41592-018-0219-4

Watanabe, A. (1958). The interaction of electrical activity among neurons of lobster cardiac ganglion. *Jpn. J. Physiol.* 8, 305–318. doi: 10.2170/jjphysiol.8.305

Weissman, T. A., and Pan, Y. A. (2015). Brainbow: new resources and emerging biological applications for multicolor genetic labeling and analysis. *Genetics* 199, 293–306. doi: 10.1534/genetics.114.172510

Wells, W. A. (2005). The discovery of synaptic vesicles. *J. Cell Biol.* 168, 12–13. doi: 10.1083/jcb1681fta2

White, J. G., Southgate, E., Thomson, J. N., and Brenner, S. (1986). The structure of the nervous system of the nematode *Caenorhabditis elegans*. *Philos. Trans. R. Soc. Lond. B Biol. Sci.* 314, 1–340. doi: 10.1098/rstb.1986.0056

Wiedenmann, B., and Franke, W. W. (1985). Identification and localization of synaptophysin, an integral membrane glycoprotein of Mr 38,000 characteristic of presynaptic vesicles. *Cell* 41, 1017–1028. doi: 10.1016/s0092-8674(85)80082-9

Willems, J., Jong, A. P. H. D., Scheefhals, N., Mertens, E., Catsburg, L. A. E., Poorthuis, R. B., et al. (2020). ORANGE: a CRISPR/Cas9-based genome editing toolbox for epitope tagging of endogenous proteins in neurons. *PLoS Biol.* 18:e3000665. doi: 10.1371/journal.pbio.3000665

Winnubst, J., Bas, E., Ferreira, T. A., Wu, Z., Economo, M. N., Edson, P., et al. (2019). Reconstruction of 1,000 projection neurons reveals new cell types and organization of long-range connectivity in the mouse brain. *Cell* 179, 268–281.e13. doi: 10.1016/j.cell.2019.07.042

Witvliet, D., Mulcahy, B., Mitchell, J. K., Meirovitch, Y., Berger, D. R., Wu, Y., et al. (2020). Connectomes across development reveal principles of brain maturation in *C. elegans*. *Nature* 596, 257–261. doi: 10.1038/s41586-021-03778-8

Xu, C. S., Hayworth, K. J., Lu, Z., Grob, P., Hassan, A. M., García-Cerdán, J. G., et al. (2017). Enhanced FIB-SEM systems for large-volume 3D imaging. *eLife* 6:e25916. doi: 10.7554/eLife.25916

Xu, H., Tong, Z., Ye, Q., Sun, T., Hong, Z., Zhang, L., et al. (2019). Molecular organization of mammalian meiotic chromosome axis revealed by expansion STORM microscopy. *Proc. Natl. Acad. Sci. U S A* 116, 18423–18428. doi: 10.1073/pnas.1902440116

Yeh, E., Kawano, T., Weimer, R. M., Bessereau, J.-L., and Zhen, M. (2005). Identification of genes involved in synaptogenesis using a fluorescent active zone marker in *Caenorhabditis elegans*. *J. Neurosci.* 25, 3833–3841. doi: 10.1523/JNEUROSCI.4978-04.2005

Yu, C.-C. J., Barry, N. C., Wassie, A. T., Sinha, A., Bhattacharya, A., Asano, S., et al. (2020). Expansion microscopy of *C. elegans*. *eLife* 9:e46249. doi: 10.7554/eLife.46249

Zhao, Y., Bucur, O., Irshad, H., Chen, F., Weins, A., Stancu, A. L., et al. (2017). Nanoscale imaging of clinical specimens using pathology-optimized expansion microscopy. *Nat. Biotechnol.* 35, 757–764. doi: 10.1038/nbt.3892

Zhong, Q., Li, A., Jin, R., Zhang, D., Li, X., Jia, X., et al. (2021). High-definition imaging using line-illumination modulation microscopy. *Nat. Methods* 18, 309–315. doi: 10.1038/s41592-021-01074-x

Zwettler, F. U., Reinhard, S., Gambarotto, D., Bell, T. D. M., Hamel, V., Guichard, P., et al. (2020). Molecular resolution imaging by post-labeling expansion single-molecule localization microscopy (Ex-SMLM). *Nat. Commun.* 11:3388. doi: 10.1038/s41467-020-17086-8

Conflict of Interest: The authors declare that the research was conducted in the absence of any commercial or financial relationships that could be construed as a potential conflict of interest.

frontiers
in Synaptic Neuroscience

PERSPECTIVE
published: 07 February 2022
doi: 10.3389/fnsyn.2021.798267

Quantitative Imaging With DNA-PAINT for Applications in Synaptic Neuroscience

Eduard M. Unterauer[1,2] *and Ralf Jungmann*[1,2]*

[1] *Max Planck Institute of Biochemistry, Martinsried, Germany,* [2] *Faculty of Physics and Center for Nanoscience, Ludwig Maximilian University, Munich, Germany*

Super-resolution (SR) microscopy techniques have been advancing the understanding of neuronal protein networks and interactions. Unraveling the arrangement of proteins with molecular resolution provided novel insights into neuron cytoskeleton structure and actin polymerization dynamics in synaptic spines. Recent improvements in quantitative SR imaging have been applied to synaptic protein clusters and with improved multiplexing technology, the interplay of multiple protein partners in synaptic active zones has been elucidated. While all SR techniques come with benefits and drawbacks, true molecular quantification is a major challenge with the most complex requirements for labeling reagents and careful experimental design. In this perspective, we provide an overview of quantitative SR multiplexing and discuss in greater detail the quantification and multiplexing capabilities of the SR technique DNA-PAINT. Using predictable binding kinetics of short oligonucleotides, DNA-PAINT provides two unique approaches to address multiplexed molecular quantification: qPAINT and Exchange-PAINT. With precise and accurate quantification and spectrally unlimited multiplexing, DNA-PAINT offers an attractive route to unravel complex protein interaction networks in neurons. Finally, while the SR community has been pushing technological advances from an imaging technique perspective, the development of universally available, small, efficient, and quantitative labels remains a major challenge in the field.

Keywords: DNA-PAINT, DNA nanotechnology, neuronal target, fluorescence microscopy, super-resolution microscopy

Edited by:
Thomas A. Blanpied,
University of Maryland, United States

Reviewed by:
Ai-Hui Tang,
University of Science and Technology of China, China
Irina Dudanova,
Max Planck Institute of Neurobiology (MPIN), Germany

****Correspondence:***
Ralf Jungmann
jungmann@biochem.mpg.de

Received: *19 October 2021*
Accepted: *21 December 2021*
Published: *07 February 2022*

Citation:
Unterauer EM and Jungmann R (2022) Quantitative Imaging With DNA-PAINT for Applications in Synaptic Neuroscience. Front. Synaptic Neurosci. 13:798267. doi: 10.3389/fnsyn.2021.798267

INTRODUCTION

In recent years, SR microscopy has been a rising technique to investigate complex biological systems and molecular mechanisms. With the availability of site-specific labeling and nanometer-scale resolutions, SR microscopy enables mapping of cellular components and single-cell heterogeneity with near molecular resolution. The investigation of neuronal tissue sections presents a unique challenge for imaging techniques. Signal transduction in this complex cellular network occurs in synaptic junctions, in which large networks of protein species are orchestrated in the space of just a few hundred nanometers. Signaling at synapses is mediated by pools of synaptic vesicles just 50 nm in size. However, they contain hundreds of surface proteins (Takamori et al., 2006).

Thus, these objects exhibit high molecular densities due to a large amount of protein copy numbers clustered in a relatively small area. To reliably identify key interactor proteins and place them into the context of larger structures, SR microscopy needs to facilitate accurate mapping of these protein networks and provide reliable molecule numbers for quantification. Both illumination-based SR techniques such as Structured illumination microscopy (SIM) (Gustafsson, 2005) or Stimulated Emission depletion microscopy (STED) (Hell and Wichmann, 1994) and localization-based SR techniques like Photoactivated-localization microscopy (PALM) (Betzig et al., 2006) or stochastic optical reconstruction microscopy (STORM) (Rust et al., 2006) have been used to study neuronal targets. The most prominent examples being the investigation of dendritic spine dynamics in living mice (Berning et al., 2012) by STED and the mapping of periodic Actin-Spectrin filaments in fixed mouse hippocampal neurons by STORM (Xu et al., 2012). While enabling unprecedented spatial resolution and quantification capabilities, SR techniques have advantages and disadvantages, with the obligation of the researcher to decide, which technique fulfills the right requirements for a given biological question under investigation. Here, we will discuss the possibilities and caveats of the localization-based SR technique DNA Points Accumulation in Nanoscale Topography (DNA-PAINT) (Jungmann et al., 2010) for quantitative and multiplexed investigation of neuronal targets.

SUPER-RESOLUTION MICROSCOPY WITH DNA-PAINT

All localization-based SR techniques aim to separate the detection of individual fluorescent molecules in space and time. The achievable localization precision in these approaches is ultimately limited by the total amount of photons and exhibits $1/\sqrt{n_{photons}}$ scaling, with $n_{photons}$ being the number of detected photons that can be detected from a single blinking or binding (Thompson et al., 2002). In contrast to PALM or STORM, where fluorescent proteins or organic dyes with photoswitching capabilities are employed, PAINT uses a different approach (Sharonov and Hochstrasser, 2006). Here, freely diffusing dyes or dye-labeled ligands that transiently interact with their targets are used to achieve the necessary molecular "blinking." In the case of DNA-PAINT, these ligands are small 6–10 nucleotides (nt) long single-stranded (ss) DNA strands, called imager strands, which bind to their complementary ssDNA strands called docking strands on a target. In comparison to other SR techniques, DNA-PAINTs advantages are the high sub-5-nm spatial resolution and—due to the technically infinite pool of imager sequences—negligible photobleaching (Dai et al., 2016). Additionally, as "blinking" is decoupled from the photophysical dye properties, DNA-barcoded targets allow for quantification and multiplexing with qPAINT (Jungmann et al., 2016) and Exchange-PAINT (Jungmann et al., 2014). However, the most severe drawbacks of DNA-PAINT have traditionally been long image acquisition times and the need for selective plane illumination due to the non-fluorogenic nature of the imager strands in solution.

QUANTITATIVE DNA-PAINT (qPAINT) FOR SYNAPTIC TARGETS

Understanding the molecular mechanisms underlying complex neuronal structures and signaling pathways requires investigations on the level of single molecules. Only when single emitters can be resolved, a complete picture of the spatial arrangement and quantitative numbers can be obtained for each relevant protein target. Out of all possible targets in neurons, the synapse presents itself as a particularly interesting entity for quantitative SR studies. The delicate machinery of signal transduction is orchestrated in a space of only a few hundreds of nanometers and varies among different types of synapses, such as inhibitory or excitatory. Furthermore, the spatial arrangement and composition of proteins in the synapses as well as its structure and plasticity is changing in important neurodegenerative and autoimmune diseases (Ladepeche et al., 2018; Jackson et al., 2019).

Recent studies have used nanoscopy methods to characterize 110 different proteins (albite in different samples) in dendritic spines and obtained ensemble numbers for each protein species (Helm et al., 2021). Combining STED nanoscopy and electron microscopy, Helm et al. (2021) have visualized protein distributions of stubby and mushroom-like dendritic spines (**Figure 1A**). They were able to show that while both types contain on average similar protein numbers and topology, stubby spines express a lower number of trafficking-related proteins in correlation to the postsynaptic density mass, indicating a lower dynamic response of those spines. This corresponds well to the general hypothesis that stubby spines represent a rather immature developmental state, while mushroom-like spines compartmentalize receptors and proteins for signal transduction cascades. (Harris et al., 1992; Berry and Nedivi, 2017) Apart from using electron microscopy as a reference, more studies use antibody titration measurements for comparison and validation of the super-resolved data. Siddig et al. (2020) determined the distribution of metabotropic glutamate receptor 4 (mGluR4) in cerebellar active zones (**Figure 1B**) and analyzed their colocalization with Cav2.1 calcium channel and the presynaptic scaffold marker Bassoon. Using direct STORM (dSTORM) super-resolution microscopy combined with cluster analysis, Siddig et al. (2020) were able to show that all three proteins in fact do colocalize. This colocalization of mGluR4 nanodomains in the active zone with Cav2.1 channels suggests that mGluR4 might regulate neurotransmitter release by influencing Calcium influx. The mGluR4 copy numbers per active zone were determined to be about 35 and the data was validated by using a ramp of different antibody concentrations and fitting the resulting to a logistic function. While the assignment of molecule numbers with sparse protein targets is a relatively straight forward, this becomes exceedingly more complex in more crowded environments of highly expressed proteins.

Quantitative counting approaches using e.g., STORM or PALM as imaging modality suffer from potential over- or undercounting due to unpredictable and hard-to-calibrate photophysics of photoswitchable proteins and organic dyes,

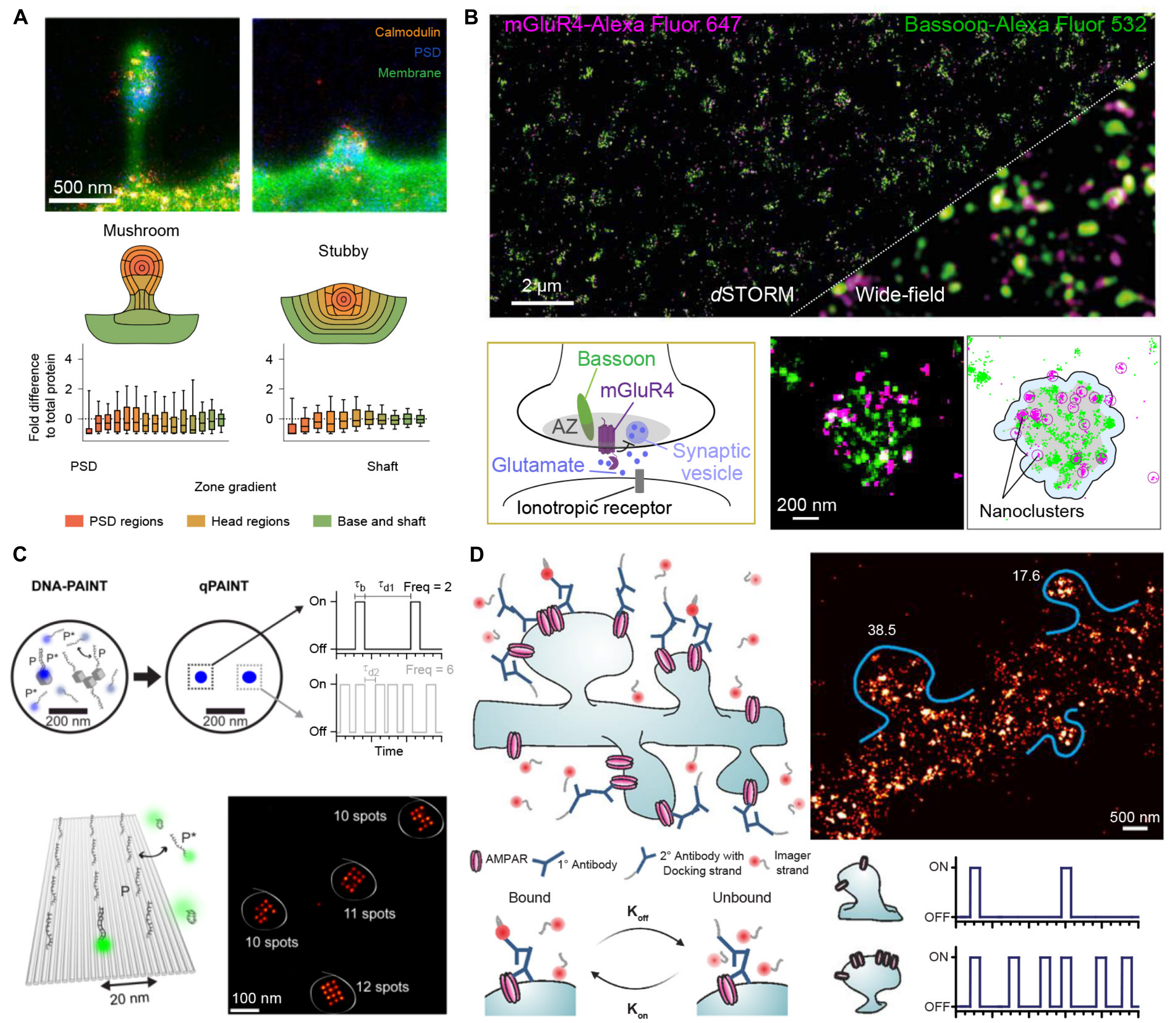

FIGURE 1 | Quantitative SR imaging of neuronal targets. **(A)** STED nanoscopy for quantification of Calmodulin protein copy numbers in dendritic spines. The top shows examples for mushroom-like and stubby dendritic spines visualized by the membrane stain DiO in green, the Postsynaptic density by Homer1 in blue and the protein of interest, Calmodulin, in orange. The bottom shows the protein enrichment separated into regions of the dendritic spines, in total $n = 150$ mushroom-like and $n = 140$ stubby spines were analyzed showing an overall similar distribution for both spine types. Adapted with permission (Helm et al., 2021). **(B)** *d*STORM microscopy for determining mGluR4 clusters at synaptic active zones. Top shows a comparison of a two-color *d*STORM image of mGluR4 (Purple) and the presynaptic active zone marker Bassoon (green) to the respective diffraction-limited image. Bottom shows a schematic of the mGluR4 located at the presynaptic active zone (AZ) and DBSCAN cluster analysis of Bassoon and mGluR4 for determining the area (gray) of the AZ and mGluR4 nanoclusters. Adapted with permission (Siddig et al., 2020). **(C)** qPAINT implementation. In DNA-PAINT, fluorescently labeled "imager" strands (P*) transiently bind from solution to complementary "docking" strands (P) attached to a target. Intensity vs. time traces show characteristic fluorescence on- and off-times (τ_b and τ_d, respectively). qPAINT uses the predictable blinking kinetics to deduct absolute molecule numbers. Top shows two exemplary regions imaged by DNA-PAINT and evaluated by qPAINT. From a single emitter (single gray cube) the imager-specific kinetics, the bright time and dark time can be extracted. Afterward this extracted dark time can be used to calculate the number of single emitters in a more crowded region where molecular resolution cannot be achieved (three cubes). Bottom shows the respective results in an exemplary 12 binding site DNA origami surface, where qPAINT correctly predicts the amount of available binding sites per structure. Adapted with permission (Jungmann et al., 2016). **(D)** Quantification of AMPA receptor complexes by qPAINT on GluA2 receptors. Top left shows an illustration of DNA-PAINT labeling and imaging of dendritic spines via primary and secondary antibodies. Bottom: By analyzing the kinetic traces of subregions of the dendrites, molecular counting can be achieved by comparing the average dark time for the regions to single binding sites for calibration. Top right shows the qPAINT results for two dendritic spines. Adapted with permission (Boger et al., 2019).

leading to downstream quantification artifacts. DNA-PAINT on the other hand offers a distinct way to deduct integer numbers of molecules from analyzing blinking kinetics of transient DNA hybridization, which enables precise and accurate counting, as the blinking fingerprint is largely independent from photophysical properties of dye molecules. This approach is called Qpaint (Jungmann et al., 2016) and uses the predictable second-order association kinetics of imager strands to their docking strands to obtain quantitative molecule numbers (**Figure 1C**). In brief, first the influx rate $\xi = k_{on} \cdot c_i$ for imager strands to targets is calibrated with a sample containing a known number of binding sites. Here, k_{on} represents the association rate for the hybridization of imager to docking strands and c_i the concentration of imager strands. In a second step, the influx rate in an analysis area with unknown quantity of binding sites (and thus target molecules) is determined. As ξ scales linearly with the number of target strands, integer numbers of molecules can be determined with qPAINT. Jungmann et al. (2016) first established this approach using DNA origami nanostructures (**Figure 1C**). As an origami can be designed with a prescribed number of docking strands, it can serve as an exquisite ground truth for developing and benchmarking new single-molecule approaches, before applying the tried and tested technique in more complex *in situ* environments (e.g., inside a cell). Optimizing acquisition conditions yielded a high qPAINT detection accuracy and precision. As a next step, the method was applied to count Bruchpilot (Brp) proteins in drosophila neuromuscular junction synaptic active zones. The individual Brp protein clusters were too dense to spatially resolve single binding sites. However, qPAINT analysis could determine ∼142 Brp molecules per cluster, in good agreement with numbers reported from an earlier study (Ehmann et al., 2014).

In a more recent study, Boger et al. (2019) were able to determine the average copy numbers of GluA2 molecules, a subpart of the AMPA-type glutamate receptor complex (AMPAR), in mouse hippocampal dendritic spines (**Figure 1D**). To optimize qPAINT for their system, the authors first performed *in silico* and *in vitro* optimizations using DNA origami structures mimicking the expected distribution and numbers of GluA2 molecules. Their simulated data yielded a detection efficiency of 84%, analyzing clusters with 40 and 15 nm docking site spacing. Their subsequent qPAINT application in dendritic spines yielded an average of 23 molecules per spine, again in good agreement with earlier studies (Nair et al., 2013). With the rise of quantitative super-resolution microscopy, it is now possible to obtain precise protein number distributions and with the help of advanced cluster analysis approaches, infer downstream mechanistic information.

Compared to more incumbent single-molecule localization microscopy counting approaches, qPAINT offers a unique advantage of immunity to under- and overcounting biases, thanks to its reliance on the predictable binding kinetics of DNA molecules to their complements and the largely photobleaching free image acquisition process. Furthermore, as qPAINT (similar to DNA-PAINT) decouples the apparent blinking from the photophysical properties of dyes, it is easily multiplexable (Jungmann et al., 2016). One potential caveat, however, might arise by inaccuracies due to altered binding kinetics in dense cellular environments such as the cell nucleus, but recent calibration-free advances could alleviate this (Stein et al., 2021).

More generally, it is important to consider that although on a conceptual level (and for *in vitro* experiments using e.g., DNA origami structures for quantification) accuracy and precision of qPAINT is excellent, this unfortunately does not hold true for the case of most cellular applications. A critical performance-determining factor in cellular applications is the efficiency and specificity of the employed labeling probes used to tag target molecules of interest with a fluorophore or DNA strand. This efficiency and specificity crucially influence the final accuracy of the imaging and counting approach for e.g., visualization and quantification of proteins in cells.

The main challenges for quantitative immunolabeling are twofold: Can we assume that the location of the emitter is a truthful representation of the target position? And second, is the number of emitters a good proxy for the true number of targets?

The two main determining factors regarding those two issues are: *(1) The size of the labeling probe*. The smaller the probe, the lower the so-called "linkage" error, which in turn leads to a more accurate representation of the true target position. *(2) The labeling stoichiometry between labeling probe and target*. Ideally, one would aim for a 1:1 labeling stoichiometry of probe to target for the most accurate and precise quantification.

The most common approach for immunolabeling are species- and host-dependent pairs of primary and secondary antibodies. While well established and available for many targets, this labeling approach unfortunately results in a relatively large probe sandwich and thus linkage error (approx. 20–25 nm) rendering not ideal for super-resolution microscopy (Tang et al., 2016; Moore and Legant, 2018; Ganji et al., 2021). Furthermore, multiple secondary antibodies (carrying potentially more than one dye or DNA strand) make precise and accurate quantification difficult. While this "amplification" effect of a target signal (due to linking many primary amines or thiol groups of antibodies to dyes or DNA) is in fact advantageous for increased signal-to-background in e.g., confocal microscopy applications, it is not ideal for absolutely quantitative single-molecule studies. However, while not enabling highest counting precision, good counting accuracy can still be achieved when single, spatially separated targets are used for calibration.

To improve labeling stoichiometry and probe size while still maintaining advantages of primary antibodies (e.g., widespread availability), labeling with secondary nanobodies has recently been introduced. Secondary nanobodies are designed to carry only a single C-terminal Cysteine for dye or DNA coupling and thus allow for a much-improved precision in counting (Pleiner et al., 2015). Additionally, being only 3 nm in size, these small secondary labeling probes significantly decrease the linkage error and show improved labeling efficiency. Finally, primary antibodies can be conjugated directly with dyes or DNA molecules, however, with potentially adverse side-effects such as reduced target binding affinity when non-site-specific labeling approaches are chosen. However, if carefully optimized, direct conjugation of primary antibodies not only "saves" the step of secondary antibody or nanobody incubation, but—more importantly—it prevents species-dependent crosstalk of antibodies in multiplexing applications.

While these labeling approaches discussed above are most common to date, substantial progress has been made in the quantitative and efficient labeling of a handful of important targets, which we will discuss later.

IMPLEMENTATION OF QUANTITATIVE SUPER-RESOLUTION MULTIPLEXING

Most quantitative SR investigations of proteins in neurons include one or several rounds of multiplexing with diffraction-limited reference targets, most prominently PSD95 or Synapsin, for identification of dendritic spines or synapses, and MAP2 for mapping the neuronal geometry. For SR quantification of multiple protein targets, spectrally distinct dyes are usually employed. However, only few optimized dye combinations are available (Dempsey et al., 2011). While this approach is relatively straightforward, the multiplexing capacity is limited by the spectral overlap of dyes. Furthermore, since many dyes are not suited for certain super-resolution approaches (Dempsey et al., 2011), a common approach to investigate multiple targets is to use one wavelength as reference and map the target localizations relative to this reference (Agasti et al., 2017). This approach has advantages and disadvantages: Imaging one important target with super-resolution in each sample allows for optimized staining and fixation conditions tailored to this specific target. Also examining one sample at a time avoids complex experimental designs for multiplexed immunostaining or automated liquid handling at the microscope.

On the other hand, although the relative distribution of targets toward a reference can yield average protein target distributions, the characteristics of single cell diversity are lost. Ensemble data cannot evaluate true colocalization nor precisely dissect multiprotein clusters or complex structures. To allow super-resolved multiplexing in the same sample, most approaches use sequential staining and imaging techniques. Sequential staining allows for spectrally unlimited multiplexing by the removal of a probe signal post image acquisition and re-staining of the sample with the next target probe. Klevanski et al. (2020) implemented this approach in STORM and called it maS^{3}TORM (**Figure 2B**). Using this strategy, the authors were able to multiplex 16 targets in the calyx of Held synapse (Klevanski et al., 2020). Although this sequential approach enables unlimited multiplexing, acquisition time increases substantially, as each antibody is incubated sequentially, which can take several hours or more per target. Also, the removal of the probe signal requires harsh treatments with SDS, generally followed by photobleaching reducing the sample quality with increasing multiplexing rounds.

DNA-PAINT offers an attractive, complementary, and relatively intuitive way to achieve spectrally unlimited super-resolution multiplexing by using different imager-docking handle pairs for imaging the individual targets. In this approach, which is called Exchange-PAINT (Jungmann et al., 2014), each protein target is labeled by an antibody with a unique docking sequence. For the multiplexing workflow, first only the transiently binding imager sequence to the first docking strand is flushed in and a super-resolution image is acquired. After this first round, the solution is washed out and the imager for the next target docking strand is incubated. The exchange of imager strands from one target to the next only takes a few minutes. In a first implementation of Exchange-PAINT to primary neurons, Wang et al. (2017) acquired super-resolved images of eight targets (**Figure 2C**). With colocalization analysis on the presynaptic active zone marker Bassoon, the inhibitory postsynaptic marker Gephyrin and the respective synaptic vesicle markers SynapsinI and VGAT, the authors were able to distinguish excitatory and inhibitory synapses and determine the geometric orientation of the synapses. The versatility of Exchange-PAINT has also been ported to STED and (d) STORM microscopy using slightly more stable imaging strands of about 12 nt, which label targets in a fixed manner during one image acquisition round. Originally demonstrated by Schueder et al. (2017) in HeLa cells, several groups have adopted the technique for diverse applications (Filius et al., 2021). A similar DNA exchange approach was also employed by Guo et al. (2019) The authors used DNA-labeled primary antibodies and DNA Exchange imaging to visualize the cross-sectional profiles of nine protein targets along the trans-synaptic axis (**Figure 2A**). In one recent study, the concept of Exchange-PAINT has also been applied to neuronal tissue sections. Using four-target Exchange-PAINT, Narayanasamy et al. (2021) were able to show the distribution of the pre- and postsynaptic scaffold proteins Bassoon and Homer1, as well as the glutamate vesicle marker VGlut1 in the calyx of Held synapse active zones with up to 25 nm resolution (**Figure 2D**).

While one of the major strengths of DNA-PAINT compared to other super-resolution techniques is the versatility in multiplexing by using programmable DNA barcodes, one substantial weakness of DNA-PAINT is its traditionally rather slow image acquisition process, practically limiting large-plex experiments. This limitation holds equally true for qPAINT, as precise counting is dependent on sufficient statistics to faithfully calculate averages from exponentially distributed times. Thus, generating sufficient statistics to truly approach the question of molecular organization in more than a few cells remains a challenge. To overcome this limitation, recent studies using secondary-structure-free sequences (Schueder et al., 2019) and sequence motif concatenation (Strauss and Jungmann, 2020) have improved DNA-PAINT's image acquisition speed by a factor of 100. While the labeling of multiple targets using species-independent probes is technically possible for most biological samples, another factor might play a crucial role when investigating dense protein clusters: labeling issues with relatively large antibodies due to molecular crowding in dense clusters. If we roughly assume a size of approx. 15 nm for primary antibodies and use this to label synaptic vesicles with 50 nm size, the problem is not only the linkage error to the true target position, but also the potential blocking of binding sites for antibodies to other targets, making subsequent imaging rounds inevitably more challenging than the first one (or even impossible). To address this problem, the labeling probes and imaging rounds for multiplexed imaging need to be designed carefully, going from more sparse protein targets to more abundant and using smaller and better labeling probes.

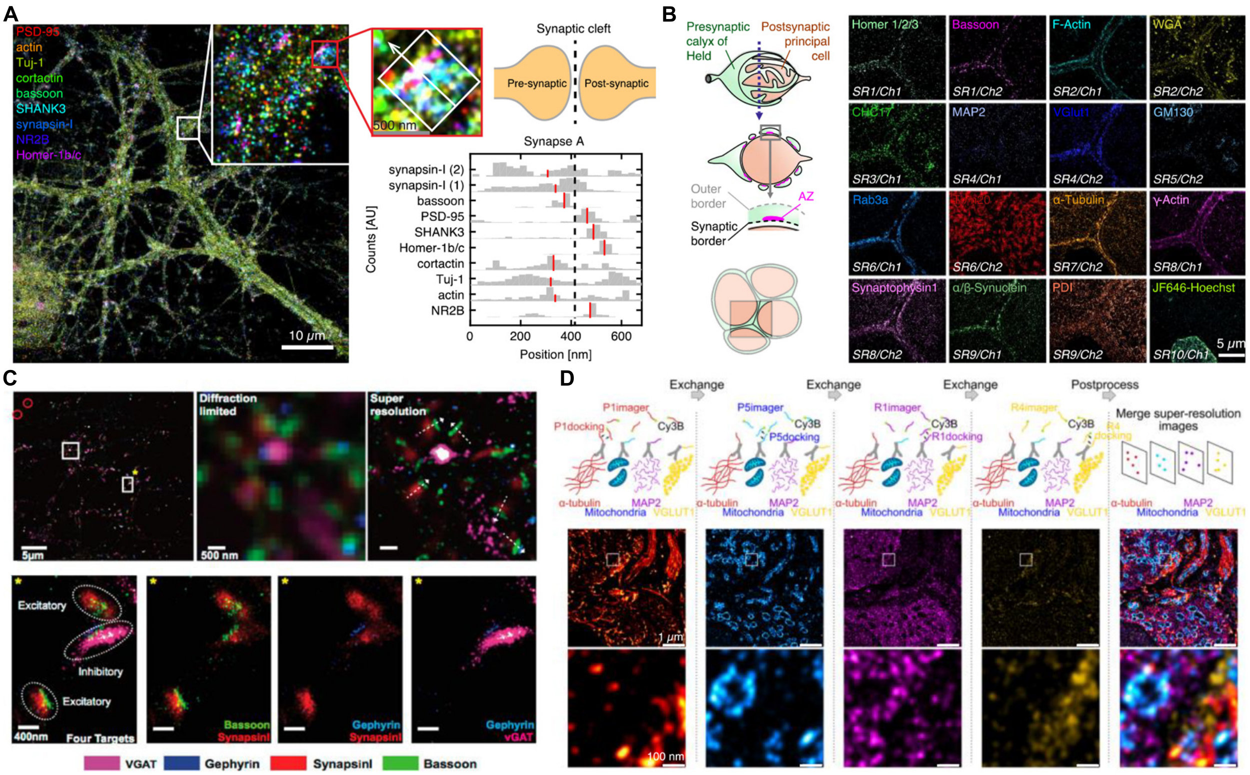

FIGURE 2 | Multiplexed SR imaging of neuronal targets. **(A)** Super-resolved DNA-PRISM multiplexing of synaptic targets. Left shows an overlayed display of nine targets imaged in neuronal cultures. The targets involve five synaptic proteins, three cytoskeleton proteins and the glutamate receptor subunit NR2B. The right shows cross-sectional profiles of the highlighted individual synapse with the median of the distributions indicated in red. Adapted with permission (Guo et al., 2019). **(B)** Automated maS^{3}TORM imaging of 16 targets in the giant calyx of Held synapse. The targets were subsequently imaged by a fully automated workflow in 10 rounds of staining utilizing one or two different fluorescent channels. Adapted with permission (Klevanski et al., 2020). **(C)** Exchange-PAINT imaging of four targets in primary neuron culture. Top shows the four-color overlay and zoom-ins with comparison to the diffraction-limited view. By determining the presynaptic and postsynaptic markers for inhibitory and excitatory synapses, the synaptic geometry can be visualized. Bottom shows a magnified view into single excitatory and inhibitory synapses, highlighting the side-by-side clustering of scaffold and marker proteins. Adapted with permission (Wang et al., 2017). **(D)** Exchange-PAINT imaging of four different targets in a calyx of Held tissue cryosection. Secondary Antibodies carrying four different docking handles were used for spectrally unlimited multiplexing. The middle panel shows the entire field of view with a zoom-in in the bottom panel and the overlayed image on the right side. Adapted with permission (Narayanasamy et al., 2021).

DISCUSSION AND OUTLOOK

The major bottleneck for almost all quantitative and multiplexed SR applications to date is the specific and efficient labeling of the target proteins. We have discussed some of the more common approaches to address the labeling challenge (Moore and Legant, 2018). While they are quite versatile, both the labeling efficiency and stoichiometry are far from perfect. If researchers only aim to address a small number of targets, several different approaches can be implemented. Among the most sophisticated labeling approaches are the use of primary nanobodies, which combine all the advantages of stochiometric labeling and small linkage error, but they are only available for very few targets. Recent developments have introduced slow off-rate modified aptamers (SOMAmers) for DNA-PAINT applications. These small (7–30 kDa) synthetic DNA probes can be functionalized with a suitable docking sequence for single-molecule quantification (Strauss et al., 2018). Aptamers have furthermore been employed in DNA-PAINT imaging to characterize size and morphology of Amyloid-beta aggregates in human cerebrospinal fluid (De et al., 2019). If aptamers or primary nanobodies are not available, a hybrid approach featuring high labeling efficiency, low linkage error and stoichiometric labeling can be applied. Here, the protein of interest is genetically tagged, either with a fluorescent protein marker (Ries et al., 2012) or a small peptide tag (Virant et al., 2018; Gotzke et al., 2019), for which direct nanobody binders are available. These nanobodies have been evaluated in numerous studies and the versatility of genetic tagging enables the investigation of a broad range of protein targets. Further examples of genetically encoded probes are self-labeling enzymes such as SNAP-tag (Keppler et al., 2003) and HaloTag (Los et al., 2008), which can be combined with DNA-PAINT to enable 1:1 labeling of single proteins (Schlichthaerle et al., 2019). Furthermore, the use of monomeric streptavidin could help to further alleviate the labeling issue (Chamma et al., 2016). Of course, the trade off in the case of genetically encoded probes is the limited amount of multiplexing and the expertise and complexity it takes to generate a genetically tagged cell line or animal.

Unfortunately, at this point there is not a single most ideal solution for universal labeling. Practically every experiment and target requires a careful probe design and optimization workflow. There will inevitably be a trade-off between achievable resolution, accuracy of molecular position and quantification, and possible targets to multiplex. While remarkable progress has been achieved in the past years, major concerted efforts are required to develop small, efficient, and quantitative labels for future applications. Ever more powerful quantitative SR approaches in the future could lay the groundwork in investigating heterogeneous morphology, plasticity, and protein compositions in synapses as well as vesicle pools. An accurate mapping of receptor nanodomains and cytoskeleton structure related to the synaptic scaffold might provide a deeper understanding of signaling cascades. Lastly, the quantitative comparison of interaction patterns of key proteins in healthy and diseased tissue could lead to a more sophisticated understanding of major neurodegenerative and autoimmune diseases.

AUTHOR CONTRIBUTIONS

EU and RJ wrote the perspective. Both authors contributed to the article and approved the submitted version.

FUNDING

EU and RJ acknowledge funding from the Human Frontier Science Program and the Max Planck Society.

REFERENCES

Agasti, S. S., Wang, Y., Schueder, F., Sukumar, A., Jungmann, R., and Yin, P. (2017). DNA-barcoded labeling probes for highly multiplexed Exchange-PAINT imaging. *Chem. Sci.* 8, 3080–3091. doi: 10.1039/c6sc05420j

Berning, S., Willig, K. I., Steffens, H., Dibaj, P., and Hell, S. W. (2012). Nanoscopy in a living mouse brain. *Science* 335:551. doi: 10.1126/science.1215369

Berry, K. P., and Nedivi, E. (2017). Spine Dynamics: are They All the Same? *Neuron* 96, 43–55. doi: 10.1016/j.neuron.2017.08.008

Betzig, E., Patterson, G. H., Sougrat, R., Lindwasser, O. W., Olenych, S., Bonifacino, J. S., et al. (2006). Imaging intracellular fluorescent proteins at nanometer resolution. *Science* 313, 1642–1645. doi: 10.1126/science.1127344

Boger, C., Hafner, A. S., Schlichtharle, T., Strauss, M. T., Malkusch, S., Endesfelder, U., et al. (2019). Super-resolution imaging and estimation of protein copy numbers at single synapses with DNA-point accumulation for imaging in nanoscale topography. *Neurophotonics* 6:035008. doi: 10.1117/1.NPh.6.3.035008

Chamma, I., Letellier, M., Butler, C., Tessier, B., Lim, K. H., Gauthereau, I., et al. (2016). Mapping the dynamics and nanoscale organization of synaptic adhesion proteins using monomeric streptavidin. *Nat. Commun.* 7:10773. doi: 10.1038/ncomms10773

Dai, M., Jungmann, R., and Yin, P. (2016). Optical imaging of individual biomolecules in densely packed clusters. *Nat. Nanotechnol.* 11, 798–807. doi: 10.1038/nnano.2016.95

De, S., Whiten, D. R., Ruggeri, F. S., Hughes, C., Rodrigues, M., Sideris, D. I., et al. (2019). Soluble aggregates present in cerebrospinal fluid change in size and mechanism of toxicity during Alzheimer's disease progression. *Acta Neuropathol. Commun.* 7:120. doi: 10.1186/s40478-019-0777-4

Dempsey, G. T., Vaughan, J. C., Chen, K. H., Bates, M., and Zhuang, X. (2011). Evaluation of fluorophores for optimal performance in localization-based super-resolution imaging. *Nat. Methods* 8, 1027–1036. doi: 10.1038/nmeth.1768

Ehmann, N., van de Linde, S., Alon, A., Ljaschenko, D., Keung, X. Z., Holm, T., et al. (2014). Quantitative super-resolution imaging of Bruchpilot distinguishes active zone states. *Nat. Commun.* 5:4650. doi: 10.1038/ncomms5650

Filius, M., Kim, S. H., Severins, I., and Joo, C. (2021). High-Resolution Single-Molecule FRET via DNA eXchange (FRET X). *Nano Lett.* 21, 3295–3301. doi: 10.1021/acs.nanolett.1c00725

Ganji, M., Schlichthaerle, T., Eklund, A. S., Strauss, S., and Jungmann, R. (2021). Quantitative Assessment of Labeling Probes for Super-Resolution Microscopy Using Designer DNA Nanostructures. *Chemphyschem* 22, 911–914. doi: 10.1002/cphc.202100185

Gotzke, H., Kilisch, M., Martinez-Carranza, M., Sograte-Idrissi, S., Rajavel, A., Schlichthaerle, T., et al. (2019). The ALFA-tag is a highly versatile tool for nanobody-based bioscience applications. *Nat. Commun.* 10:4403. doi: 10.1038/s41467-019-12301-7

Guo, S. M., Veneziano, R., Gordonov, S., Li, L., Danielson, E., Perez de Arce, K., et al. (2019). Multiplexed and high-throughput neuronal fluorescence imaging with diffusible probes. *Nat. Commun.* 10:4377. doi: 10.1038/s41467-019-12372-6

Gustafsson, M. G. (2005). Nonlinear structured-illumination microscopy: wide-field fluorescence imaging with theoretically unlimited resolution. *Proc. Natl. Acad. Sci. U. S. A.* 102, 13081–13086. doi: 10.1073/pnas.0406877102

Harris, K. M., Jensen, F. E., and Tsao, B. (1992). Three-dimensional structure of dendritic spines and synapses in rat hippocampus (CA1) at postnatal day 15 and adult ages: implications for the maturation of synaptic physiology and long-term potentiation. *J. Neurosci.* 12, 2685–2705.

Hell, S. W., and Wichmann, J. (1994). Breaking the diffraction resolution limit by stimulated emission: stimulated-emission-depletion fluorescence microscopy. *Opt. Lett.* 19, 780–782. doi: 10.1364/ol.19.000780

Helm, M. S., Dankovich, T. M., Mandad, S., Rammner, B., Jahne, S., Salimi, V., et al. (2021). A large-scale nanoscopy and biochemistry analysis of postsynaptic dendritic spines. *Nat. Neurosci.* 24, 1151–1162. doi: 10.1038/s41593-021-00874-w

Jackson, J., Jambrina, E., Li, J., Marston, H., Menzies, F., Phillips, K., et al. (2019). Targeting the Synapse in Alzheimer's Disease. *Front. Neurosci.* 13:735. doi: 10.3389/fnins.2019.00735

Jungmann, R., Avendano, M. S., Dai, M., Woehrstein, J. B., Agasti, S. S., Feiger, Z., et al. (2016). Quantitative super-resolution imaging with qPAINT. *Nat. Methods* 13, 439–442. doi: 10.1038/nmeth.3804

Jungmann, R., Avendano, M. S., Woehrstein, J. B., Dai, M., Shih, W. M., and Yin, P. (2014). Multiplexed 3D cellular super-resolution imaging with DNA-PAINT and Exchange-PAINT. *Nat. Methods* 11, 313–318. doi: 10.1038/nmeth.2835

Jungmann, R., Steinhauer, C., Scheible, M., Kuzyk, A., Tinnefeld, P., and Simmel, F. C. (2010). Single-molecule kinetics and super-resolution microscopy by fluorescence imaging of transient binding on DNA origami. *Nano Lett.* 10, 4756–4761. doi: 10.1021/nl103427w

Keppler, A., Gendreizig, S., Gronemeyer, T., Pick, H., Vogel, H., and Johnsson, K. (2003). A general method for the covalent labeling of fusion proteins with small molecules in vivo. *Nat. Biotechnol.* 21, 86–89. doi: 10.1038/nbt765

Klevanski, M., Herrmannsdoerfer, F., Sass, S., Venkataramani, V., Heilemann, M., and Kuner, T. (2020). Automated highly multiplexed super-resolution imaging of protein nano-architecture in cells and tissues. *Nat. Commun.* 11:1552. doi: 10.1038/s41467-020-15362-1

Ladepeche, L., Planaguma, J., Thakur, S., Suarez, I., Hara, M., Borbely, J. S., et al. (2018). NMDA Receptor Autoantibodies in Autoimmune Encephalitis Cause a Subunit-Specific Nanoscale Redistribution of NMDA Receptors. *Cell Rep.* 23, 3759–3768. doi: 10.1016/j.celrep.2018.05.096

Los, G. V., Encell, L. P., McDougall, M. G., Hartzell, D. D., Karassina, N., Zimprich, C., et al. (2008). HaloTag: a novel protein labeling technology for cell imaging and protein analysis. *ACS Chem. Biol.* 3, 373–382. doi: 10.1021/cb800025k

Moore, R. P., and Legant, W. R. (2018). Improving probes for super-resolution. *Nat. Methods* 15, 659–660. doi: 10.1038/s41592-018-0120-1

Nair, D., Hosy, E., Petersen, J. D., Constals, A., Giannone, G., Choquet, D., et al. (2013). Super-resolution imaging reveals that AMPA receptors inside synapses are dynamically organized in nanodomains regulated by PSD95. *J. Neurosci.* 33, 13204–13224. doi: 10.1523/JNEUROSCI.2381-12.2013

Narayanasamy, K. K., Stojic, A., Li, Y., Sass, S., Hesse, M. R., Deussner-Helfmann, N. S., et al. (2021). Visualizing Synaptic Multi-Protein Patterns of Neuronal Tissue With DNA-Assisted Single-Molecule Localization Microscopy. *Front. Synaptic Neurosci.* 13:671288. doi: 10.3389/fnsyn.2021.671288

Pleiner, T., Bates, M., Trakhanov, S., Lee, C. T., Schliep, J. E., Chug, H., et al. (2015). Nanobodies: site-specific labeling for super-resolution imaging, rapid epitope-mapping and native protein complex isolation. *Elife* 4:e11349. doi: 10.7554/eLife.11349

Ries, J., Kaplan, C., Platonova, E., Eghlidi, H., and Ewers, H. (2012). A simple, versatile method for GFP-based super-resolution microscopy via nanobodies. *Nat. Methods* 9, 582–584. doi: 10.1038/nmeth.1991

Rust, M. J., Bates, M., and Zhuang, X. (2006). Sub-diffraction-limit imaging by stochastic optical reconstruction microscopy (STORM). *Nat. Methods* 3, 793–795. doi: 10.1038/nmeth929

Schlichthaerle, T., Strauss, M. T., Schueder, F., Auer, A., Nijmeijer, B., Kueblbeck, M., et al. (2019). Direct Visualization of Single Nuclear Pore Complex Proteins Using Genetically-Encoded Probes for DNA-PAINT. *Angew. Chem. Int. Ed. Engl.* 58, 13004–13008. doi: 10.1002/anie.201905685

Schueder, F., Stein, J., Stehr, F., Auer, A., Sperl, B., Strauss, M. T., et al. (2019). An order of magnitude faster DNA-PAINT imaging by optimized sequence design and buffer conditions. *Nat. Methods* 16, 1101–1104. doi: 10.1038/s41592-019-0584-7

Schueder, F., Strauss, M. T., Hoerl, D., Schnitzbauer, J., Schlichthaerle, T., Strauss, S., et al. (2017). Universal Super-Resolution Multiplexing by DNA Exchange. *Angew. Chem. Int. Ed. Engl.* 56, 4052–4055. doi: 10.1002/anie.201611729

Sharonov, A., and Hochstrasser, R. M. (2006). Wide-field subdiffraction imaging by accumulated binding of diffusing probes. *Proc. Natl. Acad. Sci. U. S. A.* 103, 18911–18916. doi: 10.1073/pnas.0609643104

Siddig, S., Aufmkolk, S., Doose, S., Jobin, M. L., Werner, C., Sauer, M., et al. (2020). Super-resolution imaging reveals the nanoscale organization of metabotropic glutamate receptors at presynaptic active zones. *Sci. Adv.* 6:eaay7193. doi: 10.1126/sciadv.aay7193

Stein, J., Stehr, F., Jungmann, R., and Schwille, P. (2021). Calibration-free counting of low molecular copy numbers in single DNA-PAINT localization clusters. *Biophys. Rep.* 1:100032. doi: 10.1016/j.bpr.2021.100032

Strauss, S., and Jungmann, R. (2020). Up to 100-fold speed-up and multiplexing in optimized DNA-PAINT. *Nat. Methods* 17, 789–791. doi: 10.1038/s41592-020-0869-x

Strauss, S., Nickels, P. C., Strauss, M. T., Jimenez Sabinina, V., Ellenberg, J., Carter, J. D., et al. (2018). Modified aptamers enable quantitative sub-10-nm cellular DNA-PAINT imaging. *Nat. Methods* 15, 685–688. doi: 10.1038/s41592-018-0105-0

Takamori, S., Holt, M., Stenius, K., Lemke, E. A., Gronborg, M., Riedel, D., et al. (2006). Molecular anatomy of a trafficking organelle. *Cell* 127, 831–846. doi: 10.1016/j.cell.2006.10.030

Tang, A. H., Chen, H., Li, T. P., Metzbower, S. R., MacGillavry, H. D., and Blanpied, T. A. (2016). A trans-synaptic nanocolumn aligns neurotransmitter release to receptors. *Nature* 536, 210–214. doi: 10.1038/nature19058

Thompson, R. E., Larson, D. R., and Webb, W. W. (2002). Precise nanometer localization analysis for individual fluorescent probes. *Biophys. J.* 82, 2775–2783. doi: 10.1016/S0006-3495(02)75618-X

Virant, D., Traenkle, B., Maier, J., Kaiser, P. D., Bodenhofer, M., Schmees, C., et al. (2018). A peptide tag-specific nanobody enables high-quality labeling for dSTORM imaging. *Nat. Commun.* 9:930. doi: 10.1038/s41467-018-03191-2

Wang, Y., Woehrstein, J. B., Donoghue, N., Dai, M., Avendano, M. S., Schackmann, R. C. J., et al. (2017). Rapid Sequential in Situ Multiplexing with DNA Exchange Imaging in Neuronal Cells and Tissues. *Nano Lett.* 17, 6131–6139. doi: 10.1021/acs.nanolett.7b02716

Xu, K., Babcock, H. P., and Zhuang, X. (2012). Dual-objective STORM reveals three-dimensional filament organization in the actin cytoskeleton. *Nat. Methods* 9, 185–188. doi: 10.1038/nmeth.1841

Conflict of Interest: The authors declare that the research was conducted in the absence of any commercial or financial relationships that could be construed as a potential conflict of interest.

frontiers | Frontiers in Synaptic Neuroscience

BRIEF RESEARCH REPORT
published: 08 April 2022
doi: 10.3389/fnsyn.2022.852227

Complementary Use of Super-Resolution Imaging Modalities to Study the Nanoscale Architecture of Inhibitory Synapses

Sara E. Gookin, Matthew R. Taylor, Samantha L. Schwartz, Matthew J. Kennedy, Mark L. Dell'Acqua, Kevin C. Crosby and Katharine R. Smith*

Department of Pharmacology, University of Colorado School of Medicine, Aurora, CO, United States

The nanoscale architecture of synapses has been investigated using multiple super-resolution methods, revealing a common modular structure for scaffolds, neurotransmitter receptors, and presynaptic proteins. This fundamental organization of proteins into subsynaptic domains (SSDs) is thought to be important for synaptic function and plasticity and common to many types of synapses. Using 3D super-resolution Structured Illumination Microscopy (3D-SIM), we recently showed that GABAergic inhibitory synapses exhibit this nanoscale organizational principle and are composed of SSDs of $GABA_A$ receptors ($GABA_A$Rs), the inhibitory scaffold gephyrin, and the presynaptic active zone protein, RIM. Here, we have investigated the use of 3D-SIM and *d*STORM to analyze the nanoscale architecture of the inhibitory synaptic adhesion molecule, neuroligin-2 (NL2). NL2 is a crucial mediator of inhibitory synapse formation and organization, associating with both $GABA_A$Rs and gephyrin. However, the nanoscale sub-synaptic distribution NL2 remains unknown. We found that 3D-SIM and *d*STORM provide complementary information regarding the distribution of NL2 at the inhibitory synapse, with NL2 forming nanoscale structures that have many similarities to gephyrin nanoscale architecture.

Keywords: super-resolution microscopy, 3D-SIM, *d*STORM, inhibitory synapse, neuroligin-2, gephyrin

Edited by:
Thomas A. Blanpied,
University of Maryland, United States

Reviewed by:
Matteo Fossati,
Institute of Neuroscience (CNR), Italy
Corette J. Wierenga,
Utrecht University, Netherlands

***Correspondence:**
Katharine R. Smith
katharine.r.smith@cuanschutz.edu.

Received: *10 January 2022*
Accepted: *08 March 2022*
Published: *08 April 2022*

Citation:
Gookin SE, Taylor MR, Schwartz SL, Kennedy MJ, Dell'Acqua ML, Crosby KC and Smith KR (2022) Complementary Use of Super-Resolution Imaging Modalities to Study the Nanoscale Architecture of Inhibitory Synapses. Front. Synaptic Neurosci. 14:852227. doi: 10.3389/fnsyn.2022.852227

INTRODUCTION

In recent years neuronal synapses have been studied using a range of super-resolution modalities (for a recent review, see Werner et al., 2021). A key finding from this body of work is that synaptic scaffolds, neurotransmitter receptors, and adhesion molecules are not distributed uniformly at synaptic sites, but are often clustered into regions of high density within the synapse, termed nanodomains or subsynaptic domains (SSDs; Biederer et al., 2017; Yang and Specht, 2019). This organization appears to be a common feature of multiple different types of synapses and thought to be important for function and plasticity (Broadhead et al., 2016; Tang et al., 2016, Hruska et al., 2018; Crosby et al., 2019, Ramsey et al., 2021). Our recent work demonstrates that GABAergic inhibitory synapses, which mediate synaptic inhibition in the central nervous system, also exhibit this nanoscale organizational principle (Crosby et al., 2019; Garcia et al., 2021). Through the use of super-resolution three-dimensional structured illumination microscopy (3D-SIM) we found that synaptic GABA$_A$Rs, the inhibitory synaptic scaffold gephyrin, and the presynaptic active zone protein, RIM, all form SSDs. These structures associate with each other and emerge in synapses as it they grow during plasticity, suggesting that this modular structure might underlie activity-dependent synaptic plasticity (Crosby et al., 2019).

Thus far, we have delineated some key elements of inhibitory synaptic architecture with 3D-SIM. However, we reasoned that complementing this approach with a fundamentally distinct super-resolution method, direct stochastic optical reconstruction microscopy (*d*STORM), would provide further information about the synapse and its organization at different spatial scales, allowing us to compare the information provided by these two powerful techniques. 3D-SIM and *d*STORM derive a super-resolved image in distinct ways. 3D-SIM uses a series of raw images acquired with varied patterned illumination orientations that are processed in the Fourier domain, allowing access to higher-frequencies. Upon reverse transform, this higher frequency information corresponds to finer spatial resolution, ∼120 nm laterally and ∼300 nm axially, in the resulting image reconstruction (Gustafsson et al., 2008). In comparison, the raw data in *d*STORM is obtained by imaging a densely labeled sample over several thousand frames. In each individual frame only a small proportion of dye molecules emit photons, detected as "blinks" sparsely spread across the field. This spatial separation allows for fitting the point-spread function from each of these emission events to a precision on the order of 10–20 nm laterally. When the localizations from all the single-frames are aggregated, a pointillistic super-resolution representation of the labeled target emerges (van de Linde et al., 2011).

To investigate the complementary use of 3D-SIM and *d*STORM in the analysis of inhibitory synapses, we chose to image the inhibitory synaptic adhesion molecule, neuroligin-2 (NL2). NL2 is a crucial mediator of inhibitory synapse formation and organization (Oh and Smith, 2019), and interacts with gephyrin and GABA$_A$Rs (Poulopoulos et al., 2009; Yamasaki et al., 2017). This association with the key players of the inhibitory synapse suggests that NL2 could contribute to the nanoscale organization of GABA$_A$Rs and gephyrin, yet its nanoscale sub-synaptic distribution has not been described. By imaging gephyrin and NL2 with both approaches, we find that NL2 forms nanoscale structures at inhibitory synapses. 3D-SIM and *d*STORM provided complementary information and overlapping structural information about NL2 distribution, with *d*STORM providing a more detailed landscape for NL2 architecture. However, despite the difference in spatial resolution, both approaches provided similar biological conclusions, supporting the use of multiple super-resolution techniques to decipher the nanoscale architecture of synapses.

MATERIALS AND METHODS

Dissociated Hippocampal Cultures

Animal procedures were conducted in accordance with the National Institutes of Health (NIH) *Guide for the Care and Use of Laboratory Animals* and approved by the Institutional Animal Care and Use Committee at the University of Colorado. Rat primary hippocampal neurons were cultured and dissociated in papain from mixed sex postnatal day 0–1 rats as previously described (Crosby et al., 2019; Rajgor et al., 2020). The neurons were seeded on 18 mm glass #1.5 coverslips coated with poly-D-lysine at a density of 150,000–200,000 cells in MEM containing 10% FBS and Penicillin-Streptomycin. Media was replaced 24 h post seeding with Neurobasal-A Medium supplemented with B-27 and GlutaMAX. Cells were grown for 15–18 days at 37°C, 5% CO2 and fed every 5 days. Mitotic inhibitors (uridine fluorodeoxyuridine) were added at day 5 to limit growth of actively dividing cells.

Immunocytochemistry

For 3D-SIM and *d*STORM, neurons were fixed in 4% PFA solution [4% sucrose, 1× PBS and 50 mM HEPES (pH7.5)] for 5 min at room temperature followed by three washes with 1× PBS. Neurons were blocked for 1 h (5% BSA, 2% Normal Goat Serum, 0.5% NP-40 and 1× PBS) and incubated with antibodies to Gephyrin mAb7a (1:500 Synaptic Systems 147 011), VGAT (1:1000 Synaptic Systems 131 004) and NL2 (1:500 Synaptic Systems 129 203) in block for 1 h. Neurons were washed three times in 1× PBS and then labeled with secondary antibodies for 1 h at room temperature (for 3D-SIM; 1:1000 ThermoFisher Alexa Fluor 488, 568 and 647), or overnight (for *d*STORM; 1:1000 Alexa Fluor 647 anti-mouse; 1:1000 Sigma-Aldrich CF568 anti-rabbit; 1:1000 ThermoFisher Alexa Fluor 488 anti-guinea pig). Coverslips were washed four times in 1× PBS and mounted on glass microscope slides using ProLong Gold Antifade mounting media for 3D-SIM. For *d*STORM, coverslips were washed and fixed with 4% PFA in 1× PBS for 5 min at room temperature followed by final washes where they remained in 1× PBS until imaging.

3D Structured Illumination Microscopy

Images were acquired with a Nikon SIM-E Structured Illumination super-resolution microscope equipped with a 100×, 1.49 NA objective; an ORCA-Flash 4.0 sCMOS camera (Hamamatsu); and Nikon Elements software. To maximize signal to noise and reduce photobleaching, acquisition conditions and camera integration time were set in a similar manner to Crosby et al. (2019). On average, 8–15 ROIs (individual synapses) were manually selected per neuron (4–5 neurons) for each condition, with a biological replicate of 3 neuronal cultures for a total of 130–180 synapses (12–15 neurons) per condition. Synapses were within the entire Z-stack, and each selection was based off VGAT positive staining. A high throughput pipeline for analysis is as follows: synapses were processed by background subtraction (ImageJ), image segmentation (split-Bregman/MOSAIC suite) (Rizk et al., 2014), and geometric analysis (MATLAB) as further detailed in Crosby et al. (2019). For image segmentation, the following parameters were utilized: "Subpixel segmentation," "Exclude Z edge," Local intensity estimation "Medium," Noise Model "Gauss." All 3D-SIM imaging analysis was performed blind to experimental condition. 3D rendering of SIM data was achieved using the function CaptureFigVid.m.[1]

*d*STORM

Samples were imaged in a standard *d*STORM buffer containing 50 mM Cysteamine hydrochloride, 10% glucose, 0.6 mg/mL Glucose Oxidase from Aspergillus niger, 0.063 mg/mL Catalase from Bovine liver in PBS, pH between 7.5–8.0. Imaging was performed on a Zeiss Elyra P.1 TIRF microscope using a Zeiss alpha Plan Apochromat TIRF 100×/1.46 NA oil objective (Zeiss Item # 420792-9800-720) and a tube lens providing an extra factor of 1.6× magnification. Alexa647 and CF568 dyes were imaged in sequential time-series of approximately 20,000 frames each. Image size was 256 × 256 pixels, integration time was 18 ms for both channels. Alexa-647 molecules were ground-state depleted and imaged with a 100 mW 642 laser at 100% AOTF transmission in ultra-high power mode (condensed field of illumination), corresponding to approximately 1.4 W/cm^2. Emission light passed through a LP 655 filter. CF-568 molecules were ground-state depleted and imaged with a 200 mW 561 laser at 100% AOTF transmission in ultra-high power mode, corresponding to approximately 2.5 W/cm^2. Emission light was passed through a BP 570-650 + LP 750 filter. For each dye, ground-state return was elicited by continuous illumination with a 50 mW 405 laser at 0.01–0.1% AOTF transmission. Excitation light was filtered by a 405/488/561/642 filter placed in front of the camera. Images were recorded with an Andor iXon + 897 EMCCD. The camera EM gain was set to 100, which yields an effective conversion of 1 photo electron into 1.65 digital units. The image pixel size was 100 nm *xy*.

Processing

Raw data was processed through a custom written pipeline written in MATLAB (Mathworks) made up of a number of modular elements, described briefly. The Bio-Formats MATLAB toolbox (Linkert et al., 2010) was used to read Zeiss raw data files into MATLAB. Image data was transferred between MATLAB and FIJI using MIJI.[2]If necessary, raw data was pre-processed with a temporal filter (Hoogendoorn et al., 2014) to remove non-homogeneous background. The filter radius was set at 51 frames, with a key frame distance of 10 (filter is explicitly calculated only for every 10 frames and interpolated between), the quantile for the filtering was set a 20%. Localization of dye emitters was performed using the ThunderSTORM ImageJ plugin (Ovesny et al., 2014). The camera EM gain was set to 100, which resulted in a photon-to-ADU of 1.65. When the temporal median filter was used, the Offset was set to zero. Image filtering was done with the Wavelet filter setting, with a B-Spline order of 3 and scale of 2.0. A first pass approximate localization of molecules was achieved with by finding local maximum with a peak intensity threshold of 3*std(Wave.F1) and 8-neighborhood connectivity. Weighted least squares fitting of the PSF to achieve sub-pixel localizations was achieved by use of an integrated Gaussian with a fitting radius of four pixels and an initial sigma of 1.2. Localizations were filtered based on the attributes of uncertainty (<20 nm), sigma (50–150 nm), and intensity (<10,000 for CF568 and < 15,000 for Alx647). Localizations within 50 nm were merged with a frame-gap allowance of 1.

Before each experiment a calibration was calculated to correct for shifts and distortions between the acquired fluorescent channels. Sub-diffraction size beads, labeled with fluorophores in both channels were imaged. The bead positions were fitted and registered between the fluorescent channels. Registered localizations from multiple bead images were compiled into one data-set. Calibration matrices of the shift in x and y direction between the imaging channels across the full field of view were calculated by either applying a 2D polynomial fit or a localized weighted averaging to the registered bead localizations. In the raw data, the shift and distortion between the imaging channels was up to 100 nm. Applying the calibration to the STORM data yields an RMS error of less than 15 nm for the channel misalignment. Drift correction was performed using the redundant cross-correlation method described in Wang et al. (2014). The segmentation parameter was set at 500 frames, the bin size used in the cross-correlation was 10 nm, and the error threshold for the recalculation of the drift was five pixels.

Localizations were rendered into images using the ThunderSTORM visualization module using the method of average shifted histograms with a magnification of 10 and lateral shift of 2 nm. For SIM like renderings, the Normalized Gaussian method was used with a magnification of 2.5 and the lateral uncertainty locked at 60 nm.

Analysis

Coordinate analysis of our dSTORM data is conceptually similar to methods previously used to classify nanoscale organization at the excitatory synapse (Tang et al., 2016). Synapses for downstream analysis were selected manually from a composite rendered image and ROI coordinates were recorded using a custom ImageJ macro. ROI details were imported into MATLAB using the ReadImageJROI function.[3] The gephyrin scaffold and NL2 localizations were segmented using a coordinate-by-coordinate density calculation. Briefly, because labeling density could vary greatly, the thresholding parameter was determined from the overall density range of the ROI. Localizations with a local-density in the lower 10% of that range were considered to be outside of the synaptic region/clusters. Boundaries for these regions were delineated using MATLAB's alphaShape function, with an α value of 100. Only gephyrin regions with an area of 1.5 e3 nm^2 or greater were considered for analysis. High-density regions (HDRs) were defined by a cutoff determined by randomizing the experimental localizations assuming a uniform distribution across the synaptic region. The local density threshold for an experimental coordinate to be considered as part of a HDR was set at the mean local density of the randomized dataset plus 2 standard deviations. The geometric boundaries of individual HDRs were again delineated using MATLAB's alphaShape function, with an α value of 7. NL2 HDRs were classified as overlapping with the gephyrin scaffold (or gephyrin

---

[1] https://www.mathworks.com/matlabcentral/fileexchange?q=41093

[2] http://bigwww.epfl.ch/sage/soft/mij/

[3] github.com/DylanMuir/ReadImageJROI

HDR) if the overlap area had a fraction of 0.23 or greater of the total NL2 HDR area.[4]

RESULTS

Neuroligin-2 Exhibits Non-uniform, Sub-Synaptic Organization at Inhibitory Synapses

To characterize the nanoscale architecture of NL2, we imaged NL2 along with the scaffold protein, gephyrin, at inhibitory synapses with both 3D-SIM and *d*STORM. In addition, vesicular GABA transporter (VGAT) was also labeled to mark GABAergic presynaptic terminals (**Figures 1A,B**). 3D-SIM images revealed that NL2 is often non-uniformly organized into small, nanoscale SSDs, similar to those we have observed for gephyrin and synaptic GABA$_A$Rs (**Figures 1A,B**; Crosby et al., 2019; Garcia et al., 2021]. Line-scans through individual synapses supported this observation and indicated multiple peaks of intensity for NL2 and gephyrin within a single synapse (**Figure 1B**). Furthermore, 3D rendering of the 3D-SIM data underscored the modular nature of NL2 distribution at the synapse (**Figure 1C** and **Supplementary Movie 1**). *d*STORM of NL2 and gephyrin also showed a similar modular distribution for NL2 and gephyrin (**Figures 1D,E**). Both the rendered images and coordinate maps (**Figures 1D,E**) from our *d*STORM data confirmed the heterogeneous distribution of NL2 and gephyrin across the inhibitory synapse.

Nanoscale Parameters of Neuroligin-2 Nanostructures Determined by SIM and *d*STORM

Following the imaging of NL2 and gephyrin with 3D-SIM and *d*STORM, we used distinct computational methods to identify and quantify the dimensions of NL2 subsynaptic structures. To identify NL2 SSDs from our 3D-SIM images we utilized our previously developed model-based object 3D-segmentation analysis (Crosby et al., 2019). The number of NL2 SSDs within a synapse varied greatly over the synapses analyzed, with some being formed of a single SSD, whereas others harboring multiple SSDs (**Figure 2A**). The mean number of NL2 SSDs per synapse was similar to that of gephyrin and VGAT (**Figure 2B**). Our analysis also showed that NL2 SSDs are of a similar volume to those of gephyrin, but were substantially smaller than VGAT substructures in the presynaptic terminal (**Figure 2C**). Furthermore, NL2 compartment volumes were also similar to those of gephyrin, but significantly smaller than that of VGAT (**Figure 2D**), which was in agreement with our previous work (Crosby et al., 2019; Garcia et al., 2021) and the presence of NL2 within the inhibitory post-synaptic domain.

We characterized the finer scale distribution of NL2 and gephyrin captured by *d*STORM by quantifying the local density of the NL2 and gephyrin localizations (see section "Materials and Methods"). Both NL2 and gephyrin exhibited regions of relatively high-density (**Figure 2E**). We were able to delineate the boundaries of these high-density regions (HDRs) and enumerate their geometric attributes (**Figure 2F**). The number of HDRs per synapse varied across synapses for both NL2 and gephyrin, but both exhibited ∼3 HDRs per synapse (**Figure 2G**). The HDR areas for NL2 and gephyrin were also similar (**Figure 2H**). Despite the 3D/2D disparity between our SIM and *d*STORM data, it was clear from our imaging that the HDRs detected by *d*STORM were smaller and more heterogeneous than the segmented SSDs from our 3D-SIM data.

One of the motivations of this study is to compare data and analysis obtained from 3D-SIM imaging and dSTORM imaging. Ideally, we would be able to image the same synapses with both techniques to compare the resolved structures, however the technical and computational challenges of this type of correlative imaging (Reinhard et al., 2019) made these direct experiments unfeasible. Therefore, we created "pseudo-SIM" images by rendering our *d*STORM data to match the typical resolution achievable by SIM (**Figure 2I**; see section "Materials and Methods"). We then overlaid the NL2 or gephyrin *d*STORM coordinate map across the SIM-rendered image to compare HDR and SSD detection precision. By comparing these rendered images and coordinate maps we found that some, but certainly not all SSDs detected by SIM are composed of multiple smaller regions of heterogeneous density, that are only visible by higher resolution imaging techniques.

Analysis of the Association Between Gephyrin and Neuroligin-2 at the Nanoscale Level

Neuroligin-2 and gephyrin directly interact at inhibitory synapses (Poulopoulos et al., 2009). To assess whether NL2 nanoscale organization mirrors that of the gephyrin scaffold we asked whether NL2 and gephyrin SSDs are in close proximity to each other. NL2 and gephyrin SSDs were often observed paired together as shown in the example 3D-SIM images in **Figure 2A**. To assess whether this was a common feature for NL2 and gephyrin architecture across our 3D-SIM dataset, we used our segmentation work-flow to quantify the overlap and distance between neighboring SSDs within the 3D-SIM images. These data revealed a high degree of overlap between NL2 and gephyrin SSDs, compared with either NL2 or gephyrin SSDs with presynaptic VGAT substructures (**Figure 3A**). In agreement with this, ∼90% of NL2 SSDs overlapped gephyrin SSDs within an individual synapse (**Figure 3B**) indicating a high degree of association between these SSDs at the resolution of 3D-SIM. Measurement of the distance between NL2 SSDs and their nearest neighboring gephyrin SSDs showed that NL2 and gephyrin SSDs were significantly closer together than when compared to VGAT (**Figure 3C**). To give an indication of possible interdependence between NL2 and gephyrin SSD nanoscale organization we determined if the number of SSDs in the gephyrin compartment correlated with the number of SSDs in the NL2 compartment. NL2 compartments with larger numbers of SSDs were more likely to be associated with larger numbers of gephyrin SSDs (**Figure 3D**). Furthermore, larger gephyrin compartments correlated well with greater numbers of NL2 SSDs

---

[4] https://github.com/VVvanL/NL2project_SmithLab

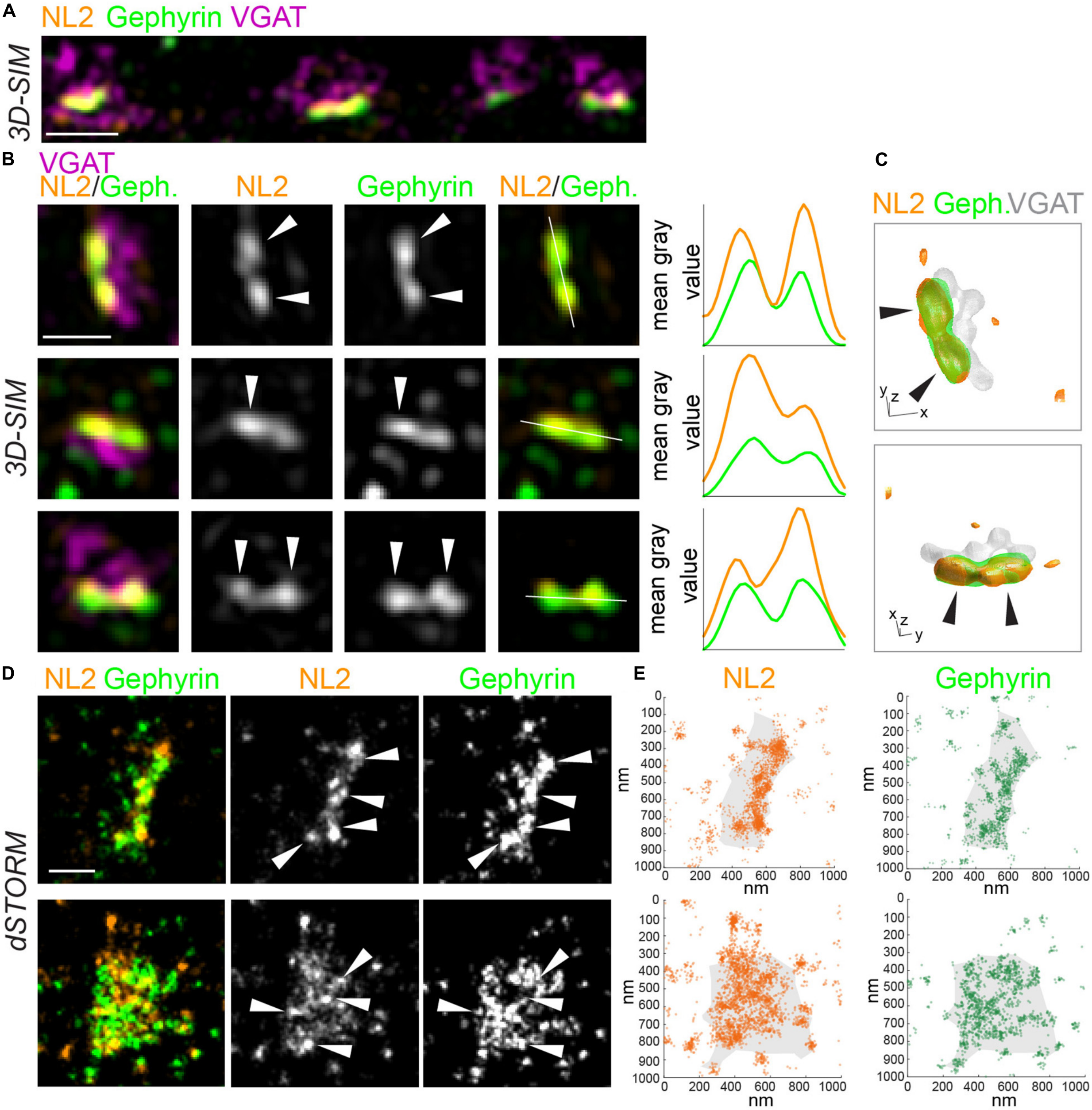

FIGURE 1 | SIM and *d*STORM reveal NL2 is organized into nanoscale structures at inhibitory synapses. **(A)** 3D-SIM maximum projection of hippocampal dendrite labeled with antibodies to NL2, gephyrin and VGAT. Scale bar = 1 μm. **(B)** Magnifications of synapses from 3D-SIM images, with line-scans showing nanoscale subsynaptic domains (SSDs) of NL2 and gephyrin. White lines show path of line scans on the right. Arrows indicate NL2 and gephyrin SSDs. Scale bar = 500 nm. **(C)** 3D reconstruction of inhibitory synapse in panel **(B)**, upper panel, labeled for NL2, gephyrin and VGAT. XY scale bar = 320 nm, Z scale bar = 600 nm. Also see **Supplementary Movie 1**. **(D)** *d*STORM rendered images of VGAT-positive inhibitory synapses labeled with antibodies to NL2 and gephyrin. Arrows indicate high-density regions. Scale bar = 250 nm. **(E)** Localization plots of *d*STORM data from panel **(D)**.

(**Figure 3E**), suggesting that larger post-synaptic domains have more NL2 distributed into SSDs. Together, analysis of our 3D-SIM data shows that at many synapses NL2 SSDs are close-to and overlap with gephyrin SSDs, suggesting that NL2 nanoscale organization may mirror that of the gephyrin scaffold.

As discussed above, *d*STORM provides a far more detailed picture of nanoscale architecture for NL2 and gephyrin. To determine whether NL2 and gephyrin HDRs associate at the resolution level of *d*STORM, we quantified the area of overlap between HDRs based on the area fraction of each individual NL2 HDR overlapping with a gephyrin HDR (**Figures 4A,B**). As expected, the higher resolution of *d*STORM compared with 3D-SIM meant that NL2 and gephyrin HDRs displayed far less overlap compared with the SSDs identified by 3D-SIM.

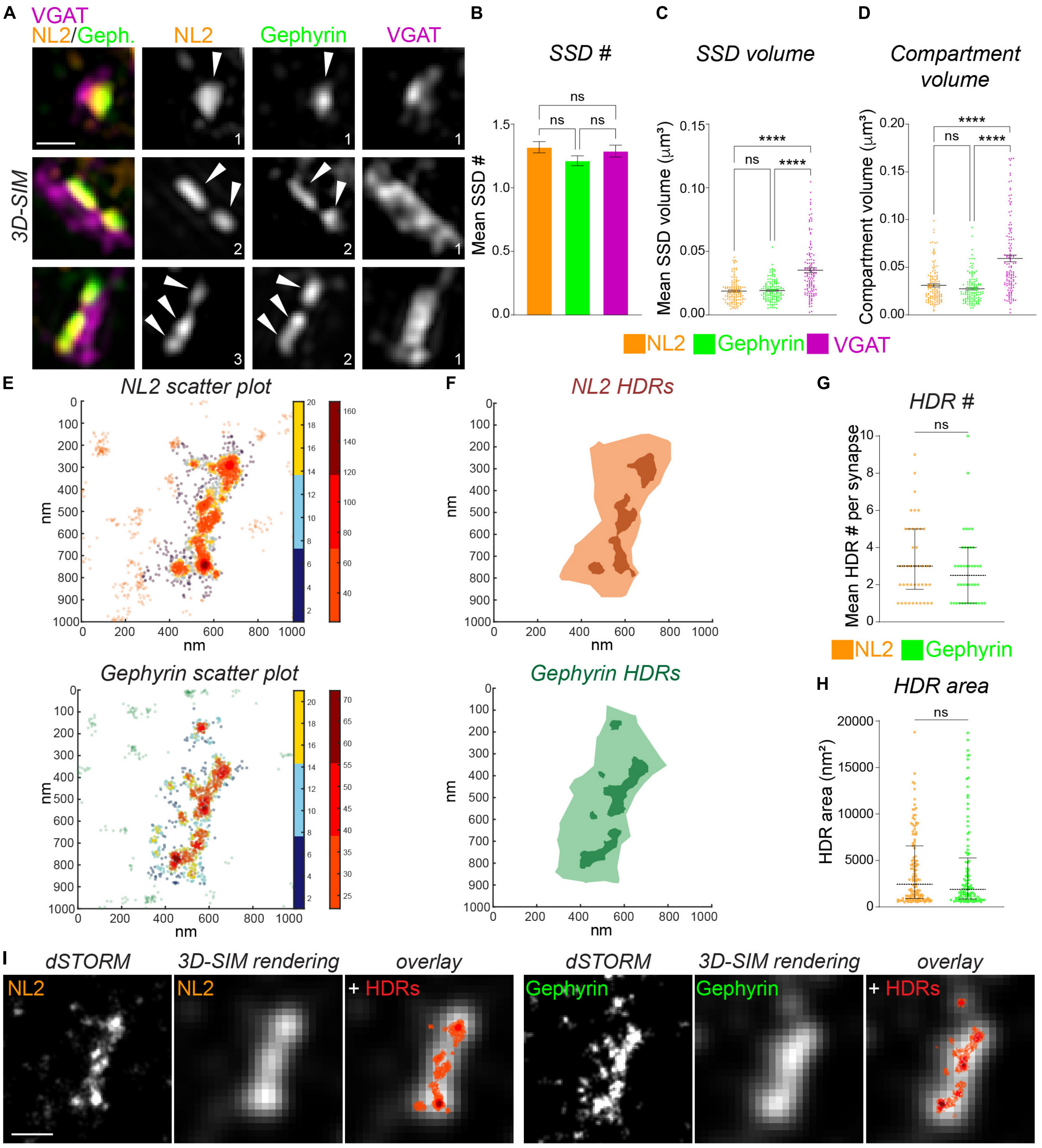

FIGURE 2 | Measurement of NL2 substructure parameters by 3D-SIM and *d*STORM. **(A)** Maximum projection 3D-SIM images of hippocampal inhibitory synapses labeled for NL2, gephyrin and VGAT. Numbers denote number of SSDs in compartment. **(B)** Mean number of SSDs per compartment. $p = 0.186$ (Kruskal–Wallis); $n = 132$ synapses. **(C)** Individual SSD volumes for NL2, gephyrin, and VGAT. $^{****}p < 0.0001$ (Kruskal–Wallis, Dunn's *post hoc*); $n = 132$ synapses. Horizontal line denotes mean. **(D)** Compartment volumes for NL2, gephyrin, and VGAT. $^{****}p < 0.0001$ (Kruskal–Wallis, Dunn's *post hoc*); $n = 132$ synapses. Horizontal line denotes mean. **(E)** Heat maps of NL2 and gephyrin localizations generated by *d*STORM. Hot colors (color-bar 2) represent localizations that are classified as high-density (HDRs), remaining synaptic localizations are shown in cooler colors (color-bar 1). **(F)** Diagrams showing the delineation of NL2 and Gephyrin HDRs (darker shades) and NL2 and gephyrin post-synaptic regions (lighter shades). **(G)** Number of HDRs per compartment for NL2 and gephyrin. Horizontal lines denote median and 25–75% quantiles. $p = 0.333$ (Mann Whitney), $n = 42$ synapses. **(H)** Individual NL2 and gephyrin HDR areas. Horizontal line denotes median and 25–75% quantiles. $p = 0.518$ (Mann Whitney), $n = 42$ synapses. **(I)** Images showing *d*STORM rendered image at *d*STORM and 3D-SIM resolution, with identified HDRs overlaid in red. Scale bar = 250 nm.

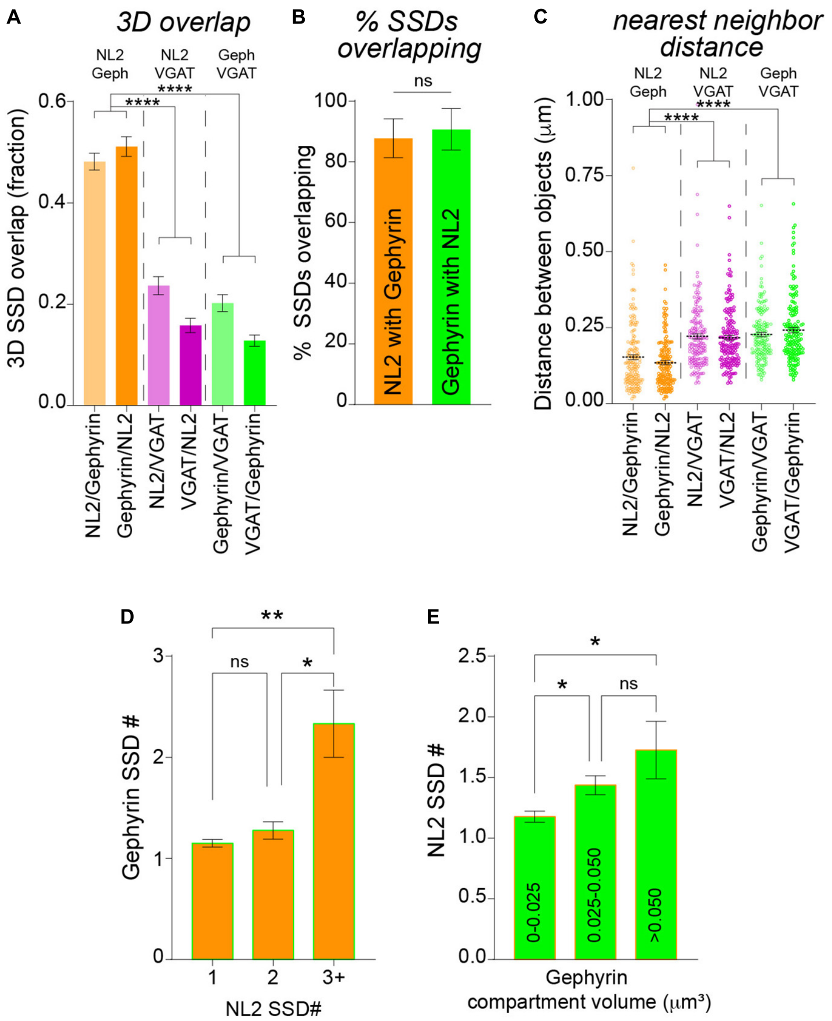

FIGURE 3 | Analysis of NL2 and gephyrin SSD association by 3D-SIM. **(A)** Mean overlap fraction for NL2, gephyrin and VGAT SSDs. ****$p < 0.0001$ (Kruskal–Wallis, Dunn's *post hoc*); $n = 132$ synapses. **(B)** Mean percentage of overlapping SSDs. $p = 0.178$ (Mann Whitney); $n = 7$ cells. **(C)** Center-to-center distances between neighboring NL2, gephyrin and VGAT SSDs. ****$p < 0.0001$ (Kruskal–Wallis, Dunn's *post hoc*); $n = 160–175$ SSDs. Horizontal line denotes mean. **(D)** Mean gephyrin SSD number for NL2 compartments with 1, 2, or 3 SSDs per compartment. *$p = 0.0225$, **$p = 0.0036$; (Kruskal–Wallis, Dunn's *post hoc*); $n = 132$ synapses. **(E)** Mean SSD number per NL2 compartment for a range of gephyrin compartment volumes. *$p < 0.05$ (Kruskal–Wallis, Dunn's *post hoc*); $n = 132$ synapses.

~ 65% of NL2 HDRs analyzed had ≤ 0.05 overlap with neighboring gephyrin HDRs (**Figure 4C**). However, in many cases NL2 HDRs were adjacent to the gephyrin HDR, with the peak of the NL2 localizations often lying next to the gephyrin HDR (as shown in **Figure 4B**). ~75% of NL2 HDRs were positioned within the gephyrin scaffold region (the shaded gray area in **Figures 4A,B**), both in and outside of gephyrin HDRs. However, ~25% of NL2 HDRs were found to be extra-synaptic. Quantification of NL2 HDR areas in and outside of the gephyrin scaffold region revealed that these extra-synaptic NL2 HDRs were significantly smaller than those inside the gephyrin scaffold (**Figure 4D**). Our 3D-SIM data suggest that larger gephyrin scaffolds contain more SSDs. To test whether this was also the case for the NL2 HDRs identified by *d*STORM we drew correlations between the number of HDRs and the area of the gephyrin scaffold (**Figures 4E,F**). There were strong correlations between the area of the scaffold and the number of either gephyrin or NL2 HDRs within the scaffold (**Figures 4E,F**), indicating that larger gephyrin scaffolds are likely able to support more NL2 HDRs. Moreover, the number of NL2 HDRs within a synapse correlated well with the number of gephyrin HDRs present (**Figure 4G**). Together, our *d*STORM analysis reveals substantially less overlap between NL2 and gephyrin HDRs than shown by 3D-SIM, with NL2 HDRs often found at the edge of neighboring gephyrin HDRs.

DISCUSSION

Multiple fluorescence-based imaging modalities have been applied to analyze the nanoscale architecture of synapses (Werner et al., 2021). These techniques increase resolution by different

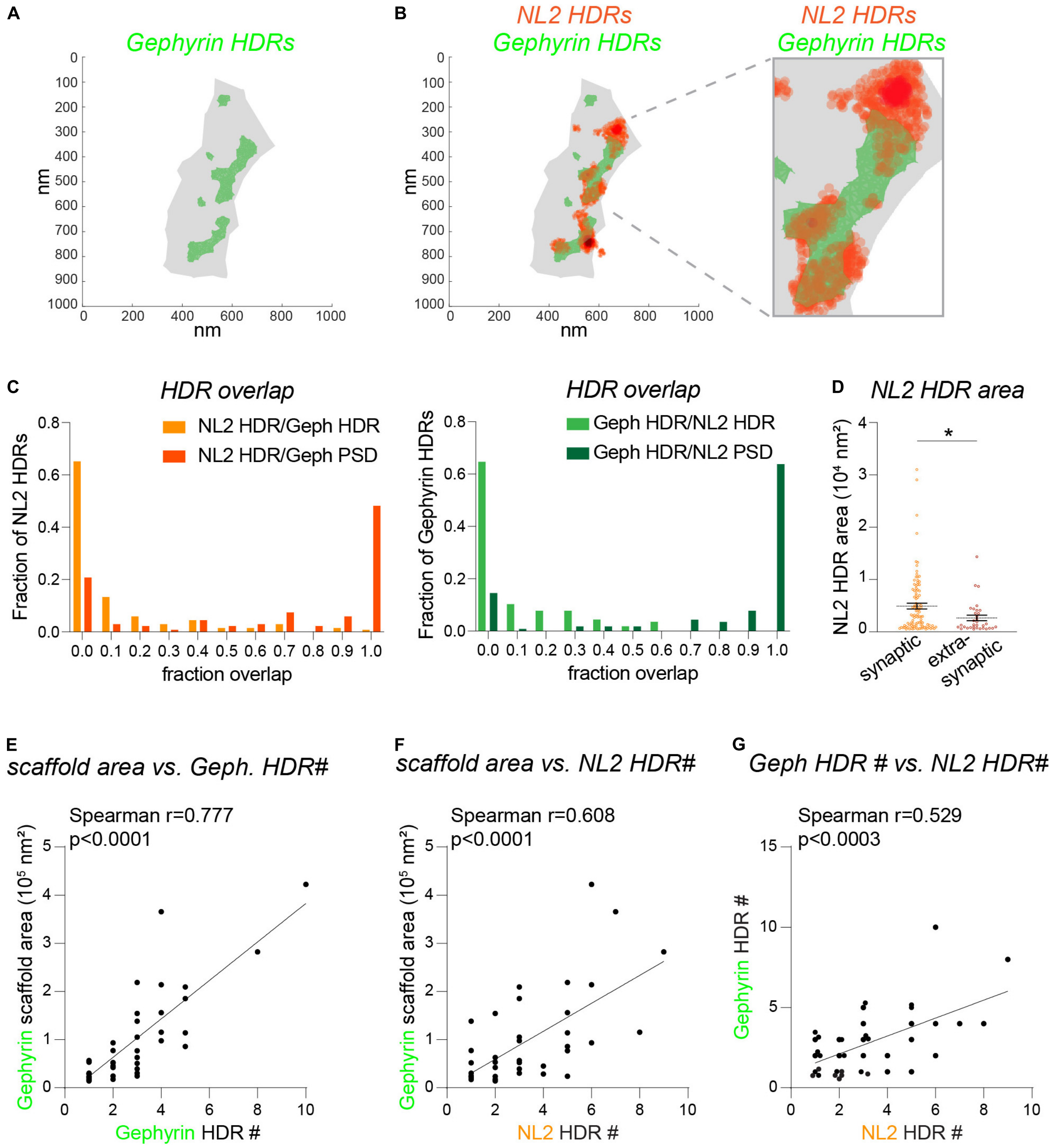

FIGURE 4 | Fine detail of NL2 and gephyrin subsynaptic structure analyzed by *d*STORM. **(A)** *d*STORM plots showing gephyrin scaffold boundary (gray) and boundaries for gephyrin HDRs (green). **(B)** *d*STORM plots showing gephyrin boundaries (green) with NL2 HDR localizations overlaid (orange). **(C)** Distribution histograms showing the relative proportion of NL2 or gephyrin HDRs with different degrees of fraction overlap with HDRs (lighter colors) or scaffold regions (darker colors). **(D)** Area distribution for synaptic and extra-synaptic NL2 HDRs. HDRs are considered synaptic with a 0.23 fraction overlap or greater with the gephyrin scaffold. Horizontal line denotes mean. $^*p = 0.016$ (Mann Whitney), $n = 33–102$ HDRs. **(E–G)** Correlation plots showing the liner relationship between the gephyrin scaffold area and the number of gephyrin HDRs **(E)** and the number of NL2 HDRs **(F)**. As a result, there is a corresponding correlation between the number of gephyrin HDRs and the number of NL2 HDRs **(G)**.

optical/computational methods, have their own set of advantages and disadvantages, and exhibit practical limits to the achievable resolution (Vangindertael et al., 2018). Here, we have used two orthogonal super-resolution imaging methods, 3D-SIM and *d*STORM, to study the subsynaptic distribution of the inhibitory synaptic adhesion protein NL2.

The two most notable differences between 3D-SIM and *d*STORM are the achievable resolution and data-type. The resolution of our 3D-SIM data is approximately half of what can be measured with standard confocal microscopy (∼120 nm laterally and ∼300 nm axially); our *d*STORM data is fit to a precision of 10–20 nm. 3D-SIM can discern distinct SSDs that are difficult/impossible to distinguish with confocal or wide-field imaging. In our previous work, we have shown that the organizational units at this resolution level (SIM-resolved SSDs) likely serve as "building blocks" of inhibitory synapses and emerge in, or are removed from, the synapses during different types of neuronal activity (Crosby et al., 2019; Garcia et al., 2021). We have found that NL2 is also organized into SSDs, of similar volume as gephyrin and GABA$_A$R SSDs (Crosby et al., 2019), suggesting that NL2 SSDs could have a role in the nanoscale organization of GABA$_A$Rs and gephyrin, and potentially the growth or shrinkage of the synapse.

With the more than five-fold improvement in resolution provided by *d*STORM, we found that the distribution of both gephyrin and NL2 localizations could be classified as either low-density or HDRs. HDRs were smaller than SIM-resolved SSDs; we postulate that SSDs are often made up of these mixed density regions, with one SSD perhaps containing multiple HDRs. Ideally, the same synapse would be imaged using each technique to confirm the smaller scale make-up of the SSDs, however, these types of experiments are technically challenging (Reinhard et al., 2019). Unsurprisingly, NL2 HDRs were more numerous and significantly smaller than NL2 SSDs identified by 3D-SIM. The higher resolution of *d*STORM also revealed reduced overlap between NL2 and gephyrin HDRs compared with that observed with 3D-SIM, with only about 25% of NL2 HDR showing an area overlap of 0.2 or greater with gephyrin HDRs. However, NL2 HDRs are often in close proximity to gephyrin HDRs and over 75% of NL2 HDR are found within the gephyrin post-synaptic scaffold. A notable consistency between our SIM and *d*STORM datasets is that the number of super-resolved substructures tended to scale with the overall size of the synapse: larger synapses generally harbored higher numbers of NL2 SSDs or HDRs. The same is true for gephyrin and GABA$_A$R sub-structures, supporting the hypothesis that SSDs underly synapse growth and shrinkage (Crosby et al., 2019). It will be interesting to determine if NL2 SSDs emerge during plasticity protocols that induce overall growth of the synapse coupled with the addition of gephyrin and GABA$_A$R SSDs. One critical distinction of our *d*STORM data is that, due in part to the single-molecule nature of the technique, we can detect smaller extrasynaptic clusters of NL2 that we have not observed using 3D-SIM. These extrasynaptic HDRs are smaller in area compared with their synaptic counterparts and could represent NL2 clusters that are trafficking to or from the synapse, or the seeding of a new synaptic site. Live super-resolution imaging such as live-cell PALM will be required to discern these possibilities.

In this study, our *d*STORM data has only been fit to provide 2D data; we therefore restricted our analysis to synapses that had a clear *en face* orientation. The implementation of 3D-STORM will improve our ability to interrogate inhibitory synapse substructure, in particular, the spatial relationship between pre- and post-synaptic elements. It is also important to note that these data represent static snap-shots of synaptic organization. We previously performed live-cell 3D-SIM experiments, imaging Gephyrin during homeostatic scaling (Crosby et al., 2019). During scaling-up of the synapse we observed the slow addition of SSDs with a corresponding growth of the gephyrin scaffold. In future studies using live-cell PALM, it will be interesting to determine the temporal stability of the HDRs we observe, and whether they increase in number during plasticity. It is possible that these regions morph and move over shorter time-scales while retaining the same overall mix of high and low-density within the boundaries of a more stable SSD.

DATA AVAILABILITY STATEMENT

The original contributions presented in the study are included in the article/**Supplementary Material**, further inquiries can be directed to the corresponding author.

ETHICS STATEMENT

All animal work was reviewed and approved by the Institutional Animal Care and Use Committee at the University of Colorado.

AUTHOR CONTRIBUTIONS

KS and KC: conceptualization and methodology and writing – original draft. SG and MT: experiments. KC, SG, MT, SS, and KS: formal analysis and figure preparation. KS, KC, and SG: writing – review and editing. KS, MD, and MK: supervision and funding acquisition. All authors contributed to the article and approved the submitted version.

FUNDING

This work was supported by a Brain and Behavior Research Foundation NARSAD Young Investigator Award, a Brain Research Foundation Seed Grant, an AHA Career Development Award, and grant R01MH119154 to KS. MD was supported by grants R01NS040701 and R01123700. MK was supported by grant R35NS116879. SS was supported by grant F32MH123053. We thank Dominik Stich for assisting with the *d*STORM imaging, which was performed at the University of Colorado Anschutz Medical Campus Advanced Light Microscopy Core, supported in part by Rocky Mountain Neurological Disorders Core grant number P30 NS048154 and by Diabetes Research Center grant number P30 DK116073.

SUPPLEMENTARY MATERIAL

The Supplementary Material for this article can be found online at: https://www.frontiersin.org/articles/10.3389/fnsyn.2022.852227/full#supplementary-material

REFERENCES

Biederer, T., Kaeser, P. S., and Blanpied, T. A. (2017). Transcellular nanoalignment of synaptic function. *Neuron* 96, 680–696. doi: 10.1016/j.neuron.2017.10.006

Broadhead, M. J., Horrocks, M. H., Zhu, F., Muresan, L., Benavides-Piccione, R., DeFelipe, J., et al. (2016). PSD95 nanoclusters are postsynaptic building blocks in hippocampus circuits. *Sci. Rep.* 6:24626. doi: 10.1038/srep24626

Crosby, K. C., Gookin, S. E., Garcia, J. D., Hahm, K. M., Dell'Acqua, M. L., and Smith, K. R. (2019). Nanoscale subsynaptic domains underlie the organization of the inhibitory synapse. *Cell Rep.* 26, 3284–3297. doi: 10.1016/j.celrep.2019.02.070

Garcia, J. D., Gookin, S. E., Crosby, K. C., Schwartz, S. L., Tiemeier, E., Kennedy, M. J., et al. (2021). Stepwise disassembly of GABAergic synapses during pathogenic excitotoxicity. *Cell Rep.* 37:110142. doi: 10.1016/j.celrep.2021.110142

Gustafsson, M. G., Shao, L., Carlton, P. M., Wang, C. J. I, Golubovskaya, N., Cande, W. Z., et al. (2008). Three-dimensional resolution doubling in wide-field fluorescence microscopy by structured illumination. *Biophys. J.* 94, 4957–4970. doi: 10.1529/biophysj.107.120345

Hoogendoorn, E., Crosby, K. C., Leyton-Puig, D., Breedijk, R. M., Jalink, K., Gadella, T. W., et al. (2014). The fidelity of stochastic single-molecule super-resolution reconstructions critically depends upon robust background estimation. *Sci. Rep.* 4:3854. doi: 10.1038/srep03854

Hruska, M., Henderson, N., Le Marchand, S. J., Jafri, H., and Dalva, M. B. (2018). Synaptic nanomodules underlie the organization and plasticity of spine synapses. *Nat. Neurosci.* 21, 671–682. doi: 10.1038/s41593-018-0138-9

Linkert, M., Rueden, C. T., Allan, C., Burel, J. M., Moore, W., Patterson, A., et al. (2010). Metadata matters: access to image data in the real world. *J. Cell Biol.* 189, 777–782. doi: 10.1083/jcb.201004104

Oh, W. C., and Smith, K. R. (2019). Activity-dependent development of GABAergic synapses. *Brain Res.* 1707, 18–26. doi: 10.1016/j.brainres.2018.11.014

Ovesny, M., Krizek, P., Borkovec, J., Svindrych, Z., and Hagen, G. M. (2014). ThunderSTORM: a comprehensive imagej plug-in for PALM and STORM data analysis and super-resolution imaging. *Bioinformatics* 30, 2389–2390. doi: 10.1093/bioinformatics/btu202

Poulopoulos, A., Aramuni, G., Meyer, G., Soykan, T., Hoon, M., Papadopoulos, T., et al. (2009). Neuroligin 2 drives postsynaptic assembly at perisomatic inhibitory synapses through gephyrin and collybistin. *Neuron* 63, 628–642. doi: 10.1016/j.neuron.2009.08.023

Rajgor, D., Purkey, A. M., Sanderson, J. L., Welle, T. M., Garcia, J. D., Dell'Acqua, M. L., et al. (2020). Local miRNA-dependent translational control of GABA $_A$ R synthesis during inhibitory long-term potentiation. *Cell Rep.* 31:107785. doi: 10.1016/j.celrep.2020.107785

Ramsey, A. M., Tang, A. H., LeGates, T. A., Gou, X. Z., Carbone, B. E., Thompson, S. M., et al. (2021). Subsynaptic positioning of AMPARs by LRRTM2 controls synaptic strength. *Sci. Adv.* 7:eabf3126. doi: 10.1126/sciadv.abf3126

Reinhard, S., Aufmkolk, S., Sauer, M., and Doose, S. (2019). Registration and visualization of correlative super-resolution microscopy data. *Biophys. J.* 116, 2073–2078. doi: 10.1016/j.bpj.2019.04.029

Rizk, A., Paul, G., Incardona, P., Bugarski, M., Mansouri, M., Niemann, A., et al. (2014). Segmentation and quantification of subcellular structures in fluorescence microscopy images using Squassh. *Nat. Protoc.* 9, 586–596. doi: 10.1038/nprot.2014.037

Tang, A. H., Chen, H., Li, T. P., Metzbower, S. R., MacGillavry, H. D., and Blanpied, T. A. (2016). A trans-synaptic nanocolumn aligns neurotransmitter release to receptors. *Nature* 536, 210–214. doi: 10.1038/nature19058

van de Linde, S., Loschberger, A., Klein, T., Heidbreder, M., Wolter, S., and Heilemann, M. (2011). Direct stochastic optical reconstruction microscopy with standard fluorescent probes. *Nat. Protoc.* 6, 991–1009. doi: 10.1038/nprot.2011.336

Vangindertael, J., Camacho, R., Sempels, W., Mizuno, H., Dedecker, P., and Janssen, K. P. F. (2018). An introduction to optical super-resolution microscopy for the adventurous biologist. *Methods Appl. Fluoresc.* 6:022003. doi: 10.1088/2050-6120/aaae0c

Wang, Y., Schnitzbauer, J., Hu, Z., Li, X., Cheng, Y., Huang, Z. L., et al. (2014). Localization events-based sample drift correction for localization microscopy with redundant cross-correlation algorithm. *Opt. Express* 22, 15982–15991. doi: 10.1364/OE.22.015982

Werner, C., Sauer, M., and Geis, C. (2021). Super-resolving microscopy in neuroscience. *Chem. Rev.* 121, 11971–12015. doi: 10.1021/acs.chemrev.0c01174

Yamasaki, T., Hoyos-Ramirez, E., Martenson, J. S., Morimoto-Tomita, M., and Tomita, S. (2017). GARLH Family proteins stabilize GABA $_A$ receptors at synapses. *Neuron* 93, 1138–1152. doi: 10.1016/j.neuron.2017.02.023

Yang, X., and Specht, C. G. (2019). Subsynaptic domains in super-resolution microscopy: the treachery of images. *Front. Mol. Neurosci.* 12:161. doi: 10.3389/fnmol.2019.00161

Conflict of Interest: The authors declare that the research was conducted in the absence of any commercial or financial relationships that could be construed as a potential conflict of interest.

frontiers | Frontiers in Synaptic Neuroscience

ORIGINAL RESEARCH
published: 25 April 2022
doi: 10.3389/fnsyn.2022.835427

High-Resolution Fluorescence Imaging Combined With Computer Simulations to Quantitate Surface Dynamics and Nanoscale Organization of Neuroligin-1 at Synapses

*Matthieu Lagardère†, Adèle Drouet†, Matthieu Sainlos and Olivier Thoumine**

CNRS, Interdisciplinary Institute for Neuroscience, IINS, UMR 5297, University of Bordeaux, Bordeaux, France

Edited by:
Thomas A. Blanpied,
University of Maryland, Baltimore,
United States

Reviewed by:
Jaewon Ko,
Daegu Gyeongbuk Institute
of Science and Technology (DGIST),
South Korea
Paul De Koninck,
Laval University, Canada

***Correspondence:**
Olivier Thoumine
olivier.thoumine@u-bordeaux.fr

†These authors have contributed equally to this work

Received: 14 December 2021
Accepted: 09 March 2022
Published: 25 April 2022

Citation:
Lagardère M, Drouet A, Sainlos M and Thoumine O (2022) High-Resolution Fluorescence Imaging Combined With Computer Simulations to Quantitate Surface Dynamics and Nanoscale Organization of Neuroligin-1 at Synapses.
Front. Synaptic Neurosci. 14:835427.
doi: 10.3389/fnsyn.2022.835427

Neuroligins (NLGNs) form a family of cell adhesion molecules implicated in synapse development, but the mechanisms that retain these proteins at synapses are still incompletely understood. Recent studies indicate that surface-associated NLGN1 is diffusionally trapped at synapses, where it interacts with quasi-static scaffolding elements of the post-synaptic density. Whereas single molecule tracking reveals rapid diffusion and transient immobilization of NLGN1 at synapses within seconds, fluorescence recovery after photobleaching experiments indicate instead a long-term turnover of NLGN1 at synapse, in the hour time range. To gain insight into the mechanisms supporting NLGN1 anchorage at post-synapses and try to reconcile those experimental paradigms, we quantitatively analyzed here live-cell and super-resolution imaging experiments performed on NLGN1 using a newly released simulator of membrane protein dynamics for fluorescence microscopy, FluoSim. Based on a small set of parameters including diffusion coefficients, binding constants, and photophysical rates, the framework describes fairly well the dynamic behavior of extra-synaptic and synaptic NLGN1 over both short and long time ranges, and provides an estimate of NLGN1 copy numbers in post-synaptic densities at steady-state (around 50 dimers). One striking result is that the residence time of NLGN1 at synapses is much longer than what can be expected from extracellular interactions with pre-synaptic neurexins only, suggesting that NLGN1 is stabilized at synapses through multivalent interactions with intracellular post-synaptic scaffolding proteins.

Keywords: adhesion molecule, membrane diffusion, single molecule tracking, computer simulation, fluorescence recovery after photo bleaching

INTRODUCTION

During neuronal development, several adhesion protein families are involved in establishing and maintaining synaptic connections, among which the neurexins (NRXNs) and their binding partners neuroligins (NLGNs) have been widely studied (Bemben et al., 2015; Südhof, 2017). These transmembrane molecules are implicated in a variety of extracellular and intracellular protein-protein interactions, including calcium-dependent *trans*-synaptic binding between NRXN and NLGN ectodomains (Levinson and El-Husseini, 2007), *cis*-interactions with neurexophilin and MDGAs, respectively (Born et al., 2014; Connor et al., 2019), and C-terminal binding to PDZ-domain containing scaffolding proteins such as CASK and PSD-95, respectively (Irie et al., 1997; Mukherjee et al., 2008). NRXNs and NLGNs are involved in regulating synaptic differentiation and potentiation through either direct or indirect connections to pre-synaptic calcium channels and post-synaptic neurotransmitter receptors, respectively (Missler et al., 2003; Poulopoulos et al., 2009; Shipman et al., 2011; Nguyen et al., 2016; Haas et al., 2018; Letellier et al., 2018, 2020; Wu et al., 2019).

The large repertoire of protein interactions displayed by NRXNs and NLGNs allows a fine regulation of the membrane trafficking and synaptic retention of these molecules. Indeed, both NRXNs and NLGNs were shown by single molecule tracking to be highly dynamic in the neuronal plasma membrane, and transiently trapped at synapses through a combination of extracellular and intracellular protein interactions (Neupert et al., 2015; Chamma et al., 2016a; Klatt et al., 2021). Synaptic confinement of these molecules increases as synapses mature during neuronal development (Chamma et al., 2016a), and super-resolution microscopy investigation in mature synapses showed that NRXN and NLGN form small confinement domains facing each other on both sides of the synaptic cleft (Chamma et al., 2016a,b; Trotter et al., 2019). Despite these advances, the molecular mechanisms that regulate the surface dynamics, synaptic anchorage and nanoscale localization of NLGNs, are still unclear. Part of the difficulty in interpreting NLGN surface dynamics or localization data arises from the various imaging techniques used i.e., Single Particule Tracking (SPT), fluorescence recovery after photobleaching (FRAP) and stochastic optical reconstruction microscopy (STORM), which are often performed at different protein expression levels, probe labeling density, and recording time scales.

To address these limitations, we provide here a detailed quantitative description of the membrane dynamics and nanoscale distribution of NLGN1 in neurons, by correlating imaging experiments and computer simulations. We previously applied such a modeling approach to evaluate the mechanisms controlling AMPA receptor trafficking at synapses (Czöndör et al., 2012). In this study, we took advantage of our recently released simulator of membrane protein dynamics, FluoSim, that was thoroughly validated against live-cell and super-resolution imaging experiments performed on lamellipodial contacts mediated by NRXN-NLGN adhesions in heterologous cells (Lagardère et al., 2020). We extended this analysis to model NLGN1 dynamics and organization in the neuronal membrane, with a systematic comparison to single molecule tracking and localization studies, as well as long-term FRAP experiments performed in primary hippocampal neurons. This approach allowed us to unify the different imaging paradigms within a single framework using a small set of parameters, i.e., diffusion coefficients outside and inside synapses, as well as binding and unbinding constants to synaptic scaffolds, and photophysical rates. Overall, we offer a simulation package of NLGN1 dynamics at the single molecule and ensemble levels, that closely matches actual imaging data and can be further used to model other types of experiments and/or to adjust labeling conditions and microscopy settings.

RESULTS

Diffusional Trapping of NLGN1 at Synapses

To characterize NLGN1 dynamics in the dendritic membrane, we first experimentally tracked single recombinant surface NLGN1 molecules in dissociated rat hippocampal neurons using universal Point Acquisition In Nanoscale Topography (uPAINT) (Giannone et al., 2010). To detect NLGN1 at near-endogenous levels we electroporated neurons with shRNA against NLGN1, resulting in a 70% knock-down of native NLGN1 within 2 weeks (Chamma et al., 2016a), and replaced it with a rescue construct bearing a 15-aa N-terminal acceptor peptide (AP) tag which is biotinylated upon the co-expression of the biotin ligase BirA^{ER} (Howarth et al., 2005). Neurons also expressed Homer1c-DsRed as a post-synaptic marker (Kuriu et al., 2006) (**Figure 1A**). Biotinylated AP-NLGN1 at the cell surface was then detected by sparse labeling with STAR635P-conjugated monomeric streptavidin (mSA) (Demonte et al., 2013; Chamma et al., 2016a), upon oblique illumination from a 647 nm laser (**Figure 1C**). Single molecule trajectories were reconstructed offline (**Figure 1E**), and their diffusion coefficient was calculated and plotted on a logarithmic scale. The global distribution of diffusion coefficients for AP-NLGN1 was rather broad, but showed two clear peaks: i) a fast diffusing population (mostly corresponding to extra-synaptic NLGN1 molecules) which peaked at 0.15 $\mu m^2/s$, and a population corresponding to more confined synaptic molecules with diffusion coefficient peaking at 0.006 $\mu m^2/s$) (**Figure 1G**). When comparing neurons between days *in vitro* (DIV) 10 and 14, the fraction of highly mobile NLGN1 molecules decreased to the benefit of confined molecules, most likely reflecting the formation and/or maturation of synapses that occurs during that time frame (Chanda et al., 2017). Independently of neuronal age, a 20% fraction of immobile molecules was also detected and placed at $D = 10^{-5}$ $\mu m^2/s$. This value is comparable to that obtained with antibodies to AMPA receptors in similar imaging conditions (Nair et al., 2013), and might correspond to a variety of processes, including receptor endocytosis during live labeling, connection to the underlying cytoskeleton, and some degree of non-specific binding of the dye-conjugated probes to the cell surface.

Introducing Biophysical Parameters in FluoSim

FluoSim is an interactive simulator of membrane protein dynamics for fluorescence live-cell and super-resolution imaging (SRI) techniques (Lagardère et al., 2020). The program calculates in real time the localization and intensity of thousands of independent molecules in 2D cellular geometries, providing simulated data directly comparable to actual experiments. FluoSim requires several inputs: (1) a realistic cellular geometry defined from a microscopy image, comprising potential sub-compartments with specific trapping properties; (2) a given

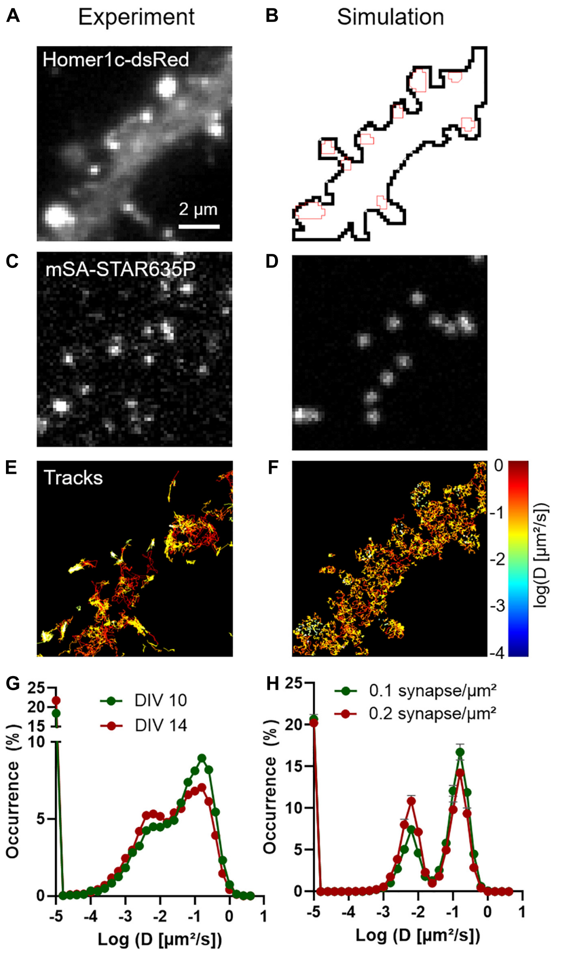

FIGURE 1 | Diffusional trapping of NLGN1 at synapses probed by uPAINT. **(A)** Raw image of a dendritic segment from a neuron co-expressing BFP + shRNA to NLGN1, AP-NLGN1, BirA^{ER}, and Homer1c-DsRed. **(B)** The Homer1c-DsRed image was used as a reference to draw the dendrite outline (black) and the PSDs (red areas) entered in the simulator. **(C)** Biotinylated AP-NLGN1 was sparsely labeled with STAR635P-conjugated mSA, allowing the tracking of individual NLGN1 molecules by uPAINT. **(D)** Realistic fluorescence rendering of simulated individual NLGN1 molecules in the defined geometry. **(E)** Image of individual NLGN1 trajectories (2667 tracks), with a color code representing the diffusion coefficient (red = fast diffusion, yellow = slow diffusion). Note the slower NLGN1 diffusion in PSDs. **(F)** Simulated NLGN1 trajectories based on the diffusion coefficients obtained from uPAINT and binding coefficients deduced from FRAP experiments (621 trajectories). The diffusion color code in logarithmic scale applies to both E and F panels. **(G,H)** Semi-log distribution of NLGN1 diffusion coefficients obtained by experiment and simulation, respectively. The experimental data is the average distribution of 13 and 9 neurons at DIV 10 and 14, respectively, the number of trajectories analyzed per cell ranging from 949 to 3113. The simulated data is the average ± sem of 5 independent simulations, with trajectory numbers between 625 and 638 per simulation, generated for two different synapse densities (0.1 and 0.2 synapse/μm^2, respectively) from the same dendritic geometry (135 μm^2). The coefficient χ^2 expressing the goodness of fit between simulated and experimental data was 5.6 and 10.5 for DIV 10 and 14 neurons, respectively, as calculated from 28 binned values.

number of molecules that populates the cellular geometry; (3) kinetic parameters (diffusion coefficients, binding and unbinding rates) characterizing the molecular system of interest; and (4) fluorescence photophysical rates related to the experiment to model (**Table 1**).

To model our experiments in dissociated neurons, we first entered in FluoSim a representative dendritic segment of 48 μm in length, populated by 24 synapses based on the Homer1c-DsRed fluorescence signal (**Figure 1B**). This represents on average one synapse every 2 μm, as previously reported in DIV 14 hippocampal cultures (Czöndör et al., 2012). In the absence of *a priori* knowledge of the surface density of recombinant NLGN1, we filled the dendritic geometry with an arbitrarily low number of molecules (i.e., 2,500 for a surface area of 70 μm^2). The synapse is considered as a trapping element for surface diffusing NLGN1 molecules, with excess number of slots based on the large number of scaffolding proteins per post-synaptic density (PSD) (>300 copies) (Chen et al., 2005; Sheng and Hoogenraad, 2007).

Regarding dynamic properties, NLGN1 molecules were allowed to diffuse relatively fast in the dendritic shaft (D_{out} = 0.15 $\mu m^2/s$), more slowly in the PSD due to steric hindrance (D_{in} = 0.06 $\mu m^2/s$), and very slowly when NLGN1 molecules were considered bound to the PSD (D_{trap} = 0.006 $\mu m^2/s$), based on the experimental peak values described above. We also defined a 20% fraction of immobile molecules, as found experimentally, that were placed randomly in the dendritic geometry. To take into account the fact that the synaptic cleft is a narrow cell-cell junction (Tanaka et al., 2012), where large molecules such as NLGN1 can have some difficulty to access, we also introduced in FluoSim a parameter called "crossing probability" ($P_{crossing}$ = 0.6) that represents the fraction of molecules allowed to enter the synapse through diffusion, based on our previous estimate of NRXN1β penetration in cell–cell contacts (Lagardère et al., 2020).

TABLE 1 | Biophysical parameters.

Category	Parameter	Notation	Unit/format	Experiment
Molecules	Copy number*		2,000–20,000	
Times	Length scale of simulations*		2,000–40,000 frames (40–1800 s)	
	Time step*	Δt	20–100 ms	
Diffusion coefficients	Outside synapse	D_{out}	0.15 $\mu m^2/s$	uPAINT
	Inside synapse	D_{in}	0.06 $\mu m^2/s$	Enrichment
	Trapped	D_{trap}	0.006 $\mu m^2/s$	uPAINT
	Crossing probability	$P_{crossing}$	60%	Enrichment
Kinetics	Binding rate	k_{on}	0.0008 s^{-1}	FRAP
	Unbinding rate	k_{off}	0.0005 s^{-1}	FRAP
	Immobile fraction		20%	uPAINT
Photophysics	Switch-on rate*	$K_{ON}{}^{Fluo}$	0.004–10 s^{-1}	uPAINT/STORM
	Switch-off rate*	$K_{OFF}{}^{Fluo}$	0–6.4 s^{-1}	uPAINT/STORM
	Photobleaching rate*	$K_{OFF}{}^{Bleach}$	4 s^{-1}	FRAP

**See the methods below for the specific molecule numbers and photo-physical parameters used in the various imaging modes (SPT, FRAP, dSTORM).*

To model the transitions between bound and unbound states, we introduced kinetic rates (k_{on} and k_{off}) as global parameters that characterize the dynamic trapping of NLGN1 at synapses through both extracellular and intracellular interactions. The reference values that describe the extracellular interaction between NLGN1 and NRXN1β are in the range of $k_{\text{on}} = 0.15\ \text{s}^{-1}$ and $k_{\text{off}} = 0.015\ \text{s}^{-1}$ (Comoletti et al., 2003; Saint-Michel et al., 2009; Lagardère et al., 2020). However, to match the FRAP experiments performed on AP-NLGN1 or NLGN1-GFP at synapses (Chamma et al., 2016a) (also see below), we had to choose interaction rates 30–150 fold lower ($k_{\text{on}} = 0{,}0008\ \text{s}^{-1}$ and $k_{\text{off}} = 0.0005\ \text{s}^{-1}$). This finding indicates that NLGN1 is not solely retained at synapses through its *trans*-synaptic binding to NRXNs, but also forms long-lived bonds with the post-synaptic scaffold, and that the combination of these extracellular and intracellular interactions overall contributes to very low kinetic rates. The molecular enrichment, defined as the ratio between NLGN1 accumulated at PSDs versus NLGN1 present in the shaft, is theoretically given by the formula ($P_{crossing}\ D_{out}/D_{in}$) $(1 + k_{on}/k_{off})$ (Lagardère et al., 2020), and is slightly lowered by the presence of immobile NLGN1 that are placed randomly. Given the chosen parameters, the synaptic enrichment of NLGN1 is predicted to be around 3.5, close to values measured earlier (Chamma et al., 2016a; Toledo et al., 2022).

With respect to photophysical parameters, we defined a fluorescence switch-on rate ($k_{\text{ON}}^{Fluo} = 0.03\ \text{s}^{-1}$) that mimics the stochastic binding of the mSA probe in uPAINT so as to match the average surface density of emitting fluorophores ($0.6/\mu\text{m}^2$) per time frame ($\Delta t = 20$ ms), which is considered as constant. Note that in the absence of knowledge about the actual number of NLGN1 molecules in the neuronal membrane (see direct stochastic optical reconstruction microscopy (dSTORM) experiments below), this value is somewhat arbitrary since the parameter $k_{\text{ON}}^{\text{Fluo}}$ is inversely related to the surface density of molecules introduced in the geometry, i.e., if we placed more molecules we would have to choose a lower $k_{\text{ON}}^{\text{Fluo}}$ and vice versa. Besides, we set a fluorescence switch-off rate ($k_{\text{OFF}}^{\text{Fluo}} = 5.4\ \text{s}^{-1}$) characterizing the photobleaching rate of the dye STAR635P in the experimental laser excitation conditions, as calculated from the exponential distribution of trajectory durations (mean 0.9 ± 0.02 s, $n = 6314$ traces). We also introduced realistic single molecule fluorescence rendering parameters for STAR635P ($\sigma = 0.22\ \mu$m, FWHM = 0.53 μm) (**Figure 1D**).

Modeling NLGN1 Diffusive and Confined Behaviors

We then performed SPT simulations of the same duration as for uPAINT experiments (2000 frames = 40 s), and analyzed the trajectories of virtual single molecules with the SPT Analysis menu in FluoSim. Using these parameters, FluoSim generated trajectory maps that mimicked experimental ones with clear confinement events inside synapses (**Figure 1F**), and global diffusion coefficient distributions that aligned well on the two experimental peaks (**Figure 1H**). Experimental distributions were somewhat more spread than theoretical ones, most likely because of local membrane heterogeneities that can contribute to NLGN1 confinement outside synapses, and/or more complex binding kinetics which are not accounted for in the model. To estimate the influence of the model parameters on the balance between mobile and confined NLGN1 populations (characterized by the relative peaks at $D_{\text{out}} = 0.15\ \mu\text{m}^2/\text{s}$ and $D_{\text{trap}} = 0.006\ \mu\text{m}^2/\text{s}$, respectively), we ran a series of simulations by individually varying D_{in}, k_{on}, or k_{off}, while adjusting P_{crossing} so as to keep a constant NLGN1 synaptic enrichment (**Supplementary Figures 1, 2**). The fraction of confined NLGN1 molecules increased at the expense of fast-diffusing molecules with increasing k_{on} or decreasing k_{off}, i.e., either way by enhancing the trapping affinity. Changing D_{in} did not influence much the ratio between confined and mobile NLGN1 molecules, most likely because the fraction of freely diffusing molecules in synapses is small compared to bound ones. To evaluate the impact of changing synapse density on the histograms of NLGN1 diffusion coefficients, we kept the same dendritic geometry but varied the number of active PSDs able to trap NLGN1 (from 0 to 24), while keeping the other parameters as constant (**Supplementary Figures 1, 2**). This is supposed to mimic the effect of neuronal development, where the number of synapses increases with time in culture (Czöndör et al., 2012; Chanda et al., 2017). The simulations show that the fraction of confined NLGN1 molecules increases significantly with synapse density, independently of changes in binding kinetics. This result indicates that the increase in overall NLGN1 confinement observed between DIV 10 and 14 might be solely due to an increase in synapse number, and not necessarily to a change in the trapping properties of the PSD. Interestingly, those data show that although NLGN1 is enriched at synapses, a large reservoir of NLGN1 (>50%) stays mobile in the dendritic shaft.

Transient Confinement Domains of NLGN1 at Synapses

In addition to providing an estimation of diffusion coefficients, uPAINT experiments can also be used to generate localization maps representing the sum of all single molecules detected over the acquisition period. For molecules that diffuse fast in the extra-synaptic space, the localization distribution is spread over a cloud of individual points, whereas for molecules that are dynamically trapped at synapses and in the dendritic shaft, the localization map forms "hot spots" that represent transient confinement domains (**Figures 2A,C**). The size of these domains depends on the diffusion coefficient of the molecule trapped in the synapse, the potential movement of the PSD during the acquisition period (a process called "morphing"; Blanpied et al., 2008), and the localization precision of the optical system. As a rule of thumb, the characteristic radius r of such domains obeys the following equation: $\langle r^2 \rangle = 4\ D_{\text{trap}}\ \tau_{\text{ON}}$, where D_{trap} is the diffusion coefficient of NLGN1 molecules trapped at synapses (in the order of $6 \times 10^{-3}\ \mu\text{m}^2/\text{s}$) and τ_{ON} is the time during which an mSA probe emits fluorescence in uPAINT illumination conditions ($t_{\text{ON}} = 1/k_{\text{OFF}}^{\text{Fluo}} = 200$ ms). Thus, r is in the range of 69 nm. As determined experimentally, the size of the NLGN1 confinement domains was 87 ± 2 nm (mean ± SEM, $n = 688$ clusters from 2 neurons) (**Figure 2E**), close to this theoretical estimate. To model the formation of such NLGN1 confinement domains, we uploaded FluoSim with the

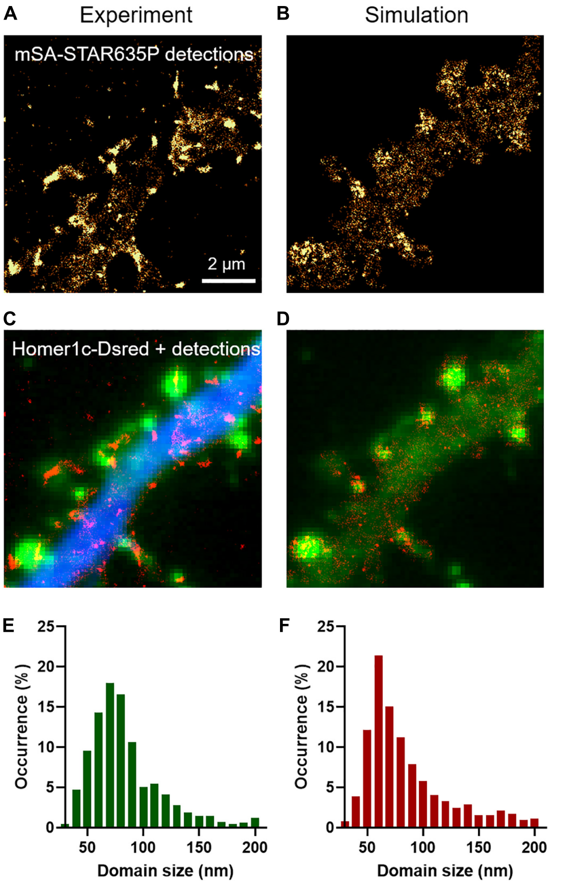

FIGURE 2 | Transient confinement domains of NLGN1. **(A)** Sum of all single mSA-STAR635P localizations detected over a live sequence of 2,000 frames of 20 ms in the dendritic segment of a neuron expressing BFP + shRNA to NLGN1, AP-NLGN1, BirA^{ER}, and Homer1c-DsRed. The total number of localizations was 29,303. The gold color codes for the surface density of accumulated NLGN1 molecules over time. **(B)** Corresponding simulated image of NLGN1 localizations, generated by considering the diffusional trapping of NLGN1 at PSDs and the photophysics of mSA-STAR635P emission. The total number of localizations is 29,730. **(C)** Merged image showing the integrated number of experimental single molecule localizations per pixel (red), Homer1c-DsRed (green), and BFP (blue). **(D)** Merged image showing the integrated number of simulated single molecule localizations per pixel (red) and Homer1c-DsRed (green). **(E,F)** Distribution of the size (FWHM) of the NLGN1 confinement domains obtained by experiment and simulation, respectively. The experimental and simulated distributions of domain sizes were compared by a non-parametric Mann–Whitney test (non-significant difference, *P*-value = 0.74).

same set of parameters as above, and generated super-resolved maps integrating all single molecule detections throughout a live uPAINT sequence of 2,000 frames, using a zoom of 5 with respect to original images (pixel size 32 nm) and a localization precision σ = 25 nm (FWHM = 58 nm). This approach resulted in the clear visualization of confinement domains localized at the PSD where NLGN1 molecules get trapped (**Figures 2B,D**). The size of the domains was on average 92 ± 2 nm (n = 541 clusters from 12 simulations), with a statistically similar distribution as the one determined experimentally (**Figure 2F**).

Long Term Turnover of NLGN1 at Synapses

To characterize the long term turnover of NLGN1 at synapses, we performed FRAP experiments using a NLGN1 construct bearing an intracellular GFP tag located just below the transmembrane domain (Dresbach et al., 2004). The NLGN1-GFP protein accumulated at synapses almost as well as AP-NLGN1 labeled with mSA (Chamma et al., 2016a) (i.e., synaptic enrichment = 3.1 ± 0.2, n = 32 synapses from nine neurons). When photobleaching was performed on synaptic NLGN1-GFP, there was a fast initial 20% recovery that likely corresponds to diffusional exchange, followed by a slower almost linear phase that reached 50% recovery in 30 min, which reflects the continuous binding and unbinding of NLGN1 at the synapse (**Figures 3A,C**). Control unbleached synapses did not display any significant drop in NLGN1-GFP fluorescence, revealing negligible observational photobleaching. Additional FRAP experiments with a lower sampling rate in neurons co-expressing NLGN1-GFP and Xph20-mRuby2, an intrabody specific to PSD-95 (Rimbault et al., 2019, 2021), showed that photobleached NLGN1-GFP was essentially post-synaptic (**Supplementary Figure 3A**). Furthermore, the NLGN1-GFP fluorescence recovery after 1 h was 60%, a value in line with the first round of experiments performed at higher sampling rate (**Supplementary Figures 3B,C**).

To mimic FRAP experiments, we introduced a large number of molecules in the simulator (25,000 copies for a dendritic region of 135 μm^2, corresponding to a surface density of 185 molecules/μm^2) and generated fluorescence-like images by defining a Gaussian intensity profile for each GFP-tagged molecule (σ = 0.17 µm, FWHM = 0.47 µm) (**Figure 3B**). To induce local photo-bleaching, we chose a bleaching rate (4.0 s^{-1}) reproducing the initial drop of fluorescence observed experimentally (~75% in 500 ms). We then entered the NLGN1 extra-synaptic and synaptic diffusion coefficients (D_{out} and D_{trap}) previously obtained from SPT data. We ran a series of simulations by individually varying D_{in}, k_{on}, or k_{off}, while adjusting $P_{crossing}$ so as to keep a constant NLGN1 synaptic enrichment of 3.5 (**Supplementary Figure 4**). D_{in} had mild effect on the simulated FRAP curve, i.e., increasing D_{in} slightly moved up the long term slope of the FRAP curve (**Supplementary Figure 4C**). Increasing k_{on} essentially reduced the fast recovering fraction, without changing much the long term slope (**Supplementary Figure 4D**). In contrast, increasing k_{off} dramatically accelerated the whole FRAP curve (**Supplementary Figure 4E**). Based on these simulated curves, we chose the best pair of coefficients that matched the experimental 30 min FRAP curve, i.e., k_{off} = 0.0005 s^{-1} and k_{on} = 0.0008 s^{-1}, as well as intermediate values D_{in} = 0.06 $\mu m^2/s$ and $P_{crossing}$ = 0.6 (**Figure 3C**), by minimizing a least squares function (**Supplementary Figure 4F**). The simulated curves also fit very well the 1 h FRAP experiment performed at lower sampling rate (**Supplementary Figures 3B,C**). With these parameters, the simulated images at steady state predicted NLGN1 enrichment in the post-synapse that matched experimental values (3.25 ± 0.05, n = 18 simulations) (unpaired t-test, no significant difference between

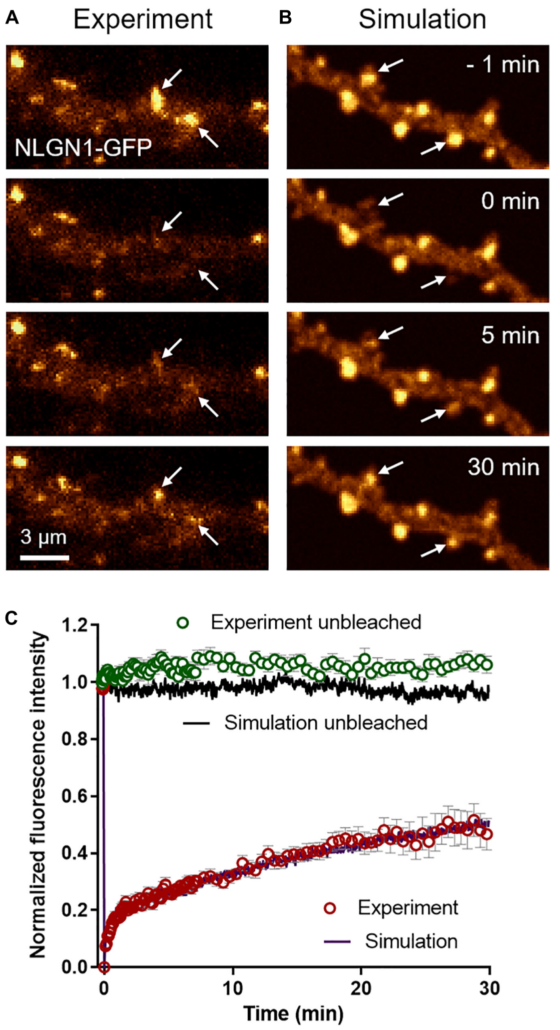

FIGURE 3 | Long term turnover of NLGN1 at synapses monitored by FRAP. **(A)** Representative time sequence of a FRAP experiment performed on a neuron expressing NLGN1-GFP. The GFP signal is color coded in gold to better visualize intensity changes over time. NLGN1-GFP was photobleached at time 0 with a focused 491-nm laser beam at two specific synapses where NLGN1 was accumulated (arrows), and fluorescence recovery was monitored for 30 min. **(B)** Corresponding simulated FRAP sequence. The dendritic geometry of 135 μm^2 was filled with 25,000 individual molecules, each with a realistic point spread function, together providing a fluorescence-like image that is also color coded in gold. The fluorescence intensity of molecules inside two PSDs was decreased by 75% at time zero (arrows), mimicking the action of the laser. **(C)** Normalized FRAP curves obtained by experiment (open circles) in bleached synapses (red, mean ± SEM of 25 synapses from 4 neurons) or unbleached synapses (green, mean ± SEM of 11 synapses from 4 neurons) and corresponding simulations (solid curves, average of 10 repetitions each, SEM < 1% mean, not shown). The Spearman correlation coefficient between experimental and simulated data for bleached synapses was 0.98, while the parameter χ^2 estimating the goodness of fit was 0.05, both values being calculated out of 100 time points.

experiment and simulation, $P = 0.6$). Thus, whereas uPAINT provides precise estimates of NLGN1 diffusion coefficients outside and inside synapses, FRAP experiments together with the measurement of NLGN1 synaptic enrichment allow for a determination of long-term trapping rates. Overall, the combination of single molecule and ensemble measurements offers a consistent set of parameters to model NLGN1 dynamics within the same framework.

Nanoscale Organization of NLGN1 at Synapses

To characterize the nanoscale organization of NLGN1 in the neuronal membrane and get access to the number of NLGN1 molecules in synapses, we performed dSTORM experiments on neurons expressing shRNA to NLGN1 plus rescue AP-NLGN1 (**Figure 4A**). Biotinylated AP-NLGN1 was densely labeled with Alexa647-conjugated mSA in live conditions, followed by fixation, and the stochastic emission of single fluorophores was induced (**Figures 4C,E**). When super-resolved images were reconstructed from individual detections, NLGN1 filled PSDs labeled with the Xph20-GFP intrabody to PSD-95 (Rimbault et al., 2019, 2021) without forming any specific sub-domain (**Figures 4G,I**), as previously reported (Chamma et al., 2016a). In the dendritic shaft, NLGN1 showed a fairly homogeneous membrane localization, likely corresponding to the fast-diffusing molecules detected live by uPAINT. To simulate stochastic fluorescence emission of Alexa647 dyes (Dempsey et al., 2011), we first calculated the switch-on rate ($k_{ON}{}^{Fluo} = 0.004\ s^{-1}$) and switch-off rate ($k_{OFF}{}^{Fluo} = 6.3\ s^{-1}$) of isolated substrate-bound mSA-Alexa647 probes in dSTORM imaging conditions (**Supplementary Figure 5**; Lagardère et al., 2020). To estimate the number of Alexa647 dyes conjugated per mSA, we counted the photobleaching steps of single substrate-bound mSA-Alexa647 molecules in Tyrode solution (**Supplementary Figure 6**). We visualized essentially one or two photobleaching steps, corresponding to an average of 1.26 Alexa dyes per mSA, in agreement with a 1.3 degree of labeling (DOL) separately measured by spectroscopy. To reproduce dSTORM experiments performed on AP-NLGN1 labeled with mSA-Alexa647, we then introduced in the imported geometry of surface area 118 μm^2 (**Figure 4B**) the number of mSA molecules corresponding to the average number of experimental detections per frame (13.3) (**Figures 4C–F**) divided by the on-off duty cycle of mSA-Alexa647 (0.0006), giving a total of 19,843 mSA molecules (surface density = 167 molecules/μm^2). After an equilibration period allowing NLGN1 molecules to accumulate at synapses with kinetic rates $k_{on} = 0.0008\ s^{-1}$ and $k_{off} = 0.0005\ s^{-1}$ as validated from FRAP experiments, we further set all diffusion coefficients to zero to mimic cell fixation. We then simulated the accumulation of single molecule localizations for 40,000 frames, including a realistic localization precision ($\sigma = 25$ nm, FWHM = 58 nm), to mimic the experimental super-resolved maps of NLGN1 distribution (**Figures 4H,J**). As expected, the overall number of single molecule detections obtained in simulations precisely matched experimental ones, thereby validating the measurement of photo-physical parameters made in parallel. In addition, simulated images faithfully reproduced the nanoscale distribution of NLGN1 outside and inside synapses observed experimentally (**Figures 4G–J**), and gave NLGN1 synaptic enrichment values (3.10 ± 0.08, $n = 44$ PSDs, two dendritic segments) similar to experimental ones (3.24 ± 0.12, n = 111 PSDs, five dendritic segments). Interestingly, we could then use the density of virtual molecules introduced in the model (19,843 mSA copies spread over the 118 μm^2 dendritic area) as a reference to predict the average copy number of mSA molecules bound to NLGN1 at steady state in each synapse. To this aim, we just generated a single frame snapshot in the super-resolution imaging (SRI) menu of FluoSim, setting the photophysical parameters $k_{ON}{}^{Fluo} = 10\ s^{-1}$ and $k_{OFF}{}^{Fluo} = 0\ s^{-1}$ so as to make all fluorophores visible, then counted the number of molecules per PSD (n = 272 ± 20, n = 44 PSDs from two dendritic segments).

DISCUSSION

In summary, we provide here a detailed description of the surface trafficking of NLGN1 in the dendritic membrane by interpreting fluorescence live-cell and super-resolution imaging experiments using a quantitative computer software, FluoSim (Lagardère et al., 2020). The advantage of this correlative approach is that different imaging paradigms can be modeled using a small set of dynamic and photophysical parameters. Interestingly, each technique is used to feed the program with critical parameters that are not easily accessible with other imaging methods. We give a schematic overview of our strategy to estimate one by one the parameters entered in the simulator (**Supplementary Figure 7**). Specifically, single molecule tracking (uPAINT) provides precise mean values of NLGN1 diffusion coefficients inside and outside synapses, but because of the short duration of the trajectories, fails to capture the long-term residence time of NLGN1 in PSDs. In contrast, FRAP gives a single curve whose fit includes several unknown dynamic coefficients, but when combined with the calculation of the synaptic enrichment of NLGN1 and the diffusion coefficients inferred from uPAINT, the long range recovery provides estimates of the binding and unbinding rates of NLGN1 to the PSD scaffold. Finally, dSTORM yields static super-resolution maps of NLGN1 distribution in the dendritic membrane that can be faithfully reproduced by filling the model with a high density of molecules made immobile to mimic chemical fixation, after an equilibration period to reach steady-state distribution. Strikingly, by considering the photophysics of the Alexa647-conjugated mSA probe, the interpretation of dSTORM sequences by FluoSim provides an estimate of the molecular density of NLGN1 in the neuronal membrane, and hence of NLGN1 copy number in single PSDs.

We thereby calculate that a PSD contains on average 272 mSA molecules bound to NLGN1. Although mSA has four potential NHS conjugation sites (N-terminus plus 3 accessible lysine residues) (Chamma et al., 2017), such that each mSA molecule may carry a different number of fluorophores (from zero to 4), we made sure to use an mSA preparation in which the average number of Alexa647 dyes was close to 1 (DOL = 1.3). In any case, the DOL should not influence much the photophysical rates in dSTORM, as reported for antibodies with up to eight conjugated Alexa647 dyes (Sauer et al., 2020). Further assuming that both NLGN1 subunits are biotinylated and that each one binds an mSA probe, we estimate the presence of ∼136 NLGN1 dimers per PSD. We can moderate this number by almost a factor of two by considering the fact that, despite our NLGN1 replacement strategy, the rescue construct is most likely over-expressed by two-fold over endogenous NLGN1 (Chamma et al., 2016a; Toledo et al., 2022). In addition, according to the kinetic parameters of the model, only a 70% fraction of synaptic NLGN1 is actually bound to the PSD, while the other 30% fraction is free to diffuse in the synapse. This finally yields a value of 48 NLGN1 dimers bound to the PSD, which is 6–10 fold lower than the estimated number of PSD-95 proteins that can accommodate NLGN1 anchoring at PSDs (between 300 and 500) (Chen et al., 2005; Sheng and Hoogenraad, 2007), especially considering that other PDZ-domain containing proteins such as PSD-93, SAP-97, SAP-102, and S-SCAM can also bind NLGN1 through its C-terminal PDZ domain binding motif (Irie et al., 1997; Hirao et al., 1998). Thus, our model hypothesis that the number of PSD binding slots is in excess of NLGN1 molecules should be valid. Based on published crystal structures (Araç et al., 2007; Fabrichny et al., 2007; Chen et al., 2008), a NLGN1 dimer is likely to occupy a projected area of 5 nm × 12 nm = 60 nm^2 in the plasma membrane, while a typical PSD has a surface area of roughly 350 nm × 350 nm, i.e., 122,000 nm^2 (Sheng and Hoogenraad, 2007). Thus, 48 NLGN1 molecules would represent 2,880 nm^2/122,000 nm^2 = 2.4% of the PSD area which is a reasonable number and leaves room to many other membrane molecules including lipids, adhesion proteins, and neurotransmitter receptors (Chen et al., 2005; Lowenthal et al., 2015). In comparison, a recent proteomics study provides an estimate of 21 NLGN3 molecules per PSD (Lowenthal et al., 2015), which is in the same order of magnitude especially considering that NLGN3 are present at both excitatory and inhibitory synapses (Budreck and Scheiffele, 2007).

The rate constants k_{on} and k_{off} introduced in the model are pooled parameters that represent the overall anchorage of NLGN1 to the synapse, taking into consideration multiple protein-protein interactions, including the extracellular binding of NLGN1 to pre-synaptic NRXNs (Dean et al., 2003), and the intracellular binding to scaffolding proteins, e.g., PDZ domain containing proteins such as PSD-95 (Irie et al., 1997; Mondin et al., 2011), and potentially other non-canonical binding partners (Shipman et al., 2011). Fitting our FRAP data indicates that NLGN1 dissociates very slowly from the synapse, potentially due to the formation of parallel interactions between dimeric NLGN1 and PDZ domain containing scaffolding proteins. In any case, the calculated dissociation rate k_{off} is two orders of magnitude lower that the dissociation rate between purified NLGN1 and NRXN1β (Comoletti et al., 2003), indicating that extracellular NRXN-NLGN interactions are not alone responsible for NLGN1 retention at the synapse. The corresponding association rate k_{on} calculated by further fitting experimental NLGN1 synaptic enrichment values was also much lower than the value previously found by quantifying the detachment rate of NRXN1β-Fc coated Quantum dots from the surface of neurons over-expressing NLGN1 (Saint-Michel et al., 2009), or from FRAP experiments performed on GFP-NRXN1β accumulated at contacts with COS-7 cells expressing NLGN1-mCherry (Lagardère et al., 2020). This finding indicates that the kinetic rate k_{on} increases

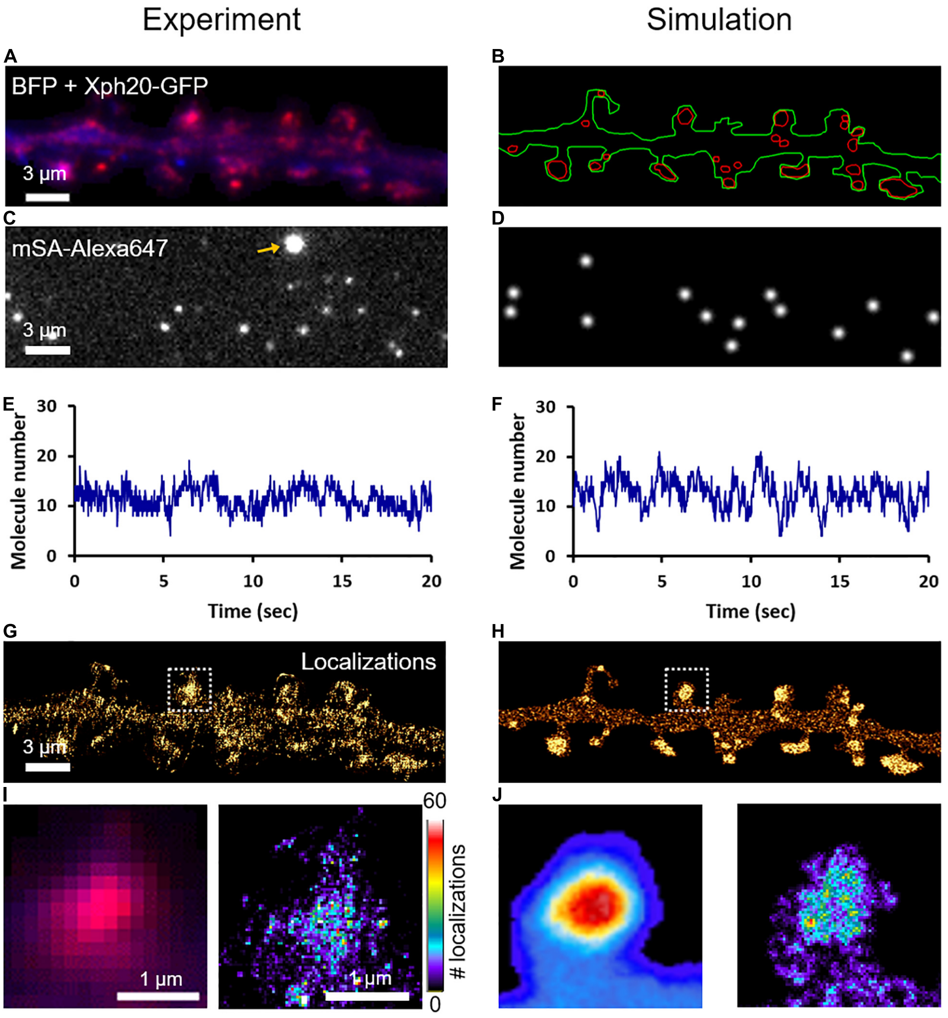

FIGURE 4 | Nanoscale organization of NLGN1 at synapses characterized by dSTORM. **(A)** Dual color image of a dendritic segment from a neuron co-expressing BFP (blue) + shRNA to NLGN1, AP-NLGN1, BirA^{ER}, and Xph20-GFP (red). **(B)** The BFP and Xph20-GFP images, respectively, were used as reference to draw the dendrite outline (green) and the PSDs (red areas) entered in the simulator. **(C)** Representative single frame image of a dSTORM sequence performed on AP-NLGN1 labeled with Alexa647-conjugated mSA. The yellow arrow indicates a bright fluorescent bead used to correct for drift. **(D)** Simulated image showing single molecule fluorescence emission in the same cell geometry, each with a Gaussian intensity profile. **(E,F)** Number of single molecules per frame detected in the defined geometry for experiment or simulation, respectively, and plotted over time. **(G)** Experimental super-resolved image generated from 470,821 single molecule localizations (pixel size 32 nm, total acquisition time 800 s). Note the accumulation of NLGN1 in PSDs. **(H)** Simulated super-resolved map with a localization precision of 58 nm (FWHM). The total number of single molecule detections is 498,447. **(I)** Zoom on one dendritic spine showing the low resolution merged image between BFP (blue) and PSD (magenta), and the super-resolved dSTORM image of NLGN1 distribution in false color. **(J)** Simulated heat map images showing the low and high resolution images of NLGN1 accumulation in the PSDs of the same spine. The color code for the number of single molecule localizations per pixel applies to the right images of both panels **(I,J)**.

with NLGN1 expression level, as expected from a ligand-receptor reaction.

A precise evaluation of the contribution of each of these protein interactions to the actual residence time of NLGN1 at synapses will require a complete structure-function analysis of the dynamics and organization of NLGN1 mutants unable to bind specific partners. In this direction, our preliminary experiments indicate that GPI-anchored NLGN1 exhibits a diffuse localization in the dendritic membrane with no particular enrichment at post-synapses (data not shown), suggesting that the NLGN1 intracellular domain is essential for the synaptic retention of NLGN1. In addition, knocking down MDGAs as endogenous competitors of NRXN-NLGN adhesion in hippocampal neurons increases the density of excitatory synapses and reduces global NLGN1 diffusion without significantly affecting the accumulation of NLGN1 at PSDs (Toledo et al., 2022), further suggesting that the binding of NLGN1 to NRXNs does not play a major role in the synaptic retention of NLGN1. Together, these results reinforce our concept that the NLGN1 intracellular domain plays a critical role in excitatory synapse differentiation (Shipman et al., 2011; Haas et al., 2018; Letellier et al., 2018, 2020). An intracellular coupling of NLGN1 to the actin network underlying the plasma membrane (Han et al., 2017) e.g., through the WAVE regulatory complex (Chen et al., 2014), might be responsible for the transient confinement of NLGN1 in dendritic sub-domains, that was not described by our model which focuses on the selective trapping of NLGN1 at PSDs.

In addition to providing a quantitative interpretation for biological data, the simulation approach described here allows a better understanding of some subtle experimental findings linked to SRI. For example, the projection of all individual molecule detections obtained in uPAINT provides a super-resolved image where hot spots of protein localization appear, corresponding to the confinement domains of a subset of molecules. Because of the live imaging conditions and the intrinsic movement of synapses, the localization of these domains can evolve over time (Nair et al., 2013). These objects are thus different from the static protein "nanodomains" that can be identified from stimulated emission depletion (STED) or dSTORM images acquired after saturating protein labeling and chemical fixation (Nair et al., 2013; Chamma et al., 2016a,b; Tang et al., 2016; Hruska et al., 2018). Things can be complicated even more by the existence of synapses containing multiple PSDs (Hruska et al., 2018). Thus, care must be taken in interpreting super-resolution images, and computer simulations can be helpful to put realistic values on the numbers of labeled molecules, the photophysical parameters behind single molecule fluorescence emission peaks, and the time frame of the acquisition sequences, that are all susceptible to affect the actual representation of the imaging data. Finally, one limitation of FluoSim is that it is currently constrained to the simulation of 2D images, while the actual dynamics of membrane molecules including NLGN1 takes place in more complex 3D geometries such as the surface of a dendrite. Theoretical analyses have been published that estimate the error made by approximating 3D diffusion by a 2D diffusion coefficient (Renner et al., 2011). This type of correction might be applied while waiting for a 3D version of the simulator in combination with 3D single molecule tracking of NLGN1.

MATERIALS AND METHODS

DNA Plasmids and Proteins

shRNA to NLGN1 (Chih et al., 2005) containing a GFP reporter was a gift from P. Scheiffele (Biozentrum, Basel, Switzerland). shRNA to NLGN1 containing a BFP reporter was described earlier (Toledo et al., 2022). NLGN1 with GFP insertion at position 728 below the transmembrane domain (Dresbach et al., 2004) was a gift from T. Dresbach (University Medical Center, Göttingen, Germany). AP-NLGN1 and BirA^{ER} (Howarth et al., 2005) were gifts from A. Ting (Stanford University, Palo Alto, CA, United States). Homer1c-DsRed was described earlier (Mondin et al., 2011). shRNA-resistant AP-NLGN1 was described earlier (Chamma et al., 2016a; Toledo et al., 2022). The specific intrabody to PSD-95, Xph20 (Addgene ID 135530) was described recently (Rimbault et al., 2019, 2021), and we used both GFP- and mRuby-tagged versions. The bacterial production of mSA, purification, and conjugation to organic dyes (STAR635P or Alexa647) to a final DOL comprised between 0.6 and 2 (dye to protein ratio), were described previously (Chamma et al., 2017).

Rat Hippocampal Cultures and Electroporation

Gestant Sprague-Dawley rat females were purchased from Janvier Labs (Saint-Berthevin, France). Animals were handled and killed according to European ethical rules. Dissociated neuronal cultures were prepared from E18 rat embryos as previously described (Kaech and Banker, 2006). Dissociated cells were electroporated with the Amaxa system (Lonza, Basel, Switzerland) using 300,000 cells per cuvette. The following plasmid combinations were used. For uPAINT: Homer1c-DsRed: shNLGN1-GFP: AP-NLGN1rescue: BirA^{ER} (1:1:1:1 μg DNA). For dSTORM: Xph20-GFP: shNLGN1-EBFP: AP-NLGN1rescue: BirA^{ER} (1:1:1:1 μg DNA). For FRAP, NLGN1-GFP (3 μg DNA) or NLGN1-GFP: Xph20-mRuby2 (1:1 μg DNA). Electroporated neurons were resuspended in Minimal Essential Medium (Thermo Fisher Scientific, Illkirch, France #21090.022) supplemented with 10% Horse serum (Invitrogen, Illkirch, France) (MEM-HS), and plated on 18 mm glass coverslips coated with 1 mg/mL polylysine (Sigma-Aldrich, Saint-Quentin-Fallavier, France #P2636) overnight at 37°C. Three hours after plating, coverslips were flipped onto 60 mm dishes containing 15 DIV rat hippocampal glial cells cultured in Neurobasal plus medium (Gibco, Illkirch, France, #A3582901) supplemented with 2 mM glutamine and 1x B27^{TM} plus Neuronal supplement (Gibco, Illkirch, France, #A3582801). Neurons were cultured during 10–14 days at 37°C and 5% CO_2. Astrocyte feeder layers were prepared from the same embryos, plated between 20,000 and 40,000 cells per 60 mm dish previously coated with 0.1 mg/mL polylysine and cultured for 14 days in MEM containing 4.5 g/L glucose, 2 mM L-glutamax (Sigma-Aldrich, Saint-Quentin-Fallavier, France #3550-038) and 10% horse serum. Ara C (Sigma-Aldrich, Saint-Quentin-Fallavier, France #C1768) was added after 3 DIV at a final concentration of 3.4 μM.

Single Molecule Tracking (uPAINT Experiments)

Universal point accumulation in nanoscale topography (uPAINT) was carried out as reported (Giannone et al., 2010; Chamma et al., 2016a). Neurons at DIV 10 or 14 were mounted in Tyrode solution (15 mM D-glucose, 108 mM NaCl, 5 mM KCl, 2 mM $MgCl_2$, 2 mM $CaCl_2$ and 25 mM HEPES, pH 7.4) containing 1% globulin-free BSA (Sigma-Aldrich, Saint-Quentin-Fallavier, France, #A7638) in an open Inox observation chamber (Life Imaging Services, Basel, Switzerland). The chamber was placed on a motorized inverted microscope (Nikon Ti-E Eclipse) equipped with perfect focus system and an APO TIRF 100x/1.49 NA oil immersion objective, and enclosed in a thermostatic box (Life Imaging Services, Basel, Switzerland) providing air at 37°C. Neurons co-expressing shRNA to NLGN1 containing a GFP reporter and Homer1c-DsRed were detected using a mercury lamp (Nikon Xcite) and the following filter sets (Semrock, Rochester, NY, United States): EGFP (Excitation: FF01-472/30; Dichroic: FF-495Di02; Emission: FF01-525/30) and DsRed (Excitation: FF01-543/22; Dichroic: FF-562Di02; Emission: FF01-593/40). Recombinant AP-NLGN1 biotinylated by BirA^{ER} was sparsely labeled using a low concentration of

STAR635P-conjugated mSA (1 nM). A four-color laser bench (405/488/561 nm lines, 100 mW each; Roper Scientific, Evry, France and 1 W 647 nm line, MPB Communications Inc., Pointe-Claire, QC, Canada) is connected through an optical fiber to the Total Internal Reflection Fluorescence (TIRF) illumination arm of the microscope. Laser power was controlled through an acousto-optical tunable filter (AOTF) driven by the Metamorph software (Molecular Devices, San Jose, CA, United States). STAR635P was excited with the 647 nm laser line (∼2 mW at the objective front lens), through a four-band beam splitter (BS R405/488/561/635, Semrock, Rochester, NY, United States). Samples were imaged by oblique laser illumination, allowing the excitation of individual mSA-STAR635P molecules bound to the cell surface, without illuminating probes in solution. Fluorescence was collected on an EMCCD camera with 16 μm pixel size (Evolve, Roper Scientific, Evry, France), using a FF01-676/29 nm emission filter (Semrock, Rochester, NY, United States). Stacks of 2,000 consecutive frames were obtained from each cell with an integration time of 20 ms. Images were analyzed using PALM-Tracer, a program running on Metamorph and based on wavelet segmentation for molecule localization and simulated annealing algorithms for tracking (generously provided by J. B. Sibarita, Bordeaux) (Izeddin et al., 2012). This program allows for the tracking of localized molecules through successive images. Trajectories longer than 10 frames (200 ms) were selected. The diffusion coefficient, D, was calculated for each trajectory, from linear fits of the first 4 points of the mean square displacement (MSD) function versus time. Trajectories with displacement inferior to the pointing accuracy (∼50 nm in uPAINT conditions) whose MSD function cannot be properly fitted are arbitrarily placed at $D = 10^{-5}$ $\mu m^2 s^{-1}$.

Direct Stochastic Optical Reconstruction Microscopy Experiments

Neurons co-expressing shRNA to NLGN1 containing an EBFP reporter, Xph20-GFP, rescue AP-NLGN1, and BirA^{ER} were surface-labeled with a high concentration (100 nM) of Alexa647-conjugated mSA in Tyrode solution containing 1% globulin-free BSA (Sigma-Aldrich, Saint-Quentin-Fallavier, France, #A7638) for 10 min, rinsed and fixed with 4% PFA-0.2% glutaraldehyde in PBS for 10 min at room temperature, and stored in PBS at 4°C until imaging (within a few days). Cells were imaged in Tris-HCl buffer (pH 7.5), containing 10% glycerol, 10% glucose, 0.5 mg/mL glucose oxidase (Sigma-Aldrich, Saint-Quentin-Fallavier, France, #G2133), 40 mg/mL catalase (Sigma-Aldrich, Saint-Quentin-Fallavier, France, #C100-0,1% w/v) and 50 mM β-mercaptoethylamine (MEA) (Sigma-Aldrich, Saint-Quentin-Fallavier, France, #M6500) (Heilemann et al., 2008). The same microscope described for uPAINT was used. Detection of the EBFP reporter was made with the following filter set from Semrock, Rochester, NY, United States (Excitation: FF02-379/34; Dichroic: FF-409Di03; Emission: FF01-440/40). Pumping of Alexa647 dyes into their triplet state was performed for several seconds using ∼60 mW of the 647 nm laser at the objective front lens. Then, a lower power (∼20 mW) was applied to detect the stochastic emission of single-molecule fluorescence, which was collected using the same optics and detector as described above for uPAINT. 10 streams of 4,000 frames each were acquired at 50 Hz. Multi-color 100-nm fluorescent beads (Tetraspeck, Invitrogen, Illkirch, France) were used to register long-term acquisitions and correct for lateral drift. The localization precision of our imaging system in dSTORM conditions is around 60 nm (FWHM). Stacks were analyzed using the PALM-Tracer program, allowing for the reconstruction of a unique super-resolved image of 32 nm pixel size (zoom 5 compared to the original images) by summing the intensities of all single molecules localized (1 detection per frame is coded by an intensity value of 1).

Fluorescence Recovery After Photobleaching Experiments and Analysis

Neurons expressing NLGN1-GFP were mounted in Tyrode solution, and observed under the same set-up used for uPAINT and dSTORM. The laser bench has a second optical fiber output connected to an illumination device containing two *x/y* galvanometric scanning mirrors (ILAS, Roper Scientific, Evry, France) steered by MetaMorph. It allows precise spatial and temporal control of the focused laser beam at any user-selected region of interest (ROI) within the sample for targeted photo-bleaching. Switching between the two fibers for alternating between imaging and bleaching is performed in the ms time range using an AOTF. Oblique illumination was performed using the 491 nm beam at low power (0.3 mW at the front of the objective) to image NLGN1-GFP molecules in the plasma membrane close to the substrate plane. After acquiring a 10 sec baseline at 0.5 Hz frame rate, rapid selective photo-bleaching of several synapses was achieved by scanning circular ROIs of diameter 2 μm at higher laser power (3 mW at the objective front lens), during 500 ms. Fluorescence recovery was then recorded immediately after the bleach sequence for 30 min. The recording period included three phases with decreasing frame rate ranging from 2 to 0.1 Hz. Observational photo-bleaching was kept very low, as assessed by observing control unbleached areas nearby. FRAP curves were obtained by computing the average intensity in the photobleached area, after background subtraction, and normalized between 1 (baseline) and 0 (time zero after photo-bleaching). In some experiments performed at lower sampling rate, several synapses from neurons expressing NLGN1-GFP + Xph20-mRuby2 were photobleached at time zero, and fluorescence recovery was monitored every 15 min, up to 1 hr.

Description of FluoSim Algorithm and Parameters

A thorough description of the FluoSim algorithm together with a detailed user manual have been previously published (Lagardère et al., 2020). We give below a general outline of the software and the important parameters used in each simulation mode (SPT, STORM, and FRAP). The contour of a 48 μm-long dendritic segment containing 23 PSDs was drawn in Metamorph using an image of a 14 DIV neuron expressing Homer1c-DsRed, and saved as a region file. This region was imported in FluoSim and randomly populated with NLGN1 molecules (1,500–25,000 copies depending on the experiment to model). Those molecules are kept within the dendrite boundaries by introducing rebound conditions. An individual molecule is characterized by its 2D coordinates x and y over time t, and its intensity. The time step Δt and total duration of the simulations T is set according to the experiment to model (SPT: Δt = 20 ms, T = 40 s; dSTORM: Δt = 20 ms, T = 800 s; and FRAP: Δt = 100 ms, T = 30–60 min). The initial position of a freely diffusing molecule is defined by $x(0) = x_0$ and $y(0) = y_0$, taken as random numbers to fall within the dendrite boundaries. The diffusion coefficient outside synapses (D_{out}) is chosen around 0.15 $\mu m^2/s$, based on SPT data, while synapses are characterized by a lower diffusion coefficient (D_{in} = 0.06 $\mu m^2/s$), owing to molecular crowding. An additional coefficient called crossing probability describes the potentially limited penetrability of molecules into the synapse because of steric hindrance ($P_{crossing}$ = 0.5). A 20% fraction of immobile NLGN1 molecules was observed in uPAINT (with $D = 10^{-5}$ $\mu m^2/s$) and introduced in the program at random positions with zero diffusion coefficient. In the synapse, NLGN1 molecules are allowed to bind reversibly to the quasi-static PSD scaffold, with first order binding and unbinding rates k_{on} and k_{off}, respectively (both in s^{-1}). The k_{on} and k_{off} values were obtained by fitting FRAP experiments. NLGN1 bound to the PSD was allowed to diffuse at a lower diffusion coefficient D_{trap} = 0.006 $\mu m^2/s$, reflecting slow PSD morphing over time (Blanpied et al., 2008). The number of PSD binding sites is assumed to be in excess, such that the binding rate k_{on} is maintained constant throughout the simulations, i.e., it does not depend on the number of NLGN1 molecules recruited at synapses over time. We further consider a non-discrete distribution of binding sites in the PSD, consistent with our previous observation that NLGN1 does not tend to form nanodomains and fills the PSD rather uniformly (Chamma et al., 2016a).

Calculation of Positions

At each time step, the (x,y) coordinates of each molecule are incremented by the distances $(\Delta x, \Delta y)$, which depend on whether the molecule is outside or inside the synapse, or bound to the PSD. If the molecule is extra-synaptic, it follows a random walk with diffusion coefficient D_{out}. The positions x(t) and y(t) are then incremented at each time step by $n_x(2D_{out}\Delta t)^{1/2}$ and $n_y(2D_{out}\Delta t)^{1/2}$, respectively, where n_x and n_y are random numbers generated from a normal distribution with zero mean and variance unity, to account for the stochastic nature of diffusion. This ensures that the mean square displacement stays proportional to time, i.e., $<x^2 + y^2> = 4D_{out}t$. If the adhesion molecule reaches a synapse, it is set to diffuse with a lower diffusion coefficient D_{in}, with increments $n_x(2D_{in}\Delta t)^{1/2}$ and $n_y(2D_{in}\Delta t)^{1/2}$. Whenever the molecule resides in the synapse, it is allowed to bind to the PSD only if the probability of coupling in this time interval, $P_{coupl} = k_{on}\Delta t$, is greater than a random number N between 0 and 1 generated from a uniform distribution. If this is not the case, the molecule continues to diffuse until both conditions are met, i.e., the molecule remains in the synapse and the probability of binding is greater than the random number N, differently chosen at each time increment. Upon binding, NLGN1 is set to diffuse with a slow diffusion coefficient D_{trap}, thus the positions x(t) and y(t) are incremented by $n_x(2D_{trap}\Delta t)^{1/2}$ and $n_y(2D_{trap}\Delta t)^{1/2}$, respectively. NLGN1 stays bound until the probability for dissociation $P_{detach} = k_{off}\Delta t$, exceeds another random number N'. It then binds again or escapes into the extra-synaptic space. An option is proposed in FluoSim to theoretically estimate the steady-state, by placing more molecules in synapses, considering both slower diffusion and adhesion. The theoretical NLGN1 synaptic enrichment is then given by the formula $(P_{crossing} \times D_{out}/D_{in})\,(1 + k_{on}/k_{off})$.

Molecule Size, Intensity, and Photophysics

In addition to its position, each molecule is defined by its size and fluorescence intensity over time. Single molecules are represented either by a discrete point of intensity 1, or by a Gaussian intensity profile with a peak value directly coded on a 16-bit gray scale (0-65535 levels), or expressed in photons/sec associated with a conversion rate, or gain, which gives the number of gray levels read on the virtual camera chip per incoming photon. The Gaussian representation comprises an adjustable width σ (the standard deviation) in the order of λ/(2 × N.A.), where λ is the emission wavelength of the fluorophore, and N.A. is the numerical aperture of the objective (1.49 in our set-up). The corresponding FWHM is then equal to $2\sigma\sqrt{(2.\ln 2)}$ (Deschout et al., 2014). In our experiments, we used NLGN1-GFP: $\sigma_{GFP} = 510/(2 \times 1.49) = 171$ nm, and $FWHM_{GFP}$ = 402 nm, STAR635P-conjugated mSA: $\sigma_{STAR635P} = 651/(2 \times 1.49) = 218$ nm and $FWHM_{STAR635P}$ = 529 nm, and Alexa647-conjugated mSA: $\sigma_{A647} = 668/(2 \times 1.49) = 224$ nm and $FWHM_{A647}$ = 527 nm. Transitions between ON/OFF intensity values are set by two photo-physical parameters: the switch-on rate (${k_{ON}}^{Fluo}$) and the switch-off rate (${k_{OFF}}^{Fluo}$). These rates are in units of sec^{-1} and represent the probabilities per unit of time that a molecule switches from a state where it emits fluorescence, to a state where it does not emit fluorescence, and vice versa. In uPAINT, ${k_{ON}}^{Fluo}$ represents the rate of binding of fluorescent mSA ligand in solution to NLGN1 molecules on the cell surface, which spontaneously appear in the oblique illumination plane, whereas ${k_{OFF}}^{Fluo}$ combines fluorophore photo-bleaching and probe detachment from the cell surface. To mimic a FRAP experiment, ${k_{OFF}}^{Fluo}$ is set to a high level in a given ROI for a few frames (500 ms) to quickly and irreversibly photo-bleach fluorophores, then recovery is monitored. In dSTORM, ${k_{ON}}^{Fluo}$ represents the frequency of stochastic fluorescence emission, and ${k_{OFF}}^{Fluo}$ the inverse of the lifetime of the fluorescence emission peaks.

Single Particle Tracking Simulations

To mimic the sparse density of NLGN1 bound to mSA-STAR635P as used in uPAINT experiments, a relatively low number of molecules were introduced in the model cell (1,500 molecules per dendrite area of 36 μm^2, corresponding to a surface density of 42 molecules/μm^2). The off-rate of the simulated trajectories was adjusted by fitting the experimental distribution of trajectory durations with an exponentially decreasing function, giving ${k_{OFF}}^{Fluo} = 5.4\ s^{-1}$ (mean trajectory duration = 220 ms). The parameter ${k_{ON}}^{Fluo}$ which determines the number of fluorescent molecules per frame was set to 0.03 s^{-1}, so as to yield approximately the same density of visible molecules per surface area as in the experiments (0.25 molecule/μm^2). Sequences of 2,000 frames were generated as in the experiments, and only trajectories longer than 10 frames were selected. Trajectories containing the spatial positions and intensity of each molecule over time are saved as .trc files, and can be loaded later for offline visualization and analysis (menu SPT Analysis). The diffusion coefficient, *D*, was calculated for each trajectory, from linear fits of the first four points of the MSD function versus time. Five independent simulations were run for each set of parameters, allowing the construction of histograms of diffusion coefficients directly comparable to SPT experiments.

Fluorescence Recovery After Photobleaching Simulations

To match the dense distribution of NLGN1 molecules that characterize FRAP experiments, a relatively large number of molecules was introduced in the virtual cell (25,000 molecules in a dendritic segment of 135 μm^2, corresponding to a surface density of ~148 molecules/μm^2). Simulations of 18,200 frames, including a baseline of 200 frames, were generated with a time step of 100 ms (total duration 30 min) and a sampling rate of 2 s. The photo-activation rate was set to a maximal value ($k_{ON}{}^{Fluo}$ = 10 s^{-1}), i.e., all molecules are initially fluorescent, while the photo-bleaching rate is set to zero during baseline and recovery acquisition (i.e., observational photo-bleaching is neglected). During the short photo-bleaching period (500 ms) applied to four PSDs, the photo-bleaching rate was set to $k_{off}{}^{Bleach}$ = 4.0 s^{-1} for five frames, to precisely match the initial drop of fluorescence observed experimentally (~75%). The number of molecules in the photo-bleached PSDs and in four control unbleached PSDs was computed over time, saved as a.txt file, and normalized between 1 (baseline number of fluorescent molecules before photo-bleaching) and 0 (number of fluorescent molecules right after photo-bleaching). FRAP simulations were repeated 10 times, and the corresponding curves were averaged. To estimate the goodness of fit between simulated and experimental FRAP curves, we calculated the coefficient $\chi^2 = (1/n)\ \Sigma_i\ [(F_i{}^{exp} - F_i{}^{sim})/\sigma_i]^2$, where n is the number of experimental values, *i* = 1 to n is the time point, F_i are the normalized fluorescence intensity values for both experiment (exp) and simulations (sim), and σ_i is the standard deviation of the experimental value.

Direct STochastic Optical Reconstruction Microscopy Simulations

The switch-on rate $k_{ON}{}^{Fluo}$ at which fluorescent dyes spontaneously emit light was determined by measuring the fluorescence intensity collected from single Alexa647-conjugated mSA molecules bound to the glass coverslip during a dSTORM sequence, and counting the number of peaks (mean ± SEM = 1.7 ± 0.2 peaks over a time period of 400 s, *n* = 43 molecules analyzed, giving $k_{ON}{}^{Fluo}$ = 0.004 s^{-1}). The switch-off rate $k_{OFF}{}^{Fluo}$ was determined by fitting the distribution of the time durations during which single Alexa647-conjugated mSA emitted light before entering again the non-emitting state with an exponentially decreasing function (average 11.1 ± 1.4 frames of 20 ms, 72 events analyzed), giving a value $k_{OFF}{}^{Fluo}$ = 6.3 s^{-1}. The on-off duty cycle $\delta = k_{ON}{}^{Fluo}/(k_{ON}{}^{Fluo} + k_{OFF}{}^{Fluo})$ is the fraction of time that fluorophores spend in the light-emitting state, and equals here 0.00067, very close to reported values for isolated Alexa647-conjugated anti-GFP nanobody (Lagardère et al., 2020) and for single Alexa647 dyes in MEA-based dSTORM buffer (Dempsey et al., 2011), thereby confirming that the fluorophore to protein ratio of our conjugates is around 1. The average number of experimentally detected mSA-Alexa647 molecules per plane in the neuronal contour was *N* = 13.3, corresponding to a total number N/δ = 19,843 actual molecules in the cell geometry that was imaged (118 μm^2), thus representing a density of 167 molecules/μm^2. To mimic dSTORM experiments that rely on the saturating labeling of biotinylated AP-NLGN1 with mSA-Alexa647, we thus introduced 19,843 molecules in the virtual dendritic segment. After the diffusion/trapping steady-state has been imposed, the simulation was paused and all diffusion coefficients were set to zero to mimic cell fixation. Then, simulations were run for 40,000 frames of 20 ms each (total time of 800 s), and a single 16-bit image was generated which contained the integration of all molecule localizations throughout time. Three parameters are used to render the super resolution image: the intensity associated with a single detection; the zoom factor which is the ratio between the pixel sizes of the super-resolved image and the low resolution reference picture (a fivefold zoom corresponds to a pixel size of 32 nm in the high resolution image); and the localization precision, which corresponds to the standard deviation of the Gaussian distribution used to spread detections around the theoretical position of the molecule (σ = 25 nm, FWHM = 58 nm). A single super-resolved image integrating all single molecule localizations is exported as a TIFF file. To estimate mSA copy numbers in PSDs at steady-state, a single TIFF image was generated from the SRI menu of FluoSim, after setting the coefficients $k_{ON}{}^{Fluo}$ = 10 s^{-1} and $k_{OFF}{}^{Fluo}$ = 0 s^{-1} so as to visualize all emitting fluorophores. The image was then opened in Metamorph and intensity values were read in PSDs defined by previously saved ROIs.

DATA AVAILABILITY STATEMENT

The original contributions presented in the study are included in the article/**Supplementary Material**, further inquiries can be directed to the corresponding author.

ETHICS STATEMENT

The animal study was reviewed and approved by the authors declare that they have complied with all relevant ethical regulations (study protocol approved by the Ethical Committee of Bordeaux CE50).

AUTHOR CONTRIBUTIONS

ML developed FluoSim. AD performed dSTORM experiments, long-term FRAP experiments and simulations. MS provided reagents and scientific insight. OT supervised the work, performed simulations, and wrote the manuscript. All authors reviewed the manuscript.

FUNDING

This work received funding from Fondation pour la Recherche Médicale (“Equipe FRM” DEQ20160334916), Agence Nationale de la Recherche (grants « SynAdh » ANR-13-BSV4-0005-01 and « Synthesyn » ANR-17-CE16-0028-01), ERA-NET Neuron “Synpathy” (ANR-15-NEUR-0007-04), Investissements d’Avenir Labex BRAIN (« SynOptoGenesis » ANR-10-LABX-43), Conseil Régional Nouvelle Aquitaine (« SiMoDyn »), and French Ministry of Research (Ph.D. fellowship to ML).

ACKNOWLEDGMENTS

We thank T. Dresbach, P. Scheiffele, and A. Ting for the generous gift of plasmids; A. Toledo for uPAINT experiments; I. Chamma for FRAP experiments; B. Tessier, M. Munier, and C. McKenzie for molecular biology; R. Sterling and J. Girard for logistics; C. Breillat, N. Retailleau, E. Verdier, and N. Chevrier from the Cell culture facility of the Institute; C. Lemoigne for probe production; C. Butler, A. Kechkar, and J. B. Sibarita for the kind gift of the PALM-Tracer and WAVE-Tracer programs; and M. Letellier for sharing reference images.

SUPPLEMENTARY MATERIAL

The Supplementary Material for this article can be found online at: https://www.frontiersin.org/articles/10.3389/fnsyn.2022.835427/full#supplementary-material

Supplementary Figure 1 | Impact of kinetic parameters and synapse density on global NLGN1 diffusion as predicted by FluoSim. **(A)** Dendritic geometry used in FluoSim, based on the image of a neuron expressing Homer1c-DsRed (in white). The green contour is the outline of the dendrite (135 μm^2), the red PSDs are considered active (i.e., able to trap NLGN1), while the blue PSDs are considered inactive (i.e., unable to trap NLGN1). **(B)** Image of all NLGN1 trajectories simulated in 2000 frames, with a color code representing the diffusion coefficient (red = fast diffusion, yellow = slow diffusion). Note the slower NLGN1 diffusion in active PSDs. **(C–F)** Semi-log plots showing the distribution of NLGN1 diffusion coefficients obtained by simulation, for individual variations of the parameters D_{in}, k_{on}, and k_{off}, respectively (all other parameters being kept constant), or for different values of synapse density, i.e., obtained by varying the number of active PSDs. Curves were plotted from 985 to 1082 simulated trajectories per condition, obtained for 2500 NLGN1 molecules introduced in the geometry. The NLGN1 confined fraction is defined as the gray zone between $-4 < \text{Log}(D) < 1.8$.

Supplementary Figure 2 | Impact of kinetic parameters and synapse density on the simulated NLGN1 confined fraction. **(A–D)** Plots showing the fraction of confined NLGN1 molecules as a function of the parameters D_{in}, k_{on}, and k_{off}, or synapse density. Values correspond to the population highlighted in gray in **Supplementary Figure 1**. When not varied, parameters were $D_{out} = 0.15\ \mu m^2.s^{-1}$, $D_{in} = 0.15\ \mu m^2.s^{-1}$, $D_{trap} = 0.006\ \mu m^2.s^{-1}$, $k_{on} = 0.0015\ s^{-1}$, $k_{off} = 0.0005\ s^{-1}$, and synapse density = 0.4 μm^{-2} (i.e., all PSDs were active). $P_{crossing}$ was adjusted so as to maintain a constant theoretical synaptic enrichment $(P_{crossing}\ D_{out}/D_{in})\ (1 + k_{on}/k_{off}) = 4$.

Supplementary Figure 3 | Long term FRAP on NLGN1-GFP. **(A)** Post-synaptic distribution of NLGN1-GFP. Representative images of a dendritic segment from a neuron co-expressing NLGN1-GFP (green) and Xph20-mRuby2 (red), an intrabody to PSD-95. The merged image shows extensive colocalization between the two proteins at post-synapses (yellow signal). **(B)** Representative 1-hr FRAP sequence performed on a neuron co-expressing NLGN1-GFP and Xph20-mRuby2. The NLGN1-GFP signal was photobleached at time 0 on two post-synapses, and epifluorescence images were acquired after 30 and 60 min. **(C)** Graph showing the fluorescence intensity of unbleached and photobleached synapses, normalized to the baseline level before photobleaching. Data are mean ± SD for 47 and 54 bleached and unbleached synapses, respectively, out of 9 neurons from 2 different experiments. The curves are computer simulations run for 1 h. The parameter χ^2 estimating the goodness of fit calculated for the two experimental points (30 and 60 min) is 0.31 for bleached synapses and 0.014 for unbleached synapses.

Supplementary Figure 4 | Impact of kinetic parameters on simulated FRAP curves. **(A)** Dendritic geometry used in FluoSim, based on the image of a neuron expressing Homer1c-DsRed. PSDs outlined in red are those which are photobleached at time zero, while PSDs outlined in blue serve as unbleached controls. **(B)** Heat map of NLGN1 localization with a color code representing the accumulation of NLGN1 in PSDs. **(C–E)** FRAP curves obtained for individual variations of the parameters D_{in}, k_{on}, and k_{off}, respectively, all other parameters in FluoSim being kept constant. When not varied, parameters were $D_{out} = 0.15\ \mu m^2.s^{-1}$, $D_{in} = 0.15\ \mu m^2.s^{-1}$, $D_{trap} = 0.006\ \mu m^2.s^{-1}$, $k_{on} = 0.0015\ s^{-1}$, $k_{off} = 0.0005\ s^{-1}$, and synapse density = 0.4 μm^{-2} (i.e., all PSDs were active). $P_{crossing}$ was adjusted so as to maintain a constant theoretical synaptic enrichment $(P_{crossing}\ D_{out}/D_{in})\ (1 + k_{on}/k_{off}) = 4$. **(F)** Graph showing the coefficient χ^2 estimating the goodness of fit, plotted as a function of k_{off}. The minimum of this curve indicates the k_{off} value giving the best fit, which was chosen thereafter in the model.

Supplementary Figure 5 | Photophysical properties of Alexa647-conjugated mSA in dSTORM conditions. **(A)** Maximum intensity projection image of a dSTORM sequence run on diluted mSA-Alexa647 molecules (1 nM) immobilized on a glass coverslip. The region of interest is 64 × 64 pixels (10 × 10 μm) and the sequence was 20,000 frames at a 20 ms exposure time per frame (total duration 400 s). **(B)** Representative single frame images of individual molecules while they emit fluorescence. **(C)** Fluorescence intensity in gray levels over time for three arbitrary regions of 6 × 6 pixels centered on individual molecules. One or several emission peaks can be clearly distinguished. The frequency of fluorescence emission by individual mSA-Alexa647 molecules, $k_{ON}{}^{Fluo}$, was taken as the average number of peaks divided by the total sequence duration ($k_{ON}{}^{Fluo} = 0.004\ s^{-1}$). **(D)** Zoom on one of the peaks (molecule 1, green), showing the lifetime of the fluorescence emission. **(E)** Distribution of the fluorescence lifetime calculated from 73 individual emission peaks (black circles). The red curve is a fit with the exponentially decreasing function $N_0\ \text{Exp}(-k_{OFF}{}^{Fluo}t)$, where N_0 is the number of values at time zero, t is the time in sec, and $k_{OFF}{}^{Fluo} = 6.3\ s^{-1}$ is the characteristic rate constant.

Supplementary Figure 6 | Estimation of the number of Alexa647 fluorophores per mSA protein by quantification of photobleaching steps. Alexa-647 conjugated mSA molecules were diluted to 3 nM in Tyrode solution, immobilized on a glass substrate, and imaged by TIRF microscopy at 30 Hz. **(A)** Representative time lapse images. Note the progressive photobleaching of the mSA molecules. **(B–D)** Representative fluorescence intensity profiles of individual molecules over time. Each color represents a different molecule. Molecules display mostly 1-step **(B)** and 2-step **(C)**, but very rarely 3-step **(D)** photobleaching profiles. **(E)** Distribution of the number of photobleaching steps computed from 250 individual Alexa647-conjugated mSA molecules. The red curve represents a binomial distribution with 4 binding sites and conjugation probability of Alexa647 to mSA of 0.35. The best fit allows the computation of a 17% fraction of unconjugated mSA, thereby undetectable by fluorescence microscopy.

Supplementary Figure 7 | General strategy to estimate model parameters entered in FluoSim. **(A)** Single molecule tracking experiments yield with relatively high precision the NLGN1 immobile fraction, the peak NLGN1 diffusion coefficient outside synapses (D_{out}), and the peak diffusion coefficient of NLGN1 molecules bound at PSDs (D_{trap}). **(B)** The fit of FRAP experiments with the model allows for the determination of the binding and unbinding rates (k_{on} and k_{off}, respectively) of NLGN1 to the PSD. Further adjustment of the remaining parameters P_c and D_{in} are based on the determination of NLGN1 synaptic enrichment. **(C)** Quantification of mSA-Alexa647 photophysical rates in dSTORM conditions combined with the other parameters of the model allows for the determination of the copy number of NLGN1 in the dendrite geometry, by matching the absolute number of single molecule detections obtained experimentally.

REFERENCES

Araç, D., Boucard, A. A., Özkan, E., Strop, P., Newell, E., Südhof, T. C., et al. (2007). Structures of neuroligin-1 and the neuroligin-1/neurexin-1β complex reveal specific protein-protein and protein-Ca^{2+} interactions. *Neuron* 56, 992–1003. doi: 10.1016/j.neuron.2007.12.002

Bemben, M. A., Shipman, S. L., Nicoll, R. A., and Roche, K. W. (2015). The cellular and molecular landscape of neuroligins. *Trends Neurosci.* 38, 496–505. doi: 10.1016/j.tins.2015.06.004

Blanpied, T. A., Kerr, J. M., and Ehlers, M. D. (2008). Structural plasticity with preserved topology in the postsynaptic protein network. *Proc. Natl. Acad. Sci. U.S.A.* 105, 12587–12592. doi: 10.1073/pnas.0711669105

Born, G., Breuer, D., Wang, S., Rohlmann, A., Coulon, P., Vakili, P., et al. (2014). Modulation of synaptic function through the α-neurexin-specific ligand neurexophilin-1. *Proc. Natl. Acad. Sci. U.S.A.* 111, E1274–E1283. doi: 10.1073/pnas.1312112111

Budreck, E. C., and Scheiffele, P. (2007). Neuroligin-3 is a neuronal adhesion protein at GABAergic and glutamatergic synapses. *Eur. J. Neurosci.* 26, 1738–1748. doi: 10.1111/j.1460-9568.2007.05842.x

Chamma, I., Letellier, M., Butler, C., Tessier, B., Lim, K.-H., Gauthereau, I., et al. (2016a). Mapping the dynamics and nanoscale organization of synaptic adhesion proteins using monomeric streptavidin. *Nat. Commun.* 7:10773. doi: 10.1038/ncomms10773

Chamma, I., Levet, F., Sibarita, J.-B., Sainlos, M., and Thoumine, O. (2016b). Nanoscale organization of synaptic adhesion proteins revealed by single-molecule localization microscopy. *Neurophotonics* 3:041810. doi: 10.1117/1.NPh.3.4.041810

Chamma, I., Rossier, O., Giannone, G., Thoumine, O., and Sainlos, M. (2017). Optimized labeling of membrane proteins for applications to super-resolution imaging in confined cellular environments using monomeric streptavidin. *Nat. Protoc.* 12, 748–763. doi: 10.1038/nprot.2017.010

Chanda, S., Hale, W. D., Zhang, B., Wernig, M., and Südhof, T. C. (2017). Unique versus redundant functions of neuroligin genes in shaping excitatory and inhibitory synapse properties. *J. Neurosci.* 37, 6816–6836. doi: 10.1523/JNEUROSCI.0125-17.2017

Chen, B., Brinkmann, K., Chen, Z., Pak, C. W., Liao, Y., Shi, S., et al. (2014). The WAVE regulatory complex links diverse receptors to the actin cytoskeleton. *Cell* 156, 195–207. doi: 10.1016/j.cell.2013.11.048

Chen, X., Liu, H., Shim, A. H. R., Focia, P. J., and He, X. (2008). Structural basis for synaptic adhesion mediated by neuroligin-neurexin interactions. *Nat. Struct. Mol. Biol.* 15, 50–56. doi: 10.1038/nsmb1350

Chen, X., Vinade, L., Leapman, R. D., Petersen, J. D., Nakagawa, T., Phillips, T. M., et al. (2005). Mass of the postsynaptic density and enumeration of three key molecules. *Proc. Natl. Acad. Sci. U.S.A.* 102, 11551–11556. doi: 10.1073/pnas.0505359102

Chih, B., Engelman, H., and Scheiffele, P. (2005). Control of excitatory and inhibitory synapse formation by neuroligins. *Science* 307, 1324–1328. doi: 10.1126/science.1107470

Comoletti, D., Flynn, R., Jennings, L. L., Chubykin, A., Matsumura, T., Hasegawa, H., et al. (2003). Characterization of the interaction of a recombinant soluble neuroligin-1 with neurexin-1β. *J. Biol. Chem.* 278, 50497–50505. doi: 10.1074/jbc.M306803200

Connor, S. A., Elegheert, J., Xie, Y., and Craig, A. M. (2019). Pumping the brakes: suppression of synapse development by MDGA–neuroligin interactions. *Curr. Opin. Neurobiol.* 57, 71–80. doi: 10.1016/j.conb.2019.01.002

Czöndör, K., Mondin, M., Garcia, M., Heine, M., Frischknecht, R., Choquet, D., et al. (2012). Unified quantitative model of AMPA receptor trafficking at synapses. *Proc. Natl. Acad. Sci. U.S.A.* 109, 3522–3527. doi: 10.1073/pnas.1109818109

Dean, C., Scholl, F. G., Choih, J., DeMaria, S., Berger, J., Isacoff, E., et al. (2003). Neurexin mediates the assembly of presynaptic terminals. *Nat. Neurosci.* 6, 708–716. doi: 10.1038/nn1074

Demonte, D., Drake, E. J., Lim, K. H., Gulick, A. M., and Park, S. (2013). Structure-based engineering of streptavidin monomer with a reduced biotin dissociation rate. *Proteins Struct. Funct. Bioinformatics* 81, 1621–1633. doi: 10.1002/prot.24320

Dempsey, G. T., Vaughan, J. C., Chen, K. H., Bates, M., and Zhuang, X. (2011). Evaluation of fluorophores for optimal performance in localization-based super-resolution imaging. *Nat. Methods* 8, 1027–1040. doi: 10.1038/nmeth.1768

Deschout, H., Zanacchi, F. C., Mlodzianoski, M., Diaspro, A., Bewersdorf, J., Hess, S. T., et al. (2014). Precisely and accurately localizing single emitters in fluorescence microscopy. *Nat. Methods* 11, 253–266. doi: 10.1038/nmeth.2843

Dresbach, T., Neeb, A., Meyer, G., Gundelfinger, E. D., and Brose, N. (2004). Synaptic targeting of neuroligin is independent of neurexin and SAP90/PSD95 binding. *Mol. Cell. Neurosci.* 27, 227–235. doi: 10.1016/j.mcn.2004.06.013

Fabrichny, I. P., Leone, P., Sulzenbacher, G., Comoletti, D., Miller, M. T., Taylor, P., et al. (2007). Structural analysis of the synaptic protein neuroligin and its β-neurexin complex: determinants for folding and cell adhesion. *Neuron* 56, 979–991. doi: 10.1016/j.neuron.2007.11.013

Giannone, G., Hosy, E., Levet, F., Constals, A., Schulze, K., Sobolevsky, A. I., et al. (2010). Dynamic superresolution imaging of endogenous proteins on living cells at ultra-high density. *Biophys. J.* 99, 1303–1310. doi: 10.1016/j.bpj.2010.06.005

Haas, K. T., Compans, B., Letellier, M., Bartol, T. M., Grillo-Bosch, D., Sejnowski, T. J., et al. (2018). Pre-post synaptic alignment through neuroligin-1 tunes synaptic transmission efficiency. *Elife* 7:e31755 . doi: 10.7554/elife.31755

Han, B., Zhou, R., Xia, C., and Zhuang, X. (2017). Structural organization of the actin-spectrin–based membrane skeleton in dendrites and soma of neurons. *Proc. Natl. Acad. Sci. U.S.A.* 114, E6678–E6685. doi: 10.1073/pnas.1705043114

Heilemann, M., Van De Linde, S., Schüttpelz, M., Kasper, R., Seefeldt, B., Mukherjee, A., et al. (2008). Subdiffraction-resolution fluorescence imaging with conventional fluorescent probes. *Angew. Chem. Int. Ed.* 47, 6172–6176. doi: 10.1002/anie.200802376

Hirao, K., Hata, Y., Ide, N., Takeuchi, M., Irie, M., Yao, I., et al. (1998). A novel multiple PDZ domain-containing molecule interacting with N-methyl-D-aspartate receptors and neuronal cell adhesion proteins. *J. Biol. Chem.* 273, 21105–21110. doi: 10.1074/jbc.273.33.21105

Howarth, M., Takao, K., Hayashi, Y., and Ting, A. Y. (2005). Targeting quantum dots to surface proteins in living cells with biotin ligase. *Proc. Natl. Acad. Sci. U.S.A.* 102, 7583–7588. doi: 10.1073/pnas.0503125102

Hruska, M., Henderson, N., Le Marchand, S. J., Jafri, H., and Dalva, M. B. (2018). Synaptic nanomodules underlie the organization and plasticity of spine synapses. *Nat. Neurosci.* 21, 671–682. doi: 10.1038/s41593-018-0138-9

Irie, M., Hata, Y., Takeuchi, M., Ichtchenko, K., Toyoda, A., Hirao, K., et al. (1997). Binding of neuroligins to PSD-95. *Science* 277, 1511–1515. doi: 10.1126/science.277.5331.1511

Izeddin, I., Boulanger, J., Racine, V., Specht, C. G., Kechkar, A., Nair, D., et al. (2012). Wavelet analysis for single molecule localization microscopy. *Opt. Express* 20, 2081–2095. doi: 10.1364/OE.20.002081

Kaech, S., and Banker, G. (2006). Culturing hippocampal neurons. *Nat. Protoc.* 1, 2406–2415. doi: 10.1038/nprot.2006.356

Klatt, O., Repetto, D., Brockhaus, J., Reissner, C., El khallouqi, A., Rohlmann, A., et al. (2021). Endogenous β-neurexins on axons and within synapses show regulated dynamic behavior. *Cell Rep.* 35:109266. doi: 10.1016/j.celrep.2021.109266

Kuriu, T., Inoue, A., Bito, H., Sobue, K., and Okabe, S. (2006). Differential control of postsynaptic density scaffolds via actin-dependent and -independent mechanisms. *J. Neurosci.* 26, 7693–7706. doi: 10.1523/JNEUROSCI.0522-06.2006

Lagardère, M., Chamma, I., Bouilhol, E., Nikolski, M., and Thoumine, O. (2020). FluoSim: simulator of single molecule dynamics for fluorescence live-cell and super-resolution imaging of membrane proteins. *Sci. Rep.* 10:19954. doi: 10.1038/s41598-020-75814-y

Letellier, M., Lagardère, M., Tessier, B., Janovjak, H., and Thoumine, O. (2020). Optogenetic control of excitatory post-synaptic differentiation through neuroligin-1 tyrosine phosphorylation. *Elife* 9:e52027. doi: 10.7554/eLife.52027

Letellier, M., Szíber, Z., Chamma, I., Saphy, C., Papasideri, I., Tessier, B., et al. (2018). A unique intracellular tyrosine in neuroligin-1 regulates AMPA receptor recruitment during synapse differentiation and potentiation. *Nat. Commun.* 9:3979. doi: 10.1038/s41467-018-06220-2

Levinson, J. N., and El-Husseini, A. (2007). A crystal-clear interaction: relating neuroligin/neurexin complex structure to function at the synapse. *Neuron* 56, 937–939. doi: 10.1016/j.neuron.2007.12.003

Lowenthal, M. S., Markey, S. P., and Dosemeci, A. (2015). Quantitative mass spectrometry measurements reveal stoichiometry of principal postsynaptic density proteins. *J. Proteome Res.* 14, 2528–2538. doi: 10.1021/acs.jproteome.5b00109

Missler, M., Zhang, W., Rohlmann, A., Kattenstroth, G., Hammer, R. E., Gottmann, K., et al. (2003). Alpha-neurexins couple Ca^{2+} channels to synaptic vesicle exocytosis. *Nature* 423, 939–948. doi: 10.1038/nature01755

Mondin, M., Labrousse, V., Hosy, E., Heine, M., Tessier, B., Levet, F., et al. (2011). Neurexin-neuroligin adhesions capture surface-diffusing AMPA receptors through PSD-95 scaffolds. *J. Neurosci.* 31, 13500–13515. doi: 10.1523/JNEUROSCI.6439-10.2011

Mukherjee, K., Sharma, M., Urlaub, H., Bourenkov, G. P., Jahn, R., Südhof, T. C., et al. (2008). CASK functions as a Mg^{2+}-independent neurexin kinase. *Cell* 133, 328–339. doi: 10.1016/j.cell.2008.02.036

Nair, D., Hosy, E., Petersen, J. D., Constals, A., Giannone, G., Choquet, D., et al. (2013). Super-resolution imaging reveals that AMPA receptors inside synapses are dynamically organized in nanodomains regulated by PSD95. *J. Neurosci.* 33, 13204–13224. doi: 10.1523/JNEUROSCI.2381-12.2013

Neupert, C., Schneider, R., Klatt, O., Reissner, C., Repetto, D., Biermann, B., et al. (2015). Regulated dynamic trafficking of neurexins inside and outside of synaptic terminals. *J. Neurosci.* 35, 13629–13647. doi: 10.1523/JNEUROSCI.4041-14.2015

Nguyen, Q. A., Horn, M. E., and Nicoll, R. A. (2016). Distinct roles for extracellular and intracellular domains in neuroligin function at inhibitory synapses. *Elife* 5:e19236. doi: 10.7554/eLife.19236

Poulopoulos, A., Aramuni, G., Meyer, G., Soykan, T., Hoon, M., Papadopoulos, T., et al. (2009). Neuroligin 2 drives postsynaptic assembly at perisomatic inhibitory synapses through gephyrin and collybistin. *Neuron* 63, 628–642. doi: 10.1016/j.neuron.2009.08.023

Renner, M., Domanov, Y., Sandrin, F., Izeddin, I., Bassereau, P., and Triller, A. (2011). Lateral diffusion on tubular membranes: quantification of measurements bias. *PLoS One* 6:e25731. doi: 10.1371/journal.pone.0025731

Rimbault, C., Breillat, C., Compans, B., Toulmé, E., Nunes Vicente, F., Fernandez-Monreal, M., et al. (2021). Engineering paralog-specific PSD-95 synthetic binders as potent and minimally invasive imaging probes. *bioRxiv* [Preprint]. doi: 10.1101/2021.04.07.438431

Rimbault, C., Maruthi, K., Breillat, C., Genuer, C., Crespillo, S., Puente-Muñoz, V., et al. (2019). Engineering selective competitors for the discrimination of highly conserved protein-protein interaction modules. *Nat. Commun.* 10:4521. doi: 10.1038/s41467-019-12528-4

Saint-Michel, E., Giannone, G., Choquet, D., and Thoumine, O. (2009). Neurexin/neuroligin interaction kinetics characterized by counting single cell-surface attached quantum dots. *Biophys. J.* 97, 480–489. doi: 10.1016/j.bpj.2009.04.044

Sauer, M., Helmerich, D. A., and Beliu, G. (2020). Multiple-labeled antibodies behave like single emitters in photoswitching buffer. *ACS Nano* 14, 12629–12641. doi: 10.1021/acsnano.0c06099

Sheng, M., and Hoogenraad, C. C. (2007). The postsynaptic architecture of excitatory synapses: a more quantitative view. *Annu. Rev. Biochem.* 76, 823–847. doi: 10.1146/annurev.biochem.76.060805.160029

Shipman, S. L., Schnell, E., Hirai, T., Chen, B.-S., Roche, K. W., and Nicoll, R. A. (2011). Functional dependence of neuroligin on a new non-PDZ intracellular domain. *Nat. Neurosci.* 14, 718–726. doi: 10.1038/nn.2825

Südhof, T. C. (2017). Synaptic neurexin complexes: a molecular code for the logic of neural circuits. *Cell* 171, 745–769. doi: 10.1016/j.cell.2017.10.024

Tanaka, H., Miyazaki, N., Matoba, K., Nogi, T., Iwasaki, K., and Takagi, J. (2012). Higher-order architecture of cell adhesion mediated by polymorphic synaptic adhesion molecules neurexin and neuroligin. *Cell Rep.* 2, 101–110. doi: 10.1016/j.celrep.2012.06.009

Tang, A.-H., Chen, H., Li, T. P., Metzbower, S. R., MacGillavry, H. D., and Blanpied, T. A. (2016). A trans-synaptic nanocolumn aligns neurotransmitter release to receptors. *Nature* 536, 210–214. doi: 10.1038/nature19058

Toledo, A., Bimbi, G., Letellier, M., Tessier, B., Daburon, S., Favereaux, A., et al. (2022). MDGAs are fast-diffusing molecules that delay excitatory synapse development by altering neuroligin behavior. *bioRxiv* [Preprint]. doi: 10.1101/2021.03.16.435652

Trotter, J. H., Hao, J., Maxeiner, S., Tsetsenis, T., Liu, Z., Zhuang, X., et al. (2019). Synaptic neurexin-1 assembles into dynamically regulated active zone nanoclusters. *J. Cell Biol.* 218, 2677–2698. doi: 10.1083/jcb.201812076

Wu, X., Morishita, W. K., Riley, A. M., Hale, W. D., Südhof, T. C., and Malenka, R. C. (2019). Neuroligin-1 signaling controls LTP and NMDA receptors by distinct molecular pathways. *Neuron* 102, 621–635.e3. doi: 10.1016/j.neuron.2019.02.013

Conflict of Interest: The authors declare that the research was conducted in the absence of any commercial or financial relationships that could be construed as a potential conflict of interest.

frontiers | Frontiers in Synaptic Neuroscience

ORIGINAL RESEARCH
published: 24 May 2022
doi: 10.3389/fnsyn.2022.748184

Correlative Assembly of Subsynaptic Nanoscale Organizations During Development

Shi-Yan Sun[1,2], Xiao-Wei Li[1], Ran Cao[1], Yang Zhao[1,3], Nengyin Sheng[3]* and Ai-Hui Tang[1,2]*

[1] Chinese Academy of Sciences (CAS) Key Laboratory of Brain Function and Disease, Ministry of Education Key Laboratory for Membrane-less Organelles and Cellular Dynamics, Division of Life Sciences and Medicine, University of Science and Technology of China, Hefei, China, [2] Institute of Artificial Intelligence, Hefei Comprehensive National Science Center, Hefei, China, [3] State Key Laboratory of Genetic Resources and Evolution in Kunming Institute of Zoology, Chinese Academy of Sciences, Kunming, China

Nanoscale organization of presynaptic proteins determines the sites of transmitter release, and its alignment with assemblies of postsynaptic receptors through nanocolumns is suggested to optimize the efficiency of synaptic transmission. However, it remains unknown how these nano-organizations are formed during development. In this study, we used super-resolution stochastic optical reconstruction microscopy (STORM) imaging technique to systematically analyze the evolvement of subsynaptic organization of three key synaptic proteins, namely, RIM1/2, GluA1, and PSD-95, during synapse maturation in cultured hippocampal neurons. We found that volumes of synaptic clusters and their subsynaptic heterogeneity increase as synapses get matured. Synapse sizes of presynaptic and postsynaptic compartments correlated well at all stages, while only more mature synapses demonstrated a significant correlation between presynaptic and postsynaptic nano-organizations. After a long incubation with an inhibitor of action potentials or AMPA receptors, both presynaptic and postsynaptic compartments showed increased synaptic cluster volume and subsynaptic heterogeneity; however, the trans-synaptic alignment was intact. Together, our results characterize the evolvement of subsynaptic protein architectures during development and demonstrate that the nanocolumn is organized more likely by an intrinsic mechanism and independent of synaptic activities.

Keywords: nanocluster, super-resolution, STORM, glutamate receptor, nanocolumn

Edited by:
Thomas Kuner,
Heidelberg University, Germany

Reviewed by:
Olivier Thoumine,
Centre National de la Recherche Scientifique (CNRS), France
Deepak Kumaran Nair,
Indian Institute of Science (IISc), India

Correspondence:
Ai-Hui Tang
tangah@ustc.edu.cn
Nengyin Sheng
shengnengyin@mail.kiz.ac.cn

Received: *27 July 2021*
Accepted: *11 March 2022*
Published: *24 May 2022*

Citation:
Sun S-Y, Li X-W, Cao R, Zhao Y, Sheng N and Tang A-H (2022) Correlative Assembly of Subsynaptic Nanoscale Organizations During Development.
Front. Synaptic Neurosci. 14:748184.
doi: 10.3389/fnsyn.2022.748184

INTRODUCTION

Synapses are highly diverse and plastic in morphology and function (Walmsley et al., 1998). Even for the same type, the sizes of both presynaptic and postsynaptic compartments can vary by two orders of magnitude (Harris and Stevens, 1989). Subsynaptic organizations of synaptic proteins have conducted a new layer of structural and functional heterogeneity. Key proteins in the presynaptic and postsynaptic compartments, including RIM, Munc13, receptors, and several postsynaptic scaffolds, are organized in the form of nanoscale assemblies with a similar size of ∼100 nm, namely, nanoclusters or nanodomains (Fukata et al., 2013; MacGillavry et al., 2013; Nair et al., 2013; Hruska et al., 2018; Kellermayer et al., 2018; Sakamoto et al., 2018). More importantly, these nanoclusters are coupled spatially within nanocolumns so that the presynaptic

RIM nanoclusters could guide the action potential-dependent transmitter release to take place preferentially on postsynaptic receptor densities (Tang et al., 2016; Petzoldt et al., 2020). This arrangement and its reorganization could play a major role in controlling the efficacy and plasticity of synaptic transmissions (Sinnen et al., 2017; Chen et al., 2018; Groc and Choquet, 2020), as has been predicted by numerical studies (Raghavachari and Lisman, 2004; MacGillavry et al., 2013). In fact, during synaptic plasticity, these subsynaptic nano-organizations undergo vigorous remodeling (Tang et al., 2016; Hruska et al., 2018). Mechanisms have been proposed for their formation and maintenance: synaptic proteins can undergo self-assembly to form condensates through phase separation (Zeng et al., 2018, 2019; Wu et al., 2019), and the alignment between presynaptic and postsynaptic nanoclusters is mediated by synaptic adhesion molecules including neuroligin1 (Haas et al., 2018) and LRRTM2 (Ramsey et al., 2021). However, it remains to be demonstrated how these nanostructures are formed in real synapses.

Early electron microscopy studies and fluorescence imaging have demonstrated a strong correlation between structural features including bouton volume, active zone (AZ) area, postsynaptic density (PSD) area, spine volume, and number of receptors and key scaffolds (Harris and Stevens, 1989; Schikorski and Stevens, 1997; Nusser et al., 1998; Takumi et al., 1999; Regalado et al., 2006; Kay et al., 2011; Holderith et al., 2012; Fisher-Lavie and Ziv, 2013; Rollenhagen et al., 2018). These correlations between structural features correspond well to the functionality of synapses. Two-photon Ca^{2+} imaging and uncaging studies revealed that presynaptic release probability scales well with the AZ size, and larger spines show larger postsynaptic responses (Matsuzaki et al., 2001; Holderith et al., 2012). Recently, with combined slice electrophysiology and correlated light microscopy and high-resolution EM, Holler et al. demonstrated a strong linear relationship between synaptic strength and PSD area (Holler et al., 2021). Consistently, further functional studies also demonstrated a correlation between presynaptic release probability and postsynaptic AMPAR abundance or EPSCs (Thiagarajan et al., 2005; Tokuoka and Goda, 2008; Kay et al., 2011). The existence of nanocolumns strongly suggests a trans-synaptic correlation between nano-organizations. However, only half of the nanoclusters are actually coupled within nanocolumns (Tang et al., 2016), whether the general heterogeneity of protein organizations in the two compartments is matched and how it is coordinated during development have not been studied.

In this study, by employing the stochastic optical reconstruction microscopy (STORM) and sophisticated analytical methods, we set out to study the nanoscale protein architecture of individual synapses in dissociated hippocampal neurons to establish how key synaptic proteins, including RIM1/2, AMPAR, and PSD-95, are subsynaptically organized during early development. We found that the subsynaptic heterogeneity of synaptic proteins was not inherent but gradually organized during development. The protein nano-organizations in presynaptic and postsynaptic compartments were largely correlated and developed coordinately with no evidence of one side leading the other. Moreover, on synaptic activity blockade, both presynaptic and postsynaptic compartments showed an increased cluster size and subsynaptic heterogeneity, and the trans-synaptic alignment remained intact. Together, our results characterize the evolvement of subsynaptic protein architectures during development and suggest an intrinsic self-organization mechanism for the formation of nanocolumn organizations.

MATERIALS AND METHODS

Neuron Culture

Dissociated hippocampal neuron cultures were prepared from E18 rat embryos and plated with a density of 50k per well on poly-lysine coated glass coverslips in a 12-well plate. All procedures conformed to the guidelines established by the Institutional Animal Care and Use Committees at the University of Science and Technology of China (USTC) and the Chinese Academy of Sciences (CAS). The activity blockade was performed by the addition of tetrodotoxin (TTX, 0.5 μM) or 2,3-dihydroxy-6-nitro-7-sulfamoylbenzo(f)-quinoxaline (NBQX, 10 μM) at DIV10. To make sure the blockade was effective through the long period, we added another dose at DIV14. Whenever the cultures were fed, TTX or NBQX was included in the fresh medium.

Immunostaining

Cells were fixed with 4% paraformaldehyde (PFA) and 4% sucrose in phosphate-buffered saline (PBS) (pH 7.4) for 10 min at room temperature (RT), followed by washing with 50 mM glycine in PBS. Cells were then permeabilized and blocked using 3% bovine serum albumin (BSA) or 5% donkey serum in PBS/Gly with 0.3% Triton X-100, followed by incubation with primary antibodies (3 h RT) and then secondary antibodies (1 h RT).

The following primary antibodies were used in this study: rabbit anti-RIM1/2 (1:500, Synaptic Systems 140213), mouse anti-PSD-95 (1:200, NeuroMab 75-028), and rabbit anti-GluA1 (1:500, Merck Millipore AB1504). For co-staining of GluA1 and RIM1/2, as both antibodies were from rabbits, staining was performed separately and the first primary antibody (GluA1) was blocked and converted with a goat anti-rabbit Fab fragment (JacksonImmuno 111-007-003) for 2 h at RT, and then recognized by secondary antibodies. The secondary antibodies were Alexa-647 conjugated donkey anti-Goat (JacksonImmuno 705-605-147), Alexa-647 conjugated donkey anti-rabbit (JacksonImmuno 711-605-152), and unconjugated donkey anti-mouse antibody (JacksonImmuno 715-005-151) or donkey anti-rabbit antibody (JacksonImmuno 711-005-152) labeled with Cy^{TM}3B (Mono NHS Ester, GE Healthcare 16889934).

STORM Imaging

Imaging was carried out on a Nikon ECLIPSE Ti2 inverted microscope equipped with a perfect focusing system and a 100×/1.49 TIRF oil-immersion objective controlled using NIS-Elements AR 4.30.02 software. The typical incident power was ∼40 mW (measured through the objective). Samples were imaged in a freshly made STORM imaging buffer containing: 50 mM Tris, 10 mM NaCl, 20% glucose, 56 μg/ml glucose oxidase

(Sigma), 18 μg/ml catalase (Sigma), and 100 mM cysteamine (Sigma). To reduce background fluorescence while maximizing the depth of view, we adjusted the incident angle of the excitation beam to near but less than the critical angle and to achieve oblique illumination of the sample. Emission was collected using a CMOS camera (ORCA-Flash4.0, Hamamatsu) at a frame rate of 50 Hz and stored as images with a pixel size of 160 nm (with an 0.4× lens in the emission path). Z positions were determined by the ellipticity of the single peaks generated by a cylindrical lens (focal length 100 mm) with a precision of 40–50 nm. Total 50k images were collected for each channel. TetraSpeck beads (100 nm; Invitrogen) deposited on a coverslip were localized for generating the calibration curves. In our system, the average deviation of the bead localizations after t correction was 10–15 nm in *x/y* and 40–50 nm in *z*. Localization detection, calibration, and drift correction were performed using the NIS-Elements AR analysis 4.40.00 software. Localization coordinates were then rendered into images (pixel size of 5 nm) using a two-dimensional Gaussian kernel ($\sigma = 20$ nm) with custom routines in MATLAB (Mathworks).

Electrophysiology

Whole-cell patch clamp was carried out with patch-clamp amplifiers (MultiClamp 700B, Axon Instruments) at RT. The data were acquired and analyzed using custom Igor Pro (WaveMetrics) programs. Intracellular pipette solution (pH 7.3) contained 136.5 mM potassium gluconate, 17.5 mM KCl, 9 mM NaCl, 1 mM $MgCl_2$, 10 mM HEPES, 0.2 mM EGTA, 2 mM ATP-Mg, and 0.3 mM GTP-Na. External bath solution (pH 7.3) contained 150 mM NaCl, 3 mM KCl, 3 mM $CaCl_2$, 2 mM $MgCl_2$, 10 mM HEPES, 5 mM glucose, 1 μM TTX, and 20 μM bicuculline.

Data Analysis

Detailed analysis on synaptic clusters was formed using custom routines in MATLAB as described previously (Tang et al., 2016; Chen et al., 2020). A synaptic cluster was identified in a 2D scatter plot of all localizations. By rotating a 3D scatterplot of localizations of a selected potential synaptic cluster pair, we evaluated the data quality and selected only those with clear edges (e.g., no nearby third cluster which may indicate more than two synaptic clusters in close proximity) for further analysis. To define a synaptic cluster on the random background, the nearest neighbor distances (NNDs) between localizations were calculated, and the mean + 2 × SD of NND was used as a cutoff to divide the localizations into subclusters. All localizations outside the primary subclusters were considered to be a background and were not used in further analysis. The border of the synaptic cluster was defined using the alpha-shape of the set of 3D localizations with $\alpha = 150$ nm.

Nanoclusters were detected based on local density which was defined as the number of molecules within a radius of 2.5 times the standard median nearest neighbor distance (MdNND) for the calculation of the density of the synaptic cluster (Chen et al., 2020). The threshold of local density for nanocluster detection was defined as mean (LD0) + 4 × SD (LD0), where LD0 is the local density of a randomized cluster with the same overall density as the synaptic cluster. All localizations with a local density over this threshold were considered within nanoclusters. These localizations were then divided into subclusters with a "top-down" divisive strategy with a minimal peak-to-peak distance of 80 nm. Finally, to be counted as nanoclusters, those subclusters had to meet a set of criteria, including the number of localizations ≥8, which was derived empirically based on tests on our measured and simulated synapses to reduce the false positives arising from repeated localizations of the same molecule.

Data analysis was performed using the Origin software. Data are reported as average ± SEM values, and statistical significance was evaluated using one-way ANOVA, Kolmogorov–Smirnov test for cumulative curves, and *z*-test for proportions. Asterisks above brackets in data bar graphs indicate the level of statistical significance ($^{*}p < 0.05$; $^{**}p < 0.01$; and $^{***}p < 0.001$). Detailed results of statistical analysis are listed in **Supplementary Table 1**.

RESULTS

Correlative Expansion of Presynaptic and Postsynaptic Protein Clusters During Development

Previous ultrastructural and fluorescence imaging studies have shown a strong correlation between the sizes of membrane compartments and the amount of synaptic proteins on presynaptic and postsynaptic sides. In this study, we reexamined this with STORM super-resolution microscopy on presynaptic RIM1/2, the key AZ protein for action potential-dependent vesicle fusion, and postsynaptic AMPAR subunit GluA1 and scaffold PSD-95. We performed the staining and imaging as pairs of RIM1/2-GluA1 and RIM1/2-PSD-95, at four developmental stages in cultured hippocampal neurons: 6–8 days *in vitro* (marked as DIV7 in the following text) when synaptic contacts are newly formed, DIV10 (±1), DIV14 (±1), and DIV18 (±1) when synapses are thought mature.

At DIV7, synaptic contacts could be identified as sites of colocalization between RIM1/2 and GluA1 (or PSD-95), while there were many protein clusters without its counter partner in the vicinity (**Figure 1A**). Synaptic clusters were filtered, and the borders were defined with an alpha-shape as previously described (Tang et al., 2016; Chen et al., 2020). When the cultures grew older, the volume of synaptic clusters expanded gradually (**Figures 1B–G**), with a 4–5-fold increase in cluster sizes of all three proteins from DIV7 to DIV18 ($p < 0.001$ for all groups, one-way ANOVA; for details, refer to **Supplementary Table 1**), similar to previous observations (Chanda et al., 2017). More importantly, we found that this expansion in synaptic size was proportional between the presynaptic and postsynaptic compartments (**Supplementary Figure 1**). Actually, even at the same developmental state, the correlations between the volumes were strong for each protein (**Figures 1H,I**; **Supplementary Figure 1**). Moreover, a similar strong correlation was also found in the localization numbers of synaptic proteins which represent the amount of synaptic proteins

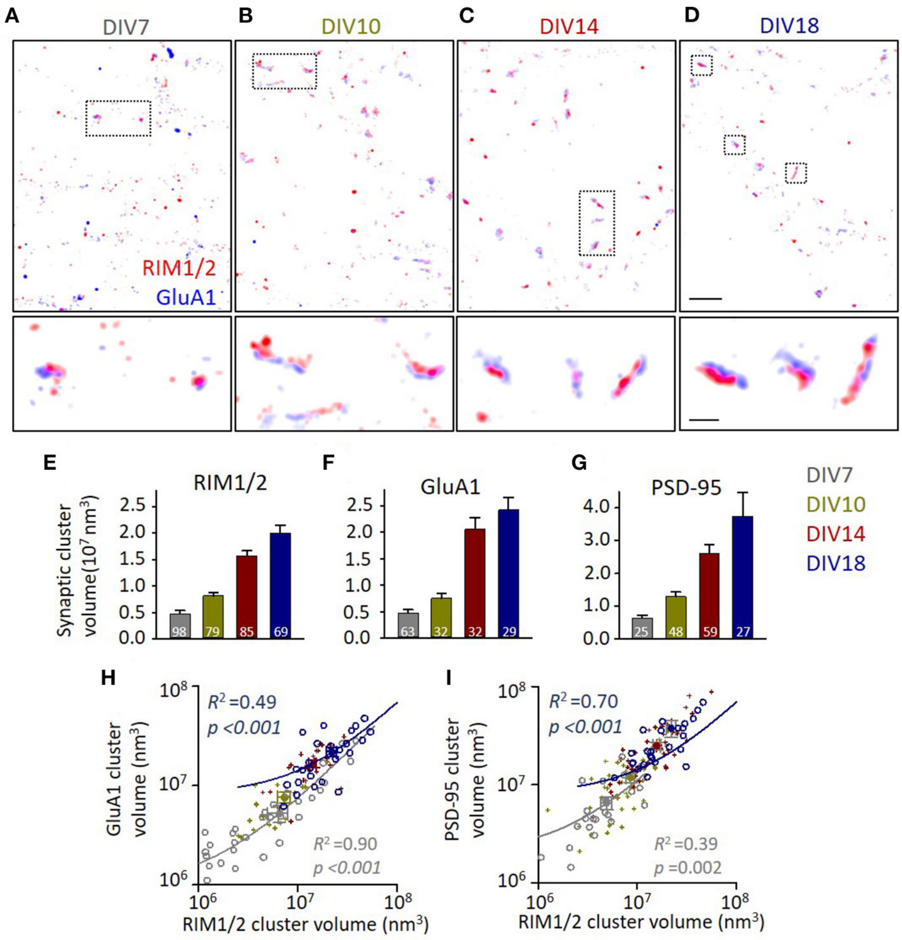

FIGURE 1 | Synapse volumes increase correlatively during synaptic maturation. **(A–D)** Representative distribution of RIM1/2 and GluA1 under stochastic optical reconstruction microscopy (STORM). Scale 2 μm in top panels and 500 nm in lower panels. **(E–G)** Volumes of identified synaptic RIM1/2, GluA1, and PSD-95 clusters across different developmental stages. Numbers in bars denote the synapse numbers. **(H,I)** Correlations between the volumes of GluA1 and RIM1/2 clusters **(H)** and the volumes of PSD-95 and RIM1/2 **(I)** within the same synapses. Linear regressions were conducted on synapses of DIV7 (gray circles and line) and DIV18 (dark blue circles and line). Data from synapses of DIV10 and 14 were plotted with dark yellow and dark red crosses. Also refer to **Supplementary Figures 1**, **2** and **Supplementary Table 1** for more details on correlations and statistics. All experiments were repeated ≥3 times.

(**Supplementary Figure 2**). These results suggest a synchronous growth of AZ and PSD during synapse maturation, and no obvious evidence indicating the remodeling in one compartment preceded that in the other.

Evolvement of Subsynaptic Protein Nano-Organizations During Development

We then set out to quantify the subsynaptic distribution of these proteins at different developmental stages. To visualize the protein pattern within the synapse, local density for each localization was calculated and color-coded in the distribution map (**Figures 2A–D**). Comparing with that in mature synapses, GluA1 at DIV7-10 distributed more homogeneously within the synapse boundaries. To quantify the heterogeneity within the synaptic cluster, we employed a normalized autocorrelation function (g_a) (Veatch et al., 2012; Tang et al., 2016). The autocorrelation showed a significant heterogeneity over a range of 0–100 nm for GluA1, RIM1/2, and PSD-95 at DIV14-18, while the amplitudes were significantly smaller and the range over which the heterogeneity was above the chance level was narrower for more immature synapses (**Figures 2E–G**). These differences were further confirmed by the properties of high-density nanoclusters identified with an automated algorithm based on local density (Chen et al., 2020). Immature synapses had a smaller number of nanoclusters, lower localization density within nanoclusters, and smaller nanocluster volume (**Figures 2H–J**). The gradually increased heterogeneity in these proteins during the maturation of synapses suggests that the well-organized subsynaptic distribution of both presynaptic transmitter release and postsynaptic receptors is a hallmark for mature synapses and may be essential for their functions.

To compare the organizations on presynaptic and postsynaptic compartments, we averaged the g_a for radius from 0 to 50 nm ($\overline{g_a}$) and used it as a simplified index of

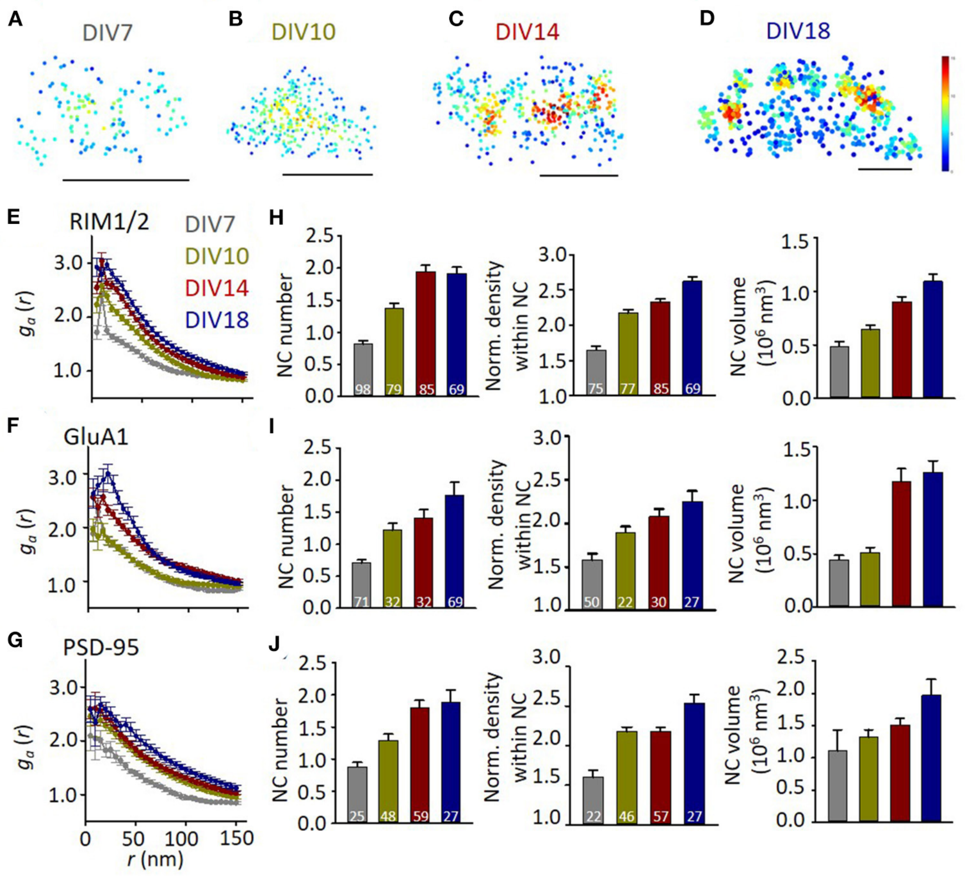

FIGURE 2 | The heterogeneity of synaptic protein distribution increases with development. **(A–D)** Representative density maps of synaptic GluA1 at different developmental stages. Scale bars, 200 nm. **(E–G)** Normalized autocorrelation functions of RIM1/2 **(E)**, GluA1 **(F)**, and PSD-95 **(G)**. g_a above 1 suggests a significant non-uniform distribution. **(H–J)** Developmental changes of nanocluster number (left), normalized density within nanocluster (middle), and nanocluster volume of RIM1/2 **(H)**, GluA1 **(I)**, and PSD-95 **(J)**. Numbers in bars denote the synapse numbers. Also refer to **Supplementary Table 1** for more statistical details. All experiments were repeated ≥3 times.

subsynaptic heterogeneity. We found a significant correlation between $\overline{g_a}$ of presynaptic RIM1/2 and postsynaptic GluA1 or PSD-95 ($p < 0.001$ for both pairs, **Figures 3A,B**). This result suggests that the subsynaptic organizations of presynaptic and postsynaptic components are evolved synchronously during development, similar to the size of both compartments. When we examined the $\overline{g_a}$ correlations in each developmental stage, we found that the correlation was only significant in mature synapses (**Figures 3C,D**). Since more mature synapses had a larger volume, we wonder whether stronger heterogeneity is an intrinsic property of larger synapses. We, therefore, plotted $\overline{g_a}$ of RIM1/2 against the cluster volume for each synapse and found that there was in fact a positive correlation (**Figure 3E**) for both mature and immature synapses. However, synapses of DIV18 showed a general larger $\overline{g_a}$ than those of DIV7. To eliminate the effect of cluster volume on $\overline{g_a}$, we picked up only those large synapses with a cluster volume of 1–4 × 10^7 nm^3 and compared the subsynaptic heterogeneity. The mature synapses showed a significantly larger $\overline{g_a}$ than the immature for both RIM1/2 and GluA1, but the heterogeneity of PSD-95 was similar (**Figure 3F**). These results suggest the subsynaptic heterogeneity of RIM1/2 or GluA1 is not an intrinsic property of the protein clusters, and there may be other active processes underlying the formation and evolvement of subsynaptic organizations during synaptic maturation.

Development of Trans-Synaptic Release-Receptor Nano-Alignments

We previously showed that the presynaptic RIM1/2 nanoscale organization represents the preferential sites for transmitter release, and its alignment with postsynaptic AMPAR densities could efficiently modulate the synaptic strength (Tang et al., 2016). Therefore, it would be crucial to examine the nanoscale alignment between nanoclusters across the cleft during development.

Representative examples showed that synapses at different developmental stages all have a certain degree of alignment between the nanoclusters of RIM1/2 and GluA1 (**Figures 4A–D**). To further quantify this, we performed the enrichment analysis by calculating the averaged local density of GluA1 along with

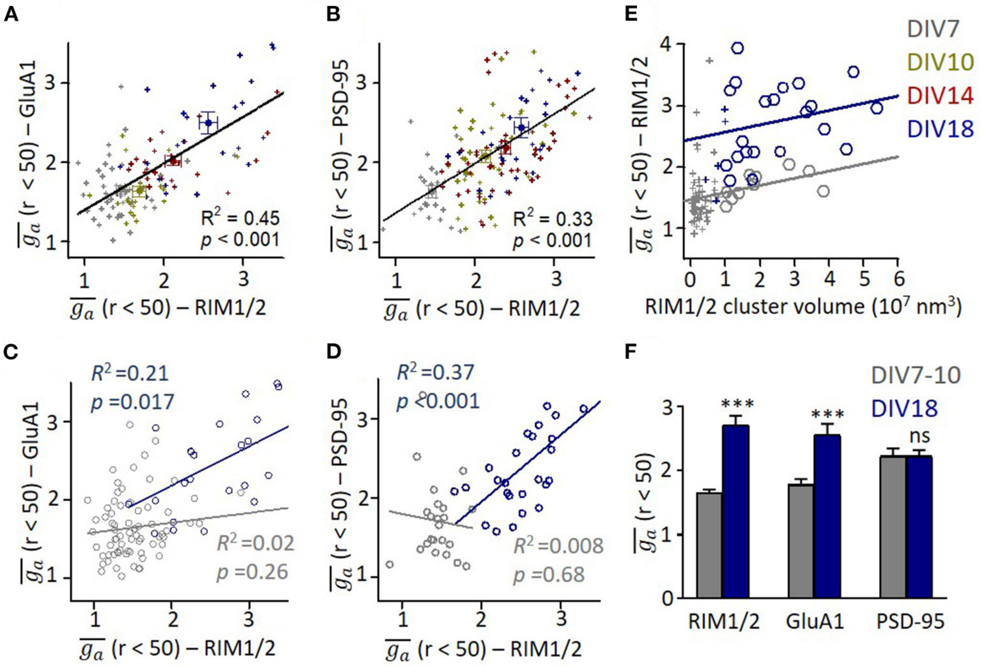

FIGURE 3 | Correlation between presynaptic and postsynaptic protein heterogeneity in mature synapses. **(A,B)** Scatter plots for heterogeneity of GluA1 **(A)** and PSD-95 **(B)** against that of RIM1/2. All data points across all developmental stages could be fitted with linear functions as shown with lines. **(C,D)** Linear regressions of the relationships between heterogeneity of GluA1/PSD-95 and RIM1/2 at DIV7 (gray) and DIV18 (dark blue). **(E)** Relationship between heterogeneity and cluster volume of RIM1/2 at DIV7 (gray) and DIV18 (dark blue). Data points with cluster volume $>1 \times 10^7$ nm^3 were fitted with linear functions. It is noted that g_a of immature synapses was significantly lower than that of matured synapses. **(F)** Averaged g_a of synapses with cluster volume of 1–4 $\times 10^7$ nm^3 for immature (DIV7-10) and mature synapses (DIV18). Also refer to **Supplementary Figure 3** for more details. ***$p < 0.001$, t-test. All experiments were repeated ≥3 times.

different distances from the projected center of defined RIM1/2 nanoclusters (**Figure 4E**). All groups showed a trend of elevated GluA1 density at distances close to the RIM1/2 nanocluster centers, but more mature synapses exhibited a more significant enrichment. To simplify the comparison, we averaged the normalized GluA1 density within the distance of 50 nm to define an enrichment index (*EI*) and compared the measured indices with that of simulated synapses with the positioning of GluA1 nanoclusters randomized within the GluA1 cluster. Synapses in cultures of DIV14 and 18 showed an *EI* significantly above the randomized simulations (**Figure 4F**; $p < 0.05$, one-way ANOVA using the Tukey's multiple comparison test, for details, refer to **Supplementary Table 1**), while the *EI*s of immature synapses at DIV7 and 10 were not significantly different from the chance level.

By performing multiple simulations on the same synapse, we could get a threshold of *EI* (usually around 1.25–1.3) above which the tested RIM1/2 nanocluster was defined as a nanocluster with significant GluA1 enrichment, or simply "enriched nanocluster," with a 95% CI (Tang et al., 2016). There were 33.3% of RIM1/2 nanoclusters above this threshold for synapses at DIV7, and the percentage increased gradually with development to 51.9% at DIV18 (**Figure 4G**). Similar results were found for the alignment between RIM1/2 and PSD-95 (**Figures 4H,I**), but one minor difference is that there were slightly more enriched nanoclusters at DIV10 compared with the GluA1-RIM1/2 pair (**Figure 4J**; 47.7% RIM1/2 and 48.1% PSD-95, vs. 10.0% RIM1/2, and 33.3% GluA1), suggesting the alignment between RIM1/2 and PSD-95 may form prior to that between RIM1/2 and GluA1.

Activity-Dependency of Synaptic Nano-Architectures

Previous studies found that the functional correlation between presynaptic and postsynaptic compartments requires neuronal activity to develop (Kay et al., 2011). We then sought to determine whether the correlation between nano-organizations was also dependent on synaptic activity. The hippocampal cultures were incubated in TTX (0.5 μM) or NBQX (10 μM) to block action potentials or AMPA receptors, respectively, at DIV10-18 during which the transsynaptic alignment and organizations show most dramatic changes (**Figures 2**, **4**). This blockade lasted much longer than the treatment commonly used for homeostatic plasticity studies, and therefore, more processes may have taken place. In fact, though the frequency of miniature EPSCs showed a similar trend of increase after TTX incubation, the effects of both treatments were much smaller and insignificant than that of the previous 1–2 days' treatment (Han and Stevens, 2009) (**Supplementary Figure 4**). We found that AMPAR blockade significantly increased the synaptic cluster volume of both RIM1/2 and PSD-95 at DIV18 (**Figures 5A,B,E,F**) as well as the nanocluster number of PSD-95 (**Figures 5C,G**). Synapses in cultures treated with TTX showed a similar trend but the

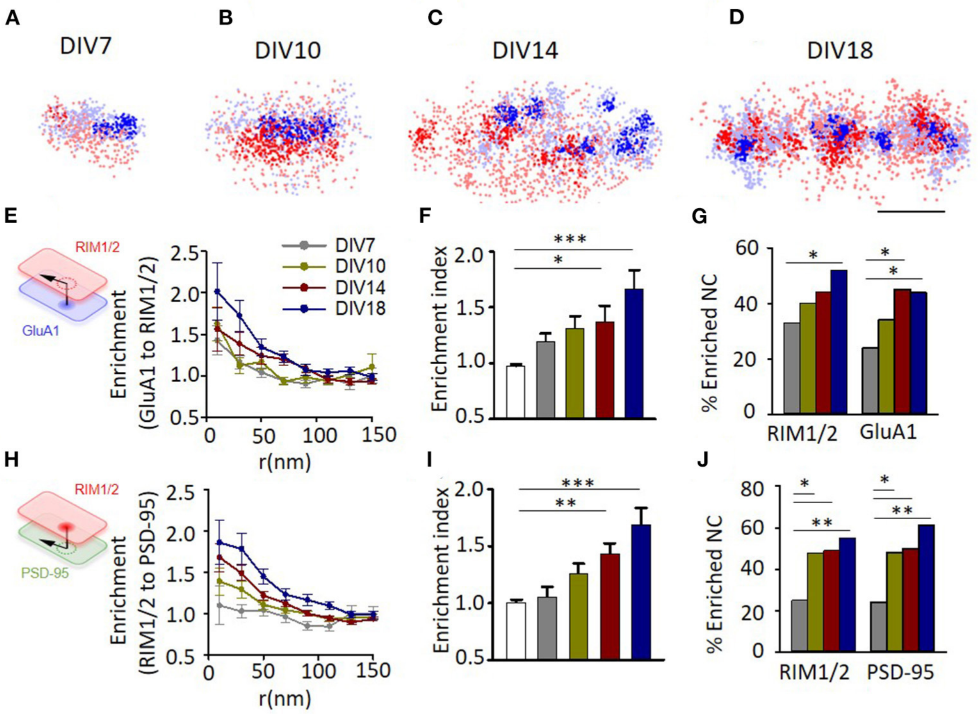

FIGURE 4 | Evolvement of trans-synaptic nano-alignment during synaptic maturation. **(A–D)** Representative examples of synapses with RIM1/2 (red) and GluA1 (blue) co-labeled and imaged with STORM. Thick color denotes detected nanoclusters. Scale bar, 200 nm. **(E)** Normalized local density of GluA1 along with distances from RIM1/2 nanoclusters for synapses at different developmental stages. **(F)**, Averaged enrichment of GluA1 within 50 nm from peaks of RIM1/2 nanoclusters ($n = 85$, 60, 30, 54, and 54 nanoclusters). The open bar represents the enrichment indices of synapses with the position of nanoclusters randomized within synaptic clusters. **(G)** Fraction of nanoclusters that were enriched with protein across the cleft. **(H–J)** Enrichment between RIM1/2 and PSD-95 for synapses at different developmental stages. $^*p < 0.05$, $^{**}p < 0.01$, $^{***}p < 0.001$, one-way ANOVA with Tukey's multiple comparisons test in **(F,I)**, *z*-test in **(G,J)**. Also refer to **Supplementary Table 1** for more statistical details. All experiments were repeated ≥3 times.

differences did not reach a significant level. These changes and trends were largely consistent with previous observations under similar treatment (MacGillavry et al., 2013; Glebov et al., 2017; Venkatesan et al., 2020).

However, the normalized density within nanoclusters showed no change with the treatment (**Supplementary Table 1**). Consistently, the autocorrelation profiles of either protein were largely overlapped (**Figures 5D,H**), except that PSD-95 showed slightly larger values of heterogeneity. To test whether this results from the larger cluster volume (**Figures 3E, 5I**), we similarly plotted $\overline{g_a}$ of PSD-95 against the cluster volume for each synapse and found that $\overline{g_a}$ of PSD-95 was, in fact, positively correlated with the cluster volume (**Figure 5J**). To rule out the effect of cluster volume, we selected only the synaptic clusters with a volume of (1–3) $\times$ 10^7 nm^3 and found that $\overline{g_a}$ of either PSD-95 or RIM1/2 showed no significant difference between control and AMPAR blockade (**Figure 5K**), suggesting that the general heterogeneity of synaptic proteins was largely unchanged by activity blockade.

We further examined whether the formation of trans-synaptic nano-alignment depends on synaptic activity. We found that neither TTX nor NBQX treatment had a significant effect on the averaged enrichment between RIM1/2 and PSD-95 (**Figures 6A–C**). The lack of changes in general heterogeneity of protein organizations and the averaged nanoscale trans-synaptic enrichments is well-consistent with the electrophysiological result that there was no significant change in either the frequency or amplitude of mEPSCs (**Supplementary Figure 4**). However, the percentage of nanoclusters (NCs) that were enriched with their counter partners showed a reducing trend on activity blockade, with the difference significant for the proportion of enriched PSD-95 nanoclusters between NBQX and control groups (**Figure 6D**; $p = 0.025$, *z*-test). Therefore, in spite of the similar average overall enrichment between RIM1/2 and PSD-95, there might be some nanoscale reorganizations that concentrate the proteins within a subset of nanocolumns, especially for the RIM1/2-to-PSD-95 enrichment.

DISCUSSION

In this study, we used super-resolution microscopy to examine the evolvement of subsynaptic protein architectures during the genesis and maturation of synapses in hippocampal neuronal cultures. We revealed a dramatic reorganization in subsynaptic protein distribution of glutamatergic synapses accompanying

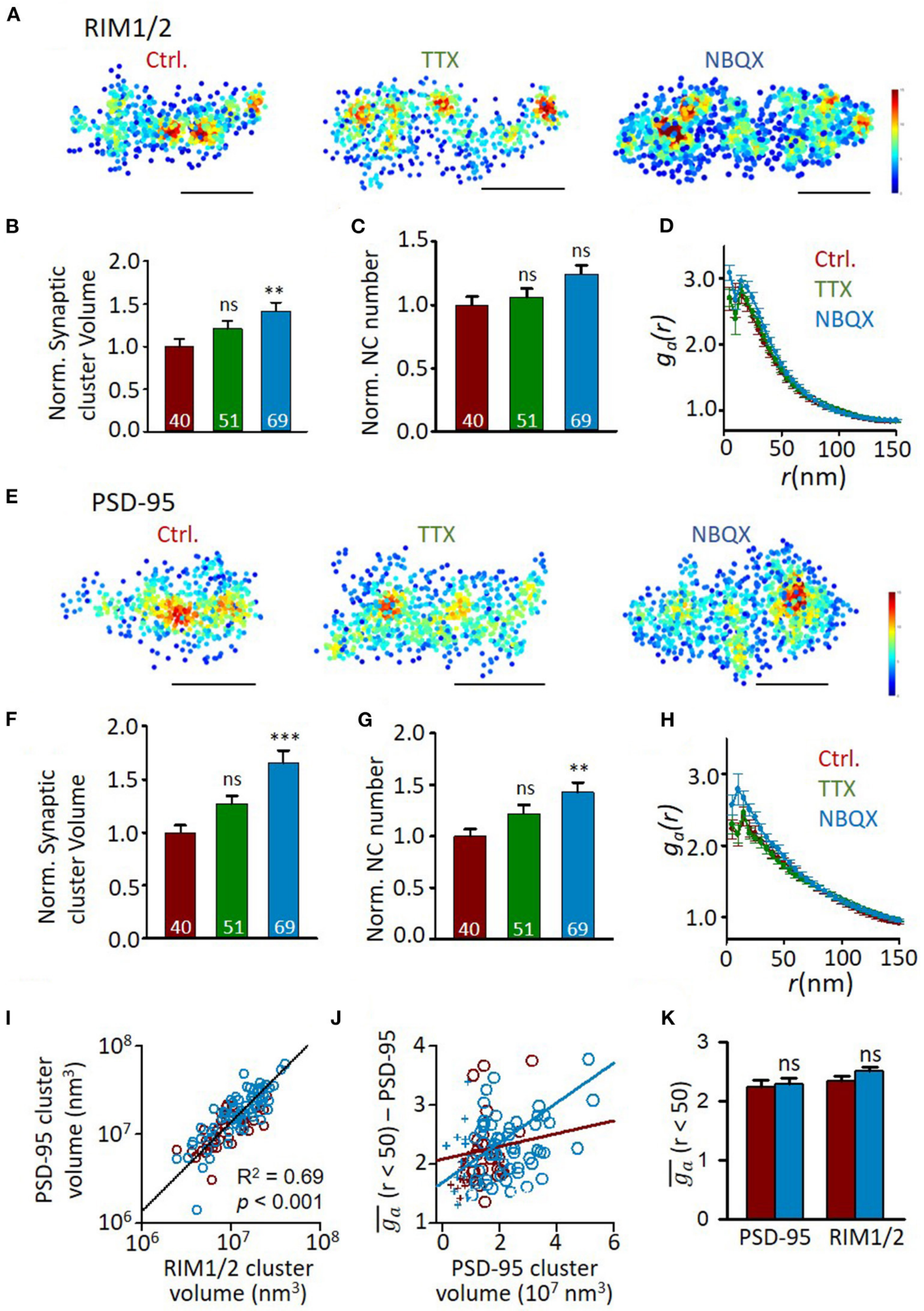

FIGURE 5 | Effects of activity blockade on development of synaptic nano-organizations. **(A)** Representative density maps of RIM1/2 by STORM in cultures with different activity levels. Scale bar, 200 nm. **(B–D)** Comparison of synaptic cluster volume **(B)**, nanocluster number **(C)**, and auto-correlation profile **(D)** between RIM1/2 distributions from normal DIV18 neurons and cultures with activity blocked with TTX or NBQX. Numbers in bars denote the synapse numbers. **(E)** Example density maps of PSD-95 in cultures with different activity levels. Scale bar, 200 nm. **(F–H)** Properties of PSD-95 clusters and nanoclusters in synapses from normal DIV18 neurons and cultures with activity blocked with TTX and NBQX. **(I)** Correlation between the volumes of RIM1/2 and PSD-95 clusters within the same synapses. Linear regressions were conducted on synapses from all three groups. **(J)** Relationship between heterogeneity and cluster volume of PSD-95 in control (dark red) and NBQX group (blue). Data points with cluster volume $>1 \times 10^7$ nm^3 were fitted with linear functions. **(K)** Averaged g_a of synapses with cluster volume of $1–3 \times 10^7$ nm^3 for control (dark red) and NBQX treated cultures (blue). $^{**}p < 0.01$, $^{***}p < 0.001$, one-way ANOVA with Tukey's multiple comparisons. Also refer to **Supplementary Table 1** for more statistical details. All experiments were repeated ≥3 times.

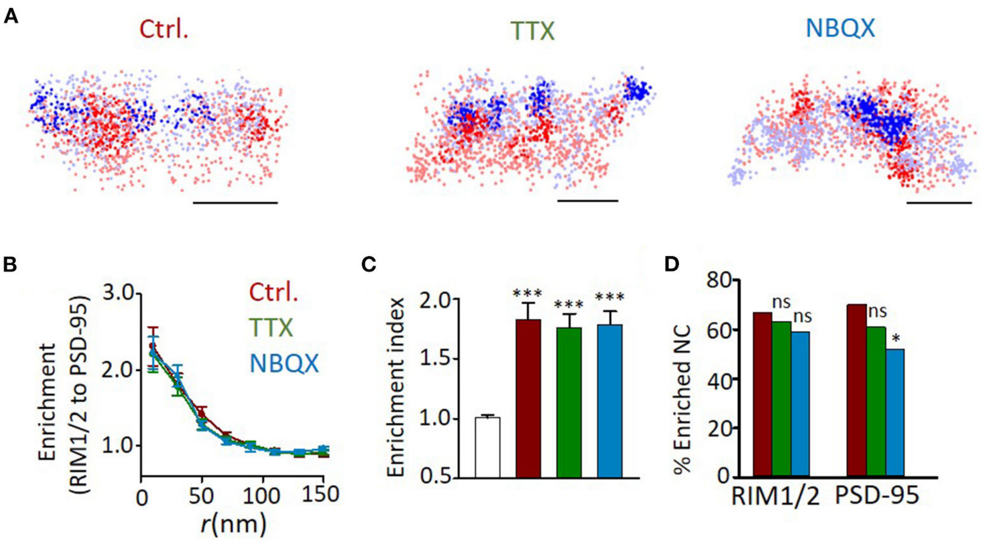

FIGURE 6 | Effects of activity blockade on development of trans-synaptic nano-alignment. **(A)** Example distribution maps of both RIM1/2 (blue) and PSD-95 (red) with nanoclusters highlighted with thick color. Scale bars, 200 nm. **(B)** Normalized local density of RIM1/2 along with distances from PSD-95 nanoclusters for synapses from DIV18 cultures with different activities. **(C)** Averaged enrichment of RIM1/2 within 50 nm from peaks of PSD-95 nanoclusters ($n = 60$, 40, 51, and 49 nanoclusters). The open bar represents the enrichment indices of synapses with the position of nanoclusters randomized within synaptic clusters. **(D)** Fraction of nanoclusters that were enriched with protein across the cleft. $^{*}p < 0.05$, $^{***}p < 0.001$, one-way ANOVA with Tukey's multiple comparisons in **(C)**, *z*-test in **(D)**. Also refer to **Supplementary Table 1** for more statistical details. All experiments were repeated ≥3 times.

a 4–5-fold increase in synapse size from DIV7 to DIV18. These changes are largely synchronous and proportional in presynaptic and postsynaptic compartments. More importantly, synaptic activities could shape the development of these nano-organizations and transsynaptic alignments in complicated ways. These findings have revealed a coordinated remodeling at the subsynaptic scale in presynaptic and postsynaptic compartments during development and suggest that both intrinsic and active mechanisms take part in controlling the formation of those nano-organizations to tune the synaptic functions.

It is well-documented that presynaptic and postsynaptic compartments of mature synapses correlate structurally in bouton and spine sizes, biochemically in protein amounts, and functionally in release probability and quantal amplitude (Harris and Stevens, 1989; Schikorski and Stevens, 1997; Nusser et al., 1998; Takumi et al., 1999; Thiagarajan et al., 2005; Regalado et al., 2006; Tokuoka and Goda, 2008; Kay et al., 2011; Holderith et al., 2012; Fisher-Lavie and Ziv, 2013; Rollenhagen et al., 2018; Holler et al., 2021). Our study has performed a systematic examination of the presynaptic and postsynaptic protein organizations at different developmental stages with super-resolution imaging methods. Our approach enables us to quantify not only the general synaptic properties, including the amount and cluster volume of key synaptic proteins but also the properties of subsynaptic nano-organizations. Consistent with an earlier pioneer study (Kay et al., 2011), we found a strong correlation between structural properties at the synapse scale, and this correlation is pronounced at every developmental stage, even after an activity blockade. These findings suggest that the coordinated development of general synaptic architecture does not require neuronal activity and is governed more likely by intrinsic mechanisms.

However, for the subsynaptic organizations which are thought to strongly modulate the action potential-dependent transmission, only the mature synapses show a significant correlation between the subsynaptic heterogeneity in presynaptic and postsynaptic compartments. Although details are still lacking, these nanocluster organizations are generally thought to result from multivalent interactions between proteins which lead to self-assembled condensates *via* phase separations in both presynaptic and postsynaptic compartments (Banani et al., 2017; Zeng et al., 2018, 2019; Wu et al., 2019), and the alignment between these condensates depends on protein interactions mediated by trans-synaptic adhesion molecules including neuroligins and LRRTM2 (Haas et al., 2018; Ramsey et al., 2021). Larger synapses generally have more presynaptic and postsynaptic proteins (Nusser et al., 1998; Holderith et al., 2012; Fisher-Lavie and Ziv, 2013); therefore, more multivalent interactions, stronger self-assembly, and higher internal heterogeneity in synaptic clusters could be expected. This is consistent with our finding that larger synapses show a higher degree of heterogeneity, regardless of the developmental stages. However, when we excluded the effect of the cluster size or protein amount by comparing only larger synapses with similar volumes, mature cultures showed significantly more subsynaptic heterogeneity. These data suggest that the evolvement, as well as the presynaptic and postsynaptic correlation of subsynaptic nano-organizations, requires active modulating mechanisms other than self-organization.

Accumulating studies suggest that spontaneous and action-potential-evoked transmitter release employs segregated vesicle pools and activates different groups of postsynaptic receptors (Reese and Kavalali, 2016; Crawford et al., 2017; Chanaday and Kavalali, 2018). Consistently, we found previously that the evoked release sites are more confined in the vicinity of RIM1/2 nanoclusters, while the spontaneous release sites distribute more broadly within the bouton (Tang et al., 2016), similar to the asynchronous release (Mendonça et al., 2021). Therefore, the simulations predict that the transsynaptic alignment directly modulates the strength of evoked transmission but not the amplitudes of spontaneous miniature currents (MacGillavry et al., 2013). This is well-consistent with the electrophysiological recordings in neurons with the alignment disrupted in response to LRRTM2 cleavage (Ramsey et al., 2021). Both miniature and evoked currents were reduced when the alignment was reduced by the expression of a truncated NL1 (Haas et al., 2018), but this may result from changes in presynaptic release probability by NL1 disturbance (Peixoto et al., 2012). Together, our finding that the development of transsynaptic alignment continued through DIV18 indicates an ongoing adjustment of action-potential (AP)-evoked transmission at this stage after the spontaneous transmission has saturated by DIV14 (Cottrell et al., 2000; Chanda et al., 2017). However, due to our limited understanding of the specific functional relevance of these subsynaptic organizations, so far it is hard to make valid predictions on the impacts on the synaptic transmission based on our structural quantifications.

Synaptic activity plays an important role in regulating synaptic morphology, transmission strength, neuronal membrane properties, and neural circuit refinement (Maletic-Savatic et al., 1999; Nick and Ribera, 2000; Groc et al., 2002; Walmsley et al., 2006; West and Greenberg, 2011; Chaudhury et al., 2016). We examined the effect of synaptic activity on subsynaptic protein nano-organizations and found a set of complicated impacts of activity blockade on the synaptic nano-architectures. Despite that reduced activity resulted in larger synaptic volumes and increased nanocluster numbers, which is largely consistent with previous studies with similar treatments (MacGillavry et al., 2013; Glebov et al., 2017), neither the general heterogeneity of protein organizations nor the averaged nanoscale trans-synaptic enrichments were significantly altered by activity blockade. These results are consistent with the electrophysiological result that there was no significant change in either the frequency or amplitude of mEPSCs. These data argue against the hypothesis that activity-dependent mechanism is directly involved in establishing nanocolumns. Instead, these results favor a self-organization model for nanocolumn organizations, and the neuronal activity may exert its influence through changing the amount of protein components. However, besides RIM1/2 and PSD-95, in this study, we examined, there are many other proteins involved in the construction of nanocolumns and the modulation of synaptic transmission in both presynaptic and postsynaptic compartments. It is very possible that other MAGUK members and scaffolding molecules are modulated by activities. In fact, the reduction in the fraction of enriched PSD-95 nanoclusters on AMPAR blockade suggests a mechanism that actively strengthens some nanocolumns while dismantling others. A similar process was observed previously after the induction of NMDA receptor-dependent long-term depression (Tang et al., 2016). This may result from changes in synaptic activity-dependent gene transcriptions (Yap and Greenberg, 2018) and activity-dependent specific rearrangements in a targeted synaptic protein interaction network (Lautz et al., 2018). The detailed mechanism needs further investigation.

Activity deprivation has been found to significantly increase the puncta size and the amount of synaptic proteins (Noritake et al., 2009; Sun and Turrigiano, 2011; Letellier et al., 2014; Venkatesan et al., 2020) through a homeostatic plasticity mechanism (Turrigiano et al., 1998; Turrigiano and Nelson, 2004). However, the changes in RIM1/2 and PSD-95 in our results are not as strong. This may result from the long duration of the activity blockade we used (8 days). The major aim of our activity blockade experiments is to test its impact on the trans-synaptic alignment. Since the largest change in enrichment index is between synapses on DIV10 and on DIV18 (synapses on DIV7 are not fully formed), we selected this period to test the effects of activity blockade. This is quite different from the 48 h treatment protocol that most people use in studies on homeostatic plasticity. More complex processes may have taken place during this prolonged treatment. There is less overlap in newly synthesized proteins for cultured hippocampal neurons within 2 and 24 h after TTX treatment (Schanzenbächer et al., 2018), and the neurons at different developmental stages undergo distinct synaptic functional reorganizations (Han and Stevens, 2009), suggesting a strong temporal dependency of the impact of activity deprivation on synapses. As another example, for homeostatic modulation of synaptic transmission by transcranial direct current stimulation in the motor cortex of healthy humans, two sets of 5-min stimulations could induce opposite plasticity depending on the time intervals (Fricke et al., 2010). Consistent with this, after the long activity blockade, neither frequency nor amplitudes of mEPSCs showed significant changes, which is quite different from the dramatic increase in these parameters in response to a 1 or 2 days incubation (Han and Stevens, 2009). More future studies are required to figure out the duration-dependent modulation of synapses in response to activity blockade.

During synaptogenesis in cultured hippocampal neurons, the presynaptic proteins accumulate before postsynaptic receptors and PSD-95 (Li and Sheng, 2003). This indicates that presynaptic differentiation precedes postsynaptic development. However, in our results, the evolvement of either the general cluster properties or features of subsynaptic nano-organizations seems synchronous between presynaptic and postsynaptic compartments. Two technical limitations may attenuate our ability of detecting the potential precedence in development. First, the temporal resolution in our design is not optimized for this purpose. This is exacerbated by the fact that the development of dissociated neurons varies with culture density and conditions. Second, we pick up synapses based on colocalization of presynaptic and postsynaptic clusters, which would exclude those early structures with one side preceding the other. However, when comparing the dependency of protein heterogeneity on cluster size, we found that both RIM1/2 and GluA1 show a significant difference between immature and mature synapses while the heterogeneity of PSD-95 is decided solely by cluster volume and independent of maturation. This result indicated a unique role of PSD-95 in organizing the subsynaptic architectures. It will be important for future studies to validate this constructing sequence of nanocolumns *in vivo* and examine the detailed molecular mechanisms.

DATA AVAILABILITY STATEMENT

The raw data supporting the conclusions of this article will be made available by the authors, without undue reservation.

ETHICS STATEMENT

The animal study was reviewed and approved by Institutional Animal Care and Use Committees at the University of Science and Technology of China (USTC) and the Chinese Academy of Sciences (CAS).

AUTHOR CONTRIBUTIONS

S-YS, X-WL, and RC conducted the experiments. S-YS, YZ, and A-HT performed the analysis and prepared the figure. NS and A-HT designed the project and wrote the manuscript. All authors contributed to the article and approved the submitted version.

FUNDING

The authors acknowledge National Key Research and Development Program of China 2021ZD0202503, National Natural Science Foundation of China (31872759, 31871032), the USTC Cultivation Fund for Innovation Team, Open Project from the State Key Laboratory of Genetic Resources and Evolution GREKF19-09 to A-HT, Strategic Priority Research Program of the Chinese Academy of Sciences XDPB17, Yunnan Applied Basic Research Projects 2019FA008 and 2019FJ003, and CAS Light of West China Program xbzg-zdsys-201913 to NS.

ACKNOWLEDGMENTS

The authors thank Dr. Jia-Hui Chen and Ms. Na Xu for their assistance on cell culture.

SUPPLEMENTARY MATERIAL

The Supplementary Material for this article can be found online at: https://www.frontiersin.org/articles/10.3389/fnsyn.2022.748184/full#supplementary-material

REFERENCES

Banani, S. F., Lee, H. O., Hyman, A. A., and Rosen, M. K. (2017). Biomolecular condensates: organizers of cellular biochemistry. *Nat. Rev. Mol. Cell. Biol.* 18, 285–298. doi: 10.1038/nrm.2017.7

Chanaday, N. L., and Kavalali, E. T. (2018). Presynaptic origins of distinct modes of neurotransmitter release. *Curr. Opin. Neurobiol.* 51, 119–126. doi: 10.1016/j.conb.2018.03.005

Chanda, S., Hale, W. D., Zhang, B., Wernig, M., and Südhof, T. C. (2017). Unique versus redundant functions of neuroligin genes in shaping excitatory and inhibitory synapse properties. *J. Neurosci.* 37, 6816–6836. doi: 10.1523/JNEUROSCI.0125-17.2017

Chaudhury, S., Sharma, V., Kumar, V., Nag, T. C., and Wadhwa, S. (2016). Activity-dependent synaptic plasticity modulates the critical phase of brain development. *Brain. Dev.* 38, 355–363. doi: 10.1016/j.braindev.2015.10.008

Chen, H., Tang, A.-H., and Blanpied, T. A. (2018). Subsynaptic spatial organization as a regulator of synaptic strength and plasticity. *Curr. Opin. Neurobiol.* 51, 147–153. doi: 10.1016/j.conb.2018.05.004

Chen, J.-H., Blanpied, T. A., and Tang, A.-H. (2020). Quantification of trans-synaptic protein alignment: a data analysis case for single-molecule localization microscopy. *Methods* 174, 72–80. doi: 10.1016/j.ymeth.2019.07.016

Cottrell, J. R., Dubé, G. R., Egles, C., and Liu, G. (2000). Distribution, density, and clustering of functional glutamate receptors before and after synaptogenesis in hippocampal neurons. *J. Neurophysiol.* 84, 1573–1587. doi: 10.1152/jn.2000.84.3.1573

Crawford, D. C., Ramirez, D. M. O., Trauterman, B., Monteggia, L. M., and Kavalali, E. T. (2017). Selective molecular impairment of spontaneous neurotransmission modulates synaptic efficacy. *Nat. Commun.* 8, 14436. doi: 10.1038/ncomms14436

Fisher-Lavie, A., and Ziv, N. E. (2013). Matching dynamics of presynaptic and postsynaptic scaffolds. *J. Neurosci.* 33, 13094–13100. doi: 10.1523/JNEUROSCI.2144-13.2013

Fricke, K., Seeber, A. A., Thirugnanasambandam, N., Paulus, W., Nitsche, M. A., and Rothwell, J. C. (2010). Time course of the induction of homeostatic plasticity generated by repeated transcranial direct current stimulation of the human motor cortex. *J. Neurophysiol.* 105, 1141–1149. doi: 10.1152/jn.00608.2009

Fukata, Y., Dimitrov, A., Boncompain, G., Vielemeyer, O., Perez, F., and Fukata, M. (2013). Local palmitoylation cycles define activity-regulated postsynaptic subdomains. *J. Cell. Biol.* 202, 145–161. doi: 10.1083/jcb.201302071

Glebov, O. O., Jackson, R. E., Winterflood, C. M., Owen, D. M., Barker, E. A., Doherty, P., et al. (2017). Nanoscale structural plasticity of the active zone matrix modulates presynaptic function. *Cell. Rep.* 18, 2715–2728. doi: 10.1016/j.celrep.2017.02.064

Groc, L., and Choquet, D. (2020). Linking glutamate receptor movements and synapse function. *Science* 368:eaay4631. doi: 10.1126/science.aay4631

Groc, L., Gustafsson, B., and Hanse, E. (2002). Spontaneous unitary synaptic activity in CA1 pyramidal neurons during early postnatal development: constant contribution of AMPA and NMDA receptors. *J. Neurosci.* 22, 5552–5562. doi: 10.1523/JNEUROSCI.22-13-05552.2002

Haas, K. T., Compans, B., Letellier, M., Bartol, T. M., Grillo-Bosch, D., Sejnowski, T. J., et al. (2018). Pre-post synaptic alignment through neuroligin-1 tunes synaptic transmission efficiency. *eLife* 7:e31755. doi: 10.7554/eLife.31755

Han, E. B., and Stevens, C. F. (2009). Development regulates a switch between post- and presynaptic strengthening in response to activity deprivation. *PNAS* 106, 10817–10822. doi: 10.1073/pnas.0903603106

Harris, K. M., and Stevens, J. K. (1989). Dendritic spines of CA 1 pyramidal cells in the rat hippocampus: serial electron microscopy with reference to their biophysical characteristics. *J. Neurosci.* 9, 2982–2997. doi: 10.1523/JNEUROSCI.09-08-02982.1989

Holderith, N., Lorincz, A., Katona, G., Rózsa, B., Kulik, A., Watanabe, M., et al. (2012). Release probability of hippocampal glutamatergic terminals scales with the size of the active zone. *Nat. Neurosci.* 15, 988–997. doi: 10.1038/nn.3137

Holler, S., Köstinger, G., Martin, K. A. C., Schuhknecht, G. F. P., and Stratford, K. J. (2021). Structure and function of a neocortical synapse. *Nature* 591, 111–116. doi: 10.1038/s41586-020-03134-2

Hruska, M., Henderson, N., Marchand, S. J. L., Jafri, H., and Dalva, M. B. (2018). Synaptic nanomodules underlie the organization and plasticity of spine synapses. *Nat. Neurosci.* 21, 671–682. doi: 10.1038/s41593-018-0138-9

Kay, L., Humphreys, L., Eickholt, B. J., and Burrone, J. (2011). Neuronal activity drives matching of pre- and postsynaptic function during synapse maturation. *Nat. Neurosci.* 14, 688–690. doi: 10.1038/nn.2826

Kellermayer, B., Ferreira, J. S., Dupuis, J., Levet, F., Grillo-Bosch, D., Bard, L., et al. (2018). Differential nanoscale topography and functional role of GluN2-NMDA receptor subtypes at glutamatergic synapses. *Neuron* 100, 106–119. doi: 10.1016/j.neuron.2018.09.012

Lautz, J. D., Brown, E. A., VanSchoiack, A. A. W., and Smith, S. E. P. (2018). Synaptic activity induces input-specific rearrangements in a targeted synaptic protein interaction network. *J. Neurochem.* 146, 540–559. doi: 10.1111/jnc.14466

Letellier, M., Elramah, S., Mondin, M., Soula, A., Penn, A., Choquet, D., et al. (2014). miR-92a regulates expression of synaptic GluA1-containing AMPA receptors during homeostatic scaling. *Nat. Neurosci.* 17, 1040–1042. doi: 10.1038/nn.3762

Li, Z., and Sheng, M. (2003). Some assembly required: the development of neuronal synapses. *Nat. Rev. Mol. Cell. Biol.* 4, 833–841. doi: 10.1038/nrm1242

MacGillavry, H. D., Song, Y., Raghavachari, S., and Blanpied, T. A. (2013). Nanoscale scaffolding domains within the postsynaptic density concentrate synaptic AMPA receptors. *Neuron* 78, 615–622. doi: 10.1016/j.neuron.2013.03.009

Maletic-Savatic, M., Malinow, R., and Svoboda, K. (1999). Rapid dendritic morphogenesis in CA1 hippocampal dendrites induced by synaptic activity. *Science* 283, 1923–1927. doi: 10.1126/science.283.5409.1923

Matsuzaki, M., Ellis-Davies, G. C. R., Nemoto, T., Miyashita, Y., Iino, M., and Kasai, H. (2001). Dendritic spine geometry is critical for AMPA receptor expression in hippocampal CA1 pyramidal neurons. *Nat. Neurosci.* 4, 1086. doi: 10.1038/nn736

Mendonça, P. R. F., Tagliatti, E., Langley, H., Kotzadimitriou, D., Zamora-Chimal, C. G., Timofeeva, Y., et al. (2021). Asynchronous glutamate exocytosis is enhanced in low release probability synapses and is widely dispersed across the active zone. *bioRxiv* 2021.05.04.441792. doi: 10.1101/2021.05.04.441792

Nair, D., Hosy, E., Petersen, J. D., Constals, A., Giannone, G., Choquet, D., et al. (2013). Super-Resolution imaging reveals that AMPA receptors inside synapses are dynamically organized in nanodomains regulated by PSD95. *J. Neurosci.* 33, 13204–13224. doi: 10.1523/JNEUROSCI.2381-12.2013

Nick, T. A., and Ribera, A. B. (2000). Synaptic activity modulates presynaptic excitability. *Nat. Neurosci.* 3, 142–149. doi: 10.1038/72082

Noritake, J., Fukata, Y., Iwanaga, T., Hosomi, N., Tsutsumi, R., Matsuda, N., et al. (2009). Mobile DHHC palmitoylating enzyme mediates activity-sensitive synaptic targeting of PSD-95. *J. Cell. Biol.* 186, 147–160. doi: 10.1083/jcb.200903101

Nusser, Z., Lujan, R., Laube, G., Roberts, J. D. B., Molnar, E., and Somogyi, P. (1998). Cell type and pathway dependence of synaptic AMPA receptor number and variability in the hippocampus. *Neuron* 21, 545–559. doi: 10.1016/S0896-6273(00)80565-6

Peixoto, R. T., Kunz, P. A., Kwon, H., Mabb, A. M., Sabatini, B. L., Philpot, B. D., et al. (2012). Transsynaptic signaling by activity-dependent cleavage of neuroligin-1. *Neuron* 76, 396–409. doi: 10.1016/j.neuron.2012.07.006

Petzoldt, A. G., Götz, T. W. B., Driller, J. H., Lützkendorf, J., Reddy-Alla, S., Matkovic-Rachid, T., et al. (2020). RIM-binding protein couples synaptic vesicle recruitment to release sites. *J. Cell. Biol.* 219, e201902059. doi: 10.1083/jcb.201902059

Raghavachari, S., and Lisman, J. E. (2004). Properties of quantal transmission at CA1 synapses. *J. Neurophysiol.* 92, 2456–2467. doi: 10.1152/jn.00258.2004

Ramsey, A. M., Tang, A.-H., LeGates, T. A., Gou, X.-Z., Carbone, B. E., Thompson, S. M., et al. (2021). Subsynaptic positioning of AMPARs by LRRTM2 controls synaptic strength. *Sci. Adv.* 7, eabf3126. doi: 10.1126/sciadv.abf3126

Reese, A. L., and Kavalali, E. T. (2016). Single synapse evaluation of the postsynaptic NMDA receptors targeted by evoked and spontaneous neurotransmission. *eLife* 5, e21170. doi: 10.7554/eLife.21170.013

Regalado, M. P., Terry-Lorenzo, R. T., Waites, C. L., Garner, C. C., and Malenka, R. C. (2006). Transsynaptic signaling by postsynaptic synapse-associated protein 97. *J. Neurosci.* 26, 2343–2357. doi: 10.1523/JNEUROSCI.5247-05.2006

Rollenhagen, A., Ohana, O., Sätzler, K., Hilgetag, C. C., Kuhl, D., and Lübke, J. H. R. (2018). Structural properties of synaptic transmission and temporal dynamics at excitatory layer 5B synapses in the adult rat somatosensory cortex. *Front. Synaptic Neurosci.* 10, 24. doi: 10.3389/fnsyn.2018.00024

Sakamoto, H., Ariyoshi, T., Kimpara, N., Sugao, K., Taiko, I., Takikawa, K., et al. (2018). Synaptic weight set by Munc13-1 supramolecular assemblies. *Nat. Neurosci.* 21, 41–49. doi: 10.1038/s41593-017-0041-9

Schanzenbächer, C. T., Langer, J. D., and Schuman, E. M. (2018). Time- and polarity-dependent proteomic changes associated with homeostatic scaling at central synapses. *eLife* 7, e33322. doi: 10.7554/eLife.33322.026

Schikorski, T., and Stevens, C. F. (1997). Quantitative ultrastructural analysis of hippocampal excitatory synapses. *J. Neurosci.* 17, 5858–5867. doi: 10.1523/JNEUROSCI.17-15-05858.1997

Sinnen, B. L., Bowen, A. B., Forte, J. S., Hiester, B. G., Crosby, K. C., Gibson, E. S., et al. (2017). Optogenetic control of synaptic composition and function. *Neuron* 93, 646–660.e5. doi: 10.1016/j.neuron.2016.12.037

Sun, Q., and Turrigiano, G. G. (2011). PSD-95 and PSD-93 play critical but distinct roles in synaptic scaling up and down. *J. Neurosci.* 31, 6800–6808. doi: 10.1523/JNEUROSCI.5616-10.2011

Takumi, Y., Ramírez-León, V., Laake, P., Rinvik, E., and Ottersen, O. P. (1999). Different modes of expression of AMPA and NMDA receptors in hippocampal synapses. *Nat. Neurosci.* 2, 618–624. doi: 10.1038/10172

Tang, A.-H., Chen, H., Li, T. P., Metzbower, S. R., MacGillavry, H. D., and Blanpied, T. A. (2016). A trans-synaptic nanocolumn aligns neurotransmitter release to receptors. *Nature* 536, 210–214. doi: 10.1038/nature19058

Thiagarajan, T. C., Lindskog, M., and Tsien, R. W. (2005). Adaptation to synaptic inactivity in hippocampal neurons. *Neuron* 47, 725–737. doi: 10.1016/j.neuron.2005.06.037

Tokuoka, H., and Goda, Y. (2008). Activity-dependent coordination of presynaptic release probability and postsynaptic GluR2 abundance at single synapses. *PNAS* 105, 14656–14661. doi: 10.1073/pnas.0805705105

Turrigiano, G. G., Leslie, K. R., Desai, N. S., Rutherford, L. C., and Nelson, S. B. (1998). Activity-dependent scaling of quantal amplitude in neocortical neurons. *Nature* 391, 892–896. doi: 10.1038/36103

Turrigiano, G. G., and Nelson, S. B. (2004). Homeostatic plasticity in the developing nervous system. *Nat. Rev. Neurosci.* 5, 97–107. doi: 10.1038/nrn1327

Veatch, S. L., Machta, B. B., Shelby, S. A., Chiang, E. N., Holowka, D. A., and Baird, B. A. (2012). Correlation functions quantify super-resolution images and estimate apparent clustering due to over-counting. *PLoS ONE* 7, e31457. doi: 10.1371/journal.pone.0031457

Venkatesan, S., Subramaniam, S., Rajeev, P., Chopra, Y., Jose, M., and Nair, D. (2020). Differential scaling of synaptic molecules within functional zones of an excitatory synapse during homeostatic plasticity. *eNeuro* 7:ENEURO.0407-19.2020. doi: 10.1523/ENEURO.0407-19.2020

Walmsley, B., Alvarez, F. J., and Fyffe, R. E. W. (1998). Diversity of structure and function at mammalian central synapses. *Trends. Neurosci.* 21, 81–88. doi: 10.1016/S0166-2236(97)01170-3

Walmsley, B., Berntson, A., Leao, R. N., and Fyffe, R. E. W. (2006). Activity-dependent regulation of synaptic strength and neuronal excitability in central auditory pathways. *J. Physiol.* 572, 313–321. doi: 10.1113/jphysiol.2006.104851

West, A. E., and Greenberg, M. E. (2011). Neuronal activity–regulated gene transcription in synapse development and cognitive function. *Cold Spring Harb Perspect Biol* 3, a005744. doi: 10.1101/cshperspect.a005744

Wu, X., Cai, Q., Shen, Z., Chen, X., Zeng, M., Du, S., et al. (2019). RIM and RIM-BP form presynaptic active-zone-like condensates via phase separation. *Mol. Cell.* 73, 971–984.e5. doi: 10.1016/j.molcel.2018.12.007

Yap, E.-L., and Greenberg, M. E. (2018). Activity-regulated transcription: bridging the gap between neural activity and behavior. *Neuron* 100, 330–348. doi: 10.1016/j.neuron.2018.10.013

Zeng, M., Chen, X., Guan, D., Xu, J., Wu, H., Tong, P., et al. (2018). Reconstituted postsynaptic density as a molecular platform for understanding synapse formation and plasticity. *Cell* 174, 1172–1187.e16. doi: 10.1016/j.cell.2018.06.047

Zeng, M., Díaz-Alonso, J., Ye, F., Chen, X., Xu, J., Ji, Z., et al. (2019). Phase separation-mediated TARP/MAGUK complex condensation and AMPA receptor synaptic transmission. *Neuron* 104, 529–543.e6. doi: 10.1016/j.neuron.2019.08.001

Conflict of Interest: The authors declare that the research was conducted in the absence of any commercial or financial relationships that could be construed as a potential conflict of interest.

Advantages of publishing in Frontiers

OPEN ACCESS
Articles are free to read
for greatest visibility
and readership

FAST PUBLICATION
Around 90 days
from submission
to decision

HIGH QUALITY PEER-REVIEW
Rigorous, collaborative,
and constructive
peer-review

TRANSPARENT PEER-REVIEW
Editors and reviewers
acknowledged by name
on published articles

Frontiers
Avenue du Tribunal-Fédéral 34
1005 Lausanne | Switzerland

Visit us: www.frontiersin.org
Contact us: frontiersin.org/about/contact

REPRODUCIBILITY OF RESEARCH
Support open data
and methods to enhance
research reproducibility

DIGITAL PUBLISHING
Articles designed
for optimal readership
across devices

FOLLOW US
@frontiersin

IMPACT METRICS
Advanced article metrics
track visibility across
digital media

EXTENSIVE PROMOTION
Marketing
and promotion
of impactful research

LOOP RESEARCH NETWORK
Our network
increases your
article's readership